Remote Sensing for Wind Energy

Peña, Alfredo; Hasager, Charlotte Bay; Lange, Julia; Anger, Jan; Badger, Merete; Bingöl, Ferhat; Bischoff, Oliver; Cariou, Jean-Pierre ; Dunne, Fiona ; Emeis, Stefan

Total number of authors:
27

Publication date:
2013

Document Version
Publisher's PDF, also known as Version of record

Remote Sensing for Wind Energy

DTU Wind Energy E-Report

Alfredo Peña, Charlotte B. Hasager, Julia Lange, Jan Anger, Merete Badger, Ferhat Bingöl, Oliver Bischoff, Jean-Pierre Cariou, Fiona Dunne, Stefan Emeis, Michael Harris, Martin Hofsäss, Ioanna Karagali, Jason Laks, Søren Larsen, Jakob Mann, Torben Mikkelsen, Lucy Y. Pao, Mark Pitter, Andreas Rettenmeier, Ameya Sathe, Fabio Scanzani, David Schlipf, Eric Simley, Chris Slinger, Rozenn Wagner and Ines Würth

DTU Wind Energy-E-Report-0029(EN)
June 2013

DTU Wind Energy
Department of Wind Energy

DTU Wind Energy-E-Report-0029(EN)

Remote Sensing for Wind Energy

Alfredo Peña, Charlotte B. Hasager, Julia Lange, Jan Anger, Merete Badger, Ferhat Bingöl, Oliver Bischoff, Jean-Pierre Cariou, Fiona Dunne, Stefan Emeis, Michael Harris, Martin Hofsäss, Ioanna Karagali, Jason Laks, Søren Larsen, Jakob Mann, Torben Mikkelsen, Lucy Y. Pao, Mark Pitter, Andreas Rettenmeier, Ameya Sathe, Fabio Scanzani, David Schlipf, Eric Simley, Chris Slinger, Rozenn Wagner and Ines Würth

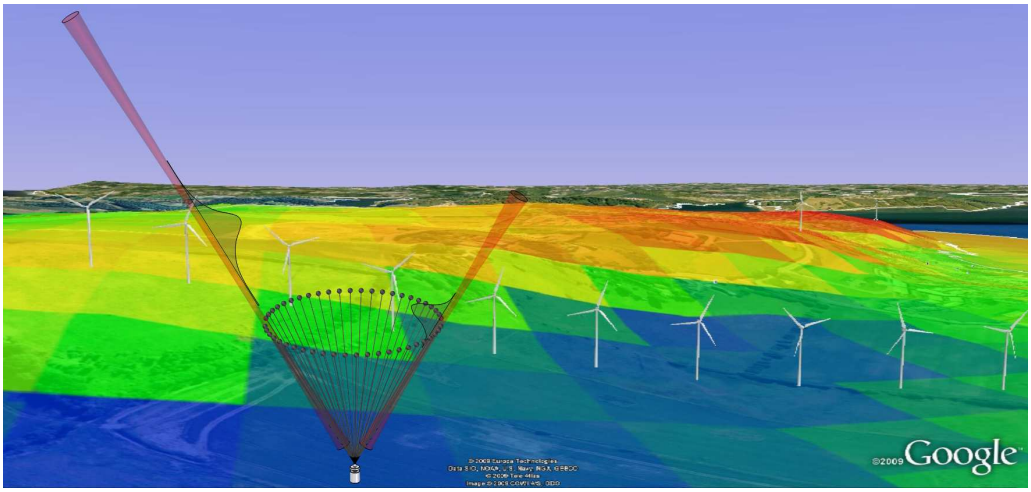

DTU Wind Energy
Department of Wind Energy

DTU Wind Energy, Risø Campus,
Technical University of Denmark, Roskilde, Denmark

June 2013

Author: Alfredo Peña, Charlotte B. Hasager, Julia Lange, Jan Anger, Merete Badger, Ferhat Bingöl, Oliver Bischoff, Jean-Pierre Cariou, Fiona Dunne, Stefan Emeis, Michael Harris, Martin Hofsäss, Ioanna Karagali, Jason Laks, Søren Larsen, Jakob Mann, Torben Mikkelsen, Lucy Y. Pao, Mark Pitter, Andreas Rettenmeier, Ameya Sathe, Fabio Scanzani, David Schlipf, Eric Simley, Chris Slinger, Rozenn Wagner and Ines Würth
Title: Remote Sensing for Wind Energy
Department: DTU Wind Energy

DTU Wind Energy-E-Report-0029(EN)
June 6, 2013

ISSN:
ISBN:
978-87-92896-41-4

Abstract (max. 2000 char)

The Remote Sensing in Wind Energy report provides a description of several topics and it is our hope that students and others interested will learn from it. The idea behind it began in year 2008 at DTU Wind Energy (formerly Risø) during the first PhD Summer School: Remote Sensing in Wind Energy. Thus it is closely linked to the PhD Summer Schools where state-of-the-art is presented during the lecture sessions. The advantage of the report is to supplement with in-depth, article style information. Thus we strive to provide link from the lectures, field demonstrations, and hands-on exercises to theory. The report will allow alumni to trace back details after the course and benefit from the collection of information. This is the third edition of the report (first externally available), after very successful and demanded first two, and we warmly acknowledge all the contributing authors for their work in the writing of the chapters, and we also acknowledge all our colleagues in the Meteorology and Test and Measurements Sections from DTU Wind Energy in the PhD Summer Schools. We hope to continue adding more topics in future editions and to update and improve as necessary, to provide a truly state-of-the-art 'guideline' available for people involved in Remote Sensing in Wind Energy.

Contract no:

Project no:

Sponsorship:

Cover: WAsP Google Earth visualization

Pages: 308
Tables: 24
Figures: 204
References: 507

Technical University of Denmark
Frederiksborgvej 399
4000 Roskilde
Denmark
Tel. +4546775024
bcar@dtu.dk
www.vindenergi.dk

Contents

Page

1 Remote sensing of wind **11**
1.1 Ground-based remote sensing for today's wind energy research . . . 11
1.1.1 Wind remote sensing (RS) methodologies . . . 11
1.2 Part I: Remote sensing of wind by sound (sodars) . . . 11
1.2.1 RS applications within Wind Energy . . . 13
1.2.2 Recent developments . . . 16
1.2.3 Summary of sodars . . . 17
1.3 Part II: RS of wind by light (lidars) . . . 17
1.3.1 Introduction to lidars . . . 17
1.3.2 Wind RS methodologies . . . 17
1.3.3 Wind lidars . . . 19
1.3.4 Wind profiling . . . 21
1.3.5 Lidar accuracy . . . 22
1.3.6 Wind lidar applications for wind energy . . . 22
1.3.7 Summary of lidar . . . 23
Notation . . . 23
References . . . 23

2 The atmospheric boundary layer **25**
2.1 Introduction . . . 25
2.2 ABL Flows . . . 25
2.3 The ideal ABL . . . 28
2.4 Surface Characteristics of real ABLs . . . 37
2.5 Homogeneous Land ABL . . . 39
2.6 Homogeneous Marine ABL . . . 39
2.7 Inhomogenous and instationary ABL . . . 42
2.8 Complex terrain . . . 46
2.9 Boundary Layer Climatology for Wind energy . . . 47
2.10 Summary . . . 48
Notation . . . 49
References . . . 50

3 Atmospheric turbulence **52**
3.1 Introduction . . . 52
3.2 Definitions . . . 53
3.3 Rapid distortion theory . . . 54
3.3.1 RDT and surface layer turbulence . . . 56
3.3.2 Eddy lifetimes . . . 56
3.3.3 The uniform shear model . . . 58
3.4 Fitting spectra to observations . . . 58
3.4.1 Uncertainties on spectra . . . 58
3.4.2 Spectral fitting and prediction of coherences . . . 59
3.5 Model spectra over the ocean and flat land . . . 61
3.5.1 Code and textbook spectra . . . 62
3.6 Comparison with the spectral tensor model . . . 65
3.7 Wind field simulation . . . 67
Notation . . . 69
References . . . 70

4 Introduction to continuous-wave Doppler lidar **72**
4.1 Introduction . . . 72
4.2 Basic principles of lidar operation and system description . . . 73
4.2.1 Brief survey of lidar types . . . 73
4.2.2 Principles underlying anemometry by coherent laser radar (CLR) . . . 73
4.2.3 Role of local oscillator and range selection by focus . . . 73
4.2.4 Doppler frequency analysis and signal processing . . . 74
4.2.5 Wind profiling in conical scan mode . . . 75
4.2.6 Pioneering a revolution: ZephIR lidar . . . 75
4.3 Lidar measurement process: Assumptions . . . 76
4.3.1 Behaviour of scattering particles . . . 77
4.3.2 Uniformity of flow and backscatter . . . 77
4.3.3 Beam positional accuracy . . . 77
4.3.4 Optical and electrical interference sources . . . 77
4.3.5 Time-of-flight considerations . . . 78
4.4 End-to-end measurement process for CW Doppler lidar . . . 78
4.4.1 Introduction . . . 78
4.4.2 Transmitter optics . . . 78
4.4.3 Light scattering by aerosols . . . 79
4.4.4 Receiver optics . . . 80
4.4.5 Light beating . . . 80
4.4.6 Photodetection . . . 81
4.4.7 Fourier analysis and lidar sensitivity . . . 81
4.4.8 Velocity estimation . . . 83
4.5 Ground based, vertical scan configuration wind field parameter determination 84
4.5.1 Least-squares fitting routine . . . 84
4.5.2 Parameter extraction . . . 85
4.5.3 Data averaging . . . 85
4.6 Uncertainty analysis . . . 85
4.6.1 Rain/snow/cloud, solid objects . . . 85
4.6.2 Cloud effects . . . 86
4.6.3 System positioning accuracy . . . 88
4.6.4 Probe volume effects and operation at greater heights . . . 89
4.6.5 Flow uniformity and complex terrain . . . 89
4.6.6 Dependence on backscatter level . . . 90
4.6.7 Beam obscuration and attenuation . . . 90
4.6.8 Wind direction . . . 90
4.7 Calibration, validation and traceability . . . 91
4.8 Turbine mounted continuous wave lidar . . . 92
4.8.1 Least-squares fitting routine for horizontal scanning (turbine mounted) operation . . . 93
4.8.2 Turbine mounted CW lidar for wind turbine power curve measurement 94
4.9 Summary, state of the art, and future developments . . . 96
Acknowledgements . . . 100
Notation . . . 100
References . . . 101

5 Pulsed lidars **104**
5.1 Introduction . . . 104
5.2 End-to-end description of pulsed lidar measurement process . . . 105
5.2.1 Architecture of pulsed lidars . . . 105
5.2.2 Differences between pulsed vs. continuous wave lidars . . . 107
5.2.3 Signal processing . . . 108

5.2.4 Coherent detection . . . 108
5.2.5 Lidar equation . . . 109
5.2.6 Spectral processing MLE . . . 110
5.2.7 Wind vector reconstruction . . . 111
5.2.8 Fiber lidars . . . 112
5.3 Lidar performances . . . 113
5.3.1 Noise . . . 113
5.3.2 Best Focus . . . 113
5.3.3 Distance range and resolution . . . 114
5.3.4 Velocity range and resolution . . . 115
5.3.5 Time-bandwidth tradeoffs . . . 116
5.3.6 Existing systems and actual performances . . . 117
5.3.7 Validation of measurements . . . 117
5.4 Conclusions and perspectives . . . 118
Notation . . . 120
References . . . 121

6 Remote sensing for the derivation of the mixing-layer height and detection of low-level jets 122
6.1 Introduction . . . 122
6.2 Mixing-layer height . . . 122
6.2.1 Acoustic detection methods (Sodar) . . . 123
6.2.2 Optical detection methods . . . 127
6.2.3 RASS . . . 130
6.2.4 Further techniques . . . 133
6.2.5 Comparison of acoustic and optical MLH detection algorithms . . . 134
6.3 Boundary-layer height . . . 134
6.4 Low-level jets . . . 135
6.4.1 Formation . . . 135
6.4.2 Frequency and properties of low-level jets . . . 136
6.5 Summary . . . 138
Notation . . . 139
References . . . 140

7 What can remote sensing contribute to power curve measurements? 143
7.1 Introduction . . . 143
7.2 Power performance and wind shear . . . 143
7.2.1 Shear and aerodynamics . . . 143
7.2.2 Consequences on the power production . . . 146
7.3 Wind speed profiles . . . 148
7.4 Equivalent wind speed . . . 150
7.4.1 Standard power curve for the two groups of wind profiles . . . 150
7.4.2 A better approximation of the kinetic energy flux . . . 151
7.4.3 Equivalent wind speed definition . . . 152
7.4.4 Choice of instrument . . . 152
7.5 Summary . . . 154
Notation . . . 154
References . . . 156

8 Nacelle-based lidar systems **157**
8.1 Summary . . . 157
8.2 Introduction . . . 157
8.3 The units of the lidar scanner . . . 157
8.3.1 Windcube . . . 157
8.3.2 Scanner . . . 158
8.4 Scan pattern . . . 159
8.5 CNR . . . 161
8.6 Wind field reconstruction . . . 162
8.7 "Visited" test sites of the SWE Scanner . . . 163
8.7.1 Onshore test site Bremerhaven, Germany . . . 163
8.7.2 Onshore test site Risø Campus - DTU Wind Energy, Denmark . . . 164
8.7.3 Onshore test site National Wind Technology Center (NWTC) - NREL, USA . . . 164
8.7.4 Offshore test site "alpha ventus" . . . 165
8.8 Measurement campaigns and some results . . . 166
8.8.1 Equivalent wind speed . . . 166
8.8.2 Rotor effective wind speed . . . 167
8.9 Outlook & Conclusions . . . 168
Notation . . . 169
References . . . 169

9 Lidars and wind turbine control – Part 1 **171**
9.1 Introduction . . . 171
9.2 Model Based Wind Field Reconstruction . . . 171
9.2.1 Ambiguity in Wind Field Reconstruction . . . 172
9.2.2 Lidar Model for Reconstruction . . . 172
9.2.3 Wind Model for Collective Pitch Control . . . 173
9.2.4 Wind Model for Cyclic Pitch Control . . . 173
9.2.5 Wind Model for Yaw Control . . . 173
9.2.6 Wind Model for Complex Terrain . . . 173
9.3 Modeling of the Wind Turbine . . . 174
9.3.1 Reduced Nonlinear Model . . . 174
9.3.2 Estimation of the Rotor Effective Wind Speed from Turbine Data . . . 175
9.3.3 Linear Model . . . 175
9.4 Correlation of a Lidar System and a Wind Turbine . . . 176
9.4.1 Simulated Lidar Measurements . . . 176
9.4.2 Reconstruction of Rotor Effective Wind Speed . . . 176
9.4.3 Correlation . . . 177
9.5 Lidar Assisted Collective Pitch Control . . . 178
9.5.1 Controller and Adaptive Filter Design . . . 178
9.5.2 Field Testing . . . 179
9.6 Lidar Assisted Speed Control . . . 180
9.6.1 Controller Design . . . 180
9.6.2 Simulation Using Real Data . . . 181
9.6.3 Discussion . . . 181
9.7 Nonlinear Model Predictive Control . . . 182
9.7.1 Controller Design . . . 182
9.7.2 Simulation Results . . . 183
9.8 Lidar Assisted Cyclic Pitch Control . . . 184
9.9 Lidar Assisted Yaw Control . . . 186
9.9.1 Simulation Using Generic Wind . . . 186
9.9.2 Simulation Using Real Data . . . 187

9.9.3 Discussion . . . 187
9.10 Conclusion and Outlook . . . 188
Acknowledgement . . . 188
Notation . . . 188
References . . . 189

10 Lidars and wind turbine control – Part 2 **192**
10.1 Introduction . . . 192
10.1.1 Lidar Measurement Strategies . . . 194
10.2 Wind Turbine Feedforward Control . . . 195
10.2.1 Feedforward Control Assuming Perfect Measurements . . . 195
10.2.2 Feedforward Control with Imperfect Measurements . . . 197
10.2.3 The Relationship between Variance and Damage Equivalent Loads . . . 198
10.3 Preview Time in Feedforward Control . . . 198
10.3.1 Ideal Feedforward Controller Preview Time . . . 198
10.3.2 Prefilter Preview Time . . . 199
10.3.3 Pitch Actuation Preview Time . . . 199
10.4 Blade Effective Wind Speed . . . 200
10.4.1 The Relative Importance of the u, v, and w Components . . . 201
10.5 Lidar Measurements . . . 201
10.5.1 Range Weighting . . . 203
10.5.2 Geometry Errors . . . 204
10.5.3 Wind Evolution . . . 205
10.5.4 Lidar Measurements of Blade Effective Wind Speed . . . 206
10.6 Lidar Measurement Example: Hub Height and Shear Components . . . 207
10.6.1 Optimizing the Measurement Scenario . . . 209
10.7 Control Example 1: Wind Turbine Preview Control In The Presence of Evolving Turbulence . . . 211
10.7.1 $\mathcal{H}_2$ Optimal Preview Control . . . 212
10.7.2 Controller Performance Simulations . . . 213
10.7.3 Simulation Results . . . 214
10.8 Control Example 2: $\mathcal{H}_2$ Optimal Control with Model of Measurement Coherence 215
10.9 Summary . . . 216
Notation . . . 217

11 Lidars and wind profiles **221**
11.1 Introduction . . . 221
11.2 Wind profile theory . . . 222
11.2.1 Surface layer . . . 222
11.2.2 Marine surface layer . . . 223
11.2.3 Boundary layer . . . 224
11.3 Comparison with observations at great heights . . . 224
11.3.1 Marine observations . . . 224
11.3.2 Neutral observations over flat land . . . 225
11.3.3 Diabatic observations over flat land . . . 226
11.4 Summary . . . 228
Notation . . . 229
References . . . 229

12 Complex terrain and lidars **231**
12.1 Introduction . . . 231
12.2 Lidars . . . 231
12.2.1 ZephIR . . . 232
12.2.2 Windcube . . . 233
12.3 Challenges and Known Issues . . . 234
12.3.1 The conical scanning error in complex terrain . . . 234
12.3.2 Predicting the error by means of a flow model . . . 235
12.4 Experimental studies . . . 236
12.4.1 Hilly site; Lavrio . . . 236
12.4.2 Mountainous site; Panahaiko . . . 238
12.5 Conclusions . . . 238
Notation . . . 240
References . . . 241

13 Turbulence measurements by wind lidars **242**
13.1 Introduction . . . 242
13.2 Theory . . . 243
13.2.1 Systematic turbulence errors for the ZephIR lidar . . . 245
13.2.2 Systematic turbulence errors for the WindCube lidar . . . 247
13.2.3 Definition of the systematic error . . . 248
13.3 Comparison of models with the measurements . . . 249
13.3.1 Comparison with the ZephIR measurements . . . 249
13.3.2 Comparison with the WindCube measurements . . . 252
13.4 Discussion . . . 253
13.5 Conclusion . . . 256
13.6 Future Perspectives . . . 257
Notation . . . 257
References . . . 258

14 Ground based passive microwave radiometry and temperature profiles **260**
14.1 Introduction . . . 260
14.2 Microwave radiometry fundamentals . . . 260
14.3 Upward-looking radiometric temperature profile measurements . . . 261
14.4 Upward-looking angular scanning microwave radiometry . . . 265
14.5 An angular scanning temperature profile radiometer . . . 269
14.6 Antarctica Dome C experimental site Radiometric measurements . . . 270
14.7 Summary . . . 271
Notation . . . 274
References . . . 275

15 SAR for wind energy **276**
15.1 Introduction . . . 276
15.2 SAR technical description . . . 276
15.3 Wind retrieval from SAR . . . 278
15.4 Beyond C-band VV . . . 280
15.5 Current practices in SAR wind retrieval . . . 280
15.6 SAR wind retrieval at DTU Wind Energy . . . 282
15.7 Mesoscale wind phenomena from SAR . . . 282
15.8 SAR wind fields near offshore wind farms . . . 284
15.9 Wind resources from SAR . . . 285
15.10S-WAsP . . . 287
15.11The wind class method . . . 288
15.12SAR wind resource maps . . . 289

15.13Lifting satellite winds to hub-height . . . 291
15.14Future advances in ocean wind mapping from SAR . . . 291
15.15Acknowledgements . . . 291
Notation . . . 291
References . . . 292

16 Scatterometry for wind energy **296**
16.1 Introduction . . . 296
16.2 Principle of Function . . . 297
16.3 Equivalent Neutral Wind . . . 298
16.4 Sources of error . . . 299
16.5 QuikSCAT . . . 300
16.6 Applications of QuikSCAT Surface Winds . . . 303
16.7 Spatial Resolution of Scatterometer Winds . . . 304
16.8 Contemporary Scatterometers . . . 304
16.9 Acknowledgements and Suggested Reading . . . 306
Notation . . . 306
References . . . 307

1 Remote sensing of wind

Torben Mikkelsen
DTU Wind Energy, Risø Campus, Roskilde, Denmark

1.1 Ground-based remote sensing for today's wind energy research

Wind turbines are being installed at an ever increasing rate today, on and offshore, in hilly and forested areas and in complex mountainous terrain. At the same time, as the wind turbines become bigger and bigger, they reach higher and higher into the atmosphere but also into hitherto unknown wind and turbulence regimes.

The traditional method for accredited measurements for wind energy is to mount calibrated cup anemometers on tall met masts. But as turbines grow in height, high meteorology masts and instrumentation becomes more and more cumbersome and expensive correspondingly. Costs for installation of tall instrumented met towers increase approximately with mast height to the third power and licensing permits can be time consuming to obtain.

With hub heights above 100 m and rotor planes nowadays reaching diameters of 120 m or more on today's 5 MW turbines, the wind speed distribution over the rotor planes will no longer be representatively measured from a single hub height measurement point, but will also require a multi-height measurement strategy with measurements ranging in heights between 50–200 m, for the purpose of capturing the simultaneous wind distribution over the entire wind turbine rotor.

1.1.1 Wind remote sensing (RS) methodologies

A simple way to remotely determine the wind speed is by observing marked cloud drift aloft from the ground on a sunny day. More quantitative and accurate remote sensing measurement techniques for wind energy applications include nowadays sound and light wave propagation and backscatter detection based instruments such as sodar, lidar and satellite-based sea surface wave scatterometry.

Today's quest within RS research for wind energy is to find useful replacement alternatives for expensive and cumbersome meteorology mast erection and installations. However, accuracy is of particular importance for site and resource assessments irrespectively of terrain, on or offshore, and measurement errors much in excess of 1% cannot be tolerated neither by banks nor by project developers, as 1% uncertainty in mean wind speed results in 3% uncertainty in mean wind power.

1.2 Part I: Remote sensing of wind by sound (sodars)

Sodar (sound detection and ranging) is based on probing the atmosphere by sound propagation, lidar (light detection and ranging) is based on probing the atmosphere by electromagnetic radiation (microwaves or laser light) and satellite RS is based on microwave scatterometry on the sea surface and synthetic aperture radar (SAR) methods. The first two (sodar and lidar) are direct measurements of wind speed based on Doppler shift, whereas the satellite scatterometry are based on proxy-empirical calibration methods. First, a description of the background and the state-of-the-art sodar is addressed. Second, the corresponding development and application lidar RS technology is addressed.

Wind turbines operate within the so-called atmospheric boundary layer, which is characterized by relatively high turbulence levels. Turbulence is here created from the strong wind

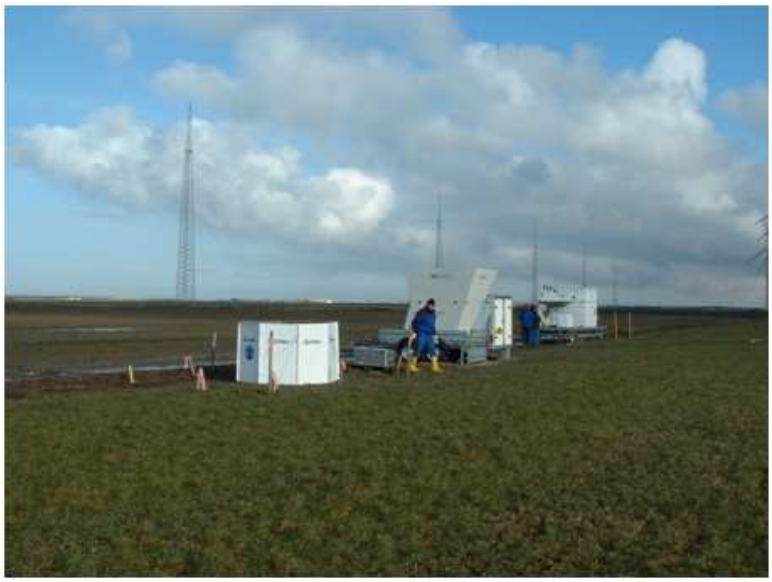

Figure 1: Commercial available sodars being inter-compared during the WISE 2004 experiment: An array of sodars (and one lidar) during inter-comparison and testing against the tall met towers (up to 168 m above ground) equipped with calibrated cup anemometers at several heights. Venue: The Test station for large wind turbines, Høvsøre, Denmark

shear due to the proximity of the Earth's surface. The wind speed at the ground is always zero, both on and offshore.

Sodar is a RS methodology for measurements of the wind speed and direction aloft at various heights in the atmosphere. Sodars are ground-based instruments that transmit a sequence of short bursts of sound waves at audible frequencies (2000–4000 Hz) upward in three different inclined directions into the atmosphere.

The sodar measurement technology was well established and in operational use for decades by now, starting in the 1980's where they served environmental protection issues and has been extensively applied to atmospheric research for environmental protection air pollution prediction measures well before the present burst in wind energy research and application. In Germany for example, sodars have been commissioned on several nuclear installations to replaced tall meteorological towers and serve now as operational monitoring devises of the local wind speed, direction and atmospheric stability.

As the sound waves from a sodar propagate forward a small fraction of the transmitted sound energy is scattered and reflected in all directions from temperature differences and turbulence in the atmosphere. A very small fraction of this scattered energy reaches back into the sodar's detector, which in principle is a directional-sensitive microphone.

The height at which the wind speed is measured is usually determined by the time delay in the backscatter from the transmitted pulse. Under standard atmospheric conditions with sound propagation speed of about 340 m s^{-1} backscatter from a sodar measurement at 170 m height above the ground will reach back into the detector after 1 s delay time.

The wind speed component in the transmitted beam direction is subsequently determined from the Doppler shift observed as frequency difference between the transmitted frequency and the frequency of the received backscattered sound wave. By combining the measured wind speed components obtained in this way from three differently inclined sound path directions, e.g. from one vertical and two inclined sound paths, the three-dimensional wind vector including wind speed and direction and tilt can be measured by sodar from preset heights from the ground and up to the limit determined by the sodar's lowest acceptable Carrier-to-Noise (C/N) ratios.

The above description is for a mono-static system, where transmitter and receivers are co-located on the ground. But alternative configurations, e.g. in the form of so-called bi-

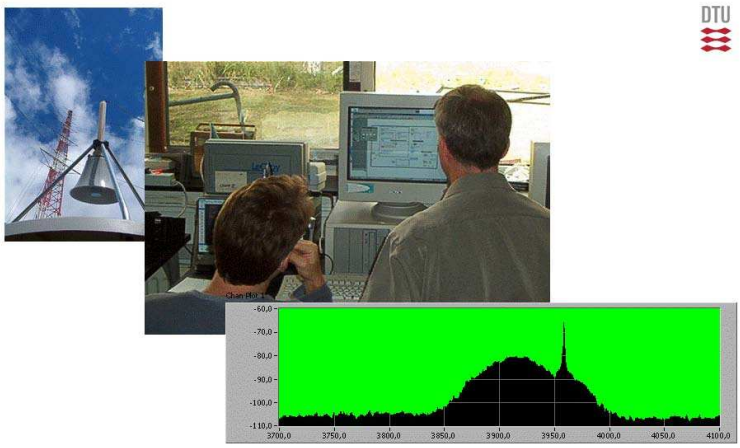

Figure 2: Calibration, laboratory work, and real-time Doppler spectrum obtained at Risø DTU with the experimental bi-static CW sodar "Heimdall" (Mikkelsen et al., 2007). Upper panel: Combined acoustic horn and parabola antenna for high-yield (+30 dB gain) backscatter receiving of sound waves. Middle panel: Two researchers at the Risø DTU Laboratory while testing of the bi-static sodar. Lower panel: A real-time obtainable continuous Doppler spectrum Heimdall bi-static sodar from wind measurements at 60 m above Risø DTU

static sodar configurations exist as well, where the transmitter and receivers are separated e.g. 100–200 meters on the ground.

Bi-static configurations have significant C/N-ratio advantages over mono-static configurations for wind energy applications. Received backscatter in a bi-static configuration is not limited to direct (180°) backscatter from temperature (density) fluctuations only, but enables also backscatter contributions from the atmospheric turbulence. And the higher the wind speed the more turbulence.

As a consequence significant improvements of the C/N- ratios can be obtained from a so-called "bi-static configuration", in which the transmitter and the receiver are separated from one another on the ground. This becomes in particular relevant during strong wind situations, where the background noise level increases with the wind speed.

A particular configuration considered for wind energy applications is therefore the bi-static continuous wave (CW) sodar configuration. Alternatively to the range gating in a pulsed system, the range to the wind speed measurement in a CW system can be determined by well-defined overlapping transmission and receiving antenna functions. At Risø DTU we have build and investigated such a sodar system for wind energy applications.

1.2.1 RS applications within Wind Energy

Remote sensed wind speed measurements are needed to supplement and extend tall met mast measurements, on and offshore, and within research to evaluate various wind flow models and wind atlases for a number of purposes, including:

1. Wind resource assessments
2. Wind park development projects
3. Power curve measurements
4. Bankability
5. Wind model and wind resource (wind atlas) uncertainty evaluation

The common denominator in most of these issues is high accuracy, and with a demand for reproducible certainty to more than 99% of what can be achieved with a corresponding

calibrated cup anemometer. A significant source for uncertainty with RS instrumentation relative to a cup anemometer, and for sodars in particular, is the remote instrument's relative big measurement volumes. A sodar measuring the wind speed from say 100 m height probes a total sampling volume of more than 1000 m^3, whereas a cup anemometer is essentially a point measurement device in this connection. In addition the sodar's measured wind components are displaced in space and time, which makes the interpretation of measured turbulence by a sodar impaired. In addition the huge sampling volumes will be putting restrictions on measurements in non-uniform flow regimes such as found near forest edges, on offshore platforms, and over hilly or complex terrain.

Sodar's RS is also in demand for direct turbine control integration, wind power optimization and turbine mounted gust warning systems, but here the demand on accuracy and reliability is correspondingly high. Today, sodars are typically used to measure 10-min averaged vertical profiles in the height interval between, say 20 and 200 m above the ground, of the following quantities:

- Mean wind speed
- Mean wind directions (including azimuth and tilt)
- Turbulence (all three wind components: longitudinal, transverse and vertical)

Albeit significant inherent scatter persists in sodar measured mean wind speed and direction data average mean wind speed compare relatively well (in most cases to within $\pm 3\%$) to that of a corresponding cup anemometer measured wind speed, cf. the slopes of the scatter plots in Figure 3.

However, the correlation coefficients between sodar and cup anemometer data is, depending on measurement height and atmospheric stability, relative poor as compared to a cup-to cup anemometer correlation, where the two cups are separated by ~ 100 m (typically less than 0.95) and reflects, among other issues, that a mono-static sodar measures the wind speed over a huge volume whereas the cup anemometer represents a point measurement. In addition, increased scatter will occur as a result of beam-bending due to the relative big wind speed to propagation speed of the sound pulses. Also notable is that sodars are able to make only a single 3D vector speed measurement about once per 6–10 s. A slow sampling rate also makes the mean prediction of a 10-min averaged quantity uncertain, due to limited independent sampling counts. In his note "Statistical analysis of poor sample statistics", Kristiansen (2010) has shown that "counting" uncertainty in terms of relative "standard deviation of the sample variance" in a small sample can give rise to a $\sim 10\%$ relative uncertainty when averaged quantities are drawn from a set of only 100 independent samples.

It is also seen from the sodar vs. cup anemometer data in Figure 3 that difficulties with the C/N ratio can occur when wind speeds exceed approximately 15 m s^{-1}, which by the way is a nominal wind speed for a wind turbine. This is due to high background noise and the loss of backscatter in neutrally stratified high wind speed regions.

Recently relative good agreements over forested areas have nevertheless been seen ($< 1\%$ discrepancy) between sodar and cup anemometer mean turbulence intensity has been reported by Gustafsson (2008). However, turbulence intensity, which is the stream wise turbulence component relative to the mean wind speed, is in a 10-min averaged quantity dominated, particularly in forested areas, by the most energy containing eddies, which in this case will be larger than the sodar's sampling volumes and therefore be well represented in the statistics. However, the smaller scales including turbulent eddies with wind gusts must be anticipated to be present also on the scales smaller than a mono-static ground based sodar will be able to capture.

While sodars appears to be able to measure accurately both the mean winds speed and the turbulence intensities at a turbines hub height it was found more difficult to use a sodar for accurate measurements over the entire rotor plane due to low C/N ratio (Wagner et al., 2008). There are several sodar manufactures on the wind RS market today including for example Remtech, Atmospheric Systems Corporation (formerly Aerovironment), Metek, Scintec,

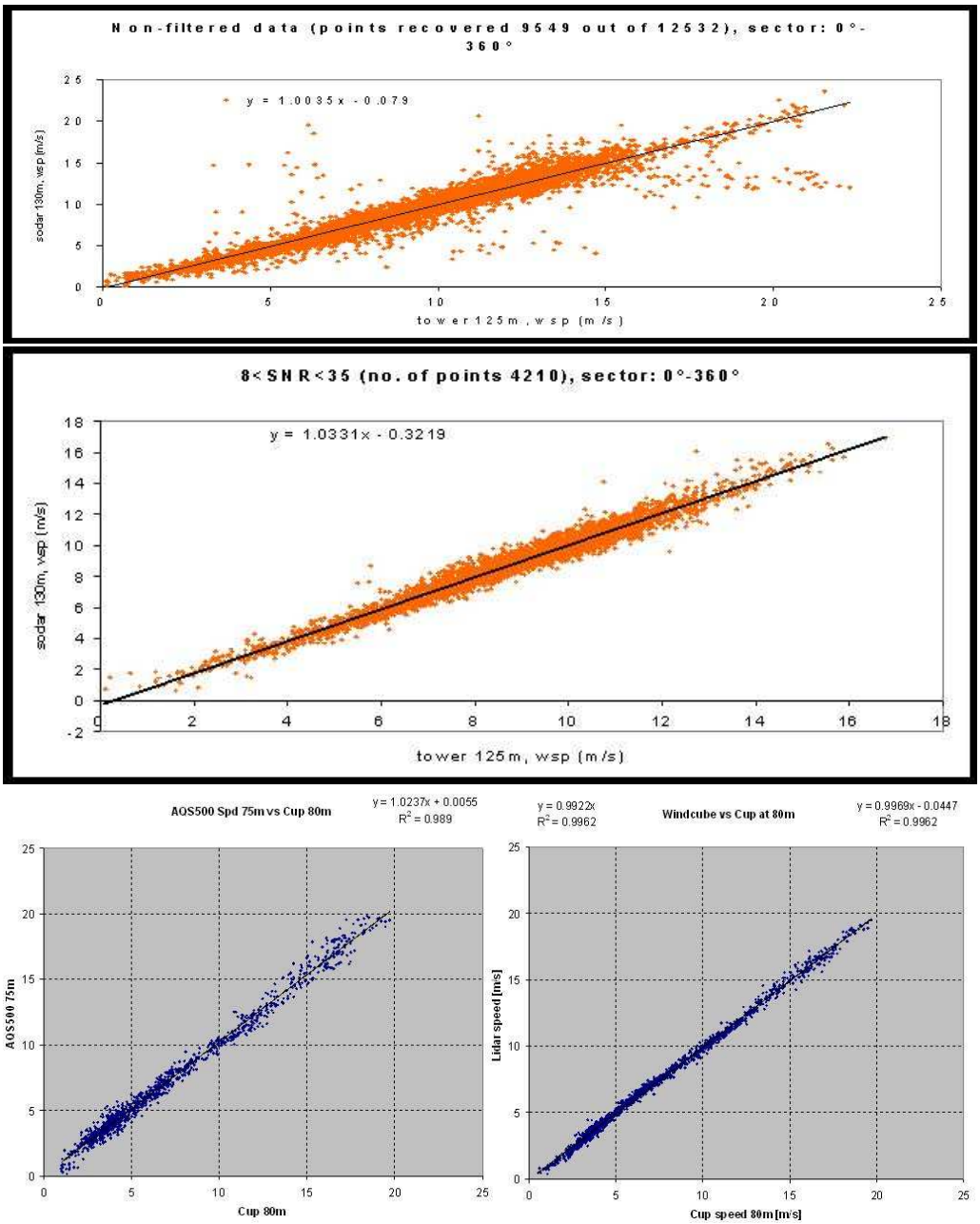

Figure 3: Example of scatter plots from sodar vs. cup anemometer data. The upper graph presents unscreened sodar wind speed data plotted against corresponding high-quality cup anemometer data measured at the Risø DTU met tower at 125 m. A data availability corresponding to 76% (9549 10-min averaged wind speeds) was obtained during this particular sodar vs cup anemometer inter-comparison test of almost three month duration (12532 10-min periods). The middle data graph shows the same data set after screening of the sodar data for high C/N-ratios. The scatter is significantly reduced, but so is also the data availability which with only 4210 data points has been reduced to almost 34%. The bottom panel shows (left) simultaneous measured sodar vs cup scatter plo tat 75 m height (0.989) and (right) lidar vs the same cup for the same data period. The lidar measurements at 80 m are seen to exhibit less scatter and high correlation coefficient (0.996)

Second Wind Inc. and Swedish AQ System to mention the most dominant. All but one base their sodar technology on mono-static phased array antenna configurations except AQ System sodars which are build on three solid dish parabolas offering a somewhat bigger antenna directivity (12° opening angle). However, only a couple of today's sodar manufacturers address directly the high accuracy demanding wind energy market.

The EU WISE project addressed and evaluated commercial sodars for wind energy (deNoord et al., 2005) and concluded then that neither of the commercial sodars were particularly close to be able to substituting standard measuring masts. In conclusion the WISE project stated that general purpose commercial sodars were unreliable, especially in case of bad weather or high background noise

1.2.2 Recent developments

A few improvements seem to have emerged since 2005. Particularly for the few sodars that addresses the wind energy marked. Replacement of the phased arrays by parabola dish seems to have contributed to the sodars overall C/N performance. Also better and improved signal processing is apparently applied today. However, it is my personal belief that we won't see any significant quantum leap in sodar performance until sodars for wind energy applications are build on bi-static configurations. Research and development along these lines are in progress, and researchers and test engineers at Risø DTU are looking forward to see and to test possible future bi-static configured sodars especially designed to meet the high accuracy demands set within wind energy RS.

Table 1: Pros & Cons of sodars

Pros	Cons
Portable	Low duty cycle (1 pulse transmitted every 3 s, and up to 6–10 s lapse times before all three wind components have been sampled)
Build on well developed and well-proven audio-frequency "low tech" technology	Limited by low S/N- ratio at: 1) high wind speed conditions 2) during neutrally stratified conditions
Sodars are relatively cheap (priced down to some 25% of a corresponding wind lidar)	Prone to solid reflections from the surroundings (including wind turbines)
Low power consumption (one solar powered version uses less than 10 W)	Prone to high background environmental noise
Sound backscatter: Relatively high yield (backscattered power at the detector of the order of 10^{-10} W)	Low wavelength/aperture ratio (1:10) results in undefined broad antenna beams
	Prone to beam bending with wind speed of the order of 5% or higher of the speed of sound
	Huge measurement and sample volumes
	Signal processing limited by pulsed sodars relative long data acquisition times (sampling time per pulse of the order of 1 s)

Table 2: Accuracy with sodars during neutral conditions

Slope mean wind speed vs. calibrated cup anemometers	$\pm 3\%$
Correlation coefficients [at 125 m, neutral stratification]	0.9–0.95
Mean turbulence intensity[at 80 m]	$< 1\%$ error

1.2.3 Summary of sodars

Most of today commercially available sodars are still build on "pre wind energy era" antenna design and processing technology, which do not in particular address nor support the high accuracy demands required within wind energy and resource assessment studies of today. The consequence is that most – if not all – of the available sodars today still exhibit insufficient accuracy to be accepted by the wind energy industry and society as an accurate RS tool for precise and "bankable" wind energy investigations.

Although some improvements seem to have occurred in accuracy since our first 2005 WISE sodar investigation, it is still not this author's belief that sodars as they come will be able to meet the high accuracy demands of the wind energy society in the future unless a major quantum jump can be demonstrated in their overall performance at high wind speed, neutral atmospheric stratification, and at present wind turbine hub heights (> 100 m).

At Risø DTU we see two venues for further research along which improved accuracy of sodars may happen: One is to switch to fully bi-static pulsed or CW based sodar configurations, however cumbersome, and the other is to take advantage of the immense, fast and cheap embeddable processing power set to our disposal from the information technology industry today, and apply these for enhanced on-line real time signal processing.

1.3 Part II: RS of wind by light (lidars)

1.3.1 Introduction to lidars

The motivation and demand in the wind energy market for wind lidars are similar to those of wind sodars. At a continuously increasing rate today wind turbines are being installed on, offshore, in hilly and forested areas, and even in complex or mountainous terrain. At the same time, as the turbines gets bigger and more powerful, they also reach higher and higher into the atmospheric flow, and thereby also into hitherto unknown wind and turbulence regimes – on as well as offshore.

The industry's traditional method for performing accredited and traceable measurements of power performance is to mount a single accurately calibrated cup anemometer at hub height two to four rotor diameters upwind in front of the turbines on a tall meteorological mast. IEC 61400-12-1 describes the accepted standard for power performance verification (power curve measurement) and prescribes measurements of power production correlated with wind speed measurements from a cup anemometer located at hub height in front of the wind turbine 2–4 rotor diameters upstream.

With turbines becoming bigger correspondingly high meteorology masts equipped with wind speed instrumentation becomes progressing more cumbersome and expensive to install, especially in mountainous and complex terrain. As wind turbines rotor planes reaches 120 m in diameter or more it is evident that the incoming wind field over the entire rotor planes is not measured representatively from a single cup anemometer mounted at hub height.

Accurate measurements of the inflow of today's huge wind turbines will require multi-point multi-height wind measurements within the entire rotor plane, to characterize the wind speed and wind shear over the entire rotor plane. Research activities addressing detailed rotor plane inflow and wakes is ongoing at Risø DTU in connection with the establishment of new research infrastructure based on wind lidars, see Windscanner.dk and Mikkelsen (2008).

1.3.2 Wind RS methodologies

RS measurement methodologies for wind energy applications are today commercially available and encompass various measurement techniques that include sound based sodars, laser based lidars and satellite borne scatterometry. The application range for wind measurements are also plentiful, and encompass for example:

1. Wind turbine power performance verification – Establishment of new RS based measure-

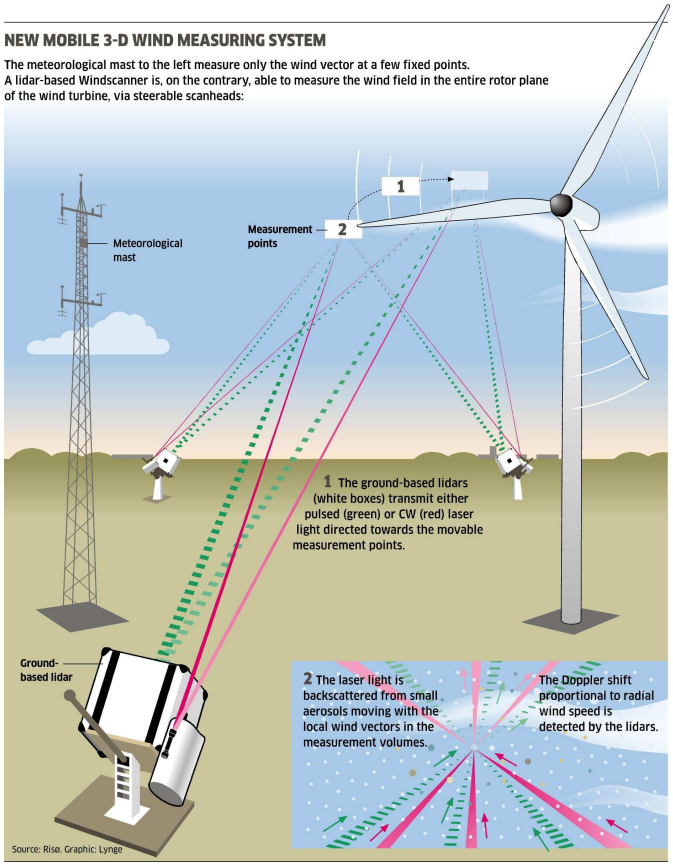

Figure 4: Windscanners in operation – CW and pulsed wind lidars engaged in measurements of the wind and turbulence fields around a spinning wind turbine (See Windscanner.dk for more details)

ment standards for the replacement of in-situ reference met masts. Work within the IEC is at the moment aiming at establishment of a new international IEC-standard for remote sensed wind measurements, as e.g. obtained by lidars, for power curve measurements.

2. Wind energy resource measurements – The global wind resources are now being mapped globally on shore, off shore, over hilly and in mountainous terrain, etc. Here also, high accuracy is of uttermost importance for accurate site and resource assessments. Measurement errors in excess of 1% are unacceptable by project developers and investment banks.

3. Wind turbine control – RS lidar instruments that are directly integrated into the wind turbines hub or spinner or even into the blades are also seen as a forthcoming RS measurement technology that can help improve the wind turbines power performance and possibly also diminish fatigue wear from extreme gusts and wind shear via active steering the wind turbines individual blade pitch or, to come one day maybe, its trailing edge flaps.

Researchers at Risø DTU have during decades now followed and contributed to the development of improved instrumentation for RS of wind. Starting out already in the 60's with more general boundary-layer meteorological investigations of flow and diffusion our present research and experimental developments within the meteorology and test and measurement programs at Risø DTU has recently become more and more directed towards applications within wind energy. Wind lidars and lidar-based wind profilers, their measurement principles, their measurement performances, and also their possible future integration within wind turbines themselves are here addressed.

1.3.3 Wind lidars

Measuring wind with a wind lidar means to probe the atmospheric flow from the ground by use of light beams. A wind lidar is wind measurement devise able to detect the Doppler shifts in backscattered light. The Doppler shift is proportional to the wind speed in the beam direction in the wind lidar's adjustable measurement volumes.

Lidars, like sodars, provide a ground-based RS measurement methodology for measuring the winds at various ranges, angles and heights aloft. Wind lidars work by transmitting electromagnetic radiation (light) from a laser with a well-defined wavelength in the near infrared band around 1.5 μm. They detect a small frequency shift in the very weak backscattered light, a Doppler shift that results from the backscattering of light from the many small aerosols suspended and moving with the air aloft.

From a meteorological point of view wind turbine are "obstacles" within the lowest part of the atmospheric boundary layer, that is, the part of the atmosphere best characterize by high wind shear, strong wind veers, and with the highest levels of turbulence.

A wind profiler is a ground-based wind lidar transmitting a continuous beam or a sequence of pulsed radiation in three or more different inclined directions. A wind profiler determines the radial wind speeds in multiple directions above its position on the ground. It does so also by determining the Doppler shifts in the detected backscattered radiation along each beam direction. Wind lidars, like sodars, therefore have both transmitting and receiving antennas, which most wind profilers today combine into a single optical telescope. The three-dimensional wind vector as function of height by measuring the radial wind speeds in three or more beam directions above the lidar. In practice, the transmitting and receiving radiation are combined in a single telescope and the beam is then steered in different directions via a rotating wedges or turning mirrors.

Wind lidars in the market for vertical mean and turbulence profile measurements are available based on two different measurement principles:

1. Continuous wave (CW) lidars
2. Pulsed lidars

Several wind lidars addressing the wind energy market are commercial available today. CW-based wind lidars are manufactured by Natural Powers (ZephIR) and OPDI Technologies & DTU Fotonik (WINDAR) while Coherent Technologies Inc. (Wind tracer), Leosphere (Wind-Cube), CatchtheWindInc (Vindicator) and Sgurr Energy (Galion) manufacture pulsed lidars for the time being.

The technology imbedded in today's CW and pulsed wind lidar systems have been spurred from the telecommunication 1.5 μm fiber and laser technology revolution in the 90's. There are however, some principally differences between CW and pulsed lidar's temporal and spatial resolution, properties that have influence on the different lidar types ability to measure and resolve the mean wind and turbulence characteristics of the atmospheric boundary layer wind field.

The CW lidar focuses a continuous transmitted laser beam at a preset measurement height and there determines, also continuously, the Doppler shift in the detected backscatter also from that particular height. When wind measurements from more than a single height are required, the CW lidar adjusts its telescope to focus on the next measurement height. The measurement ranges (measurement heights) as well as the spatial resolution of a CW lidar measurement is controlled by the focal properties of the telescope. The shorter the measurement distance, and the bigger the aperture (lens), the better defined is a CW lidar's range definition and its radial measurement confinement. A CW lidar resolves the wind profile along its beam in a similar manner as a photographer controls the focal depth in a big sport or bird telescope.

The focal depth of any telescope, however, increases proportional to the square of the distance to the focus or measurement point. This optical property limits a CW lidar build with e.g. standard 3" optics to measurement heights below, say 150 m.

Figure 5: Two CW wind lidars belonging to the Windscanner.dk research facility being intercompared and tested up against the tall meteorological masts at Høvsøre, Risø DTU.

A pulsed lidar on the other hand transmits a sequence of many short pulses, typical 30 m in effective length, and then it detects the Doppler shift in the backscattered light from each pulse as they propagate with the speed of light. While a CW lidar measures from one height at a time a pulsed lidar measures wind speeds from several range-gated distances simultaneously, typically at up to 10 range gates at a time.

The pulsed lidar's spatial resolution, in contrast to the CW lidar, is independent of the measurement range. The pulse width and the distance the pulse travels while the lidar samples the detected backscatter control its resolution. The spatial resolution in the beam direction obtainable with the 1.5 μm wavelength pulsed lidar in the market today are of the order of 30–40 m.

In addition, while a CW lidar's upper measurement distance is limited progressing unconfined measurement volume at long distances, a pulsed lidar's maximum measurement range is limited by deteriorating C/N-ratios in measurements from far distances (height).

Moreover, while a CW lidar equipped with a 1 W 1.5 μm eye-safe laser has been tested able to sample and process up to 500 wind speed measurements per second, a corresponding powered pulsed lidar can handle only 2–4 wind speed samples per second. Each of these samples, however, then on the contrary contain wind speeds from up to 10 range gates (ranges) measured simultaneously.

CW vs pulsed lidars Overall, CW lidar features high spatial resolution in the near range and very fast data acquisition rates, features that are well suitable for turbulence measurements. Today's commercial available CW lidar profilers measure radial wind speeds at ranges up to ~ 200 m and wind vectors at heights up to 150 m.

The pulsed lidar configuration on the other hand features lower but always constant spatial resolution properties (30–40 m) at all ranges. They are also inherently slower in their data acquisition rate, but then they measure wind speeds at multiple heights simultaneously, and they hold also potential for reaching longer ranges (heights) than corresponding powered CW lidars. At the test site in Høvsøre Risø DTU, commercial available pulsed wind lidar profiles have regularly measured the wind vector profiles up to 300 m height.

Figure 6: CW wind lidars (ZephIRs) under testing at Høvsøre, Risø DTU

Figure 7: Pulsed wind lidars (six WLS7 WindCubes) and one Galion (far back) during testing at Høvsøre, Risø DTU

1.3.4 Wind profiling

A wind "profiler" measures 10-min averaged quantities of the vertical wind speed profile, the vertical direction profile, and the vertical turbulence profiles, by combining a series of radial measured wind speed components from several, and at least three, different beam directions, into a three-dimensional wind vector. CW-based wind lidars, e.g. the ZephIR, measure the vertical wind profile at five consecutive heights, selectable in the range from, say 10 to 150 m height. Pulsed lidars, e.g. the WindCube or the Galion, measure correspondingly the vertical wind profile simultaneously at several (of the order of 10) heights, in the height interval from 40–~ 300 m, the upper bound depending on the amount of aerosols in the air.

True for all wind profilers in the wind energy market, however, CW and pulsed lidars irrespectively, is that they rely during combining measured radial wind speeds into a single wind vector on the assumption that the flow over the wind lidar is strictly homogeneous. Homogeneous wind flow means that the air stream is unaffected and not influenced by hills,

valleys, other wind turbine wakes, or near-by buildings within their volume of air scanned above the lidar.

For this reason, neither lidar nor sodar based wind profilers will be able measure correctly over sites located in hilly or complex terrain where the wind field is affected by the near-presence of hills or upwind turbines. Easily, up to $\sim 10\%$ measurement errors can be observed between wind speeds measured by a lidar and a mast-mounted cup anemometer co-located to take wind profile measurements from the on top of a hill. Research is therefore ongoing in order to correct wind lidar based profile measurements for flow distortion e.g. induced by terrain effects (Bingöl et al., 2008).

1.3.5 Lidar accuracy

Inherently, lidars can remotely measure the wind speeds aloft with much higher accuracy than a sodar. This is due to the nature of light, which propagates ~ 1 million times faster than a sound pulse, and because a lidar's antenna aperture size compared to the wavelength, i.e. "lens diameter-to-wavelength ratio" in a lidar is about 1000 times bigger than practically obtainable with a sodar. This result in superior beam control and also in much higher data sampling rates.

At Risø DTU's test site at Høvsøre, testing and calibration of wind lidar is now daily routine and is performed by inter-comparing and correlating lidar-measured wind speeds with wind speeds from calibrated cup anemometers in our 119-m freely exposed tall reference met mast. During "fair weather conditions", 10-min averaged wind speeds from lidars and the cups are in-situ intercompared and correlated. Linear regression coefficients with both CW and pulsed lidars could be obtained in the range of $\sim 0.99 - 1.00$, and correlation coefficients as high as ~ 0.99 (Wagner et al., 2009).

"Fair weather" means here that lidar data are screened for periods with rain, fog, mist and low-hanging clouds and mist layers. Usually this only removes a few per cent of the data. All lidars, CW and pulsed included, rely during determination of the wind speed from Doppler shift measurements on the assumption that the aerosols in the measurement volumes are homogeneously distributed and follow the mean wind flow.

Sodars for that matter, can under ideal conditions perform almost similarly well with respect to mean wind speed (linear regression coefficients as high as ~ 0.99 has been reported above). The observed scatter, however, as compared to a lidar, is bigger. Correlation coefficients observed while testing of sodars at Risø DTU's 125 m tall met mast at wind energy relevant neutrally stratified strong wind conditions (> 10 m s^{-1}) has so far not been observed to exceed the 0.90 level.

1.3.6 Wind lidar applications for wind energy

Wind lidar manufactures today address the market for replacement of tall reference meteorology mast installations at the moment required for accredited and bankable wind resource measurements and for ground-based wind turbine performance measurements. Lidar manufactures also offer their wind lidars as instruments for evaluation of model-based wind resource estimation, on and offshore (numerical wind atlases).

Wind lidars in the market today offer the wind energy industry with RS instruments, for:

- Wind speed, wind direction and turbulence profiling.
- Wind resource assessments, on and offshore.
- Wind turbine performance testing (power curves).
- Wind resource assessment via horizontal scanning over complex terrain.

Further developments Furthermore, new and improved wind lidar data and measurement technologies are under development for RS-based power performance measurements from the ground but also directly from the wind turbines. A conically scanning wind lidar (ZephIR) has during the summer 2009 been tested in a operating NM80 2.3 MW wind turbine located at Tjæreborg Enge, Denmark, with the purpose to investigate the use of wind lidars integrated directly into the wind turbine hubs, blades or spinners. The intention is to improve the wind turbine's performance by use of upstream approaching wind speed measurements from inside the turbines rotor plane as an active input to the wind turbines active control systems. Wind lidars for turbine yaw control are already nowadays on the market (Vindicator) and new and smaller wind lidars are in the near-future envisioned to become integrated as "standard" on wind turbines to provide upstream lead time wind data to the turbines control system, e.g. for:

- Enhanced wind turbine yaw control.
- Lead-time control for individual pitch control.
- Protection against fatigue from extreme wind shear and wind gusts.
- Prolonging the wind turbines longevity.
- Improving the wind turbine productivity.

1.3.7 Summary of lidar

Since the wind lidar era started at Risø DTU in 2004 new wind lidars have emerged on the wind energy market, spurred by the telecom technology revolution of the 90's. Today, wind lidars, continuous and pulsed, and properly calibrated, aligned, installed and maintained, and their volume-averaged wind measurements properly interpreted, are indeed very precise wind measuring devises, capable of matching the wind industry's needs today and in the future for precise and reproducible wind profile measurements and resource assessments.

Before, however, lidar measured wind measurements can become fully certified and accredited to industry standards, new and revised IEC lidar standards have first to be set and come into effect. It is important, however, here also to apprehend the very different nature of the previous standards point measurements as obtained from a mast-mounted cup anemometer and a volume-averaged wind vectors as obtainable from a profiling wind lidar.

Although the first generations of wind lidars, CW and pulsed, indeed had many difficulties with reliability, this era now seems to have been improved beyond their first children growth pains. Today's wind lidars offer realistic and mobile alternatives to the installation of tall meteorological masts for many wind resource estimation assessment studies, on and offshore. The near future will inevitably also show turbine mounted wind lidars fully integrated with the wind turbines control systems for improving the wind turbines productivity and longevity.

Notation

CW	continuous wave
C/N	carrier-to-noise
lidar	light detection and ranging
RS	remote sensing
SAR	synthetic aperture radar
sodar	sound detection and ranging

References

Bingöl F., Mann J., and Foussekis D. (2008) Lidar error estimation with WAsP engineering. *IOP Conf. Series: Earth and Environ. Sci.* **1**:012058

de Noord M. et al. (2005) Sodar power performance measurements, WISE WP5.

Gustafsson D. (2008) Remote wind speed sensing for site assessment and normal year correction – The use of sodar technology, with special focus on forest conditions. Master of Science Thesis in Energy Technology, KTH, Stockholm.

Mikkelsen T., Jørgensen H. E., and Kristiansen L. (2007) The Bi-static sodar "Heimdall" – you blow, I listen. Risø-R-1424(EN), Roskilde

Mikkelsen T., Courtney M., Antoniou I., and Mann J. (2008) Wind scanner: A full-scale laser facility for wind and turbulence measurements around large wind turbines. *Proc. of the European Wind Energy Conf.*, Brussels

Wagner R. and Courtney M. (2009) Multi-MW wind turbine power curve measurements using remote sensing instruments – the first Høvsøre campaign. Risø-R-1679(EN), Roskilde

Wagner R., Jørgensen H. E., Poulsen U., Madsen H. A., Larsen T., Antoniou I., and Thesberg L. (2008) Wind characteristic measurements for large wind turbines power curve. *Proc. of the European Wind Energy Conf.*, Brussels

Kristiansen L. (2010) My own perception of basic statistics. *Available on request from Torben Mikkelsen*, Roskilde

2 The atmospheric boundary layer

Søren E. Larsen
DTU Wind Energy, Risø Campus, Roskilde, Denmark

2.1 Introduction

The atmospheric boundary layer, ABL, is the lower part of the atmosphere, where the atmospheric variables change from their free atmosphere characteristics to the surface values. This means that wind speed goes from the free wind aloft to zero at the ground, while scalars, like temperature and humidity approach their surface value. An illustration of the profiles is shown on fig. 8.

Characteristics of the atmospheric boundary layer, ABL, are of direct importance for much human activity and well being, because humans basically live within the ABL, and most of our activities take place here. The importance stems as well from the atmospheric energy and water cycles. Because the fluxes of momentum, heat, and water vapour between the atmosphere and the surfaces of the earth all pass through the ABL, being carried and modified by mixing processes here. Since these mixing processes mostly owe their efficiency to the mechanisms of boundary layer turbulence, a proper quantitative description of the turbulence processes becomes essential for a satisfying description of the fluxes and the associated profiles between the surfaces and the atmosphere.

Description of the structure of the flow, relevant scalar fields, turbulence and flux through the atmospheric boundary layers necessitates that almost all types of the flows, that occur there, must be considered. For these objectives, there are very few combinations of characteristic boundary layer conditions that are not of significant importance, at least for some parts of the globe.

2.2 ABL Flows

The flow and other variables in the ABL all vary with space and time, and, neglecting the kinetic gas theory, its variability is characterized by a huge variation of the space and time scales that is involved. The larger spatial scales are related to the size of the globe, the weather systems and the depth of the atmosphere, the smaller scales are in the millimeter range. The time scales range between climate variation and milliseconds. The small scale limits are determined by the fluid properties of the atmosphere.

Important processes for ABL produced turbulence is the production of variability from the average velocity shear that has to exist in the ABL, as illustrated in fig. 8, because a fluid like the atmosphere gases cannot be dynamical stable with a mean shear as shown in fig. 8, and will start producing swirling motion, called eddies, see fig. 9. The characteristic spatial scale is the height where it happens, and the boundary layer height h. The thus created variability is called boundary layer turbulence, and is essential for the ABL mixing processes mentioned in the introduction.

For the purpose of mathematical treatment, one separates the variable in mean values and fluctuations like:

- For velocity components: $u_i =< u_i > +u_i'$, $< u_i >$ in a mean value, u_i' is fluctuating turbulence., $i = 1, 2, 3$

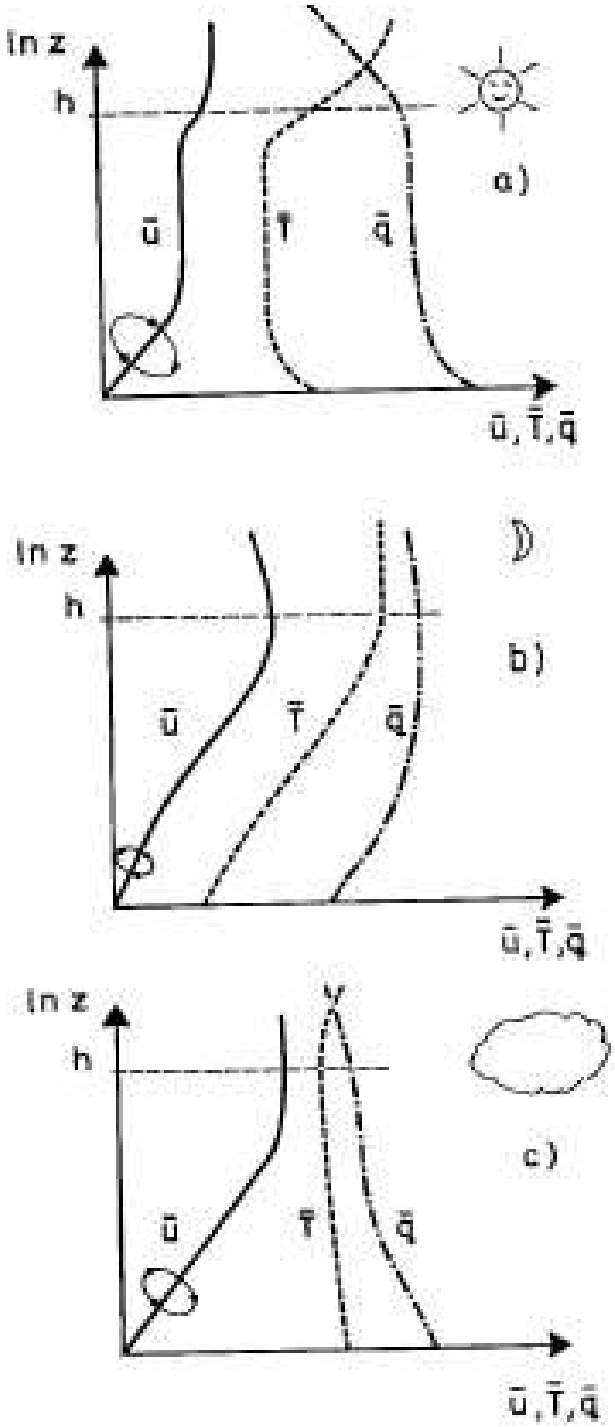

Figure 8: Profiles of mean speed, temperature and humidity (u, T and q) for clear a) day, b) night and c) cloudy conditions. Above the ABL height, h, we have the free atmosphere, while the ABL is below h down to the surface. Humidity is specified by its mixing ration q, being the ratio between the water and air density.

.

- For scalars, T , and q, temperature and humidity: $T =< T > +T'$. $q =< q > +q'$
- Variances: $< u_i'^2 >$, $< T'^2 >$ also denoted by σ^2

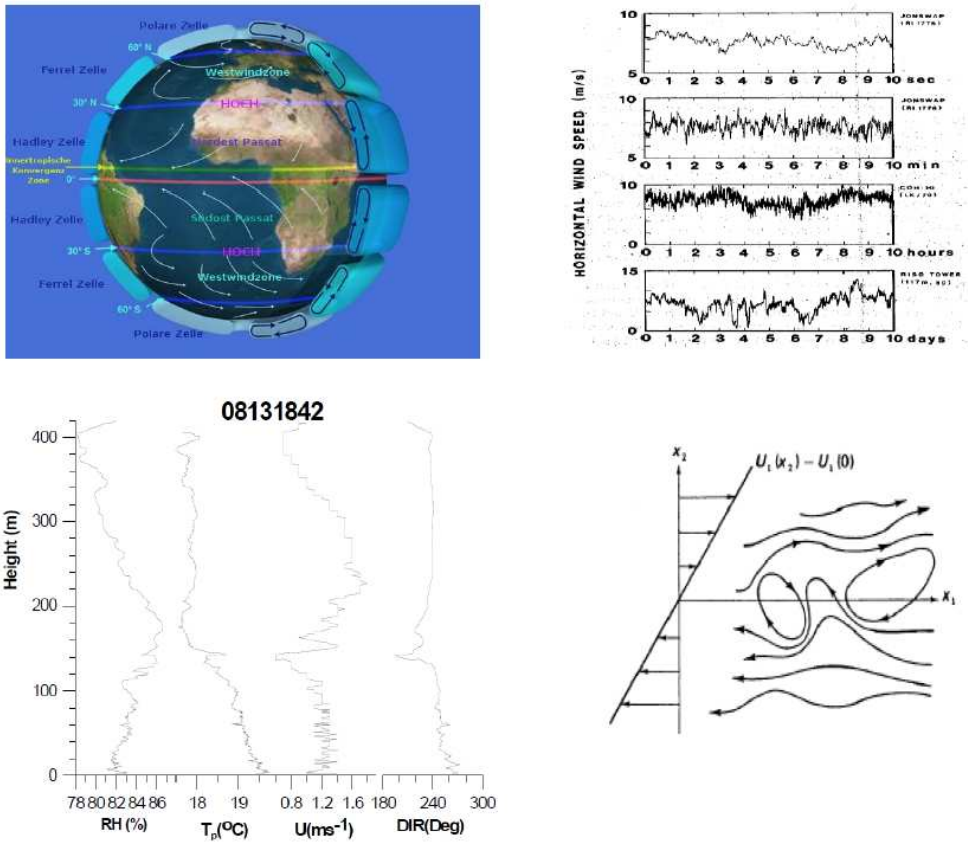

Figure 9: Large spatial scale variability for atmospheric flow at upper left, multiple temporal scale variability at upper right, and vertical multiple spatial scale Tethersonde data at lower left. A common name for the much of flow fluctuations in meteorology and fluid dynamics is turbulence, a term that further implies that at least part of its analysis and description is statistical. Production of turbulence from mean shear is illustrated at lower right (Tennekes et al., 1972)

.

- co-variances and turbulent transport: $< u_i' u_j' >$: Transport of u_i in the j direction (and vice versa).

- $< u_i T' >$, and $< u_i q' >$:Transport of temperature and water vapor in the u_i direction.

Multiplying the velocity co-variances by the air density, ρ ,we can say that the velocity transport can be considered a momentum transport, similarly multiplying the temperature transport by ρC_p is converted to a heat transport, and multiplying the water vapor transport by ρL is converted to transport of latent heat. Here C_p is the heat capacity of the air at constant pressure, L is the heat of evaporation for water. Indeed these terms are often used in the description, since they reflect the physical importance better than the statistical term correlation.

Alternatively $<>$ can be denoted with capital letters or over-bars. The coordinate system can be described at $x_i, i = 1, 2, 3$ or with x, y, z , with the corresponding u_i or u, v, w where u now is along the mean wind direction, w is vertical and v lateral (the second horizontal component).

A typical behavior of 600 seconds of ABL velocity components and temperature are shown on fig. 10.

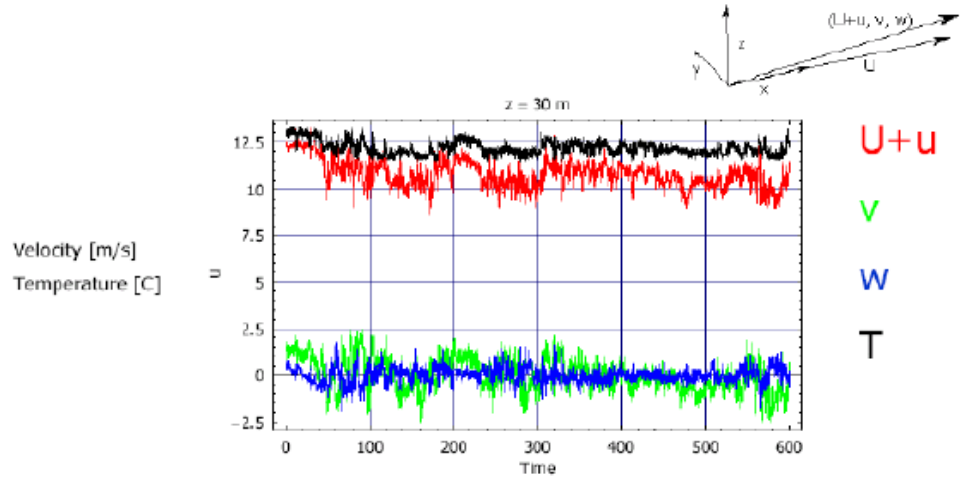

Figure 10: A 600 second record ABL mean values and turbulence: $U+u'$, $V+v'$, $W+w'$, and of $T+T'$. Notice, the coordinate system has a vertical z-axis and that the x-axis is horizontal along the direction of the mean flow, meaning that $V = 0$. The mean velocity is horizontal, because the mean vertical velocity, $W \sim 0$, since w is constrained by the nearby surface. Large spatial scale variability for atmospheric flow to the left, and temporal variability to the right.

2.3 The ideal ABL

As the simplest ABL, we assume the ABL to be limited between a homogeneous flat surface and a homogeneous boundary layer height, h, see fig. 11.

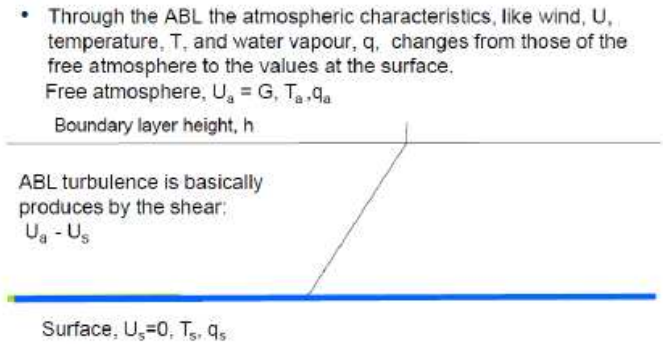

Figure 11: The ideal simplest atmospheric boundary layer, ABL, which still provides realistic results. The conditions are statistically stationary and horizontally homogeneous. The wind speed is forced to zero at the surface, and attain the free wind value U_a in the free atmosphere above the ABL height, h. The values of wind, temperature and humidity are constant at the surface and above h, giving rise to a vertical flux of momentum, heat and water vapor between the surface and the h-level

The flow is assumed statistically stationary, meaning there will be variations. But these will be statistically horizontally homogeneous and stationary. However, as seen from equation 1 we must allow a pressure gradient that, again somewhat unrealistic, is taken as constant. Without a pressure gradient, there will be no wind.

The three moment equations:

$$\frac{Du_1}{Dt} = 0 = -\frac{1}{\overline{\rho}}\frac{\partial \overline{\rho}}{\partial x_1} + f\overline{u_2} - \frac{\partial}{\partial x_3}(\overline{u_1' u_3'})$$

$$\frac{Du_2}{Dt} = 0 = -\frac{1}{\overline{\rho}}\frac{\partial \overline{\rho}}{\partial x_2} + f\overline{u_1} - \frac{\partial}{\partial x_3}(\overline{u_2' u_3'}$$

$$\frac{Du_3}{Dt} = 0 = -\frac{1}{\overline{\rho}}\frac{\partial \overline{\rho}}{\partial x_3} - 2\Omega(\eta_1\overline{u_2} - \eta_2\overline{u_1})\frac{\partial}{\partial x_3}(\overline{u_3' u_3'})$$

The scalar equations: (1)

$$\frac{D\overline{T}}{Dt} = 0 = \frac{\partial}{\partial x_3}(-\overline{u_3'\theta'})(= \frac{\partial T}{\partial t} + \overline{u_1}\frac{\partial T}{\partial t} + \overline{u_2}\frac{\partial T}{\partial x_2})$$

$$\frac{D\overline{q}}{Dt} = 0 = \frac{\partial}{\partial x_3}(-\overline{u_3' q'})$$

Equation 1 summarizes the equation form the mean flow for our pseudo homogeneous ABL. As mentioned the constant pressure gradient is necessary, but limits the horizontal scale for the model. The temperature equation further illustrates the meaning of the substantial derivative, for all the variables. The equation for u_3 is not important in this approximation and will be neglected in the following.

Additionally, in eq. 1 our simplified ABL is situated on the rotating planet Earth, reflected by appearance of the Coriolis parameter, and the Earth's rotation rate Ω, with $f = 2\Omega sin\varphi$ and with φ being the latitude on the globe. Further it is seen that we have introduced the symbol θ, the so called potential temperature. This is a modified temperature including the fact that the average pressure and density in the atmosphere decreases with height, due to gravity. This means that an adiabatically moving air packet cools moving up and heats moving down, but will remain in equilibrium with surroundings and at the same potential temperature. If θ increases with height the air is denser than equilibrium at the bottom and therefore stable against vertical perturbations. Conversely for θ decreasing with height, the air is lighter than equilibrium at the bottom and hence unstable, if perturbed vertically. Within the boundary layer, θ is often approximated by:

$$\theta = T + \Gamma \cdot z, \text{with } \Gamma = \frac{g}{C_p} \tag{2}$$

With Γ being about 0.01 K/m. It is noted that the only difference between T and θ is the linear height variation.

Equation 1 shows that the vertical fluxes of scalars are constant with height, while the momentum fluxes are slightly more complicated. Focusing on the two first equations for the horizontal velocity components, we define the geostrophic wind, G, from the pressure gradient, and perpendicular to the direction of this gradient:

$$G = (U_{1G}, U_{2G}) = (-\frac{1}{f\overline{\rho}}\frac{\partial \overline{p}}{\partial x_2}, \frac{1}{f\overline{\rho}}\frac{\partial \overline{p}}{\partial x_1}) = (-\frac{1}{f\overline{\rho}}\frac{\partial \overline{p}}{\partial y}, \frac{1}{f\overline{\rho}}\frac{\partial \overline{p}}{\partial x}) \tag{3}$$

The two first equations in eq. 1 now take the form:

$$\begin{aligned} 0 &= f(\overline{u_2} - U_{2G}) - \tfrac{\partial}{\partial x_3}(\overline{u_1' u_3'}) \\ 0 &= -f(\overline{u_1} - U_{1G}) - \tfrac{\partial}{\partial x_3}(\overline{u_2' u_3'}) \end{aligned} \tag{4}$$

This equation shows that the wind velocity approaches the geostrophic wind at the top of the boundary layer, where the turbulence disappears. Down through the boundary layer the

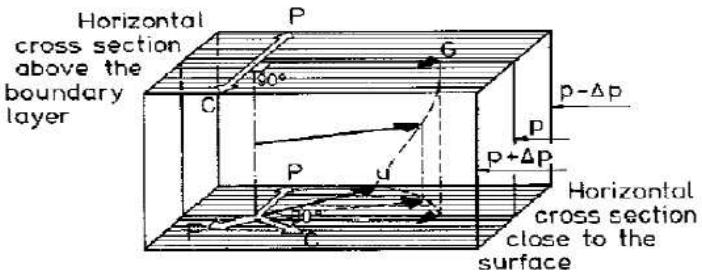

Figure 12: The variation of wind speed and wind direction from the top, through the ABL towards the ground. The wind profile can be seen as being developed through a balance between the three forces, the pressure gradient, P, the Coriolis force, C, and the Frictional force, F. (Larsen et al., 1983)

wind solution depends somewhat on the additional assumptions, but generally it undergoes a spiraling motion as it reduces to zero at the ground, see fig. 12.

The detailed behavior of the wind speed through the ABL, is simplest for atmospheric neutral stability, meaning that there is no heat flux and water vapor flux between the surface and the free atmosphere (fig. 11). This can be assured by keeping the potential temperature, $\Delta\Theta_h$, difference at zero, meaning that $Ta - Ts = \Gamma h$, compare eq. 2, and as well $q_s = q_a$. For such situations one can derive the equations in eq. 7, using so called scaling laws, where the momentum transport, is a new scale introduced from the co-variance, the so called friction velocity u_* as :

$$u_*^2 = \overline{-u'w'} \tag{5}$$

$$\begin{aligned} ABL \quad &: \quad \frac{\kappa G}{u_*} = \left((\ln(\frac{u_*}{f z_0} - A)^2 + B^2 \right)^{\frac{1}{2}} \\ ABL \quad &: \quad \alpha = tan^{-1}(\frac{-B}{(\ln(\frac{u_*}{f z_0} - A))}) \\ SBL \quad &: \quad U(z) = \frac{u_*}{\kappa} \ln \frac{z}{z_0} \end{aligned} \tag{6}$$

The first equations relate the conditions at the top of the ABL to the wind at lower heights, the so called Surface Boundary Layer, SBL. The first of these called, the resistance laws of the ABL, relating the friction velocity, u_*, to the geostrophic wind, G, and a so called roughness length, z_0, plus two three additional "universal" constants, the von Kármán, κ, and the two constants A and B. The term $\frac{u_*}{f z_0}$ is denoted the surface Rossby number. Since f is of the order of 10^{-4} A is about 2 and B about 5 , z_0 is small. The Rossby number term dominates the first of the resistance laws. The second of the resistance laws estimates the angle between the geostrophic wind and the wind in the lower part of the ABL, the ASL. In this part the wind profile is described by the last of the equations, the so called logarithmic profile.

The set of equations allow us to estimate the wind profile in the ASL for a given geostrophic wind speed for varying roughness length. Therefore the roughness length is a very important parameter, see fig. 14. In the principle it is a characteristic length, where the velocity extrapolates to its surface value, which is zero, but since it is a measure of the "roughness" of a given landscape, much work has been done to establish consensus about the roughness of characteristic real landscapes.

As seen from fig. 13, the roughness generally follows the intuitive images of what that roughness is associated with. The larger and the sharper the protruding elements, the larger the roughness. Although this image is simplistic, it still summarizes the main aspects of the roughness characteristics of landscapes, including season variation of some landscapes. To

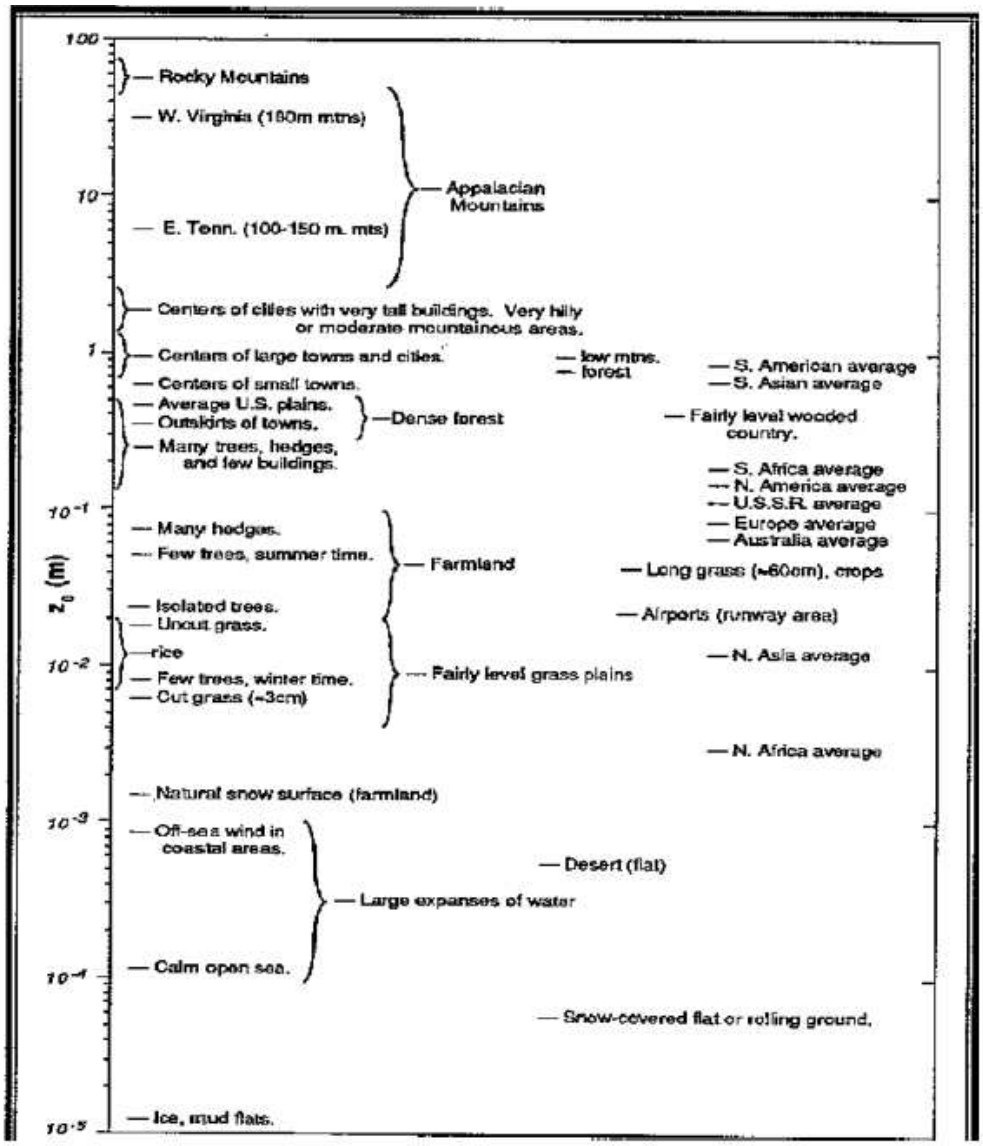

Figure 13: Consensus relations between the roughness lengths for different landscapes (Stull, 1988).

emphasize the importance of the roughness length for wind energy, we compare in fig. 14 the winds in the ASL for for different roughness values and a given geostrophic wind.

Until now we have considered only situations, where the potential temperature differences between the surface and the free atmosphere is unimportant for the dynamics, this state is called thermally neutral. Changing Ta and Ts to make $\Delta\theta_h$ different from zero, and similarly for q_s and q_a, a heat flux and water vapor must flow between the top of the ABL and the surface, and there will be a density gradient between top and bottom. For such a situation the variation of wind speed, temperature and humidity can be described by an extension of the simple scaling used for neutral conditions in eq. 7. These scaling formulations are normally denoted the Monin-Obukhov formulation. The set of scales is summarized below.

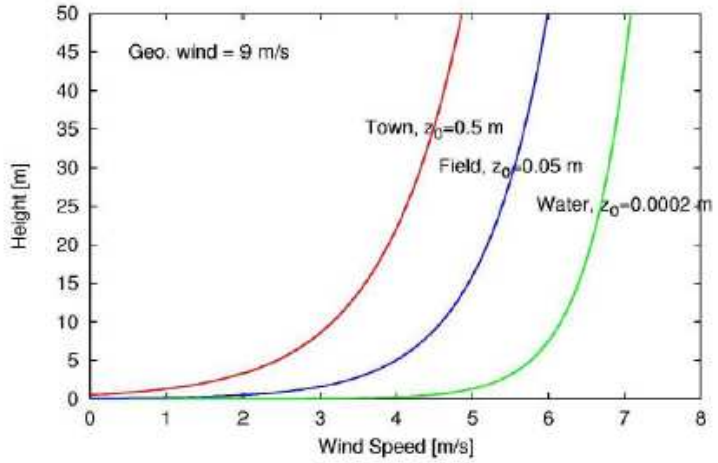

Figure 14: The change in surface wind for different roughness values, but the same Geostrophic wind, G. The roughness length z_0 is seen to be related to the indicated land scapes in fig. 13

$$\begin{aligned}
\text{Friction velocity:} u_* &= -\overline{-u'w'} \\
\text{Temperature scale:} T_* &= -\frac{\overline{-w'\theta}}{u_*} \\
\text{Water vapor scale:} q_* &= -\frac{\overline{-w'q'}}{u_*} \\
\text{Monin-Obukhov stability length:} L &= \frac{Tu_*^3}{\kappa g(T_* + 0.61 q_*)}
\end{aligned} \tag{7}$$

The water vapor concentration, q, enters into the stability measure, because both q and Θ influence the density and thereby the stability based on density fluctuations. This will be repeated throughout this text, but not always, because temperature is typically more important than humidity for the stability.

The Monin-Obukhov scales are widely used, not only in the atmospheric surface layer (ASL) that was introduced in fig. 12, but also for extension into the full ABL. In eq. 7, g is the acceleration due to gravity, and the stability length, L, is a scale that is derived from the energy budget as a measure of the importance of the heat and water vapor fluxes relative to the momentum flux. As in eq. 7, κ is the von Kármán constant (~ 0.4). The scales defined in eq. 7, change relatively little within the ASL, above this one typically uses the ASL measured parameters.

Corresponding to the neutral wind profile in eq. 7, we can now formulate the set of stability influenced profiles in eq. 9, as:

$$\begin{aligned}
\overline{u}(z) &= \frac{u_*}{k}(\ln\frac{z}{z_0} - \psi(\frac{z}{L})) \\
\overline{\theta}(z) - \theta_0 &= \frac{\theta_0}{k}(\ln(\frac{z}{z_{0T}}) - \psi_T(\frac{z}{L})) \\
\overline{q}(z) - q_0 &== \frac{q_*}{k}(\ln(\frac{z}{z_{0q}}) - \psi_q(\frac{z}{L}))
\end{aligned} \tag{8}$$

Stability influenced profiles of $< u(z) >$, $< \Theta(z) >$ and $< q(z) >$. Notice, that separate "roughness length" parameters are introduced for the scalars. These are of the order of z_0 for smooth surfaces, but typically of the order of 10 times less for rough surfaces.

From the definition of L, it is seen that $\frac{z}{L} \sim 0$ for neutral conditions, with no scalar fluxes. $\psi(0) = 0$ for all three ψ-functions, and hence the logarithmic profiles for all variable are recovered for neutral. Close to the ground $\frac{z}{L} \sim 0$ simply because z is close to zero. Hence all profiles start as being logarithmic close to the ground. For stable conditions, we have:

$\psi\frac{z}{L} \sim -\frac{5}{L}$. For unstable conditions (meaning $\frac{z}{L} < 0$) the functions are more complicated but can be approximated by is $\psi\frac{z}{L} \sim 1-(1-a\cdot\frac{z}{L})^{-n}$, with a between 10 and 15, and n $= 0.25$ for the wind and 0.5 for the scalars.

When the heat flux is positive (the ground is warmer than the air) the atmosphere is characterized by rising air. The shear produced eddies are enhanced by the thermal structure, and the situation is denoted thermally unstable. If the heat flux is downward, the shear produced eddies and the general fluctuation level is diminished, for which reason the situation is denoted stable. The enhance mixing for unstable condition reduces the wind shear, while the reduced fluctuation level for stable condition allows a larger wind shear. The situations are depicted in fig. 8, together with a neutral situation, (indicated by sun, moon and a cloud). Notice that above the ABL the temperature and the potential temperature will in general increase with height.

In reality thermal properties of the lowest atmosphere is forced either by the radiation balance at the ground, insolation at day time, and additional cooling at night time, or/and by advection of air masses with a temperature that differs from the surface temperature. The balance depends on time scale considered, on the thermal properties of the ground, cloud cover and the characteristics of the air motion around the site. We return to this when discussing real boundary layers.

As opposed to the profiles in eq. 9, in engineering literature one often find the so called power law profiles:

$$\frac{u(z)}{u(z=10)} = (z/10)^{\alpha} \tag{9}$$

where the relevant α will be function of height, stability and roughness, as seen by comparing with eq. 9. The power law profile has the advance of being simple and that α is a direct measure of the relative shear, as can be seen by differentiation of eq. 9.

For neutral conditions we have in eq. 7 not only a wind profile in the ASL, but also for the whole ABL a resistance law relating the G to u_* and the geostrophic wind angle. This can in the principle be extended also to different stabilities and to the scalar variable, letting the A and B constants, and corresponding parameters for scalars, be function of stability, typically in terms of h/L (Zilitinkevich, 1972),(Zilitinkevich, 1975). However, the quality of the data fit for these extensions are worse than for the simple neutral expression in eq. 7, and therefor they are not much used.

For our ideal boundary layer discussion, we have simply fixed the boundary layer height, just as we could fix the temperature difference between the surface and the air on the top of the ABL. In the real world the ABL height is determined as the outer range of the boundary layer turbulence. For neutral conditions one find that it must be proportional to u_*/f, since these two parameters are the only parameters available to characterize the ABL turbulence. Indeed one finds that this fits the data moderately well with a coefficient equal to about 0.3. For moderate stabilities, one can use an expression like $h \sim 0.7(u_*L/f)^{0.5}$, and for strongly stable conditions $h \sim L$, the Monin-Obukhov stability length.

For unstable and many stable situations, it is common to use an independent rate equation, to determine h, at least over land, that $h = h(t)$ is now derived from an equation like $dh/dt \sim F(\cdot\cdot)$. Especially for unstable situations, a very simple and successful equation has been developed. Assuming an unstable ABL growing, in response to sunrise, against a background stable potential temperature gradient, γ, using the in-stationary temperature equation in eq. 1. The result is:

$$h(t) = \left(2\frac{Q(t)}{\gamma}\right)^{0.5} \text{ with } Q(t) = \int_0^t \overline{w'\theta'}|_0(1+2A)dt' \tag{10}$$

Where A here is an entrainment coefficient of the order of 0.2, accounting for the flux is not only from the ground, but also from the top of the growing ABL. The boundary layer height and the roughness length in combination have importance for the existence and extent of the surface boundary layer. Formally ASL can exist for $z_0 << z << h$. For the large z_0 in fig. 13 and low values of h, the simple ASL expression of eq. 9 becomes invalid.

Note, that with equations like eq. 10, we have strictly speaking left the stationary boundary layer, and are approaching the real world, where a diurnal cycle is a basic fact of life. Experience shows, however that much of the simplified ABL described here survives, when allowing for slower changes like many, but not all, of the diurnal changes.

Not only mean values are important to characterize the ABL, also fluctuation of the individual signal are important. To a first approximation these can be characterized by the turbulence standard deviation, where especially those associated with the velocity components are important for many purposes. For velocity components one has developed expressions, corresponding to the Monin-Obukhov profile.

$$\frac{\sigma_x}{x_*} \approx F(\frac{z}{L}, \frac{h}{L}) \text{ with } x = u_i, \theta, q \tag{11}$$

Where it has been found necessary to include h/L even within the ASL. In general the function F increase with increasing instability, and become constant for neutral-stable condition. For velocity one often considers eq. 11 in term of the Turbulence Intensity (TI) derived from eq. 11 by division with the local wind speed. Thereby the TI becomes an expression for the likely relative deviation from the mean speed one will encounter for given situations, Also distributions of the vertical instantaneous shear has become an important parameter, e.g. distributions of α in eq. 9. Inserting the respective expressions we get, for the two:

$$\begin{aligned} TI &= \frac{\sigma_u}{\overline{u}} = \frac{\kappa F(z/L, n/L)}{\ln(z/z_0) - \psi(z/L)} \approx \frac{1}{\ln(z/z_0)} \text{for } \frac{z}{L} \to 0 \\ \alpha &= \frac{z}{\overline{u}} \frac{d\overline{u}}{dz} = \frac{\phi(z/L)}{\ln(z/z_0) - \psi(z/L)} \approx \frac{1}{\ln(z/z_0)} \text{for } \frac{z}{L} \to 0 \end{aligned} \tag{12}$$

where $\varphi(z/L)$ is the derivative of $\psi(z/L)$. The behavior of data on the two functions are shown in fig. 14.

Additional information about the fluctuations can be seen in the correlations or the spectral structure of the signals. Atmospheric signals vary as function of both time and space. For boundary layer turbulence, one can mostly assume that the fluctuations vary with space only, and that measured time variation at a stationary measuring station is due to advection of a spatial variation of the signal.

This, surprisingly simple assumption, is denoted the Taylor hypothesis. Take a measured $u(t)$ as an example:

$$u(\Delta t) = u(\Delta x / < u >) \tag{13}$$

where Δ signifies that the Taylors Hypothesis works on differences in space and time, not on the absolute coordinates. Equation 13 can even be used in connection with a moving sensor, like an air plane, where the speed then must be the sum of the air velocity and the sensor velocity.

To resolve frequency or wave number distribution of the turbulent variables, one uses Fourier spectra computed either as frequency or wave number spectra, with connection derived from the Taylors hypothesis, $\omega = k_1 < u >$, where k_1 is the wave number along the mean wind direction. The Fourier analysis is based on the existence of Fourier pairs. The simplest principal way is to illustrate the spectra-correlation duality by:

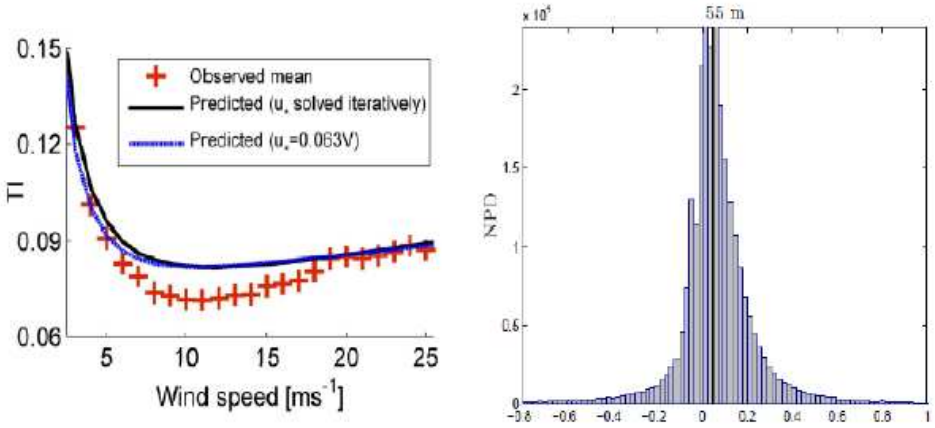

Figure 15: Behavior of the turbulent intensity the dimensionless shear from eq. 12, measured at about 60 meter over water (Wang et al., 2012; Peña et al. , 2012). The deviations between the predicted values and the data are due to stability, processes, and also to some extent to model failings, which we will comment later, but at the very least we see that the neutral limit with a constant z_0 is not adequate to explain the data. Specifically for the TI it is fairly well established that the high TI for low wind speeds is due to stability effects. For higher winds TI is expected to follow the observed mean TI is expected to be in the neutral limit of eq. 12. However, the prediction is based on land conditions with a constant z_0, while the over water measurements, reflects the growth of z_0 with wind speed, following Charnock's relation as discussed later in this chapter

$$S_{XY}(\omega) = \int \overline{X'(t)Y'(t+\tau)} \exp(i\omega\tau) d\tau$$
$$\overline{X'(t)Y'(t+\tau)} = \frac{1}{2\pi} \int S_{XY}(\omega) \exp(-i\omega\tau) d\omega \tag{14}$$

Where X and Y are two turbulent variables as function of time, with a correlation as function of a lag time, τ, with a corresponding cross spectrum $S_{XY}(\omega)$ of frequency ω. Similar expression could be formulated for the spatial correlation of $< X'Y'(x_i + \delta_i) >$ and its corresponding wave number cross spectrum, $S_{XY}(k_i)$. Here the wave number analysis is different from the frequency analysis, in that the spatial lags, δ_l, and the wave numbers, k_i, are vectors. Taylors hypothesis is relating frequency to k_1 only, the wave number one along the mean velocity direction.

The spectra are in fig. 16 are scaled with the same scales as the profiles $< u'w' >$, $< w'T' >$, etc. Thet are plotted versus a normalized frequency $n = fz/ < u >= k_1 z$, with f in Hz, and, where we have again used Taylors hypothesis for the frequency-wave number relation, the z appears from the Monin-Obukhov similarity (Kaimal et al., 1972).

The spectra in fig. 16 are empirical and other spectral expressions exist, but there is a general consensus on their form and intensity, such that the different forms agree broadly on the behavior of the spectra, although there are low frequency differences, that can be important in connection with some load modeling on structures (Andersen et al., 2010). The spectra vary systematically with height through the ABL and with stability in widely accepted ways. Olesen et al. (1984), Hojstrup (1982), Mann (1998), and the Mann-lecture at this course.

At present, there is a strong activity of extending profiles and turbulence expressions all the way through the ABL, and even further up. This is both because the growing wind turbines makes the information important and also because the breakthrough in the remote sensing

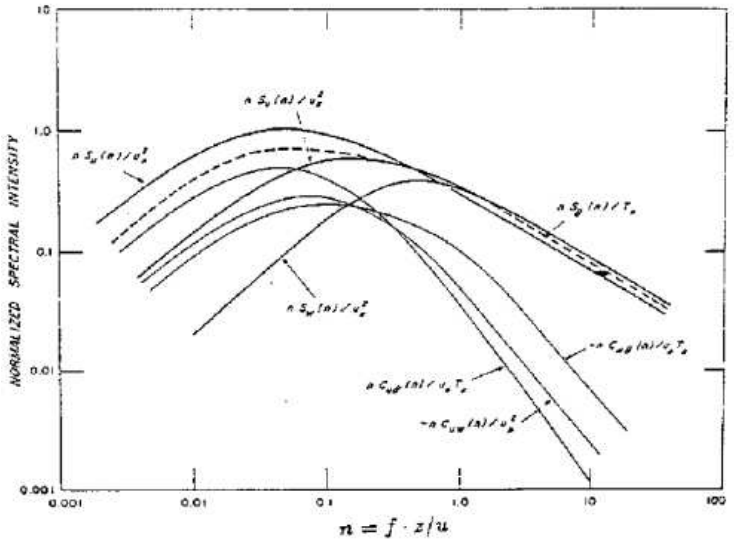

Figure 16: Neutral scaled ASL power and co-spectra from (Kaimal et al., 1972) plotted versus the normalized frequency $n = fz/U$. The spectra are scaled by the relevant Monin-Obukhov parameters defined in (7).

technology, has made systematic data gathering in these heights possible. Some progress has been made, as indicated by the illustration in fig. 17. However, it is still a speciality in development, because the profiles aloft become sensitive to many new important scales, like the ABL height, but also on the detailed characteristics of the entrainment zone above the ABL.

An often used scale for strongly unstable conditions, is a velocity scale constructed from the turbulent heat flux, to be used when the heat flux is more important than the momentum flux, and often in the upper part of the unstable ABL: $w_* = (h < w'\theta' > g/T) \sim u_*(-h/\kappa L)^{1/3}$, u_* will typically at most be a few tens of cm per second, while w_* can reach several meter per seconds. Additionally, to the new scales entering the problem,the demands to homogeneity becomes more severe, and several aspects of remote instationarity and inhomogeneity, not really influencing the profile in the ASL, will influence wind speed and wind turning aloft, like e.g baroclinity and remote changes in surface characteristics. We shall consider these aspects later. Here we present experimental and theoretical effort to describe the wind profile to greater heights.

We finally return to the concept of thermal stability, which as we have seen is a measure of the importance of the atmosphere's thermal stratification relative to the wind shear dynamics for the flow structure. In the SBL it can be described by the stability length L (Eqs. 7 and 9). Commonly used are the so called Richardson numbers, that measures the ratio between the potential and the kinetic energy across a layer. In the ABL it is mostly defined in terms of gradients of the mean temperature and the mean wind as shown in the following equation eq. 17.

$$Ri = -\frac{g\Delta z}{\overline{\rho}}\frac{\Delta\overline{\rho}}{(\Delta U)^2} \approx \frac{g\Delta z}{\overline{\theta}}\frac{\Delta\overline{\theta}}{(\Delta U)^2} \approx \frac{gz}{\overline{\theta}}\frac{\Delta\overline{\theta}}{U^2} \approx \frac{g}{\overline{\theta}}\frac{\partial\overline{\theta}/\partial z}{(\partial U/\partial z)^2} \tag{15}$$

Where the first term is the basic definition of stability in terms of density gradients for a layer of depth Δ, while the three last second forms are those most used in the ABL, and are based on a relation between the potential temperature and the potential energy. The third term characterizing a layer from the ground to height z, is denoted the Bulk Richardson Number, while the 4th form is the differential form. Inserting the profile expressions Ri can be described in terms of the SBL formalism. But Ri is more general validity than for the the SBL atmosphere. To be completely consistent with eq. 7 we should have introduced water

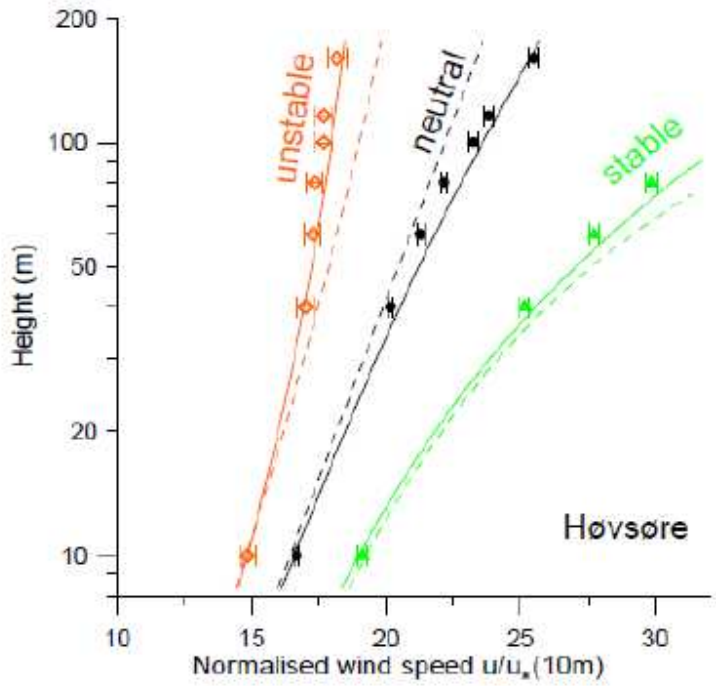

Figure 17: Newly developed models tested against data from the Høvsøre site in Denmark. The broken line are the extrapolations of the ASL models presented in fig. 14, the solid curves reflect models developed by (Gryning et al., 2007), involving the boundary layer height and one more height scale.

vapor into eq. 12 as well.

2.4 Surface Characteristics of real ABLs

We shall consider characteristic real ABLs in the light of the ideal one considered in the former section. Characteristics of a flat homogeneous land surface, a marine ABL, the effect of moderate inhomogeneity, and finally steep surfaces and complex terrain.

To understand some of the differences, we must consider layers below the turbulent ASL, because this is where the frictional processes resulting in a roughness takes place, and where the surface temperature is a result the heat flux properties. The roughness length z_0 is the height, where the logarithmic profile extrapolates to zero due to surface friction. However, below a height of about 10 z_0 the real profile is not logarithmic anymore, because of the molecular friction and because of the flow impacting on irregularities of the surface roughness elements.

Tracking the momentum transport through the viscous layer reveals that the momentum and heat transport is taken over by the surface and can be written as:

$$\begin{aligned} \overline{-w'u'}_z &= u_{*z}^2 = \left(\overline{\frac{p}{\rho}\frac{\partial \eta}{\partial x}}\right)_\eta + \nu \left(\overline{\frac{\partial u}{\partial z}}\right)_\eta \\ \overline{-w'\theta'}_z &= \nu_\theta \left(\frac{\partial \overline{\theta}}{\partial z}\right)_\eta \end{aligned} \tag{16}$$

The real irregular surface as indicated on the figure and denoted, η, while ν and ν_0 are the molecular diffusivity of momentum and heat respectively. On the left hand side of eq. 16 the transport taking place in the turbulent ASL have been indexed with a z. In the viscous layer ASL turbulence cannot exist due to the nearness of the surface, and the transport is taken

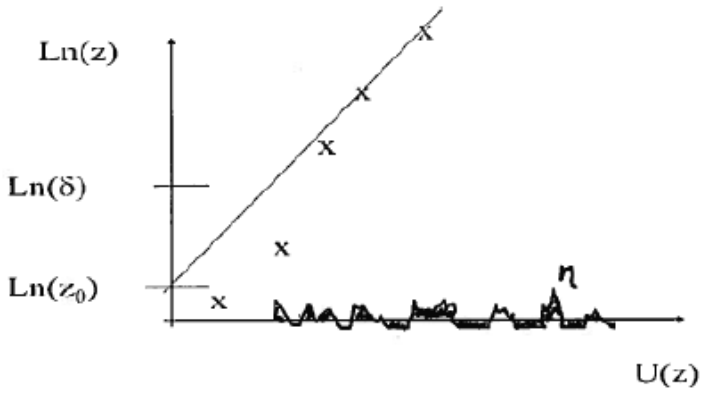

Figure 18: Extrapolation of the logarithmic profile down towards the surface below height of the viscous surface layer, δ. The logarithmic line is shown, while real velocities are indicated by x. Small scale irregularities, which we will denote roughness elements, are indicated.

over by molecular gradient diffusivity and for momentum also by the pressure perturbation around the irregularities. The correlation obviously becomes larger with steeper and sharper irregularities, roughness elements. If there is no roughness element the transport is limited by the molecular diffusion, and a scale analysis indicates the $z_0 \sim \delta \sim \nu/u_*$. With roughness elements present the roughness becomes larger. On the other hand the heat transport in eq. 16 includes no pressure term, since pressure appears in the momentum equation only. Therefore the transport of heat in the viscous sublayer is basically due to the molecular diffusion only, and z_{0T}, and correspondingly z_{0q}, must be expected to be smaller than z_0, and more so, the more rougher the surface. As mentioned earlier typically $z_{0T}/z_0 \sim 0.1$ for rough surfaces.

Next we turn to the surface temperature θ_0 appearing in eq. 9 and implicit in all our arguments about the effects of stability. The surface temperature is a boundary condition in eq. 9 but it is as well a result of the energy balance at the surface and controlled by processes above, on and below the surface. At the surface the energy balance per unit area can be written as (Bodyko, 1974):

$$C\frac{d\theta_0}{dt} = NR + H + E + G \tag{17}$$

Where, $C \cdot d\theta_0/dt$ the heat accumulation in a thin layer at the surface, with C being the heat capacity of this surface layer.

NR is the net radiation at the surface, consisting mainly of the incoming short wave radiation from the sun and outgoing long wave radiation from the surface itself. NR is positive day time, most positive around noon, and it is negative during night, when the surface undergoes additional cooling. Cloud cover, season and latitude is obviously important here.

H is the turbulent heat flux $= \rho C_p < w'\theta' >$, cooling the surface when it is warmer than the air, and heating it when it is colder, typically due to radiation at night and day. Obviously it can reflect also changes in the air temperature due to advection, from eq. 9 we have $H == \rho C_p < w'\theta' > \sim -\rho C_p(\theta(z) - \theta_0)\kappa u_*/\ln(z/z_{0T})$.

E is the latent heat flux$=\rho L < wq' >$, reflecting that the surface can regulate heat by evaporating water or condensing water vapor. Just as for temperature these processes can be driven by radiation, but also by advection.

G is the ground layer heat flux, which as all the other fluxes in eq. 17 can be both negative and positive. But it will typically be directed downwards during day time, and upwards during night.

The value of q_0 at the surface is driven by surface mass balances similar to the surface energy balance for temperature. For humidity there are of course no radiation terms, on the other hand there are two interacting balances, one for liquid water and on for water vapor, with a strong dependency on the soil type and its water content, and- if vegetated- on the vegetation types, all with different root systems and different strategies for exchanges with the atmosphere. We shall not dwell further on these complexities in this context. We just notice that if the surface is wet, it all simplifies to that q_0 can be derived from the saturated water pressure at the surface, e_s, where $e_s(\theta_0)$, since at the surface $T_0 = \theta_0$.

2.5 Homogeneous Land ABL

For a flat fairly homogeneous land surface the ABL has a number of characteristics of relevance for the detailed use of the equations and models, described in section 3.

The energy balance at the ground eq. 17 generally results into a significant diurnal and annual cycle of the surface temperature and the thermal stability of the atmosphere with instability during day, and stability during night, and the role of advection is less apparent. With this follows also a tendency to have deep ABLs at day time, following eq. 10 and shallow stable night time ABLs. The diurnal variation of the surface temperature, penetrate down to about half a meter in to the soil, where the amplitude vanishes. Hence only a shallow soil layer, with relatively little heat capacity, is involved in the diurnal heat exchange with the surface- somewhat deeper for the annual scale. For higher wind speeds the stability is often forced towards neutral by the roughness generated turbulence, even with fairly large heat fluxes. From eq. 9 is seen that a given geostrophic wind will result in a larger u_* the larger is the z_0. From eq. 7 is seen that we can write $z/L \sim z\kappa g T_*/u_*^2$, which diminish with increasing u_*. The numerics is such that we will have $z/L \sim$0 for moderately to high wind for characteristic land surface roughness.

The roughness elements of the surface consist mainly of either stone like fragment, ranging from pebbles over boulder and houses, or vegetation ranging from the tiniest to major forests. For a surface of simple roughness elements, one can often use Lettau's formula:

$$z_0 \approx 0.5 \cdot h \cdot S/A, A >> S, \tag{18}$$

where h is the height of the roughness element, S its crosswind area, and $1/A$ is the surface density of roughness elements (Lettau, 1962). For densely placed vegetation, one can often use a simple z_0 proportional to the height, and additionally introduce a so called displacement length, d, also proportional to the height of the vegetation, with different coefficients of proportionality for different types of vegetation fig. 19.

Vegetation based z_0, show some fairly weak variation with wind speed, reflecting that the wind is moving straws, branches and leaves etc. Also some stability variation of z_0 has been proposed, reflecting the structure of turbulent eddies penetrating into the canopy (Zilitinkevich et al., 2009). Further, a clear dependency on the seasonal variation of foliage is found, as in figure 12. For this kind of land roughness, the z_{0T} and z_{0q}, must be expected to be about 10% of the z_0.

Figure 13 points to a seasonal variation associated with snow cover, where such happens. The figure suggests a z_0 value of about 2 mm for a natural snow surface, which could then be the prevailing roughness for such surfaces during wintertime.

2.6 Homogeneous Marine ABL

The marine ABL has distinct features compared to the land ABL. The water is semi transparent meaning that the additional heating and cooling is distributed downwards. Additionally the water has extensive mixing properties. The surface waves and circulation systems, like the Langmuir cells, combined with turbulence give rise to extensive mixing. Additionally, when

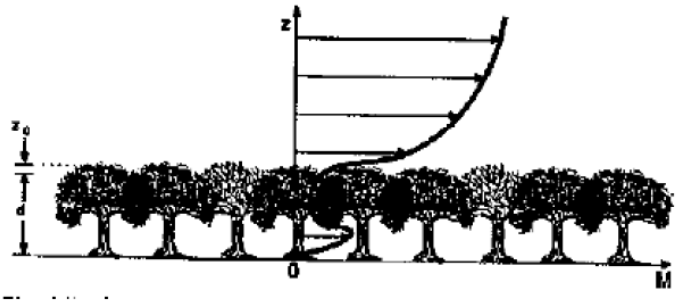

Figure 19: A forest canopy showing displacement height, d, and roughness length z_0 as being proportional to the canopy height. Additionally the wind profile is indicated. Clearly, only the wind above the canopy can be expected to be represented by an ABL profile. The displacement height indicates the ground level for the ABL profile, while the wind inside has to be described by other methods.

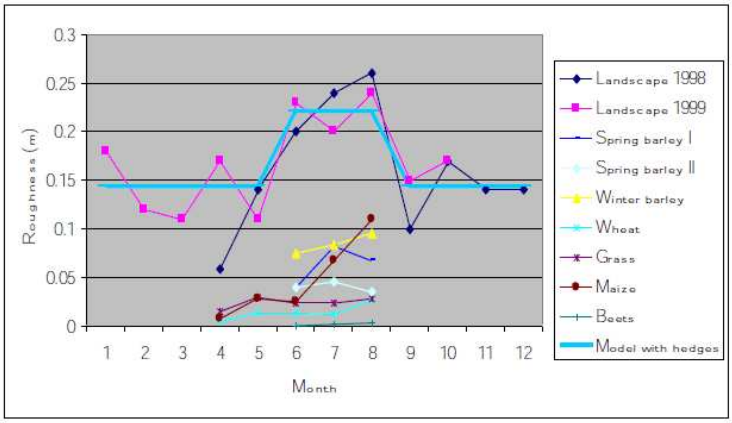

Figure 20: Measurement and modeling of seasonal variation of roughness for different types of vegetated surfaces (Hasager et al., 2003).

heated the surface water evaporates, it will start sinking; now being heavier, because it retains the salt from the evaporated water. If the surface water cools, it also becomes heavier due to the cooling and sinks. All this give rise to an intense mixing in typically the upper 10 meter of the ocean. In the heat exchange with the atmosphere the water therefore constitute a very large heat reservoir that only can change its temperature slowly, and additionally has its own heating and cooling from the ocean currents. Indeed when an air mass moves over an ocean it always ends up at the temperature of the ocean. For these reasons the homogeneous marine ABL is always close to neutral. The diurnal radiation cycle shows very little influence on the water surface temperature, although it can be measured, but typical amplitudes are less than a few tenths of a degree (Peña et al., 2008). The annual radiation cycle on the other hand has significant influence on the sea temperature, because they involve enough heat to change both the temperature and the depth of the mixed layer. However, stable and unstable conditions happens over the ocean as well on shorter timescales, but they are mostly transitional, associated with air masses moving across water surfaces with a different temperature, either coming from a nearby land or associated with moving weather systems. We shall return to these phenomena when coming to the inhomogenous and instationary ABLs.

The sea is also an obvious source of water vapor evaporation, indeed over the ocean since the q_0 is derived from the saturated pressure at the surface temperature. The ocean is also a source of liquid water in the form of sea spray converting to marine aerosols. In wintertime

the spray is the source of icing on ships and offshore structures.

The roughness elements over water mostly take the form of small steep waves of a wave length of around 5 cm, although momentum can be transferred also by larger scale breaking waves. The ocean surface is depicted in fig. 18. Since the roughness is associated with the waves and the waves are generated by the wind and modified by gravity. Charnock (1955) proposed that the roughness should depend on u_* and g. A slightly updated version of the roughness for water looks as the following:

$$z_0 = 0.11\frac{\nu}{u_*} + \beta(c/u_*, -)\frac{u_*^2}{g} \tag{19}$$

Where the first term reflects the molecular diffusion limit, discussed above, when only few roughness elements are present. The coefficient, β, denotes the Charnock's constant. It is a function of the phase speed c of the dominant waves and u_*. Since the roughness elements will be mowing with the phase speed of the waves in the direction of the wind. The term c/u_* is denoted wave age, because c increases with the duration of the acting wind. β is varying between 0.01 and 0.07, being smallest for mid-ocean mature waves with large phase speed. A "typical" value is 0.015. β can be a function of other parameters as well: e.g bottom topography, swells, and very high winds (e.g. hurricanes) resulting in foam covered waters that reduces β further (Makin, 2005).

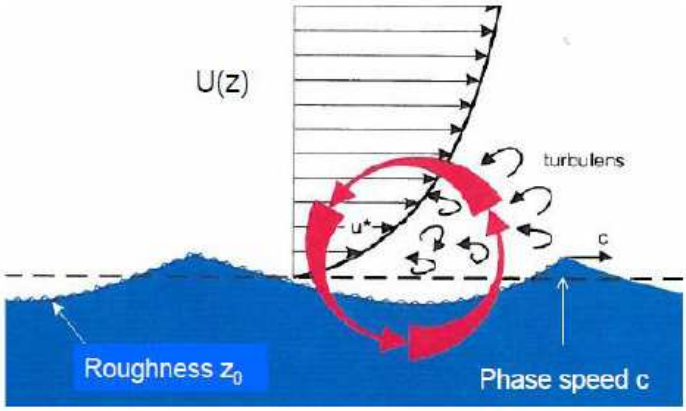

Figure 21: The wind profile close to the water surface, with the wave induced vorticity and the small scale roughness element riding on the larger scale waves, with a phase speed c.

In spite of the functions shown in eq. 19 the roughness of the sea surface still remains one of the smallest, one can encounter in nature. This means that high wind speeds will be less efficient in forcing the stability towards neutral over water than over land, although over water frequency of neutral stability increases with wind speed. Still high winds can be encountered, associated with strongly stable flows over water, again reflecting an inhomogeneous situation where warm air is advected over cold water. Here the friction almost disappears. Again we shall return to this issue. Just as winter snow can modify the roughness of a land surface strongly, the winter will some part of the world cover the water with ice, see again fig. 13, and the roughness now will depend on the characteristics of the ice surface, ranging from extremely low for smooth solid ice, to quite rough for pack ice. The small z_0 also means that the turbulence typically is lower over the water than over land, reflected also in a lower ABL height over water than over land. The small z_0 also means that the z_{0T} and z_{0q} are close to z_0 for low wind speeds, and start deviating only for rough pack ice or larger wind speeds, with rough sea.

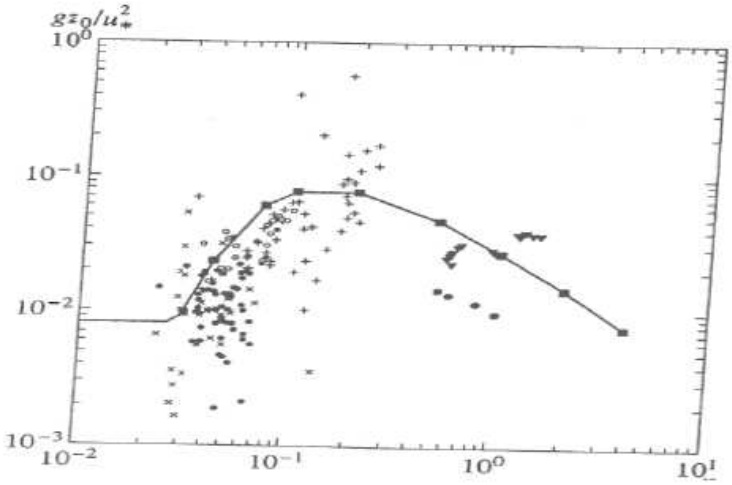

Figure 22: The Charnock's function, β is shown versus reciprocal wave age, u_*/c. Typical wave ages in nature lie between 5 and 30, (Jones et al., 2001)

2.7 Inhomogenous and instationary ABL

No ABL is strictly homogenous and simple models have been developed to handle the inhomogneity to organise the ideas about the complex subject.

Starting with an abrupt roughness change as depicted in fig. 23. Here the wind blows from a surface with one roughness over a surface with another roughness. The stability is neutral. The turbulence associated with the new roughness growths into the upstream boundary layer by diffusion. This new boundary layer is called and Internal Boundary Layer, IBL, because it growths within the already existing boundary layer.

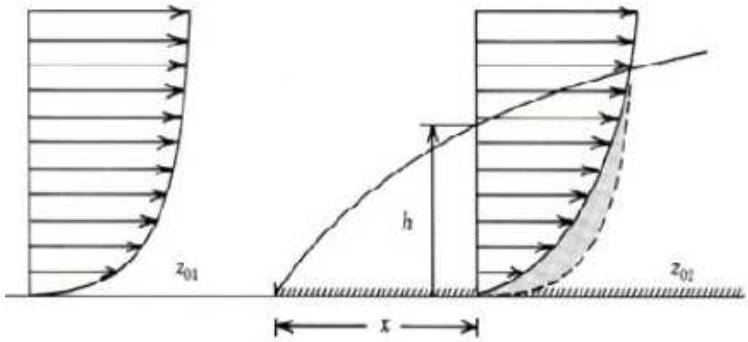

Figure 23: Description of the structure of the internal boundary, of height $h(x)$, due to a step change in terrain roughness. Rule of thumb $h \sim 0.1x$

$$\frac{dh}{dt} = \overline{u}(h)\frac{\partial h}{\partial x} = Au_{*0} \rightarrow \frac{\partial h}{\partial x} = \frac{\kappa A}{\ln(h/z_0)} \rightarrow C_x h \ln(h/z_0) \tag{20}$$

Where we have used that $u(h)$ follows the logarithmic profile. C is found to be about 1. Notice, we measure u_* as u_* at the surface, because u_{*2} must be expect to vary with height in the IBL. The system works for both a smooth- to -rough transition, and the opposite, as long as one uses the largest roughness of the two in the IBL growth equation eq. 18. With $h(x)$ determined in eq. 18, we can find the new surface, the new u_{*2}, matching the upstream and downstream profile at h to yield:

$$\overline{u_1}(h) = \frac{u_{*1}}{k}\ln\left(\frac{h}{z_{01}}\right) = \frac{u_{*2}}{k}\ln\left(\frac{h}{z_{02}}\right) \rightarrow$$

$$\frac{u_{*2}}{u_{*1}} = \frac{\ln\left(\frac{h}{z_{01}}\right)}{\ln\left(\frac{h}{z_{02}}\right)} = \frac{\ln\left(\frac{h}{z_{01}}\frac{z_{02}}{z_{02}}\right)}{\ln\left(\frac{h}{z_{02}}\right)} = 1 + \frac{\ln\left(\frac{z_{02}}{z_{01}}\right)}{\ln\left(\frac{h}{z_{02}}\right)} \equiv 1 + \frac{M}{\ln\left(\frac{h}{z_{02}}\right)} \tag{21}$$

Equation 21 provides a very successful estimate of the ratio between the upstream and downstream u_* values with fetch, x, since $h = h(x)$. Additionally it provides us with a way of characterizing magnitude of roughness changes, through the factor M (in the last term). From eq. 13 we get that the roughness change between a water surface and a smooth land surface with a roughness of 1 cm has the same roughness change magnitude as the roughness change between the same land surface and a city or a major forest. Both roughness changes are associated with a roughness ratio of about 1000. We may also use the results to estimate, how wide a homogenous area that is needed for the assumption about homogeneity, need to be. This is height dependent. The growth rate of the IBL given by eq. 20 is slightly slower than $h = 0.1x$, meaning the measuring height should be less than 10 times the fetch, x, to feel the new IBL. It can show that the height below, which the flow is in approximate equilibrium with the new surface, is about 0.01x, meaning that we will need a homogeneous new fetch of 100 times the measuring height to consider the upstream conditions homogeneous. Under all circumstances the demands to a homogenous fetch, depends on the measuring height. This is one explanation of why it has been found to be more difficult to obtain consistent estimates of the profiles aloft. For example the profiles obtained up to 200 m in fig. 14, demands homogeneous fetches of 20 km to be in equilibrium with the underlaying surface. Uncritically, we could extend the theory to a full ABL, find as a rough estimate we should have a fetch of 100h to have a new equilibrium situation.

From eq. 21 one can estimate also the ratio between the upstream and down stream wind speeds. Unfortunately, the formulation is wrong for very large fetches. Where it predicts the u_*-ratio, it becomes unity, which is not in accordance with the resistance law for a new ABL with the new z_0. Also stability effects are not included. Both deficiencies can be repaired, but the results miss the appealing simplicity of eq. 21, and will not be treated here.

Instead we turn towards the flow over low hills: As the flow approach the hill a pressure perturbation develops, reaching both up-stream and down-stream and breaking the air on the front slope and back slope of the hill and and developing an acceleration on the top of the hill.

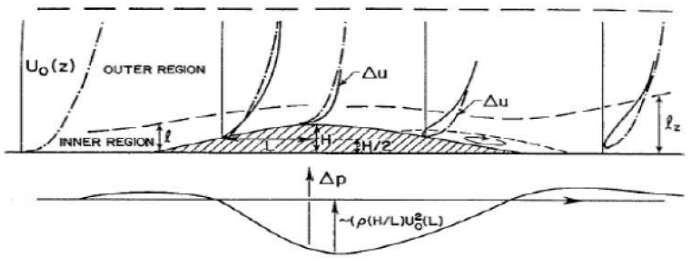

Figure 24: The principles for flow over a low hill according to (Jackson et al., 1975) from (Hunt et al., 1982), with the width, L, the height, H, defined.

The flow over the hill is described for three regions in the vertical. At a height L the pressure perturbation has disappeared, and the flow is undistorted. In the inner region the maximum flow perturbation takes place, while the wind is still forced to zero at the ground. Therefore, this is the region with the largest wind shear. The maximum wind perturbation takes place at the top of the inner layer, and gradually decreases to zero at the height, L. The hight of the

inner layer is of the order of 0.1 L, and the perturbation of the top of the hill, the so-called relative speed up, is found as:

$$\frac{\Delta u}{u_0} \approx 2\frac{H}{L} \tag{22}$$

Troen & Petersen (1989) have developed the theory into a Fourier form, allowing one to build an arbitrary landscape as a superposition of low hills, which when combined with the roughness changes, becomes the model in the WAsP system Troen & Petersen (1989). If the slope becomes too large, of the order of 20%, flow separation develops on both the upstream and the downstream slope.

We next turn towards the situations which are driven by a changing heat flux. Here we start with the diurnal cycle for a horizontally homogeneous area at midlatitude, where the boundary layer show obvious diurnal changes. As we have discussed the changes, they will be smaller if the wind is high, and the atmosphere is cloudy, than when the wind is low and the sky is clear. But it will always be present, and limiting the degree of stationarity one can expect for such a surface. A similar changing rate can be found in frontal passages, which take a time of the order of one day or longer.

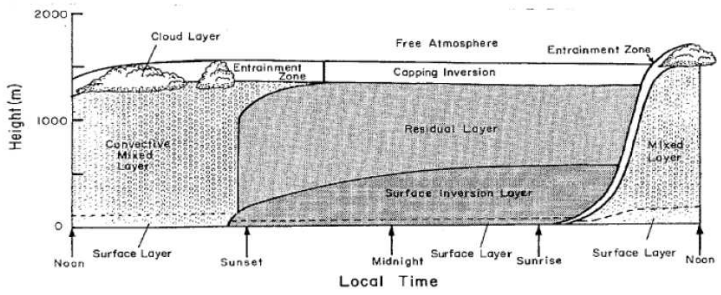

Figure 25: A heat flux driven diurnal change of the ABL for a homogeneous midlatitude land surface (Stull, 1988).

We next turn towards an IBL controlled by the surface heat flux, where the IBL, here denoted TIBL, growths against a stable upstream ABL. Here, we can use the growth of the unstable boundary layer equation in eq. 10, also depicted in fig. 25. Just assuming that the upward heat flux now happens as function of fetch, x, instead of time, inserting $t = u/x$ in eq. 10. A more comprehensive description of these types of models are found in Gryning et al. (1990). The situation can happen for both land and water surfaces, being dependent on differences in surface heat flux and/or surface temperature of the two surfaces involved. However, it is quite easy to imagine, that it is developing at a coast line. Here the surface temperature of the land and the sea is quite often different. Due to the two different surfaces response in the surface energy budget (eq. 17) on a diurnal scale. As the time and space scales for such coastal system increase, the differential heating between two surfaces, will influence the atmospheric dynamics, because air will tend to rise over the relatively warm surface and sink over the colder area. The resulting circulation is called a land-sea breeze system. At night the land cools relatively to the sea, and the flow reverses. The land-sea breeze is the best known one of the breeze systems. However, breeze systems occur also as breeze systems around major cities, because of the "urban heat island" effect. When the spatial scale of a land-breeze system increase to continental scale, one talk about Monsoons, which will typical be seasonal rather than diurnal. However breeze systems of many scales can exist at the same location, and will often interact.

A more complex situation appears for a transition from an unstable ABL passing over a colder surface, where the more intensive unstable ABL has to decay before the stable IBL can establish itself. Also, these situations occur quite often in some coastal areas.

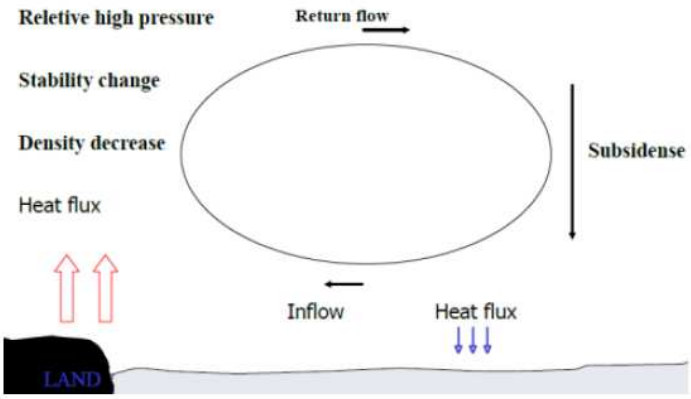

Figure 26: Land-sea breeze system, where a hot land results in rising air, while over the relative cold water air sinks.

Especially the transition from relatively warm unstable/neutral land ABL into a stable IBL over the water (Melas, 1998). Several things happens. The air gradually looses heat to the water and reach the water surface temperature at the interface, where a small neutral layer establishes itself. This neutral layer slowly growths up through the stable IBL, until the original temperature gradient between the two air masses is concentrated at the top of a new boundary layer that however can take many hundred kilometers to establish itself.

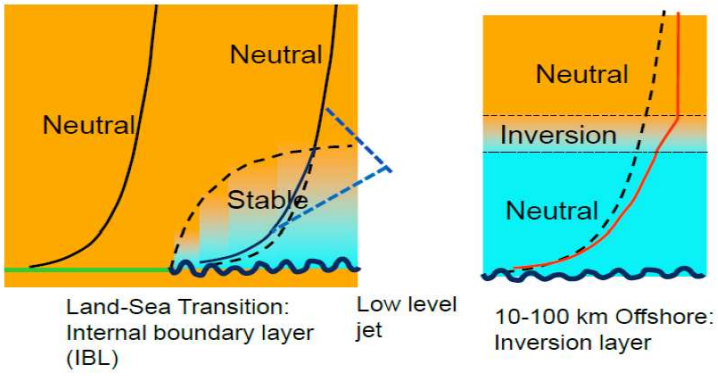

Figure 27: Warm neutral air flowing over cold water, and develops a stable IBL, SIBL, gradually transitioning to a neutral ABL with an inversion on the top. Over the water for off-winds. (Lange et al., 2004). The broken triangular line indicates the possibility for a low level jet at the transition.

A low level jet may happen in the transition between land and water, because the surface friction in the boundary layer suddenly disappears, for the air crossing the coastal line. Considering eq. 1, we see that the wind above the boundary layer is unchanged,friction is unimportant here. The velocity within the ABL must accelerate because the friction is reduced, finally the wind has to go to zero at the surface. It is a transitional phenomenon that gradually disappears as the full profile and stress profile reasserts themselves downstream from the coast line. These low level jets can appears, wherever the surface stress reduces because of increasing stability or decreasing roughness or both. It is quite well known over the nighttime Plains of US, where they are a result of the growing night time stability.

The heat/temperature controlled IBLs may happen also especially over water, when synoptic air masses are advected over relatively cold or warm water. Here especially, the second one, will give rise to a thermally induced convective IBL, which over the water typically will

be associated with mesoscale structures like rolls and cells.

The large scale temperature differences may also influence the basic equation system in eq. 1. In this system only pressure was allowed to change to ensure a pressure gradient and thereby a geostrophic wind. If the large scale temperature is allowed to change horizontally, meaning that T_s and T_a changes together in fig. 11, the simple relation for the geostrophic wind in eq. 3 changes to:

$$G = (U_{1G}, U_{2G}) = (-\frac{1}{f\overline{\rho}}\frac{\partial \overline{p}}{\partial y} - \frac{gz}{f\overline{\rho}}\frac{\partial T_l}{\partial y}, \frac{1}{f\overline{\rho}}\frac{\partial \overline{p}}{\partial x} - \frac{gz}{f\overline{\rho}}\frac{\partial T_l}{\partial x}) \tag{23}$$

In eq. 23 the original G is present at the surface only, and the deviations are seen to increase with z. Also they will influence both the magnitude and the direction of the geostrophic wind for baroclinic situations. Indeed a low level jet can result from this type of baroclinicity as well (Garreaud et al., 2005). The subscript l refers to that the temperature must be considered a layer average. The thermal contribution is often called "The Thermal Wind".

We finally mention coast line changes that firstly happens in the water, but may still influence the air above the water: For deep water coasts, currents and wind may carry the surface water outwards, and upwelling of deeper colder water replaces it closer to the shore. This means that the flow approaching the land is in the process of cooling and developing a stable internal boundary layer over the coastal water, as in fig. 27, before making landfall. A well known example is the Californian west coast upwelling sea- breeze system. For shallow coasts, on the other hand the coastal water reflects the land surface temperature more, because the radiation balance reaches all the way to the bottom. Additional wave breaking may also enhance the mixing through the water of both momentum and heat (Johnson et al., 1999).

2.8 Complex terrain

With complex terrain, we will understand a terrain composed of randomly steep slopes. As we discussed in the former section, we can in the principle model flow over terrain composed of random slopes and roughness changes at least as long as the thermal conditions are less important, (Troen et al., 1989). But if there are too many steep slopes in an area, there are no simple models available for the flow computation. For such work a system RIX, Ruggedness Index (Mortensen et al., 1997) has been developed that compare steepness around a meteorological station, from which the data are extrapolated to potential wind turbines sites, with the steepness of the potential sites. Hereby it has been possible to estimate and reduce the errors of the simple flow models, associated with larger steepness somewhat.

Often the varying terrain will give rise to different temperature fields, and if slopes are additionally of a height that is comparable or larger than a typical boundary layer height, the boundary layer can break down into several different boundary layers, at different levels above ground or in different parts of the terrain. Therefore the diurnal radiation changes will modify different terrain parts differently. fig. 25 show and example of the diurnal change for a simple valley.

At night drainage flow of cold air down the mountains dominates, while a valley wind upslope of the sun heated slopes dominate in the late afternoon. The morning shows upslope flow on the part of the slopes that is reached by the sun, while down slope drainage wind prevails in the valley, not yet reached by the sun. The depth and strength of the flows can vary from deep and strong catabatic flows down stream to high winds upslope, down to shallow weak breezes in both directions. Obviously such flows can also exhibit sharp gradients in all direction as well a remarkable unsteadiness. The detailed flow structure will depend both on the solar input and also on synoptic pressure gradients across the landscape. Again, they depend on the detailed orientation of the slopes of the landscape. Therefore measurements must be recommended combined with modeling if detailed knowledge about such flows is required.

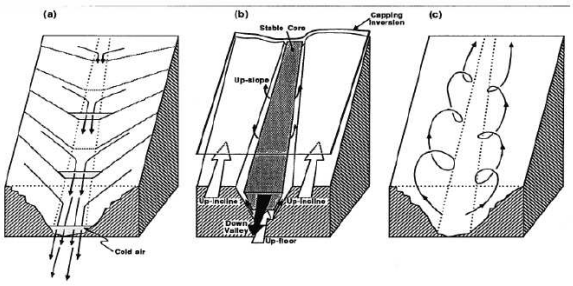

Figure 28: Three dimensional picture of idealized local mountain circulations (a) at night, with cold air drainage, (b) morning with mixed up-and down slope flows, dependent on sun-rise, and (c) afternoon up-slop flow along the sun-heated slopes (Stull, 1988).

2.9 Boundary Layer Climatology for Wind energy

Until now we have discussed the processes controlling the different boundary layer parameters and how the processes and parameters were forced by processes and conditions outside the ABL. The resulting climate at any location develops from a specific local mix of the processes and forcings described above, and must be determined either from measurements or integrated modeling.

It is important to limit the scope of such a climate study, one starts by specifying the focus, which is here offshore wind energy, meaning that one needs sufficient site specific environmental data for wind resource estimation and for establish the external conditions for the design or choice of turbine type. The data base can be established using existing data, new in situ measurements or modeling- or combinations of all these. There will be considerations about "Need to know and nice to know" and about the price and project duration for the different solutions.

For wind resource estimations, data of wind speed and direction distributions at hub height should be available for at least one year, since a year is the longest simple cycle in the climate. Preferably are several years, to account for the known inter-annual variability. Nice to know would be some stability information for comparison with models, since the offshore site is likely to be in a coastal zone for some wind directions, where conditions are influenced by the nearby land. However, pressure and temperature and humidity provide also the air density influencing directly the wind resource.

Next we come to the effort to establish environmental data for design basis and turbine details. The required statistics are summarized in Bredmose et al. (2012) and detailed in the Design Standards (2007-11). For load estimation one needs to establish hub-height distributions of turbulence intensity and shear at the location and estimate extreme values of these parameters see fig. 15.

For an offshore site, also the wave climate has to be established, both with respect to wave height and wave direction. This is not to estimate the roughness, but to estimate the wave loads and combined wind- wave loads on the wind turbine and foundation. The wind and wave extreme load analysis are formulated in terms of return periods of 1 to 100 years, utilizing Gumbel statistics (Bredmose et al., 2012), and in terms of joined distribution for wind and waves.

Some of this information can best be obtained on site, and here the new advances of the LIDAR technology (Peña et al. , 2012) have made it possible, and economically feasible, to have in-situ measurements offshore at larger heights than before, corresponding to the hub-heights today. But aside from the prize of offshore measuring stations, also the necessary project duration for obtaining the long return period makes it necessary to use other data of other types, either long term measurements from nearby sites, that can be model translated to values at the site, or full scale model generated data. This has for some time been used for wave data, and can now be used on wind and other meteorological data as well, with the

progress of mesoscale meteorological models to compute a sufficiently detailed climatology based on a climate from reanalysis data ((Hahmann et al., 2012)). Some available global reanalysis data bases are listed in fig. 29.

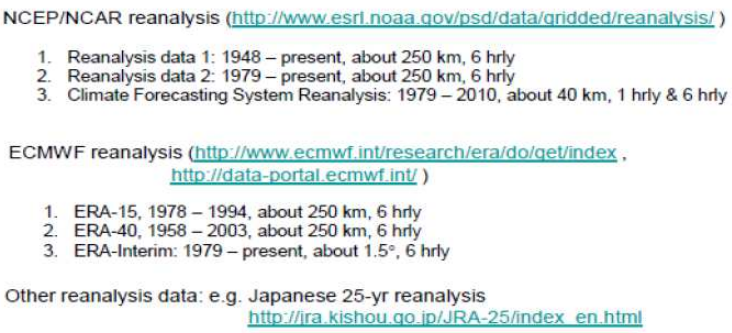

Figure 29: Different reanalysis sets, with start time, and horizontal grid size and time resolution. The vertical resolution corresponds to 20-30 levels.

Stability (temperature and humidity) and other possible data are here again "Nice to know", for the same reasons as for the wind resource estimation.

Finally we mention that it is quite normal that wind farm operators keep a meteorology mast running when the farm has started to operate, both to support the monitoring of the farm performance, and to support the service and maintenance function.

2.10 Summary

We have all most entirely avoided discussions of the different measuring systems in this presentation and concentrated on meteorological climatological aspects.

We have summarized knowledge about atmospheric boundary layers, starting with the simplest ideal form, being statistically stationary and horizontally homogenous. We have thereafter introduced aspect of reality into the picture, considering stability and unstability, typical terrestrial boundary layers and marine boundary layers, and the important points of instationarity and inhomogeneity.

Over land we have seen that stability changes have a clear diurnal cycle, the importance of which becomes the smaller for the boundary layer structure, the higher the wind speed and the larger the cloud cover. On the other hand the thermal properties become more and more important the greater the height within the boundary layer. Over water stability is more associated with advection of air masses than daily variation of insolation. On the other hand high wind does not force the stability towards neutral to the same degree as for the terrestrial boundary layers.

When the surface change, the boundary layer reacts by forming an internal boundary layer. Orography changes, induce a pressure perturbation that reaches out in all directions within a range of the same scale as the width the terrain change. The pressure perturbation also perturbs the oncoming flow. Changes due to roughness and thermal changes on the other hand diffuse into the flow as it moves across the surface. The transition zone for these changes will typically be between 10 and 50 kilometers before a new boundary layer establishes itself as a homogeneous boundary layer. The highest levels in the boundary layer reach equilibrium the latest. The stable internal boundary layer over water for offshore flow takes the longest fetch to reach equilibrium up to more than 100 km, meaning for example that an enclosed sea as the Baltic Sea, with relatively cold water, must be considered entirely coastal.

We find that for complex terrain some general methodologies are possible, but one must expect to have into invest more specific studies for projects within such areas, before having

sufficient information.

Finally, we compare the two regional seas of the region, the Baltic and the North Sea, in the light of the discussion of the ABL in the rest of the manuscript. The main differences are derived from the large scale features of the two seas, The North Sea region with an additional Gulf Stream heat input, is relatively mild coastal maritime climate. This becomes more continental as we move east along the Baltic shore, where the Baltic Sea additionally is fed by colder input. We conclude that there is a high probability of transient stable internal boundary layers over the Baltic Sea. It would be interesting to see it confirmed by independent data and analyses, from the measuring station in the region. Wind-wise the southern Baltic Sea seems very similar to the inner danish waters, but with a larger open high wind area in the center, where winds get closer to the North Sea level.

Notation

A	Coefficient in the resistance laws (6)
	an entrainments coefficient in (10), area (15)
	coefficient of proportionality in (17)
ABL, ASL	Atmospheric Boundary Layer, Atmospheric Surface Layer
α	Power in power law wind profile (9), Geostrophic angle (6)
B	Another coefficient in the resistance laws (6)
β	Charnock's coefficient as function of wave age in (16)
C	Surface heat capacity in (14), coefficient of proportionality in (17)
C_p	The heat capacity at constant pressure for air
c	Phase velocity of surface water waves (16)
δ	Length scale lag-length, height of interfacial layer fig. 17
E	Latent heat flux (14)
$e_s : e_s = e_s(T)$	saturated water vapor pressure in the atmosphere
η	detailed surface height (13)
F	unspecified function used in (11) and in deriving (10)
F	Coriolis paramert (1)
G, U_{1G}, U_{2G}	Geostrophic wind (3)
	Soil energy flux (14)
g	acceleration due to gravity (1)
H	Height of hill (Fig 8), turbulent heat flux (14)
h	height of ABL, and height of IBL (Figs. 11 and 20)
	height of roughness element (15)
IBL	Internal Boundary Layer
κ	von Kármán constant in Monin-Obukhov turbulence description (6)
$< psi(z/L)$	Stability function for profiles (8)
L	Monin-Obukhov stability length scale (7)
	width of the hill (fig. 21)
	heat of evaporation
Γ	The dry adiabatic lapse rate (2)
NR	Net radiation (14)
ν, ν_θ	Molecular viscosity and heat conductivity (13)
ρ	density of air (1)
p	air pressure (1)
q	water vapor mixing ratio defined as density of water vapour/air density,
	surface value of q (1)
q_*	Turbulence scale for q (7)
S	Cross wind area of roughness element (15)
σ	Standard deviation
T	Temperature in K (1)
$T*$	Turbulence scale for T or θ (7)
t	time (1)
θ, θ_0	Potential temperature in K, surface value of θ , (2)
$U_i = u_1, u_2, u_3 = u, v, w$	Three components of the wind velocity
$X_i = x_1, x_2, x_3, = x, y, z$	Three spatial coordinates
z_0, z_{0T}, z_{0q}	Roughness length for u, T and q

References

Andersen, O.J. and J. LÃ¸vseth (2010) Stability modifications of the FrÃ¸ya wind spectrum. *Journ. Wind Engeneering Industrial Aerodynamics, 236-242*

Bodyko, M.I. (1974) Climate and Life. *International Geophysical Series, Vol. 18, Academic Press, New York* **18**:508

Bredmose, H., S.E.Larsen, D. Matha, A. Rettenmeier, E. Marino, L. Saettran (2012) D2.04: Collation of offshore Wind Wave Dynamics. *MARINET Report, EU-FP7 Grant no. 262552, 50p*

Brutsaert, W.H. (1982) Exchange processes at the earth atmosphere interface *Engineering Meteorology, Ed. E. Platte, Elsevier, 319-369*

Charnock H. (1955) Wind stress over a water surface. *Quart. J. Roy. Meteorol. Soc.* **81**:639–640

Design Standards, (2007-2011) IEC 61400-3: Wind turbines- Part 3: Design of offshore wind turbines, 2009 DNV-OJ-J101. OFF SHORE STANDARD: Design of offshore wind turbine structures. DNV, 2007. ABS(American Bureau of Shipping), Offshore Wind Turbine Installation, American Bureau of Shipping, 2010 ABS(American Bureau of Shipping), Design Standards for offshore wind farms, American Bureau of Shipping, 2011 IEC 61400-1, Design requirements, 2008. IEC 61400-1, Design requirements-amendment1, 2010

Garreaud, R. D. and R. Munoz, 2005. The low level jet off the subtropicalwest coast of South America, Structure and Variability. *Monthly Weather Review* **133**:2246-2261

Gryning, S.E. and E. Batchvarova, (1990) Analytical model for the growth of the coastal internal boundary layer during onshore flow. *Quart. J. Roy. Met. Soc.* **116**:187-203

Gryning S.-E., Batchvarova E., Brümmer B., Jørgensen H., and Larsen S. (2007) On the extension of the wind profile over homogeneous terrain beyond the surface layer. *Bound.-Layer Meteorol.* **124**:251–268

Hahmann, A. N., J. Lange, A. Peña and C. Hasager The NORSEWInD numerical wind atlas for the South Baltic *DTU Wind Energy-E-Report-0011(EN)*

Hasager, C.B.; Nielsen, N.,W.; Jensen, N.O.; Bøgh, E.; Christensen, J.H.; Dellwik, E.; Søgaard, G.. (2003) Effective roughness calculated from satellite-derived land cover maps and hedge-information used in a weather forecasting model *Boundary-Layer Meteorology* **109**:227-254

Hunt, J.C.R. and J.E.Simpson, (1982) Atmospheric Boundary Layers over Non-Homogeneous terrain *Engineering meteorology (E.: E. Plate) Elsevier, Amsterdam 269-318*

Håkanson, L. (1991) The Baltic Sea Environment *Session 1: Physical Oceanography of the Baltics. The Baltic University Programme, Uppsala University, Swedem, 35 p*

Højstrup, J., (1982) Velocity spectra in the unstable planetary boundary layer *J. Atmos. Sci.* **39**:2239-2248

Jackson, P.S. and J.R.C. Hunt, (1975) Turbulent wind flow over a low hill *J. Roy. Met. Soc.* **101**:929–955

Jones, I S F, Y Volkov, Y Toba, S Larsen, N Huang, M Donelan (2001) Overview. Chapter 1 *Wind stress over the ocean (Ed. I.S.F.Jones and Y.Toba). Cambridge University Press, 1 - 31.*

Johnson, H K, H.J Vested, H. Hersbach, J HÃ¸jstrup and S E Larsen (1999) The coupling between wind and waves in the WAM model *Journ. Atmos. Ocean. Tech* **16**(11):1780 - 1790

Kaimal, J.C., J.C. Wyngaard, Y. Izumi, and O.R. Cote, (1972) Spectral characteristics of surface-layer turbulence *Quart. J. Roy. Met. Soc., 563–589*

Karagali, I,, A. Peña, M. Badger and C.B. Hasager (2012) Wind characteristics of the North Sea and the Baltic Seas from QuickScatt satellite *Wind Energy*

Lange, B., S.E.Larsen, J. Højstrup and R. Barthelmie, (2004) The influence of thermal effects on the wind speed profile of the coastal marine boundary layer *Boundary-Lay. Meteorol.* **112**:587-617

Larsen, S.E. and Jensen, N.O. (1983) Summary and Interpretation of Some Danish Climate Statistics *Risø-R-399, 76 pp*

Larsen, S.E., N. E. Tarp-Johansen, S. Frandsen and E. R. Jørgensen (1990) Södra Midsjöbanken Environmental Data-Initial analysis *Risø-I-2505. FP6 Integrated project DOWNVInd*

Lettau H. H. (1962) Theoretical wind spirals in the boundary layer of a barotropic atmosphere. *Beitr. Phys. Atmos.* **35**:195–212

Makin, V. K. (2005) A note on the drag of the sea surface at hurricane winds *Boundary Layer Meteorology* **115**:169-175

Mann, J. (1998) Wind field simulation *Prob. Engng. Mech* **14**(4):269-282

Melas, D., (1998) The depth of the stably stratified internal boundary layer over the sea *Geophysical Research Letters* **25**(13):2261-2264

Mortensen, N. G. and E.L. Petersen (1997) Influence of topographical input data on the accuracy of wind flow modeling in complex terrain *European Wind Energy Conference, Dublin, Ireland*

Olesen, H.R., S.E. Larsen, and J. Højstrup, (1984) Modelling velocity spectra in the lower part of the planetary boundary layer *Boundary-Layer Meteorol.* **29**:285–312

Peña A., Gryning S.-E., and Hasager C. B. (2008) Measurements and modelling of the wind speed profile in the marine atmospheric boundary layer. *Bound.-Layer Meteorol.* **129**:479–495

Peña A. and Gryning S.-E. (2008) Charnock's roughness length model and non-dimensional wind profiles over the sea. *Bound.-Layer Meteorol.* **128**:191–203

Peña A., Mikkelsen T., Gryning S.-E., Hasager C. B., Hahmann A. N., Badger M., Karagali I., and Courtney M. (2012) Offshore vertical wind shear. Final report on NORSEWInD's work task 3.1 *DTU Wind Energy-E-Report-005(EN), DTU Wind Energy, Risø, Campus, Roskilde*

Smedman, A-S., H. Bergström and B. Grisogono, (1997) Evolution of stable internal boundary layers over a cold sea *Journ. Geophys. Research* **102**:1091-1099

Stull R. B. (1988) An introduction to boundary layer meteorology, Kluwer Academic Publishers, 666 pp

Tennekes, H. and J.L. Lumley (1972) A first course in turbulence *MIT, Cambridge, Mass. 300p.*

Troen, I. and E.L. Petersen (1989) European Wind Atlas *Risø National Laboratory, Roskilde, Denmark*

Wang, H., R. Barthelmie, S.G. pryor, and H-G. Kim (2012) A new Turbulence model for offshore wind standards *Subm. Geophysical Researh*

Zilitinkevich, S.S. (1972) On the determination of the height of the Ekman boundary layer *Boundary-Layer Meteorol.* **3**:141–145

Zilitinkevich, S.S. (1975) Resistance laws and prediction equations for the depth of the planetary boundary layer *J. Atmos. Sci.* **32**:741–752

Zilitinkevich, S. , I. Mamarella, A. Baklanov and S. Joffre (2009) The effect of Stratefication on the aerodynamic roughness length *Meteorological and Air quality models for urban areas. Springer Berlin*

3 Atmospheric turbulence

Jakob Mann
DTU Wind Energy, Risø Campus, Roskilde, Denmark

3.1 Introduction

For many civil engineering structures, including wind turbines, dynamic wind loading caused by the atmospheric turbulence is a serious concern for the designer. Gust loading on streamlines bridge decks requires knowledge of the vertical wind field fluctuations not only in one point, but also how the fluctuations are correlated in space Simiu and Scanlan (1996); Larose and Mann (1998). Also the horizontal components may be of importance in bridge aerodynamics. For dynamical load calculations on a wind turbine, for example at an off-shore location knowledge of all three wind components and their spatial correlations are needed because the gusts are 'sampled' in a complicated way by the sweeping blades. Yet other structures such as tension leg platforms used for extracting oil on deep waters are sensitive to slow variation in the direction of the wind. Thus various engineering structures are sensitive to various components of wind fluctuations at a wide range of frequencies and also to the spatial correlations of these fluctuations.

The spatial structure of turbulence is also important in order to understand how remote sensing instruments such as lidars measure in a turbulent flow fields. That is because the lidar's sampling volume is rather extended and thus very far from the almost point-like measurements of a ultra-sonic anemometer. The description of how lidars measure turbulence may be found in Mann et al. (2009) for a pulsed lidar, or in Sjöholm et al. (2009) for a continuous wave (cw) lidar.

The purpose of this contribution is to model the *spectral tensor* of neutral atmospheric surface layer turbulence. The spectral tensor contains all information on spectra, cross-spectra and coherences, which usually are the input requested by wind engineers. We also want to devise a general algorithm to simulate three-dimensional fields of all three components of the wind velocity fluctuations. Such simulations are particular useful for time domain simulations of gust loading of wind turbines and other structures.

In section 3.3 rapid distortion theory (RDT) is used to estimate the tendency of shear to make turbulence anisotropic. RDT is a linearization of the Navier–Stokes equations and has as such limited applicability. The influence of the non-linearity is modeled by postulating some limit as to how much shear is allowed to make the turbulence anisotropic. This modelling uses the concept of eddy lifetime. Despite the various assumptions and postulates the tensor model only contains three adjustable parameters: a length scale describing the size of the energy containing eddies, a non-dimensional number used in the parametrization of eddy lifetime, and the third parameter is a measure of the energy dissipation.

These three parameters are estimated by comparing the model to measurements over the sea in section 3.4. In section 3.5 the model is compared to various widely used wind engineering spectral formulations. Finally, in section 3.7 the spectral tensor is used in a numerical algorithm to simulate three-dimensional fields of all three components of the wind vector. This is done by recasting the Fourier representation of the wind field in the discrete wave-vector space, i.e. as a trigonometric series, where the statistics of the random coefficients are determined by the spectral tensor. The method is considerably simpler, faster and in some aspects more physical than many other currently used simulation algorithms. The method is now used in bridge aerodynamics and in load calculations on wind turbines.

Much of the material presented here has previously been reported in Mann (1994, 1998), and more details on many aspects may be found in these papers. Newer comparison with neutral atmospheric data taken from Risø's test station Høvsøre may be found in Peña et al.

(2010) and comparison under different atmospheric stabilities are under way.

3.2 Definitions

The atmospheric turbulent velocity field is denoted by $\tilde{\boldsymbol{u}}(\boldsymbol{x})$, where $\boldsymbol{x} = (x, y, z)$ is a right-handed coordinate system with the x-axis in the direction of the mean wind field and z as the vertical axis. The fluctuations around the mean wind, $\boldsymbol{u}(\boldsymbol{x}) = (u_1, u_2, u_3) = (u, v, w) = \tilde{\boldsymbol{u}}(\boldsymbol{x}) - (U(z), 0, 0)$, are assumed to be homogeneous in space, which is often the case in the horizontal directions but is only a crude approximation in the vertical. Since turbulence over the sea at high wind speeds is primarily shear-generated, the mean wind field is allowed to vary as a function of z. Because of homogeneity, the covariance tensor

$$R_{ij}(\boldsymbol{r}) = \langle u_i(\boldsymbol{x}) u_j(\boldsymbol{x} + \boldsymbol{r}) \rangle \tag{24}$$

is only a function of the separation vector $\boldsymbol{r}$ ($\langle \quad \rangle$ denotes ensemble averaging).

We shall use *Taylor's frozen turbulence hypothesis* to interpret time series as 'space series' and to serve as a 'dispersion relation' between frequency and wave number (Panofsky and Dutton, 1984). Therefore, we can suppress the time argument in $\boldsymbol{u}$.

We only aim at modelling the second order statistics of turbulence, such as variances, cross-spectra, etc. For simulation purposes the velocity field is otherwise assumed to be Gaussian (see section 3.7). It is still not clear how much influence the statistics of third order, such as skewness, has on load calculations.

All second order statistics can be derived from the covariance tensor or its Fourier transform, the spectral tensor:

$$\Phi_{ij}(\boldsymbol{k}) = \frac{1}{(2\pi)^3} \int R_{ij}(\boldsymbol{r}) \exp(-\mathrm{i}\boldsymbol{k} \cdot \boldsymbol{r}) \mathrm{d}\boldsymbol{r}, \tag{25}$$

where $\int \mathrm{d}\boldsymbol{r} \equiv \int_{-\infty}^{\infty} \int_{-\infty}^{\infty} \int_{-\infty}^{\infty} \mathrm{d}r_1 \mathrm{d}r_2 \mathrm{d}r_3$. The spectral tensor is the basis of the Fourier simulation in section 3.7.

The stochastic velocity field can be represented in terms of a generalized stochastic Fourier-Stieltjes integral:

$$\boldsymbol{u}(\boldsymbol{x}) = \int \mathrm{e}^{\mathrm{i}\boldsymbol{k}\cdot\boldsymbol{x}} \mathrm{d}\boldsymbol{Z}(\boldsymbol{k}), \tag{26}$$

where the integration is over all wave number space. The orthogonal process $\boldsymbol{Z}$ is connected to the spectral tensor by

$$\langle \mathrm{d}Z_i^*(\boldsymbol{k}) \mathrm{d}Z_j(\boldsymbol{k}) \rangle = \Phi_{ij}(\boldsymbol{k}) \mathrm{d}k_1 \mathrm{d}k_2 \mathrm{d}k_3, \tag{27}$$

which is valid for infinitely small $\mathrm{d}k_i$ and where * denotes complex conjugation (Batchelor, 1953).

Is it very difficult to measure the spectral tensor directly. Instead cross-spectra, defined as

$$\chi_{ij}(k_1, \Delta y, \Delta z) = \frac{1}{2\pi} \int_{-\infty}^{\infty} R_{ij}(x, \Delta y, \Delta z) \mathrm{e}^{-\mathrm{i}k_1 x} \mathrm{d}x \tag{28}$$

are often measured, say by two instruments separated by Δy in the horizontal direction perpendicular to the wind and Δz in the vertical, and are used in practical applications. The connection between the components of the spectral tensor and the cross-spectra is

$$\chi_{ij}(k_1, \Delta y, \Delta z) = \int_{-\infty}^{\infty} \int_{-\infty}^{\infty} \Phi_{ij}(\boldsymbol{k}) \mathrm{e}^{\mathrm{i}(k_2 \Delta y + k_3 \Delta z)} \mathrm{d}k_2 \mathrm{d}k_3. \tag{29}$$

When the two indices i and j are the same and $\Delta y = \Delta z = 0$ Eq. (29) becomes the one-point spectrum $F_i(k_1) = \chi_{ii}(k_1, 0, 0)$. This definition implies that spectra are *two-sided*, i.e. we get the variance by integrating from $-\infty$ to ∞. This convention is used throughout this chapter.

To distinguish between spectra as functions of wave number k_1 ($= 2\pi f/U$) and frequency f we use F for the former and S for the latter, i.e. $S_i(f)\mathrm{d}f = F_i(k)\mathrm{d}k$. The *coherence* is defined as

$$\mathrm{coh}_{ij}(k_1, \Delta y, \Delta x) = \frac{|\chi_{ij}(k_1, \Delta y, \Delta z)|^2}{F_i(k_1) F_j(k_1)}, \tag{30}$$

which can be interpreted as a normalized cross-spectrum.

3.3 Rapid distortion theory

The incompressible Navier-Stokes equation may be written as

$$\frac{\mathrm{D}\boldsymbol{u}}{\mathrm{D}t} + \boldsymbol{u}\cdot\boldsymbol{\nabla}\ \boldsymbol{U} = -\frac{1}{\rho}\boldsymbol{\nabla}\ p + \text{non-lin. and viscous terms}, \tag{31}$$

where p is the pressure, and $\mathrm{D}/\mathrm{D}t \equiv \partial/\partial t + \boldsymbol{U}\cdot\boldsymbol{\nabla}$ is the 'average Lagrangian derivative.' Assuming a linear shear ($\boldsymbol{\nabla}\ \boldsymbol{U}$ constant), taking the curl, and dropping the non-linear and viscous terms we get

$$\frac{\mathrm{D}\boldsymbol{\omega}}{\mathrm{D}t} = \boldsymbol{\Omega}\cdot\boldsymbol{\nabla}\ \boldsymbol{u} + \boldsymbol{\omega}\cdot\boldsymbol{\nabla}\ \boldsymbol{U}, \tag{32}$$

where $\boldsymbol{\Omega}$ and $\boldsymbol{\omega}$ are the mean and the fluctuating part of the vorticity. It is not at all clear that this linearization is permissible. For example, it can be shown that if the curl of Eq. (31) is used to estimate the change in mean square vorticity the non-linear terms will dominate the linear. However, Hunt and Carruthers (1990) argue that when used for the calculation of the response of velocity fluctuations ($\boldsymbol{u}$ or R_{ij}) to a sudden application of a large scale shearing or straining motion the linearization Eq. (32) is valid.

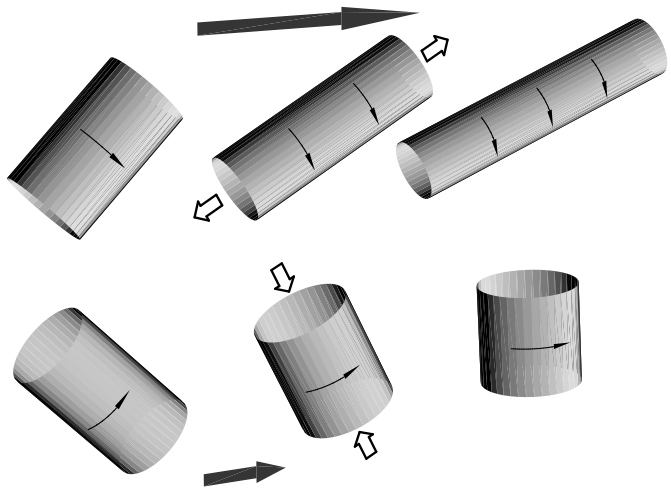

Figure 30: Interpretation of the interplay of shear and turbulence: Two differently oriented eddies are followed over three successive times. Shear stretches (along the axis of rotation) and speeds up the upper eddy while the lower eddy is compressed and slowed down.

Physically, the last term on the right hand side of Eq. (32) may be interpreted as the stretching of vorticity by the mean shear (see Figure 30). The first term is a distortion of the mean vorticity by velocity fluctuations.

In order to solve Eq. (32) we have to Fourier transform the equation. In order to do so, it is important to notice that wave fronts are advected by the mean flow i.e.

$$\frac{\mathrm{d}\boldsymbol{k}}{\mathrm{d}t} = -(\boldsymbol{\nabla}\ \boldsymbol{U})\boldsymbol{k}. \tag{33}$$

The solution to this wave front advection equation is

$$\boldsymbol{k}(t) = \exp(-\boldsymbol{\nabla}\ \boldsymbol{U}t)\boldsymbol{k}_0 \tag{34}$$

where $\exp$ means the matrix exponential.

For a general linear $\boldsymbol{U}$ Eq. (32) does not have analytic solution. However, for many simple situations such as unidirectional shear, non-rotational stretching or compression, etc. such solutions exists (Townsend, 1980).

To get the velocity field from the vorticity we shall express $\mathrm{d}Z$ in terms of $\mathrm{d}\boldsymbol{\Omega}$, which is the Fourier transform of $\boldsymbol{\omega}$ defined in parallel to Eq. (26):

$$\boldsymbol{\omega} = \boldsymbol{\nabla} \times \boldsymbol{u} \Rightarrow \mathrm{d}\boldsymbol{\Omega} = \mathrm{i}\boldsymbol{k} \times \mathrm{d}\boldsymbol{Z} \Rightarrow -\mathrm{i}\boldsymbol{k} \times \mathrm{d}\boldsymbol{\Omega} = \boldsymbol{k} \times (\boldsymbol{k} \times \mathrm{d}\boldsymbol{Z}). \tag{35}$$

Because of the general identity $\boldsymbol{A} \times (\boldsymbol{B} \times \boldsymbol{C}) = \boldsymbol{B}(\boldsymbol{A} \cdot \boldsymbol{C}) - \boldsymbol{C}(\boldsymbol{A} \cdot \boldsymbol{B})$ and that $\boldsymbol{k} \cdot \mathrm{d}\boldsymbol{Z} = 0$ we get

$$-\mathrm{i}\boldsymbol{k} \times \mathrm{d}\boldsymbol{\Omega} = -k^2 \mathrm{d}\boldsymbol{Z} \Rightarrow \mathrm{d}\boldsymbol{Z} = \mathrm{i}\frac{\boldsymbol{k} \times \mathrm{d}\boldsymbol{\Omega}}{k^2}. \tag{36}$$

We shall re-derive (3.11) in Mann (1994), i.e. set up the equations of motion for

$$\boldsymbol{\nabla}\ \boldsymbol{U} = \begin{pmatrix} 0 & 0 & 0 \\ 0 & 0 & 0 \\ \frac{\mathrm{d}U}{\mathrm{d}z} & 0 & 0 \end{pmatrix}. \tag{37}$$

In this case

$$\boldsymbol{k}(t) = \exp(-\boldsymbol{\nabla}\ \boldsymbol{U}t)\boldsymbol{k}_0 = \begin{pmatrix} 1 & 0 & 0 \\ 0 & 1 & 0 \\ -\frac{\mathrm{d}U}{\mathrm{d}z}t & 0 & 1 \end{pmatrix} \boldsymbol{k}_0, \tag{38}$$

in accordance with (3.13) of Mann (1994), and $\boldsymbol{\Omega} = (0, \mathrm{d}U/\mathrm{d}z, 0)$. The equations of motion Eq. (32) becomes

$$\frac{\mathrm{D}\boldsymbol{k} \times \mathrm{d}\boldsymbol{Z}}{\mathrm{D}\beta} = k_2 \mathrm{d}\boldsymbol{Z} + \begin{pmatrix} \mathrm{d}\Omega_3 \\ 0 \\ 0 \end{pmatrix}. \tag{39}$$

Taking the cross product with $\boldsymbol{k}$ and adding $\dot{\boldsymbol{k}} \times (\boldsymbol{k} \times \mathrm{d}\boldsymbol{Z})$ on both sides we get

$$\begin{aligned} -\frac{\mathrm{D}k^2 \mathrm{d}\boldsymbol{Z}}{\mathrm{D}\beta} &= \frac{\mathrm{D}\boldsymbol{k}}{\mathrm{D}\beta} \times (\boldsymbol{k} \times \mathrm{d}\boldsymbol{Z}) + \boldsymbol{k} \times \frac{\mathrm{D}\boldsymbol{k} \times \mathrm{d}\boldsymbol{Z}}{\mathrm{D}\beta} \\ &= \frac{\mathrm{D}\boldsymbol{k}}{\mathrm{D}\beta} \times (\boldsymbol{k} \times \mathrm{d}\boldsymbol{Z}) + k_2 \boldsymbol{k} \times \mathrm{d}\boldsymbol{Z} + \begin{pmatrix} 0 \\ k_3 \\ -k_2 \end{pmatrix} \mathrm{d}\Omega_3. \end{aligned} \tag{40}$$

Writing this more explicitly we get

$$\frac{\mathrm{D}k^2 \mathrm{d}\boldsymbol{Z}}{\mathrm{D}\beta} = \begin{pmatrix} (k_1^2 - k_2^2 - k_3^2)\mathrm{d}Z_3 - 2k_1 k_3 \mathrm{d}Z_1 \\ 2k_1(k_2 \mathrm{d}Z_3 - k_3 \mathrm{d}Z_2) \\ 0 \end{pmatrix} \tag{41}$$

and using $\mathrm{D}k^2/\mathrm{D}\beta = -2k_1 k_3$ from Eq. (38) this can be shown to be equivalent to (3.11) in Mann (1994).

The differential equations Eq. (41) are easily solved given the initial conditions $\boldsymbol{k}(0) = \boldsymbol{k}_0 = (k_1, k_2, k_{30})$ and $\mathrm{d}\boldsymbol{Z}(\boldsymbol{k}_0, 0)$. Instead of time, t, we shall use the non-dimensional time, β, defined as

$$\beta = \frac{\mathrm{d}U}{\mathrm{d}z}t. \tag{42}$$

The solution to Eq. (41) is

$$\mathrm{d}\boldsymbol{Z}(\boldsymbol{k}, \beta) = \begin{bmatrix} 1 & 0 & \zeta_1 \\ 0 & 1 & \zeta_2 \\ 0 & 0 & k_0^2/k^2 \end{bmatrix} \mathrm{d}\boldsymbol{Z}(\boldsymbol{k}_0, 0), \tag{43}$$

where

$$\zeta_1 = \left[C_1 - \frac{k_2}{k_1} C_2 \right] \quad , \quad \zeta_2 = \left[\frac{k_2}{k_1} C_1 + C_2 \right] \tag{44}$$

with

$$C_1 = \frac{\beta k_1^2 (k_0^2 - 2k_{30}^2 + \beta k_1 k_{30})}{k^2 (k_1^2 + k_2^2)} \tag{45}$$

and

$$C_2 = \frac{k_2 k_0^2}{(k_1^2 + k_2^2)^{\frac{3}{2}}} \arctan \left[\frac{\beta k_1 (k_1^2 + k_2^2)^{\frac{1}{2}}}{k_0^2 - k_{30} k_1 \beta} \right]. \tag{46}$$

Eqs. (38) and (43) give the temporal evolution of individual Fourier modes.

3.3.1 RDT and surface layer turbulence

In this section we first discuss the connection between RDT and stationary surface-layer turbulence, then the key concept of eddy lifetime, and finally we combine the different parts to obtain the spectral tensor model. The theory in the previous section describes how turbulence react to a sudden and fast application of a linear shear. It is natural to ask what this has to do with turbulence in the surface layer over the ocean.

If the initial conditions can be represented by the isotropic von Kármán tensor,

$$\Phi_{ij}(\boldsymbol{k}) = \frac{E(k)}{4\pi k^4}\left(\delta_{ij}k^2 - k_i k_j\right), \tag{47}$$

with the energy spectrum

$$E(k) = \alpha\varepsilon^{\frac{2}{3}}L^{\frac{5}{3}}\frac{(Lk)^4}{(1+(Lk)^2)^{\frac{17}{6}}}, \tag{48}$$

then the tensor $\Phi_{ij}(\boldsymbol{k},t)$ will become more and more 'anisotropic' with time.

The linearization implied by RDT is unrealistic, and at some point (in time) the stretched eddies will break up. We postulate that eddies of linear dimension $\approx |\boldsymbol{k}|^{-1}$ (or more precisely the Fourier modes) are stretched by the shear over a time which is proportional to their lifetime. The lifetime τ is

$$\tau(k) \propto \varepsilon^{-\frac{1}{3}}k^{-\frac{2}{3}} \tag{49}$$

pertaining, at least in the inertial subrange, to eddies with wave vector magnitude $k = |\boldsymbol{k}|$ (Landau & Lifshitz 1987, § 33).

The basic *postulate* is that the *stationary* spectral tensor

$$\Phi_{ij}(\boldsymbol{k}) \equiv \Phi_{ij}\left(\boldsymbol{k}, \tau(k)\right) \tag{50}$$

describes the surface layer turbulence well. The combination of RDT and scale dependent eddy lifetimes has previously been used by Derbyshire and Hunt (1993).

Maxey (1982) has described a similar model with the exception that the lifetime τ was assumed to be constant for all wavevectors. ($\tau \mathrm{d}U/\mathrm{d}z$ is called 'the equilibrium value of the effective distortion strain' by Maxey.) Maxey's model gives a reasonable, but not perfect, description of the ratios between σ_u^2, σ_v^2, σ_w^2 and $\langle uw\rangle$ for turbulent shear flows. There are, however, two grave drawbacks when the model of Maxey (1982) is used to calculate spectra:

1. The uw-cross-spectrum in the inertial subrange decays as $k_1^{-\frac{5}{3}}$ whereas Wyngaard & Coté (1972) observe and give scaling arguments for $k_1^{-\frac{7}{3}}$.
2. For typical values of the effective distortion strain the model predicts $F_u/F_w \approx 7$ in the inertial subrange whereas it should be $F_u/F_w = \frac{3}{4}$.

The models presented here do not suffer from these shortcomings.

3.3.2 Eddy lifetimes

At scales larger than the inertial subrange Eq. (49) is not necessarily valid. We construct an alternative model for the 'eddy lifetime' assuming that the destruction of an eddy with size k^{-1} is mainly due to eddies comparable to or smaller than k^{-1}. The characteristic velocity of these eddies may be written as $\left(\int_k^\infty E(p)\mathrm{d}p\right)^{\frac{1}{2}}$, and we simply assume the lifetime to be proportional to the size k^{-1} divided by this velocity:

$$\begin{aligned}\tau(k) &\propto k^{-1}\left(\int_k^\infty E(p)\mathrm{d}p\right)^{-\frac{1}{2}} \\ &\propto k^{-\frac{2}{3}}\left[{}_2F_1\left(\frac{1}{3},\frac{17}{6};\frac{4}{3};-(kL)^{-2}\right)\right]^{-\frac{1}{2}} \propto \begin{cases} k^{-\frac{2}{3}} & \text{for } k\to\infty \\ k^{-1} & \text{for } k\to 0\end{cases}\end{aligned} \tag{51}$$

where we have chosen E as the von Kármán energy spectrum Eq. (48) and where ${}_2F_1$ is the hypergeometric function.

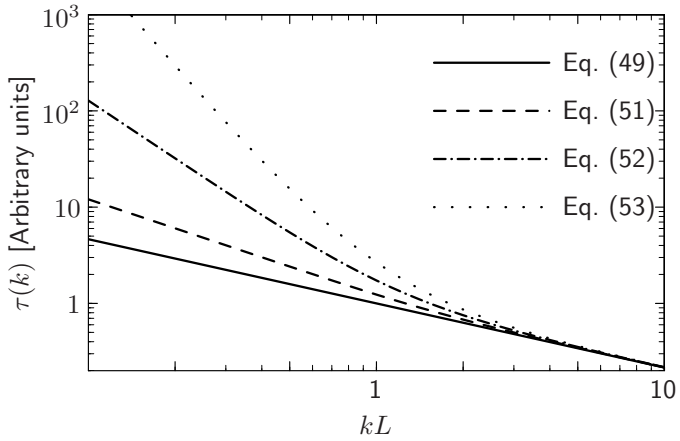

Figure 31: Eddy lifetimes as functions of the magnitude of the wave vector. The lifetimes given by Eq. (51) give the most realistic results.

Comte-Bellot and Corrsin (1971) give another lifetime model which has the right asymptotic behaviour for $k \to \infty$, the 'coherence-destroying diffusion time' :

$$\begin{aligned} \tau_D(k) &\propto k^{-2}\left[\int_k^\infty p^{-2}E(p)\mathrm{d}p\right]^{-\frac{1}{2}} \\ &\propto k^{-\frac{2}{3}}\left[{}_2F_1\left(\frac{4}{3},\frac{17}{6};\frac{7}{3};-(kL)^{-2}\right)\right]^{-\frac{1}{2}} \propto \begin{cases} k^{-\frac{2}{3}} & \text{for } k\to\infty \\ k^{-2} & \text{for } k\to 0 \end{cases} \end{aligned} \tag{52}$$

which was constructed as the square of the eddy size divided by a k-dependent 'turbulent viscosity'.

Further, the inverse 'eddy-damping rate'

$$\tau_E(k) \propto \left(k^3E(k)\right)^{-\frac{1}{2}} \propto \begin{cases} k^{-\frac{2}{3}} & \text{for } k\to\infty \\ k^{-\frac{7}{2}} & \text{for } k\to 0 \end{cases} \tag{53}$$

is used by Lesieur (1987) in eddy-damped quasi-normal theories of turbulence as a characteristic non-linear relaxation time.

All lifetime models are shown in Figure 31 normalized such that they coincide in the inertial subrange. It turns out that σ_u^2 becomes infinite using Eq. (52) or (53), while Eq. (49) and (51) give reasonable results. It also turns out that the spectra calculated from Eq. (51) fit the data better than Eq. (49) for which reason Eq. (51) is used in the rest of this chapter. Some support for Eq. (51) may be found in Panofsky, Larko, Lipschutz, Stone, Bradley, Bowen and Højstrup (1982) who measured eddy 'response times' of eddies in the neutral atmospheric surface-layer. Also Kristensen and Kirkegaard (1987) were in their theoretical model of the growth of a puff in a turbulent fluid compelled to use Eq. (51) rather than Eq. (52) or (53).

It is convenient to write Eq. (51) as

$$\tau(k) = \Gamma\left(\frac{\mathrm{d}U}{\mathrm{d}z}\right)^{-1}(kL)^{-\frac{2}{3}}\left[{}_2F_1\left(\frac{1}{3},\frac{17}{6};\frac{4}{3};-(kL)^{-2}\right)\right]^{-\frac{1}{2}}, \tag{54}$$

where Γ is a parameter to be determined. [1]

It should be emphasized that at low wave numbers the assumptions made so far are not valid. F.ex. the assumptions of linear shear is only valid over small distances, i.e. for large k. Similarly, homogeneity is a dubious assumption for large vertical separations. Finally, despite

[1] Keith Wilson has reformulated this expression in terms of the incomplete beta function.

talking about eddy lifetimes, there is no real modelling of the decay process, because there is no equation describing the non-linear transfer of energy among various wave vectors.

In an attempt to relax the assumption of vertical homogeneity Mann (1994) modelled the influence of the blocking of the surface in addition to shear. This gave slightly better coherence predictions than the present model, but greatly complicated the mathematics and had also other negative consequences.

3.3.3 The uniform shear model

To make a stationary model we use Eqs. (54) and (50) discussed in the beginning of this section, i.e. we substitute t with τ given by Eq. (54). For the 33-component we get

$$\Phi_{33}(\boldsymbol{k}) = \Phi_{33}^{\text{iso}}(\boldsymbol{k}_0)\frac{k_0^4}{k^4} = \frac{E(k_0)}{4\pi k^4}(k_1^2 + k_2^2), \tag{55}$$

where Φ_{33}^{iso} refers to the isotropic von Kármán tensor and E to the energy spectrum Eq. (48). The other components become

$$\Phi_{11}(\boldsymbol{k}) = \frac{E(k_0)}{4\pi k_0^4}\left(k_0^2 - k_1^2 - 2k_1k_{30}\zeta_1 + (k_1^2 + k_2^2)\zeta_1^2\right) \tag{56}$$

$$\Phi_{22}(\boldsymbol{k}) = \frac{E(k_0)}{4\pi k_0^4}\left(k_0^2 - k_2^2 - 2k_2k_{30}\zeta_2 + (k_1^2 + k_2^2)\zeta_2^2\right) \tag{57}$$

$$\Phi_{12}(\boldsymbol{k}) = \frac{E(k_0)}{4\pi k_0^4}\left(-k_1k_2 - k_1k_{30}\zeta_2 - k_2k_{30}\zeta_1 + (k_1^2 + k_2^2)\zeta_1\zeta_2\right) \tag{58}$$

$$\Phi_{13}(\boldsymbol{k}) = \frac{E(k_0)}{4\pi k_0^2 k^2}\left(-k_1k_{30} + (k_1^2 + k_2^2)\zeta_1\right) \tag{59}$$

and

$$\Phi_{23}(\boldsymbol{k}) = \frac{E(k_0)}{4\pi k_0^2 k^2}\left(-k_2k_{30} + (k_1^2 + k_2^2)\zeta_2\right). \tag{60}$$

Eqs. (55)–(60) with Eq. (54) constitute the uniform shear model (US).

These equations have two differences from the expressions of Townsend (1976) for plane shearing of homogeneous turbulence. The first is the elimination of time by Eq. (54) and the second and related difference is that we do not use the turbulent viscosity of Townsend, which would make the decay time for all eddies equal, independent of their sizes.

3.4 Fitting spectra to observations

First the uncertainties on estimated spectra are discussed. Theses are either caused by variations in atmospheric stability, which persists even at high wind speeds (> 16 m s^{-1}) over water, or by statistical variations. Secondly, the measured neutral spectra are fitted to the spectral tensor model. Based on this fit the coherences are finally predicted and compared to the measurements.

3.4.1 Uncertainties on spectra

Often spectra are averaged over, say, n consecutive frequencies or wave numbers to decrease the random error of the estimate. Alternatively, the time series could be divided into n segments of equal duration. Each segment is then Fourier transformed and the spectrum determined as the average of the absolute square of these Fourier transforms. For either definition the statistical uncertainty on spectral density F calculated from a stationary time series is (under the assumption that the time series is long compared to the time scale of the process)

$$\frac{\sigma(F)}{\langle F\rangle} = \frac{1}{n^{\frac{1}{2}}} \tag{61}$$

(Koopmans, 1974; Bendat and Piersol, 1986).

Figure 32 shows the result of an analysis of 14 two-hour time series from the Great Belt. The series have mean speeds U between 16 and 20 m s^{-1} and the mean directions are within a narrow range around south where there is an uninterrupted fetch over water for at least 20 km.

Assuming the stability to be neutral, the variation of spectral densities should obey Eq. (61) and the standard deviation at the lowest wavenumbers should be around 25% and 5% at $k_1 = 0.1$ m^{-1}. The observed rms variations are clearly larger, at least 50% at the lowest frequencies and maybe 20% at higher frequencies. Most noticeably, there are spectra with only 10% of the spectral density of the others.

This variation is due to the stability of the atmosphere not being neutral. The case with suppressed turbulence is slightly stable and has $U = 16$ m s^{-1}. From the point of view of aerodynamic loads this may imply enhanced loads on a bridge deck. While the buffeting loads are smaller the loads from vortex shedding can be much larger. Usually vortex shedding from a bridge deck is suppressed or even destroyed by the turbulence in the atmosphere, but if turbulence is absent as in a stably stratified atmosphere (e.g. warm air flowing out over a cold sea) the vortex shedding might be strong. Stable stratification might also alter loads on off-shore wind turbines because of increased shear.

Unstable stratification also alters the spectrum. Though none of the spectra from the Great Belt are obtained under very unstable situations, an analysis of unstable, high-wind spectra on the west coast of Norway indicate that the spectra are mainly enhanced (by more than 100%) at *very* low frequencies ($f < 0.02$ Hz). These might be relevant for various off-shore production units (Mann, 1992).

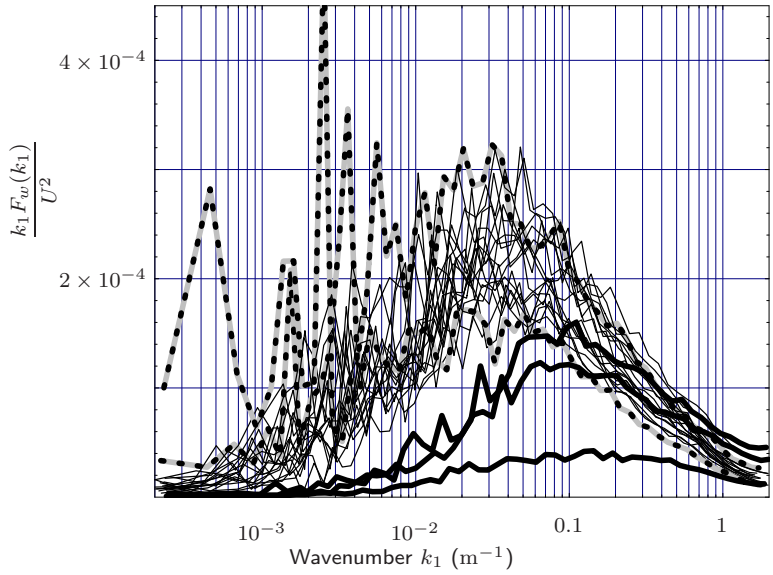

Figure 32: Spectra of w from the Great Belt Coherence Experiment. Mean wind speeds are between 16 and 20 m s^{-1} and directions are in a narrow interval around the South. Dashed spectra have slightly unstable stratification, gray have stable, and the thin have neutral.

3.4.2 Spectral fitting and prediction of coherences

In order to conduct simultaneous measurements of spectra and coherence over the sea a 70 m high mast was erected 40 m from an existing mast on the easterly spit of Sprogø, an island in the midst of the Great Belt separating the two Danish islands Funen and Zealand. A 15 m long horizontal boom was mounted symmetrically at the top of the new mast so that the whole construction has the form of a letter "T". A Kaijo-Denki DAT-300 omni-directional sonic

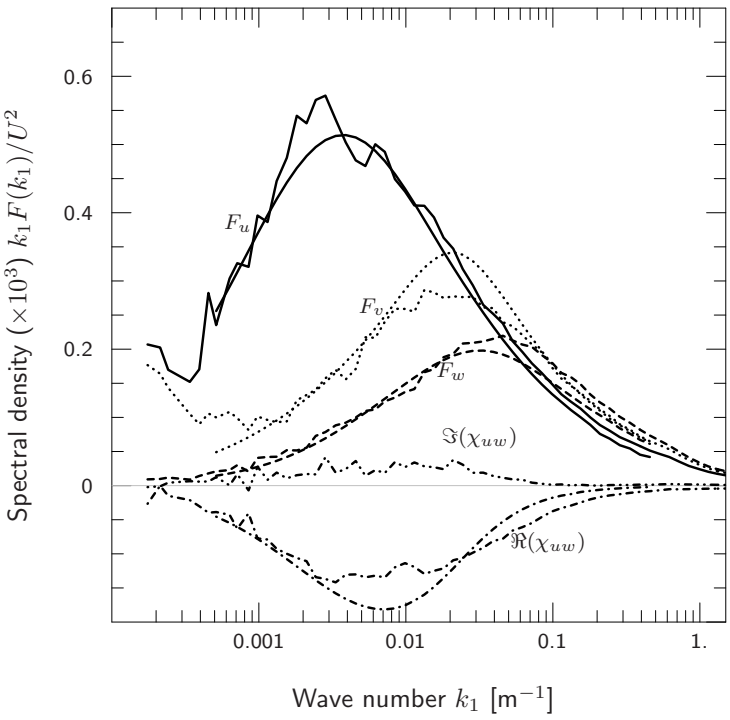

Figure 33: Average u-, v-, w-, and cross-spectra of all the *neutral* runs present in Figure 32. The ragged curves are measurements while the smooth are the model spectra. The model has zero imaginary part of the cross-spectrum (quadrature spectrum).

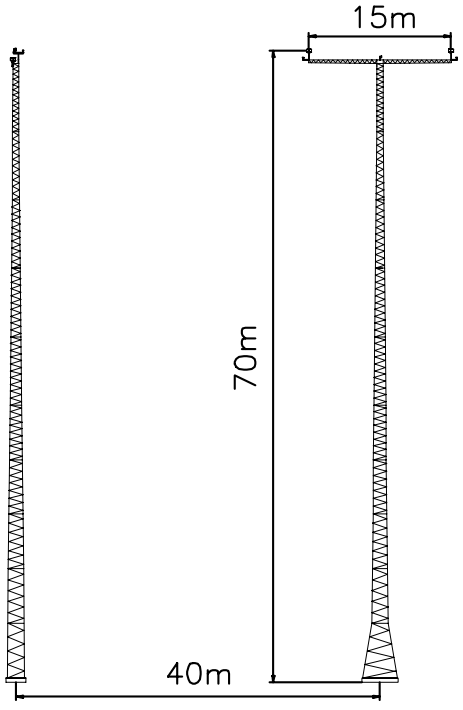

Figure 34: The mast array on Sprogø viewed from SSE. The tiny dots at the top of the masts are the omni-directional sonic anemometers.

anemometer was installed at each end of the boom and at the top of the old mast, providing 15.0, 32.5 and 47.5 m horizontal separations between the three co-linear instruments. The mast array is shown in Figure 34. More details about the experiment including correction for flow distortion by the sonic anemometers may be found in Mann et al. (1991).

The measured spectra shown in Figure 33 are an average of 16 *neutral* two hour runs with wind speeds between 16 and 20 m s^{-1}. The smooth curves are model spectra derived from the spectral tensor model with the parameters $\Gamma = 3.2$, $L = 61$ m, and $\alpha\varepsilon^{2/3}/U^2 = 1.810^{-4}$ $m^{-2/3}$, which are taken from Mann (1994), who used fewer two hour runs but slightly higher wind speeds.

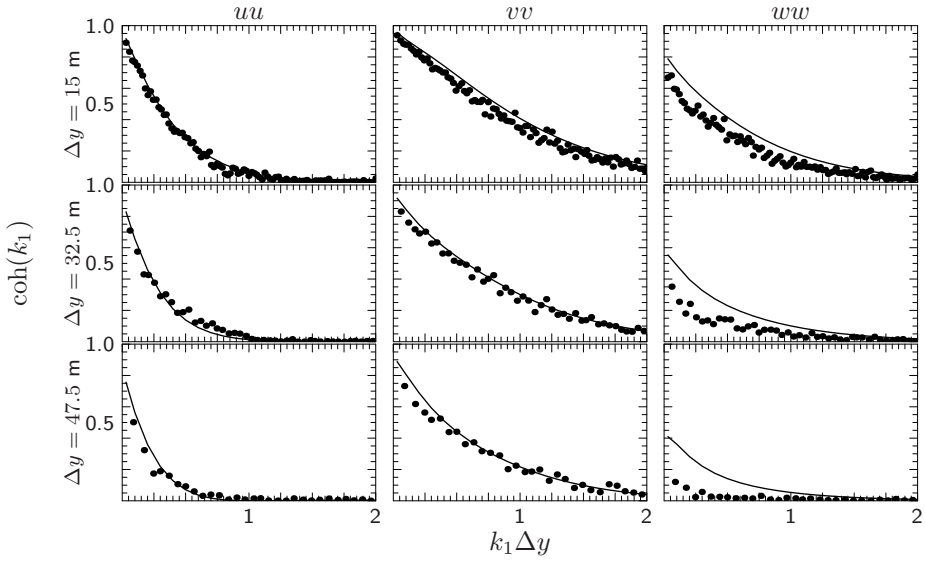

Figure 35: The dots are measured coherences from the same set of data as used for Figure 33 for various horizontal separations Δy and for all three velocity components. The lines are the coherences predicted by the model.

These parameters are in turn used to predict the coherences as shown in Figure 35. As seen from this figure the predictions agree well with the measurements except for the w coherence, especially at the largest separation.

3.5 Model spectra over the ocean and flat land

Here we compare the tensor model of section 3.3.1 to spectra and coherences from the literature. We will not give an exhaustive review of spectral models but select a few modern models which the author believes is used in wind engineering. The purpose is to estimate the parameters Γ, L and $\alpha\varepsilon^{2/3}$ for a given mean wind speed U and height above the water surface z.

The logarithmic mean wind profile defines the roughness length:

$$U(z) = \frac{u_*}{\kappa}\ln(z/z_0), \tag{62}$$

where $u_* \equiv (-\langle uw\rangle)^{1/2}_{z\to 0}$ is the friction velocity and $\kappa = 0.40$ the von Kármán constant (Landau and Lifshitz, 1987; Panofsky and Dutton, 1984).

ESDU International (1982) gives a slightly more accurate wind profile:

$$U(z) = \frac{u_*}{\kappa}\left(\ln(z/z_0) + 34.5fz/u_*\right) \tag{63}$$

with the Coriolis parameter $f \equiv 2\Omega\sin\phi$, where Ω is the angular velocity in rad s^{-1} of the Earth and ϕ the geographical latitude. The profile Eq. (63) is valid up to $z = 300$ m, below

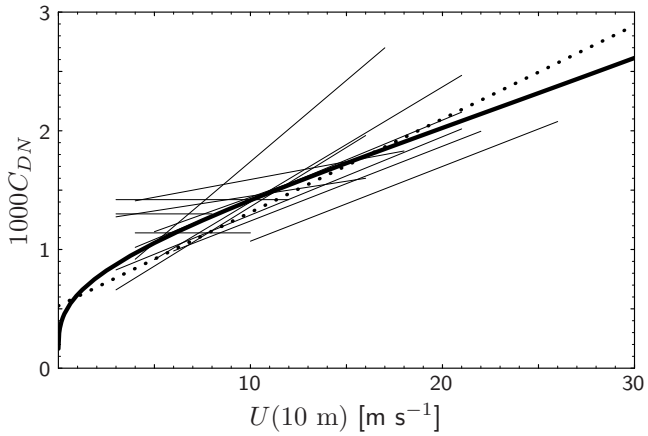

Figure 36: The neutral drag coefficient C_{DN} as a function of mean wind speed at $z = 10$ m. The broad line is from Charnock's relation Eqs. (64) and (62). The thin lines are empirical relations from Geernaert (1987) and the dotted line is from NDP (1998), see Eq. (73).

30 m Eq. (62) is a good approximation to Eq. (63). Throughout this comparison we use $f = 10^{-4}$ s^{-1}.

Charnock (1955) argued that over the sea the roughness length is related to $g = 9.8$ m s^{-2} the acceleration due to gravity and the friction velocity by

$$z_0 = A\frac{u_*^2}{g} \tag{64}$$

where A, the Charnock constant, must be determined experimentally. On basis of an extensive literature study of ocean data Garratt (1977) found that the best fit of Eq. (64) is $A = 0.0144$. A slightly newer value is given by ESDU International (1982):

$$A = 0.0167, \tag{65}$$

which will be used here. Over the ocean the neutral drag coefficient

$$C_{DN} = \left(\frac{u_*}{U(10\ \mathrm{m})}\right)^2 \tag{66}$$

increases monotonicly with U as can be seen by solving Eqs. (64) and (62). This is shown in Figure 36 as a broad line together with several recent empirical relations. The figure gives a good impression of the uncertainty in estimates of drag coefficients. Among the various reasons for this variability are atmospheric stability, surface currents, 'wave age', length of the fetch over water, and water depth (Garratt, 1977; Geernaert, 1987; Brown and Swail, 1991). The spectral density of velocity fluctuations is in general proportional to the drag coefficient so the uncertainty of the former is probably of the same order of the latter.

3.5.1 Code and textbook spectra

Surface layer scaling is used in many spectral models, implying that length scales are proportional to z and that variances are proportional to u_*^2. Therefore, it is convenient to normalize the spectra with u_*^2 and present them as functions of either $n \equiv fz/U$ or $k_1 z$. All spectra in this paper are 'two-sided' implying $\int_{\infty}^{-\infty} S(f)\mathrm{d}f$ is equal to the variance[2].

The spectra of Kaimal are (Kaimal et al., 1972; Kaimal and Finnigan, 1994)

$$\frac{fS_u(f)}{u_*^2} = \frac{k_1 F_u(k_1)}{u_*^2} = \frac{52.5n}{(1+33n)^{5/3}}, \tag{67}$$

$$\frac{fS_v(f)}{u_*^2} = \frac{8.5n}{(1+9.5n)^{5/3}}, \tag{68}$$

[2]The so-called 'one-sided' spectra, where $\int_0^{\infty} S(f)\mathrm{d}f$ is equal to the variance, are probably more commonly used.

and

$$\frac{fS_w(f)}{u_*^2} = \frac{1.05n}{1+5.3n^{5/3}}. \tag{69}$$

Kaimal's spectra are based on measurements over flat homogeneous terrain in Kansas.

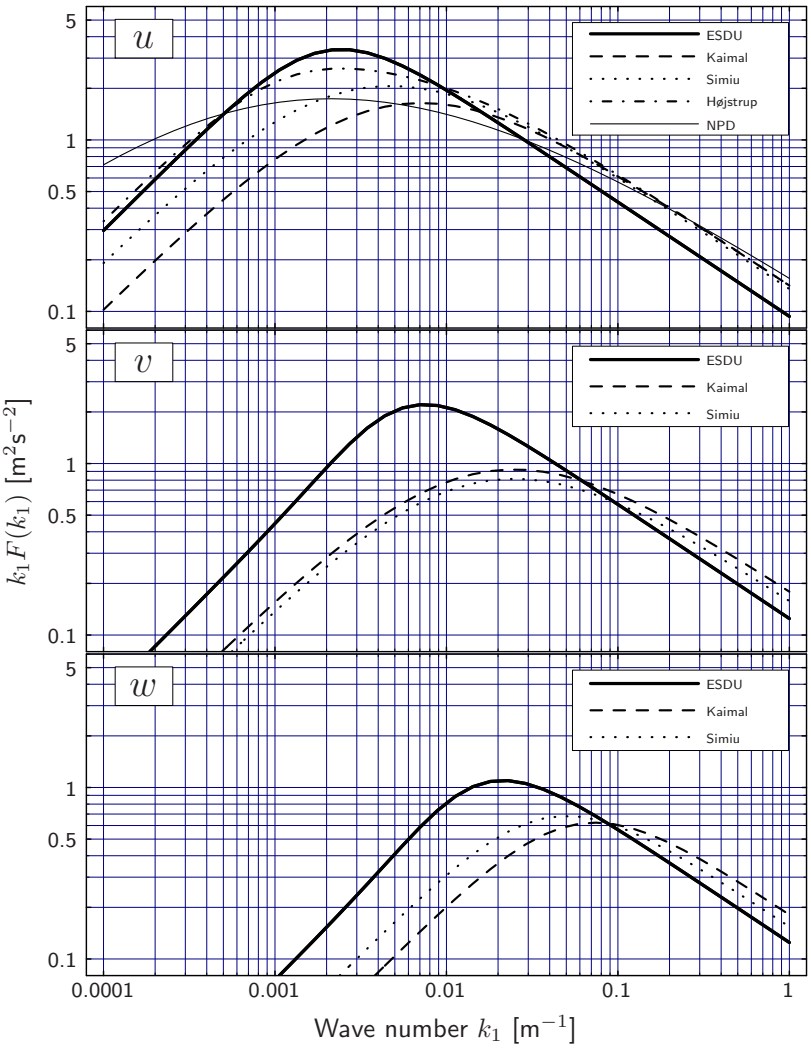

Figure 37: Comparison of spectral models. For the comparison $z = 40$ m and $U = 40$ m s^{-1} (over the sea) is chosen. For u (ESDU International, 1985), Eqs. (67), (70), (80), (76) are used. For v and w (ESDU International, 1985), Eqs. (68) and (71), and (ESDU International, 1985), Eqs. (69) and (72), respectively. Eq. (63) together with Eq. (64) gives $u_* = 1.78$ m s^{-1} and $z_0 = 0.0054$ m.

The spectra of Simiu and Scanlan (1996) have the same functional shapes as Kaimal's but the numerical constants are different:

$$\frac{fS_u(f)}{u_*^2} = \frac{100n}{(1+50n)^{5/3}}, \tag{70}$$

$$\frac{fS_v(f)}{u_*^2} = \frac{7.5n}{(1+9.5n)^{5/3}}, \tag{71}$$

and

$$\frac{fS_w(f)}{u_*^2} = \frac{1.68n}{1+10n^{5/3}}. \tag{72}$$

Deviations from surface layer scaling are found in the model spectra from ESDU International (1985). Also the spectra of Norwegian Petroleum Directorate NDP (1998) and Højstrup,

Larsen and Madsen (1990) do not obey surface layer scaling, but they are only limited to u-spectra.

The Engineering Science Data Unit (ESDU) wind profile, spectra and coherences (ESDU International, 1982, 1985 and 1986) are derived from many sources from all over the world during several decades. ESDU proposes that the turbulence intensities and length scales in the surface layer are dependent on mean wind speed. The argument is that the boundary layer depth increases with increasing wind speed implying larger scales of the turbulence. The other models, relying on surface layer scaling do not contain any information on the boundary layer depth and they contain no explicit reference to the mean wind speed. The equations of ESDU are, compared to all other spectral models discussed here, by far the most complicated. Therefore we shall not cite them explicitly. The most important input parameters are, as for the other spectral models, the height above the surface z, and the mean wind speed at some height. Of less important input is the Coriolis parameter which, as mentioned previously, is taken to be $f = 10^{-4}$ s^{-1}. The models we use are valid for the neutral atmosphere.

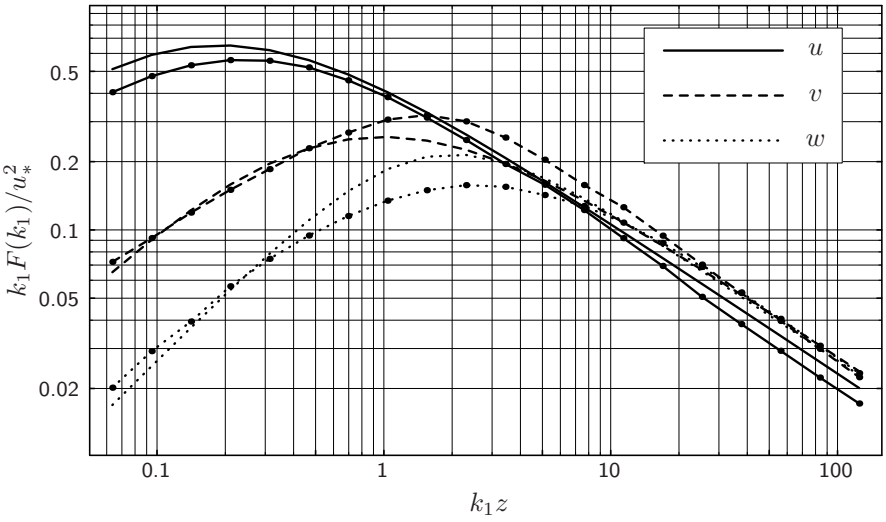

Figure 38: The 'sheared spectral tensor' of section 3.3.1 (curves with dots) fitted to the models by Simiu and Scanlan Eqs. (70)–(72). The result is given by Eq. (83).

The u-spectrum of NDP (1998) applies to winds over oceans and assumes the drag coefficient to be

$$C_{DN} = 0.525 \times 10^{-3}(1 + 0.15U_{10}), \tag{73}$$

see Figure 36. Integrating $\mathrm{d}U/\mathrm{d}z = u_*/(\kappa z) = \sqrt{C_{DN}}U_{10}/(\kappa z)$ Eq. (73) implies that

$$U(z) = U_{10}\left(1 + C\ln\frac{z}{10\ \mathrm{m}}\right) \tag{74}$$

with

$$C = 0.0573(1 + 0.15U_{10})^{1/2} \tag{75}$$

where U_{10} has to be measured in meters per second. While discussing the NPD spectrum we also assume the unit of z to be meter, f is Hz and S_u is m^2 s^{-2} Hz^{-1}. The spectral density of the longitudinal wind component is

$$S_u(f) = \frac{160\left(\frac{U_{10}}{10}\right)^2\left(\frac{z}{10}\right)^{0.45}}{\left(1 + \tilde{f}^n\right)^{\frac{5}{3n}}} \tag{76}$$

with

$$\tilde{f} = 172f\left(\frac{z}{10}\right)^{2/3}\left(\frac{U_{10}}{10}\right)^{-3/4} \tag{77}$$

and $n = 0.468$. This spectrum implies that the variance

$$\sigma_u^2 = 0.00309 \frac{U_{10}^{2.75}}{z^{0.217}} \tag{78}$$

will decrease with height and not constant as implied by surface layer scaling. Furthermore, the integral length scale

$$\text{length scale} \propto z^{2/3} U_{10}^{1/4} \tag{79}$$

will not be proportional with height but will grow somewhat slower and it will also increase a little with wind speed. This is not consistent with surface layer scaling where it under neutral conditions is constant with wind speed.

Højstrup et al. (1990) suggested that spectra at low frequencies do not obey surface layer scaling because the low frequency part scales with the height of the boundary layer, not z. To verify their model they used data selected for neutrality and high wind speeds ($11 < U < 23$ m s^{-1}) from both over sea and land sites in Denmark. The u-model is[3]

$$\frac{fS_u(f)}{u_*^2} = \left(\frac{2.5 n_t}{1 + 2.2 n_t^{5/3}} + \frac{52.5 n}{(1 + 33n)^{5/3}} \right) \frac{1}{1 + 7.4(z/A)^{2/3}} \tag{80}$$

where the 'neutral length scale' $A = 3000$ m and $n_t = fA/U$. The second term in the parenthesis is the Kaimal spectrum Eq. (67).

All spectral models are compared in Figure 37 for a specific choice of U and z. Generally, ESDU has larger length scales compared to those by Kaimal and by Simiu & Scanlan, which are similar. NPD and Højstrup support ESDU's large u-scale. ESDU, though, has the most peaked spectra and, at high wave numbers, slightly lower spectral densities. All spectra agree fairly well at high wave numbers but have substantial scatter at low wave numbers.

3.6 Comparison with the spectral tensor model

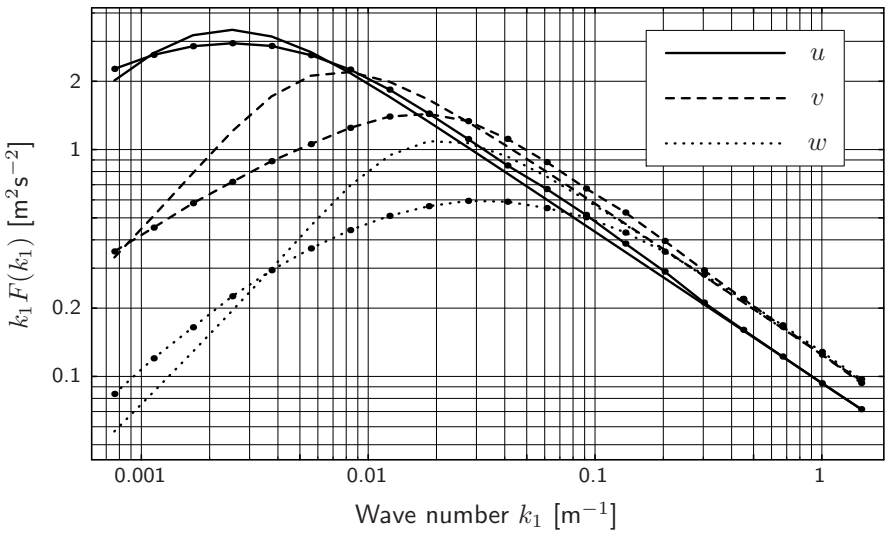

Figure 39: Example with $z = 40$ m and $U = 40$ m s^{-1} of the fit of the spectral tensor model (curves with dots) to the ESDU models.

Here we fit the spectral tensor of section 3.3.1 to models that describe all three component spectra, namely the ones by Kaimal, Simiu & Scanlan and ESDU.

We obtain the parameters Γ, L and $\alpha\varepsilon^{2/3}$ by making a simultaneous least squares fit to the u-, v- and w-model spectra for wave numbers in the range $0.05 < k_1 L < 100$. For the

[3]Højstrup, Larsen and Madsen (1990) also gives a model for the v spectrum, but it was never compared with data, so it will not be discussed here.

Kaimal spectra we get

$$\begin{aligned} \Gamma &= 3.9 \\ L &= 0.59z \\ \alpha\varepsilon^{2/3} &= 3.2\frac{u_*^2}{z^{2/3}}, \end{aligned} \tag{81}$$

where the dependence on z is a consequence of surface layer scaling. For the Simiu & Scanlan spectra, where the fit is shown in Figure 38, we get

$$\begin{aligned} \Gamma &= 3.8 \\ L &= 0.79z \\ \alpha\varepsilon^{2/3} &= 2.8\frac{u_*^2}{z^{2/3}} \end{aligned} \tag{82}$$

and for both models u_* can be obtained from Figure 36.

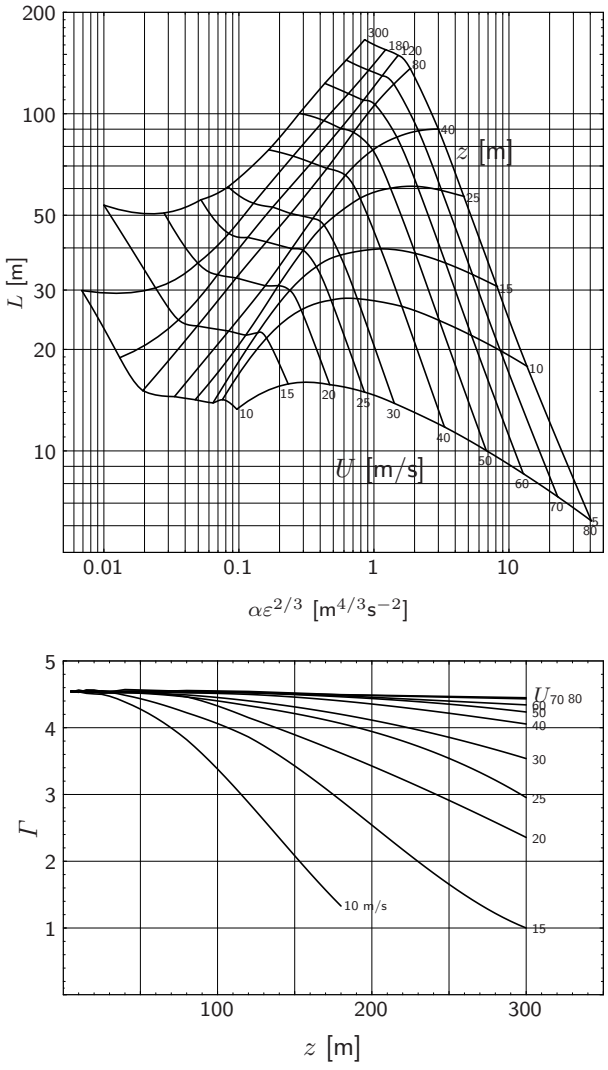

Figure 40: The parameters of the spectral tensor model derived from fits to the ESDU model spectra for turbulence over the sea. Given U and z, all three parameters can be extracted from these plots.

It is more complicated to get the parameters from the ESDU models because the spectra no longer depend on U and z in a simple way. For each set $\{U, z\}$, a fit to the tensor model has

to be calculated. We do that on a mesh limited by $10 < U < 80$ m s^{-1}, $5 < z < 300$ m over the sea. The result is shown in Figure 40. As an example of use of these graphs, suppose that the parameters for $U(z = 80 \text{ m}) = 20$ m s^{-1} are wanted. From the upper plot of Figure 40 we get $L = 33$ m and $\alpha\varepsilon^{2/3} = 0.1$ m$^{4/3}$ s^{-2}. The lower plot gives $\Gamma = 4.5$.

Table 4: Parameters of the spectral tensor derived from different sources for $U(40 \text{ m}) = 40$ m s^{-1} at sea.

	Γ	L [m]	$\alpha\varepsilon^{2/3}$ [m$^{4/3}$ s^{-2}]
Great Belt	3.2	35	0.79
Kaimal	3.9	24	0.86
Simiu	3.8	31	0.76
ESDU	4.5	66	0.62

Another example is shown in Table 4 where the Great Belt data from Mann (1994) are extrapolated using neutral surface layer scaling to $U(40 \text{ m}) = 40$ m s^{-1}. The spectral fit for these values of U and z is shown in Figure 39.

Literature coherences and coherences derived from the spectral tensor by Eqs. (29) and (30) are compared in Mann (1998). Generally, the agreement is good.

3.7 Wind field simulation

Having discussed the spectral tensor in relation to commonly used literature spectra we now describe how to simulate a velocity field $\boldsymbol{u}(\boldsymbol{x})$, which can be used for calculating loads on engineering structures. We approximate the integral Eq. (26) by a discrete Fourier series:

$$u_i(\boldsymbol{x}) = \sum_{\boldsymbol{k}} \mathrm{e}^{\mathrm{i}\boldsymbol{k}\cdot\boldsymbol{x}} C_{ij}(\boldsymbol{k}) n_j(\boldsymbol{k}), \tag{83}$$

where the l'th component of $\boldsymbol{x}$ is $x_l = n\Delta L_l$ with $n = 1, ..., N_l$. The symbol $\sum_{\boldsymbol{k}}$ denotes the sum over all wave vectors $\boldsymbol{k}$ with components $k_i = m2\pi/L_i$, with the integer $m = -N_i/2, ..., N_i/2$, $n_j(\boldsymbol{k})$ are independent Gaussian stochastic complex variables with unit variance and $C_{ij}(\boldsymbol{k})$ are coefficients to be determined. The great advantage of Eq. (83) is that, once the coefficients are known, it can be evaluated very fast by the fast Fourier transform (FFT) (Shinozuka and Deodatis, 1991).

Solving Eq. (83) we get approximately (Mann, 1998)

$$C_{ij}(\boldsymbol{k}) n_j(\boldsymbol{k}) = \frac{1}{V(B)} \int_B u_i(\boldsymbol{x}) \mathrm{e}^{-\mathrm{i}\boldsymbol{k}\cdot\boldsymbol{x}} \mathrm{d}\boldsymbol{x}, \tag{84}$$

where $V(B) = L_1 L_2 L_3$ is the volume of B and $\int_B \mathrm{d}\boldsymbol{x}$ means integration over the box B. From Eq. (84) it is easy to see that $n_j(\boldsymbol{k})$ *have* to be Gaussian when $u_i(\boldsymbol{x})$ is a Gaussian field. Many authors relax this constraint and let $n_j(\boldsymbol{k})$ have random phase but a fixed absolute value (Shinozuka and Jan, 1972; Shinozuka and Deodatis, 1991, 1996). Using this approach every sample will get exactly the same variance and, given a wavenumber (or vector), the estimated power spectral density at this wavenumber will be the same for all realizations of the same process. This might be advantageous in some situations, but it is in contrast to power spectral density estimates of stationary time series which have 100% rms (Press et al., 1992; Bendat and Piersol, 1986). The difference between the two approaches is discussed in detail in Grigoriu (1993). In practice there is little difference and both models could be used. However, the Gaussian approach is usually easier to analyze theoretically and we shall stick to that here.

To find the coefficients $C_{ij}(\boldsymbol{k})$ we calculate the covariance tensor of Eq. (84) obtaining

$$\begin{aligned} & C^*_{ik}(\boldsymbol{k})C_{jk}(\boldsymbol{k}) \\ &= \frac{1}{V^2(B)}\int_B\int_B \langle u_i(\boldsymbol{x})u_j(\boldsymbol{x}')\rangle \,\mathrm{e}^{\mathrm{i}\boldsymbol{k}\cdot\boldsymbol{x}}\mathrm{e}^{-\mathrm{i}\boldsymbol{k}\cdot\boldsymbol{x}'}\mathrm{d}\boldsymbol{x}\mathrm{d}\boldsymbol{x}' \\ &= \frac{1}{V^2(B)}\int\int R_{ij}(\boldsymbol{x}-\boldsymbol{x}')1_B(\boldsymbol{x})1_B(\boldsymbol{x}')\mathrm{e}^{\mathrm{i}\boldsymbol{k}\cdot(\boldsymbol{x}-\boldsymbol{x}')}\mathrm{d}\boldsymbol{x}\mathrm{d}\boldsymbol{x}', \end{aligned} \tag{85}$$

where $1_B(\boldsymbol{x}) = 1$ if $\boldsymbol{x} \in B$ and 0 otherwise. Using the change of variables $\boldsymbol{r} = \boldsymbol{x} - \boldsymbol{x}'$ and $\boldsymbol{s} = \boldsymbol{x} + \boldsymbol{x}'$ having the Jacobian $|\partial(\boldsymbol{r},\boldsymbol{s})/\partial(\boldsymbol{x},\boldsymbol{x}')| = 8$ we get

$$C_{ik}(\boldsymbol{k})C_{kj}(\boldsymbol{k}) = \frac{1}{8V^2(B)}\int R_{ij}(\boldsymbol{r})\mathrm{e}^{-i\boldsymbol{k}\cdot\boldsymbol{r}}\int 1_B\left(\frac{\boldsymbol{s}+\boldsymbol{r}}{2}\right)1_B\left(\frac{\boldsymbol{s}-\boldsymbol{r}}{2}\right)\mathrm{d}\boldsymbol{s}\mathrm{d}\boldsymbol{r} \tag{86}$$

The inner integration can be carried out according to

$$\int 1_B\left(\frac{\boldsymbol{s}+\boldsymbol{r}}{2}\right)1_B\left(\frac{\boldsymbol{s}-\boldsymbol{r}}{2}\right)\mathrm{d}\boldsymbol{s} = \begin{cases} \prod_{l=1}^{3} 2(L_l - |r_l|) & \text{for } |r_l| < L_l \text{ for all } l \\ 0 & \text{otherwise} \end{cases} \tag{87}$$

so, using the convolution theorem and noting that the Fourier transform of $L-|r|$ (for $|r| < L$ and else 0) is $L^2\,\mathrm{sinc}^2(kL/2)$, we get

$$C^*_{ik}(\boldsymbol{k})C_{jk}(\boldsymbol{k}) = \int \Phi_{ij}(\boldsymbol{k}')\prod_{l=1}^{3}\mathrm{sinc}^2\left(\frac{(k_l - k'_l)L_l}{2}\right)\mathrm{d}\boldsymbol{k}', \tag{88}$$

where $\mathrm{sinc}\,x \equiv (\sin x)/x$. For $L_l \gg L$, the sinc^2-function is 'delta-function-like', in the sense that it vanishes away from k_l much faster than any change in Φ_{ij}, and the area beneath the sinc^2-curve is $2\pi/L_l$. Therefore, we get

$$C^*_{ik}(\boldsymbol{k})C_{jk}(\boldsymbol{k}) = \frac{(2\pi)^3}{V(B)}\Phi_{ij}(\boldsymbol{k}). \tag{89}$$

The solution to Eq. (89) is

$$C_{ij}(\boldsymbol{k}) = \frac{(2\pi)^{3/2}}{V(B)^{1/2}}A_{ij}(\boldsymbol{k}) = \left(\Delta k_1\Delta k_2\Delta k_3\right)^{1/2}A_{ij}(\boldsymbol{k}) \tag{90}$$

with $A^*_{ik}A_{jk} = \Phi_{ij}$ and $\Delta k_l = 2\pi/L_l$. This result should be expected when comparing Eq. (26) to (83).

Two problems occur by simulating a field by the Fourier series Eq. (83) with the coefficients Eq. (90). The first is that for many applications the dimensions of the simulated box of turbulence need *not* to be much larger than the length scale of the turbulence model L. Therefore Eq. (89) may not be a good approximation to Eq. (88). The second problem is that the simulated velocity field Eq. (83) is periodic in all three directions. Both problems have been addressed in Mann (1998).

The algorithms above simulate a three-dimensional vector field on a three-dimensional domain, but it can easily be modified to simulate one- or two-dimensional vectors in a 2- or 3-D domain (Mann, 1998). The algorithms are not needed for a one-dimensional domain, i.e. simulation of wind fluctuations in one point as a function of time.

The implementation of the model includes three steps:

1. Evaluate the coefficients $C_{ij}(\boldsymbol{k})$, either by Eq. (90) or a modification of this (Mann, 1998).
2. Simulate the Gaussian variable $n_j(\boldsymbol{k})$ and multiply.
3. Calculate $u_i(\boldsymbol{x})$ from Eq. (83) by FFT.

The time consumption in the first step is proportional to the total number of points $N = N_1N_2N_3$ in the simulation. The required time to perform the FFT is $O(N\log_2 N)$ (Press et al., 1992). In practice, simulating a three-dimensional field, used for load calculations on wind turbines, with millions of velocity vectors takes of the order of a few minutes on a modern pc.

Notation

A	Charnock constant
	neutral length scale
B	box of e.g. turbulence
coh_{ij}	coherence or normalized cross-spectrum
cw	continuous wave
C_{ij}	coefficients for a discrete Fourier series
C_{DN}	neutral drag coefficient
$E(k)$	energy spectrum
ESDU	engineering science data unit
f	frequency
	Coriolis parameter
F	spectrum (function of wave number)
FFT	fast Fourier transform
g	gravitational acceleration
i	tensor index
j	tensor index
k	wave number/component
$\mathbf{k}$	wave vector
L	turbulence length scale or length of a volume
m	integer number
n	number of segments
	normalized frequency
$n_j(\mathbf{k})$	Gaussian variable
n_t	normalized neutral frequency
N	number of points
NPD	Norwegian Petroleum Directorate
p	pressure
$\mathbf{r}$	separation vector
$R_{ij}(r)$	covariance tensor
RDT	rapid distortion theory
S	spectrum (function of frequency)
t	time
u	longitudinal wind component
$\tilde{\boldsymbol{u}}(\boldsymbol{x})$	turbulent velocity field
u_*	friction velocity
U	mean wind speed
$\boldsymbol{U}$	mean flow
US	uniform shear model
v	transversal wind component
$V(B)$	volume of the box B
w	vertical wind component
x	direction of the mean wind field
$\boldsymbol{x}$	coordinate system
y	transversal direction
z	vertical axis direction or height
z_0	roughness length
Z	orthogonal process
$\alpha\varepsilon$	energy dissipation measure
β	non-dimensional time
Γ	anisotropy parameter
δ	Kronecker delta
κ	von Kármán constant
σ_X	standard deviation of a variable X
τ	eddy lifetime
τ_D	coherence-destroying diffusion time
τ_E	eddy-damping rate
ϕ	geographical latitude
$\Phi_{ij}(\mathbf{k})$	spectral tensor
χ_{ij}	cross-spectra
ω	fluctuating part of the vorticity

Ω	angular velocity
$\mathbf{\Omega}$	mean part of the vorticity
∂	partial derivate
∇	vector differential operator
$\langle X \rangle$	ensemble average of the variable X

References

Batchelor G. K. (1953) The theory of homogeneous turbulence, Cambridge University

Bendat J. S. and Piersol A. G. (1986) Random data: Analysis and Measurement Procedures, 2 edn, Wiley-Interscience

Brown R. D. and Swail, V. R. (1991) Over-water gust factors. *Ocean Engng.* **18**(4):363–394

Charnock H. (1955) Wind stress on a water surface. *Q. J. Royal Meteorol. Soc.* **81**:639–640

Comte-Bellot G. and Corrsin S. (1971) Simple Eulerian time correlation of full- and narrow-band velocity signals in grid generated, 'isotropic' turbulence. *J. Fluid Mech.* **48**:273–337

Derbyshire S. H. and Hunt J. C. R. (1993) Structure of turbulence in stably stratified atmospheric boundary layers; comparison of large eddy simulations and theoretical models. *in* S. D. Moobs and J. C. King (eds), Waves and Turbulence in Stably Stratified Flows, Clarendon, Oxford, 23–59 pp

ESDU International (1982) Characteristics of wind speed in the lower layers of the atmosphere near the ground: strong winds (neutral atmosphere), ESDU International, London

ESDU International (1985) Characteristics of atmospheric turbulence near the ground. Part II: single point data for strong winds (neutral atmosphere), ESDU International, London

Garratt J. R. (1977) Review of drag coefficients over oceans and continents, *Mon. Wea. Rev.* **105**:915–929

Geernaert G. L. (1987) On the importance of the drag coefficient in air-sea interactions. *Dynamics Atmos. Oceans* **11**:19–38

Grigoriu M. (1993) On the spectral representation method in simulation. *Prob. Eng. Mech.* **8**:75–90

Højstrup J., Larsen S. E. and Madsen P. H. (1990) Power spectra of horizontal wind components in the neutral atmospheric boundary layer. *in* N. O. Jensen, L. Kristensen and S. E. Larsen (eds), Ninth Symposium on Turbulence and Diffusion, American Meteorological Society, 305–308 pp

Hunt J. C. R. and Carruthers D. J. (1990) Rapid distortion theory and the 'problems' of turbulence. *J. Fluid Mech.* **212**:497–532

Kaimal J. C. and Finnigan J. J. (1994) Atmospheric Boundary Layer Flows, Their Structure and Measurement, Oxford University Press, New York

Kaimal J. C., Wyngaard J. C., Izumi Y. and Coté O. R. (1972) Spectral charcteristics of surface-layer turbulence, *Q. J. R. Meteorol. Soc.* **98**:563–589

Koopmans L. H. (1974) The Spectral Analysis of Time Series, Academic Press

Kristensen L. and Kirkegaard P. (1987) Puff kinematics, Technical Report R–548, Risø National Laboratory

Landau L. D. and Lifshitz E. M. (1987) Fluid Mechanics, Pergamon Press

Larose G. L. and Mann J. (1998) Gust loading on streamlined bridge decks, *J. Fluids Structures* **12**(5):511–536

Lesieur M. (1987) Turbulence in fluids, Martinus Nijhoff Publishers

Mann J. (1992) Investigation of atmospheric low-frequency turbulence over the ocean, Technical Report I–634(EN), Risø National Laboratoty, Roskilde

Mann J. (1994) The spatial structure of neutral atmospheric surface-layer turbulence. *J. Fluid Mech.* **273**:141–168

Mann J. (1998) Wind field simulation, *Prob. Engng. Mech.* **13**(4):269–282

Mann J., Cariou J.-P., Courtney M. S., Parmentier R., Mikkelsen T., Wagner R., Lindelöw P., Sjöholm M. and Enevoldsen K. (2009) Comparison of 3D turbulence measurements using three staring wind lidars and a sonic anemometer. *Meteorol. Z.* **18**(2):135–140

Mann J., Kristensen L. and Courtney M. S. (1991) The great belt coherence experiment – a study of atmospheric turbulence over water, Technical Report R–596, Risø National Laboratory, Roskilde

Maxey M. R. (1982) Distortion of turbulence in flows with parallel streamlines. *J. Fluid Mech.* **124**:261–282

NDP (1998) Acts, regulations and provisions for the petroleum activities, Vol. 2,, Norwegian Petroleum Directorate

Panofsky H. A. and Dutton J. A. (1984) Atmospheric Turbulence, John Wiley & Sons, New York

Panofsky H. A., Larko D., Lipschutz R., Stone G., Bradley E. F., Bowen A. J. and Højstrup J. (1982) Spectra of velocity components over complex terrain. *Q. J. R. Meteorol. Soc.* **108**:215–230

Peña A., Gryning S.-E., Mann J. and Hasager C. B. (2010) Length scales of the netural wind profile over homogeneous terrain *J. Appl. Meteor. Climat.* **49**:792–806

Press W. H., Flannery B. P., Teukolsky S. A. and Vetterling W. T. (1992) Numerical Recipes, 2nd edn, Cambridge University Press

Shinozuka M. and Deodatis G. (1991) Simulation of stochastic processes by spectral representation, *Appl. Mech. Rev.* **44**(4):191–203

Shinozuka M. and Deodatis G. (1996) Simulation of multi-dimensional gaussian stochastic fields by spectral representation. *Appl. Mech. Rev.* **49**(1):29–53

Shinozuka M. and Jan C.-M. (1972) Digital simulation of random processes and its applications. *J. Sound Vibration* **25**(1):111–128

Simiu E. and Scanlan R. H. (1996) Wind Effects on Structures, 3. ed., John Wiley & Sons

Sjöholm M., Mikkelsen T., Mann J., Enevoldsen K. and Courtney M. (2009) Time series analysis of continuous-wave coherent Doppler lidar wind measurements. *Meteorol. Z* **18**(3):281–287

Townsend A. A. (1976) The Structure of Turbulent Shear Flow, 2nd edn, Cambridge University Press

Townsend, A. A. (1980) The response of sheared turbulence to additional distortion. *J. Fluid Mech.* **98**:171–191

4 Introduction to continuous-wave Doppler lidar

Mark Pitter, Chris Slinger and Michael Harris
Zephir Limited, The Old Barns, Fairoaks Farm, Hollybush, Ledbury, HR8 1EU, U.K.

4.1 Introduction

Remote sensing offers the wind industry an attractive alternative or complement to the traditional methods for obtaining accurate wind measurements that involve the siting of tall meteorological masts. Laser anemometry (lidar) has now demonstrated its capacity for resource assessment, wind turbine power curve measurement, and turbine mounted deployment for advance wind speed detection. Widespread acceptance of lidar by the industry has required that this technique be extensively validated, aiming towards a certifiable and traceable measurement standard and formal accreditation of lidar methods for different applications in a range of terrain types. This chapter outlines the lidar measurement process and capabilities specifically for the case of continuous wave (CW) systems.

Wind lidar systems were first demonstrated in the 1970's (Jelalian, 1992) and have since been applied to a wide variety of applications including aviation and meteorology. Although applications to wind energy were explored in the 1980's (Hardesty and Weber, 1987; Vaughan and Forrester, 1989), the lidar systems that existed at that time were too large, complex and expensive to achieve serious acceptance in the industry. The situation has now changed dramatically, with rapid growth of the wind generation industry coinciding with development of a new generation of lidars based on optical fibre and other components that emerged from the telecommunications boom of the 1990's. The first all-fibre lidars were demonstrated in the late 1990's, and a commercial prototype unit (ZephIR) was mounted on a turbine to demonstrate wind speed detection in front of the rotor plane in early 2003. A demonstration of ground-based wind profiling followed shortly afterwards. ZephIR is a CW coherent lidar system, and this approach was selected as a means to combine simplicity with high sensitivity at measurement ranges relevant to wind energy resource assessment, and hence achieve a robust, reliable system at relatively low cost. Following this pioneering work, the pace of development has accelerated, and lidars have increasingly become an established tool in the wind industry.

Section 4.2 of this chapter provides an overview of lidar techniques and technology. Different types of lidar system are surveyed, and the generic physical principles underlying their operation are reviewed. The specific case examined in detail here is that of wind profiling by a ground-based conically-scanned continuous-wave lidar, which has rapidly become established as a powerful tool in the wind energy industry, and is exemplified by the ZephIR lidar, initially developed by QinetiQ, the Natural Power, and now by Zephir Limited.

A number of assumptions must be made in order to extract values of wind speed from raw lidar data; these are reviewed in section 4.3. The necessary steps that are required during the end-to-end measurement process in order to arrive at a value of wind speed are detailed in section 4.4. It is important to understand the potential sources of error and uncertainty, and these are reviewed and analysed in section 4.6. Section 4.7 examines the important requirement for lidar calibration and traceability and 4.8 discusses the emerging area of turbine mounted lidar. Finally, section 4.9 draws together some conclusions and a summary of the future outlook for lidar in wind energy.

4.2 Basic principles of lidar operation and system description

4.2.1 Brief survey of lidar types

There are many different types of lidar (Jelalian, 1992) and these are capable of performing a diverse range of tasks (e.g. 3D imaging and range finding, gas species detection, remote measurement of vibrations). We concern ourselves here specifically with systems for the measurement of wind speed in the atmosphere (Zak, 2003). Such systems fall into two broad categories: coherent lidar and direct detection lidar. Coherent lidar measures Doppler shifts by comparing the frequency of backscattered radiation to that of a reference beam via a light beating process, whereas direct detection lidar (Chanin et al., 1989) performs its frequency-shift measurements by passing the light through an optical filter, such as a Fabry-Perot etalon. By operating in the ultra-violet, direct detection lidars can exploit molecular scattering processes, guaranteeing signal returns even in very clean air where there is an absence of aerosols. A further type of direct detection lidar that uses cross-correlation of the backscatter signal measured at several points to determine wind speed and direction is also emerging, but this chapter concentrates on systems that use the Doppler shift from aerosols or molecules.

Coherent wind lidar systems can be categorised according to their emission waveform (pulsed or continuous), waveband (UV, visible, near-IR, far-IR), and their transmit/receive geometry (monostatic or bistatic). This chapter concentrates specifically on continuous-wave coherent monostatic lidar systems that operate in the telecommunications near-IR band around 1.55 μm (Karlsson et al., 2000). At this wavelength, reliable components including optical fibre and circulators are readily available. Such systems can route the light within the lidar via fibre cables (creating an "all-fibre" lidar'), rather than using mirrors to direct the beams in free space. This confers an enormous design advantage, simplifying alignment and improving robustness and stability. Pulsed all-fibre lidar has also been developed as reported in Pearson et al. (2002) and is discussed in other chapters.

4.2.2 Principles underlying anemometry by coherent laser radar (CLR)

The principle by which coherent lidar measures the velocity of a target is simple: a beam of coherent radiation illuminates the target, and a small fraction of the light is backscattered into a receiver. Motion of the target along the beam direction leads to a change in the light's frequency via the Doppler shift: motion towards the lidar brings about a compression of the wave and an increase in its frequency (a "blue shift"), while movement away stretches the wave reducing its frequency (a "red shift"). This frequency shift is accurately measured by mixing the return signal with a portion of the original beam, and sensing the resulting beats at the difference frequency on a photodetector. Like the Doppler effect, the beat phenomenon is perhaps most familiar in the context of acoustics as, for example, when two closely (but not identically) tuned guitar strings are simultaneously plucked.

The essential features are readily seen in the simplified generic CLR depicted in Figure 41. In order to illustrate the concept this is drawn as a bistatic system, in which the transmit and receive optics are separate and distinct. In practice a monostatic geometry is more usual, in which the transmit and receive paths share common optics, since this is a much more stable arrangement and allows for far simpler alignment.

4.2.3 Role of local oscillator and range selection by focus

The reference beam, or local oscillator (LO), plays a crucial role in the operation of a CLR (Sonnenschein and Horrigan, 1971). Firstly, it defines the region of space from which light must be scattered for efficient detection of the beat signal; radiation from other sources (e.g. sunlight) is rejected both spatially and spectrally, so that CLR systems are usually completely immune to the effect of background light. The LO also provides a stable reference frequency

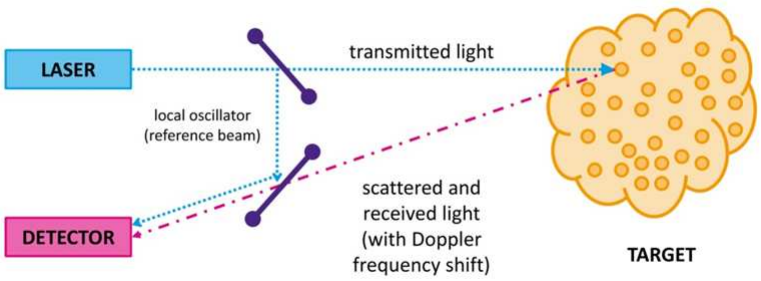

Figure 41: Generic bistatic lidar system. A small fraction of the transmitted light is tapped off by a beamsplitter to form a reference beam. This is superimposed at a second beamsplitter with the weak return scattered from moving aerosols. The detector picks up the resulting beat signal; this undergoes spectral analysis to determine aerosol velocity.

to allow very precise velocity determination; as a consequence the Doppler shift measurement by a CLR system is inherently calibrated. Finally, the LO amplifies the signal via the beating process to allow operation at a sensitivity that approaches the shot-noise (or quantum) limit. This very high sensitivity permits the operation of CLR systems in an unseeded atmosphere, relying only on detection of weak backscattering from natural aerosols.

CW systems are the simplest form of lidar possessing the advantage of reduced complexity, and their performance can be tailored closely to the requirements of the wind industry. However, the overall trade-off between the pulsed and CW options for each specific application must take into account a number of factors including sensitivity, cost, velocity resolution, and maximum and minimum ranges. Unlike pulsed lidar systems, which use time of flight to discriminate between returns from different ranges, a CW lidar achieves operation at a given range by beam focusing. Wind profiling is achieved by continuously scanning the beam, focusing in turn at a number of predetermined ranges. For each range, a circular scan is typically used. The rapid sampling rate inherent to CW lidar permits 1-s "snapshots" of the flow across the scan disk at each measurement range. Focusing of the lidar beam results in a Lorentzian spatial weighting function along the beam axis, with the sensitivity peak located at the beam waist (Sonnenschein and Horrigan, 1971; Karlsson et al., 2000). This function has a half-width given by the Rayleigh range (the distance from the waist at which the beam area has doubled).

The beam diameter at the waist increases linearly with range while the Rayleigh range increases roughly as the square. Hence the effective probe volume varies as the 4th power of the focus range, and this strong dependence has some implications for the signal statistics at shorter ranges (Harris et al., 2001b). The minimum range for a CW lidar is very short with detection possible in principle at zero range, whereas a pulsed system is blinded while the pulse is leaving the transmitter leading to a minimum range of 10's of metres, typically around 40–50 m.

4.2.4 Doppler frequency analysis and signal processing

The stages of signal processing required for CLR wind signals are discussed in section 4.4. The detector output, containing the beat signal information embedded in broadband noise, is typically digitised by an analogue-to-digital converter (ADC). Spectral analysis (e.g. by fast Fourier transform methods) leads to the generation of Doppler spectra. It is usually necessary to average a number of these spectra in order to improve the signal-to-noise ratio (SNR), after which the Doppler peak stands clearly above a flat shot-noise floor. A value for the line-of-sight wind speed can then be computed via a velocity estimation algorithm. This might calculate, for example, the peak, median or centroid value of the Doppler signal.

4.2.5 Wind profiling in conical scan mode

Since a single lidar measurement only provides the component of wind speed along the beam direction, it is necessary to scan the direction of the beam in order to generate a measurement of the wind speed vector. A conical or VAD (velocity-azimuth-display) scan pattern has been widely used (Banakh et al., 1993) (see Figure 42); as the beam moves, it intercepts the wind at different angles, thereby building up a series of measurements around a disk of air from which the wind speed vector can be derived. In uniform flow, a plot of the measured line-of-sight wind speed (V_{LOS}) versus scan azimuth angle (ϕ) takes the form of a cosine wave (or a rectified cosine for a homodyne lidar system that cannot distinguish the sign of the Doppler shift). The peak Doppler shifts correspond to measurements when the azimuth scan angle aligns with the upwind and downwind directions. Doppler shifts close to zero are obtained when the azimuth angle is perpendicular to the flow.

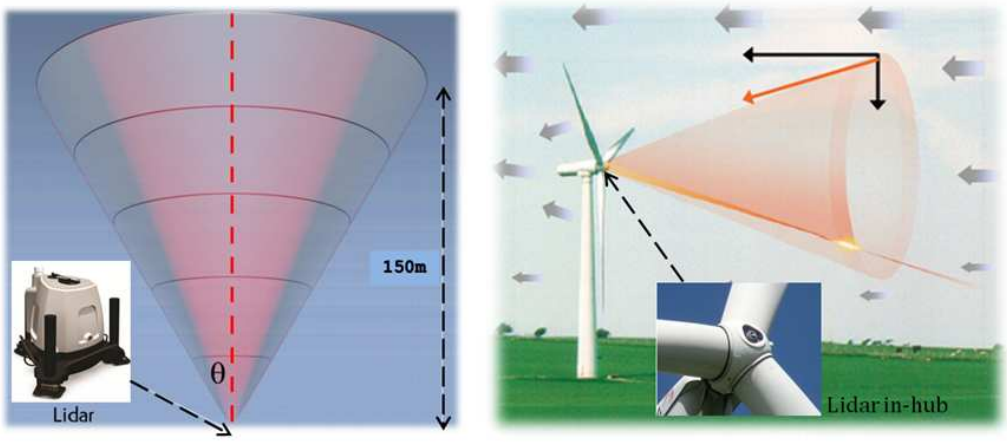

Figure 42: Conical scan pattern as used for lidar wind profiling. Left: ground based vertical scanning. The cone half-angle (θ) is typically of order 30°. The lidar can operate successfully even when part of its scan is obscured, e.g. by an adjacent met mast. To build up a wind profile, the lidar operates in a repeating sequence during which all the heights are interrogated in series. Right: one of several wind turbine mounted configurations, where the lidar scans around a horizontal axis, usually pointing into the wind.

4.2.6 Pioneering a revolution: ZephIR lidar

Many different research groups have built and successfully deployed wind lidars over the past 30 years. However, commercial lidar products have until very recently been available from only a few companies. In 2003 the UK company QinetiQ (formerly the government-funded establishment RSRE, later DRA then DERA), launched the first commercial all-fibre lidar ("ZephIR$^{\mathrm{TM}}$") which exploited decades of research in the coherent lidar area. QinetiQ began a programme to develop a commercial fibre-based lidar in 2001; the resulting ZephIR product is now an established tool for wind profiling in the wind energy industry. Systems have been deployed successfully around the world in several demanding applications that illustrate the flexibility and robustness of the solution. Initial deployment of the ZephIR lidar (March 2003) was on the nacelle of a large (2.3 MW) wind turbine (Figure 43-left frame), remotely measuring for the first time the wind speed up to 200 m in front of the blades (Harris et al., 2006, 2007). The lidar consisted of a 19 inch rack unit containing laser source, detector and signal processing computer, situated in the base of the tower and connected via over 100 m of electrical and optical fibre cable to the transceiver head mounted on the top of the nacelle. The lidar system was installed and was fully operational after just a few hours, thus allowing a demonstration of advance warning of oncoming gusts and providing valuable experience in

practical deployment issues.

Figure 43: Stages of evolution of the ZephIR lidar. The upper left-hand picture (a) shows the lidar head mounted on the nacelle of a Nordex N-90 wind turbine (March 2003). The top central picture (b) shows a prototype ground-based wind profiler at the Risø wind energy test site at Høvsøre, Denmark. The top right picture (c) shows an early ZephIR production model deployed in the field. The lower pictures show a more recent dual mode ZephIR DM300 deployed on an offshore platform (d) and on a turbine nacelle (e).

The system achieved several weeks of successful operation. It was then converted into a ground-based scanning unit for wind profiling (Figure 43-upper middle frame). The ground based system was first trialled in December 2003, and subsequently deployed in numerous campaigns in the UK, Europe, and other parts of the world. The experience gained through these trials has built confidence in the robustness and reliability of the core ZephIR design. In late 2004, work started on a production instrument (Figure 43-upper right frame), designed to perform autonomous wind profiling measurements at heights up to 200 m (Smith et al., 2006), primarily for site surveys at proposed wind farm sites. The technology was transferred to Natural Power in 2007, and subsequent development resulted in the more integrated ZephIR Z300 system (Figure 43-lower frames), and the dual mode DM300 which can be both turbine and ground mounted. ZephIRs have logged more than 3.6 million hours of deployment (May 2013 figures) around the world and Zephir Limited was eventually established as a standalone member of the Fred Olsen Limited group in 2012.

4.3 Lidar measurement process: Assumptions

The following sections discuss generic CW lidar considerations (most of which apply equally to pulsed systems). Where appropriate, application to the ZephIR lidar is used to provide an illustrative example.

4.3.1 Behaviour of scattering particles

The lidar signals from which wind speeds are derived originate via backscattering of the beam by particles in the atmosphere. The exact constitution of these aerosols is generally unknown, but they are normally assumed to consist of dust, organic matter (e.g. pollen), soot, or water droplets. Knowledge of the aerosols' make-up is not a requirement for lidar wind speed measurement. The particles must provide sufficient backscatter signal for Doppler analysis and their motion must faithfully follow that of the wind flow. The latter assumption is very good, since viscous forces are dominant for such small particles. Larger particles, for which this does not apply, will rapidly fall to ground. Raindrops or snowflakes provide a strong contribution to the lidar signal. Their gravity induced downward motion can lead to an error in the vertical component of wind speed (just one parameter of interest, and affected data can be easily identified and filtered), but the important horizontal component will be correct.

A further excellent assumption is that the return signal is dominated by light generated by single-scattering events. While it is possible for light to suffer multiple scattering in dense fog, it is a valid assumption that any effect on the Doppler spectrum is almost always negligible.

4.3.2 Uniformity of flow and backscatter

A least-squares fitting to the azimuthal variation of line-of-sight wind speed allows the derivation of wind parameters from conical scan data. These parameters pertain to a significant volume of atmosphere – the signal originates from a disk whose diameter commonly exceeds 100 m, and whose depth along the beam direction can be over 10 m. Except in situations of strong shear, turbulence or highly complex terrain the wind speed is reasonably uniform throughout this sampled volume, and the best fit wind parameters are used to indicate the average values over the volume. In fact, ZephIR data itself can provide a straightforward check on wind field uniformity since conical scanning provides measurements at many different azimuth angles; where the assumptions have broken down, measurements with less certainty can be flagged.

The contribution to the lidar signal from different regions of the lidar probe volume is weighted by the value of the atmospheric backscatter coefficient $\beta(\pi)$ at each point. The value of $\beta(\pi)$ is typically constant to $\sim 10\%$ throughout the probe volume (Banakh et al., 1993) except in conditions that lead to stable mist layers, or when the lidar beam is incident on a low cloud base.

4.3.3 Beam positional accuracy

Lidar scan angle and focus calibration are performed in the laboratory, and these must be correctly maintained throughout a period of deployment in the field. Obviously errors in the focus setting would result in wind speed measurement at the wrong height. Careful design eliminates the risk of uncertainty in the beam focus: thermal expansion, which could change the length of the transceiver telescope, can be compensated and the position of the focus mechanism can be automatically checked to provide information on any malfunction.

The lidar must be correctly set up, with the vertical and azimuthal orientation adjusted appropriately during installation. External to the lidar, it has been established that small-scale refractive-index atmospheric fluctuations will have negligible effect on the propagation of the lidar beam (Clifford and Wandzura, 1981; Lading et al., 1984).

4.3.4 Optical and electrical interference sources

The lidar identifies the presence of a wind signal when the power density in the Doppler spectrum exceeds a threshold level. In the absence of any significant source of spurious signal, the only mechanism that can lead to such detection events is the backscatter of Doppler-shifted light into the lidar receiver. Optical interference is extremely unlikely - even when the

lidar points directly at the sun the spectral power density is insufficient to cause a problem, and the interaction between two adjacent lidars can be neglected. Thorough electromagnetic screening eliminates the risk of spurious spectral features caused by electrical interference for any normal deployment.

4.3.5 Time-of-flight considerations

The round-trip time for light interrogating the atmosphere at a height of 100 m is less than 1 μs. On this timescale the ZephIR scanner moves the focused beam a distance of only 300 μm, and the laser phase drifts by an insignificant amount. The polarisation state of the lidar output is similarly frozen on this timescale, so no appreciable misalignment of loss of interference efficiency is incurred.

4.4 End-to-end measurement process for CW Doppler lidar

4.4.1 Introduction

The wind parameter measurement process can be divided into a number of sequential steps. This section describes the overall end-to-end process of the wind speed measurement process for a CW coherent Doppler lidar wind profiler. Again, where appropriate, the ZephIR lidar is used as an example.

4.4.2 Transmitter optics

The role of the transmitter is to provide a focused beam at a desired location. This location can be moved around in space with a combination of (i) altering the focus range and (ii) passing the beam through a scanning element such as a rotating prism (wedge). Wind profiling lidars conveniently employ a conical scan with its axis aligned vertically; the cone half-angle is commonly of order 30° (i.e. the beam elevation angle is $\sim 60°$). Some turbine mounted lidars use lower cone angles, the optimum choice depending upon a variety of factors including the mounting position on the turbine, the rotor diameter and the measurement ranges of most interest.

In a monostatic CW system, a Doppler-shifted contribution to the signal is generated via light scattering from any moving part of the atmosphere that the beam illuminates. The contribution from any point is weighted by the square of the beam's intensity at that point (Harris et al., 2001a). Hence it can be shown that focusing of an ideal Gaussian beam (Siegman, 1986) gives rise to a spatial sensitivity along the beam direction that depends on the inverse of beam area. It follows that the sensitivity rises to a peak at the beam waist, and falls symmetrically on either side. There is also a spatial dependence of sensitivity transverse to the beam, but because the beam is very narrow this is of little interest and can be ignored. To a good approximation the axial weighting function for a CW monostatic coherent lidar is given by a Lorentzian function (Sonnenschein and Horrigan, 1971; Karlsson et al., 2000):

$$F = \frac{\Gamma/\pi}{\Delta^2 + \Gamma^2}, \tag{91}$$

where Δ is the distance from the focus position along the beam direction, and Γ is the half-width of the weighting function to the -3 dB point, i.e. 50% of peak sensitivity. Note that F has been normalised such that it's integral from $-\infty$ to ∞ gives unity. To another good approximation, Γ is given by:

$$\Gamma = \frac{\lambda R^2}{\pi A^2}, \tag{92}$$

where λ is the laser wavelength, here assumed to be the telecommunications wavelength $\lambda \sim 1.55 \times 10^{-6}$ m, R is the distance of the beam focus from the lidar output lens, and A is

the beam radius at the output lens. The beam intensity profile is assumed to be an axially-symmetric 2D Gaussian; A is calculated for the point at which the intensity has dropped to $1/e^2$ of its value at the beam centre. For example, if A takes the value 28 mm (broadly equivalent to the current production ZephIR) then, at a focus range R of 100 m, Γ has a value of ~ 5.5 m, or a probe length (to -3 dB points) of ~ 11 m. Figure 44 shows the behaviour of the theoretical sensitivity curves for the two example cases ($A = 20$ mm, 28 mm) at several focus heights above ground level. In addition the theoretical curve corresponding to one of the calibration ranges has been plotted, with experimental calibration data for comparison. (Section 4.7 contains more detail of the calibration processes). The minimum range is determined by the focusing capability of the transceiver optics, and for ZephIR it takes the value 10 m.

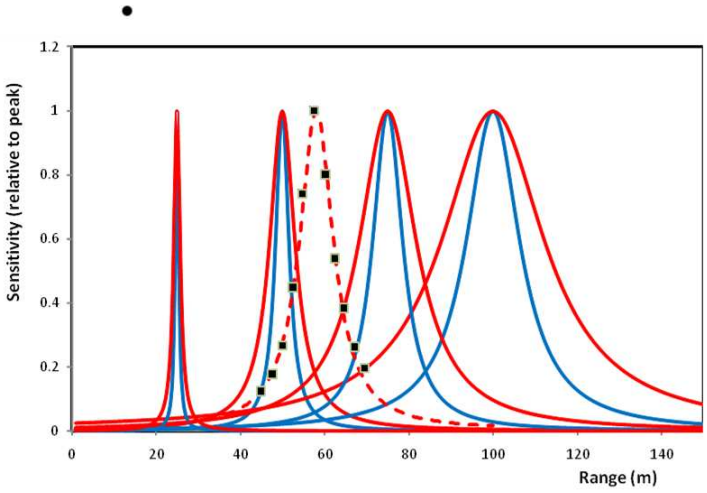

Figure 44: Theoretical lidar sensitivity curves at focus heights 25, 50, 75 and 100 m for the two cases listed above with $A = 20$ mm and 28 mm, corresponding to respectively the original (red curve) and current (blue curve) ZephIR design. The peak is normalised to unity in each case; the absolute peak value decreases as the inverse of height squared, so that the area under each curve (representing the overall sensitivity) is always the same. This illustrates a useful feature of focused CW coherent lidar that in uniform scattering, the signal-to-noise ratio is independent of focus range. Data obtained in calibration measurements (black squares) at a calibration range $R = 68$ m are in close agreement with the corresponding theoretical values (dashed curve) at the equivalent height 58 m (=68 m$\times \cos 30°$)

4.4.3 Light scattering by aerosols

Coherent lidar measures the Doppler shift resulting from the component of target velocity along the beam (or line-of-sight) direction. Motion of the target transverse to the beam direction produces no net Doppler shift. Hence, for a lidar at (0,0,0) measuring at a specific location (x, y, z) where wind components are (u, v, w), the lidar will detect a line-of-sight velocity given by the dot product of the wind vector (u, v, w) and the unit vector along the beam direction:

$$V_{\mathrm{LOS}} = \left| (\mathbf{u} + \mathbf{v} + \mathbf{w}) \cdot \left(\frac{\mathbf{x} + \mathbf{y} + \mathbf{z}}{\sqrt{x^2 + y^2 + z^2}} \right) \right|, \tag{93}$$

where V_{LOS} is the component of aerosol speed along the line of sight (i.e. the beam direction), and the modulus applies to homodyne systems that cannot distinguish the sign of the Doppler shift.

In the backscattering geometry considered here, the scattered light experiences a Doppler

shift in frequency given by:

$$\delta\nu = \frac{2V_{\mathrm{LOS}}\nu}{c} = \frac{2V_{\mathrm{LOS}}}{\lambda}, \tag{94}$$

where c is the speed of light (2.998×10^8 m s^{-1}) and ν and λ are the laser frequency and wavelength respectively.

Since the signal originates from a finite probe length, the overall return exhibits a spectrum of frequencies. This results from the contributions from different velocities (with strengths determined by the weighting function, Eq. 91) over all the space occupied by the lidar beam. Note that in the absence of additional information it is not possible to identify from what range each component of the spectrum has originated. Section 4.6 will outline how information from additional focus ranges can be used to identify and reject spectral components originating from strongly-scattering objects (e.g. clouds) situated outside the probe length.

For a CW coherent system, the time-averaged optical signal power, P_s, backscattered by the aerosols into the receiver is given to a good approximation by:

$$P_s = \pi P_T \beta(\pi)\lambda, \tag{95}$$

where P_T is the transmitted laser power. It is notable that Eq. (95) contains no dependence on either the focus range or the system aperture size. With a value of 10^{-8} (m srad)$^{-1}$ for $\beta(\pi)$ in clear boundary-layer air, a transmitted power $P_T \sim 1$ W and $\lambda \sim 1.5$ μm, the received power P_s derived from Eq. (95) is only of order 5×10^{-14} W emphasising the need for high sensitivity.

4.4.4 Receiver optics

In a monostatic system, the backscattered light returns through the transmission optics (the term transceiver is commonly used to denote this dual role). After entering the transceiver, optical means are used to isolate the return light, and this is passed to the next stages of the detection process.

4.4.5 Light beating

In coherent laser radar, the incoming Doppler-shifted radiation is optically mixed with a reference LO beam. The mixing of two waves in this manner leads to the well-known "beat" phenomenon in which the resulting amplitude oscillates at the difference frequency. In lidar, the process conveniently "downmixes" the optical frequency of the Doppler shifted return at $\sim 2 \times 10^{14}$ Hz to a more manageable signal in the MHz range. The efficiency of the beating process is optimised when the signal and LO beams overlap perfectly in space (i.e. they occupy identical spatial "modes"). This condition is ensured when both beams propagate in the same single-mode optical fibre, assuming that they share the same polarisation state.

It is instructive to consider a simple classical description of the light beating process. Superposition of a LO field $E_{\mathrm{LO}}\cos(\omega_{\mathrm{LO}}t)$ and a stable signal field $E_{\mathrm{s}}\cos(\omega_{\mathrm{s}}t)$ results in a fluctuating detector output:

$$i(t) \propto \left(E_{\mathrm{LO}}\cos(\omega_{\mathrm{LO}}t) + E_{\mathrm{s}}\cos(\omega_{\mathrm{s}}t)\right)^2. \tag{96}$$

This is conveniently separated into a "constant" term and a cross term oscillating at the difference frequency:

$$i(t) \propto \left(E_{\mathrm{LO}}^2 + E_{\mathrm{s}}^2\right) + 2E_{\mathrm{LO}}E_{\mathrm{s}}\cos\left|\omega_{\mathrm{s}} - \omega_{\mathrm{LO}}\right| t. \tag{97}$$

Since the optical power of the local oscillator beam typically exceeds that of the signal beam by many orders of magnitude, the first term is given by E_{LO}^2 to a very good approximation, and after high pass filtering produces only quantum fluctuations which give rise to the shot noise floor of the instrument (section 4.7). For a system in which there is no frequency shift between the LO and transmitted beams, the measured Doppler shift is given simply by:

$$\delta\nu = 2\pi\left|\omega_{\mathrm{s}} - \omega_{\mathrm{LO}}\right| \tag{98}$$

from which the value of V_{LOS} is derived via Eq. (94). In practice a signal field originating from atmospheric scattering exhibits fluctuations in both its amplitude and phase (or frequency). The coherent detection process ensures that these properties are reproduced in the detector output so that, in the limit of high SNR, its spectral analysis gives a correct representation of the scattered light's spectrum (Harris et al., 1994).

The coherent detection process described above is also commonly referred to as homodyne or heterodyne detection. A rigorous quantum-mechanical theoretical treatment of the detection process is given in Loudon (2000). Note that although the detection process is described as coherent, the backscattered radiation itself is incoherent in nature, meaning that its phase is uncorrelated with that of either the transmitted beam or the local oscillator. The phase and intensity are typically subject to random fluctuations on a timescale that is related to the inverse of the signal bandwidth (see section 4.9).

4.4.6 Photodetection

The beat signal is detected by directing the optically-mixed beam onto a photodetector which measures fluctuations in the light's intensity. In the telecommunications wavelength band around 1.55 μm, reliable photodiodes are readily available that are well suited to this purpose. The photodiode converts the incident photons into photoelectrons, which generate a measurable current (or voltage) that is normally amplified before digitisation. There are generally four contributions to the output of the photodetector module:

- Dark noise – the intrinsic wideband noise floor generated by the detector and amplifier combination in the absence of any incident light. Dark noise is due to the random generation of electrons and holes within the depletion region of the photodetector device that are then swept by the photodetector's electric field.
- Photon shot noise (Bleaney and Bleaney, 1976) (sometimes called quantum noise) – the random generation of photoelectrons by the incident LO beam leads to a wideband, spectrally flat (white) Gaussian noise source. The shot noise power spectral density increases in proportion to the optical power of the LO beam.
- Laser relative intensity noise (RIN) – intensity fluctuations that are in excess of shot noise, caused for example by relaxation oscillation of the laser output (Siegman, 1986). For a RIN-dominated noise floor, the power spectral density increases as the square of LO power. Such oscillation is typically at relatively low frequency, peaking below 1 MHz, and hence only affects the sensitivity of the lidar at low line-of-sight wind speeds around 1 m s^{-1}. In some systems it is possible to cancel the RIN by use of a dual-channel balanced detector.
- Beat term resulting from the wind signal – this is the contribution that contains the information on Doppler shifts from which the wind speed is derived. Its power spectral density increases in proportion both to the LO power and the signal power.

The requirements for the detector are high quantum efficiency, sufficient bandwidth to cope with the maximum Doppler frequencies of interest, and for the shot noise contribution to significantly exceed that of dark noise. This latter requirement depends on a combination of the detector's intrinsic noise floor and the optical saturation threshold.

4.4.7 Fourier analysis and lidar sensitivity

In order to extract the Doppler frequency information, it is necessary to perform a spectral analysis of the detector output. This is conveniently done digitally; an example of a typical signal processing procedure is described below and illustrated in Figure 45. An ADC with a sampling rate of 100 MHz permits spectral analysis up to a maximum frequency of 50 MHz, corresponding to a wind speed V_{LOS} of ~ 38.8 m s^{-1} for an upwardly pointing 30° scan (Eq.

(95), with $\lambda = 1.55$ μm). An analogue low-pass filter with a cut-off frequency of 50 MHz, inserted between the detector and ADC, eliminates aliasing. Spectra are calculated by digital Fourier transform (DFT) methods; a 512 point DFT gives rise to 256 points in the output spectrum with a bin width of ~ 200 kHz, corresponding to a line-of-sight velocity range of ~ 0.15 m s^{-1}. Each DFT represents ~ 5 μs of data; successive DFTs are then calculated, and the resulting "voltage" spectra are squared in order to generate a power spectrum. These power spectra are then averaged to find a mean spectrum for the averaging period. The random fluctuation in the shot noise floor of the spectrum reduces as the square root of the number of averages: the sensitivity increases by this same factor. For 4000 averages, the measurement time amounts to ~ 20 ms (or a data rate of ~ 50 Hz). This requires that the processing is capable of 100% duty cycle, which is achieved in ZephIR with a fast Fourier transform (FFT) block within a field-programmable gate array (FPGA). It has been shown that a standard PC with no additional duties to perform can achieve a similar performance. It is possible to accommodate reasonable variations in any of the above parameters (sample rate, DFT size and number of averages) and maintain the 100% duty cycle.

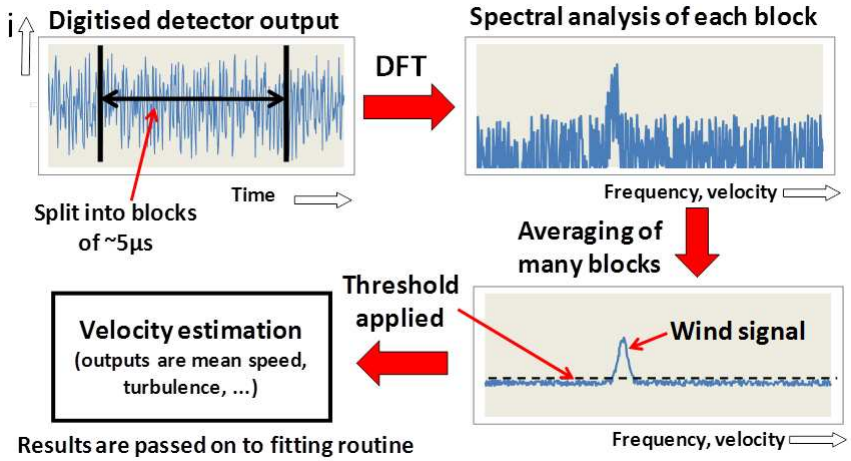

Figure 45: Stages in typical lidar signal processing: DFT analysis is carried out by a computer integrated into the lidar system. As an example, 4000 individual spectra might be averaged to achieve high sensitivity and measurable returns even in very clear air. This entire process takes only 20 ms, giving ~ 50 measurements of line-of-sight wind velocity per second

The width of the Doppler spectrum is determined by three elements:

- Instrumental width: this corresponds closely to the ~ 200 kHz bin width mentioned above.
- Transit-time broadening: during the conical scan, the beam passes through the aerosol particles in a timescale of $\sim 10 - 15$ μs, independent of the lidar focus setting. The corresponding broadening is again of order 200 kHz.
- Turbulence broadening: the probing of a significant volume results in a range of Doppler shifts from parts of the atmosphere that are moving at different speeds (see section 4.3). In general, this contribution increases with turbulence and shear, and occasionally there is more than one peak in the spectrum as a result. There is potential for using this broadening to measure and characterise turbulence at a fundamental level.

The turbulence broadening dominates except under conditions of very uniform airflow. High system sensitivity is of crucial importance for a wind lidar reliant on weak backscatter from

the atmosphere. The SNR[4] for a wind speed measurement by a CW CLR is given by:

$$\mathrm{SNR} = \frac{\eta P_s}{(hc/\lambda)\,\Delta\nu\,[1 + D(\nu) + R(\nu)]}. \tag{99}$$

Here η is an efficiency term incorporating optical losses and photodetector sensitivity (typically $\eta \sim 0.5$, approaching the value 1.0 only for a "perfect" system), P_s is the input signal power, as defined in Eq. (95) and hc/λ is the light quantum energy, of order 1.3×10^{-19} J. The signal bandwidth $\Delta\nu$ is determined by the three contributions listed above, and the term inside the square brackets denotes the various noise sources listed in section 4.7. $D(\nu)$ and $R(\nu)$ represent the power spectral density (at frequency ν) from dark noise and RIN respectively in units of the power spectral density of the local oscillator shot noise. Ideally $D(\nu)$ and $R(\nu)$ should both be $\ll 1$ over the range of Doppler frequencies of principal interest, so that the shot noise is the dominant noise source.

The SNR as defined here is the power spectral density at the Doppler peak divided by that in the surrounding noise floor. The averaging of many spectra (described in the following sections) ensures that good performance can be obtained even when the SNR is well below unity. For example, an SNR of 0.1 will easily exceed a 5σ threshold level (see next section) for an average of 4000 spectra. From the above it is possible to derive an approximate value of $\beta(\pi)_{\min} \sim 10^{-9}$ (m srad)$^{-1}$ for the minimum detectable backscatter, assuming a transmitted intensity 1 W and a 20 ms measurement time.

4.4.8 Velocity estimation

From the preceding sections it is apparent that each measurement of line-of-sight wind speed, obtained over a timescale of ~ 20 ms, generates a Doppler spectrum consisting of one or more peaks of variable width, superimposed on a noise floor that is predominantly white, but which may have spectral features originating from RIN and dark noise sources. This section outlines steps that can be followed to derive an appropriate estimate of the wind speed.

First, the noise floor is "whitened" so that each spectral bin contains the same mean noise level, achieved by dividing the power value in each bin of the spectrum by a previously-measured value for the same bin obtained with the shutter closed. A flat threshold is then applied at a pre-determined level above the mean noise; see Figure 45. A suitable and conservative choice for the threshold is 5 standard deviations (5σ) above the mean noise level. In the absence of any wind signal (e.g. with the output of the lidar blocked) such a setting will give rise to negligible occurrences in which the noise alone exceeds threshold. It follows that any bin whose level exceeds the threshold is deemed to contain a valid contribution to the wind signal. For each 20 ms measurement, the wind spectrum is reconstructed by subtracting the mean noise contribution from the contents of each bin that exceeds threshold, and applying a small re-correction for any distortion resulting from the noise whitening. In order to proceed to the next stage, a single velocity value is derived from the resulting spectrum. A number of options are available, including peak and median values; a common solution is to calculate the mean (or centroid) value $\langle V_{\mathrm{LOS}} \rangle$.

A series of these values of mean line-of-sight wind speed is generated as the ZephIR lidar performs a conical scan. Wind parameters are usually calculated from data obtained from a single revolution of the scanner. With a rotation time of ~ 1 s, up to 50 line-of-sight values are available for the next stage, in which a least-squares fitting algorithm is applied. Data is generally generated for a 1-s, single scan rotation as this is appropriate for most applications e.g. gust detection for turbine control or mechanical load mitigation.

[4] In the lidar community, this is commonly, and more properly, referred to as the carrier-to-noise ratio (CNR)

4.5 Ground based, vertical scan configuration wind field parameter determination

4.5.1 Least-squares fitting routine

The data that are fed to the fitting routine consist of up to 150 pairs of values of $\langle V_{\mathrm{LOS}} \rangle$ and azimuth angle ϕ. In conditions of uniform wind flow, this gives rise to a rectified cosine wave of the form:

$$\langle V_{\mathrm{LOS}} \rangle = |a \cos(\phi - b) + c| \,. \tag{100}$$

The derivation of this function is straightforward and can be found in a number of publications, e.g. Banakh et al. (1993). The peaks of the function correspond to the azimuth angle aligned parallel or anti-parallel to the wind direction. The function passes through zero when the azimuth angle is perpendicular to wind bearing since there is no component of velocity along the line of sight. The data are also conveniently displayed on a polar plot (Figure 46), which provides information at a glance on the speed, direction and vertical wind component. A standard least-squares fitting routine provides the best estimates of the values of the three floating parameters (a, b and c).

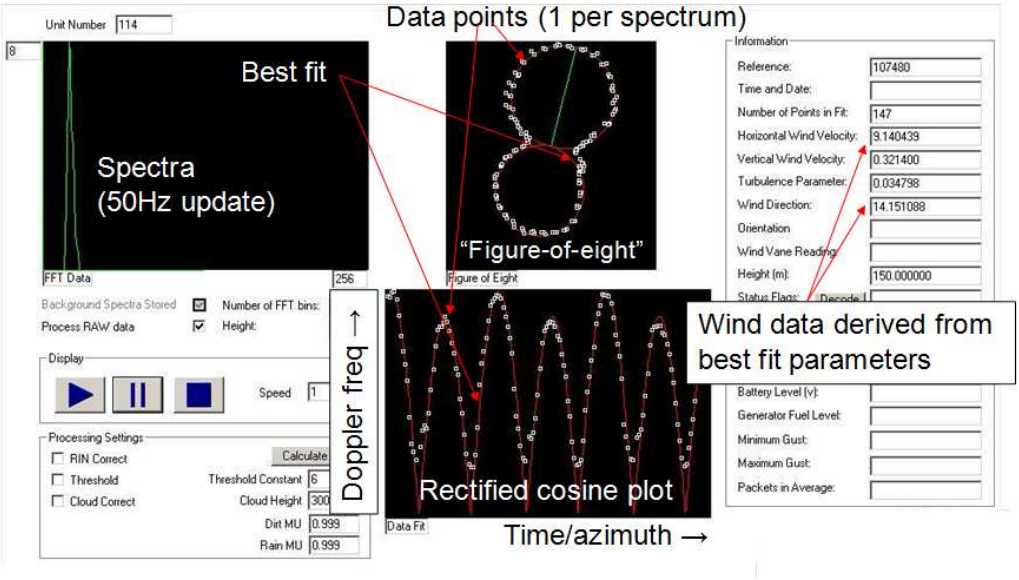

Figure 46: Wind lidar output for a ground-based, vertical scan ZephIR, illustrating many of the features of a wind profile measurement. This example has been obtained at a height 150 m above ground level, one of several heights being probed in sequence. The lower trace shows 147 individual line-of-sight wind speed values, obtained over a total period of 3 seconds (plotted as white squares against azimuth scan angle). The same data, along with the least-squares fit in red, are displayed above in polar coordinates on the figure-of-eight plot showing the wind bearing to lie slightly to the East of North. The wind parameters, derived from the fit, appear in the table on the right; the horizontal wind speed at this height is determined to be 9.1 m s^{-1}. The plot on the upper left shows one of the spectra from which each point on the other graphs is derived.

The high level of redundancy in the fitting process is advantageous and can be used to identify non-uniform flow. The root mean square deviation of the points from the optimum solution gives an indication of the quality of fit, and this can be related to the value of turbulent kinetic energy (TKE; see Wagner et al. (2009)). More work is needed to establish a full understanding of the turbulence information available from lidar signals (Banakh et al., 1999). Note that information on turbulence is also available from the spectral widths of the

individual line-of-sight wind speed measurements, but this is not currently used to evaluate turbulence parameters.

4.5.2 Parameter extraction

The wind parameters for each measurement period are extracted from the best fit as follows, where (θ is the scan cone half angle of order $30°$):

$$\begin{aligned} \text{Horizontal speed} \quad V_H &= a/\sin\theta, \\ \text{Vertical speed} \quad w &= -c/\cos\theta, \\ \text{Bearing} \quad B &= b, \quad \text{or} \quad b \pm 180°. \end{aligned} \tag{101}$$

Where there is an ambiguity in the sign of the Doppler shift, there are two equally valid best-fit solutions corresponding to values of b separated by 180°. The correct choice is usually easily made by choosing the solution that lies closest to a conventional measurement from a met station situated close to ground. Conventionally, a wind profiling lidar incorporates such a station that performs these (and other) measurements and feeds the results to the analysis software.

The 1–second wind parameter values are stored internally for subsequent analysis; they can also undergo further processing for extraction of average values.

4.5.3 Data averaging

It is a common requirement to calculate 10–minute averaged wind data for compatibility with industry standards. This is most easily achieved by calculation of the arithmetic mean ("scalar average") of the individual values of V_H, w and B that have been obtained during the required period. A vector average is also possible in which the resultant of the individual measurements is calculated over each 10 minute period. In practice the results from the two methods differ negligibly in reasonably stable conditions. In accordance with industry standards, ZephIR computes a scalar average for V_H and w, and a vector average for B.

When a CW lidar is operating as a wind profiler it is necessary to measure each height in series. Hence, at any given height the wind is not monitored continuously. Instead, an individual measurement (taking 1 to 3 s to obtain) is followed by a period of order 7–20 s during which the lidar is focused at other heights. Since this sampling is carried out randomly with respect to any behaviour of the wind, this duty cycle of order 15% has negligible impact on the validity of the resulting 10–minute averaged values. Also the typically large scan area ensures the beam samples a much higher fraction of the overall turbulent fluctuations.

4.6 Uncertainty analysis

4.6.1 Rain/snow/cloud, solid objects

In general the Doppler shift measured by coherent laser radar is very accurate. This is apparent from Eq. (95) as long as the laser wavelength remains stable and the signal processing has been correctly performed - both good assumptions in practice. The laser wavelength is defined by the manufacturer's specification to within ± 1 nm of the nominal wavelength (1565 nm). So the contribution to velocity uncertainty from wavelength variation is $1/1565 = \pm 0.07\%$. The Doppler frequency spectra are calculated in a dedicated DSP board with a manufacturer's specification of clock stability to within ± 50 ppm. The clock stability is directly proportional to uncertainty in wind velocity and therefore the uncertainty due to this potential source of error is again small at $\pm 0.05\%$ The values of $\langle V_{\mathrm{LOS}} \rangle$ that are derived from the centroids of the spectra can be measured to considerably better than a bin width. Confirming the above instrumental considerations, the line-of-sight velocity calibration was experimentally verified in a recent wind-tunnel trial (Pedersen et al., 2012). A modified ZephIR 300 configured to

stare directly along the flow reported measurements in very good agreement with a reference pitot tube for a wide range of wind speeds from 5-75 m s^{-1}. (Figure 47),

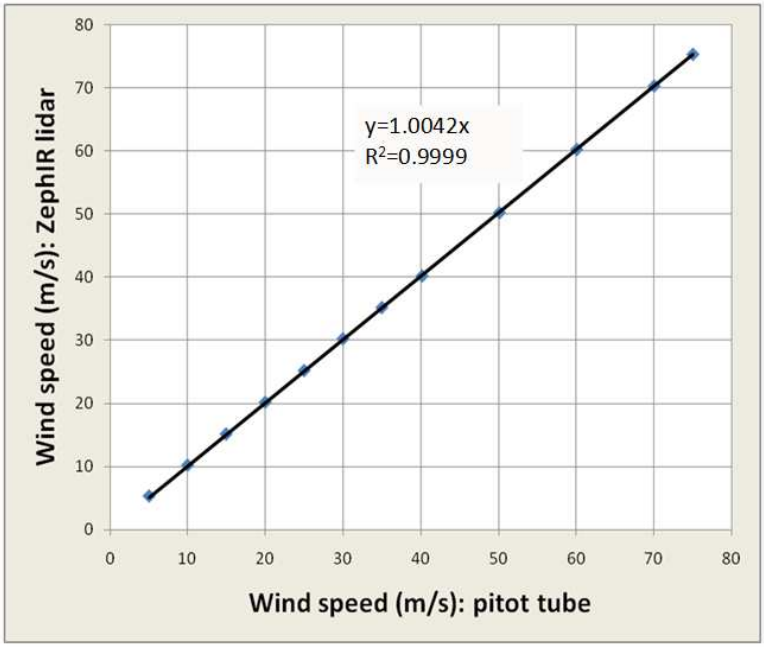

Figure 47: ZephIR lidar wind speed correlation with instrumented wind tunnel pitot tube. Courtesy of LM Wind Power, DTU Wind Energy, and NKT Photonics.

A greater source of error arises from uncertainty about what provides the scattering from which the Doppler shift is derived. The scattering is assumed to originate from atmospheric particles moving at the same speed as the wind and positioned close to the focus of the lidar beam (section 4.3). An obvious example where this breaks down is when the beam intersects a solid object (e.g. a bird) that is moving at a different speed from the wind giving a measurement which could be in error. However, in such a case the value of $\langle V_{\mathrm{LOS}} \rangle$ so derived will stand out as clearly anomalous on the polar plot (Figure 46). The presence of such points will be diluted by approximately 50 correct values of $\langle V_{\mathrm{LOS}} \rangle$ obtained from uncontaminated parts of the atmosphere, and their inclusion should not introduce any bias. A further safeguard against these erroneous points is provided by a simple "outlier removal" algorithm. This identifies points that lie anomalously far from the best fit solution to Eq. (100) and eliminates them. The least-squares routine is then rerun on this slightly reduced set of $\langle V_{\mathrm{LOS}} \rangle$, data pairs. The presence of precipitation within the probe volume leads to a different source of uncertainty. The downward motion of rain and snow inevitably leads to some error in the vertical component of wind speed. However, the presence of rain and snow is normally easily identified from the measurement process (for example by detecting activation of a rain sensor), and the resulting values of vertical wind eliminated from the data. Other wind parameters are unaffected and can still be correctly inferred.

4.6.2 Cloud effects

CW laser wind profilers focus the beam in order to measure wind speed at a given height. This technique has the advantage of uniformly high sensitivity independent of the measurement range, and of very small probe volumes at lower ranges where detailed investigation of shear or accurate prediction of high turbulence wind fields is important. However, the signals do require correct processing when the beam impacts a cloud base at higher altitude since the contribution to the Doppler signal from cloud provides an additional contribution to that from the aerosols at the desired height.

A general approach to mitigating this problem needs first to identify the presence of a cloud return and then remove its contribution from the Doppler spectra. Cloud returns have a number of characteristics that allow them to be distinguished from aerosol returns:

- Their velocity usually higher
- Their spectral width usually narrower
- For horizontally scanned lidars, only a section (generally the upper part) of the circular scan is generally affected by cloud
- The power in Doppler peak has clear dependence on lidar focus; the power is maximised when the lidar beam is focused close to the height of the cloud base
- The Doppler spectrum from cloud is independent of focus range

The latter two characteristics are highly dependable and form the basis for identification and elimination of spurious cloud returns. The general strategy for removal of cloud signals is outlined in the following steps (and illustrated in Figure 48):

1. Routinely run the lidar at an additional greater height (e.g. 800 m - essentially a collimated beam output) immediately before or after the maximum height of interest (say 150 m in this example).
2. For each azimuth angle around scan at 150 m, identify the 800 m ("cloud") spectrum obtained at the closest value of azimuth angle.
3. Apply test conditions to the 150 m spectra to determine whether any cloud signal is present in the spectral data, then if necessary apply cloud removal algorithm.
4. Run standard thresholding and centroiding routines on resulting "clean" spectra and fit to the rectified cosine wave (Eq. (100)) to obtain wind parameters.

A cloud removal algorithm based on this approach is implemented in ZephIR; this has been extensively tested in a number of locations, and its effectiveness demonstrated by correlation analysis against calibrated tall masts. During the 800 m ("wind profile") scan, background measurements are taken to quantify the specific cloud return and any cloud effect is then removed from the processed data.

In general, lidars of various types of design will all have difficulty measuring in very low cloud and fog scenarios where the light emitted from the lidar is unable to reach all the heights of interest due to absorption in the atmosphere. While this atmospheric condition mostly occurs during low wind speed periods, it is important that these periods be identified. In the majority of cases they are removed by filtering methods.

Trials of a ZephIR unit at Risø DTU's test site at Høvsøre (Courtney and Gottschall, 2010) took place in long periods of low cloud and hence provide a demonstration of the performance in challenging cloud conditions. The data set summarised in Table 5 below was taken during a period of 4 weeks in October and November 2009. Cloud height was measured using a ceilometer; 25% of data was obtained with the cloud base below 300 m, and 43% obtained with the cloud base below 600 m. A more recent independent evaluation of a ZephIR 300 system in similar conditions is available at: http://www.zephirlidar.com/sites/yourwindlidar.com/files/ZephIR-301-Evaluation-at-Risoe-Test-Site.pdf.

The results of the trial (Table 5) indicate a good agreement between lidar and mast at all heights from 40 up to 116 m. Filtering has been applied to remove sectors prone to the influence of turbine wakes, and speeds below 4 m s^{-1}, to ensure measurement within the calibration range of the mast cups.

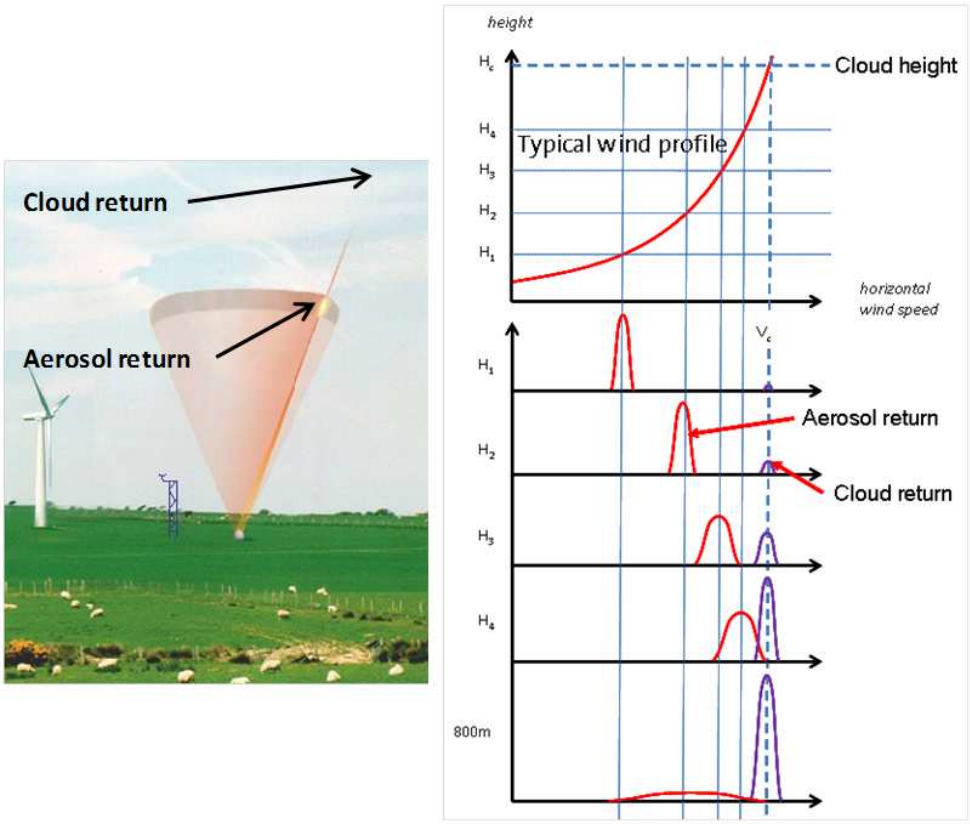

Figure 48: Cloud removal for a vertical scan CW lidar. The left plot shows the lidar conical scan focused at a typical height above ground level. The Lorentzian sensitivity curve is also shown; a spurious return is generated when the far wing of this curve intersects a strongly scattering low cloud layer. The right plot shows the aerosol (red) and cloud (purple) returns as the lidar is focused at various heights - the level of cloud contamination increases with focus height. The cloud signal is easily identified from the 800 m focus, and these data are then used to eliminate the cloud return at the measurement heights.

Table 5: Results of correlation analysis of 10-minute averaged horizontal wind speed for a ZephIR 300 trial at Høvsøre, Denmark in March 2011. Gradients, m, (forced through the origin) and coefficients of determination, R2, of unity would imply perfect agreement between the lidar and the mast-mounted cup anemometers. (It should be noted that the slopes very close to unity are slightly fortuitous, since the cup anemometer measurements have uncertainties at least of order $\pm 1\%$, due to calibration and mounting/shadowing effects).

Height AGL [m]	Slope m	R^2
116	0.993	0.977
100	0.987	0.988
80	0.984	0.992
60	0.990	0.992
40	1.007	0.992

4.6.3 System positioning accuracy

Correct alignment ensures the risks are low, but errors in aligning the lidar during set-up will have an impact on the measurement of wind bearing (if the lidar is rotated from its correct orientation) and vertical wind speed (if the lidar is tilted, so that the axis of its conical scan is not precisely vertical). For a small tilt angle δ, the error in vertical wind speed w will vary

from $\pm V_H \sin\delta$ (if the tilt is towards or away from the direction of the wind) to zero (if the tilt is perpendicular to the wind). Any bias on V_H is negligible to first order.

4.6.4 Probe volume effects and operation at greater heights

As discussed in section 4.2, the lidar samples the motion of air from a finite volume, centred on the beam waist at the focus. Clearly there is minimal risk of bias while all the air within the probe volume moves at the same speed. However, for vertical scan lidars, there is usually some degree of shear across the sample region. For a linear shear this leads to spectral broadening of the returns, but no overall bias. A strong non-linear shear profile across the probe volume is required to induce any bias of significance. In practice such conditions are rare, in particular for measurement heights around hub height and below where the probe length is relatively small.

Most lidar comparisons have taken place beside masts of heights around 100 m or less. However, in early 2009 a study took place in Iowa, USA against a 200 m mast in flat terrain. The results showed high correlation (Table 6, taken from Barker (2009)) even at the greater heights examined (150 and 200 m), which approach the expected maximum operating range for focused CW lidar.

Table 6: Results of a comparative trial of a ZephIR lidar against a very tall mast, equipped with two types of cups at each height. The data indicate that the extended probe length at greater heights did not result in excessive bias or errors. [1]: Forced through the origin; [2]: Only hourly average containing 6 valid 10 min measurements are compared

	NRG IceFree3				NRG MAX#40C			
	Ten min average		Hourly average[2]		Ten min average		Hourly average[2]	
Height AGL [m]	R^2	Slope[1]	R^2	Slope[1]	R^2	Slope[1]	R^2	Slope[1]
193	0.984	0.987	0.987	0.987	0.982	0.993	0.988	0.992
157	0.982	1.006	0.988	1.005	0.984	1.000	0.989	1.000

4.6.5 Flow uniformity and complex terrain

Because only line-of-sight wind components are measured, a single ground-based lidar unit inevitably provides an incomplete picture of the 3D vector flow, regardless of the scan pattern employed. Firstly, this "cyclops" LOS velocity determination at any one probe point is unable to disambiguate the full wind vector information, merely measuring one component. The full vector at a given point can only be measured by the provision of three (or more) lidar units positioned on the ground at an appropriate separation distance (comparable to the measurement height for best accuracy), such as the Windscanner system under development by Risø DTU, web address below: `http://www.risoe.dtu.dk/research/sustainable_energy/wind_energy/projects/vea_wind_scanner.aspx?sc_lang=en/`

Secondly, whilst a given scan pattern can provide more information about the wind flow, certain assumptions, for example uniformity of flow across the probed area, linear or logarithmic vertical shears, are often reasonably made. However, in complex terrain, the flow undergoes stable and unstable non-uniformities, and the figure-of-eight plot (Figure 46):) can distort systematically for a given wind direction, reflecting the speeding up and slowing down in certain regions of the scan. The ZephIR lidar provides some information about the flow non-uniformity, with up to 50 points per second being interrogated around the scan disk.

In the presence of non-uniformity in flow (section 4.2), a lidar measurement can indicate a wind speed different to that from a point measurement by a mast-mounted cup anemometer.

Lidar data has been successfully combined with the output from flow-modelling software, using both linear models (Bingöl et al., 2008, 2009; Bingöl, 2010) and computational fluid dynamics, CFD (Harris et al., 2010; Pitter et al., 2012). This pragmatic approach generates measurements equivalent to a "point-in-space" sensor by using the results of flow modelling to adjust the measured lidar wind speed. This topic will is dealt with elsewhere in this lecture series, examining possible improvement of lidar resource assessment capability in complex terrain.

4.6.6 Dependence on backscatter level

Under conditions of high backscatter, the spectrum provides an accurate measure of the distribution of line-of-sight velocities within the probe volume, weighted according to Eq. (91). As the backscattering strength drops (usually associated with increased air clarity) this has a similar effect to raising the detection threshold, and will lead to elimination from the spectrum of weaker components of velocity. The impact of the system noise floor on the detailed spectral shape will also be increased. The centroid values $\langle V_{\mathrm{LOS}} \rangle$ will be unbiased and independent of threshold level when the spectrum is symmetrical. However, for a skewed (asymmetric) spectrum the precise value of $\langle V_{\mathrm{LOS}} \rangle$ will be sensitive to the threshold. Hence a small difference in measured wind speed is possible between two measurements under conditions that are identical in every way apart from the level of backscatter. However, there is no evidence from comparisons so far to suggest that this leads in practice to a significant discrepancy.

A further possibility to be considered is the effect of saturation (by very strong scattering returns from thick cloud) of the lidar detector, electronics or signal processing. In the event that the input signal exceeds these limits, the spectrum will become distorted, possibly featuring higher harmonic components of the true Doppler frequencies. In practice, the range of inputs to the ADC can be tailored to accommodate the highest levels of backscatter that will reasonably be encountered, eliminating the risk of bias.

4.6.7 Beam obscuration and attenuation

Lidar can operate successfully even when part of its scan is obscured. This confers great flexibility so that the system can easily be located adjacent to masts, buildings or in forests. Stationary objects pose no major problem other than the loss of wind measurements from the relevant obscured sector of the scan. Slowly moving objects can also easily be filtered, based on the magnitude of their Doppler shift.

In the above cases, the fit to Eq. (100) will no longer contain data over the full 360° range of ϕ. Laboratory experiments on moving belt targets have indicated that accurate measurements are obtained even when over half of the scan is obscured. Large errors in the least-squares fitting process become possible as the obscuration increases yet further; such conditions are identified and a null result returned.

4.6.8 Wind direction

For ground based, vertically scanning ZephIR, the two best-fit solutions ZephIR obtains to Eq. (100) give values of wind direction that are 180° apart. Selection between the two options is made with reference to the measurement of wind direction from a ground-based anemometer. This needs to be in disagreement by over 90° with the direction at the chosen height for the incorrect choice to be made. While such a directional shear (veer) is conceivable in highly complex terrain and at very low wind speed, it is much less likely in the reasonably uniform conditions of interest for wind energy applications, and the wind direction selection can be propagated upwards from measurements at several heights. In the event of the wrong choice being made, leading to a wind direction that is in error by 180°, the value of vertical component of the wind w will have the wrong sign. In other words, an updraught will be wrongly identified

as a down draught (of the same absolute speed) and vice versa.

4.7 Calibration, validation and traceability

For historical reasons, the clearest demonstration of validity is provided by direct side-by-side comparisons between the lidar system and a fully instrumented IEC-compliant meteorological mast of suitable height. Rigorous comparisons must be carried out with great care to avoid a number of problems associated with cup anemometers (Kristensen, 1999). These are well known and include the following:

- Shadowing of the cup anemometer by the mast from certain directions
- Cup over-speeding in turbulence and sensitivity to any vertical wind component
- Cup icing
- Valid cup anemometer calibration
- Topographic effects leading to non-uniform flow across the area occupied by mast and lidar scan (including turbine wakes)

A lidar/mast comparison is commonly used to provide a validation of lidar performance, and examples of such checks were provided by the results in Tables 5 and 6. The lidar can then be used as a traceable reference for comparison with other units.

Lidar systems are normally calibrated in the laboratory before shipping. Routine checks on the calibration of units on their return to base provide confidence of long-term stability. As an example, the calibration process undertaken for a ZephIR lidar is outlined below. This consists of three stages:

1. Velocity and direction check against a calibrated moving belt. The process provides a direct check of laser wavelength and scanner cone angle, each of which affects the velocity calibration (via Eqs. (94) and (100) respectively).
2. A focus range check is carried out with a moving target located at precise distances from the lidar. The closed loop positioning system ensures no drifts over time. An example of the output data from a focus calibration test was plotted in Figure 44 (section 4.4).
3. Finally, each unit undergoes an outdoor test to measure wind speed at several heights using an industry-certified, 92 m, meteorological mast. Figure 49 shows an example correlation plot of 10 min average horizontal wind speed, obtained over a period of 7 days.

Each of the three tests above gives information on the sensitivity of the unit; for deployments in "clean" air, it is important to ensure this aspect of performance is fully optimised and has not deteriorated, or there is a risk of reduced data availability.

It is important that no adjustments are performed during validation trials, or afterwards for as long as the lidar remains a traceable reference unit. The certification process outlined above has been defined in collaboration with industry experts including Garrad Hassan and provides the traceability that is a key element of formal energy prediction reports used by the financial community.

In addition to its velocity measurements being closely traceable to primary units of time and length, lidars offer a potential advantage for accurate shear profiling, for both speed and direction, in that the same instrument is used to make the measurements at all heights. By contrast, a mast relies on consistent calibration of the full set of cups and vanes; any differences in calibration of the individual instruments will lead to uncertainty and error in the shear assessment. An example of the difficulty in calibrating instruments such as cup anemometers that rely on relatively complex, non-linear physical interactions is illustrated in Figure 50, where calibration results from four high quality cups are compared.

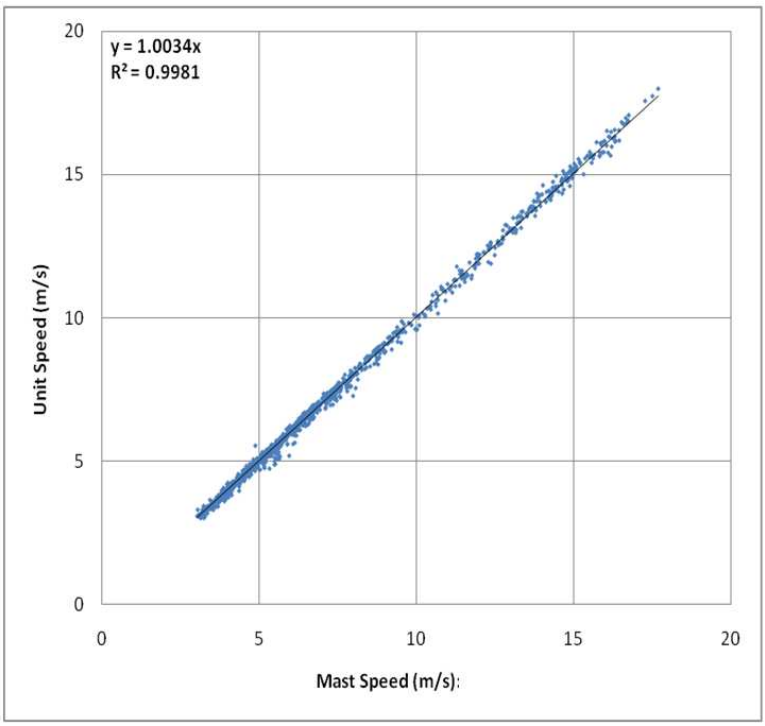

Figure 49: A ground based ZephIR 300 system compared to the industry-certified met mast at Pershore, demonstrating strong correlation and a gradient very close to unity. In this example, comparison was carried out at a height of 70.5 m. From (Rutherford et al., 2012).

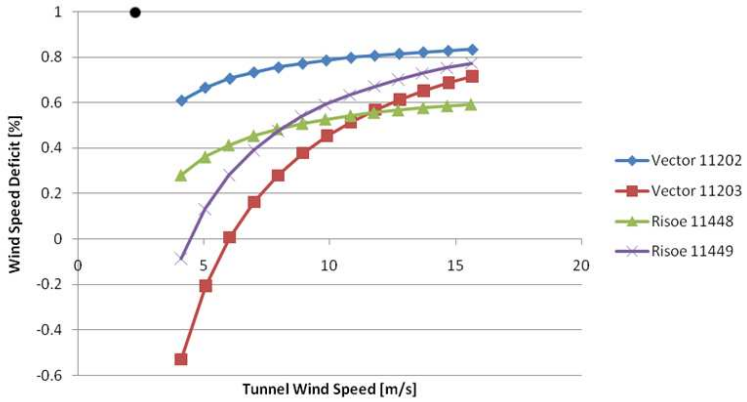

Figure 50: Graph showing results from routine re-calibration of four cups to be used at an accredited met mast site. The vertical axis shows differences when the same cup was calibrated at two independent wind tunnel standards facilities. The tunnel-to-tunnel calibrations of the same cups show variability of the order of 1%.

4.8 Turbine mounted continuous wave lidar

An application that has recently generated much interest is the use of remote sensors, such as lidar, to measure the wind field ahead of an operating wind turbine generator. Since, for a correctly yawed turbine, the lidar is always pointing into the incident wind field; this can be very useful for power curve measurement as no sectors need to be eliminated for turbine shadow, as is the case when using a fixed meteorological mast and cup anemometers (of course sectors affected by the wakes of adjacent turbines will still need to be filtered). Providing advance wind data to the turbine control system also has many potential advantages such as reducing stress loads by warning of incoming gusts or optimising rotor pitch control. The lidar can

Table 7: Combined results from 28 ZephIR 300 units. The mean and standard deviation of the mast comparison parameters, gradient and R^2, were calculated from the first batch of 28 ZephIR 300 units. These results confirm the consistency of the lidars' performance.

Height [m]	Gradient		R^2		Laser sensitivity	
	Mean	Std. Dev.	Mean	Std. Dev.	Mean	Std. Dev.
91	1.0039	0.0072	0.9894	0.0059	1.0350	0.0893
70	1.0033	0.0072	0.9928	0.0059		
45	1.005	0.0050	0.9924	0.0050		
20	0.9967	0.0045	0.9925	0.0048		

be mounted on the nacelle roof, within the rotor spinner (Figure 51) or built into the rotor blades.

Figure 51: Continuous wave dual mode ZephIR 300 lidars mounted on a nacelle roof (left) and within a wind turbine spinner (right).

The high sensitivity and hence fast data rates of circular scanning CW lidar make it very well suited to turbine mounted applications. By adopting different signal processing and data analysis strategies; hub height wind speed, direction, shear exponent and turbulence can be measured, or speed, direction and turbulence at discrete heights across the rotor can calculated (or both). The latter technique can be used to generate rotor equivalent wind data which has been shown to produce more precise and representative wind turbine power curves, especially for large rotor diameters (Wagner et al., 2008; Wharton and Lundquist, 2012).By measuring the inclination of the lidar in real-time, the circular scan CW approach allows the effects of nacelle motion on both line-of-sight velocity and measurement height to be negated.

4.8.1 Least-squares fitting routine for horizontal scanning (turbine mounted) operation

The use of a CW lidar for turbine mounted applications is fundamentally a quite different arrangement when compared to a ground based, vertical scanning configuration. Unlike the latter, the scan axis is approximately horizontal, and the lidar is almost always predominantly staring into the wind. A consequence of this is that the polar plot (of the measured line-of-sight wind speeds as a function of scan angle) is no longer a figure-of-eight shape, but instead takes on a more circular appearance (Figure 52).

Important quantities of interest for turbine relevant wind field determination include hub height horizontal wind speeds, the vertical wind shear, and the yaw misalignment. The latter is an angular measurement of the difference between the horizontal direction of the lidar scan axis and the wind direction, and it is useful for yaw control of the turbine or calibration of wind turbine nacelle vanes. Horizontal shear and wind inflow angles are also of interest.

As before, a wind model can be constructed. This must take into account the mounting geometry on the turbine e.g. (Mikkelsen et al., 2010; Angelou et al., 2010). A least squares fit of the measured wind field can be performed to extract the parameters of interest.

One of the attractive features of the CW lidar's circular scan pattern is that it samples the wind field around the full range of rotation of the turbines rotor. Typically 50 line-of-sight measurements are obtained over one circular scan in 1 second (i.e. 20 ms sample rate). This dense sampling of the wind field around the rotor disk can give valuable preview data to allow feed-forward control for both collective and individual pitch control of the blades of the turbine.

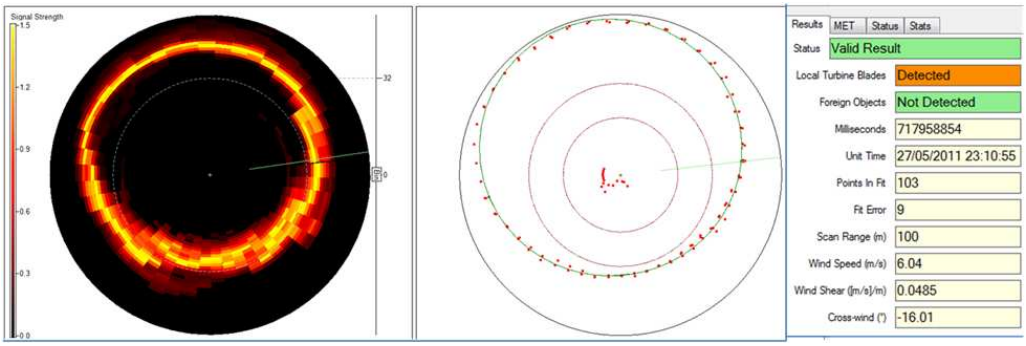

Figure 52: An example of visualisation and analysis of data from a turbine-mounted ZephIR. Left: polar plot of raw data, showing line-of-sight wind speeds with scan angle. The radial axis is the LOS speed. The breadth and structure of plotted distribution gives an indication of the spatial turbulence within the scan volume e.g. ground induced shear and turbulence can be seen in the lower range of angles. Low level wind jets and wakes from other turbines can also be detected in this manner. Centre: real time analysis of the received polar plot, showing centroids of the received line-of-sight spectra (red dots) and fitted wind parameters (indicated by the green curve). The central red dots are turbine blade returns and are automatically filtered prior to fitting. Right: reference data and wind characteristics calculated from the fit.

An example of filtering that can be required is for the case of turbine blades. For a turbine mounted CW lidar, situated on the roof of a turbine's nacelle, and scanning upwind through the turbine blades, the lidar must contend not only with quasi-periodic blocking of the beam, but also strong Doppler returns from the blades themselves. Although the intensity of the back reflected laser signals can be very high from these blades (typically 50 times higher than the wind returns), this can help distinguish them from the line of sight Doppler returns from the incoming wind. Additionally, the relatively slow, near perpendicular path of the blade surfaces means that the Doppler shifts are relatively low frequency (giving Doppler returns corresponding to typically < 2 m s^{-1}). Hence efficient blade rejection filters, which remove these signals from the wind field fitting process, are simple to implement. However, blade effects do reduce the number of data points around the scan, and for this reason, hub (or spinner) mounted CW lidars can have some advantages.

4.8.2 Turbine mounted CW lidar for wind turbine power curve measurement

Continuous wave lidar have now been deployed in a number of wind turbine power curve measurement campaigns. Some results from two of these are reproduced in this section. The first campaign discussed here was organised by ROMO Wind and carried out in flat terrain

in Eastern Jutland between January and April, 2012 (Slinger et al., 2013). The lidar, a dual mode ZephIR 300, was mounted on the nacelle roof of a NEG-Micon 2 MW wind turbine with a 72 m rotor diameter. There was no meteorological mast data from the site - the trial was intended to measure relative, rather than absolute power curves, in order to demonstrate and quantify turbine performance improvements after turbine tuning.

Lidar data from the first part of the trial, before wind turbine tuning was carried out, identified a turbine yaw error of between 14° and 16° (Figure 53). This was remedied by a nacelle vane recalibration before the second phase of the trial was undertaken. The effects on the lidar measured power curve (at a measurement range of 180 m or 2.5 rotor diameters) are clearly visible (Figure 53). ROMO Wind estimated an improved annual energy production (AEP) of approximately 5% after yaw recalibration.

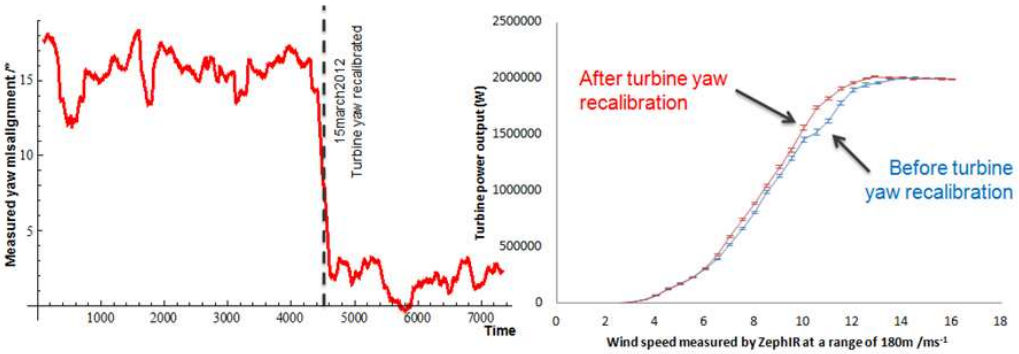

Figure 53: (a) Measured turbine yaw misalignment before and after nacelle vane recalibration. (b)Wind turbine power curves measured by nacelle mounted lidar before and after nacelle vane recalibration at a measurement range of 180 m.

Measurements were also made at a series of other ranges between 10 m and 180 m and are shown in Figure 54). While the measurements at close range "flatter" the power curve due to the rotor induction effect, they demonstrate that high quality power curves can be obtained very close to the rotor. While these would have to be corrected to be quantitative, they are very representative of the true wind field incident on the turbine rotor and can be expected to be immune to say, the effects of complex terrain, as compared to more remote measurements.

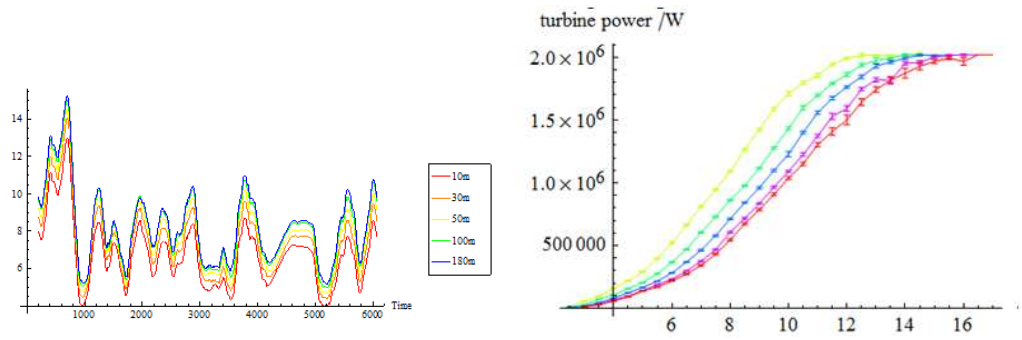

Figure 54: (a) time series of wind speed measurements taken at a series of measurement ranges. The measurements are highly correlated, but rotor induction (blockage) effect is clearly visible.(b) Series of wind turbine power curves generated from measurements at several ranges. The upper curve is from the closest range (10 m), the lower curves were measured at 30, 50, 100 and 180 m respectively.

The second study reported here took place on a DTU test turbine situated at Roskilde,

Denmark. The turbine was a 500 kW Nordtank turbine with a rotor diameter of 41 m and a hub height of 36 m. A meteorological mast was situated at a distance of approximately 2.2 rotor diameters, so absolute as well as relative measurements could be carried out. The met mast was equipped with cup anemometers at heights of 18, 27, 36, 45 and 54 m above ground level, spanning the entire swept area of the rotor. Figure 55. below shows a comparison of hub height wind speed measured by the lidar (at a range of 2.2 rotor diameters) and the met mast, when the wind direction was in a sector that was unaffected by shadowing or wake effects from adjacent turbines. It can be seen that the measurements demonstrate a high level of correlation, particular when the sloping nature of the terrain at this site is taken into account.

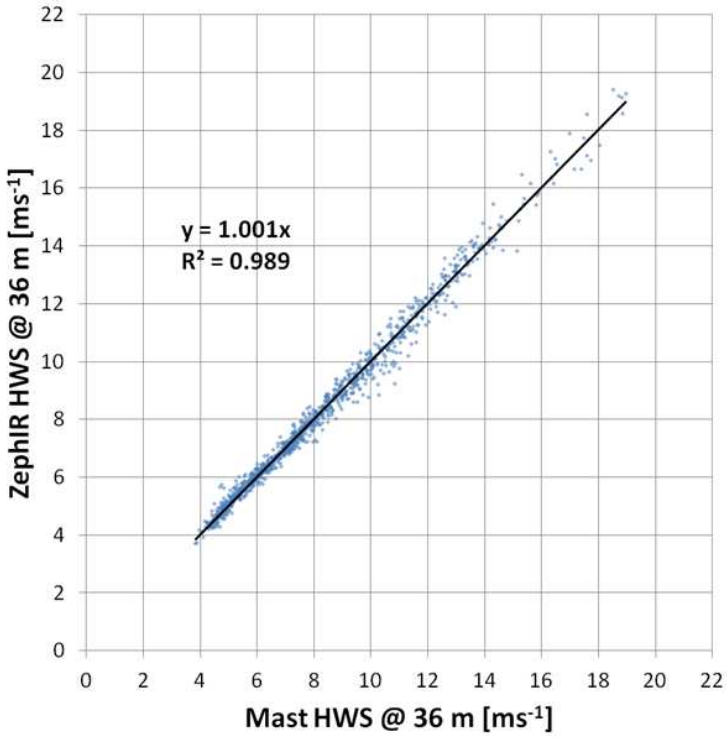

Figure 55: Correlation plot of hub height wind speeds measured by a nacelle mounted CW lidar and a pair of cup anenometers on a 500 kW Nordtank wind turbine at Roskilde, Denmark.

The lidar data was then reprocessed to measure wind speed and direction at the height of each of the cups listed above, taking full account of any nacelle motion on both measurement height and line-of-sight velocity. Turbine SCADA power output data was corrected for air density and temperature and used to generate rotor equivalent power curves from both the met mast and the lidar data (Figure 56). This preliminary result indicates that turbine mounted CW lidars are capable of measuring power curves of comparable quality to met masts, but with the advantage of easy redeployment. These are believed to be the first reported rotor equivalent power curve measurements using a commercially available nacelle mounted lidar.

Subjects of current research in the turbine mounted lidar area include feed-forward control for stress load reduction and short range (i.e. less than 2 rotor diameters) wind speed measurement for turbines situated in more complex terrain where long range measurements are less representative of the actual wind field incident on the turbine rotor.

4.9 Summary, state of the art, and future developments

Coherent monostatic CW lidar is a method capable of rapid wind speed measurement at relatively short ranges (all the way from 10 m to 200 m) and hence is well suited to several

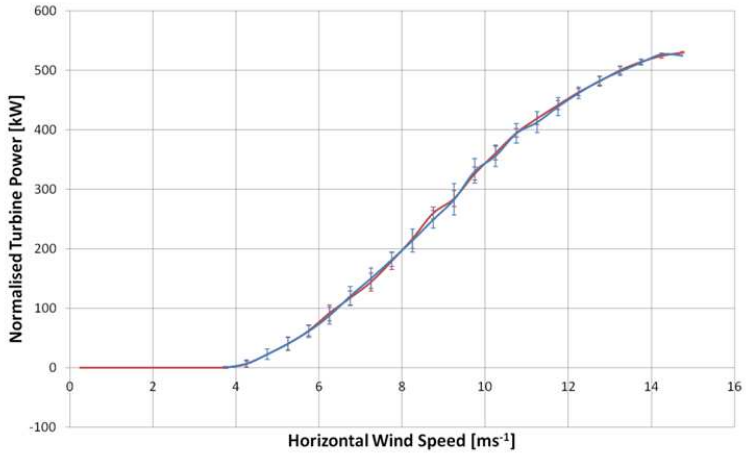

Figure 56: Normalized power curves using rotor-equivalent wind speeds measured by a nacelle mounted CW lidar (blue) and mast mounted cups (red) at heights of 18, 27, 36, 45 and 54 m above ground level. Wind speed bin size was 0.5 m s^{-1} and the error bars indicate the standard deviation of the scatter in the measured data.

requirements in the field of wind energy. Examination of the measurement process reveals that the basic acquisition of line-of-sight Doppler spectra is a well-established method with little scope for gross errors and miscalibration. The subsequent steps required to convert these spectra into a profile of wind speed are more complex, however, and their validity relies on a number of well-established assumptions. Much work has been performed to test the validity of the assumptions outlined in section 4.3, and to understand the uncertainties and other issues discussed in section 4.6.

Complex terrain remains a topic of great interest as it becomes increasingly necessary to explore less ideal locations as potential wind farm sites. In such sites the horizontal wind speed deduced by conically-scanned lidar can be subject to differences in comparison to that measured by co-located cup anemometers when the flow is non-uniform across the lidar measurement disk. A method has recently been developed in which the impact of inhomogeneous flow at complex flow sites is examined using computational fluid dynamics (CFD modelling to predict the bias that will be experienced by a lidar in comparison to a conventional met mast equipped with cup anemometers. Similar percentage changes in wind speed as measured by a mast are shown to occur if the mast were to be moved by ± 50 m from its original location. This suggests a methodology for resource assessment in complex terrain in which lidar is used in combination with CFD modelling in order to (i) adjust the lidar data for the impact of non-uniform flow and (ii) investigate the wind variations across the site that are a major source of uncertainty for current techniques.

Lidar offers some potential advantages in turbine power curve measurement. The measurement over an extended volume may give a more representative estimate of the wind energy content of the air interacting with the blades, and the ability to re-position the lidar quickly is clearly advantageous. A study reported by Wagner et al. (2008) has shown that exploiting the lidar wind profile data can reduce the scatter of points in a measured power curve. In another recent study (Cayla, 2010) a ZephIR lidar gave an almost identical power curve to an IEC-instrumented power performance mast. The scatter of the points in the power curve obtained using the ZephIR data at hub height was somewhat lower than that for the mast. This result needs further investigation and possibly is a consequence of the more effective sampling of the wind around the scan disk. It follows, interestingly, that remote sensing equipment that agrees perfectly with the mast would therefore have provided higher scatter in the power curve than ZephIR!

The extraction of turbulence data relevant to the wind industry from lidar signals is an area that will benefit from further research and verification through field comparisons. Turbulence

can manifest itself as gusts, eddies, and fluctuations in wind speed. It is important in wind energy applications to characterise the levels of turbulence encountered at a specific site location. A commonly-used basic measure of turbulence is turbulence intensity (TI). ZephIR calculates the turbulence intensity that a conventional cup would have obtained at the same measurement height by analysing the variation in individual wind speed values during a 10-minute averaging period. This value of TI is automatically logged in the output data. The calculation takes into account the difference between point measurements obtained from a cup anemometer, and spatially-averaged lidar data where a volume is interrogated (Barker et al, 2012).ZephIR's measurements of turbulence have been investigated in a number of independent studies against calibrated met masts in flat, offshore and complex terrain, and at different heights above ground (Wagner et al., 2009).

Resource assessment in maritime locations is becoming increasingly relevant as offshore wind farms assume greater importance. The cost of installing an offshore tall mast is very high, so remote sensing may prove particularly advantageous in such locations. ZephIR lidars have been involved in successful trials on several offshore platforms in the North Sea (e.g. Peña et al. (2009)), the Baltic, and around the lakes and coasts of North America. A floating lidar platform offers an exciting future concept; an early attempt to develop a ZephIR system on a buoy (SeaZephIR) took place in 2004/5. After a redesign, the system took to the water off S Norway in 2009. A world-first demonstration trial took place over a period of several weeks in late 2009, involving one ZephIR unit stationed on land, with the floating SeaZephIR unit positioned 800 m out to sea. The wind speeds measured by the two ZephIR units showed excellent correlation, with differences in mean wind of $\sim 1\%$ or less at all heights over a 3 week test period (see Table 8, from Wiggins (2009)). In this trial there was no attempt to compensate for the platform motion; it may be necessary in very severe conditions to use measurements of the 6 degrees of freedom (3 rotational and 3 translational) that can in principle distort the lidar measurement. The low impact of the motion observed in trials so far may be a consequence of the high stability of the buoy combined with the very fast 50 Hz measurement rate for the ZephIR lidar, which allows a snapshot of the wind around a 360° disk to be obtained in 1 s. Further development of SeaZephIR is ongoing.

Table 8: Correlation analysis from the first SeaZephIR trial in 2009: the table shows gradient (m) and coefficient of determination R^2 for plots of 10-minute wind speed for SeaZephIR on a floating platform versus those measured by a second ZephIR unit positioned 800 m away on land

Height AGL [m]	Slope m	R^2
120	0.993	0.972
90	0.998	0.970
60	1.004	0.968
30	0.990	0.954
10	0.984	0.953

Forward-looking turbine mounted lidar, either on the nacelle or in the hub, is another exciting lidar development. Applications include turbine power curve measurement, energy yield optimisation (e.g. by reducing turbine yaw misalignment) and gust and fatigue load reduction allowing longer turbine lives and/or turbine build cost reduction. As already remarked, CW lidar seems particularly well suited to this type of application, owing to its high sensitivity (high average photon flux), high sample rate (50 Hz), and scan path that probes the wind around the rotation path of the rotor. Another of its benefits is its flexibility in terms of turbine mounting. In addition to nacelle roof mounting, it is, to date, the only class of lidar that has been installed in a rotor hub (or spinner). Interest in the concept has increased significantly since the world-first proof-of-principle demonstration of turbine-mounted lidar in 2003 (Harris et al., 2006, 2007), with several groups currently working towards evaluating

the concept. Developments include incorporation of a conical-scanning ZephIR lidar in the spinner of a large turbine (Mikkelsen et al., 2010; Angelou et al., 2010) giving an unobscured view of the approaching wind. More recent still has been research and development activity funded by the Danish High Technology Fund (DHTF) studying implementation of CW turbine blade mounted lidar. Here the concept is to have a ZephIR base unit installed in a turbine hub, connected by fibre optics to small, fixed focus telescopes mounted on the blades of the turbine. The rotation of the blades naturally allows scanning of the wind field around the blade path, and this approach holds some promise for blade pitch optimisation, for example. Initial experiments in a wind tunnel (Figure 57) (Pedersen et al., 2012) have confirmed the potential of the approach and turbine trials are currently underway.

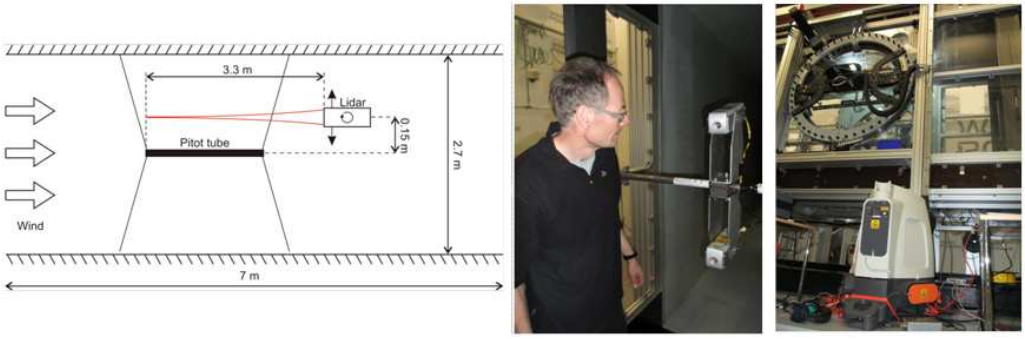

Figure 57: CW lidar experiments in a wind tunnel, prior to blade lidar deployment experiments. Left: wind tunnel schematic. Centre: CW lidar twin telescopes. Right: External view of the wind tunnel, showing the ZephIR 300 base unit.

In connection with turbine mounted lidars, significant recent efforts in the industry have focussed on quantifying their potential benefits, as well as looking at the optimum lidar configurations to use. For CW lidars, the cone scan angle, the number of ranges to scan over (if indeed more than one is required), scan rates and the LOS processing algorithms are all being investigated. Recent results in the literature have included:

1. Conical scan CW lidar was used to determine yaw alignment of a lidar (Kragh et al., 2013) and demonstrated the ability to achieve a sub 4° yaw error over a 2 hour period, even during periods of high turbulence.
2. Simulations examining the ability of turbine mounted lidar for accurate yaw alignment (Kragh and Hansen, 2011) indicated yield, at below rated power, could be raised by 1% to 5%.
3. A study reported in Schlipf et al. (2011) comparing conventional nacelle based wind vane with lidar yaw alignment control, indicated that the yearly energy output of a 5 MW turbine could be enhanced by ˜ 2% using the lidar.
4. Schlipf and Kuhn (2008) modelled the benefits of a nacelle mounted lidar for feed-forward control, in particular turbine speed control. The study found reductions in standard deviations of 91%, 90% and 71% for rotor speed, tower fore-aft moment and blade root flap moment for gusts. For turbulent airflows, the reductions in standard deviations were 77%, 32% and 17% respectively.
5. Simley et al. (2011) simulated a conical scan CW lidar and showed accurate yaw alignment should be possible. Even in highly turbulent airflow, a precision of a few degrees was achievable. The same paper also showed that RMS wind speed measurement errors were lower for a CW system than a pulsed system for ranges ¡125m
6. Simulations using lidar feed-forward control (Laks et al, 2011) showed turbine fatigue load reductions of approximately 20%.

7. A recent study by Rogers et al. (2012) analysed a variety of scenarios that could be addressed by turbine mounted lidar, including retrofitting lidar to existing turbines, larger rotors and taller towers. Benefits of turbine mounted lidar included a 6 year life extension and 30% increase in total energy production (when a lidar was retrofitted to a 2.5 MW turbine); an increase in permitted rotor area of 6% and an associated energy output increase of 4% (larger rotor on 5 MW turbine); a 3% energy output increase from a greater allowable tower height, achieved through reduced fatigue loads (again on a 5 MW turbine). The same study also estimated an achievable increase in energy output due to optimisation of lidar control alone to be just 0.6%.

Clearly, turbine mounted lidars have an important role to play in reducing costs of energy generated by wind turbines. This application is discussed in more detail and in broader scope in other lectures.

Acknowledgements

The authors are grateful for the support and enthusiasm of their colleagues and collaborators. Without them, wind power lidar technology could not have evolved to its current advanced state.

Notation

a	floating parameter for the fit of the line-of-sight velocity
A	beam radius at the output lens
ADC	analogue-to-digital converter
b	floating parameter for the fit of the line-of-sight velocity
B	wind bearing
c	speed of light
	floating parameter for the fit of the line-of-sight velocity
CFD	computational fluid dynamics
CLR	coherent laser radar
CNR	carrier-to-noise ratio
CW	continuous wave
DFT	digital Fourier transform
$D(\nu)$	power spectral density from dark noise
E_{LO}	LO field
E_{s}	stable signal field
FFT	fast Fourier transform
FPGA	field-programmable gate array
h	Planck constant
i	fluctuating detector power output
IR	infrared
LO	local oscillator
m	slope of the linear regression
P_s	time-average optical signal power
P_T	transmitted laser power
R	distance of the beam focus from the lidar output lens
R^2	coefficient of determination
RIN	laser relative intensive noise
$D(\nu$	power spectral density from RIN
SNR	signal-to-noise ratio
t	time variable
TI	turbulence intensity
TKE	turbulent kinetic energy
u	wind speed component in the x-direction
v	wind speed component in the y-direction
VAD	velocity-azimuth-display
V_H	horizontal wind speed
V_{LOS}	line-of-sight wind speed
w	wind speed component in the z-direction

x	horizontal position in longitudinal direction
y	horizontal position in transverse direction
z	position perpendicular to the horizontal plane
β	atmospheric backscatter coefficient
Γ	half-width of the lidar's peak sensitivity
δ	lidar's tilt angle
$\delta\nu$	Doppler shift in frequency
Δ	target distance from the focus position along the beam direction
η	lidar efficiency
θ	lidar's cone half-angle
λ	laser wavelength
ν	laser frequency
ϕ	lidar's azimuth angle
σ	standard deviation
ω_{LO}	local oscillator frequency
ω_{s}	stable signal frequency
$\langle X \rangle$	ensemble average of a variable X

References

Angelou N., Mikkelsen T., Hansen K. H., Sjöholm M., and Harris M. (2010) LIDAR Wind Speed Measurements from a Rotating Spinner: SpinnerEx 2009. *Project Upwind and Risø report* **34**: Risø-R-1741(EN)

Banakh V. A., Smalikho I. N., Köpp F., and Werner C. (1993) Representativeness of wind measurements with a CW Doppler lidar in the atmospheric boundary layer. *Appl. Opt.* **34**:2055–2067

Banakh V. A., Smalikho I. N., Köpp F., and Werner C. (1999) Measurements of turbulent energy dissipation rate with a CW Doppler lidar in the atmospheric boundary layer. *J. Atmos. Oceanic Tech.* **16**:1044–1061

Barker W. (2009) Analysis of ZephIR data from Mason City, Iowa. Natural Power internal report

Barker W., Pitter M., Burin de Roziers E., Harris M., and Scullion R. (2012) Can lidars measure turbulence. *EWEA conference PO74*

Bingöl F., Mann J., and Foussekis D. (2008) Lidar error estimation with WAsP engineering. *IOP Conf. Series: Earth and Environ. Sci.* **1**:012058

Bingöl F., Mann J., and Foussekis D. (2009) Conically scanning lidar error in complex terrain. *Meteorol. Z.* **18**:189–195

Bingöl F. (2010) Complex terrain and wind lidars. Risø-PhD-52(EN), Roskilde

Bleaney B. I. and Bleaney B. (1976) Electricity and magnetism, Oxford University Press, Section 23.4

Cayla M. (2010) Comparison of ZephIR measurements against cup anemometry and power curve measurements. Natural Power internal report (http://www.zephirlidar.com/resources/publications)

Chanin M. L., Gariner A., Hauchecorne A., and Portneuve J. (1989) A Doppler lidar for measuring winds in the middle atmosphere. *Geophys. Res. Lett.* **16**:1273–1276

Clifford S. F. and Wandzura S. (1981) Monostatic heterodyne lidar performance: the effect of the turbulent atmosphere. *Appl. Opt.* **20**:514–516

Courtney M. and Gottschall J. (2010) ZephIR 145 validation test. Risø report for Natural Power

Hardesty R. M. and Weber B. F. (1987) Lidar measurement of turbulence encountered by horizontal-axis wind turbines. *J. Atmos. Oceanic Tech.* **67**:191–203

Harris M., Pearson G. N., Hill C. A., and Vaughan J. M. (1994) Higher moments of scattered light fields by heterodyne analysis. *Appl. Opt.* **33**:7226–7230

Harris M., Constant G., and C Ward (2001) Continuous-wave bistatic laser Doppler wind sensor. *Appl. Opt.* **40**:1501–1506

Harris M., Pearson G. N., Ridley K. D., Karlsson C. J., Olsson F. A., and Letalick D. (2001) Single-particle laser Doppler anemometry at 1.55 μm. *Appl. Opt.* **40**:969–973

Harris M., Hand M., and Wright A. (2006) Lidar for turbine control. Tech. Report NREL/TP-500-39154

Harris M., Bryce D. J., Coffey A. S., Smith D. A., Birkemeyer J., and Knopf U. (2007) Advance measurements of gusts by laser anemometry. *J. Wind Eng. Ind. Aerodyn.* **95**:1637–1647

Harris M., Locker I., Douglas N., Girault R., Abiven C., and Brady O. (2010) Validated adjustment of remote sensing bias in complex terrain using CFD. *European Wind Energy Conf.*, Warsaw

Jelalian A. V. (1992) Laser radar systems, Artech House, Boston

Karlsson C. J., Olsson F. A., Letalick D., and Harris M. (2000) All-fiber multifunction CW 1.55 micron coherent laser radar for range, speed, vibration and wind measurements. *Appl. Opt.* **39**:3716–3726

Kristensen L. (1999) The perennial cup anemometer. *Wind Energy* **2**:59–75

Kragh K. A., and Hansen M. H (2011) Individual Pitch Control Based on Local and Upstream Inflow Measurements. Proceedings of 49th AIAA Aerospace Sciences, American Institute of Aeronautics and Astronautics, AIAA 2011–813, Orlando, Florida

Kragh K. A., Hansen M. H, and Mikkelsen T. (2013) Precision and shortcomings of yaw error estimation using spinner-based light detection and ranging. *Wind Energy* **16**:353–366

Lading L., Hanson S., and Skov Jensen A. (1984) Diffraction-limited lidars: the impact of refractive turbulence. *Appl. Opt.* **23**:2492-2497

Laks J., Pao L. Y., Simley E., Wright A., Kelley N., and Jonkman B. (2011) Model Predictive Control Using Preview Measurements From LIDAR. Proceedings of 49th AIAA Aerospace Sciences, American Institute of Aeronautics and Astronautics, AIAA 2011–813, Orlando, Florida.

Loudon R. (2000) The quantum theory of light, Oxford University Press, 3rd edition

Mikkelsen T., Hansen K., Angelou N., Sjöholm M., Harris M., Hadley P., Scullion R., Ellis G., and Vives G. (2010) Lidar wind speed measurements from a rotating spinner. *European Wind Energy Conf.*, Warsaw

Pearson G. N., Roberts P. J., Eacock J. R., and Harris M (2002) Analysis of the performance of a coherent pulsed fiber lidar for aerosol backscatter applications. *Appl. Opt.* **41**:6442-6450

Pedersen A. T., Montes B. F., Pedersen J. E., Harris M., and Mikkelsen T. (2012) Demonstration of short-range wind lidar in a high-performance wind tunnel, EWEA conference PO78, Copenhagen

Peña A., Hasager C. B., Gryning S.-E., Courtney M., Antoniou I., Mikkelsen T. (2009) Offshore wind profiling using light detection and ranging measurements. *Wind Energy* **12**:105-124

Pitter M., Abiven C., Harris M., Barker W., and Brady O. (2012) Lidar and computational fluid dynamics for resource assessment in complex terrain. *EWEA conference PO80*, Copenhagen.

Rogers T., Byme A., McCoy T., and Briggs K. (2012) Expected impacts on cost of energy through lidar based wind turbine control. *EWEA 2012*.

A Rutherford A, M Harris M, W Barker W, E Burin de Roziers E., R Pitter M., R Scullion R., and C Slinger C. (2012) Lidar calibration and performance validation process. AWEA 2012, Atlanta.

Schlipf D., and Kuhn M. (2008) Prospects of a collective pitch control by means of predictive disturbance compensation assisted by wind speed measurements. German Wind Energy Conference (DEWEK 2008), pp. 1–4

Schlipf D., Anger J., Kapp S., Bischoff O., Hofsäß M., Rettenmeier A., and Kühn M. (2011) Prospects of optimization of energy production by lidar assisted control of wind turbines Proceedings of European Wind Energy Conference and Exhibition, *EWEA 2011*.

Siegman A. E. (1986) Lasers, University Science Books, Mill Valley

Simley E., Pao L. Y., Frehlich R., Jonkman B., and Kelley N (2011) Analysis of Wind Speed Measurements using Continuous Wave LIDAR for Wind Turbine Control. Proceedings of 49th AIAA Aerospace Sciences, American Institute of Aeronautics and Astronautics, AIAA 2011-263, Orlando, Florida

Slinger C., Leak M., Pitter M., and Harris M. (2013) Relative Power Curve Measurements Using Turbine Mounted, Continuous Wave Lidar. *EWEA 2013*.

Smith D. A., Harris M., Coffey A. S., Mikkelsen T., Jørgensen H. E., and Mann J. (2006) Wind lidar evaluation at the Danish wind test site in Høvsøre. *Wind Energy* **9**:87–93

Sonnenschein C. M. and Horrigan F. A. (1971) Signal-to-noise relationships for coaxial systems that heterodyne backscatter from the atmosphere. *Appl. Opt.* **10**:1600–1604

Vaughan J. M. and Forrester P. A. (1989) Laser Doppler velocimetry applied to the measurement of local and global wind. *Wind Eng.* **13**:1–15

Wagner R., Jørgensen H. E., Paulsen U. S., Larsen T. J., Antoniou I., and Thesbjerg L. (2008) Remote sensing used for power curves. *IOP Conf. Series: Earth and Environ. Sci.* **1**:012059

Wagner R., Mikkelsen T., and Courtney M. (2009) Investigation of turbulence measurements with a continuous-wave conically scanning lidar. Risø-R-1682(EN), Roskilde

S Wharton S., and Lundquist J. K. (2012) Atmospheric stability affects wind turbine power collection. *Environmental Research Letters* textbf7: 014005.

Wiggins J. (2009) Unpublished internal report. Natural Power

Zak J. A. (2003) Atmospheric boundary layer sensors for application in a wake vortex advisory system. NASA/CR-2003-212175

5 Pulsed lidars

Jean-Pierre Cariou
Leosphere, Orsay, FR

This section complements the description of the measurement process for a Doppler lidar for wind speed and direction determination, by focusing more on the pulsed lidar technology, and particularly on the WINDCUBE^{TM} Doppler pulsed lidar, one of the most accurate remote sensing devices available at the present time in the wind industry.

5.1 Introduction

There is a pressing need for good wind-speed measurements at greater heights and at more site locations to assess the availability of the resource in terms of power production and to identify any frequently occurring atmospheric structural characteristics that may impact the operational reliability and lifetime of wind turbines and their components. To measure the wind field up to the height of new generation wind turbines and at any location of interest, remote sensors are needed to complement masts.

Different technologies are in use in this field, among them pulsed lidars (LIght Detection And Ranging). The underlying principle of pulsed lidar measurement of wind and aerosols is the use of optical heterodyne (coherent) detection, in which laser pulses are transmitted into the atmosphere and scattered off of naturally-occurring small dust particles (aerosols) entrained in the ambient flow field (Frehlich et al., 1994; Huffaker and Hardestry, 1996; Soreide et al., 1997; Frehlich et al., 1998). Even though the measurement principle is well known and similar to pulsed radars, pulsed lidars have only been used in wind energy site assessment only since 2008. Their recent introduction is mainly due to laser revolution coming from fiber telecommunication development in the late 1990s.

In this section, we describe the architecture of pulsed lidars, based on the WINDCUBE^{TM} lidar developed by LEOSPHERE and ONERA, the French Aerospace Lab. We define the different modules of a pulsed lidar, their specific functions and the individual level of uncertainties they might bring to the lidar wind speed retrieval. We also show the differences between pulsed and continuous wave (CW) lidars, used as well for wind sensing. We eventually give the lidar equation in pulsed mode, giving the relationship between parameters, and we focus on range and speed accuracy and resolution.

Figure 58: Leosphere Windcube7, first version (left) and V2 (right).

5.2 End-to-end description of pulsed lidar measurement process

5.2.1 Architecture of pulsed lidars

Figure 59 illustrates the general set up of a pulsed lidar. The following paragraphs provide more details of the key hardware components and explain the requirements and trade-offs on solutions for the main parts of the lidar

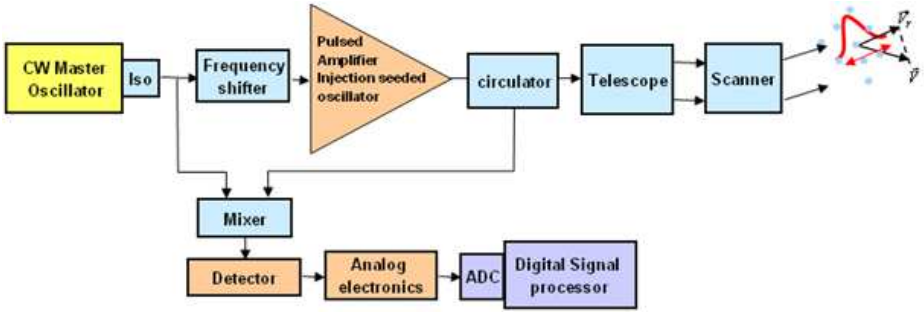

Figure 59: Pulsed lidar set up.

Laser source A pulsed lidar needs a continuous wave laser, called master oscillator (MO) to generate the local oscillator (LO) beam and a pulsed laser to generate the powerful transmitted pulse. The frequency offset between the two sources need to be stable with time to allow an unbiased measurement of the Doppler shift.

The master oscillator provides the laser wavelength, the laser linewidth, the laser intensity noise and the state of polarization. Each of these parameters has to be well known and stable to guarantee the lidar performance. The required CW power is at least some milliwatts.

The pulsed laser delivers cyclic pulses of high energy. The pulse duration is some hundreds of nanoseconds, that determines the length of the pulse in the atmosphere and so the spatial resolution.

Table 10: Spatial resolution versus pulse duration

Pulse duration [ns]	Pulse length [m]	Minimum spatial resolution [m]
200	60	30
400	120	60
800	240	120

The pulse repetition frequency (PRF) is as high as possible, but cannot exceed a maximum value $\mathrm{PRF}_{\max}$. To avoid ambiguity between return signals, the time between pulses (1/PRF) must be longer than the round trip time of flight of the pulse to the greatest height to be measured $Z_{\max}$, $\mathrm{PRF}_{\max} = c/(2Z_{\max})$, where c is the speed of light.

Table 11: $\mathrm{PRF}_{\max}$ versus lidar range

PRF [KHz]	Maximum range [m]
10	15000
20	7500
50	3000

Two technologies are used for the pulsed laser. In the first one, called MOPA (master oscillator power amplifier), pulses are emitted from the MO by use of an optical pulse modulator. Resulting low power pulses are amplified into a single pass high bandwidth optical amplifier to generate high power pulses, having the same duration, frequency and polarization state as the incoming pulses. In the second scheme, the MO is used as a seeder in a Q-Switched pulsed laser. Cavity frequencies have to be matched to allow the seed frequency to be amplified. Pulse duration and PRF depend on the cavity parameters. First solution allows higher PRF but lower energy/pulse than the second one. Both deliver an equivalent average power.

Laser wavelength is an important parameter. Following the recent improvement of solid state lasers in late 90s, the near Infrared spectrum (1.4–2.2 μm) is widely used for operational wind lidars. Efficient technology, good Doppler sensitivity, fiber architecture, eye safety and good atmospheric transmission are the main reasons (Cariou et al., 2006).

Circulator Figure 60 describes the circulator and the different elements which compose it. The function of the circulator is to transmit the laser pulse from the laser (1) to the telescope (2) and to direct the backscattered light from the telescope (2) to the receiver (3). Power handling, transmission efficiency and isolation between (1) and (3) ports are critical parameters. In coherent pulsed lidars, most circulators use polarization to perform this function. Polarization is rotated in the telescope thanks to a quarter wave plate. The transmitted polarization is circular.

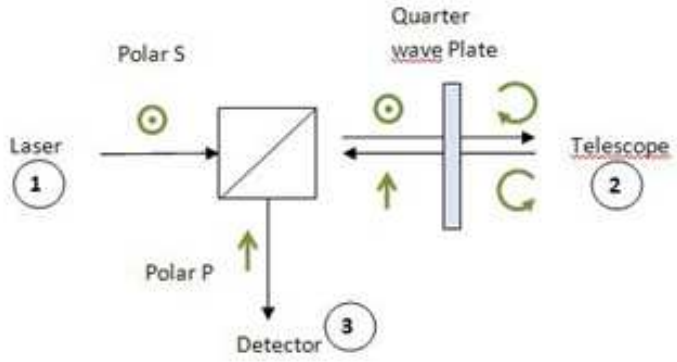

Figure 60: Circulator.

Telescope The telescope magnifies the laser beam in order to reduce its divergence in the far field, and focuses the beam at any distance. The larger the beam, the smaller the divergence and the better the signal-to-noise ratio (SNR) at long range. Since the lidar SNR is inversely proportional to the beam area, beam diameter must be minimized over the global measurement range to ensure maximum efficiency.

The telescope can use reflective or refractive optics, perfectly corrected from geometrical aberrations. In order to lose less than 3 dB on the detection efficiency, wavefront distortion on the global roundtrip optical path has to be less than $\lambda/4$ RMS, including components and atmospheric distortion.

Atmospheric turbulence as well creates wave distortion that degrades heterodyne efficiency. To keep this distortion negligible, the telescope aperture has to be smaller than the coherence diameter of the beam expressed by:

$$d_o = 2.4\text{e}10^{-8}\lambda^{6/5}Z^{-3/5}C_n^{-6/5}. \tag{102}$$

Considering maximum values of index structure constant ($C_n^2 = 10^{-13}$ m$^{-2/3}$) and propagation over about $Z = 1$ km, this limits the size of the telescope to about 10 cm at ground level.

Scanner Coherent lidar measure the radial component of the wind, i.e. the projection of the wind vector on the line of sight (LOS). To provide two or three components of the vector, the beam has to be directed in two or three independent different directions (more details in Section 2.6). The scanner can move the entire telescope, for example Mitsubishi (Ando et al., 2008), or only the beam. Some manufacturers prefer skipping the scanner and duplicate the telescope to suppress all moving parts from the lidar (for example Catch The Wind or Leosphere WindcubeV2).

To perform the vertical wind profile, beams are directed upwards along a cone around the zenithal direction. For that, a single rotating prism or dual flat mirrors are used (see Figure 61).

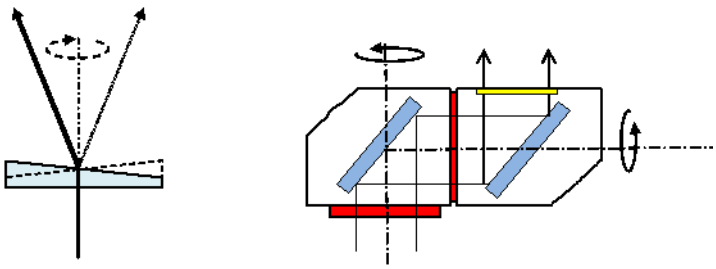

Figure 61: Prism scanner and dual flat mirror scanner.

To measure the wind speed in any direction, and display 2D or 3D wind maps, a more flexible scanner is needed. Double flat mirror scanners are mostly used (CTI, Halophotonics, Leosphere), while double prism scanners, like those in Risø DTUs Windscanners (Mikkelsen, 2008), offer a more original and compact solution. A global hemispherical field of view can be obtained with both solutions.

5.2.2 Differences between pulsed vs. continuous wave lidars

In CW lidars, light is continuously transmitted to the atmosphere. Assuming atmospheric parameters do not vary, the backscattered signal average power is constant, coming from all distances at the same time. The distance weighting function is defined by the beam aperture and the focus distance (see chapter on CW lidars from Mike Harris). Spectral bandwidth is limited by atmospheric turbulence if laser line width is narrow. The size of the range gate (contributing to the signal) increases as the square of the distance. The range gate can be small and well defined at short distance but is always too large when the range exceeds few hundreds of meters. Table 12 summarizes the main differences between CW and pulsed lidars:

In pulsed lidars, short pulses are transmitted to the atmosphere, illuminating at each instant only a limited part of the line of sight. Therefore, backscattered signal arriving onto the detector at a time only comes from a given range of distance. The time delay between the pulse start and the measurement time informs on the distance of the analyzed zone. The range gate length is always the same, at short and long range.

Pulsed LIDARs, as their name implies, emit regularly spaced emissions of highly collimated light energy for a specified period of time (pulse length). Precision timing circuits then isolate the returned signals to a period of time that corresponds to a specified segment of radial distance along the beam called a range gate. The backscattered signals contained within each gate are then processed to derive the radial velocities along the path of the LIDAR beam.

Table 12: Main differences between CW and pulsed lidars

	CW lidar	Pulsed lidar
Velocity accuracy	limited by coherence time of the atmosphere	limited by the pulse duration
Range gate	determined by focus, increases as R^2	constant, around $c\tau/2$
Number of range gates	less than 10, sequentially addressed	more than 100 simultaneously addressed
Sensitivity to targets out of focus	high	limited by SNR at long range no
Maximum range	few hundreds of meters	some kilometers
Laser source	1000 mW laser	10 mW MO + 200 mW power amplifier
Linear polarization	not necessary	mandatory

5.2.3 Signal processing

After the pulse has left by the laser, the detector starts to collect the backscattered signal from the successive range gates. It first crosses the telescope optics and provides a zero Doppler signal, used as a marker for the zero distance. Even if the stray light is small thanks to optimized coatings (10^{-6} order), this signal is always larger than the light backscattered by the atmosphere (10^{-12} order).

Each layer of atmosphere then backscatters light to the lidar. The power is proportional to the backscattering atmospheric coefficient β while the frequency shift is proportional to the radial velocity. For each pulse, the collected signal contains the total wind speed information on the LOS.

However, both the signal and the noise fluctuate from pulse to pulse and it is necessary to average signals to get a good estimation of the spectral content. Because of the short wavelength (10^4 less than radars and sodars), signal phase changes quickly with particle motion, atmospheric turbulence and small laser spectral drifts. This is useless to average time series. To improve SNR on the Doppler spectrum, successive spectra corresponding to the same range gate are summed. SNR increases as the square root of the number of average pulses N. This computation is performed for all range gates.

To sum up, the successive steps for the signal processing are for every LOS (Figure 62):

- Break the time series into gates
- Compute the spectrum for each gate
- Average spectra for same range gate from different pulses
- Find frequency peak for each gate to find Doppler shift and convert to radial velocity
- Reconstruct wind vector for each gate with radial velocity on the different LOS.

5.2.4 Coherent detection

Basic principles of coherent detection are the same than for CW lidars (see chapter on CW lidars from Mike Harris). The return signal mixes with local-oscillator creating the beat signal. The electronic signal on the detector contains the same amplitude, frequency and phase information as the optical signal, but is frequency downshifted to allow detection with conventional high speed detectors. So the Doppler shift, which is small in comparison to the optical frequency ν can be measured in base band. To allow both negative and positive shifts

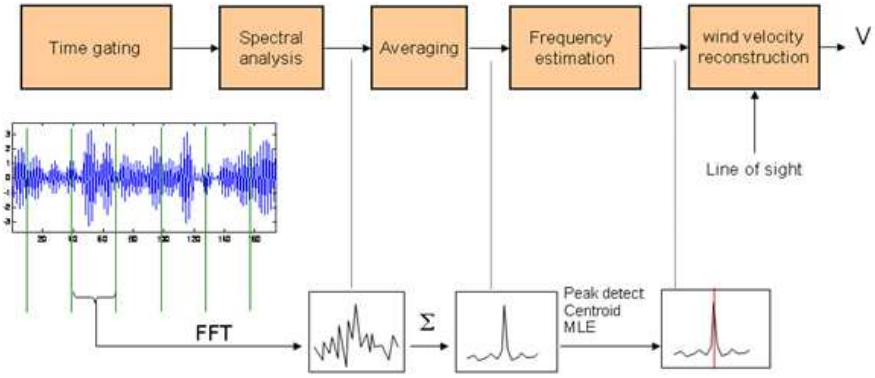

Figure 62: Radial wind velocity retrieval process.

to be measured, an offset frequency F_i (intermediate frequency) is added on one arm of the interferometer.

$$F_{dop} = (\nu + F_i)_{\mathrm{LO}} - (\nu + F_{dop})_{\mathrm{signal}} = F_i + F_{dop}. \tag{103}$$

An important advantage of coherent detection is that it can be limited by signal photon noise, if some conditions are fulfilled. First condition is that the amplitude and phase match between signal beam and the LO beam must be perfect. The second condition is that temporal coherence is optimum, i.e the spectral width of the main oscillator must be narrower than the spectral width of the electronic signal. The third condition is that polarization state must be the same on the LO and the signal. System and component limitations lead however to a loss in heterodyne efficiency. Frehlich and Kavaya (1991) demonstrated that the heterodyne efficiency is limited to 40% by spatial coherence for a perfect Doppler lidar using a circular aperture and a Gaussian beam. A good actual operational lidar heterodyne efficiency is more than 20%.

5.2.5 Lidar equation

The lidar equation gives the expected signal power returning from the atmosphere within the range gate to be analyzed. The signal power can then be compared to the noise power in order to determine the range of the lidar. The total optical power $P_r(z)$ reflected back in the receiver telescope from the range gate at Z is:

$$P_r(Z) = P_{peak} T_{inst} T_{atm} \beta_\pi(Z) \frac{c\tau}{2} \Omega, \tag{104}$$

where P_{peak} is the transmitted pulse peak power, T_{inst} is the instrumental round trip transmission and T_{atm} is the atmospheric round trip transmission, expressed as:

$$T_{atm} = \exp\left(-2 \int_0^Z \alpha(x) dx\right). \tag{105}$$

$T_{atm} = \exp(-2\alpha Z)$ if the atmosphere is homogeneous and $\beta_{pi}(Z)$ is the backscattering coefficient of the atmosphere at a distance Z, τ is the full-width-half-maximum (FWHM) pulsed duration and Ω is the reception solid angle:

$$\Omega = \frac{\pi \sigma^2}{Z^2}, \tag{106}$$

where σ is the efficient telescope aperture radius and α and β_π are roughly proportional since they both depend on aerosol concentration in the atmosphere.

However, because of the limited heterodyne efficiency, only a part of $P_r(Z)$ is efficient for the coherent detection. The lost part of $P_r(Z)$ comes from phase and polarization mismatches. An interesting way to estimate the detection antenna diagram is to propagate back in the atmosphere the LO, and to compute the overlap integral of the signal and LO along the LOS.

This defines the transverse and longitudinal efficiency of the lidar (BPLO theory (Siegman, 1966)). The efficient signal power incoming onto the detector is:

$$P_s(Z) = P_{peak} T_{inst} T_{atm} \beta_\pi(Z) \frac{c\tau}{2} \lambda I(Z), \tag{107}$$

where $I(Z)$ is a Lorentzian function including Ω and Z depending focus function:

$$I(Z) = \frac{\Delta Z}{(Z - Z_o)^2 + \Delta Z^2}, \tag{108}$$

with $Z_o = F_t/(1 + (F_t/Z_r)^2)$, $Z_r = \pi\sigma^2/\lambda$, $\Delta Z = Z_o F_t / Z_r$ being Z_o the distance where $I(Z)$ is maximum, i.e. maximum SNR, Z_r the Rayleigh distance, F_t the instrumental geometrical focus distance (wave curvature radius at telescope) and ΔZ half of FWHM geometric depth of focus.

Figure 63 shows different plots of the Lorentzian function $I(Z)$ for different values of the focus distance F_t. Short focus improves signal power at short range whereas long focus averages the power along the distance, leading to a more constant signal on the different range gates, but with a lower value.

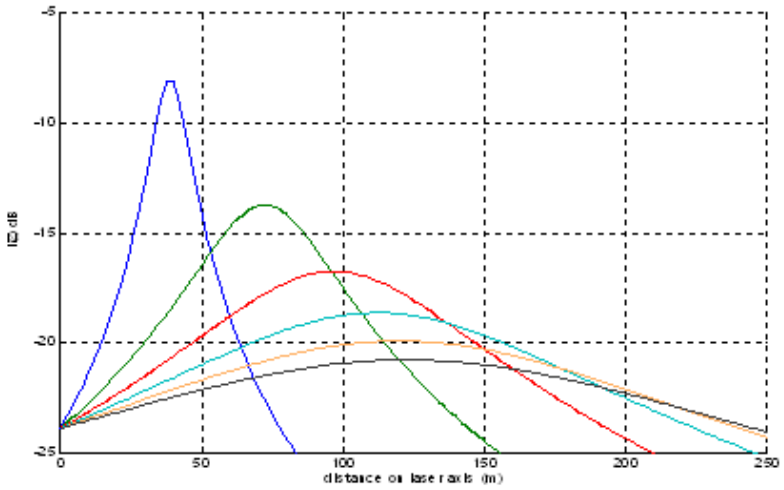

Figure 63: Variations of $I(Z)$ with focus distance $F_t = 40, 80, 120, 160, 200, 240$ m respectively.

The current power on the detector can then be derived using the same equations as in CW mode,

$$< i_{het}^2 >= 2\eta_{het} S^2 P_{\mathrm{LO}} P_s(Z), \tag{109}$$

where P_{LO} is the local oscillator power, η_{het} the heterodyne efficiency, which depends on phase, amplitude and polarization matching and S the detector sensitivity.

$$\eta_{het} = \frac{\left[\int\int_{Ad} E_s(x,y) E^*_{\mathrm{LO}}(x,y) dxdy\right]^2}{\int\int_{Ad} E_s^2(x,y) dxdy \int\int_{Ad} E^2_{\mathrm{LO}}(x,y) dxdy}, \tag{110}$$

$$< i_{het}^2 >= \eta_{het} T_{inst} T_{atm} S^2 \beta_\pi(Z) P_{\mathrm{LO}} P_{peak} \tau c I(Z). \tag{111}$$

The lidar equation shows that the signal power is proportional to pulse energy $P_{peak}\tau$ and proportional to LO power. LO amplifies the signal allowing it to be detected over the detector noise.

5.2.6 Spectral processing MLE

A maximum likelihood estimator (MLE) based on the likelihood of the Fourier transform of the signal is used as spectral processing. This estimator assumes an uncorrelated Fourier

transform in order to use data obtained from the accumulated spectrum. The estimator is slightly different from the likelihood of the spectrum traditionally used for spectral maximum likelihood estimators but still shows the same efficiency.

Signal spectrum is calculated using a temporal model such as the Feuilleté model (Cariou et al., 2006) and thus takes into account all the FFT algorithm disturbing effects such as the spectral leakage, which must be carefully characterized in the case of a pulsed atmospheric lidar.

5.2.7 Wind vector reconstruction

Pulsed lidars provide radial wind components on different lines of sight at different altitudes. In an ideal case, and to mimic local sensors such as cup or sonic anemometers, beams intersect at the point of interest within a small volume. This is the goal of the Windscanner project with three lidars. In an operational situation, only one lidar is available. To reconstruct the 3D components of the wind vector, some assumptions are then necessary.

- Horizontal homogeneity: the three components of the wind are the same for the different points of the disc at a given altitude. The numerous measurement campaigns have proven that this assumption is valid on flat terrains and offshore, but not perfect on complex terrains (hills, mountains, forest boarders)
- Temporal variations are slower than the inter-beam distance divided by the horizontal wind speed. This time increases with altitude and matches the conical geometry.
- Wind slowly varies within a range gate. Wind dispersion lowers the SNR and provides a bias if the shear is non linear.

The scanning configuration can be either velocity azimuth display (VAD) or Doppler beam swinging (DBS). VAD uses information from a continuous scan in a part or total cone angle and is mostly used in CW lidars. DBS is used in pulsed lidars to average more information on the LOS. Since VAD is described in the "Remote Sensing QinetiQ Lidar Measurement Report", we focus here on DBS reconstruction.

First is important to define an orthogonal frame. The orthogonal frame of the WINDCUBE is described in Figure 64:

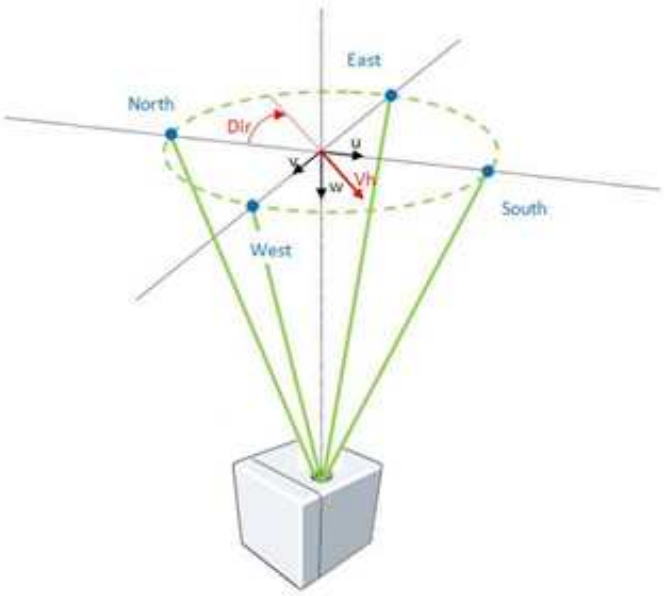

Figure 64: Orthogonal frame of the WINDCUBE for retrieving the wind speed components

Suppose the lidar probes the atmosphere with three beams in the three directions North, East, and Zenith. Then the three measured LOS velocities Vr_i are described as following (θ being the angle between Zenith and North and East, the so-called cone-angle):

$$Vr_N = u\sin\theta + w\cos\theta, \quad (112)$$

$$Vr_E = v\sin\theta + w\cos\theta, \quad (113)$$

$$Vr_Z = w. \quad (114)$$

So the u, v and w wind speed components can be retrieved as,

$$u = \frac{Vr_N - Vr_Z\cos\theta}{\sin\theta} \quad (115)$$

$$v = \frac{Vr_E - Vr_Z\cos\theta}{\sin\theta} \quad (116)$$

$$w = Vr_Z. \quad (117)$$

Supposing the lidar probes the atmosphere at four different locations, the LOS being East, West, North, South, the system of wind equations will be,

$$u = \frac{Vr_N - Vr_S}{2\sin\theta} \quad (118)$$

$$v = \frac{Vr_E - Vr_W}{2\sin\theta} \quad (119)$$

$$w = \frac{Vr_N + Vr_S + Vr_E + Vr_W}{4\cos\theta}. \quad (120)$$

Horizontal wind speed V_h and wind direction Dir are then retrieved as following:

$$V_h = \sqrt{u^2 + v^2} \quad (121)$$

$$Dir = mod(360 + \mathrm{atan2}(v, u), 360). \quad (122)$$

If the North beam of the lidar is offset from the geographical North with an angle α, the wind direction is:

$$Dir = mod(360 + \alpha + \mathrm{atan2}(v, u), 360). \quad (123)$$

With three beams, the solution is unique. The vertical component w is perfectly determined if the one of the three axis is accurately vertical. No check of assumptions mentioned above is possible. With four beams, the additional equation allows wind homogeneity to be checked and skip undesired values.

Cone-angle θ is a trade-off between lidar velocity resolution and atmosphere homogeneity. The smaller is θ, the better is the wind homogeneity but worse is the projection of the wind vector on every beam. Boquet et al. (2010a) demonstrated that best θ values are between 15° and 30°. Even in complex terrains, in general wind non homogeneity condition, no better estimation is obtained when reducing the cone angle (Boquet et al., 2009).

5.2.8 Fiber lidars

Before early 2000s, LIDAR systems were based on solid-state laser technologies that do not meet operational requirements for remote site wind assessment due to high power consumption, size, weight, reliability, and life cycle cost. It was therefore the purpose of Leosphere, thanks to a partnership with French Aerospace Lab ONERA to introduce a unique fiber laser technology geared for the wind industry requirements, enabling efficient realization of compact wind Doppler lidar systems.

Fiber lidars use fiber amplifiers and coherent detection and fiber architecture based on mainstream telecommunication components. Fiber amplifiers use codoped Erbium Ytterbium silica fibers to amplify with a large bandwidth low power pulses cut out of a CW laser at 1.5 μm (MOPA configuration). The electrical to optical efficiency of 1.5 μm fiber laser sources is of the order of 10%, thus allowing low electrical consumption.

This wavelength is also the most favorable for eye-safe lidar designs: the eye-safety laser energy limitation being high, the laser power can be increased with little constraints on the lidar operation or design. One advantage of the IR fiber technology is its reliability. It is now well established that a fiber architecture is easy to adjust and mechanically reliable in a vibrating environment. The other advantages of fiber architectures are their compactness and flexibility in terms of installation. The lidar can be split up into subsystems spatially far apart and linked together using fiber optics. The new technologies of large-mode-area (LMA) fibers enable high peak power generation without nonlinear effects, while maintaining a good spatial mode and polarization state. The average power exceeds several watts and high PRF compensates efficiently the relative low pulse energy. Moreover, the MOPA architecture flexibility in terms of pulse duration allows fulfilling a large panel of requirements, either with high spatial resolution or long range.

5.3 Lidar performances

5.3.1 Noise

In coherent detection, noise sources come principally from 3 origins:

$$< i_{SN}^2 > \;=\; 2eS\ P_{LO}B \qquad \text{LO shot noise} \tag{124}$$

$$< i_{NEP}^2 > \;=\; 2eS\ NEP\ B \qquad \text{Detector noise} \tag{125}$$

$$< i_{RIN}^2 > \;=\; (S\ P_{LO})^2 10^{RIN/10} B \qquad \text{RIN noise,} \tag{126}$$

where NEP is the noise equivalent power density, B is the detection bandwidth and,

$$< i_n^2 > = < i_{SN}^2 > + < i_{NEP}^2 > + < i_{RIN}^2 > . \tag{127}$$

For optimum detection, LO shot noise must be the main noise contributor. When other sources are negligible, CNR (Carrier to Noise Ratio), describing the signal to noise ratio on the carrier frequency is,

$$\text{CNR} = \frac{< i_{het}^2 >}{< i_n^2 >} = \eta_{het} T_{inst} T_{atm} \frac{S}{2eB} \beta_\pi(Z) P_{peak} \tau c\ I(Z). \tag{128}$$

5.3.2 Best Focus

Focus distance can be adjusted in order to optimize CNR over the measurement range. Figure 65 shows the simulated CNR variation versus focus distance, expressed as the wave radius of curvature at the instrument exit (beam radius being 11 mm@1/e^2 at the lens).

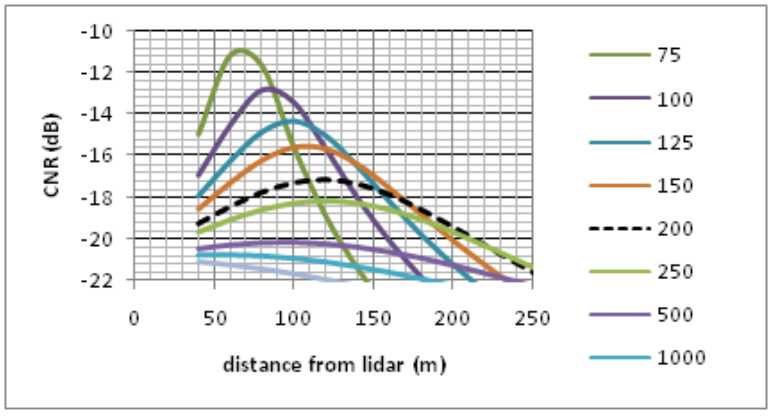

Figure 65: Variation of CNR vs distance (Altitude/cos(θ-dev)) for different beam radius of curvature

Best focus corresponds to maximizing the data availability at all altitudes, from $H = 40$ m ($Z = 46$ m) to $H = 200$ m ($Z = 230$ m). Practically, it corresponds to balancing and

maximizing the CNR for $H = 40$ m and $H = 200$ m. For the Windcube WLS7, Fopt=120 m (Hopt=104 m), corresponding to a beam curvature of 200 m at lens (black dot line).

For a beam radius of curvature of 200 m, the beam diameter slowly varies along the propagation in the range of interest. Beam radius ($1/e^2$) is $\sigma = 11$ mm at lens, 9 mm at 46 m, 7 mm at 120 m and 10 mm at 230 m, giving a maximum of 2 dB difference along the total range. (CNR is proportional to $1/\sigma^2$).

Maximum focus distance corresponds to half of the Rayleigh distance Z_r:

$$Z_{max} = \frac{Z_r}{2} = \frac{\pi\sigma^2}{2\lambda}, \tag{129}$$

where $Z_{max} = 123$ m for the WINDCUBE7 v2 parameters. This configuration minimizes the beam diameter variation from $Z = 0$ to $Z = Z_r$.

Lindelöw (2007) demonstrated a velocity error coming from the unbalanced velocity weighting function due to a variation of CNR within the range gate. In the case of the WINDCUBE7 v2, the difference of CNR is always less than 0.5 dB/range gate, leading to a maximum bias in the velocity of around 0.06 m s^{-1} under a vertical linear wind shear of 0.02 m s^{-1}/m.

5.3.3 Distance range and resolution

Because of the footprint of the laser pulse on the line of sight, range resolution is limited. Moreover, during the measurement time τ_m, the pulse has moved further, enlarging the range resolution. Figure 66 describes the pulse space and time propagation and the portion of atmosphere illuminated during a time window analysis of length τ_m.

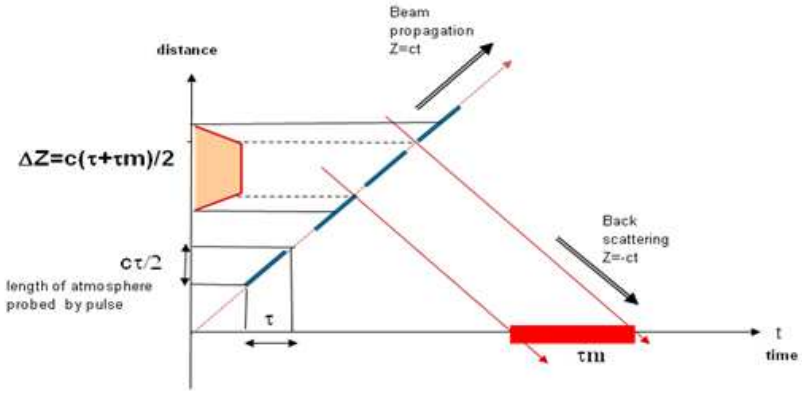

Figure 66: Pulse propagation and width of range gate represented on a time-distance plot

Velocity measurement at one point $V_d(Z)$ depends on the velocity $Vr(R)$ at close points and on the range weighting function $RWF(R)$,

$$Vd(Z) = \int_{-\infty}^{\infty} RWF(R)Vr(R)dR. \tag{130}$$

For a pulsed lidar, Banakh and Smalikho (1994) gave an analytical equation for RWF, when the pulse is Gaussian ($\mathrm{FWHM} = \tau$) and range gate is flat (width τ_m), as the convolution between the pulse power profile and the range gate profile:

$$RWF(Z) = \frac{1}{\tau_m c}\left[\mathrm{erf}\left(\frac{4\sqrt{\ln 2}}{c\tau}(Z - Z_o) + \frac{\sqrt{\ln 2}}{\tau}\right) - \mathrm{erf}\left(\frac{4\sqrt{\ln 2}}{c\tau}(Z - Z_o) - \frac{\sqrt{\ln 2}}{\tau}\right)\right]. \tag{131}$$

Range resolution is defined as the FWHM of the function RWF which is roughly:

$$\Delta z1 = \frac{c\tau_m}{2\mathrm{erf}\left(\sqrt{\ln 2}\tau_m/\tau\right)}. \tag{132}$$

Eq. (132) is adapted for collimated system but does not give accurate results for focused lidars, i.e. focusing the laser beam leads to better resolution near the focusing point. Moreover, this method is only valid for a Gaussian pulse and a flat measurement window.

In order to make this calculation more general, Lindelöw (2007) proposed multiplying the focusing efficiency by the convolution of the pulse and the range gate profile:

$$RWF(Z) = \eta_{foc}(Z)\,(Pulse\ FFT_{window})\,(Z), \tag{133}$$

where $\eta_{foc}(Z)$ is the focusing efficiency,

$$\eta_{foc}(Z) = \left(1 + Z_r^2\left[\frac{1}{Z} - \frac{1}{Z_{foc}}\right]\right)^{-1}. \tag{134}$$

These methods can be applied to the current WINDCUBE7 v2 pulse shape and range gate profile. The "impulse response" FWHM is calculated to be 27 m. The altitude resolution is therefore around 23.8 m (LOS zenithal deviation angle is 28°). Lindelöw's RWF is 26.3 m, i.e. ~ 23.2 m altitude resolution.

5.3.4 Velocity range and resolution

Velocity range ambiguity Radial velocity is proportional to Doppler frequency shift. Velocity range is then determined by frequency range. The intermediate frequency F_i used in most pulsed lidars allows the measurement of both positive and negative shifts. Maximum downshift is limited by the value of F_i, since no negative frequency can be measured. Maximum upshift is limited by the Nyquist frequency, half of the sampling frequency F_s. Figure 67 describes the spectrum and velocity ranges.

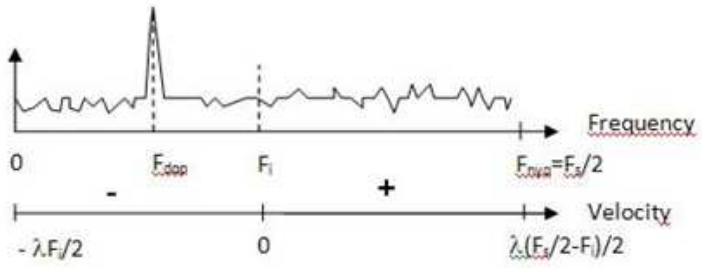

Figure 67: Lidar spectrum and velocity range

Because of spectral extent of the signal and low frequency noise, this range is in fact a bit smaller. For example, with $\lambda = 1.55$ μm, $F_i = 68$ MHz and $F_s = 250$ MHz, the practical horizontal velocity range is [-50 m s^{-1}, $+50$ m s^{-1}]. A passband filter cancels outband Doppler shifts to avoid Doppler ambiguities.

Velocity resolution Velocity precision depends on both atmospheric parameters and lidar parameters. Both are broadening the Doppler spectrum and hence limit the frequency estimation. Atmospheric parameters are wind gradient within the range gate and turbulence. Lidar parameters are pulse duration CNR and number N of average spectra. The smaller the pulse duration, the smaller the range gate and the velocity dispersion but larger the frequency spectrum.

Eq. (135) gives the minimum velocity resolution as a function of relative parameters. It is called Cramer Rao lower bound (CRLB),

$$\sigma v_{crlb} = \frac{\sqrt{2}\lambda}{2\tau}\frac{\sqrt{1+\mathrm{CNR}}}{\sqrt{N}\mathrm{CNR}}. \tag{135}$$

Eq. (135) assumes an infinite correlation time of the signal. In an actual lidar, σv is limited by the finite correlation time τ_c , the smallest value between the pulse duration and the

correlation time of the atmosphere,

$$\sigma v_{sat} = \frac{\lambda}{2\sqrt{N}4\pi\tau_c}. \tag{136}$$

The global velocity resolution is then:

$$\sigma v = \sqrt{\sigma v_{crlb}^2 + \sigma v_{sat}^2}. \tag{137}$$

Figure 68 illustrates the variation of σv with CNR for $N = 100$ and $N = 10000$.

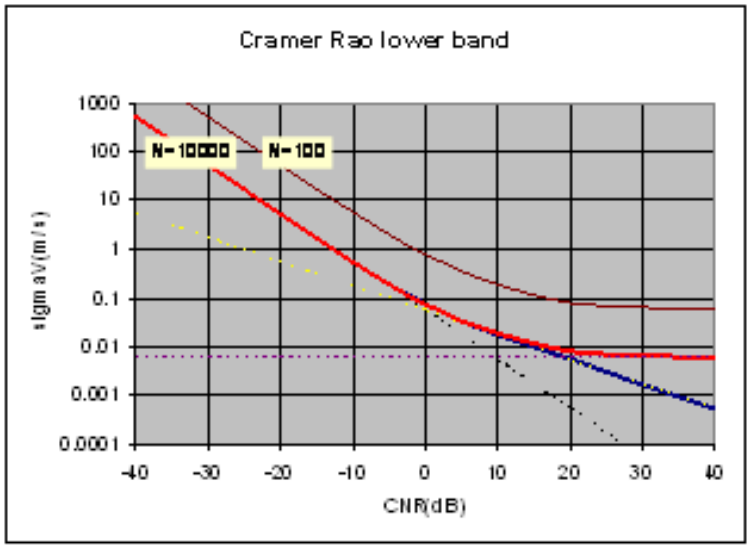

Figure 68: Cramer Rao boundary for 100 averaged spectra (dark red) and 10000 averaged spectra (light red). CNR is measured in narrow band ($B = 1/\tau_m$)

For low CNR values, σv decreases as 1/CNR. Doubling the pulse energy divides by 2 the velocity resolution. For high CNR values, σv is constant. Spectral broadening comes from speckle fluctuations in the signal. The only way to reduce σv is to increase N. For intermediate CNR, σv varies as $1/\sqrt{\text{CNR}}$. It is therefore equivalent to increase pulse energy or number of pulses. In this region, σv depends only on the average laser power. Using a low energy, high pulse repetition rate (PRF) laser is then equivalent to using a high energy, low PRF laser, assuming the average power is constant. This is one for the reasons of the recent raise of high PRF fiber lasers for pulsed Doppler lidars.

Range ambiguity The rate at which pulses are transmitted, the PRF limits the range over which heights can be unambiguously determined. To avoid ambiguity between return signals, the inter pulse period (IPP=1/PRF) must be longer than the round trip time of flight of the pulse to the greatest height. For example, to measure without ambiguity up to 5 km, the PRF needs to be less than 30 KHz,

$$\text{PRF}_{\max} = \frac{c}{2Z_{\max}}. \tag{138}$$

5.3.5 Time-bandwidth tradeoffs

Spatial resolution is proportional to pulse duration. The shorter the pulse, the smaller the resolution. Velocity resolution is proportional to spectrum width and is smaller when the spectrum is narrow. Because the spectrum width is inversely proportional to the pulse duration, range resolution and velocity resolution are also inversely proportional.

5.3.6 Existing systems and actual performances

In 2013, only a few pulsed lidars are available. Table 13 summarizes the characteristics of commercial ones, which can be used in the wind industry, meteorology or airport safety. All are based on coherent detection. In 2011, Pentalum introduced a new pulsed lidar, based on backscatter correlation on two adjacent beams and direct detection. This technique is currently under evaluation.

Table 13: Comparison of commercially available pulsed lidars

System	Wave length [μm]	Range/ accuracy [m]/[m s^{-1}]	Data update [s]	Sample volume length [m]	pulse duration/ energy [ns]/[μJ]	PRF [kHz]	Beam config.
Leosphere WindCube7	1.54	40–200/0.1	1/10 alt	20	175/10	30	Five beams DBS
WindCube 200S	1.54	100–6000/0.3	1	75	400/100	10	LOS mapping
WindCube 400S	1.54	200–12000/0.5	1	150	800/200	10	LOS mapping
LMCT Windtracer	1.6	400–15000/1	0.1	80	300/2000	0.75	LOS mapping
Mitsubishi	1.5	100–1500/NA	1	90	600/6.5	1	Scanning head
Sgurr Gallion G250	1.5	40–250/0.1	0.1–30	24	150/10	20	LOS mapping
G4000	1.5	80–4000/NA	NA	30	NA	NA	LOS mapping

5.3.7 Validation of measurements

Since the instrumental sources of uncertainty are now well identified and the range of deviation they might incur in the wind speed measurement are well estimated, it is necessary to compare the measurement of a new lidar unit against a tall mast equipped with traditional anemometry or against a well-known and validated lidar in a double phase verification/validation.

Validation is the process of ensuing that a WINDCUBE measures wind speed characteristics in conformity with what a reference instrument would give. Today, validation is done against well-known traditional anemometry, like a mast equipped with calibrated cup anemometers. This instrument comparison introduces additional uncertainties, not related to the inner performances of each individual instrument but related to the differences in the measurement process between the two instruments. These differences in the measurement process might incur differences in measured values, which will be site and time specific. Even if these are small, it is important to closely define the range of variation that might occur on the validation site.

With more than 140 field deployments worldwide for the past 4 years, the Windcube has been extensively tested in different conditions and under a diversity of climates. Several authors have reported very good measurement accuracy with reference to calibrated cup anemometers in good operating conditions (Oldroyd et al., 2009; Faghani et al., 2009; Jaynes, 2009).

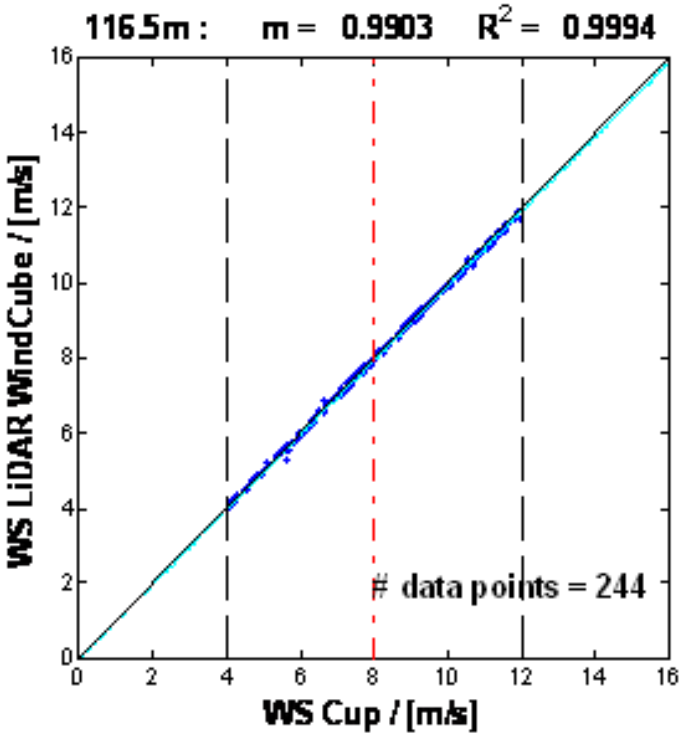

Figure 69: Comparison of Windcube 10-min averages with calibrated mast at Risø Høvsøre

5.4 Conclusions and perspectives

This chapter summarizes the principles of operation, the performances and critical parameters of Doppler pulsed wind lidars, such as the WINDCUBE lidar from LEOSPHERE. It takes into account the different steps of the velocity measurement process. This detailed process analysis provides the backbone for a pulsed lidar development, optimization and issues related to serial production.

More generally, pulsed and CW lidars have shown great reliability and accuracy in the measurement of wind characteristics such as horizontal and vertical wind speed and wind direction at various heights on flat terrains and offshore (Courtney et al., 2009; Westerhellweg et al., 2010). The high data recovery rate up to above blade top ensures a high quality analysis of the wind conditions available on the project site, leading to an optimized layout design and the choice of the suitable turbines.

Regarding future improvements, the measurement of additional wind parameters like turbulence intensities, kinetic fluxes or inflow-angles is under investigation at the present time and should be available in the near future.

One of the remaining challenges is also reaching high accuracy in complex terrains where flow distortion occurs and impairs the lidar wind components retrieval from measured radial velocities. Since lidar radial velocities are still very accurate even on complex and rough terrains, a methodology using CFD modeling has been recently developed to avoid taking the flow homogeneity assumption (Boquet et al., 2009; Bingöl et al., 2009; Boquet et al., 2010a). Even though new, this methodology has already shown good results on sites of various complexities. The measurement of additional wind parameters like turbulence intensities, kinetic fluxes or inflow angles is under investigation at the present time and should be available in the near future.

To sum up, lidar anemometry has already proven its great utility in the development of wind farm projects, as an instrument allowing considerable financial gains through a better understanding of the wind conditions at a site and therefore reducing the capital risk of the investors (Boquet et al., 2010b), but also for operational power curves measurements

(Gottshall et al., 2010; Albers et al., 2010). With the general trend to develop larger wind turbines and wider wind farms, the lidar technology is elected to be more and more widely used.

Notation

B	detector bandwidth
c	speed of light
C_n	index structure constant
CNR	carrier-to-noise ratio
CRLB	Cramer Rao lower bound
CW	continuous wave
d_o	coherence diameter of the beam
DBS	Doppler beam swinging
FFT	fast Fourier transform
F_i	intermediate frequency
F_s	sampling frequency
F_t	instrumental geometrical focus distance (wave curvature radius at telescope)
FWHM	full width half maximum
$< i^2_{NEP} >$	detector noise
$< i^2_{RIN} >$	rin noise
$< i^2_{SN} >$	shot noise
$I(Z)$	Lorentzian function
IPP	inter pulse period
LMA	large mode area
LOS	line of sight
LO	local oscillator
MLE	maximum likelihood estimator
MO	master oscillator
MOPA	master oscillator power amplifier
NEP	noise equivalent power density
P_{LO}	local oscillator power
P_{peak}	transmitted pulse peak power
P_r	total optical power
PRF	pulse repetition frequency
$\mathrm{PRF}_{\max}$	maximum pulse repetition frequency
N	number of average pulses
R	focus distance
$RWF(Z)$	range weighting function
S	detector sensitivity
SNR	signal to noise ratio
T_{atm}	atmospheric round trip transmission
T_{inst}	instrumental round trip transmission
u	north-south wind speed component
v	east-west wind speed component
VAD	velocity azimuth display
$V_d(Z)$	velocity measurement at one point
Vr_i	LOS velocities, $i = N$ North, $i = E$ East, $i = S$ South, $i = W$ West and $i = Z$ Zenith
w	vertical wind speed component
Z	height
$Z_{\max}$	maximum height to be measured
Z_o	distance where $I(Z)$ is maximum, i.e. signal to noise is maximum
Z_r	Rayleigh distance
β	backscattering atmospheric coefficient
ΔZ	half of FWHM geometric depth of focus
η_{foc}	focusing efficiency
η_{het}	heterodyne efficiency
θ	lidar cone angle
λ	laser wavelength
ν	optical frequency
σ	efficient telescope aperture radius
σv	global velocity resolution
σv_{crlb}	Cramer Rao lower bound of velocity resolution
σv_{sat}	smallest value of the velocity resolution
τ	pulse duration
τ_c	finite correlation time
τ_m	measurement time

References

Albers A., Janssen A. W. and Mander J. (2010) Hot to gain acceptance for lidar measurements. *DEWEK*

Ando T., Kameyama S. and Hirano Y. (2008) All-fiber coherent Doppler lidar technologies at Mitsubishi Electric Corporation. *IOP Conf. Series: Earth and Environ. Science* **1**:012011

Banakh V. and Smalikho I. (1994) Estimation of the turbulence energy dissipation rate from the pulsed Doppler lidar data. *J. Atmos. Oceanic Technol.* **10**

Bingöl F., Mann J. and Foussekis D. (2009) Conically scanning lidar error in complex terrian. *Meteorol. Z.* **18**:1–7

Boquet M., Parmentier R. and Cariou J. P. (2009) Analysis and optimization of pulsed Doppler lidar in complex terrain. *EWEC*, Marseille

Boquet M., Parmentier R. and Cariou J. P. (2010) Correction of pulsed wind lidars bias in complex terrain. *ISARS*

Boquet M., Callard P., Neve N. and Osler E. G. (2010) Return on investment of a lidar remote sensing device. *DEWI Magazin* **37**:56–61

Cariou J.-P., Augere B. and Valla M. (2006) Laser source requirements for coherent lidars based on fiber technology. *Comptes Rendus Physique* **7**:213–223

Courtney M., Wagner R. and Lindelöw P. (2009) Commercial lidar profilers for wind energy. A comparative guide. *EWEC*, Marseille

Faghani D. et al. (2009) Remote sensing: practical use for wind power project. *AWEA Wind Resource & Project Energy Assessment Workshop*, Portland

Frehlich R. G. and Kavaya M. J. (1991) Coherent laser radar performance for general atmospheric refractive turbulence. *Appl. Opt.* **30**

Frehlich R. G., Hannon S. M., Henderson S. W. (1993) Performance of a 2-coherent Doppler lidar for wind measurements. *J. Atmos. Oceanic. Technol.* **11**:1517–

Frehlich R. G., Hannon S. M. and Henderson S. W. (1998) Coherent Doppler lidar measurements of wind field statistics. *Bound.-Layer Meteorol.* **86**:233–256

Gottshall J., Courtney M. S., Lindelöw P. and Albers A. (2010) Classification of lidar profilers: How to introduce lidars to power performance testing. *EWEC*, Brussels

Huffaker R. M. and Hardestry R. M. (1996) Remote sensing of Atmospheric wind velocities using solid state and CO2 coherent laser systems. *Proc. IEEE* **84**

Jaynes D. (2009) Lidar validation and recommendations for wind resource assessments. *Wind Power Conf.*, Chicago

Lindelöw P. (2007) Effective sample volume fiber based coherent lidars for remote sensing of wind. PhD thesis from Ørsted-DTU, Lyngby

Mikkelsen T. (2008) WindScanner: a facility for wind and turbulence measurements around large wind turbines. *In Nordic Conf. on: Global Challenges-Regional Opportunities: How can research infrastracture and Science support Nordic competiveness?*, Stockholm

Oldroyd A. et al. (2009) Testing and calibration of various lidar remote sensing devices for a 2 year offshore measurement campaign. *EWEC*, Marseille

Siegman A. E. (1966) The antenna properties of optical heterodyne receivers. *Appl. Optics* **5**:1588–1594

Soreide D., Boque R. K., Seidel J. and Ehernberger L. J. (1997) The use of a lidar forward looking turbulence sensor for mixed-compression inlet unstart avoidance and gross weight reduction on a high speed civil transport Nasa Technical memorandum

Westerhellweg A., Beeken A., Canadillas B., Neumann T. (2010) One year of lidar measurements at Fino1-platform: comparison and verification to met-mast data. *DEWEK*

6 Remote sensing for the derivation of the mixing-layer height and detection of low-level jets

Stefan Emeis
Institute of Meteorology and Climate Research,
Atmospheric Environmental Research Division (IMK-IFU),
Karlsruhe Institute of Technology, Garmisch-Partenkirchen, Germany

6.1 Introduction

This chapter gives an overview of the derivation of mixing-layer height (MLH) and the detection of low-level jets (LLJs) by surface-based remote sensing instruments such as sodar, lidar, ceilometer and RASS. The detection of vertical profiles indicating the structure of the atmospheric boundary layer (ABL) is one of the principal tasks of experimental boundary-layer research. MLH has become an important input parameter for the description of wind profiles above the surface layer (Gryning et al., 2007; Peña et al., 2010). LLJs are secondary wind maxima which occur at the top of a stable boundary layer. Over land, they are observed at several hundred metres above ground at night-time. Over the sea, they are found with offshore winds when warmer air flows over cooler water at the top of the shallow stable internal boundary layer at any time of the day. These shallow internal boundary layers are often considerably less than 100 m deep.

The next section describes methods to detect the mixing-layer height, while Section 6.3 briefly mentions methods to capture the boundary-layer height. Section 6.4 gives more information on low-level jets. Acoustic (sodar) and optical sounding techniques (lidar) have got a broad coverage elsewhere in this volume. RASS techniques are still quite unusual in the assessment of wind resources. Therefore, a subsection on technical details of this instrumentation has been added in section 6.2. A more complete survey of remote sensing instrumentation is given in Emeis (2010), an overview of applications of ground-based remote sensing is presented in Emeis (2011). The full scope of wind energy meteorology is presented in Emeis (2012).

6.2 Mixing-layer height

We must distinguish between the mixing-layer height, MLH (see section 6.2) and the boundary-layer height, z_i (see section 6.3). The boundary-layer height is the height up to which the influence of the presence of the lower surface is detectable. The mixing-layer height is the height up to which atmospheric properties (such as wind speed and turbulence) or substances originating from the surface are dispersed by turbulent vertical mixing processes. The mixing-layer – if it is present at all – is a part of the ABL. The mixing-layer height is usually shallower than the boundary-layer, but it fills the whole ABL in deep convective boundary layers.

Sometimes the terms mixed-layer height or mixing height are used as well for MLH, but we will stick here to the most common term mixing-layer height. The mixing-layer height is the height up to which atmospheric properties or substances originating from the Earth's surface or formed within this layer are dispersed almost uniformly over the entire depth of this layer by turbulent vertical mixing processes. Therefore, the existence and the height of a mixing layer can either be analyzed from a detection of the presence of the mixing process, i.e. turbulence, or from the verification that a given conservative atmospheric variable is distributed evenly over the full height range of the well-mixed layer. The level of turbulence can for instance be

derived from fluctuations of the wind components or from temperature fluctuations. Suitable conservative atmospheric variables for the identification of the mixing layer and its height are, e.g., potential temperature, specific humidity or aerosol particle concentrations. Temperature can be measured with RASS, temperature gradients may be assessed from sodar data and aerosol concentration data from lidar and ceilometer measurements. Therefore, these instruments offer the opportunity to detect mixing-layer heights. A suitable remote sensing method for deriving humidity profiles with high vertical resolution (comparable to sodar, RASS and lidar) is still missing.

A well-known overview of methods to determine MLH from in-situ measurements and surface-based remote sensing had been given by Seibert et al. (2000). Since then considerable development has taken place, especially concerning the usage of optical surface-based remote sensing methods (see the review paper by Emeis et al. (2008)) and RASS. Updates are given in Emeis (2011) and Emeis (2012).

Optical methods for MLH detection may be used to illustrate this recent progress. Seibert et al. (2000) still classified lidar methods as expensive, not eye-save, with a high lowest range gate, limited range resolution, and sometimes subject to ambiguous interpretation. This has changed drastically in the last ten years when and smaller Doppler wind lidars have been built and the simpler non-Doppler ceilometers have been discovered to be a nearly ideal sounding instrument for the detection of the vertical structure of the boundary layer. Progress has been made in the field of acoustic sounding as well. Similarly, algorithms for the determination of MLH from vertical profiles of the acoustic backscatter intensity as described in Beyrich (1997) and Seibert et al. (2000) have been enhanced by using further variables available from sodar measurements such as the wind speed and the variance of the vertical velocity component (Asimakopoulos et al., 2004; Emeis and Türk, 2004). Such enhancements had been named as possible methods in Beyrich (1995) and Seibert et al. (2000) but obviously no example was available at that time.

A variety of different algorithms have been developed by which the MLH is derived from ground-based remote sensing data (see Table 14 for a short overview). We will mainly concentrate on acoustic and optical remote sensing because electro-magnetic remote sensing (by RADAR and wind profiler) has too high lowest range gates for a good coverage of shallow MLH. The disadvantage of a too high lowest range gate can partly be circumvented by slantwise profiling or conical scanning if the assumption of horizontal homogeneity can be made.

6.2.1 Acoustic detection methods (Sodar)

Acoustic methods either analyze the acoustic backscatter intensity, or, if Doppler shifts in the backscattered pulses can be analyzed, features of vertical profiles of the wind components and its variances as well. The acoustic backscatter intensity is proportional to small-scale fluctuations in atmospheric temperature (usually generated by turbulence) or by stronger vertical temperature gradients. The latter feature may be an indication for the presence of temperature inversions, which can often be found at the top of the mixing layer.

Beyrich (1997) listed possible analyses which can mainly be made from acoustic backscatter intensities measured by a sodar. Later, Asimakopoulos et al. (2004) summarized three different methods to derive MLH from sodar data: (1) the horizontal wind speed method (HWS), (2) the acoustic received echo method (ARE), and (3) the vertical wind variance method (VWV). We will mainly follow this classification here and finally add a fourth method, the enhanced ARE method (EARE).

Figure 70, showing an acoustic sounding taken in an Alpine valley, gives an impression what wealth of detailed vertical information can be derived from acoustic boundary-layer sounding. The left-hand frame displays the acoustic backscatter intensity and the right-hand frame the wind direction as time-height sections over one day (from midnight to midnight) and over a height range of 700 m. The depicted wintry situation from a day in January exhibits a multiple layering of the air in that valley due to the very stable thermal stratification of the

Table 14: Overview of methods using ground-based remote sensing for the derivation of the mixing-layer height mentioned in this chapter (see right most column to find its placement in section 6.2).

method	short description	which section?
acoustic ARE	analysis of acoustic backscatter intensity	6.2.1
acoustic HWS	analysis of wind speed profiles	6.2.1
acoustic VWV	analysis of vertical wind variance profiles	6.2.1
acoustic EARE	analysis of backscatter and vertical wind variance profiles	6.2.1
optical threshold	detection of a given backscatter intensity threshold	6.2.2
optical gradient	analysis of backscatter intensity profiles	6.2.2
optical idealized backscatter	analysis of backscatter intensity profiles	6.2.2
optical wavelet	analysis of backscatter intensity profiles	6.2.2
optical variance	analysis of backscatter intensity profiles	6.2.2
acoustic/electro-magnetic	RASS	6.2.3
acoustic/electro-magnetic	sodar-RASS and windprofiler-RASS	6.2.3
acoustic/electro-magnetic/in situ	sodar-RASS plus surface heat flux data	6.2.3
acoustic/electro-magnetic	sodar plus windprofiler	6.2.4
acoustic/optical	sodar plus ceilometer	6.2.4

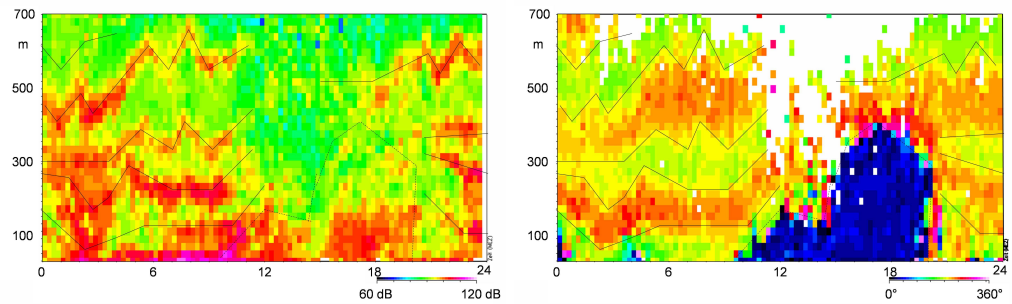

Figure 70: Sample time-height cross-section from acoustic sounding with a sodar. Left: acoustic backscatter intensity, right: horizontal wind direction. Thin black lines demark inversions.

valley air over a snow-covered valley floor. The multiple layering originated from an interlacing of down-valley (wind direction around 190°) and down-slope (wind direction around 230°) flows. The layers are separated by temperature inversions and each higher layer is potentially warmer than the next lower layer. They persisted nearly the whole day because no vertical mixing took place in the stably stratified valley atmosphere.

Acoustic received echo (ARE) method The ARE method is the most basic method of determining MLH from acoustic remote sensing. Most of the methods listed in Beyrich (1997) belong to this method. The method does not require an analysis of the Doppler shift of the backscattered signals. The method makes use of the assumption that turbulence is larger in the mixing layer than in the atmosphere above, and that this turbulence is depicted in the intensity of the acoustic backscatter. MLH is analyzed either from the maximum negative slope or from the changing curvature of the vertical profile of the acoustic backscatter intensity or it is analyzed from the height where the backscatter intensity decreases below a certain pre-specified threshold value.

Horizontal wind speed (HWS) method The HWS method requires the analysis of the Doppler shift of the backscattered acoustic signals. The algorithm is based on the analysis of the shape of hourly-averaged vertical wind speed profiles using the assumption that wind speed and wind direction are almost constant within the mixing layer but approach gradually towards the geostrophic values above the mixing layer. Beyrich (1997) listed this method in his Tab. 2 but did not discuss it further. The applicability of the method is probably limited to the well-developed convective boundary layers (CBL) due to the underlying assumptions. Such CBLs are often higher than the maximum range of a sodar. Even if the CBL height is within the range of the sodar the algorithm for the analysis of the Doppler shift often fails above the inversion topping of the CBL due to too low signal-to-noise ratios. Today, small Doppler wind lidars are available to derive wind speed and direction profiles through the whole depth of the boundary layer. This facilitates the application of the HWS method.

Vertical wind variance (VWV) method The VWV method is also working only for CBLs. It is based on the vertical profile of the variance of the vertical velocity component σ_w. In a CBL σ_w reaches a maximum in a height az_i. Typical values for a are between 0.35 and 0.40. Thus, in principle, this is an extrapolation method. It has been tried for sodar measurements because it permits a detection of MLH up to heights which are 2.5 times above the limited maximum range (usually between 500 and 1000 m) of the sodar. Beyrich (1997) classified this method as not reliable. A related method, which is based on power spectra of the vertical velocity component, is integrated in the commercial evaluation software of certain sodars (Contini et al., 2009). The application of the VWV method is now also been facilitated by the easy availability of small Doppler wind lidars.

Enhanced acoustic received echo (EARE) method The EARE algorithm has been proposed by Emeis and Türk (2004) and Emeis et al. (2007). The method is an enhancement of the ARE method in two ways. Firstly, it includes further variables into the MLH algorithm that are available from Doppler-sodars. The benefits of the additional usage of the variance of the vertical velocity component have been demonstrated by Emeis and Türk (2004). Secondly, it determines not only MLH from sodar measurements but also the heights of additional lifted inversions. Especially in orographically complex terrain, the vertical structure of the ABL can be very complicated. Emeis et al. (2007) have shown that several persistent inversions one above the other which form in deep Alpine valleys can be detected from sodar measurements (Fig. 70).

EARE determines three different types of heights based on acoustic backscatter intensity and the variance of the vertical velocity component. Because the horizontal wind information above the inversion is not regularly available from sodar measurements, horizontal wind data have not been included into this scheme. In the following a letter "H" and an attached number will denote certain derived heights which are related to inversions and the MLH; while the variable z is used to denote the normal vertical coordinate. The EARE algorithm detects:

- the height ($H1$) of a turbulent layer characterised by high acoustic backscatter intensities $R(z)$ due to thermal fluctuations (therefore having a high variance of the vertical velocity component σ_w),

- several lifted inversions ($H2_n$) characterized by secondary maxima of acoustic backscatter due to a sharp increase of temperature with height and simultaneously low σ_w (like those depicted in the left-hand frame of Fig. 70), and
- the height of a surface-based stable layer ($H3$) characterised by high backscatter intensities due to a large mean vertical temperature gradient starting directly at the ground and having a low variance of the vertical velocity component.

The height $H1$ corresponds to a sharp decrease $\partial R/\partial z < DR_1$ of the acoustic backscatter intensity $R(z)$ below a threshold value R_c with height z usually indicating the top of a turbulent layer:

$$H1 = z, \quad \text{if} \quad (R(z) < R_c \quad \text{and} \quad R(z+1) < R(z) + zDR_1 \quad \text{and} \quad R(z+2) < R(z) + 2zDR_1). \tag{139}$$

$R_c = 88$ dB and $DR_1 = -0.16$ dB m^{-1} have proven to be meaningful values in the above mentioned studies. R_c is somewhat arbitrary because the received acoustic backscatter intensities from a sodar cannot be absolutely calibrated. An absolute calibration would require the knowledge of temperature and humidity distributions along the sound paths for a precise calculation of the sound attenuation in the air. DR_1 is, at least for smaller vertical distances, independent from the absolute value of R_c. An application-dependent fine-tuning of R_c and DR_1 may be necessary.

Elevated inversions are diagnosed from secondary maxima of the backscatter intensity that are not related to high turbulence intensities. For elevated inversions increase in backscatter intensity below a certain height $z = H2$ and a decrease above is stipulated while the turbulence intensity is low:

$$H2_n = z, \quad \text{if} \quad (\partial R/\partial z|_{z+1} < -DR_2 \quad \text{and} \quad \partial R/\partial z|_{z-1} > DR_2 \quad \text{and} \quad \sigma_w < 0.70 \text{ m s}^{-1}) \tag{140}$$

for $n = 1$, ..., N. In Emeis et al. (2007) N was chosen to be five. A threshold value $DR_2 = 0.08$ dB m^{-1} has proven suitable. But again, an application-dependent tuning may be advisable.

The determination of the height of the stable surface layer $H3$ is started if the backscatter intensity in the lowest range gates is above 105 dB while σ_w is smaller than 0.3 m s^{-1}. The top of the stable layer $H3$ is at the height where either the backscatter intensity sinks below 105 dB or σ_w increases above 0.3 m s^{-1},

$$\begin{aligned} H3 \quad = \quad & z, \text{ if } (R(z) > 105 \text{ dB and } R(z+1) < 105 \text{ dB and } \sigma_w(z) < 0.3\text{m s}^{-1}) \text{ or} \\ & \text{if } (\sigma_w(z) < 0.3 \text{ m s}^{-1} \text{ and } \sigma_w(z+1) > 0.3 \text{ m s}^{-1} \text{ and } R(z) > 105 \text{ dB}) \end{aligned} \tag{141}$$

The σ_w values used in Eqs. (140) and (141) have been determined by optimizing the automatic application of the detection algorithm. In doing so it turned out that no lifted inversions occurred with a variance σ_w higher than 0.7 m s^{-1} and that the variance σ_w in nocturnal stable surface layers was always below 0.3 m s^{-1}. The first σ_w threshold made it possible to distinguish between inversions and elevated layers of enhanced turbulence. The latter σ_w threshold made it possible to differentiate between nocturnal stable surface layers and daytime super-adiabatic surface layers although both types of surface layers yield more or less the same level of backscatter intensity. Finally MLH from the acoustic remote sensing is determined as the minimum of $H1$, $H2_1$, and $H3$:

$$\text{MLH}_{\text{ac}} = \min\left(H1, H2_1, H3\right). \tag{142}$$

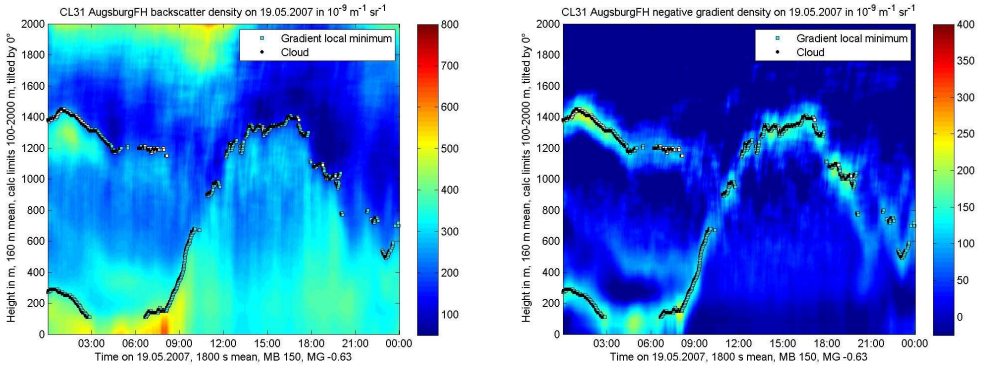

Figure 71: Sample time-height cross-section from optical sounding with a ceilometer. Left: optical backscatter intensity, right: vertical derivative of this backscatter intensity. Dots mark mixing-layer height derived from a gradient algorithm.

6.2.2 Optical detection methods

Usually the aerosol content of the mixing layer is higher than in the atmospheric layer above, because the emission sources for aerosol are in most cases on the ground. Aerosol formation from precursors mainly takes place near the surface as well. Making the assumption that the vertical aerosol distribution adapts rapidly to the changing thermal structure of the boundary layer, MLH can be determined from the analysis of the vertical aerosol distribution. This also includes the assumption that the vertical aerosol distribution is not dominated by horizontally advected aerosol plumes or layers. The heights of the near surface aerosol layers ($H4_n$) can be analysed from the optical vertical backscatter profile obtained from optical remote sensing. Several methods have been developed, the most prominent of these being: (1) the threshold method, (2) the gradient or derivative method, (3) the idealised gradient method, (4) the wavelet method, and (5) the variance method. In addition, the horizontal wind speed method and the vertical wind variance method mentioned in section 6.2.1 above are available to derive the vertical structure of the boundary layer from Doppler wind lidar data.

The application of optical remote sensing for MLH determination has focussed on the use of ceilometers in recent years. Ceilometers can be regarded as a small lidar. They are simpler and they have a much lower lowest range gate than lidars. For the detection of MLH below 150 to 200 m a ceilometer with one optical axis for the emitted and the received beam should be used. Due to the thin light beams the overlap of the emitted and received beam from a ceilometer with two parallel optical axes can be insufficient in this height range. Further on, Doppler shifts are not analyzed by ceilometers. Therefore, in contrast to acoustic remote sensing with Doppler-sodars, additional variables in addition to the backscatter intensity are not available from ceilometers for the design of determination schemes for MLH. Thus the schemes listed below all resemble to the ARE methods for acoustic remote sensing.

Figure 71 shows a sample measurement with a mono-axial ceilometer. The left-hand frame displays the optical backscatter intensity and the right-hand frame the negative vertical derivative of this intensity as time-height sections over one day (from midnight to midnight) and over a height range of 2000 m. The data was received on a clear day in spring and the vertical structure of the ABL was dominated by surface heating due to incoming solar radiation during daytime and radiative surface cooling during night-time. In the morning hours until about 0900 LST a shallow stable nocturnal surface layer with a depth of about 200 m and a residual layer with a depth of about 1200 to 1400 m can be distinguished. From 0900 LST onwards the evolution of a daytime convective boundary layer with a maximum depth of about 1400 m can be clearly seen. The dots in both frames of Fig. 71 indicate the mixing-layer height determined with the gradient method described below. The right-hand frame in Fig. 71 demonstrates that the analysed MLH values indeed coincide with maxima of the negative vertical gradient of the optical backscatter intensity.

Threshold method Melfi et al. (1985) and Boers et al. (1988) used simple signal threshold values, though this method suffers from the need to define them appropriately (Sicard et al., 2006). $H4$ is defined here as the height within the vertical profile of the optical backscatter intensity where the backscatter intensity first exceeds a given threshold when coming downward from the free unpolluted troposphere. The determination of several heights $H4_n$ would require the definition of several thresholds which probably cannot be done a priory to the analysis. Therefore this will always lead to a subjective analysis of MLH. The left-hand frame in Fig. 71 shows that the threshold value cannot be kept constant during the diurnal evolution of the boundary layer in order to get a result which is comparable to the one from the gradient method applied in Fig. 71.

Gradient or derivative methods Hayden et al. (1997) and Flamant et al. (1997) proposed to use the largest negative peak of the first derivative of the optical attenuated backscatter intensity ($B(z)$) for the detection of $H4$ from LIDAR data (height of gradient minimum $H4_{\mathrm{GM}}$):

$$H4_{\mathrm{GM}} = \min(\partial B(z)/\partial z). \tag{143}$$

The right-hand frame of Fig. 71 demonstrates that this is a very meaningful assumption. Likewise Wulfmeyer (1999) used the first minimum of the slope to detect the top of a convective boundary layer from DIAL data. Münkel and Räsänen (2004) and Schäfer et al. (2004, 2005) applied the gradient method to ceilometer data. Menut et al. (1999) took the minimum of the second derivative of $B(z)$ as the indication for MLH:

$$H4_{\mathrm{IPM}} = \min(\partial^2 B(z)/\partial z^2). \tag{144}$$

This method is called inflection point method (IPM). It usually gives slightly lower values for $H4$ than the gradient method in Eq. (143). A further approach was suggested by Senff et al. (1996). They looked for the largest negative gradient in the logarithm of the backscatter intensity (height of logarithmic gradient minimum $H4_{\mathrm{LGM}}$):

$$H4_{\mathrm{LGM}} = \min(\partial \ln B(z)/\partial z). \tag{145}$$

This approach usually gives the largest value for $H4$. According to Sicard et al. (2006) $H4_{\mathrm{IPM}}$ from Eq. (144) is closest to the MLH derived from radiosonde ascents via the Richardson method. The other two algorithms in Eqs. (143) and (145) give slightly higher values.

In Emeis et al. (2007) the gradient method in Eq. (143) has been further refined and extended to enable the calculation of up to $n = 5$ lifted inversions. This algorithm, which has also been used for the MLH analysis shown in Fig. 71, is described in the following. Prior to the determination of gradient minima the overlap and range corrected attenuated backscatter profiles have to be averaged over time and height to suppress noise generated artefacts. Therefore the $H4$ values are determined in a two-step procedure. Between 140 and 500 m height sliding averaging is done over 15 min and a height interval Δh of 80 m. In the layer between 500 and 2000 m Δh for vertical averaging is extended to 160 m. Two additional parameters have been introduced to further reduce the number of false hits. The minimum accepted attenuated backscatter intensity $B_{\min}$ right below a lifted inversion is set to 200×10^{-9} m^{-1} srad^{-1} in the lower layer and 250×10^{-9} m^{-1} srad^{-1} in the upper layer. Additionally the vertical gradient value $\partial B/\partial z_{\max}$ of a lifted inversion must be more negative than 0.30×10^{-9} m^{-2} srad^{-1} in the lower layer and more negative than -0.60×10^{-9} m^{-2} srad^{-1} in the upper layer.

If $B(z)$ denotes the measured attenuated backscatter intensity in the height z above ground averaged over time and height and Δh is the height averaging interval, then the gradient $\partial B/\partial z$ in the height z is calculated as

$$\partial B/\partial z|_z = \left(B(z + \Delta h/2) - B(z - \Delta h/2)\right)/\Delta h. \tag{146}$$

A gradient minimum is characterized by a change of sign from minus to plus of the second derivative of $B(z)$. The height interval under examination is searched from bottom to top for these gradient minima $H4_n$.

The second derivative of $B(z)$ in the height z is

$$\partial^2 B/\partial z^2|_z = \left(\partial B/\partial z|_{z+\Delta h/2} - \partial B/\partial z|_{z-\Delta h/2}\right)/\Delta h. \quad (147)$$

There is a gradient minimum $H4_n$ in the height z if the second derivative of $B(z)$ one range gate below z is not positive, if the second derivative of $B(z)$ in the height z is positive, and if the false hit conditions mentioned above are fulfilled:

$$H4_n = z, \qquad \text{if } \partial^2 B/\partial z^2|_{z-1} \leq 0 \text{ and } \partial^2 B/\partial z^2|_z > 0 \text{ and } B(z-\Delta h/2) \geq B_{\min} \text{ and } \partial B/\partial z|_z \leq \partial B/\partial z_{\max} \text{ for } n = 1, ..., 5. \quad (148)$$

The MLH from optical remote sensing is taken as the lowest height $H4_n$:

$$\mathrm{MLH_{op}} = H4_1. \quad (149)$$

Idealised backscatter method A parallel development by Eresmaa et al. (2006) using an idealised backscatter profile, originally described by Steyn et al. (1999), is also an extension of the gradient method. MLH is not determined from the observed backscatter profile, but from an idealised backscatter profile fitted to the observed profile. The robustness of this technique is founded on utilising the whole backscatter profile rather than just the portion surrounding the top of the mixing layer. In this method an idealized backscattering profile $B_i(z)$ is fitted to measured profile by the formula

$$B_i(z) = \left((B_m + B_u)/2 - (B_m - B_u)/2\right)\mathrm{erf}((z-h)/\Delta h) \quad (150)$$

where B_m is the mean mixing layer backscatter, B_u is the mean backscatter in air above the mixing layer and Δh is related to the thickness of the entrainment layer capping the ABL in convective conditions. Two new parameters $A1$ and $A2$ are defined so that $A1 = (B_m + B_u)/2$ and $A2 = (B_m - B_u)/2$. The value of $A1$ is kept constant during the fitting procedure. A good estimation of $A1$ based on an initial order-of-magnitude guess for the MLH is crucial for the quality of the result.

Wavelet method A Wavelet method has been developed for the automatic determination of mixing layer height from backscatter profiles of an LD-40 ceilometer by de Haij et al. (2006). Before that wavelet transforms have been applied in recent studies for MLH determination from LIDAR observations (Cohn and Angevine, 2000; Davis et al., 2000; Brooks, 2003; Wulfmeyer and Janjić, 2005). The most important advantage of wavelet methods is the decomposition of the signal in both altitude as well as vertical spatial scale of the structures in the backscatter signal.

The Wavelet algorithm in de Haij et al. (2006) is applied to the 10 minute averaged range and overlap corrected backscatter profile $B(z)$ within a vertical domain of 90–3000 m. For each averaged profile the top of two significant aerosol layers are detected in order to detect MLH as well as the top of a secondary aerosol layer, like e.g. an advected aerosol layer or the residual layer. This Wavelet MLH method uses the scale averaged power spectrum profile $W_B(z)$ of the wavelet transform with 24 dilations between 15 and 360 m and step size 15 m. The top of the first layer, $H4_1$, is detected at the first range gate at which the scale averaged power spectrum $W_B(z)$ shows a local maximum, exceeding a threshold value of 0.1. This threshold value is empirically chosen, based on the analysis of several cases with both well pronounced and less clearly pronounced mixing layer tops. $H4_2$ is optionally determined in the height range between $H4_1$ and the upper boundary of detection. A valid $H4_2$ is detected at the level with the strongest local maximum of $W_B(z)$ provided that this maximum is larger than the $W_B(z)$ of $H4_1$. MLH is set equal to $H4_1$.

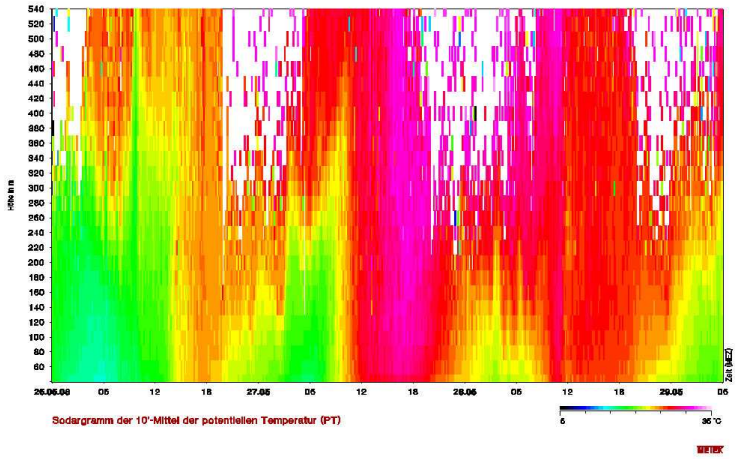

Figure 72: Sample time-height cross-section from a potential temperature sounding with RASS.

However, problems with this method arise e.g. in case of multiple (well defined) aerosol layers, which renders the selection of the correct mixing layer top ambiguous. Furthermore, in spring and summer the detection of the MLH for deep (convective) boundary layers often fails. This is mostly due to the high variability of the aerosol backscatter signal with height which limits the range for MLH estimation in those conditions (de Haij et al., 2006).

Variance method At the top of the CBL we have entrainment of clear air masses from the free troposphere into the ABL. The entrainment process is temporarily variable and leads locally to considerable fluctuations in the aerosol concentration. Therefore the maximum in the vertical profile of the variance of the optical backscatter intensity can be an indicator for an entrainment layer on top of a CBL (Hooper and Eloranta, 1986; Piironen and Eloranta, 1995). The method is called variance centroid method in Menut et al. (1999). The variance method for the CBL height is also described in Lammert and Bösenberg (2006). Due to the assumptions made this method is suitable for daytime convective boundary layers only. An elucidating comparison between the gradient method and the variance method can be found in Martucci et al. (2004) although they used a Nd:YAG LIDAR at 532 nm instead of a ceilometer and thus suffered from a high lowest range gate in the order of 300 m.

6.2.3 RASS

The acoustic and optical methods for MLH determination, which have been described in the sections above, are all indirect methods that try to infer the mixing-layer height from other variables which usually adapt to the vertical structure of the ABL. The only direct and key variable for the analysis of the presence of a mixing layer is the vertical profile of virtual temperature. Temperature profiles can directly be measured with a radio-acoustic sounding system (RASS). Fig. 72 shows an example. We start here with a short description of the available RASS methods.

Instrumentation A radio-acoustic sounding system (RASS) operates acoustic and electro-magnetic sounding simultaneously (Marshall et al., 1972). This instrument is able to detect acoustic shock fronts of the acoustic pulses and to determine their propagation speed from the Doppler shift of the backscattered electro-magnetic waves. This propagation speed is equal to the speed of sound which in turn is a known function of air temperature and humidity. To different types of RASS have been realised (Engelbart and Bange, 2002): a Bragg-RASS and

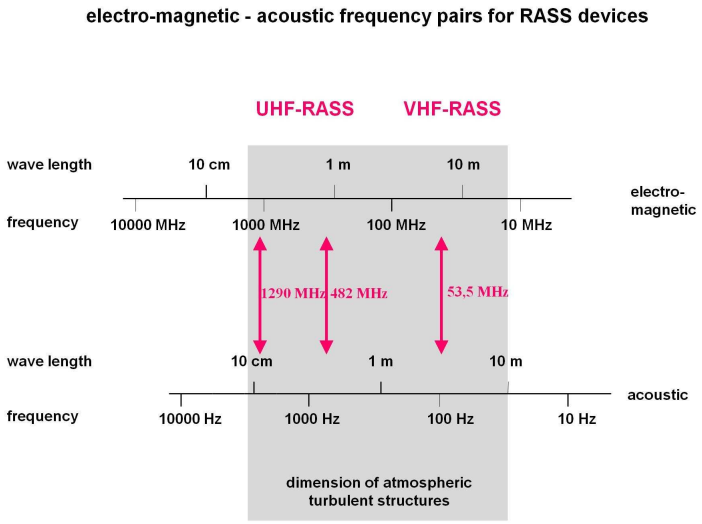

Figure 73: Bragg-related acoustic (below) and electro-magnetic (above) frequencies for RASS.

a Doppler-RASS.

Bragg-(windprofiler) RASS A Bragg-RASS (or windprofiler-RASS) is basically a windprofiler with an additional acoustic emitter. When the Bragg condition is fulfilled (Fig. 73), i.e. the wavelength of the sound waves λ_a is half the one of the electro-magnetic waves λ_e, then there is optimal backscatter of the electro-magnetic waves from the acoustic waves (Fig. 74). The electro-magnetic signal is emitted at a fixed frequency, but the emitted sound signal is a chirp signal with varying frequency f_a. From the sound wave length $\lambda_{a,B}$ at which optimal backscatter occurs the propagation speed of the sound signal can be determined via the following dispersion relation:

$$c_a = \lambda_{a,B} f_a / 2. \tag{151}$$

For a VHF windprofiler operating at 50 MHz a sound frequency of about 100 Hz is used, for a UHF windprofiler operating at 1 GHz a sound frequency around 2 kHz is most suitable to fulfil the Bragg condition. Because the attenuation of sound waves in the atmosphere is strongly frequency dependent, a UHF RASS can detect temperature profiles up to about 1.5 km height whereas a VHF RASS can observe temperature profiles throughout the troposphere.

Doppler-(sodar) RASS A Doppler-RASS (or sodar-RASS) is a sodar with an additional electro-magnetic emitter and receiver (Fig. 75) operating at a frequency $f_{e,0}$. From the Doppler shift Δf_e of the electro-magnetic radiation which is backscattered at the density fluctuations caused by the sound waves the propagation speed c_a of the sound waves is determined:

$$c_a = -c\Delta f_e / (2 f_{e,0}) \tag{152}$$

where c denotes the speed of light. A Doppler-RASS like a Bragg-RASS also emits a chirp sound signal in order to assure that the Bragg condition is optimally met due to the varying temperature over the entire height range.

The so determined propagation speed c_a is a sum of the speed of sound c_s and of the vertical movement of the air w within which the sound waves propagate:

$$c_a = c_s + w. \tag{153}$$

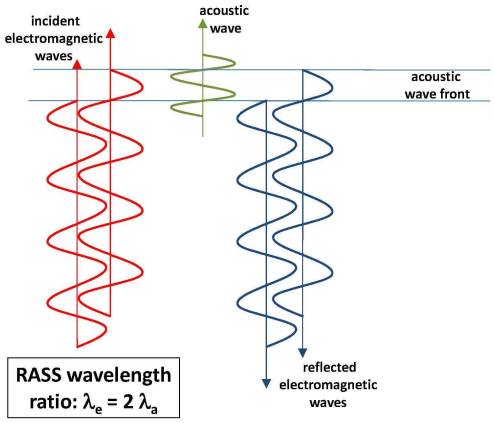

Figure 74: Bragg condition for RASS sounding.

Figure 75: Sodar-RASS. The acoustic antenna is in the middle, the electro-magnetic antennas to the left and right.

The vertical air speed component w can be determined separately from the Doppler shift of the backscattered electro-magnetic clear-air signal when operating a Bragg-RASS or from the Doppler shift of the backscattered acoustic signal when operating a Doppler-RASS. Using the definition of the acoustic temperature the height profile of c_s can then be converted in a height profile of the acoustic temperature T_a. For many purposes this acoustic temperature is a sufficiently accurate approximation of the virtual air temperature. The maximum range of a sodar-RASS is usually less than thousand metres so that such an instrument covers the lower part of the boundary layer. Due to the high vertical resolution and the low minimum range of about 30 to 40 m, which is comparable to the abilities of a sodar, a sodar-RASS is well suited for the detection of shallow nocturnal boundary layers.

MLH detection algorithms MLH can be determined from the lowest height where the vertical profile of potential temperature increases with height indicating stable thermal stratification of the air. The great advantage of RASS measurements is that the magnitude of

stability (inversion strength) can be assessed quantitatively which is not possible from the acoustic and optical sounding devices described before. Fig. 72 displays a time-height cross-section of potential temperature over three days starting at midnight for a height range of 540 m. On the afternoons of the second and the third day well-mixed boundary layers formed, which can be deduced from the vertically constant potential temperature. New surface layers form on the evenings of all three days at about 1800 LST. The depth of these new surface layers increase during the night to about 200 to 300 m. Above these nocturnal surface layers low-level jets (see below) form, indirectly visible from the white areas indicating missing data in Fig. 72. Stronger winds like those in low-level jets blow the sound pulses from the RASS out of the focus of the electro-magnetic antenna and hence lead to a failure of the temperature detection.

Ideally, thermal stratification of air should be analyzed from the virtual potential temperature ($\Theta_v = \Theta(1 + 0.609q)$, where q is specific humidity) in order to include the effects of the vertical moisture distribution on the atmospheric stability. Unfortunately, no active remote sensing device for the determination of high-resolution moisture profiles is available. Therefore, the acoustic potential temperature ($\Theta_a = \Theta(1 + 0.513q)$), which actually is the temperature that is delivered by a RASS, is often used as a substitute. This is sufficient for cold and dry environments, but somewhat underestimates the virtual potential temperature in humid and warm environments. In case of larger vertical moisture gradients and small vertical temperature gradients this can lead to a switch in stability from stable to unstable or vice versa.

Engelbart and Bange (2002) have analyzed the possible advantages of the deployment of two RASS instruments, a sodar-RASS and a high-UHF windprofiler-RASS, to derive boundary-layer parameters. With these instruments, in principle, MLH can either be determined from the temperature profiles or from the electro-magnetic backscatter intensity. The latter depends on temperature and moisture fluctuations in the atmosphere. The derivation of MLH from the temperature profile requires a good vertical resolution of the profile which is mainly available only from the sodar-RASS. But even if the inversion layer at the top of the boundary layer is thick enough, due to the high attenuation of sound waves in the atmosphere, also the 1290 MHz-windprofiler-RASS used by Engelbart and Bange (2002) can measure the temperature profile only up to about 1 km. Therefore, in the case of a deeper CBL, MLH was determined from a secondary maximum of the electro-magnetic backscatter intensity which marks the occurrence of the entrainment zone at the CBL top. Thus, with this instrument combination the whole diurnal cycle of MHL is ideally monitored by interpreting the temperature profile from the sodar-RASS at night-time and by analyzing the electro-magnetic backscatter intensity profile from the windprofiler-RASS during daytime.

Hennemuth and Kirtzel (2008) have recently developed a method that uses data from a sodar-RASS and surface heat flux data. MLH is primarily detected from the acoustic backscatter intensity received by the sodar part of the sodar-RASS and verified from the temperature profile obtained from the RASS part of the instrument. Surface heat flux data and statistical evaluations complement this rather complicated scheme. The surface heat flux is used to identify situations with unstable stratification. In this respect this observable takes over an analogous role as the σ_w in the EARE algorithm (see above). The results have been tested against radiosonde soundings. The coincidence was good in most cases except for a very low MLH at or even below the first range gate of the sodar and the RASS.

6.2.4 Further techniques

Beyrich and Görsdorf (1995) have reported on the simultaneous usage of a sodar and a wind profiler for the determination of MLH. For the sodar data the ARE method was used. From the wind profiler data MLH was likewise determined from the height of the elevated signal intensity maximum (Angevine et al., 1994; Grimsdell and Angevine, 1998; White et al., 1999). Good agreement between both algorithms was found for evolving CBLs. The vertical ranges of the two instruments (50 to 800 m for the sodar and 200 to 3000 m for the wind profiler)

allowed following the complete diurnal cycle of MLH.

6.2.5 Comparison of acoustic and optical MLH detection algorithms

There is an interesting difference between the schemes for the determination of MLH from acoustic and optical backscatter intensities which should be noted carefully. While the acoustic backscatter intensity itself is taken for the detection of $H1$ and $H3$ (see Eqs. (139) and (141)) and the first derivative of this backscatter intensity for the determination of $H2$ (see Eq. (140)), the first and the second derivative of the optical backscatter intensity (but not the optical backscatter intensity itself) is used to determine $H4$ (see Eq. (143)). This discrepancy in the processing of the two backscatter intensities is due to the different scattering processes for acoustic and optical waves: Acoustic waves are scattered at atmospheric refractivity gradients and thus at temperature gradients (Neff and Coulter, 1986) while optical waves are scattered at small particles. Therefore the optical backscatter intensity is proportional to the aerosol concentration itself. The MLH on the other hand, which we desire to derive from these backscatter intensities, is in both cases found in heights where we have vertical gradients of the temperature and of the aerosol concentration. Therefore, in principle, the vertical distribution of the acoustic backscatter intensity should look very much alike the vertical distribution of the vertical gradient of the optical backscatter intensity.

Simultaneous measurements with different remote sensing devices have mainly been made in order to evaluate one remote sensing method against the other (Devara et al., 1995). But one could also think of combining the results two or more remote sensing devices for determining the structure of the ABL. The analysis of the sodar data and the ceilometer data can be combined to one single piece of MLH information by forming the minimum from Eqs. (142) and (149):

$$\mathrm{MLH} = \min\left(\mathrm{MLH}_{\mathrm{ac}}, \mathrm{MLH}_{\mathrm{op}}\right). \tag{154}$$

6.3 Boundary-layer height

Often, the boundary layer consists of more layers than just the mixing layer. For example, at night, a residual layer may persist over a newly formed near-surface stable surface layer. The deployment of sophisticated lidars (Bösenberg and Linné, 2002) may be a choice to detect such features as well as the combined deployment of a sodar and a ceilometer. Such a combination of parallel measurements of the vertical structure of the atmospheric boundary layer by a ceilometer and a sodar is described in Emeis and Schäfer (2006). Fig. 76, which is taken from this study, shows a daytime convective boundary layer, shallow nocturnal surface layers in the morning and the evening, and a residual layer above the nocturnal surface layers. The ceilometer detects the overall boundary layer height (blue triangles) whose height is partly modified by large-scale sinking motion in the anticyclone dominating the weather during the measurement period. Stable nocturnal surface layers with a depth of a few hundred metres can be detected underneath the black squares derived from the sodar soundings. The convective boundary layer during daytime fills the full depth of the boundary layer. This combination offers the same advantages as the combination of sodar and windprofiler presented in Beyrich and Görsdorf (1995). First results from a combined deployment of a RASS and a ceilometer are given in Emeis et al. (2009).

In such combined remote sensing measurements a sodar better detects the near-surface features such as nocturnal stable layers (a RASS instead of a sodar directly delivers the near-surface temperature profile) while the ceilometer is able to follow the diurnal variation of the daytime convective boundary layer and the top of the whole boundary layer. The residual layer then becomes visible as the layer between the new nocturnal surface layer below and the top of the boundary layer above.

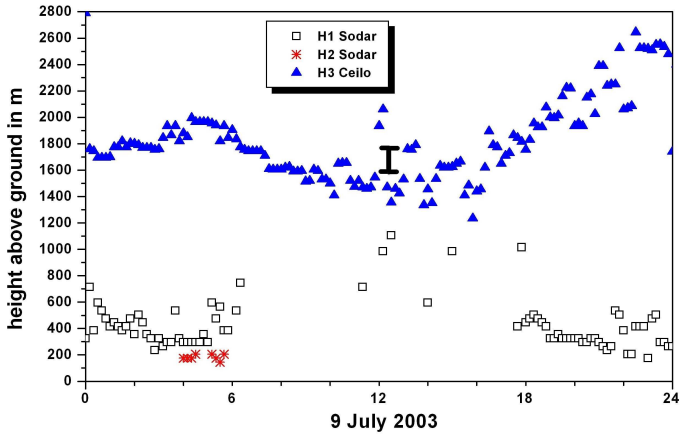

Figure 76: Combined sounding with a sodar (black squares and red asterisks) and a ceilometer (blue triangles) giving a complete view of the diurnal variation of the vertical structure of the ABL.

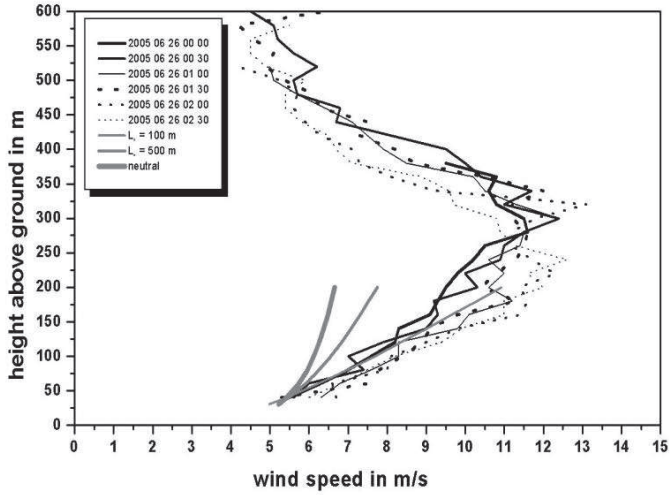

Figure 77: Example of a sodar observation of a nocturnal low-level jet.

6.4 Low-level jets

Sometimes vertical wind profiles exhibit secondary maxima in heights which are relevant for today's large wind energy converters, because the vertical wind shear underneath these maxima may be enhanced considerably. Figure 77 shows an example for a nocturnal low-level jet over land.

6.4.1 Formation

The formation of low-level jets requires a temporal or spatial change in the thermal stability of the atmospheric boundary layer which leads to a sudden change between two different equilibria of forces. The flow must transit from an unstable or neutral condition where friction, pressure-gradient and Coriolis forces balance each other to a stable condition where only pressure-gradient and Coriolis force balance each other (see Fig. 78). The sudden disappear-

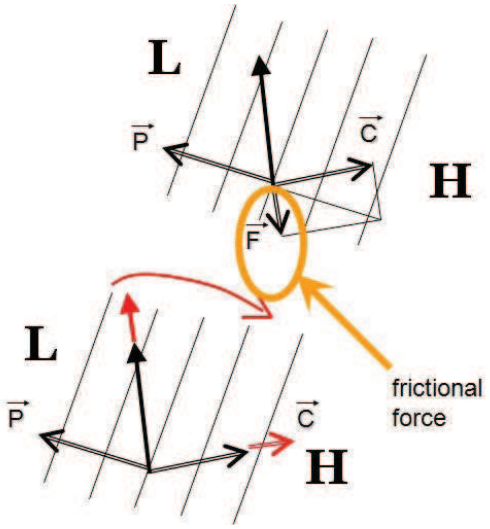

Figure 78: Balance of forces before (upper frame) and after (lower frame) the onset of a low-level jet. The red arrows indicate the changes leading to the low-level jet.

ance of the retarding friction in the equilibrium of forces leads to an inertial oscillation of the horizontal wind vector. Wind speed shoots to much higher values and the increased wind speed leads to a stronger Coriolis force which provokes a turning of the wind vector as well. The relevant equations for the wind components u and v at the moment of the disappearance of the frictional force read:

$$\frac{\partial u}{\partial t} = -f\,(v - v_g) \tag{155}$$

$$\frac{\partial v}{\partial t} = f\,(u - u_g) \tag{156}$$

where f is the Coriolis parameter and u_g and v_g are the components of the geostrophic wind. The terms on the left-hand side involve a dependence on time. Therefore, the analytical solution of Eqs. 155 and 156 describes an oscillation with time, t:

$$u - u_g = D_v \sin ft + D_u \cos ft \tag{157}$$

$$v - v_g = D_v \cos ft - D_u \sin ft \tag{158}$$

where D_u and D_v are the ageostrophic wind components at the beginning of the oscillation in the moment when the retarding frictional force vanishes.

In the temporal domain this corresponds to a sudden change from an unstable daytime convective boundary layer to a nocturnal stable boundary layer. This requires clear skies in order to have rapid changes in thermal stratification but still non-vanishing horizontal synoptic pressure gradients. Therefore, nocturnal low-level jets usually appear at the edges of high-pressure systems (see shaded area in Fig. 79).

In the spatial domain this corresponds to a sudden transition of the flow from a surface which is warmer than the air temperature to a smooth surface which is colder than the air temperature. This may happen when the flow crosses the coast line from warm land to a colder ocean surface or from bare land to snow or ice-covered surfaces.

6.4.2 Frequency and properties of low-level jets

It was mentioned in the preceding subchapter that the occurrence of nocturnal low-level jets depends on certain synoptic weather conditions. Therefore, it can be expected that the frequency of occurrence is linked to the appearance of certain weather or circulation types. For Central Europe the "Grosswetterlagen" (large-scale weather types) have proven to give a good classification of the weather situation (Gerstengarbe et al., 1999). Figure 80 shows

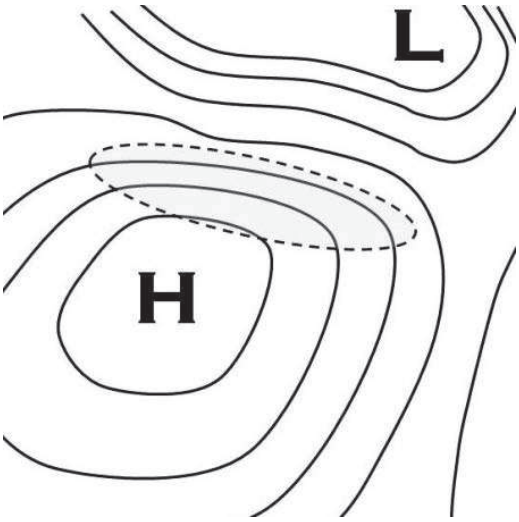

Figure 79: Favorite regions (shaded area) for the formation of nocturnal low-level jets.

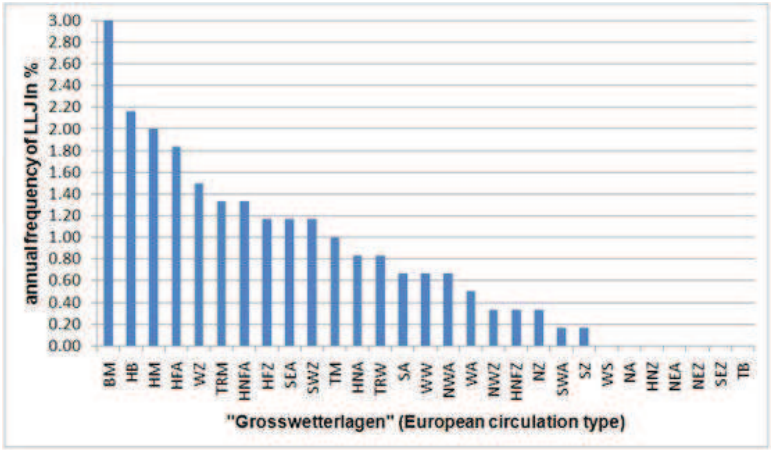

Figure 80: Annual frequency of low-level jet events ordered by large-scale synoptic weather patterns (Grosswetterlagen). From two years of sodar data for Hannover, Germany.

the frequency of occurrence of low-level jets over Northern Germany as function of these 29 large-scale weather types. The two most relevant types (the two left-most columns in Fig. 80) are a high-pressure bridge over Central Europe (type "BM") and a high-pressure area over the British Isles (type "HB"). All in all a low-level jet appeared in 23% of all nights

Figure 80 showed the frequency of occurrence of a low-level jet as function of the weather type. The relevance of a certain weather type for the formation of a low-level jet can be assessed when comparing the frequency of low-level jet occurrence with the overall frequency of occurrence of the respective weather type. Figure 81 has been produced by dividing the frequencies shown in Fig. 80 by the occurrence frequency of the respective weather types during the same observation period. There are two weather types where the occurrence frequency is identical to the occurrence frequency of the low-level jets during this weather type. This means that in every night when this weather type prevailed a low-level jet was observed. This is indicated by a low-level jet efficiency of 1.0 in Fig. 81. Small deviations from unity are due to the limited sample size evaluated for this purpose. These two weather types are "HNFA" and "HFZ" which are both related to high-pressure systems to the North of the investigation site

Such a high efficiency for forming a low-level jet allows for a quite certain forecast of the occurrence of a low-level jet. Once such weather types are forecasted a low-level jet will form with a very high probability. The values given in Fig. 81 can be used to give the low-level jet

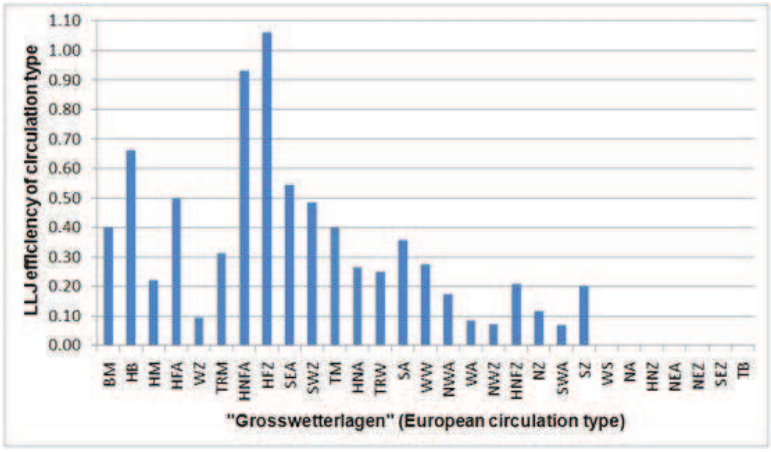

Figure 81: Efficiency of a large-scale synoptic weather pattern (Grosswetterlage) to form a low-level jet. From two years of sodar data for Hannover, Germany.

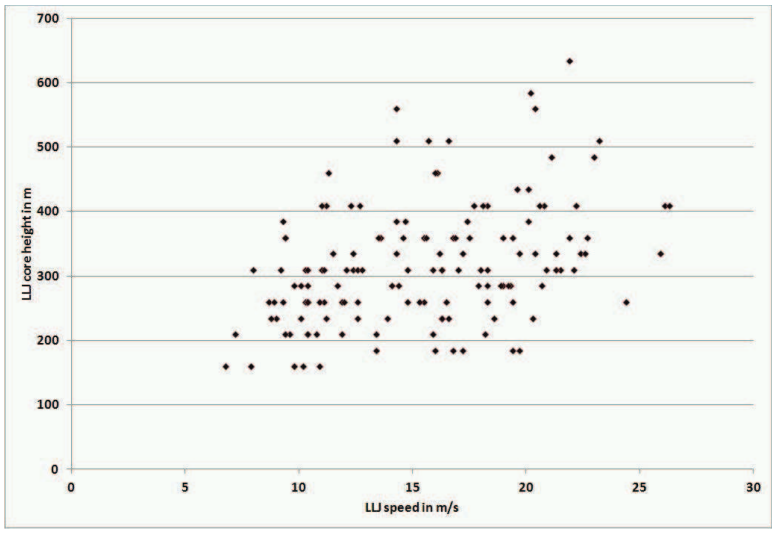

Figure 82: Correlation between the height of the core of a low-level jet and its maximum wind speed over Northern Germany (from two years of sodar measurements).

formation probability for Northern Germany for each of the weather types. For other areas the investigation has to be repeated with local low-level jet data.

The height of the core of a low-level jet and its maximum wind speed seems to be correlated. Figure 82 shows a correlation analysis from two years of sodar measurements in Northern Germany. Weaker jet cores may appear at heights between 150 m and 200 m above ground while stronger events (20 m s^{-1} core wind speed) usually appear at about 400 m with considerable scatter. Typical wind shear values for the layer between the surface and 160 m above ground vary between 0.04 and 0.10 s^{-1}. An analysis of daily wind speed amplitudes at 160 m above ground from these sodar data shows that amplitudes of up to 14 m s^{-1} are possible due to low-level jet events.

6.5 Summary

Wind resources depend on the large-scale weather conditions as well as on the local vertical structure of the atmospheric boundary layer. Ground-based remote sensing is now a viable technique to monitor the vertical structure of the atmospheric boundary layer. Three different techniques are presently available: acoustic sounding (sodars), optical sounding (wind lidars and ceilometers) and the combination of acoustic and electro-magnetic sounding (RASS).

Direct detection of MLH from acoustic backscatter intensities is limited to the order of about 1 km due to the rather high attenuation of sound waves in the atmosphere. In contrast, optical remote sensing offers much larger height ranges of at least several kilometres, because the attenuation of light waves in the atmosphere is small unless there is fog, clouds or heavy precipitation. This now offers the possibility to introduce information on boundary layer structure such as mixing-layer height and the frequency of occurrences of low-level jets into the monitoring and description of wind resources.

Notation

a	factor of proportionality
$A1$	$(B_M + B_U)/2$
$A2$	$(B_M - B_U)/2$
ABL	atmospheric boundary layer
ARE	acoustic received echo (method)
$B_{\min}$	threshold value for $B(z)$
B_M	mixing-layer mean of $B(z)$
B_U	value of $B(z)$ above the mixing layer
$B(z)$	optical backscatter intensity
$B_i(z)$	idealized optical backscatter intensity
$\partial B/\partial z_{\max}$	threshold value for the vertical derivate of $B(z)$
c	speed of light
c_a	RASS speed of sound ($= c_s + w$)
c_s	true speed of sound
CBL	convective boundary layer
D_u	initial ageostrophic wind component
D_v	initial ageostrophic wind component
DR_1	threshold value for the vertical gradient of $R(z)$
DR_2	threshold value for the vertical gradient of $R(z)$
EARE	enhanced acoustic received echo (method)
f	Coriolis parameter
f_a	acoustic frequency
f_e	electro-magnetic frequency
Hn	analysed height (n is a one-digit number)
$H4_{\mathrm{GM}}$	height of minimum of vertical gradient of $B(z)$
$H4_{\mathrm{IPM}}$	height of minimum of second vertical derivate of $B(z)$
$H4_{\mathrm{LGM}}$	height of minimum of logarithmic vertical gradient of $B(z)$
HWS	horizontal wind speed (method)
MLH	mixing-layer height
$\mathrm{MLH_{ac}}$	mixing-layer height from acoustic sounding
$\mathrm{MLH_{op}}$	mixing-layer height from optical sounding
q	specific humidity
R_c	threshold value for $R(z)$
$R(z)$	acoustic backscatter intensity
RASS	radio-acoustic sounding system
t	time
T_a	acoustic temperature
u	horizontal wind component (Eastwards)
u_g	horizontal component of geostrophic wind (Eastwards)
v	horizontal wind component (Northwards)
v_g	horizontal component of geostrophic wind (Northwards)
VWV	vertical wind variance (method)
w	vertical wind component
$W_B(z)$	scale averaged power spectrum profile
z	height above ground
z_i	boundary-layer height
Δf_e	Doppler shift of electro-magnetic frequency
Δh	height interval
Θ	potential temperature
Θ_a	acoustic potential temperature
Θ_v	virtual potential temperature
λ_a	wavelength of sound wave

$\lambda_{a,B}$ wavelength of sound wave fulfilling the Bragg condition
λ_e wavelength of electro-magnetic wave
σ_w standard deviation of the vertical wind component

References

Angevine W., White A. B., and Avery S. K. (1994) Boundary layer depth and entrainment zone characterization with a boundary layer profiler. *Bound.-Layer Meteorol.* **68**: 375–385

Asimakopoulos D. N., Helmis C. G., and Michopoulos J (2004) Evaluation of SODAR methods for the determination of the atmospheric boundary layer mixing height. *Meteorol. Atmos. Phys.* **85**: 85–92

Beyrich F. (1995) Mixing height estimation in the convective boundary layer using sodar data. *Bound.-Layer Meteorol.* **74**: 1–18

Beyrich F. (1997) Mixing height estimation from sodar data - a critical discussion. *Atmosph. Environ.* **31**: 3941–3954

Beyrich F. and Görsdorf U. (1995) Composing the diurnal cycle of mixing height from simultaneous SODAR and Wind profiler measurements. *Bound.-Layer Meteorol.* **76**: 387–394

Boers R., Spinhirne J. D., and Hart W. D. (1988) Lidar Observations of the Fine-Scale Variability of Marine Stratocumulus Clouds. *J. Appl. Meteorol.* **27**: 797–810

Bösenberg J. and Linné H. (2002) Laser remote sensing of the planetary boundary layer. *Meteorol. Z.* **11**: 233–240

Brooks I. M. (2003) Finding boundary layer top: application of a wavelet covariance transform to lidar backscatter profiles. *J. Atmos. Oceanic Technol.* **20**: 1092–1105

Cohn S. A. and Angevine W. M. (2000) Boundary Layer Height and Entrainment Zone Thickness Measured by Lidars and Wind-Profiling Radars. *J. Appl. Meteorol.* **39**: 1233–1247

Contini D., Cava D., Martano P., Donateo A., and Grasso F. M. (2009) Comparison of indirect methods for the estimation of Boundary Layer height over flat-terrain in a coastal site. *Meteorol. Z.* **18**: 309–320

Davis K. J., Gamage N., Hagelberg C. R., Kiemle C., Lenschow D. H., and Sullivan P. P. (2000) An objective method for deriving atmospheric structure from airborne lidar observations. *J. Atmos. Oceanic Technol.* **17**: 1455–1468

de Haij M., Wauben W., and Klein Baltink H. (2006) Determination of mixing layer height from ceilometer backscatter profiles. In: Slusser J. R., Schäfer K., Comerón A. (eds) Remote Sensing of Clouds and the Atmosphere XI. *Proc. SPIE* Vol 6362: paper 63620R.

Devara P. C. S., Ernest Ray P., Murthy B. S., Pandithurai G., Sharma S., and Vernekar K. G. (1995) Intercomparison of Nocturnal Lower-Atmospheric Structure Observed with LIDAR and SODAR Techniques at Pune, India. *J. Appl. Meteorol.* **34**: 1375–1383

Emeis S. (2010) Measurement methods in atmospheric sciences. In situ and remote. Vol. 1 of Quantifying the Environment. Borntraeger, Stuttgart, XIV+257 pp., 103 Figs, 28 Tab. ISBN 978-3-443-01066-9.

Emeis S. (2011) Surface-Based Remote Sensing of the Atmospheric Boundary Layer. Series: Atmospheric and Oceanographic Sciences Library, Vol. 40. Springer Heidelberg etc., X+174 pp. 114 illus., 57 in color., H/C. ISBN: 978-90-481-9339-4, e-ISBN 978-90-481-9340-0, ISSN 1383-8601, DOI: 10.1007/978-90-481-9340-0

Emeis S. (2012) Wind Energy Meteorology - Atmospheric Physics for Wind Power Generation. Springer Heidelberg etc., XIV-196 pp. ISBN 978-3-642-30522-1, e-book: ISBN 978-3-642-30523-8

Emeis S. and Schäfer K. (2006) Remote sensing methods to investigate boundary-layer structures relevant to air pollution in cities. *Bound.-Layer Meteorol.* **121**: 377–385

Emeis S. and Türk M. (2004) Frequency distributions of the mixing height over an urban area from SODAR data. *Meteorol. Z.* **13**: 361–367

Emeis S., Jahn C., Münkel C., Münsterer C., and Schäfer K (2007) Multiple atmospheric layering and mixing-layer height in the Inn valley observed by remote sensing. *Meteorol. Z.* **16**: 415–424

Emeis S., Schäfer K., and Münkel C (2008) Surface-based remote sensing of the mixing-layer height - a review. *Meteorol. Z.* **17**: 621–630

Emeis S., Schäfer K., and Münkel C (2009) Observation of the structure of the urban boundary layer with different ceilometers and validation by RASS data. *Meteorol. Z.* **18**: 149–154

Engelbart D. A. M. and Bange J. (2002) Determination of boundary-layer parameters using wind profiler/RASS and sodar/RASS in the frame of the LITFASS project. *Theor. Appl. Climatol.* **73**: 53–65

Eresmaa N., Karppinen A., Joffre S. M., Räsänen J., and Talvitie H. (2006) Mixing height determination by ceilometer. *Atmos. Chem. Phys.* **6**: 1485–1493

Flamant C., Pelon J., Flamant P. H., and Durand P. (1997) Lidar determination of the entrainement zone thickness at the top of the unstable marin atmospheric boundary-layer. *Bound.-Layer Meteorol.* **83**: 247–284

Gerstengarbe F.-W., Werner P. C., and Rüge U. (Eds.) (1999) Katalog der Großwetterlagen Europas (1881 - 1998). Nach Paul Hess und Helmuth Brezowsky. 5th edition. German Meteorological Service, Potsdam/Offenbach a. M. (available from: http://www.deutscher-wetterdienst.de/lexikon/download.php?file=Grosswetterlage.pdf or http://www.pik-potsdam.de/ uwerner/gwl/gwl.pdf)

Grimsdell A. W. and Angevine W. M. (1998) Convective Boundary Layer Height Measurement with Wind Profilers and Comparison to Cloud Base. *J. Atmos. Oceanic Technol.* **15**: 1331–1338

Gryning S.-E., Batchvarova E., Brümmer B., Jørgensen H., and Larsen S. (2007) On the extension of the wind profile over homogeneous terrain beyond the surface layer. *Bound.-Layer Meteorol.* **124**:251–268

Hayden K. L., Anlauf K. G., Hoff R. M., Strapp J. W., Bottenheim J. W., Wiebe H. A., Froude F. A., Martin J. B., Steyn D. G., and McKendry I. G. (1997) The Vertical Chemical and Meteorological Structure of the Boundary Layer in the Lower Fraser Valley during Pacific '93. *J. Atmos. Environ.* **31**: 2089–2105

Hennemuth B. and Kirtzel H.-J. (2008) Towards operational determination of boundary layer height using sodar/RASS soundings and surface heat flux data. *Meteorol. Z.* **17**: 283–296

Hooper W. P. and Eloranta E. (1986) Lidar measurements of wind in the planetary boundary layer: the method, accuracy and results from joint measurements with radiosonde and kytoon. *J. Clim. Appl. Meteorol.* **25**: 990–1001

Lammert A. and Bösenberg J. (2006) Determination of the Convective Boundary-Layer Height with Laser Remote Sensing. *Bound.-Layer Meteorol.* **119**: 159–170

Marshall J. M., Peterson A. M., and Barnes A. A. (1972) Combined radar-acoustic sounding system. *Appl. Opt.* **11**: 108–112

Martucci G., Srivastava M. K., Mitev V., Matthey R., Frioud M., and Richner H. (2004) Comparison of lidar methods to determine the Aerosol Mixed Layer top. In: Schäfer K., Comeron A., Carleer M., Picard R. H. (eds.): Remote Sensing of Clouds and the Atmosphere VIII. *Proc of SPIE* 5235: 447–456

Melfi S. H., Spinhirne J. D., Chou S. H., and Palm S. P. (1985) Lidar Observation of the Vertically Organized Convection in the Planetary Boundary Layer Over the Ocean. *J. Clim. Appl. Meteorol.* **24**: 806–821

Menut L., Flamant C., Pelon J., and Flamant P. H. (1999) Urban Boundary-Layer Height Determination from Lidar Measurements Over the Paris Area. *Appl. Opt.* **38**: 945–954

Münkel C. and Räsänen J. (2004) New optical concept for commercial lidar ceilometers scanning the boundary layer. *Proc. SPIE* Vol 5571: 364–374

Neff W. D. and Coulter R. L. (1986) Acoustic remote sensing. In: Lenschow D. H. (ed) Probing the Atmospheric Boundary Layer. Amer. Meteorol. Soc., Boston, MA, 201–239

Peña A., Gryning S.-E., and Hasager C. B. (2010) Comparing mixing-length models of the diabatic wind profile over homogeneous terrain. *Theor. Appl. Climatol.* **100**:325–335

Piironen A. K. and Eloranta E. W. (1995) Convective boundary layer depths and cloud geometrical properties obtained from volume imaging lidar data. *J. Geophys. Res.* **100**: 25569–25576

Schäfer K., Emeis S. M., Rauch A., Münkel C., and Vogt S. (2004) Determination of mixing-layer heights from ceilometer data. In: Schäfer K., Comeron A. T., Carleer M. R., Picard R. H., and Sifakis N. (eds.): Remote Sensing of Clouds and the Atmosphere IX. *Proc. SPIE* Vol 5571: 248–259

Schäfer K., Emeis S., Junkermann W., and Münkel C. (2005) Evaluation of mixing layer height monitoring by ceilometer with SODAR and microlight aircraft measurements. In: Schäfer K., Comeron A. T., Slusser J. R., Picard R. H., Carleer M. R., and Sifakis N. (eds) Remote Sensing of Clouds and the Atmosphere X. *Proc. SPIE* Vol 5979: 59791I-1–59791I-11

Seibert P., Beyrich F., Gryning S.-E., Joffre S., Rasmussen A., and Tercier P. (2000) Review and intercomparison of operational methods for the determination of the mixing height. *Atmosph. Environ.* **34**: 1001-1-027

Senff C., Bösenberg J., Peters G., and Schaberl T. (1996) Remote Sesing of Turbulent Ozone Fluxes and the Ozone Budget in the Convective Boundary Layer with DIAL and Radar-RASS: A Case Study. *Contrib. Atmos. Phys.* **69**: 161–176

Sicard M., Pérez C., Rocadenbosch F., Baldasano J. M., and García-Vizcaino D. (2006) Mixed-Layer Depth Determination in the Barcelona Coastal Area From Regular Lidar Measurements: Methods, Results and Limitations. *Bound.-Layer Meteorol.* **119**: 135–157

Steyn D. G., Baldi M., and Hoff R. M. (1999) The detection of mixed layer depth and entrainment zone thickness from lidar backscatter profiles. *J. Atmos. Ocean Technol.* **16**: 953–959

White A. B., Senff C. J., and Banta R. M. (1999) A Comparison of Mixing Depths Observed by Ground-Based Wind Profilers and an Airborne Lidar. *J. Atmos. Oceanic Technol.* **16**: 584–590

Wulfmeyer V. (1999) Investigation of turbulent processes in the lower troposphere with water-vapor DIAL and Radar-RASS. *J. Atmos. Sci.* **56**: 1055–1076

Wulfmeyer V. and Janjić T. (2005) 24-h observations of the marine boundary layer using ship-borne NOAA High-Resolution Doppler Lidar. *J. Appl. Meteorol.* **44**: 1723–1744

7 What can remote sensing contribute to power curve measurements?

Rozenn Wagner
DTU Wind Energy, Risø Campus, Roskilde, Denmark

7.1 Introduction

Power performance measurement is central to the wind industry since it forms the basis for the power production warranty of the wind turbine. The power curve measurement has to be realised according to the IEC 61400-12-1 standard. The power curve is obtained with 10-min mean power output from the turbine plotted against simultaneous 10-min average wind speeds. The standard requires the wind speed to be measured by a cup anemometer mounted on top of a mast having the same height as the turbine hub and located at a distance equivalent to 2.5 rotor diameters from the turbine.

Such a plot usually shows a significant spread of values and not a uniquely defined function. The origin of the scatter can mainly be grouped into three categories: the wind turbine components characteristics, sensor error and the wind characteristics. Within the last group, the current standard only requires the wind speed at hub height and the air density measurement. However, other wind characteristics can influence the power production like the variation of the wind speed with height (i.e. wind speed shear). The influence of wind speed shear on the power performance was shown in several studies: some based on aerodynamic simulations (Antoniou, 2009; Wagner et al., 2009) others based on measurements (Elliot and Cadogan, 1990; Sumner an Masson, 2006).

A major issue is to experimentally evaluate the wind speed shear. The wind speed profile is usually assumed to follow one of the standard models such as the logarithmic or power law profiles. However, these models are valid for some particular meteorological conditions, and therefore, cannot represent all the profiles experienced by a wind turbine. Measurements are then a better option but are also challenging. Indeed characterising the wind speed profile in front of the rotor of a multi-MW wind turbine requires measurements of wind speed at several heights, including some above hub height, i.e. typically above 100 m. Remote sensing instruments such as lidar or sodar then appear as a very attractive solution.

This chapter starts with a description of the influence of the wind speed shear on the power performance of a multi-MW turbine. The challenge of describing the wind speed profile is then discussed followed by a description of an experiment using a lidar for its characterisation. This is followed by the introduction of the definition of an equivalent wind speed taking the wind shear into account resulting in an improvement of the power performance measurement. Finally, some recommendations about remote sensing instruments are given to successfully apply this method.

7.2 Power performance and wind shear

7.2.1 Shear and aerodynamics

In order to see the effect of the wind speed shear on a wind turbine, aerodynamic simulations were carried out for two inflow cases:

1. constant wind speed profile (same wind speed everywhere) with 8 m s^{-1}
2. power law profile with 8 m s^{-1} at hub height and a shear exponent of 0.5

The power law profile is defined as:

$$u = u_{hub}\left(\frac{z}{z_{hub}}\right)^{\alpha}, \tag{159}$$

where u is the wind speed at height z, z_{hub} the hub height, u_{hub} the wind speed at that height and α the shear exponent. Both profiles are shown in Figure 83.

The model used was HAWC2Aero. The modeled turbine was a Siemens 3.6 MW with a rotor diameter of 107 m and a hub height of 80 m.The wind speed is assumed horizontally homogeneous (i.e. the wind speed is the same everywhere on each horizontal plane). In order to emphasize the effect of wind speed shear, the simulations were carried out with laminar inflow, the tower shadow was turned off and the tilt angle of the rotor was set to 0°.

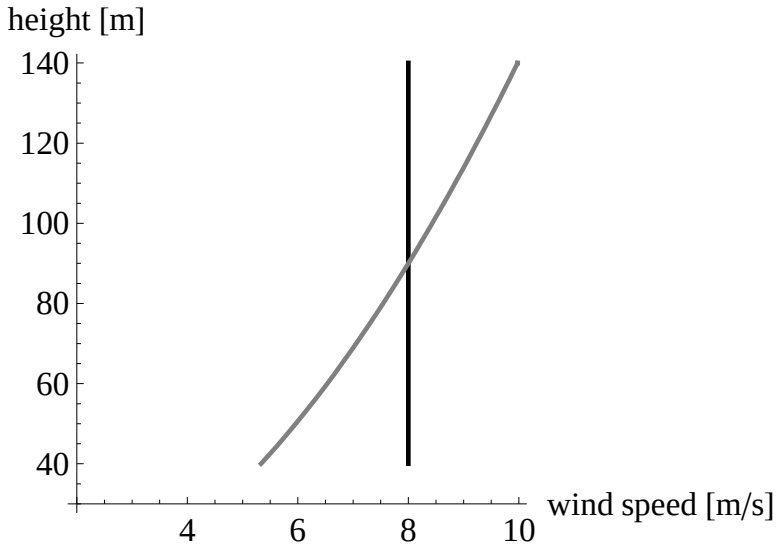

Figure 83: Wind profiles used as input for the wind speed shear aerodynamic investigation. Black curve: no shear; grey curve: power law profile with shear exponent of 0.5. Both profiles have the same wind speed at hub height

Figure 84 shows the free wind speed (i.e. the absolute wind speed in absence of a turbine) seen by a point at a radius of 30 m from the rotor centre, rotating at the same speed as the rotor as a function of time for the 2 inflow cases. Whereas in a uniform flow the blade is subjected to a constant wind speed, in a sheared flow, the point is exposed to large variations of wind speed even though the inflow is laminar. The variation of the wind speed seen by this rotating point in time is only due to the fact that it is rotating within a non uniform flow (wind speed varying with height).

Figure 85 shows the variations of the free wind speed seen by the same rotating point as function of the azimuth position ($0° = \mathrm{downwards}$). The point experiences the hub height wind speed (same as uniform inflow) when it is horizontal ($\pm 90°$), lower wind speed when it is downward ($0°$) and higher wind speed when it is upward ($180°$).

A rotating blade does not experience the free wind speed because of the induction from the drag of the rotor. In reality, a rotating blade is directly subjected to the relative wind speed w (i.e. the speed of the wind passing over the airfoil relative to the rotating blade) and the angle of attack ϕ (i.e. the angle between the blade chord line and the relative wind speed) with the effects of the induced speed included. The variations of these two parameters as function of θ are shown in Figure 86. As these two parameters directly depend on the free wind speed, they vary with the azimuth angle in a sheared inflow, whereas they remain constant in a uniform inflow.

The relative speed and the angle of attack are derived from the rotor speed and the induced velocity. Therefore, they depend on the way that the induction is modeled and it is difficult

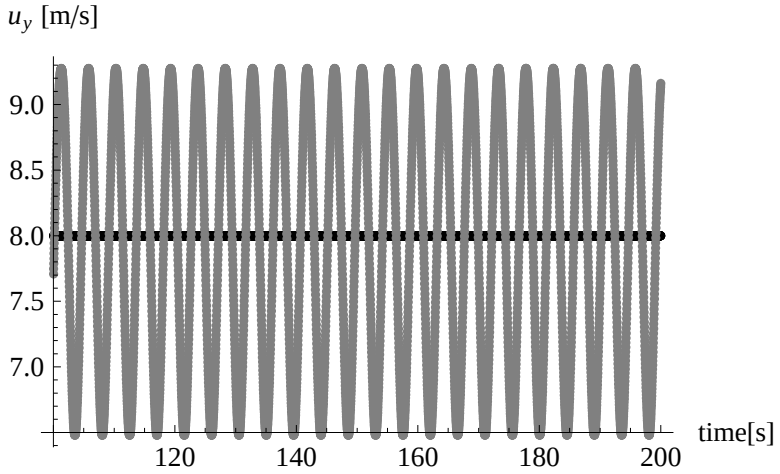

Figure 84: Time series of free wind speed seen from a rotating point, positioned at a radius of 30 m, rotating at rotor rotational speed (no induced velocity). Black curve: no shear; grey curve: power law profile with shear exponent of 0.5

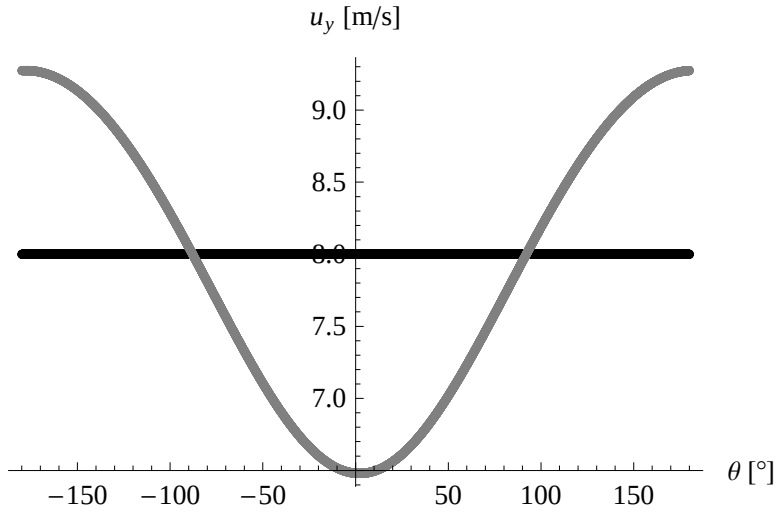

Figure 85: Free wind speed seen from a rotating point, positioned at a radius of 3 0m, rotating at rotor rotational speed, as function of the azimuth angle θ. Black curve: no shear; grey curve: power law profile with shear exponent of 0.5

to evaluate their variations due to a non uniform flow in a simple way. However, some basic considerations (ignoring the induction) can give a basic insight to the variation of the relative speed and the angle of attack as the blade rotates. In case of uniform inflow, the free wind speed is the same at any point of the swept rotor area. Therefore, the angle of attack and the relative speed are the same at any azimuthal position (see Figure 87).

In case of sheared inflow, the free wind speed depends on the position of the blade. When the blade is horizontal, the free wind speed is the speed at hub height and the speed triangle is the same as in Figure 87. Below hub height, the wind speed is lower than the hub height speed, see Figure 88 (left). Consequently w and ϕ are lower than those at hub height. Above hub height, the wind speed is higher than the hub height wind speed. Consequently w and ϕ are higher than those at hub height, see Figure 88 (right). The variations in ϕ and w cause a variation of the local lift and drag as the blade rotates, which finally results in the variation of the local tangential force contributing to the wind turbine power (see Figure 89). For a given ϕ, local lift dF_L and local drag dF_D, the local tangential force dF_T is given by (Manwell

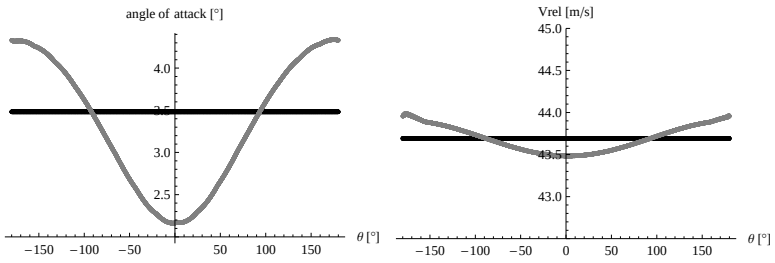

Figure 86: phi (left) and w (including induction) (right) as a function of θ, seen from a point at radius $r = 30$ m on a rotating blade. Black curve: no shear; grey curve: power law profile with shear exponent of 0.5

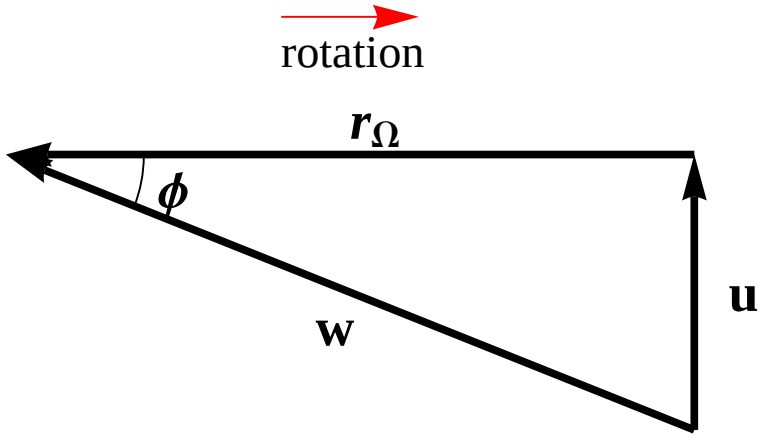

Figure 87: Speed triangle for a blade element at radius r. r_Ω is the blade speed and w corresponds to the sum of the pitch angle, the twist angle and ϕ. As the twist angle is constant for a given position on the blade and the pitch angle is 0° for wind speeds below rated speed, ϕ represents the variation of the angle of attack

et al., 2002):

$$dF_T = dF_L \sin\phi - dF_D \cos\phi. \tag{160}$$

As the wind speed increases with height (e.g. in the case of the power law profile), the amplitude of the variations of the free wind speed seen by a rotating point increases with the radius (not shown here). The local tangential force consequently varies with the radius too. As the torque results from the integral of the tangential force over the whole rotor, it thus depends on the wind speed profile.

7.2.2 Consequences on the power production

A series of cases were simulated with theoretical wind speed shear defined from the power law in Eq. (159), with $-0.1 < \alpha < 0.5$ and 5 m s^{-1} $< u_{hub} <$ 10 m s^{-1}. The relative variations in power (defined as the percentage difference between the power outputs obtained with a shear inflow and an uniform inflow) are shown in Figure 90. According to the simulations results, the power output obtained with shear inflow is generally smaller than the power output obtained with an uniform inflow. Moreover, it decreases as the shear exponent increases except at 5 m s^{-1} where the power output reaches a minimum for $\alpha = 0.2$ and increases for larger shear exponents, even exceeding the power output from uniform inflow with $\alpha = 0.5$.

The first difference between a sheared and an uniform inflow is the kinetic energy flux. In case of horizontally homogeneous inflow, the kinetic energy flux can be expressed by:

$$KE_{\text{profile}} = \int_{H-R}^{H+R} 0.5\rho u^3 c\,(z - (z_{hub} - R))\,dz, \tag{161}$$

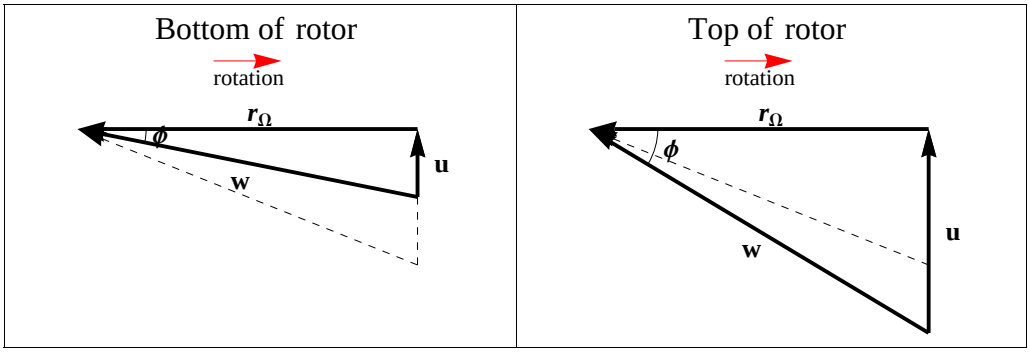

Figure 88: Speed triangles at the top and bottom of the rotor showing the effect of wind speed shear. The speed triangle at hub height is shown with dashed arrows

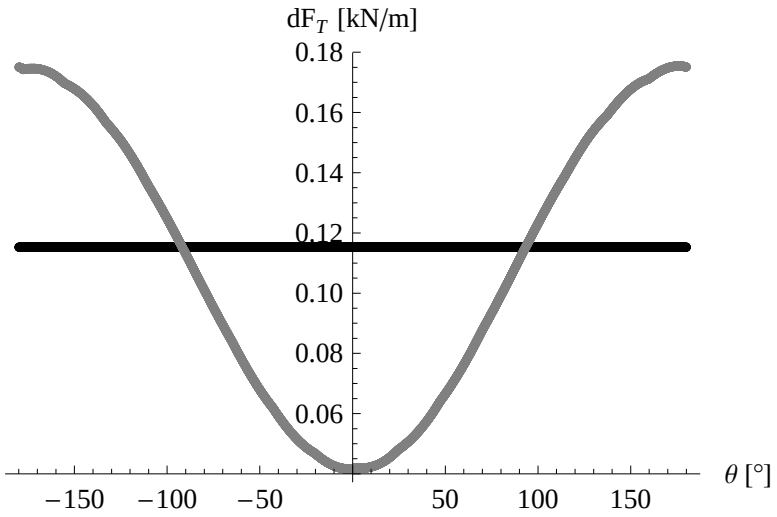

Figure 89: Local tangential force seen from a point $r = 30$ m on a rotating blade as function of θ. Black curve: no shear; Gray curve: power law profile with shear exponent of 0.5

where ρ is the air density, R the rotor radius and c is the chord (of the circle defined by the rotor swept area) as function of z which varies between the bottom and the top of the rotor:

$$c = 2\sqrt{2Rz - z^2}. \tag{162}$$

In order to compare to the power output variations, Figure 90 also shows the difference between the kinetic energy flux for a power law profile and a constant profile, normalised with the power obtained with a constant profile $KE_{\text{profile}} - KE_{\text{hub}}/KE_{\text{hub}}$ (see gray dashed line) [5]. Figure 90 shows two other interesting results:

1. The kinetic energy flux varies with shear exponent.
2. The power output of the turbine does not follow the same trend as the kinetic energy flux.

Despite the high uncertainty in the modeled power output for a sheared inflow, the results highlight that the influence of the shear on the power performance of a turbine can be seen as the combination of two effects:

- The variation in kinetic energy flux (power input).
- The ability of the turbine to extract the energy from the wind, which depends on the details of the design and the control strategy of the turbine.

[5] The kinetic energy flux is not an output of HAWC2Aero, it has been here estimated and for power law profiles, the normalized difference does not depend on the wind speed

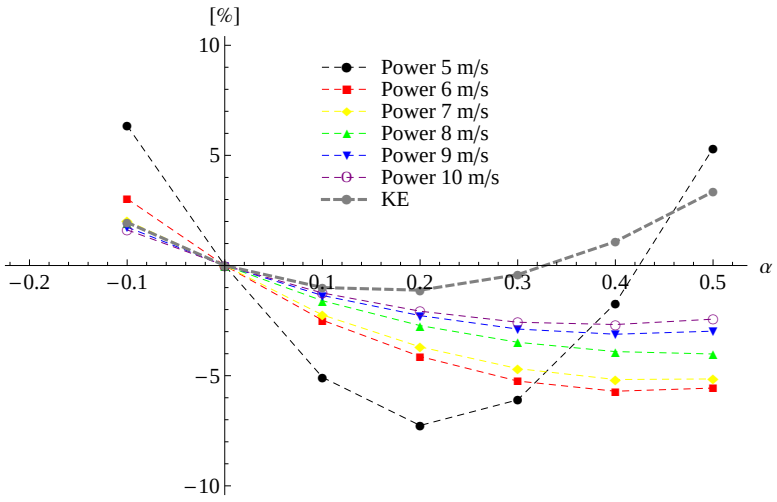

Figure 90: Normalised difference in power output and kinetic energy flux between shear and uniform case as function of the shear exponent, for various wind speed at hub height

These results clearly indicate that wind speed profiles encountered by the turbine during a power performance measurement should be known and taken into account.

7.3 Wind speed profiles

Within the power performance evaluation context, the wind speed shear is often described by α obtained from the assumption of a power law profile (Eq. (159)). This procedure was applied to profiles measured by a high meteorological mast located at the test site for large wind turbines, at Høvsøre, on the west coast of Denmark with $z_{hub} = 80$ m and $z = 40$ m to determine α. For some cases, this model fits the measured profile very well, but it cannot represent all kinds of profiles observed at Høvsøre. Figure 91 shows two examples of measured profiles and their corresponding modelled profiles.

The distribution of the error made by such an approximation is shown in Figure 92. We define the error as the difference between the wind speed at 116.5 m (top of the mast) estimated by the power law model and the speed measured by the cup anemometer. Over a year of measurements, for a large wind sector 60°–300° degrees (with predominant wind from west), 7% of the profiles show a wind speed error at 116.5 m larger than 10%. We should keep in mind that all the anemometers are mounted on a boom except the top anemometer, and this can induce an error in the profile extrapolation to the top (116.5 m).

As shown by the simulations presented in section 7.2, such an error in the wind speed profile can significantly affect the power curve. The shear exponent from wind speed measurements at two heights is not acceptable for this application. Therefore it is important to measure the wind speeds at several heights below and above hub height. For this purpose remote sensing instruments such as lidar and sodar are highly relevant since in many cases they can measure up to 200 m with the required degree of accuracy.

An experimental campaign using a lidar to measure the wind speed profile in front of a multi-MW turbine showed the importance of measuring the complete profile for power performance. In our experiment, the lidar measured the wind speed at 9 uniformly distributed heights covering 90% of the vertical rotor diameter. Each wind speed profile measured by the lidar was fitted to a power law profile in order to find the most representative shear exponent for this profile (α_{fit}). The fit is forced through the point of coordinate (u_{hub}, z_{hub}):

$$u_{fit}(z) = u_{hub}\left(\frac{z}{z_{hub}}\right)^{\alpha_{fit}}. \tag{163}$$

In order to separate the profiles for which the power law assumption was acceptable, we

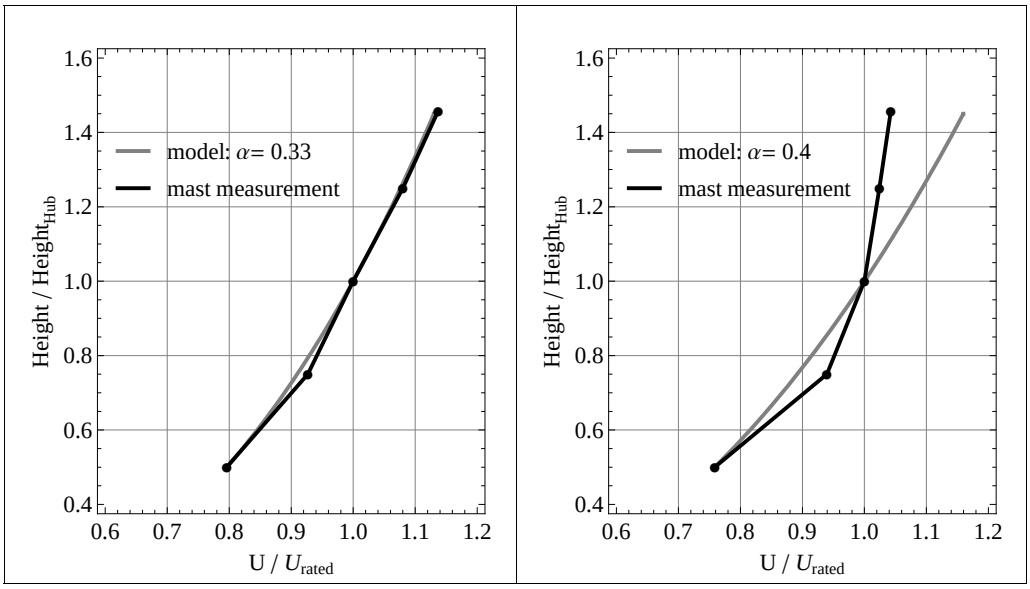

Figure 91: Two examples of profiles and their fit to the power law model (using the wind speed values at 40 and 80 m). The model fits very well the measured profile on the left, but it does not work for the profile on the right

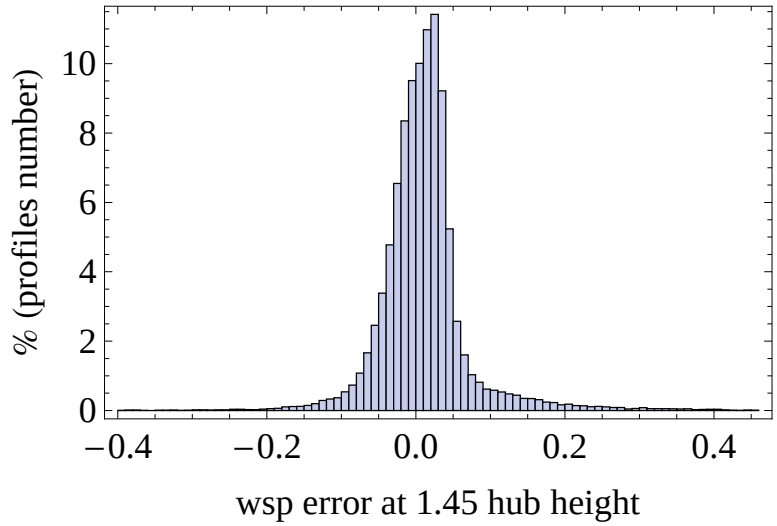

Figure 92: Distribution of the error made on the wind speed at 116.5 m height when assuming a power law profile with a shear exponent estimated with the wind speeds at 40 and 80 m

evaluated the goodness of fit with the residual sum of squares RSS, defined as:

$$\mathrm{RSS} = \sum_i \left(u_{fit}(z_i) - u_i\right)^2, \tag{164}$$

where u_{fit} is the fit function defined in Eq. (163) and u_i the wind speed measured by the lidar at height z_i ($i = 1$ to 9). Figure 93 shows two examples of measured profiles with their shear exponents and RSSs.

The profiles were then divided into two groups according to the RSS:

- Group 1: $\mathrm{RSS} \leq 0.1$ – the profiles from this group have a shape close to a power law profile and are referred to as the power law profiles.
- Group 2: $\mathrm{RSS} > 0.1$ – the profiles from this group have a shape that cannot be well represented by a power law profile and are referred to as the non power law profiles.

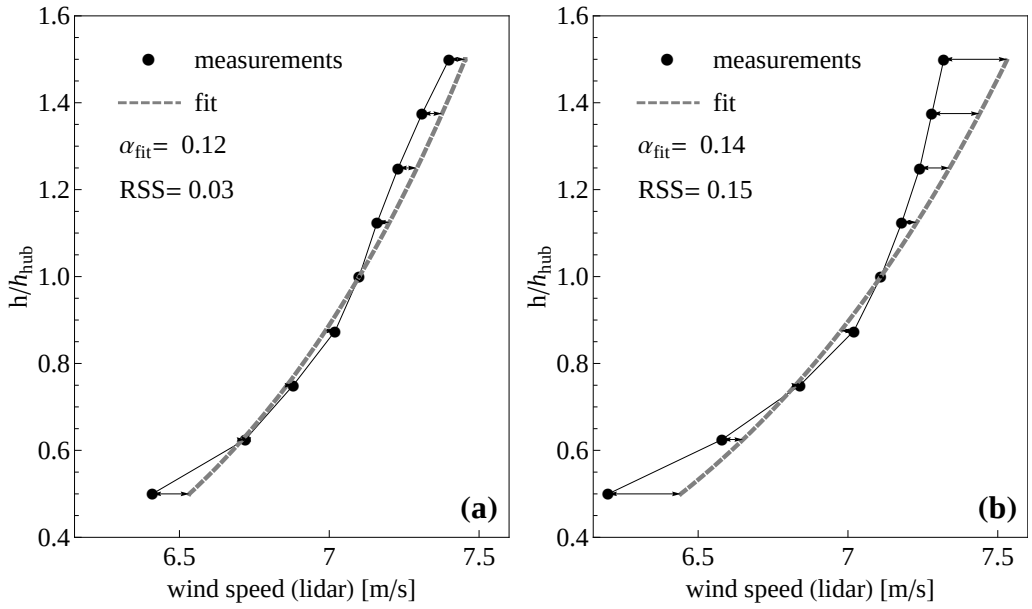

Figure 93: Example of measured wind profiles and their fit to a power law profile. (a) $\mathrm{RSS} \leq 0.1$, (b) $\mathrm{RSS} > 0.1$

According to this classification, profile (a) in Figure 93 would be in group 1 and profile (b) in group 2. The value of 0.1 was chosen here as threshold for the RSS, because it gave two groups of data showing two trends (shown below) while being statistically comparable (as they count similar numbers of data: 511 in group 1 and 396 in group 2). It is recognized that this threshold is somewhat arbitrary and should subsequently be "fine-tuned" using a large number of datasets.

7.4 Equivalent wind speed

7.4.1 Standard power curve for the two groups of wind profiles

Figure 94 shows the standard scatter plot of the power (a) and the C_p (b) as function of the wind speed at hub height. C_p is defined as in the current IEC standard 61400-12-1:

$$C_p = \frac{P}{0.5\rho u_{hub}^3 A}, \tag{165}$$

where P is the electrical power output of the turbine and A is the rotor swept area. The two colours represent the two groups of wind profiles: points obtained with the group 1 profiles ($\mathrm{RSS} \leq 0.1$) are displayed in black and those obtained with group 2 profiles ($\mathrm{RSS} > 0.1$) are displayed in red.

Figures 94(a) and (b) show two trends (one for each group) leading to two mean power curves and C_p curves (obtained after binning the data into 0.5 m s^{-1} wind speed bins and averaging as required by the IEC 614000-12-1 standard) (Figures 94(c) and (d)). The power output of the turbine for a given wind speed (at hub height) is smaller for data from group 2 (non power-law profiles) than for data from group 1 and the data from group 2 generally give a lower C_p.

What might appear here, for the non-power law profiles, as an underperformance of the wind turbine is an overestimation of the kinetic energy flux of the wind. Indeed, the C_p definition given by Eq. (165) implicitly assumes that the wind speed is constant over the entire rotor swept area:

$$u(z) = u_{hub} \qquad KE_{\text{hub}} = 0.5\rho u_{hub}^3 A, \tag{166}$$

or, in other words, the wind speed shear is ignored.

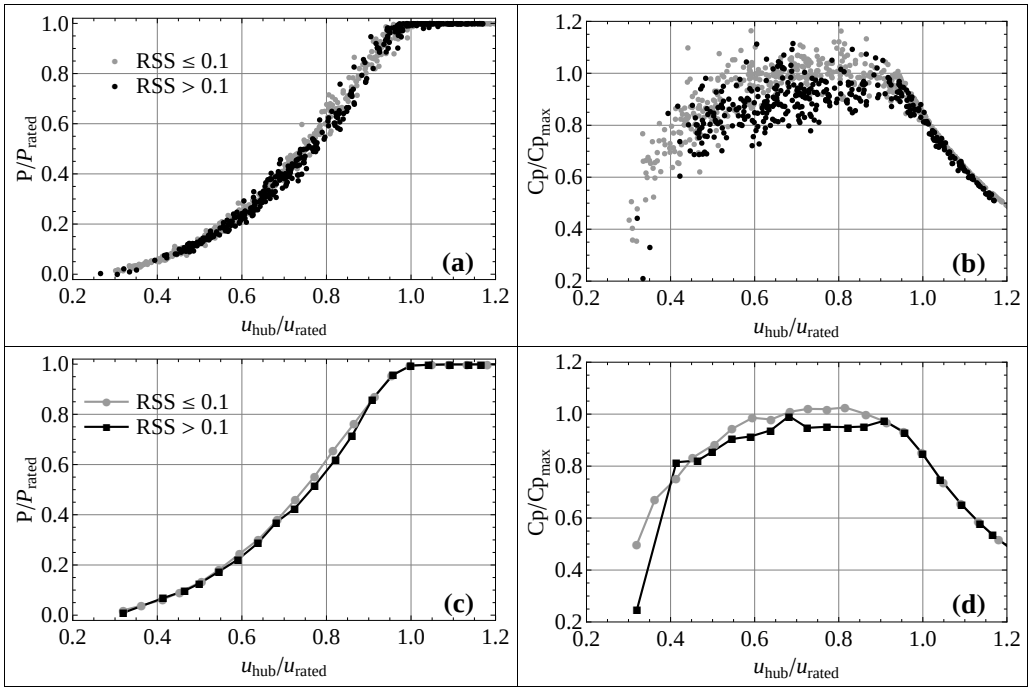

Figure 94: (a) Scatter plot of power curves, (b) Scatter plot of Cp curves, (c) Averaged power curves, (d) Averaged Cp curves. These plots are obtained by using the wind speed at hub height only and Cp calculated as in the IEC standards

7.4.2 A better approximation of the kinetic energy flux

However, as mentioned earlier, the real kinetic energy flux is obtained with Eq. (159). The kinetic energy flux for each profile measured by the lidar can be approximated by:

$$KE_{\text{profile}} = \sum_i 0.5\rho_i u_i^3 A_i, \tag{167}$$

where u_i is the wind speed measured at the ith height in the profile and corrected for the air density and A_i is the area of the corresponding segment of the rotor swept area (see Figure 95).

The ratio $KE_{\text{profile}}/KE_{\text{hub}}$ is displayed in Figure 89. The profiles from group 1 (black points) follow rather well the analytical results showing a moderate error due to the constant wind profile assumption.

The non power-law profiles (group 2), on the other hand, do not follow the analytical curve and show a much larger difference between the two ways of evaluating the kinetic energy flux. The approximation of a constant wind speed over the whole rotor swept area overestimates the kinetic energy flux for most of the data of group 2 and underestimates it for a few of them.

Two wind speed profiles can have the same wind speed at hub height but different kinetic energy. In a standard power curve, such profiles would have the same abscissa (hub height wind speed), whereas they would almost certainly result in different power outputs. This is partially why the two groups of wind profiles give two different power curves. The kinetic energy flux overestimation has even more impact on C_p, explaining the lower C_p for the group 2 wind profiles compared to that for group 1.

Another contribution to the differences between the power curves in figure 94 can be the influence of the wind speed shear on the power output. Indeed, two wind profiles resulting in the same kinetic energy may give different turbine power output, because for some wind speed shear conditions (e.g a power law profile with a large shear exponent), the turbine is not able to extract as much energy as in other shear conditions (e.g. a constant profile).

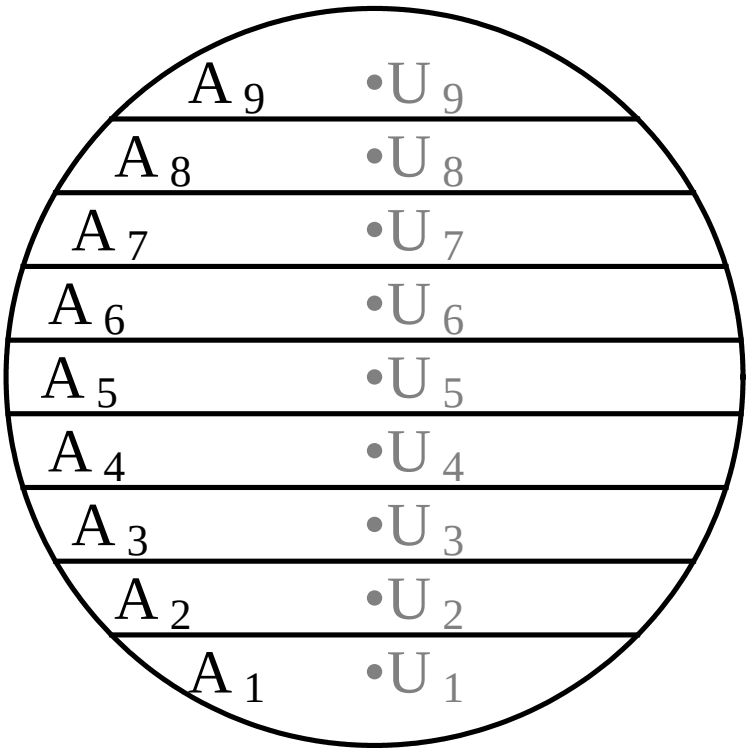

Figure 95: Rotor swept area divided into 9 segments corresponding to the 9 heights where lidar observations are performed. Each wind speed is assumed to be constant in each segment

7.4.3 Equivalent wind speed definition

Intuitively, the power output of the turbine should be more closely related to the kinetic energy flux derived from the whole profile than that derived from the wind speed at hub height. We should then consider the power output of the turbine as a function of the kinetic energy flux. In order to do so, an equivalent wind speed is suggested:

$$u_{eq} = \left(\sum_i u_i^3 \frac{A_i}{A} \right)^{1/3}. \tag{168}$$

Then C_p becomes:

$$\begin{aligned} C_p &= \frac{P}{0.5\rho_0 u_{eq}^3 A} = \frac{P}{0.5\rho_0 \left(\sum_i \left(\left[\frac{\rho_i}{\rho_0} \right]^{1/3} u_i \right)^3 \frac{A_i}{A} \right) A} \\ &= \frac{P}{\sum_i 0.5\rho_i u_i^3 A_i} = \frac{P}{KE_{\text{profile}}}. \end{aligned} \tag{169}$$

Figure 97 shows plots comparable to the plots in Figure 94: in Figure 97, the power and C_p are plotted as a function of the equivalent wind speed defined in Eq. (168) (instead of the wind speed at hub height in Figure 87) and C_p is calculated according to Eq. (169) (instead of Eq. (165) in Figure 94). In Figure 97, profiles from both groups follow the same trend. The mean power and C_p curves obtained with each group of points overlap each other. This shows that the difference in power curves between the two groups shown in Figure 97 was mainly due to the error in kinetic energy flux.

7.4.4 Choice of instrument

The question now is: can any remote sensing instrument be used to measure a power curve and reduce the scatter with the equivalent wind speed method? Figures 98(a) and (b) show

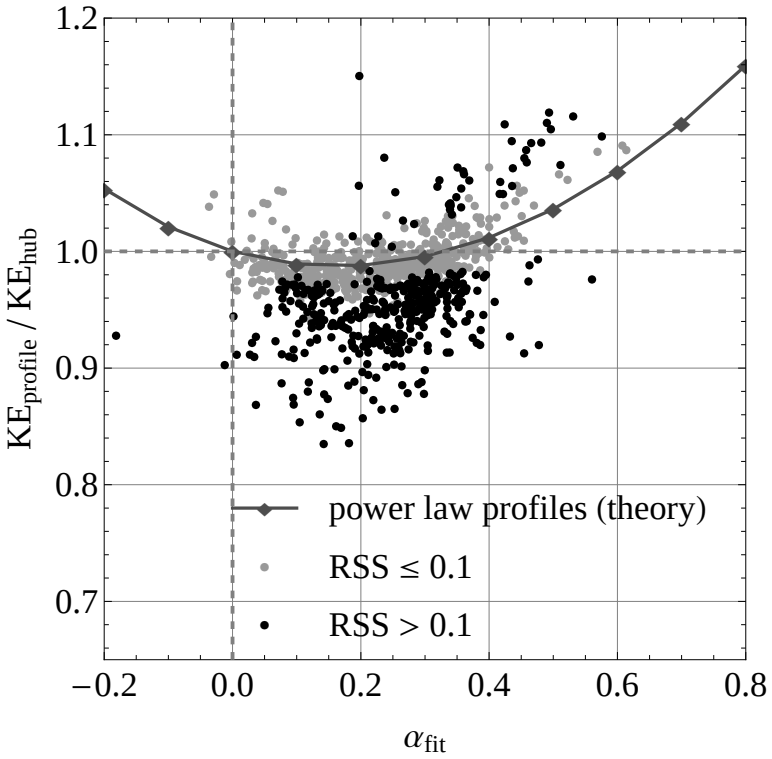

Figure 96: Ratio between the kinetic energy flux obtained with the wind speed profiles (KE_{profile} for the theoretical and measured profiles) and the kinetic energy assuming a constant wind speed with height equal to the hub height wind speed (KE_{hub})

the comparison of the simultaneous 10-min mean wind speed measured by a remote sensing instrument (sodar and lidar respectively), and a cup anemometer at the same height. The lidar and the sodar were placed next to each other but with a lateral distance of 100 m from a mast equipped with a top-mounted cup anemometer used for the comparisons. Both datasets include the same 10-min periods. It can be clearly seen that the sodar data are noisier than the lidar data. There was no indication of any major problem with the sodar during this experiment. The difference in measurements from the two instruments can be explained by the difference in the way they operate. Because sodar measurements are based on sound properties, they are sensitive to noise from the surroundings and obstacles (which is not the case for light beams). Moreover, the sampling frequency of a sodar is much smaller than that of a lidar. A sodar measures one wind speed every 10 min, whereas a lidar can measure the wind speed 30 to 100 times during that time.

The power curve obtained with such noisy measurements (at hub height) presents a much larger scatter than the power curve obtained with the cup anemometer (Figure 98(c)), whereas the scatter in power curve obtained with better remote sensing measurements is similar to that obtained with the cup anemometer (Figure 98(d)). If the remote sensing instrument increases the scatter in power curve compared to a cup anemometer, it is very unlikely that the observation of wind speed profiles from that same instrument can help to reduce the scatter. Thus, an instrument presenting noisy measurements is not suitable for power curve measurement and cannot be used to calculate an equivalent wind speed in order to reduce the scatter. This restricts very much the possibility of using sodar because of the inherent noise in the measurements. However, the point here is not to disqualify sodars, but to make the difference between an instrument which is suitable and one which is not suitable for the application of the equivalent wind speed method.

Figure 99 shows a lidar cup comparison for two lidar systems (same brand, same test location). Even though the gain factor and the coefficient of determination (R^2) is good for both instruments, a clear difference appears when we look at the lidar error (i.e. difference

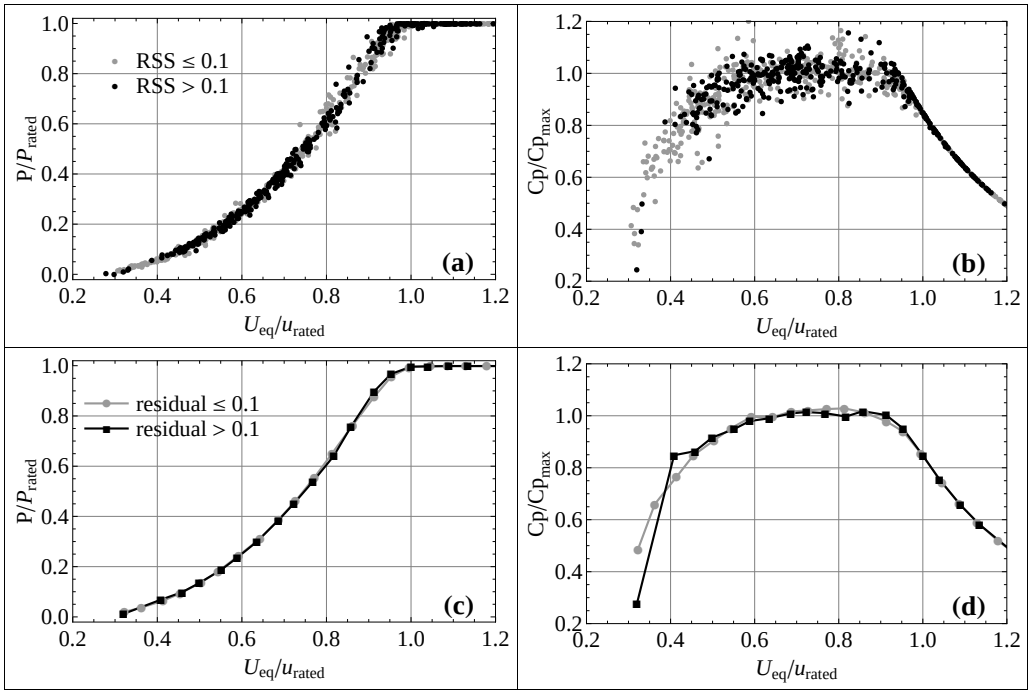

Figure 97: (a) Scatter plot of power curves, (b) Scatter plot of $C : p$ curves, (c) Averaged power curves, (d) Averaged C_p curves. These plots are obtained using the equivalent wind speed Eq. (168) and a C_p definition taking the wind shear into account

between wind speed measured by the lidar and the cup). Lidars are very attractive because of their capacity to measure wind speed and direction profiles with the convenience of a ground based measurement device. However, this is still a new and rather immature technology and it is strongly recommended to verify each instrument against a tall mast (equipped with good wind speed sensors at several heights) in flat terrain. A remote sensing classification and a verification procedure are currently being defined within the standard committee.

7.5 Summary

As wind speed shear influences the power performance of multi-MW turbines, it is necessary to characterize the wind speed profile in front of the turbine rotor. Remote sensing instruments are of great interest, since they can measure the wind speed profile over the whole rotor range. Such measurements avoid the use of assumptions about the shape of the wind speed profile. A more accurate kinetic energy flux can then be calculated resulting in a better evaluation of the power performance of the turbine. The use of an equivalent wind speed taking the wind speed shear into account reduces the scatter in the power curve and the uncertainty in power performance measurement. In that sense, the use of remote sensing measurements can improve the power performance measurements. However, this can only be achieved with a good instrument. Finally, the remote sensing instrument should not show more scatter in the power curve than that of a cup at a given height. This requires a verification of the instrument prior to the power performance measurement.

Notation

A	rotor swept area
A_i	area of the ith element
c	chord defined by the rotor swept area
C_p	power coefficient
dF_D	local drag force
dF_L	local lift force

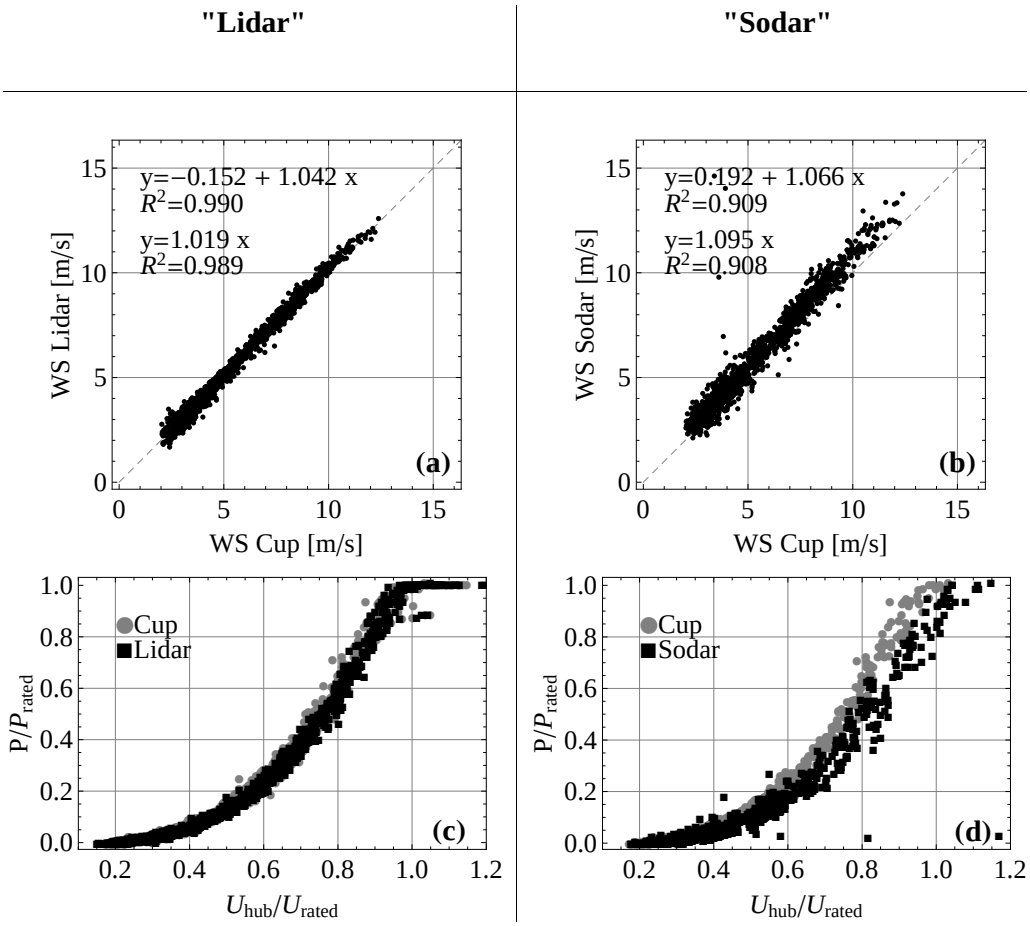

Figure 98: (a) Linear regression of 10-min mean wind speed measured by a lidar and a cup anemometer; (b) Linear regression of 10-min mean wind speed measured by a sodar and the same cup anemometer as in (a) for the same 10-min periods; (c) power curve obtained with wind speed measurement at hub height with a cup and a lidar; (d) power curve obtained with wind speed measurement at hub height with a sodar and the same cup anemometer as in (c) for the same 10-min periods

dF_T	local tangential force
KE_{hub}	kinetic energy flux of a constant wind profile
KE_{profile}	kinetic energy flux of the wind profile
P	electrical power output of the turbine
r	radial position
r_Ω	blade speed
R	coefficient of determination
R	rotor radius
RSS	residual sum of squares
u	wind speed
u_{eq}	equivalent wind speed
u_{fit}	fit wind speed function to the power profile
u_{hub}	hub height wind speed
u_i	wind speed at height z_i
w	relative wind speed
z	height above the ground
z_{hub}	hub height
z_i	lidar height
α	shear exponent of the power law
α_{fit}	shear exponent fit
θ	azimuth angle
ρ	air density
ϕ	angle of attack

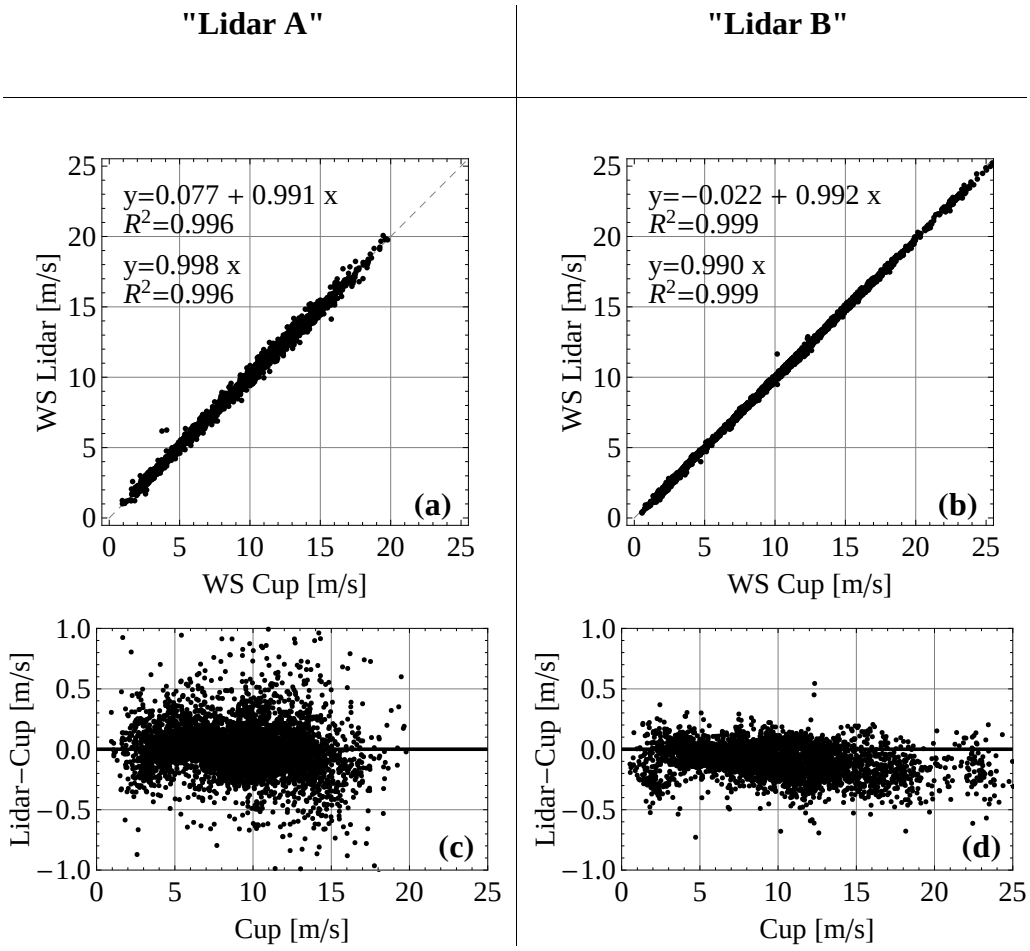

Figure 99: (a and b) Linear regression of 10-min mean wind speeds measured by a lidar and a cup anemometer from two lidar systems; (c and d) lidar error for each system

References

Antoniou I. (2009) Wind shear and uncertainties in power curve measurement and wind resources. *WindPower*

Elliot D. L. and Cadogan J. B. (1990) Effects of wind shear and turbulence on wind turbine power curve. *Proc. of the European Community Wind Energy Conf.*, Madrid

IEC (2005) IEC 61400-12-1 Wind turbines - Power performance measurements of electricity producing wind turbines. Int. Electrotechnical Commission

Manwell J. F., McGowan J. G., and Rogers A. L. (2002) Wind energy explained: Theory, design and application, John Wiley & Sons Ltd, 577 pp

Sumner J. and Masson C. (2006) Influence of atmospheric stability on wind turbine power performace curves. *J. Solar Energy Eng.* **128**:531–538

Wagner R., Antoniou I., Pedersen S. M., Courtney M., and Jørgensen H. E. (2009) The influence of the wind speed profile on wind turbine performance measurements. *Wind Energy* **12**:348–362

8 Nacelle-based lidar systems

**Andreas Rettenmeier, Jan Anger, Oliver Bischoff,
Martin Hofsäss, David Schlipf and Ines Würth**
*Stuttgart Chair of Wind Energy, Institute of Aircraft Design,
Universität Stuttgart, Stuttgart, Germany*

8.1 Summary

The use of a nacelle-based lidar system allows measuring turbine inflow and wake in a very high spatial and temporal resolution. The new measurement techniques to be developed have direct applications on- and offshore for the verification of wake models, predictive control strategies and new methods for power curve determination and load estimation.

An adaptive scanning device was developed for the standard pulsed lidar system Windcube. This additional system has been conceived with a certain flexibility to allow different trajectories and to scan horizontally the flow field in front and behind of turbines covering the whole rotor disc. The design and construction of the device was supported by a software tool for wind turbine lidar simulation. Based on the results of the simulation of different trajectories, requirements to the hardware and software adaptation could be defined.

8.2 Introduction

Installation of the lidar system on the nacelle of a turbine is advantageous because in this way the lidar yaws with the turbine and the laser beam is always orientated along the up- or downwind wind direction, depending on the application.

If the lidar system "is looking" upwind one can measure the incoming wind for e.g. predictive turbine control, load estimation or power curve determination. If the lidar is looking downwind it is possible to measure the turbine's wake wind and thus making the validation of wake models possible. The wind speed component of the line-of-sight vector is much higher when operating horizontally from a nacelle than from the ground.

The development of different nacelle-based lidar systems are on the one hand commercial products (e.g. Blue Scout, Avent) with two/three beam directions which mainly focus to support the yaw control of the turbine. On the other hands different research lidar were developed for nacelle applications. For this reason one of the first CW-lidars from QinetiQ was used for the first investigations regarding turbine control (Harris et al., 2006) and wake (Trujillo et al., 2008). Another CW-lidar was mounted in the rotating spinner of a wind turbine (Mikkelsen et al., 2010). The lidar system presented here is based on the pulsed lidar device "Windcube" of Leosphere (Rettenmeier et al., 2010).

8.3 The units of the lidar scanner

The SWE lidar system consists of two components. The first component is the commercial "Windcube WLS-7" from Leosphere. The second part of the used system is a scanner specifically created for nacelle-based lidar measurements.

8.3.1 Windcube

The "Windcube WLS 7" was developed to measure wind speed and wind direction from the ground in order to replace the conventional met masts for wind potential analyses in some areas and to support the certification process regarding power curve and load measurements

in the future. The working principle of the pulsed lidar system is described by Cariou and Boquet (2010).

In order to use the standard Windcube for a nacelle-based measurement campaign several adaptations had to be made. The internal deflection mirror with 45° was removed and the optical axis from the Windcube to the scanner had to be ensured. The software had to be adapted insubstantially:

- The Windcube has to be synchronized with the controller unit of the scanner so that the movement of the mirror and the measuring of the laser is synchronized.
- The ten arbitrary heights from the ground-based system have been reduced to five arbitrary focus distances in front of the lidar system for the nacelle-based version. With a fixed focus length the scanning figure is described on a cubic surface (Figure 100(left)). It is possible to vary the focus length at each measurement point so that the focus plane is vertical which means a "slicing" of the wind field (Figure 100(right)).
- The maximum number of measurement points of a scanning pattern is limited to 49.
- The scanning modes are either "Start-Stop" or "Bang-Bang". At the Start-Stop mode the mirror stops at the measurement point, the measurements involve shooting and averaging the spectra to the line-of-sight wind speed. Afterwards the mirror moves to the next measurement point. The employment of this mode allows to average a higher number of shots which are taken into account to calculate the line-of-sight velocity. The result is a good carrier to noise ratio (CNR) and a higher maximum measurement range. In the "Bang-Bang" mode the mirror always moves, but decelerates shortly before reaching the measurement point and accelerates after passing the measurement point. In this mode the number of shots to be averaged has to be lowered. This means that the carrier to noise ration (CNR) is worse compared to the "Start-Stop" mode, but the movement is much faster and therefore the temporal resolution is better.

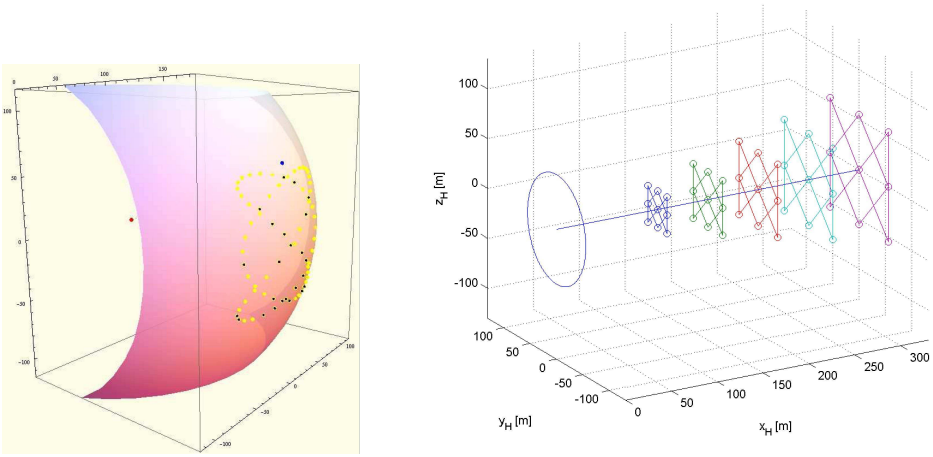

Figure 100: Measuring on a cubic shape with a fixed focus length (left) and using variable focus length to "cut" the wind field vertically (right).

8.3.2 Scanner

A scanner device with two degrees of freedom has been developed for the nacelle measurement campaigns in order to be able to position the laser beam of a standard Windcube lidar system in any direction. The requirements for the development of the scanner system were:

- Angle of projection: 53.2°. In a distance of 1D the measurement area should cover the whole swept rotor disc.

- Flexible trajectories. Depending on the different applications, various scan patterns should be possible.
- High speed and acceleration. To get a good temporal and spatial resolution, it is necessary that the measurements are fast and have a high repeatable accuracy.

The scanner system developed is based on a single mirror which is moved by a mechanical system with two independent rotation stages (Figure 101(left)). The mirror has a mechanical angle range of $\pm 15^{\circ}$ in the pan and tilt direction (horizontal and vertical). The motors are controlled by an external unit which is synchronized with the Windcube. The two mentioned rotation stages and the supporting structure with the transmission rods form the scanning system which was mounted in a modular way in order to simplify attachment to the standard Windcube (Figure 101(right)). The scanner was integrated in a second housing so that an adaptation to the original Windcube was easy and water tightness as well as structural stability could be assured. Thus, the orientation of the laser beam and the alignment of the optical axis could be guaranteed.

The mirror which deflects the beam in the original Windcube system is removed so that the laser beam goes through both casings and is deviated by the 2-DOF mirror (Figure 102(left)).

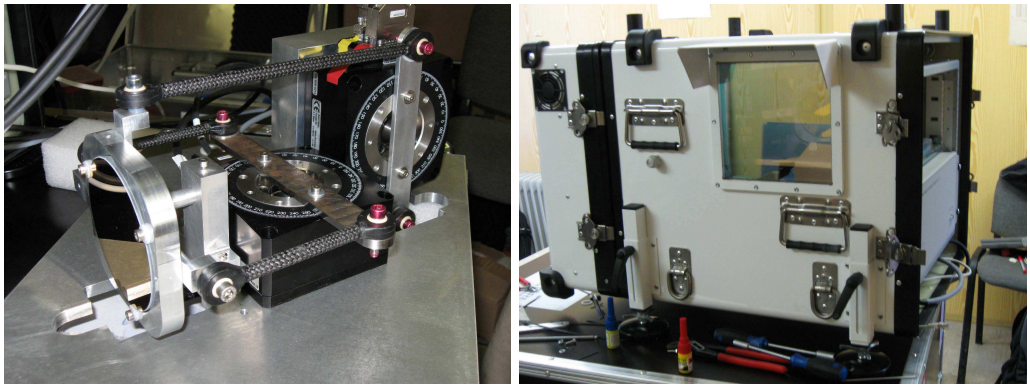

Figure 101: Scanner assembly (left) and integration to a second housing (right).

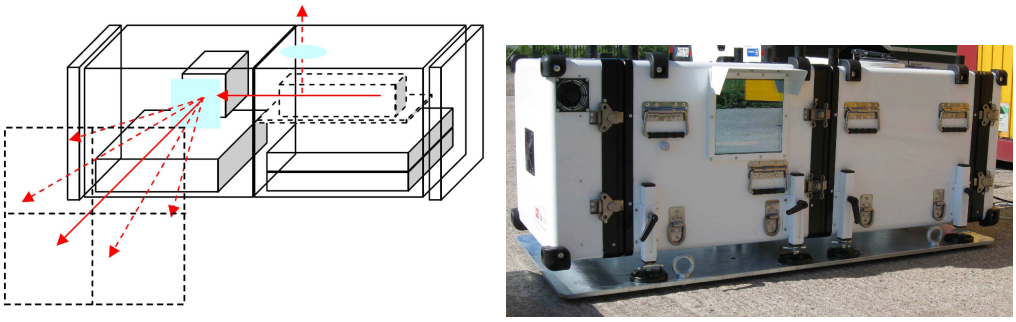

Figure 102: Way of the laser beam and the optical axis (left) and the assembled system modules (right).

8.4 Scan pattern

Measuring the wind field from the nacelle of a turbine makes it possible to gather wind field information (wind speed, wind direction, shear) in a high temporal and spatial resolution. To scan a wind field in any vertical and horizontal direction, the laser beam runs along a predetermined path and executes the measurement at predefined points. For designing a scan pattern the wind turbine simulator WiTLiS was developed (Schlipf et al., 2009). This software supports the development of trajectories considering the motor speed and acceleration.

WiTLiS scans a synthetic wind field generated with Vindsim and interpolates the measurements to a defined grid. Then the calculated wind field is compared with the synthetic one. Some investigations were carried out in accordance with the planned application of inflow and wake measurements taking into account the maximum measurement points per focus plane. The software WiTLiS is also used to post-process the measured data.

As a result of the consideration to scan as many points as possible in the shortest possible time inside a square, the trajectories based on Lissajous-figures show the best ratio of temporal and spatial resolution. A Lissajous figure can be created by superposing two harmonious waves that can be driven from the two independent rotation stages used. In mathematics, a Lissajous curve (Lissajous figure or Bowditch curve) is the graph of a system of parametric equations which describe complex harmonic motion. (Eqs. (170) and (171)):

$$x = A\sin(at + \delta), \tag{170}$$

$$x = B\sin(bt + \delta). \tag{171}$$

This family of curves was investigated by Nathaniel Bowditch in 1815, and later in more detail by Jules Antoine Lissajous in 1857. The appearance of the figure is highly sensitive to the ratio a/b. For a ratio of 1, the figure is an ellipse, with special cases including circles ($A = B$, $\delta = \pi/2$ radians) and lines ($\delta = 0$). Another simple Lissajous figure is the parabola ($a/b = 2$, $\delta = \pi/2$). Other ratios produce more complicated curves, which are closed only if a/b is rational. The visual form of these curves is often suggestive of a three-dimensional knot, and indeed many kinds of knots, including those known as Lissajous knots, project to the plane as Lissajous figures. [http://en.wikipedia.org/wiki/Lissajous_curve]

One of the basic trajectories used in different measurement campaigns was a Lissajous figure with a ratio of 3:4. If a lidar scans the figure in such a way, it becomes more difficult to evaluate and recalculate a wind field from the measured points. Therefore, specific measurement points have to be defined, and the figure was adapted to 7×7 measurement grid points. The time needed to scan the 49 measurement points was 5.5 s. which led to a good temporal and spatial resolution. Based on the pulsed lidar technology, each trajectory point is measured at 5 focus planes simultaneously which even allows an interpolation between the different focus planes.

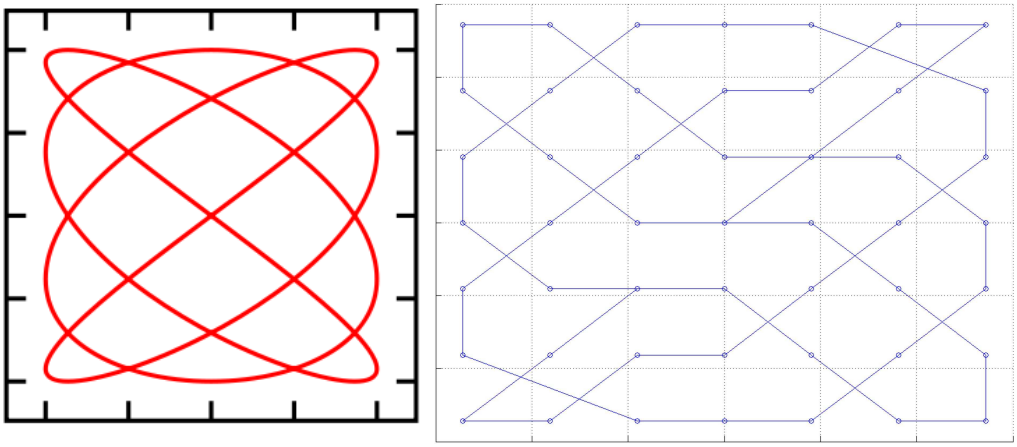

Figure 103: Lissajous figure with a frequency ratio of 3:4 (left) and adapted to 7×7 measurement grid (right).

To ensure that the scan pattern works with a high accuracy a visible red laser was used and the scan pattern was photographed with a long exposure time (Figure 105(left)). As a second step, the use of an infrared camera and an IR-sensitive card makes even the real eye-safe beam visible.

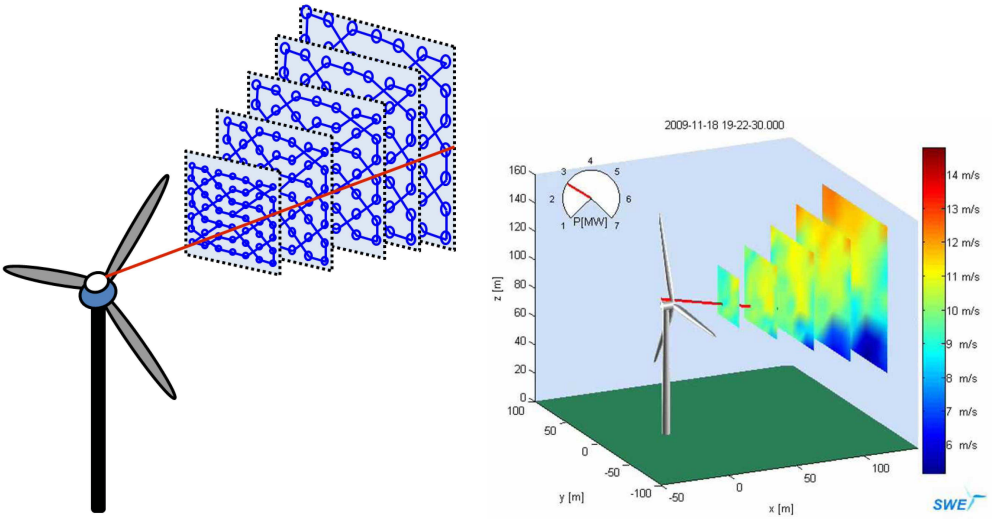

Figure 104: Sketch of simultaneous measurements at different distances (left) and real measured data with an interpolation within one focus plane (right).

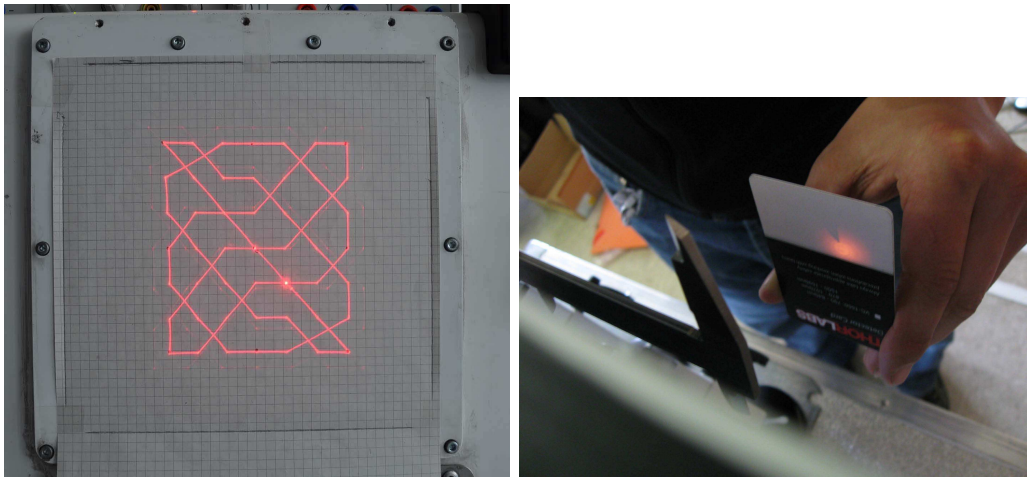

Figure 105: Photo of Liss2Grid trajectory taken with long exposure time (left). Use of an IR-sensitive card for the invisible laser beam (right.

8.5 CNR

CNR is deemed to be as an indication of the quality of the measurement. It describes the ratio of sent photons C to the number of reflected photons N using the unit dB (see chapter 4),

$$\mathrm{CNR} = \frac{C}{N}, \tag{172}$$

$$\mathrm{CNR(dB)} = 10 \log_{10} \frac{C}{N}. \tag{173}$$

The CNR value of every point measurement can be used to obtain information about the quality of the line-of-sight velocity. Measurements with a bad CNR value (< -17 dB) have to be ignored. There are several reasons for poor CNR values, from a dirty window/prism to the quantity and kind of the aerosols in the air. During -and directly after- a heavy rain the air is very clean and contains fewer aerosols to reflect the laser beam. Here the ratio between carriers to noise is quite bad. In offshore conditions the value of CNR is often higher due to the salty air.

If we examine nacelle-based measurements, the impact on the rotor blades causes a bad

CNR signal when the system is installed behind the rotor. About 30% of the data has to be removed due to rotor impact. Synchronizing the scan pattern with the rotor position or scanning the pattern in the opposite direction of the rotor direction will reduce the ignored data sets. If any faults in the lidar system occur, there is a need to know that issue especially when the output data and information is linked to the control of the turbine.

8.6 Wind field reconstruction

To reconstruct the wind speed and the wind field some assumptions have to be made. This is due to the fact that one can measure only the line-of-sight velocity along the laser beam. Based on the assumption that the wind field is parallel to the ground, the following drawings show how the wind speed vector is mapped by the line-of-sight vector. The absolute values of the line-of-sight velocity v_{LOS} at points P_i for every focus area m and the angles of the vertical and horizontal beam deflection are needed to recalculate the wind field. By means of these angles the coordinates of the measured points (for every five focus planes) can be calculated.

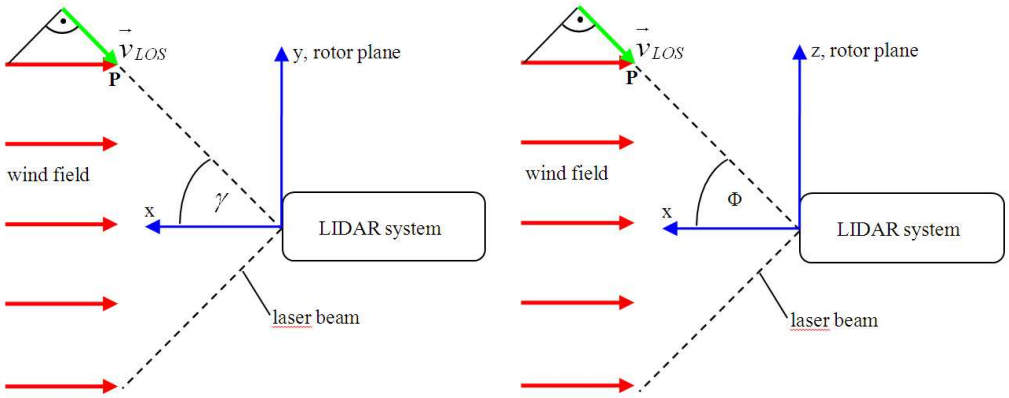

Figure 106: Schematic drawing of the lidar coordinate system from top and lateral views (left, right).

For a Cartesian coordinate system, where the lidar system is the origin of the coordinate system, the coordinates of a measured point P_i are x_p, y_p, z_p. Using these coordinates the normal vector $\mathbf{n}_{LOS} = [x_n, y_n, z_n]^T$ of the laser beam can be defined as

$$x_n = \frac{x_p}{\sqrt{x_p^2 + y_p^2 + z_p^2}}, \tag{174}$$

$$y_n = \frac{y_p}{\sqrt{x_p^2 + y_p^2 + z_p^2}}, \tag{175}$$

$$z_n = \frac{z_p}{\sqrt{x_p^2 + y_p^2 + z_p^2}}. \tag{176}$$

Therefore $|v_{LOS,fpm,Pi}|$ at focus plane m and point i yields to,

$$|v_{LOS,fpm,Pi}| = u_p \cdot x_n + v_p \cdot y_n + w_p \cdot z_n, \tag{177}$$

where the wind speed coordinates at point P_i, u_p, v_p, w_p, are unknown. Assuming that a plane parallel wind field prevails, the wind speed vector can be simplified by setting the wind speed coordinate in horizontal direction v_p and the wind speed coordinate in vertical direction w_p to zero.

$$v_p = 0, \tag{178}$$

$$w_p = 0. \tag{179}$$

The normal wind direction vector $\mathbf{n}_{winddir}$ for a plane parallel wind field (that always inflows right-angled to the rotor area) without vertical wind component can be described as followed:

$$\mathbf{n}_{winddir} = \begin{bmatrix} 1 \\ 0 \\ 0 \end{bmatrix}.$$

The angle $\cos\varphi$ between $\mathbf{n}_{winddir}$ and $\mathbf{n}_{los}$ can be calculated,

$$\cos\varphi = \frac{\mathbf{n}_{los} \cdot \mathbf{n}_{winddir}}{||\mathbf{n}_{winddir}||||\mathbf{n}_{los}||}. \tag{180}$$

The wind speed component u in x-direction, is the projection of v_{los} in the direction of $\mathbf{n}_{winddir}$. It can be calculated with the angle between the vectors.

$$u_{los} = \frac{v_{los}}{\cos\varphi} \tag{181}$$

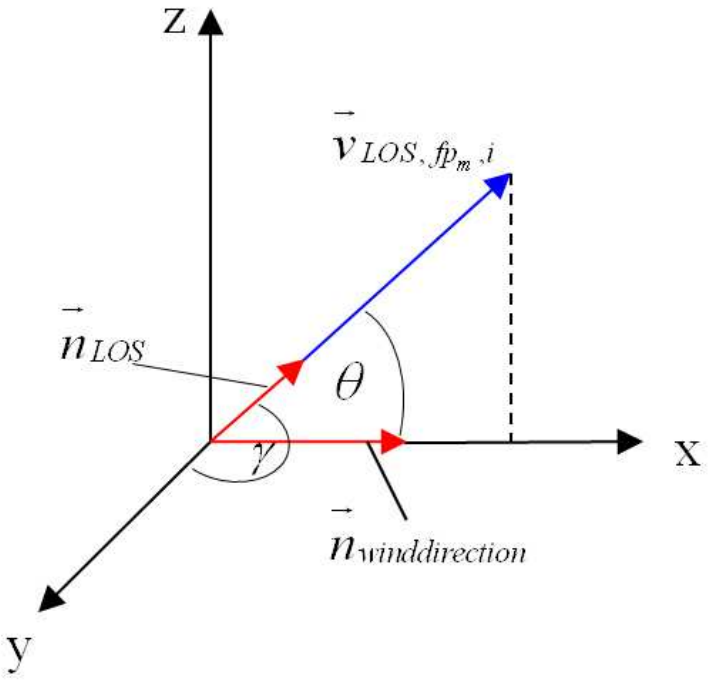

Figure 107: Schematics of the normalized vectors and v_{los}.

Assuming a plane parallel wind field and no vertical wind speed component enables a reconstruction of the wind field. But what's about horizontal and vertical shear, yaw error, turbulence? One possibility is shown with an "Estimator"-approach by Schlipf (2011).

8.7 "Visited" test sites of the SWE Scanner

8.7.1 Onshore test site Bremerhaven, Germany

The prototype of the AREVA Wind M5000 wind turbine was erected in December 2004 in Bremerhaven, close to the North Sea. In cooperation with DEWI (German Wind Energy Institute) and AREVA Wind the SWE started a thorough measurement program in spring 2005. In 2007 the national funded project "Development of lidar measurement techniques for the German offshore test site" started with the objective to develop reliable and standardized remote sensing techniques for various new applications in the wind energy community and to support in a later step other RAVE (research at alpha ventus) projects at the German offshore

test site "alpha ventus". Except for a FINO1 campaign, all lidar measurements from ground and from nacelle were carried out in Bremerhaven.

The M5000 is a 5 MW wind turbine designed for offshore purposes. With a hub height of 102 m and a rotor diameter of 116 m the M5000 is currently one of the largest wind turbines. The cut-in wind speed is 4 m s^{-1}, the rated wind speed is 12 m s^{-1} and the cut-out wind speed 25 m s^{-1}. The M5000 is a pitch-controlled, variable speed wind turbine with a permanent magnet generator.

Figure 108: Onshore test site with AREVA M5000 and SWE met mast (102 m) (left) Installation of the lidar system on the nacelle of the turbine (approx. 105 m AGL) (right).

8.7.2 Onshore test site Risø Campus - DTU Wind Energy, Denmark

The measurement campaigns at this test site mainly focus on fundamental investigations concerning the minimum number of trajectory points for equivalent wind speed, turbulence measurements, horizontal/ vertical wind shear and mean wind speed accuracy compared to a cup and sonic anemometer on a met mast. The test site of DTU Wind Energy is located close to the research center on the Risø Campus (Denmark). The SWE-Lidar system was first installed on ground, tilted up with 25° and pointed towards the met mast. In a second campaign, the Lidar system was installed on a platform of a Nordtank wind turbine in about 38m height. From this platform, the Lidar system shot almost horizontally to a met mast where the laser pointed to three sonic anemometers at different heights.

8.7.3 Onshore test site National Wind Technology Center (NWTC) - NREL, USA

The measurement campaigns at this test site mainly focus on the first test and validation of Lidar assisted control worldwide (see next chapter). The SWE scanner was installed on the nacelle of the two-bladed Controls Advanced Research Turbine (CART-2).

Figure 109: Test site at DTU Wind Energy, Risø campus, with SWE scanner installed on the Nordtank turbine (left). Tilted SWE lidar system pointing to a met mast (right).

Figure 110: SWE scanner mounted on the CART-2 machine for Lidar Assisted control purposes.

8.7.4 Offshore test site "alpha ventus"

The offshore test site "alpha ventus" is located 45 km north of the island of Borkum next to the research platform FINO 1. It comprises twelve offshore wind turbines with a total capacity of 60 MW. Six AREVA Wind M5000 turbines were installed in summer 2009, six REpower 5M turbines followed in 2010. The German Federal Environment Ministry supports alpha ventus with a major research funding. The RAVE initiative is accompanying the construction and operation of the test site to attain a broad basis of experience and expertise for future offshore wind parks. Several research projects are currently carried out. Within the RAVE-

OWEA research project two scanning lidar systems, one installed on the nacelle of the AREVA Wind M5000 the other one on REpower 5M, measure the inflow and the wake of the turbines under offshore conditions.

Figure 111: Lidar system (scanner unit and Windcube) on the top of a Repower 5M measuring the inflow.

8.8 Measurement campaigns and some results

Different measurement campaigns regarding different applications such as the verification of Taylor's frozen turbulence hypothesis, validation of wake models, predictive control, load estimation and power curve determination are still on-going or have been terminated. If we look at the power curve determination and load measurements, the wind field information has to be summed up to equivalent wind speed and turbulence intensity (Klausmann, 2010; Bischoff et al., 2010; Rettenmeier et al., 2012a,b).

8.8.1 Equivalent wind speed

The advantage of measuring from the nacelle of a turbine is that the whole swept rotor area is covered and that horizontal and vertical wind shear can be taken into account. According to the standard, fewer sectors have to be excluded because there is no met mast in the wake of the turbine or of other obstacles. Thus measurement campaigns can be carried out in a shorter time.

To determine a power curve, the mean values as well as the standard deviation of the electric power and the average wind speed over 10 min are necessary. The main goal is to get a power curve including all wind field information, as well as to get a smaller standard deviation. A second goal consists in the definition of relevant trajectory points. Both methods presented here are based on the trajectory Liss2Gridopt (Rettenmeier et al., 2011). With 7×7 measuring points a variety of different methods is feasible.

Arithmetic average of all points The first method is a simple arithmetic average over all mean wind speeds of measurement points during a 10 min period of time.

$$u_{mean} = \frac{1}{N} \sum_{i=1}^{N} v_i, \tag{182}$$

where N is the number of layers and v_i the average wind speed of trajectory layer i. The used trajectory for this example, Liss2Gridopt, has seven layers.

The curve is relatively similar to the power curve measured with a met mast and a cup anemometer according to the IEC standard. One can see that the bars of the standard deviation are significantly smaller. That means that the uncertainties in the measurements are lower and the accuracy is higher. In another approach, five single points were picked out of

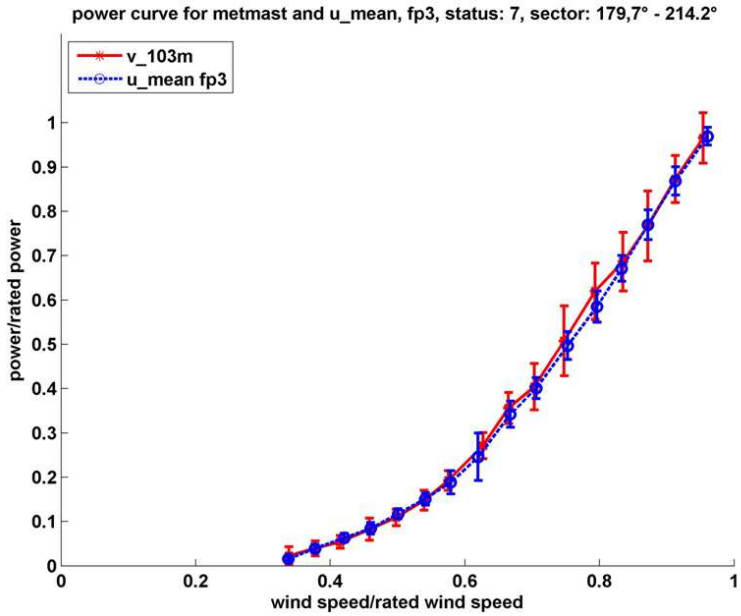

Figure 112: Power curve met mast and u_{mean} method.

the 49 measurement points (Big-Cross). Even when reducing the measurement points the standard deviation is still very small.

$$u_{bigcross} = \frac{1}{5}\sum_{i=1}^{5} \mathbf{u}_i. \tag{183}$$

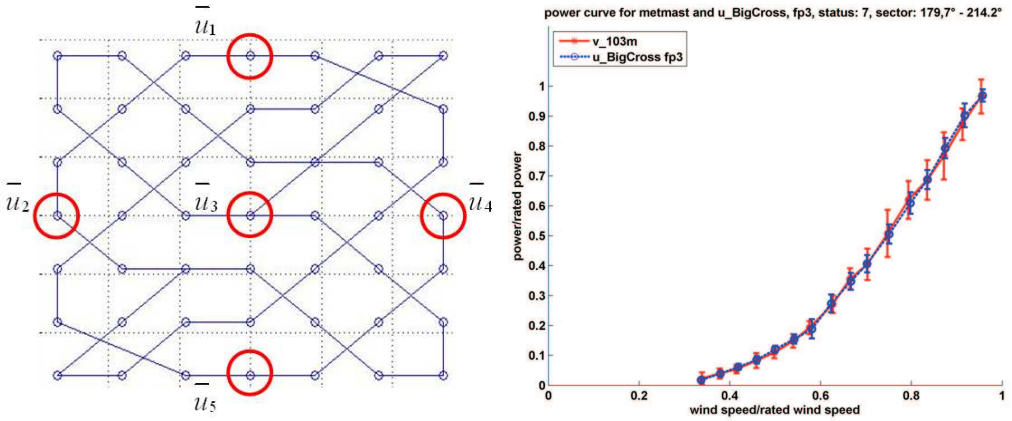

Figure 113: Five points out of 49 for the Big cross method (left) and calculated power curve (right).

8.8.2 Rotor effective wind speed

In this case the six measurement points of a circle are measured at each of the five focus distances (Figure 114(left)). For quite good wind field information a high spatial and temporal resolution of the wind fields is needed. Therefore all of these thirty measurement points in space are taken into account and are calculated to one single speed, which is further called rotor effective wind speed v_0: In (Schlipf et al., 2012) one describes how to calculate this rotor effective wind speed. The line-of-sight wind speeds are measured by the laser in six points at five different fixed distances. By the use of assumptions the wind speeds are corrected and averaged over the last trajectory at each focus distance. In a further step the resulting preview

of the rotor effective wind speed $v_0(t)$ is a weighted average over all available v_i available during time t (Figure 114(right)). That means that the five focus distances are shifted to one single distance. This shift can be done by the use of Taylor's frozen turbulence hypothesis which is valid for horizontally Lidar measurements (Schlipf et al., 2010).

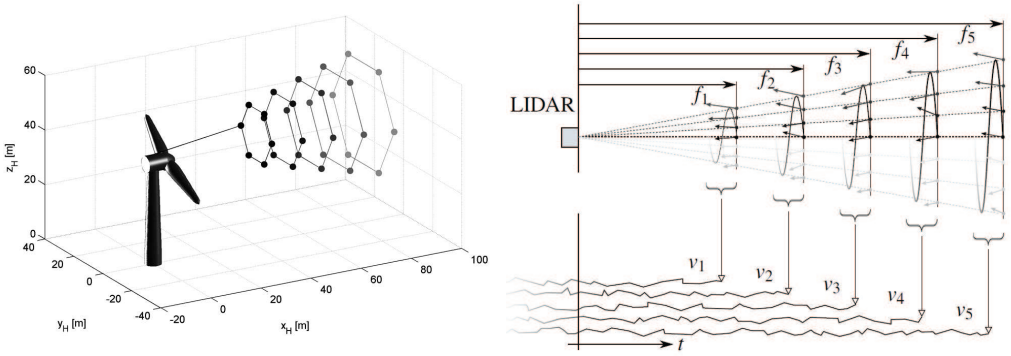

Figure 114: Circle trajectory used for the CART-2 campaign (left) and schematic drawing of the incoming wind field measured by a lidar at different focus distances (right).

In (Figure 115(left)) three different wind speeds are shown in a 10-min time series: one is measured by the anemometer on the met mast v_M, the other one shows the rotor effective wind speed v_{0L} measured with the Lidar. The third wind speed is recalculated from the turbine data as e.g. the pitch angle, rotor speed and power output data. Here the turbine represents a big horizontal axes anemometer with a rotor effective wind speed v_0. It is visible that the turbine's wind speed corresponds much better to the rotor effective wind speed of the Lidar than to the anemometer on the met mast.In a further step, the power production of the CART-2 turbine was simulated with FAST. As input for the wind two different data sets were used: the real met mast data and the rotor effective wind speed measured with the Lidar. In (Figure 115(right)) the result of the simulated power output is shown together with the real electrical power from the turbine. As one can see, the simulation with the rotor effective wind speed corresponds very well with the real data (Rettenmeier et al., 2012b).

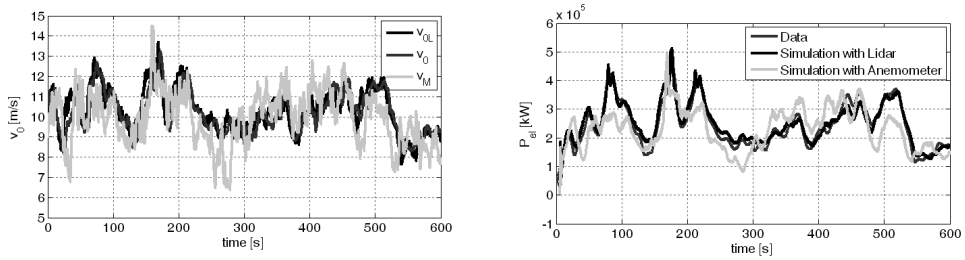

Figure 115: Time series of the rotor effective wind speed from Lidar and turbine and of the anemometer mounted on a mast (left) and simulation of the power production with met mast and Lidar data in comparison with the real production data. (right).

8.9 Outlook & Conclusions

The use of a lidar system from the nacelle offers various applications in wake wind field analysis, wind turbine control, power curve determination and load estimation. The whole swept rotor area can be taken into account, but assumptions have to be made. Nacelle-based measurement methods show a great potential on- and offshore and even in complex terrain. But there are still some investigations that have to be done concerning turbulence, vertical and horizontal shear, comparison criteria and equivalent wind speed.

Notation

C	number of sent photons
CNR	carrier to noise ratio
DEWI	German wind energy institute
i	index of layers of points
m	beam focus plane
$\mathbf{n}_{los}$	line of sight normal vector
$\mathbf{n}_{windir}$	normal wind direction vector
N	number of reflected photons and number of layers
P_i	beam focus area points
SNR	signal to noise ration
SWE	Stuttgart Chair of Wind Energy
$u_{bigcross}$	5-point average wind speed
u_{los}	wind speed component in x-direction
u_{mean}	10-min mean wind speed
u_p	longitudinal wind speed at point P
v_i	average wind speed of trajectory layer i
v_{los}	line-of-sight velocity
v_m	wind speed measured on met mast
v_0	rotor effective wind speed, recalculated from turbine data
v_{0L}	rotor equivalent wind speed, calculated by lidar data
v_p	transversal wind speed at point P
WiTLiS	wind turbine simulator
w_p	vertical wind speed at point P
x_n	longitudinal coordinate of normal vector $\mathbf{n}_{los}$
x_p	longitudinal coordinate of point P
y_n	transversal coordinate of normal vector $\mathbf{n}_{los}$
y_p	transversal coordinate of point P
z_n	vertical coordinate of normal vector $\mathbf{n}_{los}$
z_p	vertical coordinate of point P
φ	angle between $\mathbf{n}_{los}$ and $\mathbf{n}_{winddir}$

References

Bischoff O. Hofsäss M, Rettenmeier A., Schlipf D. and Siegmeier B, (2010) Statistical load estimation using a nacelle-based lidar system. *DEWEK*, Bremen

Canadillas B., Schlipf D., Neumann T. and Kuehnel D. (2011) Validation of Taylor's hypothesis under offshore conditions. *EGU*, Vienna

Cariou J.-P. and Boquet M. (2010) Leosphere pulsed lidar principles. Contribution to EU-project UpWind WP6

Harris M., Hand M. and Wright A. (2006) lidar for turbine control. Tech Report NREL/TP-500-39154

Klausmann P. (2010) Calculation of power curves based on interpolated line-of-sight velocities of nacelle-based lidar-measurements. Study thesis, SWE

Mikkelsen T., Hansen K., Angelou N., Sjöholm M., Harris M., Hadley P., Scullion R., Ellis G. and Vives G. (2010) lidar wind speed measurements from a rotating spinner. *EWEC*, Warsaw

Rettenmeier A., Bischoff O. Hofsäss M, Schlipf D. and Trujillo J. J. (2010) Wind field analysis using a nacelle-based lidar system. *EWEC*, Warsaw

Rettenmeier A., Klausmann P., Bischoff O., Hofsäss M, Schlipf D., Siegmeier B. and Kühn M. (2011) Determination of Power Curves Based on Wind Field Measurements Using a Nacelle-based Lidar Scanner. *EWEA*, Brussels

Rettenmeier A., Wagner R., Courtney M., Mann J., Bischoff O., Schlipf D., Anger J., Hofsäss M. and Cheng P. W. (2012) Turbulence and wind speed investigations using a nacelle-based Lidar scanner and a met mast. *EWEA*, Copenhagen

Rettenmeier A., Schlipf D., Würth I., Cheng P. W., Wright A., Fleming P., Scholbrock A., Veers P. (2012) Power Performance Measurements of the NREL CART-2-Wind Turbine Using a nacelle-based Lidar scanner. *ISARS*, Boulder

Schlipf D., Trujillo J. J., Basterra V. and Kühn M. (2009) Development of a wind turbine lidar simulator. *EWEC*, Marseille

Schlipf D., Trabucchi D., Bischoff O. Hofsäss M, Mann J., Mikkelsen T., Rettenmeier A., Trujillo J. J. and Kühn M. (2010) Testing for frozen turbulence hypothesis for wind turbine applications with a scanning lidar system. *ISARS*, Paris

Schlipf D., Schlipf D. J. and Kühn M. (2010) Nonlinear Model Predictive Control of Wind Turbines Using LIDAR. *Wind energy Journal*

Trujillo J. J., Bingöl F., Larsen G., Mann J. and Kühn M (2008) lidar measurement and modelling of wind turbine far-wake dynamics *DEWEK*, Bremen

Trujillo J. J. (2009) Measurements of a multi-MW turbine near-wake using lidar from the nacelle. *Euromech Colloquium*, Madrid

Trujillo J. J., Trabucchi D., Bischoff O. Hofsäss M., Mann J., Mikkelsen T., Rettenmeier A., Schlipf D. and Kühn M. (2010) Testing for frozen turbulence hypothesis for wind turbine applications with a staring lidar. *EGU*, Vienna

Trujillo J. J., Kühn M, Bischoff O. Hofsäss M., Rettenmeier A. and Schlipf D. (2010) Meandering model with near wake lidar measurements. *DEWEK*, Bremen

9 Lidars and wind turbine control – Part 1

David Schlipf
Stuttgart Chair of Wind Energy, Institute of Aircraft Design, Universität Stuttgart, Germany

9.1 Introduction

In recent years lidar technology found its way into wind energy. The main application is still the site assessment, but the possibility to optimize the energy production and reduce the loads by nacelle or spinner based lidar systems is becoming an important issue. In terms of control the inflowing wind field is the main disturbance to the wind turbine and most of the wind turbine control is designed to deal with variations in this disturbance. From control theory, the control performance can be improved with the knowledge of the disturbance. Due to the measurement principle and the complexity of the wind lidar assisted control is a wide field of research. The main idea is to divide the problem in a measurement and a control problem.

The presented work describes first how wind characteristics, such as wind speed, direction and shears, can be reconstructed from the limited provided information (see Section 9.2). Based on the models of the wind turbines (see Section 9.3) it is investigated in Section 9.4, how well the lidar information can be correlated to the turbines reaction.

In the next sections, several controllers are presented, see Table 15. All controllers are designed first for the case of perfect measurement and then adjusted for realistic measurements. The most promising approach is the collective pitch feedforward controller using the knowledge of the incoming wind speed providing an additional control update to assist common collective pitch control. Additional load reduction compared to the sophisticated feedback controllers could be archived (Schlipf et al., 2010a). The concept has been successfully tested on two research wind turbines (Schlipf et al., 2012a; Scholbrock et al., 2013). Then a feedforward control strategy to increase the energy production by tracking optimal inflow conditions is presented. The comparison to existing indirect speed control strategies shows a marginal increase in energy output at the expense of raised fluctuations of the generator torque (Schlipf et al., 2011). A Nonlinear Model Predictive Control (NMPC) is also presented, which predicts and optimizes the future behavior of a wind turbine using the wind speed preview adjusting simultaneously the pitch angle and the generator torque. The NMPC achieves further load reductions especially for wind conditions near rated wind speed (Schlipf et al., 2012b). Furthermore, a cyclic pitch feedforward controller using the measured horizontal and vertical shear is introduced to assist common cyclic pitch control for further reduction of blade loads. Simulations results from Dunne et al. (2012) are promising, but they have to be further investigated under more realistic conditions. Finally, the benefit of lidar assisted yaw control is explored. A promising way to obtain a accurate measurement of the wind direction is to measure it over the full rotor plane ahead of the turbine by lidar. The expected increase of the energy output is about one percent of the annual energy production, when using the wind direction signal from the lidar system instead of the sonic anemometer (Schlipf et al., 2011).

9.2 Model Based Wind Field Reconstruction

In this section a method is proposed to retrieve the necessary information for lidar assisted control out of lidar data. First the ambiguity in wind field reconstruction is presented. Then lidar and wind models are introduced which can be applied to reconstruct wind characteristics. Further details can be found in Schlipf et al. (2011) and Schlipf et al. (2012c).

Table 15: Possible application and benefit of lidar assisted control.

	benefit	potential	Section
collective pitch feedforward	less loads	$< 20\%$	9.5
direct speed control	more energy	marginal	9.6
model predictive control	more energy + less loads	$< 1\% + < 30\%$	9.7
cyclic pitch feedforward	less loads	$< 20\%$	9.8
lidar assisted yaw control	more energy	$< 2\%$	9.9

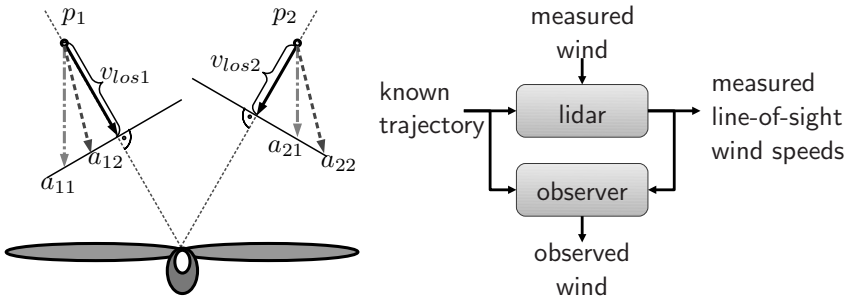

Figure 116: (left) Ambiguity in wind field reconstruction. (right) System theoretical view on lidar measurements and wind field reconstruction.

9.2.1 Ambiguity in Wind Field Reconstruction

It is not possible to measure a three-dimensional wind vector with a single nacelle or spinner based lidar system due to the limitation to the line-of-sight wind speed. But with simple assumptions the wind vector can be reconstructed:

1. no vertical and no horizontal wind component
2. no vertical component and homogeneous flow

In Figure 116 the effect of both assumptions is shown. In this example the 3D vectors in the locations p_1 and p_2 (measured at the same height) are reconstructed from the line-of-sight wind speeds $v_{los,1}$ and $v_{los,2}$. The first assumption yields a_{11} and a_{21} representing a horizontal shear. By the second assumption the resulting vectors a_{12} and a_{22} are equal representing a cross-flow. A dilemma ("Cyclops Dilemma") exists, if the lidar is used for yaw and cyclic pitch control at the same time: If the first assumption is used to calculate the inhomogeneous inflow, perfect alignment is assumed. If the second assumption is used to obtain the misalignment, homogeneous flow is assumed.

9.2.2 Lidar Model for Reconstruction

All known settings of a lidar system can be considered as inputs, all unknown influences as disturbances and the measurements as outputs (see Figure 116). In system theory a disturbance observer can be used to reconstruct the disturbances from the system in- and outputs, if observability is given. Robustness evaluates, how well this is done in the presence of model and measurement uncertainties. For static systems observability and robustness can be simplified to the questions, whether a unique disturbance can be found which caused the measured output with given input and how sensible it is for uncertainties. For this purpose, a model of the system is needed, similar to a simulation model and the observation can be considered to be inverse to a simulation.

A lidar measuring in point i can be modeled by

$$v_{los,i} = \frac{x_i}{f_i}u_i + \frac{y_i}{f_i}v_i + \frac{z_i}{f_i}w_i, \tag{184}$$

which is a projection of the wind vector $[u_i\ v_i\ w_i]$ and the normalized vector of the laser beam focusing in the point $[x_i\ y_i\ z_i]$ with a focus length f_i. Since there is only one equation

for three unknowns, it is impossible to reconstruct the local wind vector. Observability can be restored by changing the wind model, which has to be chosen according to the application and the quality of the results depends on the model validity.

9.2.3 Wind Model for Collective Pitch Control

The simplest model assumes that only the rotor effective wind v_0 is present and no shears or inflow angles. In this case, the u_i component is equal to the rotor effective wind, v_i and w_i are neglected. Using (184) the rotor effective wind estimate v_{0L} can be defined for n points measured in the same vertical measurement plane in front of the turbine as:

$$v_{0L} = \frac{1}{n}\sum_{i}^{n} v_{los,i}\frac{f_i}{x_i}. \tag{185}$$

9.2.4 Wind Model for Cyclic Pitch Control

In the second model, it is assumed that the wind is homogeneous in a vertical measurement plane in front of the turbine. If there is no tilted inflow and no misalignment, the turbulent wind vector field is reduced to v_0 and the horizontal and vertical shear (δ_H and δ_V):

$$u_i = v_0 + \delta_H y_i + \delta_V z_i. \tag{186}$$

The advantage of this reduction is that n measurements gathered simultaneously in the same measurement plane can be combined to get an estimation for the rotor effective wind characteristics. For non simultaneous measurements of scanning systems, the last n focus points of a scan can be used. Following equation is obtained using (186) and (184):

$$\underbrace{\begin{bmatrix} v_{los,1} \\ : \\ v_{los,n} \end{bmatrix}}_{m} = \underbrace{\begin{bmatrix} x/f_1 & xy_1/f_1 & xz_1/f_1 \\ : & : & : \\ x/f_n & xy_n/f_n & xz_n/f_n \end{bmatrix}}_{A} \underbrace{\begin{bmatrix} v_0 \\ \delta_H \\ \delta_V \end{bmatrix}}_{s}. \tag{187}$$

A solution for all three wind characteristics can only be found, if $rank(A) = 3$. For $n = 3$ there is one unique solution

$$s = [v_0 \ \delta_H \ \delta_V]^T = A^{-1}m. \tag{188}$$

For $n > 3$ a solution can be selected by the method of least squares.

9.2.5 Wind Model for Yaw Control

This model assumes that there is no shear and no tilted inflow and that the u and v wind component are homogeneous. Using (184) a linear system in u and v can be formulated:

$$\underbrace{\begin{bmatrix} v_{los,1} \\ : \\ v_{los,n} \end{bmatrix}}_{m} = \underbrace{\begin{bmatrix} x/f_1 & y_1/f_1 \\ : & : \\ x/f_n & y_n/f_n \end{bmatrix}}_{A} \underbrace{\begin{bmatrix} u \\ v \end{bmatrix}}_{s}. \tag{189}$$

This system can be solved using the estimator (188), if $rank(A) = 2$.

9.2.6 Wind Model for Complex Terrain

In the presence of inflow angles and shears the measurement in point i can be defined as

$$u_{Wi} = v_0 + \delta_H y_{Wi} + \delta_V z_{Wi}, \tag{190}$$

The wind coordinates $[x_{Wi} \ y_{Wi} \ z_{Wi}]$ can be transformed to the lidar coordinate system by a rotation of the horizontal and vertical inflow angle, α_H and α_V. A numerical inversion for

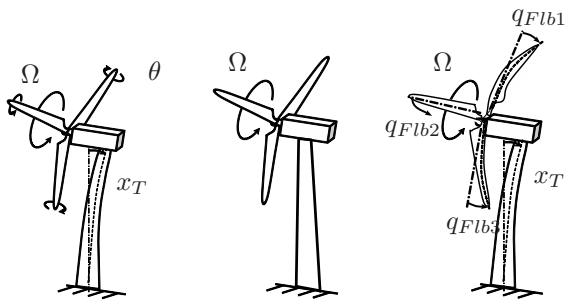

Figure 117: Degrees of freedom for the reduced nonlinear model (left), the first order model (center) and the linear model (right).

the nonlinear equations can be achieved with the least-squares minimization problem

$$\min_{v_0,\alpha_H,\alpha_V,\delta_H,\delta_V} \sum_{i=1}^{n} \left(v_{los,i} - \frac{x_{Wi}}{f_i} u_{Wi} \right)^2, \tag{191}$$

and the wind vector can be calculated with (190) and the inverse transformation.

9.3 Modeling of the Wind Turbine

The crucial part of a successful feedforward and model predictive controller design is the adequate modeling of the dynamic system to be controlled. The model should be simple enough to allow a partial system inversion (for the feedforward controller design) and simulations in reasonable computation time (for the NMPC) and at the same time it should be accurate enough to capture the system dynamics that are relevant for the wind turbine control. The reduced model can also be used in an estimator to estimate the rotor effective wind speed from turbine data.

9.3.1 Reduced Nonlinear Model

Classically aeroelastic simulation environments for wind turbines such as FAST (Jonkman and Buhl, 2005) (used later in this work) provide models close to reality but far to complex to be used for controller design. In addition, current remote sensing methods such as lidar are not able to provide a wind field estimate with comparable details to a generic wind field used by aeroelastic simulations (generated in this work with TurbSim (Jonkman and Buhl, 2007)). In this section a turbine model with three degrees of freedom (see Figure 117) is derived from physical fundamentals and the wind field is reduced to the rotor effective wind speed which is measurable with existing lidar technology.

The first tower fore-aft bending mode, the rotational motion and the collective pitch actuator are based on Bottasso et al. (2006):

$$J\dot{\Omega} + M_g/i = M_a(\dot{x}_T, \Omega, \theta, v_0) \tag{192a}$$

$$m_{Te}\ddot{x}_T + c_T\dot{x}_T + k_T x_T = F_a(\dot{x}_T, \Omega, \theta, v_0) \tag{192b}$$

$$\ddot{\theta} + 2\xi\omega\dot{\theta} + \omega^2(\theta - \theta_c) = 0. \tag{192c}$$

Equation (192a) models the drive-train dynamics, where Ω is the rotor speed, M_a is the aerodynamic torque and M_g the electrical generator torque, x_T the tower top fore-aft displacement, θ the effective collective blade pitch angle, and v_0 the rotor effective wind speed. Moreover, i is the gear box ratio and J is the sum of the moments of inertia about the rotation axis of the rotor hub, blades and the electric generator. Equation (192b) describes the tower fore-aft dynamics, F_a is the aerodynamic thrust and m_{Te}, c_T, and k_T are the tower equivalent modal mass, structural damping and bending stiffness, respectively. These values were calculated according to Jonkman et al. (2009). Finally, equation (192c) is a second-order

model of the blade pitch actuator, where ω is the undamped natural frequency and ξ the damping factor of the pitch actuator and θ_c is the collective blade pitch control input. The nonlinearity in the reduced model resides in the aerodynamic thrust and torque acting on the rotor with the radius R:

$$M_a(\dot{x}_T, \Omega, \theta, v_0) = \frac{1}{2}\rho\pi R^3 \frac{c_P(\lambda,\theta)}{\lambda} v_{rel}^2 \tag{193a}$$

$$F_a(\dot{x}_T, \Omega, \theta, v_0) = \frac{1}{2}\rho\pi R^2 c_T(\lambda,\theta) v_{rel}^2, \tag{193b}$$

where ρ is the air density, λ the tip-speed ratio, defined as

$$\lambda = \frac{\Omega R}{v_{rel}}, \tag{194}$$

and c_P and c_T are the effective power and thrust coefficients, respectively. The nonlinear c_P and c_T coefficients can be obtained from steady state simulation. The relative wind speed v_{rel} is defined as a superposition of tower top speed and mean wind speed

$$v_{rel} = (v_0 - \dot{x}_T), \tag{195}$$

and is used to model the aerodynamic damping. The equations (192) to (195) can be organized in the usual nonlinear state space form:

$$\begin{aligned} \dot{x} &= f(x,u,d) \\ y &= h(x,u,d), \end{aligned} \tag{196}$$

where the states x, the inputs u, disturbance d and measurable outputs y are

$$x = \begin{bmatrix} \Omega & x_T & \dot{x}_T & \theta & \dot{\theta} \end{bmatrix}^T, \qquad u = \begin{bmatrix} M_g & \theta_c \end{bmatrix}^T,$$

$$d = v_0, \qquad y = \begin{bmatrix} \Omega & \ddot{x}_T & \theta & \dot{\theta} \end{bmatrix}^T.$$

9.3.2 Estimation of the Rotor Effective Wind Speed from Turbine Data

The nonlinear reduced model (192) can be further reduced to a first order system (see Figure 117) by ignoring the tower movement and the pitch actuator:

$$J\dot{\Omega} + M_g/i = M_a(\Omega, \theta, v_0) \tag{197a}$$

$$M_a(\Omega, \theta, v_0) = \frac{1}{2}\rho\pi R^3 \frac{c_P(\lambda,\theta)}{\lambda} v_0^2 \tag{197b}$$

$$\lambda = \frac{\Omega R}{v_0}. \tag{197c}$$

This model is used to estimate the rotor effective wind speed v_0 from turbine data. If parameter such as inertia J, gear box ratio i and rotor radius R as well as the power coefficient $c_P(\lambda,\theta)$ are known, and data such as generator torque M_g, pitch angle θ, rotor speed Ω and air density ρ are measurable, the only unknown in (197) is the rotor effective wind v_0.

Due to the λ-dependency of the power coefficient $c_P(\lambda,\theta)$ no explicit solution can be found. A solution could be found by solving (197) by iterations. But this would produce high computational effort for high resolution data. Therefore, a three dimensional look-up-table $v_{0R}(M_a, \Omega, \theta)$ is calculated a priori from the cubic equation (197b), similar to van der Hooft and van Engelen (2004). Here, the equation (197b) is solved first in λ for numerical reasons. The aerodynamic torque M_a can then be calculated online from turbine data with (197a).

9.3.3 Linear Model

For the cyclic pitch feedforward controller (see Section 9.8), a model including the blade bending degree of freedom is needed. It is obtained from an azimuth dependent nonlinear aeroelastic model considering the rotor motion, first flapwise bending modes of each blade and the first tower fore-aft bending mode as depicted in Figure 117. The aeroelastic model is linearized, transformed with the Coleman-Transformation and decoupled, details see Schlipf et al. (2010b).

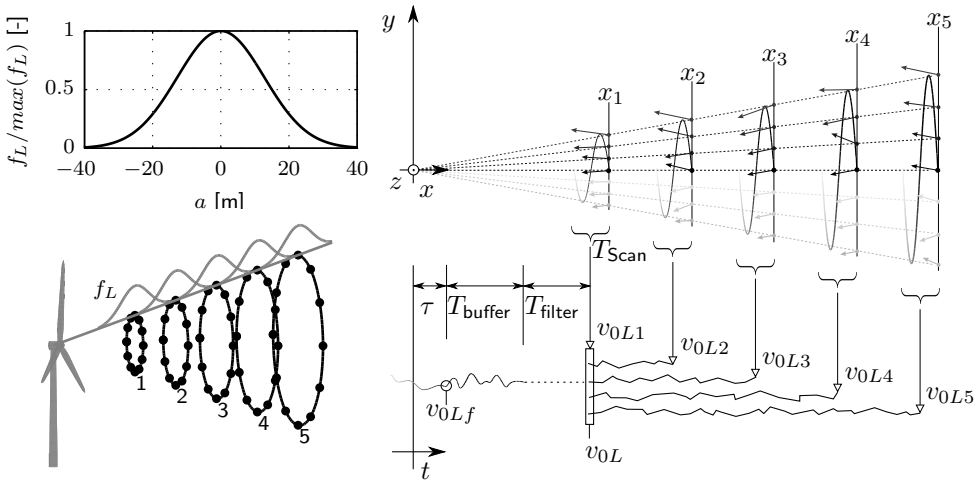

Figure 118: (left top) Normalized range weighing function $f_L(a)$ for a pulsed lidar system. (left bottom) Scope of circular scan (right) and the wind prediction.

9.4 Correlation of a Lidar System and a Wind Turbine

9.4.1 Simulated Lidar Measurements

Compared to (184) lidar measurements can be modeled more realistically for simulations by the following equation:

$$v_{los,i} = \int_{-\infty}^{\infty} \left(\frac{x_i}{f_i} u(a) + \frac{y_i}{f_i} v(a) + \frac{z_i}{f_i} w(a) \right) f_L(a) da. \tag{198}$$

The weighting function $f_L(a)$ at the distance a to the focus point depends on the used lidar technology (pulsed or continuous wave). Here, a Gaussian shape weighting function with full width at half maximum (FWHM) of $W = 30$ m is used, see Figure 118, following the considerations of Cariou (2011). 3D Wind fields generated e.g. with TurbSim (Jonkman and Buhl, 2007) over time t and the coordinates y and z can be scanned at a trajectory point $[t_i + T_{\text{Taylor},i}, y_i, z_i]$ by assuming Taylor's Hypothesis of Frozen Turbulence with

$$T_{\text{Taylor},i} = x_i / \bar{u}. \tag{199}$$

In this work, a pulsed system with a circular trajectory is used, which is performed within $T_{scan} = 2.4$ s with 12 focus points in 5 focus distances equally distributed between $0.5D$ and $1.5D$ with the rotor diameter $D = 126$ m, resulting in an update rate of 0.2 s, see Figure 118. This trajectory was realized by a real scanning lidar system installed on the nacelle of a 5 MW turbine (see Rettenmeier et al. (2010)). In the simulation, effects such as collision of the laser beam with the blades, volume measurement and mechanical constraints of the scanner from data of the experiment are considered to obtain realistic measurements.

9.4.2 Reconstruction of Rotor Effective Wind Speed

The wind characteristics are then reconstructed using (185): For each distance i the longitudinal wind component is averaged over the last trajectory for a rotor effective value and the obtained time series of the measurements v_{0Li} is time-shifted according to Taylor's frozen turbulence hypothesis, see Figure 118. The rotor effective wind speed $v_{0L}(t)$ is then calculated by

$$v_{0L}(t) = \frac{1}{5} \sum_{i=1}^{5} v_{0Li}(t - T_{\text{Taylor},i}). \tag{200}$$

This improves the short term estimation, because the measurements of further distances can be stored and used to obtain more information when reaching the nearest distance.

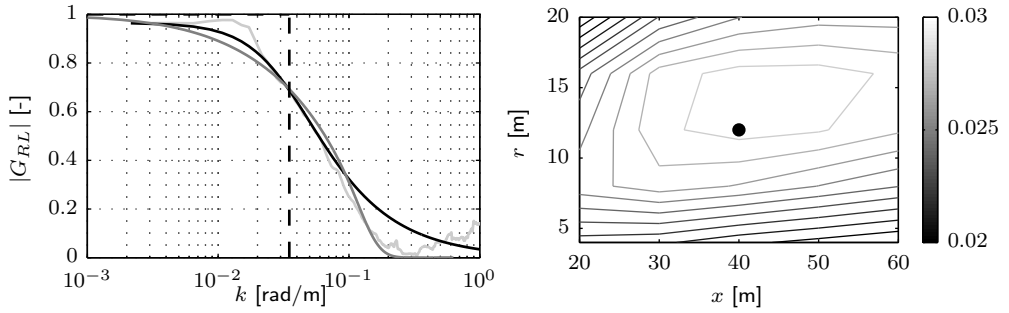

Figure 119: (left) Transfer function for a scanning lidar and a turbine: analytic (dark gray), measured (light gray), and fitted (black); maximum coherent wavenumber (dashed). (right) Optimization of the maximum coherent wavenumber.

9.4.3 Correlation

The correlation between the lidar estimate of the rotor effective wind speed v_{0L} and the rotor effective wind speed v_0 can be calculated by the transfer function

$$G_{RL} = \frac{S_{RL}}{S_{LL}} \tag{201}$$

and the squared coherence

$$\gamma^2_{RL} = \frac{|S_{RL}|^2}{S_{RR}S_{LL}} \tag{202}$$

using the auto spectrum S_{LL} from the lidar signal and S_{RR} from the rotor signal as well as the cross spectrum S_{RL} between the rotor and the lidar signal. With the definition of Bendat and Piersol (1971) cross and auto spectra can be calculated, omitting all scaling constants, by

$$\begin{aligned} S_{RR} &= \mathcal{F}\{v_0\}\mathcal{F}^*\{v_0\} \\ S_{RL} &= \mathcal{F}\{v_0\}\mathcal{F}^*\{v_{0L}\} \\ S_{LL} &= \mathcal{F}\{v_{0L}\}\mathcal{F}^*\{v_{0L}\}, \end{aligned} \tag{203}$$

where $\mathcal{F}\{\}$ and $\mathcal{F}^*\{\}$ are the Fourier transform and its complex conjugate, respectively. The same idea is used for the blade effective wind speed in Simley and Pao (2013).

For real time applications the spectra can be obtained from lidar measurements and turbine data using the estimator (197). The transfer function can be approximated by a standard low pass filter. Therefore, the maximum coherent wavenumber can be found with the cut-off frequency (-3 dB) of the corresponding filter (see Figure 119 in Schlipf and Cheng (2013)).

The correlation between a lidar system and a turbine can be calculated also analytically using analytic wind spectra, e.g. the Kaimal model. The measured wind can be considered as a sum of signals and due to the linearity of the Fourier transformation, the spectra can be calculated by a sum of auto and cross spectra, using (185), (198), and (200). In the full-analytical case, already the case of a staring lidar is very complicated. In the semi-analytical case, the rotor effective wind can be expressed by the mean of all n longitudinal wind components u_i hitting the rotor plane:

$$v_0 = \frac{1}{n}\sum_{i=1}^{n} u_i. \tag{204}$$

This model can then be used to design an optimal filter which is the crucial part of the controller described in the following sections. Another application is to optimize lidar systems (Schlipf et al., 2013a): Figure 119 shows how the maximum coherent wavenumber changes, if the focus distance x from a turbine with a rotor diameter of 40 m and the radius r of a scan with three measurements are varied. Furthermore, lidar measurements can be evaluated, whether the provided signal quality is sufficient for control, see e.g. Schlipf et al. (2012a); Scholbrock et al. (2013).

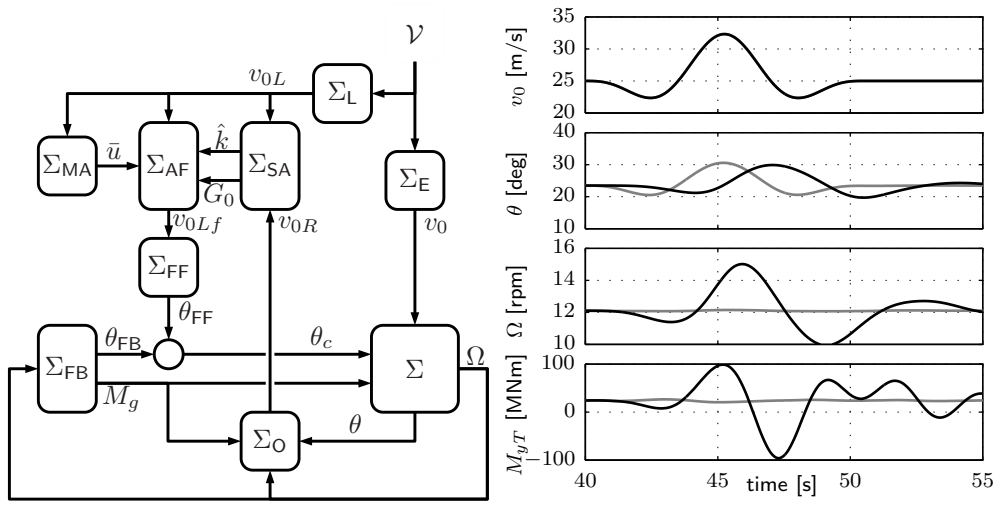

Figure 120: (left) Feedforward controller with adaptive filter. (right) Reaction to an EOG in case of perfect measurement using the 5 MW NREL turbine in FAST (Jonkman et al., 2009): Baseline controller only (black) and with additional feedforward (grey).

9.5 Lidar Assisted Collective Pitch Control

The lidar based collective pitch feedforward controller is the most promising approach for load reduction. In this section the controller and adaptive filter design will be presented and some results from the initial field testing.

9.5.1 Controller and Adaptive Filter Design

The collective pitch feedforward controller (see Figure 120) is based on the work in Schlipf et al. (2010a); Schlipf and Cheng (2013) and combines a baseline feedback controller with a feedforward update. The main control goal of the collective pitch feedback controller Σ_{FB} is to maintain the rated rotor speed Ω_{rated}. The system Σ is disturbed by a wind field $\mathcal{V}$, which can be measured by a lidar system Σ_{L} in front of the turbine before reaching the rotor. If the wind would not change on its way ($\Sigma_{\mathsf{E}} = 1$) and in the case of perfect measurement the measured wind speed v_{0L} and the rotor effective wind speed v_0 are equal. In this case and assuming a simple nonlinear wind turbine model (197), the effect of the wind speed on the rotor speed can perfectly compensated moving the collective pitch angle along the static pitch curve $\theta_{SS}(v_0)$ without any preview. If a more detailed model is used along with a pitch actuator, the proposed feedforward controller still can achieve almost perfect cancellation of an Extreme Operating Gust (EOG), see Figure 120. In this case, only a small preview time τ is necessary to overcome the pitch actuator dynamics.

In reality v_0 cannot be measured perfectly due to the limitation of the lidar system and Σ_{E} is quite complex to model. However, if the transfer function (201) from the measured wind speed to the rotor effective wind speed is known, it can be used to obtain a signal as close as possible to the rotor effective wind speed. Therefore, an adaptive filter is proposed along with a time buffer which can be fitted to the transfer function:

$$\Sigma_{\mathsf{AF}} = G_{\mathsf{filter}} e^{-T_{\mathsf{buffer}} s} \approx \Sigma_{\mathsf{E}}\ \Sigma_{\mathsf{M}}^{-1}. \tag{205}$$

The filter depends on the mean wind speed $\bar{u}$, which can be obtained with a moving average Σ_{MA}, and on the maximum coherent wavenumber $\hat{k}$ and the static gain G_0, which can be identified with a spectral analysis Σ_{SA} and the observer Σ_O from (188). The buffer time (see Figure 118) is necessary to apply the signal with the prediction time τ, considering the delay of the filter T_{filter} and the scan T_{scan}, assuming Taylor's Hypothesis:

$$T_{\mathsf{buffer}} = T_{\mathsf{Taylor}} - \frac{1}{2} T_{\mathsf{scan}} - T_{\mathsf{filter}} - \tau. \tag{206}$$

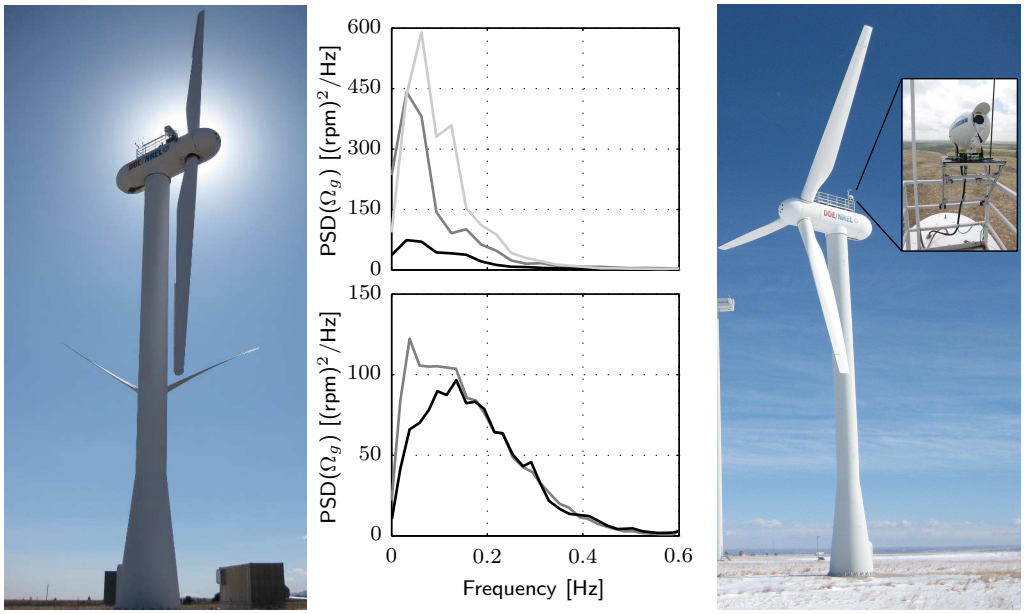

Figure 121: (left) The SWE-Scanner on the CART2. (middle) Spectra of the generator speed for the CART2 (top) and CART3 (bottom): FF off (dark gray), FF on with high (black) and low (light gray) correlation. (right) The OCS on the CART3.

9.5.2 Field Testing

The collective pitch controller has been successfully tested together with the National Renewable Energy Laboratory (NREL) in Boulder, Colorado in two different control campaigns. The scanning SWE-Lidar system was installed on the two-bladed CART2 and the OCS from Blue Scout Technologies on the three-bladed CART3. The main purpose of these campaigns was to provide a proof-of-concept of the feedforward controller. More details can be found in Schlipf et al. (2012a); Scholbrock et al. (2013).

In a first step the correlation between both turbines and the installed lidars was investigated, using the estimator (188). The maximum coherent wavenumber in the transfer function (201) was identified for the CART2 and the scanning lidar at $\hat{k} = 0.06$ rad/m and for the CART3 and the OCS at $\hat{k} = 0.03$ rad/m.

Then the adaptive filter and the feedforward controller was applied to each turbine. Here, a pitch rate update $\dot{\theta}_{\mathsf{FF}}$ instead of θ_{FF} was used:

$$\dot{\theta}_{\mathsf{FF}}(t) = \dot{v}_0(t+\tau)\frac{d\theta_{ss}}{dv_{0ss}}(v_0(t+\tau)) \tag{207}$$

Figure 121 shows the main result of the field testing, which is a reduction of the generator speed variations with the feedforward pitch rate update on, compared to the case with only the feedback controller. In the case of high correlation, the standard deviation of the rotor speed has been reduced by 30% for the CART2 and by 10% for the CART3. The difference is due to the lower correlation of the OCS on the CART3: The rotor speed is only reduced up to the frequency corresponding to the maximum coherent wavenumber.

However, in the case of low correlation, which was due to the impact with the met mast and guy wires, an increment of the generator speed variations can be seen, because of the wrong pitch action by the feedforward controller. This confirms, that it is possible to assisted wind turbine controllers with lidar measurements, but the signal has to be carefully filtered to have a beneficial effect.

Although load reductions have been detected as well, in next campaigns the feedback controller should be tuned: The benefit gained in rotor speed variation can be transformed in further load reduction by relaxing the feedback controller gains (Schlipf and Cheng, 2013).

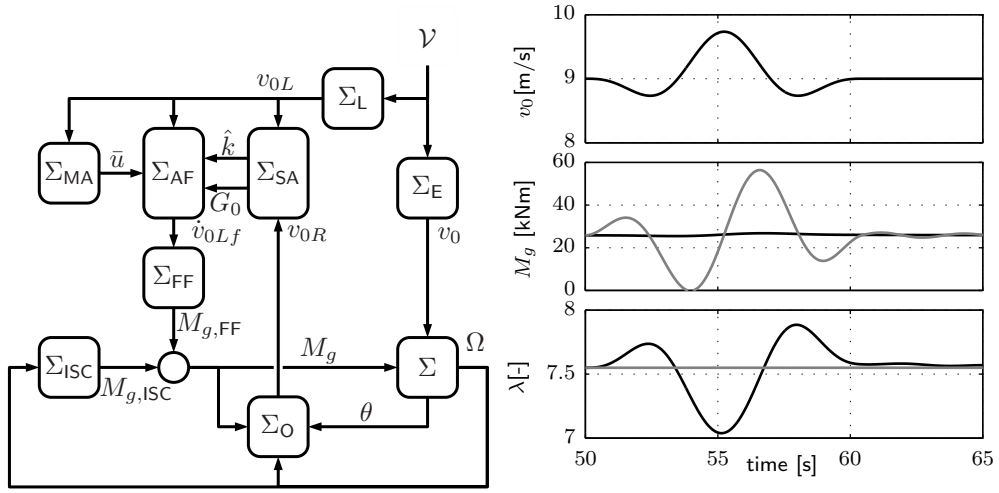

Figure 122: (left) Direct Speed Controller with adaptive filter. (right) Reaction to a gust in case of perfect measurement using the 5 MW NREL turbine in FAST (Jonkman et al., 2009): Baseline controller only (black) and with additional feedforward (grey).

9.6 Lidar Assisted Speed Control

The main purpose of variable speed control for wind turbines below rated wind speed is to maximize the electrical power extraction (Burton et al., 2001). Therefore, the turbine has to operate with the rotor blades held at the optimal angle of attack. This blade inflow angle is represented by λ (197c). The optimal tip speed ratio λ_{opt} can be found at the peak $\hat{c}_P$ of the power coefficient. The aerodynamic optimum can be achieved by tracking λ_{opt} via adjusting the generator torque M_g. This section depicts how tracking λ_{opt} can be done dynamically by using the knowledge of the incoming wind, more details see Schlipf et al. (2011, 2013b).

9.6.1 Controller Design

The baseline speed control (Burton et al., 2001) to maintain in steady state the maximum power coefficient $\hat{c}_P$ can be determined with the reduced nonlinear model (197) by:

$$M_{g,\mathsf{ISC}} = \underbrace{\frac{1}{2}\rho\pi R^5 \frac{\hat{c}_P}{\lambda_{opt}^3} i^3}_{k_{\mathsf{ISC}}} \Omega_g^2. \tag{208}$$

Equation (208) with constant k_{ISC} is known as the indirect speed control (ISC). Using the lidar technology, v_0 and thus λ become measurable, and therefore, the proposed controller is considered as direct speed control (DSC). The basic idea of the proposed DSC is to keep the ISC feedback law (208) and to find a feedforward update $M_{g,\mathsf{FF}}$ to compensate changes in the wind speed similar to the one used for collective pitch control, see Figure 120. With the derivative of the rotor effective wind speed $\dot{v}_0$ the DSC is:

$$M_{g,\mathsf{DSC}} = M_{g,\mathsf{ISC}} \underbrace{-iJ\frac{\lambda_{opt}}{R}\dot{v}_0}_{M_{g,\mathsf{FF}}}. \tag{209}$$

Higher order DSCs can be found (Schlipf et al., 2013b). Similar to the collective pitch feedforward controller, this controller in the nominal case perfectly maintains λ at its optimal value. This still holds, using a full aero-elastic model, assuming perfect measurement of v_0. But Figure 122 shows, that M_g has to be negative already with a small gust with 1 m/s amplitude due to the high inertia J, introducing high loads on the shaft.

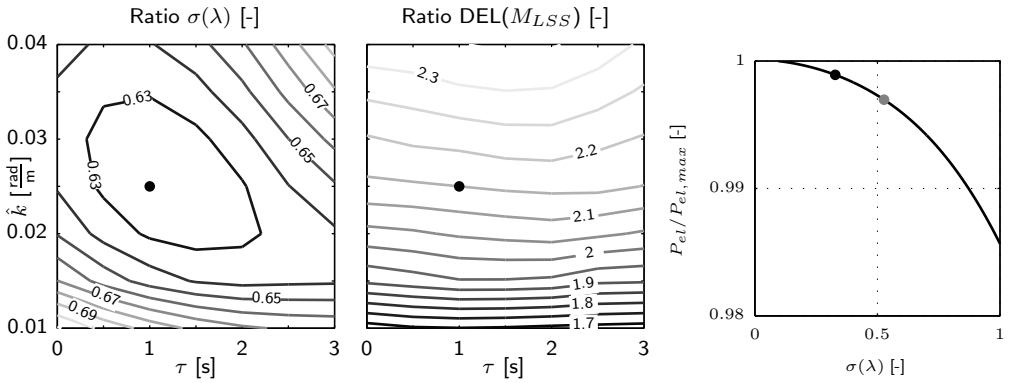

Figure 123: (left) Relative changes of the DSC in the standard deviation of λ and low-speed shaft loads compared to the ISC. Dots: optimal case. (right) Relative power extraction for the CART3. Dots: Field test results: ISC (gray) and DSC (black).

9.6.2 Simulation Using Real Data

The lidar raw data and the estimated v_{0R} obtained with (188) from the CART3 control campaign (see Figure 121) are used for simulations to test the DSC. The simulations are done with an aeroelastic model of the CART3 implemented in FAST (Jonkman and Buhl, 2005), disturbed by a hub height wind field of v_{0R}. The same adaptive filter (205) is used, see Figure 122. In this case the benefits over conventional simulations with lidar simulation and wind evolution models (Bossanyi, 2012) are that effects such as measurement errors and delays, real wind evolution, and site specific problems can be included into the simulations. If used along with the ISC controller, the simulated turbine's reaction will be close to the measured turbine data due to the fact that the used estimation of the rotor effective wind speed v_{0R} is an inverse process to the simulation. If used along with the DSC controller, it can be estimated in a realistic way, which effect the DSC would have produced in this specific situation. Furthermore, the DSC can be tuned to the real data.

A set of simulations with different $\hat{k}$ and τ are done. Figure 123 shows the changes from the DSC to the ISC in the standard deviation of λ and damage equivalent loads (DEL) on the low-speed shaft. The optimal values for $\hat{k} = 0.025$ rad/m and $\tau = 1$ s from this brute force optimization (minimizing $\sigma(\lambda)$) are close to the value from Section 9.5. This confirms, that it is important to filter the data according to this specific correlation.

Here, the standard deviation $\sigma(\lambda)$ can be reduced from 0.527 to 0.328, resulting in a power production increase of 0.3%, which is close to the theoretical value of 0.2% from Figure 123. The loads on the shaft are approximately doubled. This proofs, that only marginal benefit can be gained by tracking the optimal tip speed ration, which does not justify the usuage due to the higher loads on the shaft.

9.6.3 Discussion

The fluctuation of the tip speed ratio can be used as a measure for the potential of energy optimization. Assuming the distribution of the tip speed ratio $\varphi_{\lambda_{opt};\sigma}$ to be Gaussian with mean λ_{opt} and a standard deviation $\sigma(\lambda)$, then the generated power can be estimated by

$$P_{el}(\sigma(\lambda)) = P_{el,max} \int_{-\infty}^{\infty} \varphi_{\lambda_{opt};\sigma(\lambda)} c_P(\lambda) d\lambda. \tag{210}$$

The collected data from the CART3 field testing justify a Gaussian distribution (Schlipf et al., 2013b). In Figure 123 this potential is quantified for the CART3.

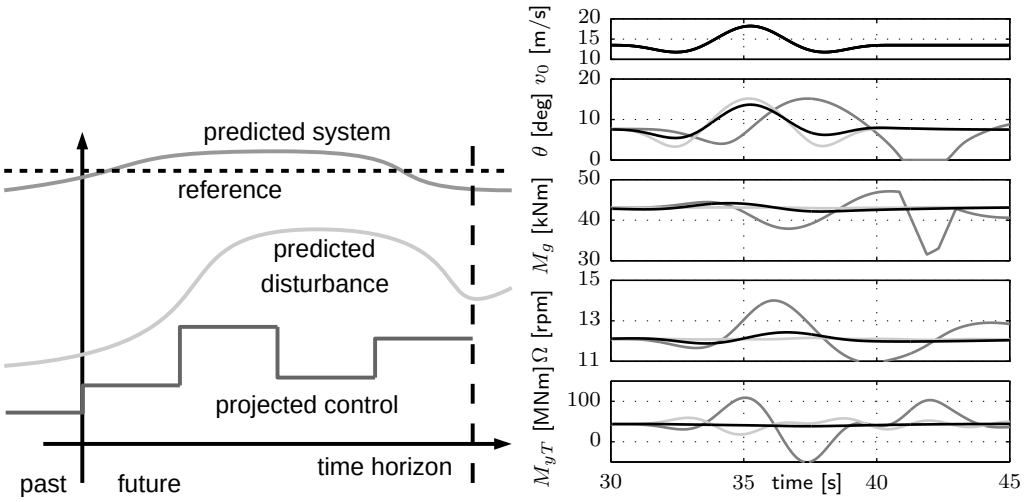

Figure 124: (left) Principle of NMPC. (rigth) Reaction to an EOG in case of perfect measurement using the 5 MW NREL turbine in FAST (Jonkman et al., 2009): Baseline controller only (dark gray), baseline with feedforward (light grey) and NMPC (black).

9.7 Nonlinear Model Predictive Control

Model predictive control (MPC) is an advanced control tool, which predicts the future behavior of the system using an internal model and the current measurements. With this information the control actions necessary to regulate the plant are computed by solving an optimal control problem over a given time horizon. Part of the solution trajectory for the control inputs are transfered to the system, new measurements are gathered and the optimal control problem is solved again. The feedforward controller presented in the previous sections are updates to existing pitch and torque feedback controllers. In contrast the MPC is a control strategy which in the presented case controls pitch angle and generator torque independently from the common feedback controllers. This provides the possibility for further improvements, but also makes real applications more complex. Here, the basic principle and simulation results of a nonlinear model predictive control (NMPC) are presented. More details can be found in Schlipf et al. (2012b,d).

9.7.1 Controller Design

There are several advantages of MPC in general. One is that it can handle multi-variable and non-quadratic (different number of inputs and outputs) control tasks naturally: additional control inputs or outputs will merely increase the number of optimization variables. Another advantage is that it considers actuator and system constraints during solving the optimal control problem. Furthermore, it provides a framework for incorporating a disturbance preview dynamically and tuning of MPC controllers is done intuitively by changing weights of a definable objective function. However, the main advantage of MPC is that it is in a mathematically sense an optimal controller. Solving the optimal control problem is not an easy task and several methods exist. Independent of the used method, the basic principle of model predictive control is illustrated in Figure 124 using piecewise constant parametrization: Future control action is planned to fulfill the control goal, e.g. reference signal tracking, considering a predicted disturbance. The considered optimal wind turbine control problem can be described by the following problem: The objective is to find the optimal control trajectory which minimizes the cost function, which is defined as the integral over the time horizon of the objective function from the actual time to the final time, with the reduced nonlinear model (192) and the set of constraints. The crux of designing the NMPC is to translate the verbal formulation of the control goal to a mathematical formulation. In wind energy the overall goal of development can be stated very roughly as “minimizing energy production cost”. In

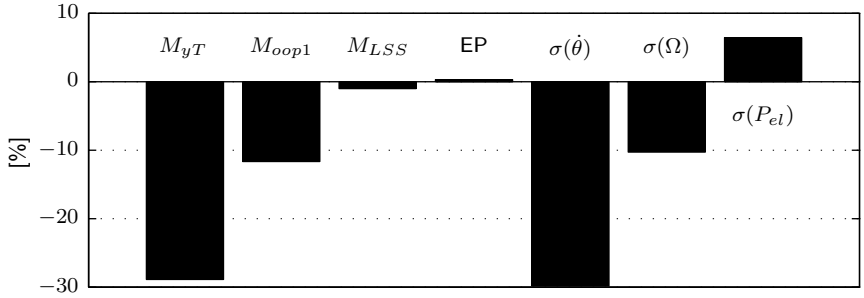

Figure 125: Overall improvement for the NMPC with respect to the baseline: Lifetime weighted DEL for tower base fore-aft bending moment M_{yT}, out-of-plane blade root bending moment of blade 1 M_{oop1} and low-speed shaft torque M_{LSS}, lifetime energy production, lifetime weighted standard deviation of pitch rate, rotor speed and electrical power.

classic wind turbine control (Burton et al., 2001) this is in general done by tracking optimal tip speed ratio below a certain wind speed defined as rated wind speed and by limiting rotor speed and power above the rated wind speed. The used objective function and constraints can be found in Schlipf et al. (2012b).

The optimal control problem is converted by the Direct Multiple Shooting method (Findeisen, 2005) into a nonlinear program. The control inputs are discretized in piecewise constant stages and the ODEs of the model are solved numerically on each interval. The optimization is performed over the set of initial values and the control outputs. Additional constraints are applied to ensure that the states at the end of each stage coincide with the initial conditions of the subsequent stage.

The nonlinear program can be solved iteratively with Sequential Quadratic Programming (SQP). The separation of the optimization problem into multiple stages results in a faster solution. Here Omuses (Franke, 1998) is used, a front-end to the large-scale SQP-type nonlinear optimization solver HQP.

9.7.2 Simulation Results

In a first step the different control strategies are compared with their reaction to gusts. For this purpose, hub-height time series are created with extreme operation gusts at $v_{rated} + 2$ m/s $= 13.2$ m/s. At first the simulations are run with the reduced nonlinear model such that the internal model and the simulation model are identical. Furthermore, the wind speed is directly fed into the NMPC assuming perfect measurements and the tower states are assumed to be measurable. This is done to make results more apparent and to show the effect of different optimization goals: The NMPC tries to reduce rotor speed variation and the tower movement. Figure 124 compares the pitch angle, generator torque, rotor speed, and tower base fore-aft bending moment for the baseline controller, the feedforward controller of Section 9.5 and the NMPC. The NMPC and the feedforward controller are able to minimize the rotor speed deviation. The feedforward controller only uses the pitch angle to achieve this goal. The NMPC additionally uses the generator torque to achieve the minimization of the tower movement and the variation of the rotor speed due to its competence to incorporate multivariable control.

In a second step various simulations with a set of turbulent TurbSim wind fields are conducted, featuring A-type turbulence intensity according to IEC 61400-1 and a Rayleigh distribution with $C = 12$ m/s, to estimate the benefit for fatigue load reduction. The adaptive filter (205) and a nonlinear estimator (Schlipf et al., 2012b) are used.

Figure 125 summarizes the results for all 33 simulations. Even if the NMPC controller is computationally more complex, the framework provides a high performing benchmark for development and comparison of less computationally-complex controllers.

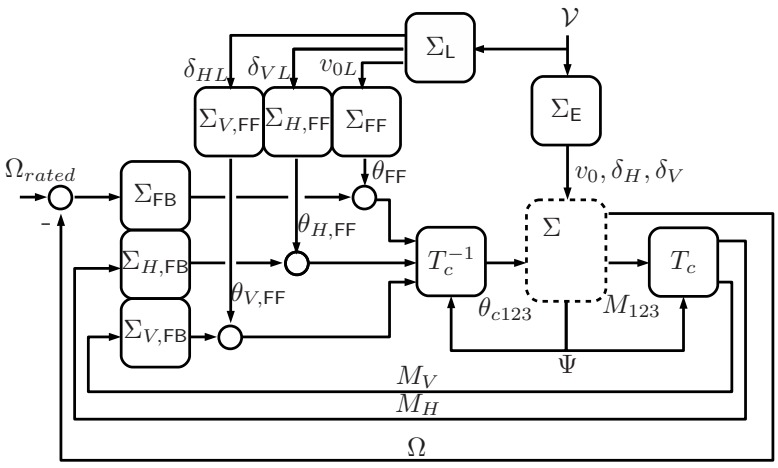

Figure 126: Cyclic pitch feedforward control: The feedforward controllers try to compensate the effects of the wind field $\mathcal{V}$ on the rotor speed Ω and the horizontal and vertical blade root bending moments, M_H and M_V.

9.8 Lidar Assisted Cyclic Pitch Control

The block diagram in Figure 126 illustrates the used feedforward control schema for the cyclic pitch control problem. More details can be found in Dunne et al. (2012), Schlipf et al. (2010b) and Laks et al. (2011).

The collective pitch controller is extended by two additional control loops: The flapwise blade root bending moments of the three blades M_{123} are transformed by the Coleman transformation T_c into a yaw and tilt moment M_H and M_V. These signals are fed back into two additional feedback controllers $\Sigma_{H,\mathsf{FB}}$ and $\Sigma_{V,\mathsf{FB}}$. Here, standard PI controllers are used following those of Bossanyi et al. (2012). The horizontal and vertical blade root bending moment M_H and M_V are mainly disturbed by the horizontal and vertical shear δ_H and δ_V. The shears can also be estimated by a lidar system (see Section 9.2) and can be used to calculate the feedforward updates $\theta_{H,\mathsf{FF}}$ and $\theta_{H,\mathsf{FF}}$ for the horizontal and vertical control loop. Static functions are proposed, which can be obtained from simulations or from modeling:

$$\theta_{H,\mathsf{FF}} = g_H \delta_{HL} \tag{211}$$

$$\theta_{V,\mathsf{FF}} = g_V \delta_{VL}$$

Furthermore, the same filter (205) is used to avoid wrong pitch action. Also the time tracking issue is solved similar to the collective pitch feedforward controller: The feedforward update is added to the feedback with the prediction time τ before the shears reach the turbine.

To demonstrate the benefit of lidar assisted cyclic pitch control, a collective pitch feedback only controller is compared to a cyclic pitch feedback only controller and a combined collective and cyclic feedback and feedforward controller. A wind field with mean wind speed $\bar{u} = 16$ m/s and a turbulence intensity of 18% is used. Figure 127 shows the power spectral densities of pitch rate and out-of-plane blade root bending moment of blade 1. Both individual pitch controllers decrease variation of the blade root bending moment especially at the $1P$ frequency, but only the feedforward controller can reduce the loads around 0.1 Hz due to the collective feedforward part. Further investigations have to be done to investigate, whether similar load reduction can be obtained without the cyclic feedforward part. A validation of the lidar reconstructed rotor effective wind characteristics can be achieved by comparing to those estimated from turbine data. Figure 128 compares the shears obtained from model (186) with shears obtained by a simple estimation from blade root bending moment, showing as expected a better correlation for δ_V than for δ_H. Further investigations have to be done in addition to investigate, if the correlation between the lidar measurement and the turbine reaction regarding the shears is sufficient to use it for feedforward control.

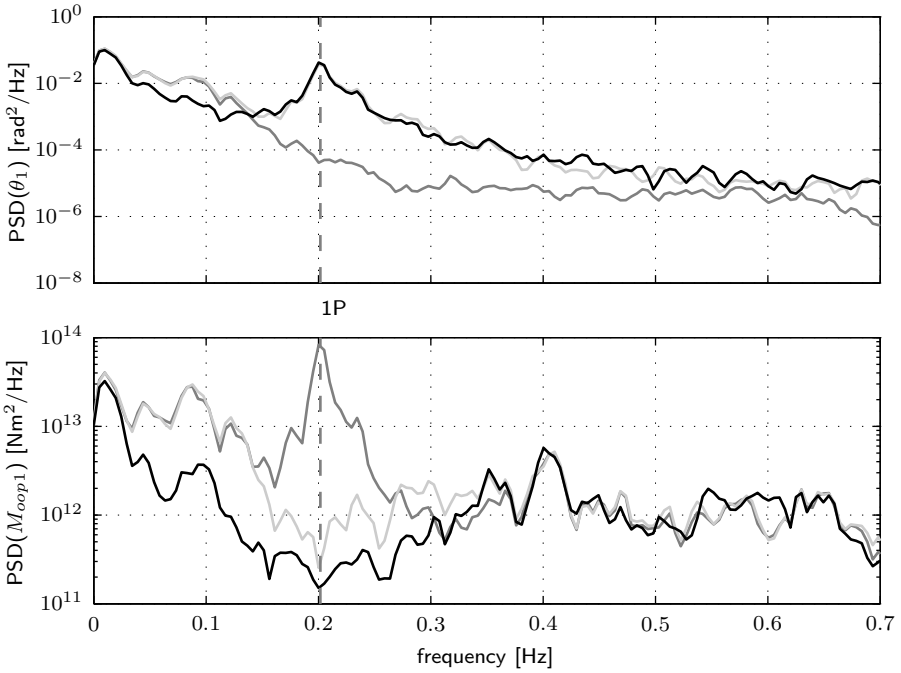

Figure 127: Power spectral density of pitch rate and out-of-plane blade root bending moment of blade 1: Collective pitch feedback (dark gray), cyclic pitch feedback (light gray) and combined collective and cyclic feedback and feedforward (black). The cyclic pitch controller decrease the spectra around the 1P frequency at the expense of higher pitch action in this frequency section.

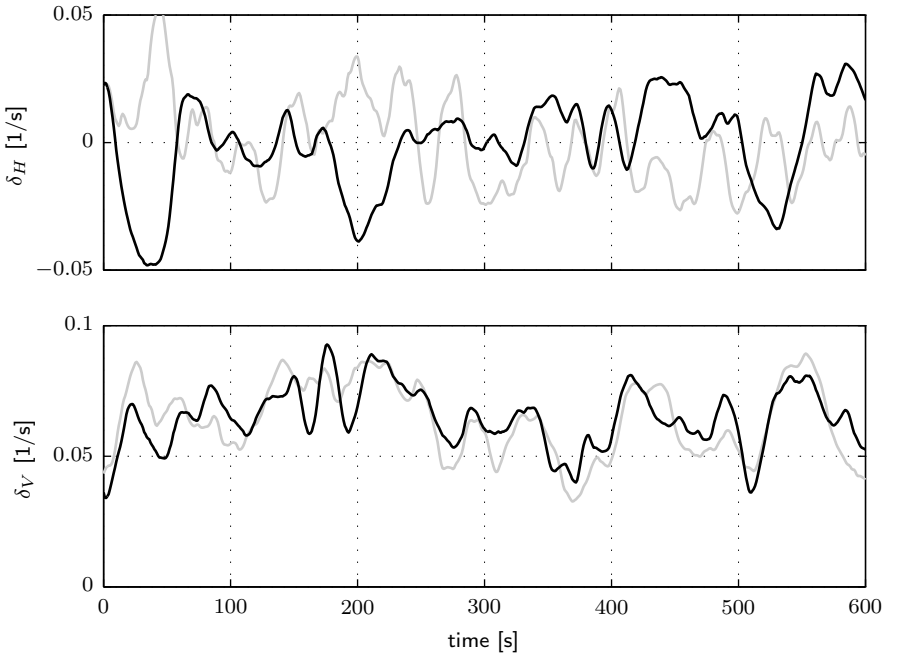

Figure 128: Estimated (1 min average) shears using lidar (black) and turbine data (gray). The correlation of the vertical shear (bottom) is higher than the correlation of the horizontal shear (top).

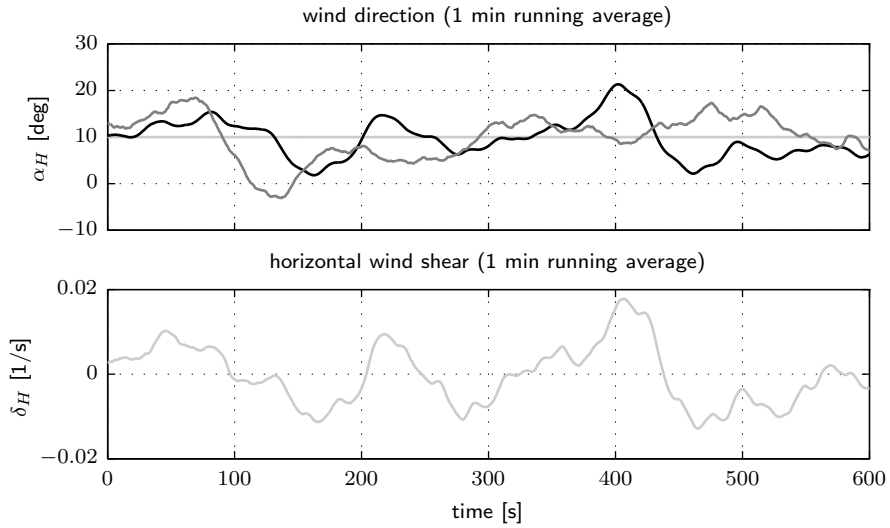

Figure 129: Misalignment and horizontal shear. From a wind field (light gray), lidar estimation (black) and sonic anemometer simulation (dark gray).

9.9 Lidar Assisted Yaw Control

Due to the large moment of inertia of the rotor, the nacelle is aligned with the wind with slow rates and only, if the misalignment exceeds a certain value (Hau, 2008). The demand signal is normally calculated from a nacelle mounted wind vane or sonic anemometer. These sensors are heavily disturbed for an operating turbine and are measuring at only one single point. A nacelle mounted lidar system avoids these disadvantages, being able to measure the undisturbed inflow over the entire rotor area. The first part of this section shows the capability and the problems of a simulated lidar system. In the second part data is analyzed and finally in the third part the improvements in energy yield by lidar assisted yaw control are discussed theoretically. More details can be found in Schlipf et al. (2011).

9.9.1 Simulation Using Generic Wind

The scope of the presented simulation study is to test if the methods presented in Section 9.2 are robust and can be applied to turbulent wind fields. This is not obvious, because the simulation model of the wind (here IEC Kaimal) and of the lidar (198) are more complex than the wind (189) and lidar (184) model used in the reconstruction. Similar work has been presented (Kragh et al., 2011), using an empiric reconstruction method and Mann turbulence.

The 33 Class A wind fields from Section 9.6 are generated with a horizontal mean flow angle of $\alpha_H = 10$ deg. The 10 min-wind fields are scanned again with the mentioned lidar simulator, imitating the SWE-lidar system (Rettenmeier et al., 2010) using a Lissajous-like trajectory. The misalignment detected by the lidar α_{HL} is estimated with the model (189) using those focus points from the last n points, where no impact with the turbine blades is simulated. Due to the positioning on top of the nacelle, similar to the one used in the experiment, this usually results in a loss of $\approx 30\%$. The resulting α_{HL} signal is very oscillating and for better illustration a 1 min running average is used in Figure 129. Due to the effects described in Section 9.2 the misalignment signal estimated with the lidar is disturbed by the horizontal shear. For comparison, the misalignment signal of a point measurement is plotted, which could be obtained from an undisturbed sonic anemometer on hub height.

For all 33 simulations the error of the misalignment estimation in the 10 min mean is below 1 deg due to the fact that the mean of the effective horizontal shear for the wind field is close to zero. The results of this simulation study show that with the proposed method of wind reconstruction it is possible for a simulated lidar to estimate the misalignment of a turbine in the scale of 10 min similar to the simulated undisturbed sonic anemometer.

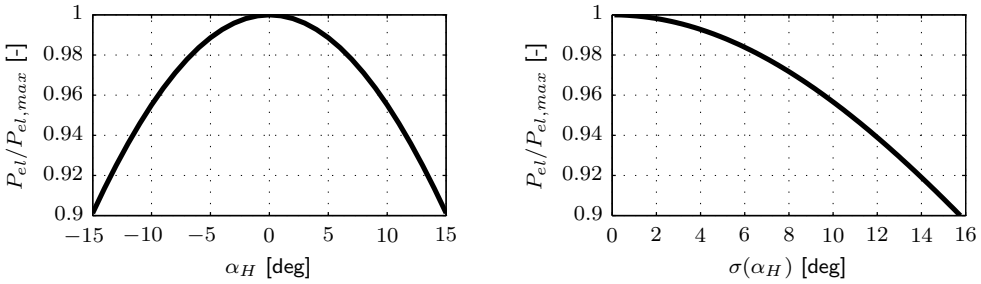

Figure 130: Power loss due to static (left) and dynamic (right) misalignment.

9.9.2 Simulation Using Real Data

From the simulation study above it is hard to estimate the improvement of lidar assisted yaw control compared to the standard control. Therefore, a simulation study can be done using data from a real experiment. The absolute yaw direction signal is superposed with the relative, 10 min averaged misalignment signals from the nacelle mounted lidar and sonic anemometer. With this method it can be simulated, how the turbine would have been yawed for both instruments, if the same yaw control strategy is applied. Finally, the resulting yaw misalignment for both instruments can be calculated by comparing the simulated turbine positions with the lidar wind direction, assuming the lidar is able to perfectly estimate the averaged misalignment. Due to the average time and the threshold in the control strategy, the difference in the fluctuation of both signals is relatively low.

9.9.3 Discussion

Both studies above show, the yaw misalignment can be divided in a static and a dynamic subproblem. In reality there will be a mixture of both, but this perception is helpful to rate the benefits which can be achieved by using a lidar system for yaw control. If there is a static misalignment $\bar{\alpha}_H$, the loss in power can be modeled as (Burton et al., 2001):

$$P_{el}(\bar{\alpha}_H) = P_{el,max} \cos^3(\bar{\alpha}_H). \tag{212}$$

Figure 130, shows e.g. that $\approx 10\%$ of power is lost, if the turbine is misaligned by ≈ 15 deg to one side. This value can be considered as a lower bound, because a misalignment in full load operation will not have an effect on the power. A static misalignment can be solved by better calibration of the standard nacelle anemometer and does not need a constant use of a lidar system. In the case of the investigated data the detected static misalignment of 0.7 deg only would cause a power loss of 0.02%. A constant use of a nacelle mounted lidar system is justified, if the fluctuation of yaw misalignment can be reduced. Similar to the discussion in Section 9.6.3 the misalignment can be assumed to be Gaussian distributed with zero mean and a standard deviation $\sigma(\alpha_H)$. Then the loss in power can be modeled by:

$$P_{el}(\sigma(\alpha_H)) = P_{el,max} \int_{-\infty}^{\infty} \varphi_{0;\sigma(\alpha_H)} \cos^3(\alpha_H) d\alpha_H. \tag{213}$$

The loss in power due to the dynamic misalignment is plotted in Figure 130 and again is only applicable to partial load operation. The reduction of $\sigma(\alpha_H)$ and an improvement of the power output is limited to the control strategy: a reduction to 0 deg would require immediate yawing of the rotor which is neither feasible nor reasonable due to the induced loads. In the presented investigation a reduction from 6.4 deg to 4.1 deg yield to an improvement from $99.3\% - 98.2\% = 1.1\%$ using (213). This low value despite of assumed perfect reconstruction of the alignment by the lidar system gives an estimation of improvement which can be expected.

9.10 Conclusion and Outlook

Lidar systems are able to provide preview information of wind disturbances at various distances in front of wind turbines. This technology paves the way for new control concepts, helping to compensate changes in the inflowing wind field. The complexity of the wind field, the limitation due to the measurement principle and the combined aero-elastic character of wind turbines makes this an interdisciplinary and challenging task. This field of research has increased significantly in recent years and several controllers have been proposed for load reduction or increasing the energy yield.

In this work a method is presented to reconstruct wind characteristics based on lidar measurements and shortcomings are shown. This method is used in various approaches to increase the energy production and to reduce loads of wind turbines: Collective pitch feedforward control and direct speed control uses the knowledge of the incoming wind speed to calculate a control update to existing feedback controllers. Collective pitch feedforward control is a promising strategy to reduce extreme and fatigue loads and has been successfully tested. Filtering the lidar signal is an important issues, because not all turbulences can be measured. The filter can be designed based on the correlation between the lidar measurement and the reaction of the wind turbine. With the direct speed control only marginal benefit can be gained. This is due to the fact that the standard variable speed control is already close to the aerodynamic optimum. The approach of the Nonlinear Model Predictive Control differs from the feedforward approaches: the future behavior of a wind turbine is optimized by solving an optimal control problem repetitively using the wind speed preview adjusting simultaneously the pitch angle and the generator torque. Therefore, loads on tower, blades and shaft can be further reduced especially for wind conditions near rated wind speed. Further load reduction of the blades can be gained with cyclic pitch feedforward control, extending the feedforward approach to reduce also tilt and yaw moments of the rotor. Another approach uses the wind direction estimation by a lidar system for yaw control. Here, an increase of energy production by a couple of percent can be expected, depending on the control strategy and the inhomogeneity of the wind.

Acknowledgement

This research is funded by the German Federal Ministry for the Environment, Nature Conservation and Nuclear Safety (BMU) in the framework of the German joint research project "LIDAR II - Development of nacelle-based LIDAR technology for performance measurement and control of wind turbines" . Thanks all the people getting the lidar systems and the different measurement campaigns working, special thanks to Jan Anger, Oliver Bischoff, Florian Haizmann, Martin Hofsäß, Andreas Rettenmeier and Ines Würth of the SWE Lidar group, Paul Fleming, Andrew Scholbrock and Alan Wright from NREL, my supervisors Po Wen Cheng, Martin Kühn and Lucy Pao and my students Valeria Basterra, Patrick Grau, Stefan Kapp, Timo Maul and Davide Trabucchi. Thanks to Björn Siegmeier from AREVA Wind GmbH for his help and the access to the turbine measurement data.

Notation

DEL	Damage Equivalent Loads
EOG	extreme operating gust
NMPC	Nonlinear Model Predictive Control
PI	proportional-integral (controller)
a	distance to focus point
A	constant variables for least squares method
c_P,c_T	power and thrust coefficient
d	system disturbance
D	rotor diameter
f_i	focus length of measurement point i

f_L	weighting function
G_{RL}	transfer function from the lidar estimate to the rotor effective wind speed
i	gearbox ratio
J	sum of the moments of inertia about the rotation axis of the rotor hub
$\hat{k}$	maximum coherent wave number
m	known variables for least squares method
m_{Te}, c_{Te}, k_{Te}	the tower equivalent modal mass, structural damping and bending stiffness
M_g	generator torque
M_a, F_a	aerodynamic torque and aerodynamic
M_{yT}	tower fore-aft bending moment
M_{LSS}	low speed shaft torque
M_{oop1}	out-of-plane bending moment
n	number of measurements
R	rotor radius
S_{RL}	cross spectrum between the lidar estimate to the rotor effective wind speed
S_{LL}	auto spectrum of the lidar estimate of the rotor effective wind speed
S_{RR}	auto spectrum of the rotor effective wind speed
s	unknown variables for least squares method
$T_{\text{Taylor},i}$	time delay based on Taylor's Hypothesis of Frozen Turbulence from point i
T_{scan}	time to finish a full scan
T_{buffer}	time to buffer data before applying the feedforward command
T_{filter}	time delay due to filtering
u	system input
u_i, v_i, w_i	local wind components in measurement point i
$\bar{u}$	mean wind speed
v_0	rotor effective wind speed
v_{0L}	estimate of rotor effective wind speed from lidar data
v_{0Lf}	filtered estimate of rotor effective wind speed from lidar data
v_{0R}	estimate of rotor effective wind speed from turbine data
$v_{los,i}$	line-of-sight wind speed in measurement point i
v_{rel}	relative wind speed
x	system states
x_i, y_i, z_i	coordinates of measurement point i in lidar coordinate system
x_{Wi}, y_{Wi}, z_{Wi}	coordinates of measurement point i in wind coordinate system
x_T	tower top displacement
y	system output
α_H, α_V	horizontal and vertical inflow angle
γ^2_{RL}	coherence between the lidar estimate to the rotor effective wind speed
δ_H, δ_V	horizontal and vertical shear
λ	tip speed ratio
ξ, ω	damping factor and undamped natural frequency of the pitch actuator
ρ	air density
τ	prediction time of a signal
$\varphi_{\bar{x};\sigma(x)}$	Gaussian probability density function depending on mean $\bar{x}$ and standard deviation $\sigma(x)$
θ, θ_c	collective pitch angle and collective pitch angle demand
θ_{FF}	feedforward pitch angle
Ω, Ω_g	rotor and generator speed
$\mathcal{V}$	wind field

References

D. Schlipf, T. Fischer, C. E. Carcangiu, M. Rossetti, and E. Bossanyi, "Load analysis of look-ahead collective pitch control using LiDAR," in *Proceedings of the German Wind Energy Conference DEWEK*, Bremen, Germany, 2010.

D. Schlipf, P. Fleming, F. Haizmann, A. Scholbrock, M. Hofsäß, A. Wright, and P. W. Cheng, "Field testing of feedforward collective pitch control on the CART2 using a nacelle-based lidar scanner," in *Proceedings of The Science of Making Torque from Wind*, Oldenburg, Germany, 2012.

A. Scholbrock, P. Fleming, L. Fingersh, A. Wright, D. Schlipf, F. Haizmann, and F. Belen, "Field testing LIDAR based feed-forward controls on the NREL controls advanced research turbine," in *51th AIAA Aerospace Sciences Meeting Including the New Horizons Forum and Aerospace Exposition*, Dallas, USA, 2013.

D. Schlipf, S. Kapp, J. Anger, O. Bischoff, M. Hofsäß, A. Rettenmeier, U. Smolka, and M. Kühn, "Prospects of optimization of energy production by LiDAR assisted control of wind turbines," in *Proceedings of the EWEA Annual event*, Brussels, Belgium, 2011.

D. Schlipf, D. J. Schlipf, and M. Kühn, "Nonlinear model predictive control of wind turbines using LIDAR," *Wind Energy*, 2012.

F. Dunne, D. Schlipf, L. Y. Pao, A. D. Wright, B. Jonkman, N. Kelley, and E. Simley, "Comparison of two independent lidar-based pitch control designs," in *Proc. 50th AIAA Aerospace Sciences Meeting Including the New Horizons Forum and Aerospace Exposition*, 2012.

D. Schlipf, A. Rettenmeier, M. Hofsäß, M. Courtney, and P. W. Cheng, "Model based wind vector field reconstruction from lidar data," in *Proceedings of the German Wind Energy Conference DEWEK*, Bremen, Germany, 2012.

J. Jonkman and M. L. Buhl, "FAST user's guide," NREL, Tech. Rep. NREL/EL-500-38230, August 2005.

B. J. Jonkman and M. L. Buhl, "TurbSim user's guide," NREL, Tech. Rep. NREL/TP-500-41136, April 2007.

C. L. Bottasso, A. Croce, B. Savini, W. Sirchi, and L. Trainelli, "Aero-servo-elastic modelling and control of wind turbines using finite-element multibody procedures," *Multibody System Dynamics*, vol. 16, pp. 291–308, 2006.

J. Jonkman, S. Butterfield, W. Musial, and G. Scott, "Definition of a 5-MW reference wind turbine for offshore system development," *Technical Report NREL/TP-500-38060*, 2009.

E. van der Hooft and T. G. van Engelen, "Estimated wind speed feed forward control for wind turbine operation optimization," *European Wind Energy Conference, London*, vol. 1, p. 9, 2004.

D. Schlipf, S. Schuler, P. Grau, F. Allgöwer, and M. Kühn, "Look-ahead cylcic pitch control using LiDAR," in *Proceedings of The Science of making Torque from Wind*, Heraklion, Greece, 2010.

J. P. Cariou, "Pulsed lidars," in *Remote Sensing for Wind Energy. Risøreport Risø-I-3184(EN)*. Roskilde, Denmark: A. Peña and C. B. Hasager, June 2011, pp. 65–81, Risø-DTU.

A. Rettenmeier, O. Bischoff, M. Hofsäß, D. Schlipf, J. J. Trujillo, and M. Kühn, "Wind field analysis using a nacelle-based lidar system," in *Presentation at the European Wind Energy Conference*, Warsaw, Poland, 2010.

J. S. Bendat and A. G. Piersol, *Random data; analysis and measurement procedures*. New York, USA: John Wiley & Sons, 1971.

E. Simley and L. Pao, "Correlation between rotating LIDAR measurements and blade effective wind speed," in *51th AIAA Aerospace Sciences Meeting Including the New Horizons Forum and Aerospace Exposition*, Dallas, USA, 2013.

D. Schlipf and P. W. Cheng, "Adaptive Vorsteuerung für Windenergieanlagen," *at - Automatisierungstechnik*, vol. 61, pp. 329–338, 2013.

D. Schlipf, J. Mann, and P. W. Cheng, "Model of the correlation between lidar systems and wind turbines for lidar assisted control," *submitted to Journal of Atmospheric and Oceanic Technology*, 2013.

T. Burton, N. Jenkins, D. Sharpe, and E. Bossanyi, *Wind Energy Handbook*. New York, USA: John Wiley & Sons, 2001.

D. Schlipf, P. Fleming, S. Kapp, A. Scholbrock, F. Haizmann, F. Belen, A. Wright, and P. W. Cheng, "Direct speed control using lidar and turbine data," in *Proceedings of the American Control Conference*, Washington, USA, 2013.

E. Bossanyi, "Un-freezing the turbulence: improved wind field modeling for investigating lidar-assisted wind turbine control," in *Proceedings of the EWEA Annual event*, Copenhagen, Denmark, 2012.

D. Schlipf, L. Y. Pao, and P. W. Cheng, "Comparison of feedforward and model predictive control of wind turbines using LIDAR," in *Proceedings of the Conference on Decision and Control*, Maui, USA, 2012.

R. Findeisen, "Nonlinear model predictive control: A sampled-data feedback perspective," Ph.D. dissertation, Universität Stuttgart, 2005.

R. Franke, "Omuses - a tool for the optimization of multistage systems and HQP a solver for sparse nonlinear optimization," TU Ilmenau, Tech. Rep., 1998.

J. Laks, L. Y. Pao, E. Simley, A. Wright, N. Kelley, and B. Jonkman, "Model predictive control using preview measurements from LIDAR," in *Proceedings of the 49th AIAA Aerospace Sciences Meeting Including the New Horizons Forum and Aerospace Exposition*, Orlando, USA, 2011.

E. Bossanyi, B. Savini, M. Iribas, M. Hau, B. Fischer, D. Schlipf, T. van Engelen, M. Rossetti, and C. E. Carcangiu, "Advanced controller research for multi-MW wind turbines in the UpWind project," *Wind Energy*, vol. 15, no. 1, pp. 119–145, 2012.

E. Hau, *Windkraftanlagen*, 4th ed. Springer, 2008.

A. Kragh, M. Hansen, and T. Mikkelsen, "Improving yaw alignment using spinner based LIDAR," in *Proc. 49th AIAA Aerospace Sciences Meeting Including the New Horizons Forum and Aerospace Exposition*, 2011.

10 Lidars and wind turbine control – Part 2

Eric Simley[1], Fiona Dunne[1], Jason Laks[2], and Lucy Y. Pao[1]
[1]*Department of Electrical, Computer, and Energy Engineering, University of Colorado, Boulder, CO, USA*
[2]*National Renewable Energy Laboratory, Golden, CO, USA*

10.1 Introduction

Modern utility-scale wind turbines are typically controlled using yaw, generator torque, and blade pitch actuation (Pao and Johnson, 2011). The yaw motor is used to align the rotor with the wind direction for the purpose of maximizing power capture. Generator torque is controlled during below-rated (region 2) operation to maximize power capture by maintaining the optimal tip speed ratio. In above-rated conditions (region 3), the blades are pitched to regulate rotor speed and power capture by limiting the amount of aerodynamic torque produced by the rotor. In addition to regulating rotor speed, region 3 control systems are often designed to reduce structural loads on the turbine caused by turbulence.

A block diagram of a wind turbine's feedback control system is shown in Fig. 131. In region 2, feedback measurements of generator speed are used to maintain the optimal tip speed ratio by adjusting generator torque. The generator torque command is traditionally set equal to the square of the generator speed multiplied by a constant whose value is chosen to maintain the optimal tip speed ratio (Pao and Johnson, 2011). If the wind speed is above the turbine's rated wind speed, the region 3 controller employs blade pitch control to decrease the fraction of the available power in the wind extracted by the rotor. Feedback measurements of generator speed are input to a feedback blade pitch controller designed to both regulate rotor speed to the rated value and reduce structural loads caused by fluctuations in wind speed, which act as a disturbance to the wind turbine. With a single feedback measurement of generator speed, all of the blades are usually pitched together using a strategy called collective pitch (CP) control. When additional feedback measurements are available, such as the blade root bending moment at each blade, the blades can be pitched separately using individual pitch (IP) control (Bossanyi, 2005). Utilizing separate pitch commands for each blade allows for the reduction of loads due to variations in wind speed across the rotor disk, especially blade loads at the once-per-revolution (1P) frequency.

A drawback to feedback control is that the wind disturbance must first act on the turbine before a corrective control action can be made based on a feedback measurement. To address this delay, feedforward control has been proposed, whereby a preview measurement of the

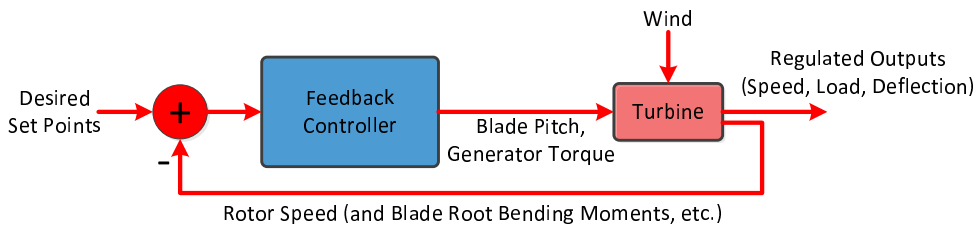

Figure 131: Feedback control scenario.

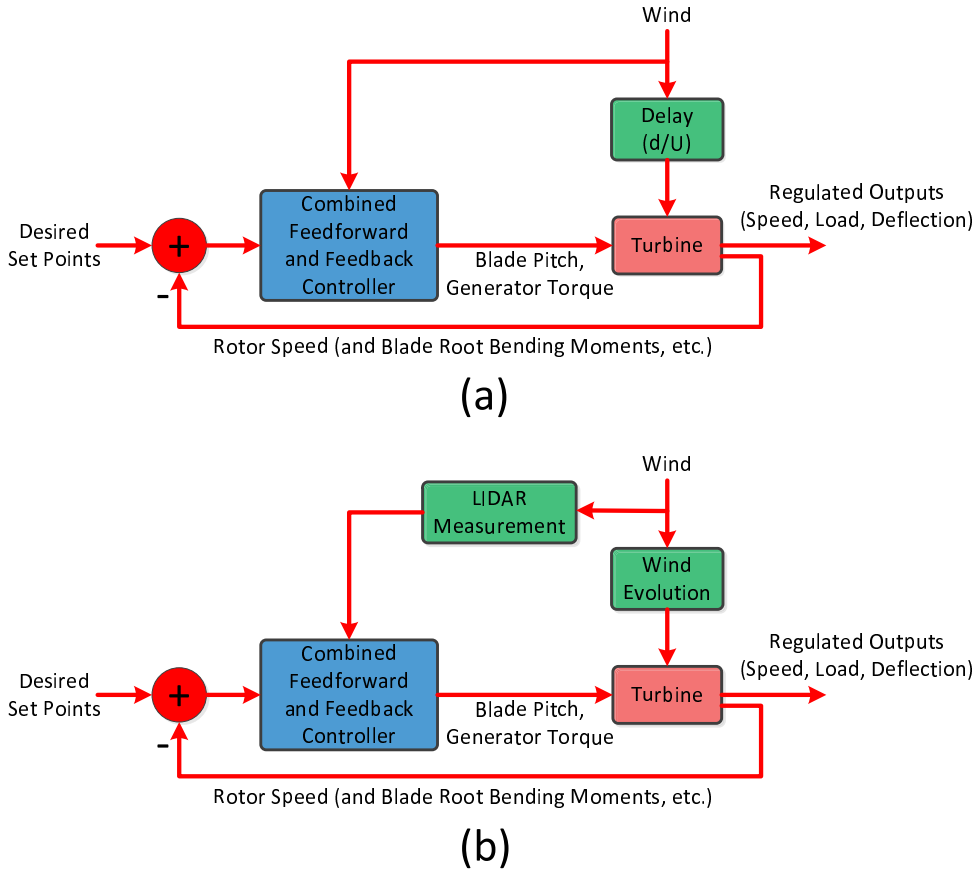

Figure 132: Combined feedback and feedforward control scenarios with (a) perfect preview measurements and (b) lidar measurements and the effects of wind evolution.

wind disturbance is used directly as an input to the controller (see Fig. 132a). Original work in feedforward control focused on regulating power capture in fluctuating wind conditions using preview measurements provided by an upstream meteorological tower (Kodama et al., 1999). Later, research concentrated on using lidar to remotely sense the wind speeds from the turbine nacelle (Harris et al., 2005).

Lidar-based control has been investigated for use in both below-rated and above-rated conditions. In below-rated region 2 control, turbine-mounted lidar measurements have been proposed for correcting yaw error (Schlipf et al. 2011; Kragh et al. 2013) and increasing power capture (Schlipf et al. 2011; Wang et al. 2012a; Bossanyi et al. 2012b). Through simulation, it was found that a scanning lidar system can effectively estimate yaw error and fine-tune the yaw alignment of a turbine as long as the inflow is not too complex (Kragh et al., 2013). Lidar-assisted feedforward control in below-rated conditions has been shown to provide a small increase in power capture $(0.1 - 2\%)$. However, the additional structural loads caused by aggressively tracking the optimal tip speed ratio usually outweigh the power capture improvement (Schlipf et al. 2011; Bossanyi et al. 2012b).

Recently, much of the lidar-based feedforward control research has focused on regulating rotor speed and mitigating structural loads in above-rated conditions, where potential for significant load reduction has been shown. As with feedback control, lidar-assisted control in region 3 can be classified as either collective pitch or individual pitch control. Collective pitch feedforward control strategies use the lidar measurements to estimate the effective wind speed that the entire rotor will experience to regulate rotor speed and reduce tower and collective blade loads (Wang et al. 2012b; Schlipf et al. 2012b; Bossanyi et al. 2012b). Individual blade pitch control, however, allows for reduction of the loads experienced by each separate blade, which could also be transferred to non-rotating components on the

turbine (Bir, 2008). Information from lidar measurements must be used to estimate the wind speeds encountered by each individual blade. One class of controller designs uses information from lidar measurements to estimate the hub-height, horizontal shear, and vertical shear components of the wind, which are in turn used as inputs to the controller (Schlipf et al. 2010; Laks et al. 2011b; Bossanyi et al. 2012b). The other class of controllers uses a separate measurement of the expected wind speed for each individual blade (Dunne et al. 2011b; Laks et al. 2011b; Dunne et al. 2012). During the summer of 2012, a simple lidar-based collective pitch feedforward controller designed to regulate rotor speed was tested at the US National Renewable Energy Laboratory (NREL) with promising results (Scholbrock et al., 2013).

The simulation of lidar-based controllers is progressing toward more realistic preview measurement modeling. Preliminary research included the assumption that upstream wind speeds could be measured perfectly (Schlipf and Kühn 2008; Dunne et al. 2011b; Laks et al. 2011b). An additional assumption was that the measured wind speeds would reach the turbine unchanged after a delay time of d/U, where d is the preview distance and U is the mean wind speed (see Fig. 132a). The next generation of feedforward control simulations contained realistic lidar models including spatial averaging of the wind speeds along the lidar beam (discussed in Section 10.5.1) (Schlipf et al. 2009; Dunne et al. 2011a; Laks et al. 2011a; Simley et al. 2013c; Kragh et al. 2013). Recently, control simulations have included models of the important source of error commonly referred to as "wind evolution" (discussed in Section 10.5.3) (Bossanyi 2012; Laks et al. 2013). Wind evolution describes how the wind speeds change, or evolve, as they travel downstream toward the turbine. The more realistic lidar measurement scenario including wind evolution is shown in Fig. 132b. An additional source of measurement error that has recently been included in simulation is uncertainty in the time it takes for the measured wind to reach the rotor (Mirzaei et al., 2013).

10.1.1 Lidar Measurement Strategies

Several lidar technologies suitable for wind turbine control have been field tested in the past decade. Harris et al. (2007) performed the first turbine-mounted lidar test using a continuous-wave (CW) lidar (see Section 10.5.1) mounted on top of the nacelle. This lidar was simply configured to stare straight ahead into the wind and focus at a particular distance. Rettenmeier et al. (2010) employ a customized pulsed lidar system (see Section 10.5.1) that is also mounted on top of the nacelle. The pulsed lidar provides measurements at a number of points along the beam and can be aimed in any direction in front of the rotor using a mirror with two axes of motion. Mikkelsen et al. (2013) have developed a circularly scanning CW lidar that can be mounted in the hub, or spinner, of a turbine (see Fig. 133). This configuration allows for continuous measurements without periodic blockage from passing blades. Recently, Pedersen et al. (2013) have tested a CW lidar mounted directly on a turbine blade, allowing for direct measurement of the wind speed and angle-of-attack that a rotating blade will experience.

The lidar measurement analyses in the rest of this chapter assume a circularly scanning spinner-mounted lidar similar to the system developed by Mikkelsen et al. (2013). Figure 133 contains an illustration of the measurement scenario. The hub-mounted lidar measures a circle of wind with scan radius r at a preview distance d upstream of the rotor. Although it is possible to scan faster than the rotational speed of the rotor (Mikkelsen et al., 2013), the analyses in this chapter assume that the lidar spins with the rotor, allowing the lidar to measure the wind that a single blade will experience. The relative simplicity of this measurement scenario allows for careful analysis of measurement performance. Unless otherwise specified, the lidar investigations in this chapter are performed using the NREL 5-MW reference turbine model (Jonkman et al., 2009) which has a hub height of 90 m and a rotor radius of 63 m.

The remainder of this chapter is organized as follows. Section 10.2 presents the region 3 feedforward control scenario using a linear wind turbine model. The feedforward control strategy that minimizes the variance of an output error variable such as generator speed or a structural load is derived for the case of imperfect lidar measurements. An explanation of why measurement preview is required in feedforward wind turbine control is presented in

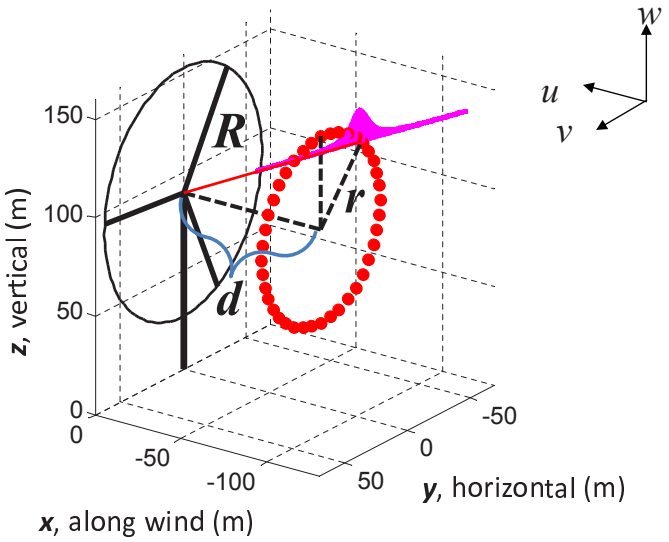

Figure 133: Measurement scenario for the 5-MW reference turbine. The variable d represents the preview distance upwind of the turbine where measurements are taken. r represents the radius of the scan circle and R indicates the 63 m rotor radius. The dots represent where measurements are taken for the circularly scanning lidar and the magenta curve illustrates the range weighting function along the lidar beam (see Section 10.5.1).

Section 10.3. Section 10.4 describes the wind speed quantity of interest for blade pitch control, referred to as "blade effective wind speed." Section 10.5 describes how measurements from a hub-mounted lidar can be used to estimate blade effective wind speed. The main sources of lidar measurement error are discussed here as well. The topics in Sections 10.2, 10.4, and 10.5 are combined to illustrate a lidar measurement design scenario in Section 10.6, with the objective of minimizing the mean square value of blade root bending moment using feedforward control. Examples of lidar-based feedforward controller designs using simulation are included in Sections 10.7 and 10.8. Finally, Section 10.9 summarizes the material presented in the chapter.

10.2 Wind Turbine Feedforward Control

The combined feedback/feedforward control scenario for above-rated conditions used in this chapter is described in Fig. 134. A blade pitch control loop using feedback from rotor speed regulates an output variable y (such as generator speed error or a structural load), which represents the deviation from a set point. Generator torque is controlled to be inversely proportional to generator speed to maintain the rated 5 MW of power (Jonkman et al., 2009). The feedback control loop is designed for the mean wind speed U such that any wind speed deviation acts as a disturbance w_t on the turbine. The feedback control loop is augmented with a blade pitch feedforward controller F which uses the preview wind disturbance measurement w_m, provided by a lidar. Additionally, a prefilter H_{pre} can be introduced between the lidar measurement and the feedforward controller to provide an estimate $\hat{w}_t$ of the wind disturbance based on w_m. The original upstream wind w_{orig} is measured by the lidar yielding the distorted measurement w_m. As w_{orig} travels downstream toward the turbine, it will undergo distortion due to wind evolution until it interacts with the turbine as w_t after a delay of d/U.

10.2.1 Feedforward Control Assuming Perfect Measurements

When feedforward is not used ($F = 0$), the output variable y is given by

$$y = T_{yw_t} w_t \tag{214}$$

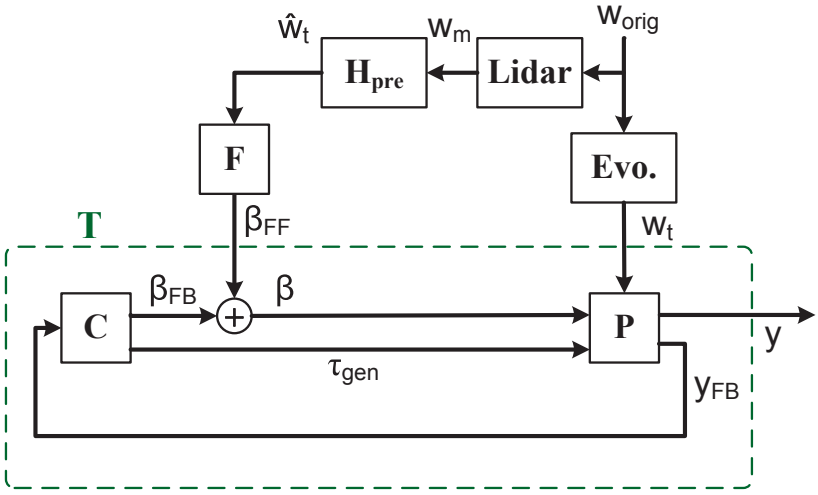

Figure 134: Block diagram of the feedforward control scenario. P is the linearized turbine model and C is the feedback controller, controlling blade pitch and generator torque deviations from the operating point using a measurement of generator speed error y_{FB}. T represents the turbine with feedback control, as enclosed in the dashed box. y is the output error variable of interest, which is intended to be regulated to 0. F represents the ideal feedforward controller (assuming perfect measurements) and H_{pre} is the prefilter used to estimate a preview of the wind disturbance w_t based on the lidar measurement w_m. w_{orig} is the original upstream wind speed which becomes w_m after lidar measurement and w_t after experiencing wind evolution and arriving at the turbine.

where T_{yw_t} is the transfer function from the wind disturbance w_t to y. With the introduction of feedforward control without a prefilter ($H_{pre} = 1$), y becomes a function of both w_t and w_m:

$$y = T_{yw_t} w_t + T_{y\beta_{FF}} F w_m \tag{215}$$

where $T_{y\beta_{FF}}$ is the transfer function from the feedforward blade pitch command β_{FF} to y. When measurements are perfect ($w_m = w_t$) and there is perfect turbine modeling, the feedforward controller that completely cancels the effect of the disturbance w_t on the turbine is given by

$$F = -T_{y\beta_{FF}}^{-1} T_{yw_t}, \tag{216}$$

which yields the output $y = 0$ in Eq. (215). In reality, non-minimum phase (unstable) zeros in $T_{y\beta_{FF}}$ can cause the ideal F to be unstable (Dunne et al., 2011b). In this case, a stable approximation to the ideal F is used (Dunne et al., 2011b). For the analysis in this chapter, however, it is simply assumed that $F = -T_{y\beta_{FF}}^{-1} T_{yw_t}$. When the measurements are not perfect ($w_m \neq w_t$), the output is

$$y = T_{yw_t} (w_t - w_m). \tag{217}$$

Due to the distorting effects of the lidar and wind evolution along with the spatial averaging of the wind caused by the area of the turbine rotor, in general $w_m \neq w_t$. In this case, the variance, or mean square magnitude, of y in the frequency domain is given by

$$\begin{aligned} \overline{|Y(f)|^2} &= |T_{yw_t}(f)|^2 \, \overline{|W_t(f) - W_m(f)|^2} \\ &= |T_{yw_t}(f)|^2 \left(S_{w_t w_t}(f) + S_{w_m w_m}(f) - 2\Re\left\{S_{w_t w_m}(f)\right\}\right) \end{aligned} \tag{218}$$

where $S_{w_t w_t}(f)$ represents the power spectral density (PSD) of the wind disturbance, $S_{w_m w_m}(f)$ is the PSD of the lidar measurement, $S_{w_t w_m}(f)$ is the cross-power spectral density (CPSD) between the wind disturbance and the lidar measurement, and $\Re\{\}$ indicates the real part of a complex value. The variance of y in the time domain is calculated by integrating Eq. (218) over all frequencies:

$$\mathrm{Var}(y) = \int_{-\infty}^{\infty} |T_{yw_t}(f)|^2 \left(S_{w_t w_t}(f) + S_{w_m w_m}(f) - 2\Re\left\{S_{w_t w_m}(f)\right\}\right) df. \tag{219}$$

With feedback only, on the other hand, the variance of y is simply

$$\overline{|Y(f)|^2} = |T_{yw_t}(f)|^2 S_{w_t w_t}(f) \tag{220}$$

in the frequency domain and

$$\mathrm{Var}(y) = \int_{-\infty}^{\infty} |T_{yw_t}(f)|^2 S_{w_t w_t}(f)\, df \tag{221}$$

in the time domain. Section 10.2.3 provides an explanation for treating reduction in variance as a control objective.

By comparing Eq. (218) with Eq. (220), the frequencies where feedforward control with $\hat{w}_t = w_m$ is beneficial can be found. Ideal feedforward control with no prefilter reduces the variance of y at the frequencies where Eq. (222) is satisfied:

$$S_{w_t w_t}(f) + S_{w_m w_m}(f) - 2\Re\{S_{w_t w_m}(f)\} < S_{w_t w_t}(f). \tag{222}$$

Equation (222) can be rearranged as

$$\frac{1}{2} < \frac{\Re\{S_{w_t w_m}(f)\}}{S_{w_m w_m}(f)}. \tag{223}$$

10.2.2 Feedforward Control with Imperfect Measurements

By introducing a prefilter H_{pre}, shown in Fig. 134, to form an estimate of w_t based on the measured w_m, the variance of the output variable y can be reduced below the value without prefiltering so that feedforward control is always an improvement over feedback only (Simley and Pao, 2013b). With prefiltering, the output variable y is given as

$$y = T_{yw_t}(w_t - H_{pre} w_m). \tag{224}$$

In the frequency domain, the variance of y is given by

$$\overline{|Y(f)|^2} = |T_{yw_t}(f)|^2 \overline{|W_t(f) - H_{pre}(f) W_m(f)|^2}. \tag{225}$$

The optimal prefilter should minimize the variance of y in Eq. (225) at all frequencies. The classical solution to this minimization problem is the transfer function

$$H_{pre}(f) = \frac{S_{w_t w_m}(f)}{S_{w_m w_m}(f)}. \tag{226}$$

When the optimal minimum-variance prefilter is employed, the variance of y in the frequency domain reduces to

$$\overline{|Y(f)|^2} = |T_{yw_t}(f)|^2 S_{w_t w_t}(f) \left(1 - \gamma^2_{w_t w_m}(f)\right) \tag{227}$$

where $\gamma^2_{w_t w_m}(f)$ is the coherence function between the true wind disturbance and the lidar measurement. The coherence function describes the correlation between two signals as a function of frequency, with an output of 0 indicating no correlation and 1 describing perfect correlation. The coherence between signals $a(t)$ and $b(t)$ is defined as

$$\gamma^2_{ab}(f) = \frac{|S_{ab}(f)|^2}{S_{aa}(f) S_{bb}(f)}. \tag{228}$$

Eq. (227) reveals that when measurement coherence is 1 (perfect correlation), the variance of y can be reduced to zero. When measurement coherence is 0 (the measurement contains no information about the true disturbance), on the other hand, feedforward control is not used and the variance of y reduces to the feedback only case (Eq. (220)).

In reality, the optimal prefilter defined by Eq. (226) cannot be realized because of constraints on the preview time available to the filter (Simley and Pao, 2013b). Instead, the optimal filter can be calculated using time domain methods where the available preview time appears as a hard constraint. Further details on implementation of the optimal measurement filter can be found in Simley and Pao (2013b).

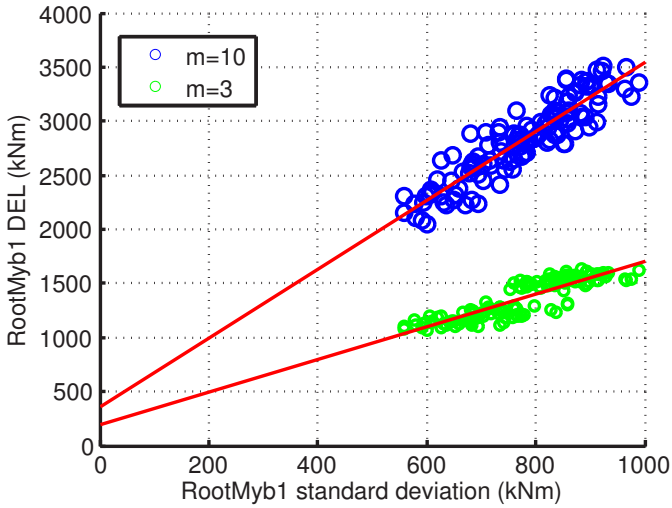

Figure 135: DEL vs STD values of blade root flapwise bending moment (RootMyb1) from various simulations of the NREL 5-MW wind turbine. The DEL calculation depends on m, the slope of the S-N (stress vs. cycles to failure) curve for the particular material. The value m=3 is typical for welded steel, and m=10 is typical for composite blades.

10.2.3 The Relationship between Variance and Damage Equivalent Loads

Aside from regulating generator speed, the objective of the control in above-rated conditions is to minimize variations in stress on turbine components because they cause material fatigue, which over time leads to failure. The damage equivalent load (DEL) (IEC, 2001) is the standard method of quantifying fatigue damage. However, the DEL is a fairly complicated nonlinear function of a load on a turbine component, and it is difficult to minimize directly. Instead, the standard deviation (STD) of a load can be minimized, and this is correlated with reduction in the DEL, as shown in Fig. 135. Minimizing variance is the same as minimizing standard deviation because the variance is simply the standard deviation squared.

10.3 Preview Time in Feedforward Control

10.3.1 Ideal Feedforward Controller Preview Time

The ideal feedforward controller (Eq. (216)) is typically non-causal, and therefore not implementable except by causal approximation or by using a preview measurement of the wind. This non-causality appears whenever $T_{y\beta_{FF}}$ has more phase delay than T_{yw_t}, or in other words, the blade pitch command takes longer to affect the output of interest than does the wind disturbance. This happens whenever a blade pitch actuator model is included, and it has also been observed when blade-flexibility is modeled. The difference in phase delay between $T_{y\beta_{FF}}$ and T_{yw_t} determines how much preview time is required to implement the ideal controller. A smaller-than-ideal amount of preview time is still useful, allowing a better approximation to the ideal controller than would be possible with no preview time at all.

The pitch actuator for the NREL 5-MW wind turbine is typically modeled as a 2nd-order low-pass filter with a natural frequency of 1 Hz and a damping ratio of 0.7. This results in a delay of about **0.225 seconds** that appears in $T_{y\beta_{FF}}$ but not T_{yw_t}. Phase delay is converted to time delay using the equation

$$\text{time delay} = -\text{phase}/360^\circ/\text{frequency}.$$

The time delay is a function of frequency, but remains fairly constant at low frequencies, and we use this low-frequency value of the time delay.

When blade flexibility is modeled on the NREL 5-MW wind turbine, and when the output y is chosen to be generator speed error, the delay in $T_{y\beta_{FF}}$ further increases relative to T_{yw_t}.

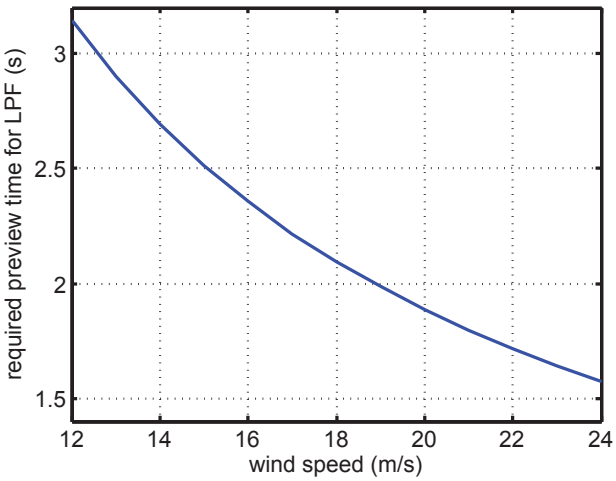

Figure 136: Estimated preview required to cancel the delay of the prefilter, as a function of wind speed. The prefilter is assumed to be a 2nd order low-pass Butterworth filter with cutoff frequency corresponding to 0.04 rad/m.

The physical reason for this blade-flexibility delay is not understood, but it does conincide with non-minimum phase zeros in the linearized turbine model. The resulting delay ranges from **0.05 to 0.3 seconds** depending on average wind speed. Additional or different delay in $T_{y\beta_{FF}}$ relative to T_{yw_t} may appear when a different output of interest is chosen.

10.3.2 Prefilter Preview Time

In addition to the preview time required to implement the ideal feedforward controller, preview time is needed to implement the minimum mean square error prefilter (Eq. (226)). The prefilter generally takes the form of a low-pass filter, where the better the wind measurements are, the higher the cutoff frequency of the low-pass filter is. Every low-pass filter introduces delay (or requires equivalent advance knowledge of the incoming signal). The higher the cutoff frequency of the low-pass filter, the less delay is introduced at any given frequency. Therefore better measurements mean less delay introduced in the prefilter and less required preview time.

A typical nacelle-mounted lidar, designed for control, yields good measurements up to a wavenumber of about 0.04 rad/m. For a wind speed of 13 m/s for example, this frequency is

$$0.04 \text{ rad/m} \times 13 \text{ m/s}/(2\pi \text{ rad}) \approx 0.08 \text{ Hz}.$$

Figure 136 shows the preview time required (the time delay introduced at low frequencies) by the prefilter, assuming it is a 2nd-order low-pass Butterworth filter with a cutoff frequency corresponding to 0.04 rad/m. (The amount of delay introduced depends on the order of the filter in addition to the cutoff frequency. A higher-order means a steeper cutoff and more delay introduced.) We see that the preview time needed for the prefilter is much greater than the preview time needed for the ideal feedforward controller, and it decreases with increasing wind speed, ranging from about **1.5 to 3 seconds**. Preview time available from the lidar measurement also decreases with increasing wind speed because it is determined by the preview distance divided by the average wind speed. More detail on required preview time due to pitch actuators, blade flexibility, and imperfect wind measurements can be found in Dunne et al. (2012).

10.3.3 Pitch Actuation Preview Time

The ideal model-inverse feedforward controller design method assumes we want to minimize a single output or set of outputs, such as generator speed error or blade root bending moments,

with no restriction on pitch actuation. However, we may want to minimize pitch actuation in addition to generator speed error or particular loads of interest. It is possible that additional preview time may be useful in meeting this combined objective. This topic is currently under investigation.

10.4 Blade Effective Wind Speed

Before analyzing lidar measurement error in depth, it is important to define the wind speed quantities that are of interest for blade pitch control. For collective pitch control, the effective wind speed experienced by the rotor is often calculated by integrating the wind speeds across the entire rotor disk using the formula:

$$u_{rotor} = \left(\frac{\int_0^{2\pi} \int_0^R u^3 (r,\phi)\, C_P (r)\, r dr d\phi}{\int_0^{2\pi} \int_0^R C_P (r)\, r dr d\phi} \right)^{\frac{1}{3}}, \tag{229}$$

where $C_P(r)$ is the radially-dependent coefficient of power and R is the rotor radius (Schlipf et al., 2012b). The resulting u_{rotor} is the uniform wind speed that would produce the same power as the actual distribution of wind speeds across the rotor disk. Note that Eq. (229) is only a function of the u component of wind, which is perpendicular to the rotor plane (see Fig. 133), rather than also including the horizontal v and vertical w components. Because u has a significantly greater impact on the turbine's aerodynamics than v or w, the calculation of effective wind speeds at the turbine is performed solely for the u component. Section 10.4.1 describes the relative importance of the u, v, and w wind speed components in further detail.

For individual pitch control, the effective wind speeds experienced by each individual blade are of interest, rather than a rotor averaged quantity. The blade effective wind speed used here is a weighted sum of wind speeds along the blade span such that wind speeds at each location are weighted according to their contribution to overall aerodynamic torque. Aerodynamic torque $\delta Q(r)$ produced by a segment of the blade with spanwise thickness δr at radial distance r along the blade can be described using the radially dependent coefficient of torque $C_Q(r)$ as

$$\delta Q(r) = \rho \pi r^2 u^2 (r)\, C_Q (r)\, \delta r, \tag{230}$$

where ρ is the air density and $u(r)$ is the u component of the wind speed at radial distance r along the blade (Moriarty and Hansen 2005; WT_Perf 2012). Although other weighting variables could be chosen for the definition of blade effective wind speed, aerodynamic torque is used here because it is directly related to the power generated by the turbine.

Using Eq. (230), the torque-based blade effective wind speed is given by

$$u_{blade} = \left(\frac{\int_0^R u^2 (r)\, C_Q (r)\, r^2 dr}{\int_0^R C_Q (r)\, r^2 dr} \right)^{\frac{1}{2}}. \tag{231}$$

A linearized form of Eq. (231) is used to calculate blade effective wind speed by integrating the wind speeds along the blade using the linear weighting function

$$W_b (r) = \frac{C_Q (r)\, r^2}{\int_0^R C_Q (r)\, r^2 dr}. \tag{232}$$

A linear blade effective wind speed is used because of its simplicity and because the statistics of a linear combination of wind speeds are generally easy to calculate. Figure 137 illustrates the blade effective weighting function $W_b(r)$ calculated using WT_Perf (2012) for the NREL 5-MW turbine model at the rated wind speed $U = 11.4$ m/s, and two above-rated wind speeds (13 m/s and 15 m/s). In above-rated conditions, the weighting curves change with wind speed because the steady-state blade pitch angle increases as wind speed increases (Jonkman et al., 2009).

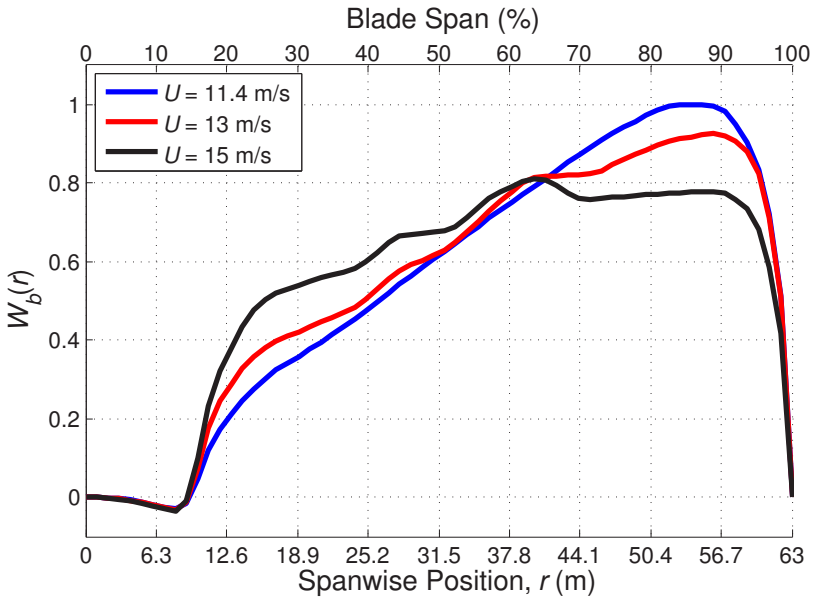

Figure 137: Aerodynamic torque-based blade effective weighting function $W_b\,(r)$ for the NREL 5-MW turbine model at the rated wind speed 11.4 m/s and two above-rated wind speeds.

10.4.1 The Relative Importance of the u, v, and w Components

When a turbine is operating in above-rated wind speeds, variations in the u component of the wind have a much greater effect than variations in the v and w components, in terms of their effect on generator speed and structural loads. To illustrate this point, linearized transfer functions from wind speed to variables of interest were generated for the 5-MW model using NREL's FAST software (Jonkman and Buhl, 2005). For example, in Fig. 138, which shows the magnitude frequency responses of several transfer functions, the effect of the u component is generally about ten times (20 dB) greater than that of the v and w components, when looking at the frequencies where the turbine speed and loads are most affected. There are some frequencies at which v and w have a greater effect than u on the vertical and horizontal components of blade root bending. However, all wind inputs shown are uniform over the rotor plane, and shear was not included. It is expected that the magnitude of the transfer functions from vertical and horizontal shear in the u component of the wind to the vertical and horizontal components of blade root bending would be much higher than the magnitude of the transfer functions from the v and w components.

The u component likely has a greater effect than v and w in part because the turbine blades move quickly in the direction of the v and w components. In above-rated wind speeds, a turbine's tip speed is typically around 70 m/s, so the outboard half of the blade (which is most influential in power capture and loads) is moving through the v and w wind components at 35 to 70 m/s. The angle of attack seen by a blade section is more influenced by a small change in the 13 m/s u component than a small change in the 35 to 70 m/s v or w component it sees.

10.5 Lidar Measurements

The performance of lidar measurements is investigated using the hub-mounted, circularly scanning lidar scenario shown in Fig. 133. The lidar model is based on the ZephIR 300 continuous-wave lidar (Slinger and Harris, 2012), which has a sampling rate of 50 Hz. Measurement performance is assessed as a function of the two scan parameters: scan radius r and preview distance d.

In general, measurement quality is described using the coherence between the lidar measurement and the blade effective wind speed. The coherence calculations require a frequency

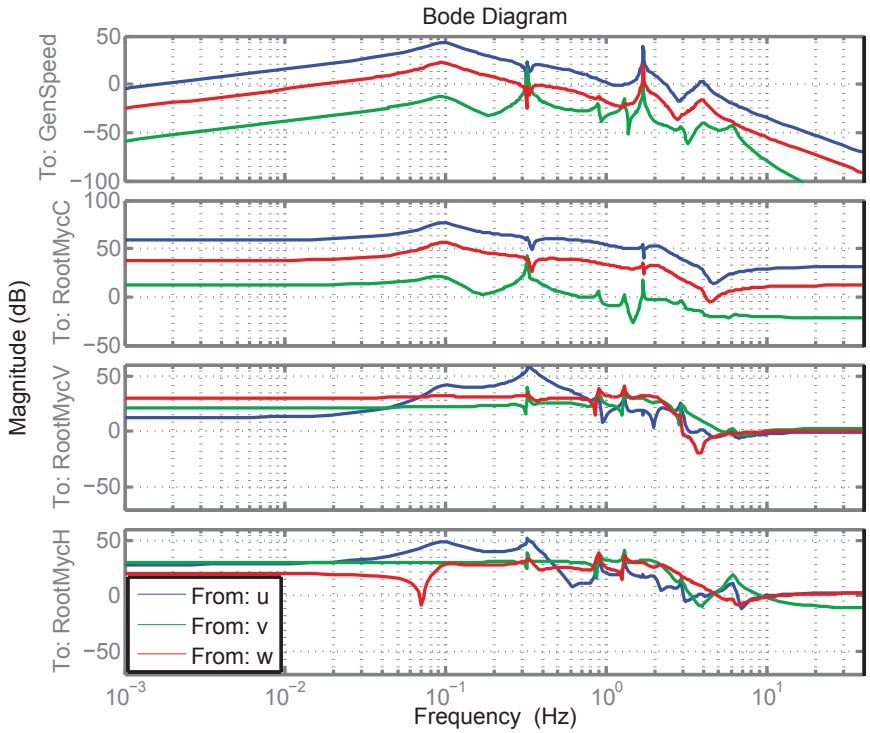

Figure 138: Plots of the magnitude frequency response of the closed-loop transfer functions from the u, v, and w components of wind speed (m/s) to (from upper to lower plots) generator speed error (rpm) and the collective, vertical, and horizontal components of blade root bending moment (kN·m) for the NREL 5-MW turbine, with all 16 degrees of freedom, linearized at 13 m/s.

domain model of the wind field. The wind field used here is based on the IEC von Karman isotropic model for neutral atmospheric stability (Jonkman, 2009). An above-rated mean wind speed $U = 13$ m/s is used, along with a turbulence intensity of 10%. Wind speeds are spatially correlated in the transverse y and vertical z directions using the IEC coherence formula (Jonkman 2009; IEC 2005). Whereas the IEC standard only defines spatial coherence for the u component of wind speed, we apply the coherence formula to the spatial correlation of the v and w components as well.

Lidar measurements and blade effective wind speeds are calculated as weighted sums of wind speeds along the lidar beam and blade span. Conveniently, the spectra of weighted sums of wind speeds are easy to calculate. For example, the CPSD between signals $a(t) = \sum_{m=0}^{M} \alpha_m a_m(t)$ ($A(f)$ in the frequency domain) and $b(t) = \sum_{n=0}^{N} \beta_n b_n(t)$ ($B(f)$ in the frequency domain), which are linear combinations of other signals, can be calculated as

$$\begin{aligned} S_{ab}(f) &= \overline{A(f)\,B^*(f)} \\ &= \overline{\left(\sum_{m=0}^{M} \alpha_m A_m(f)\right)\left(\sum_{n=0}^{N} \beta_n^* B_n^*(f)\right)} \\ &= \sum_{m=0}^{M}\sum_{n=0}^{N} \alpha_m \beta_n^* S_{a_m b_n}(f), \end{aligned} \tag{233}$$

as long as the CPSDs $S_{a_m b_n}(f)$ are known for each m and n. The symbol $\{\}^*$ represents the complex conjugate operator. The wind field model used here defines the CPSDs between wind speeds at any two locations, allowing the spectra of lidar measurements and blade effective wind speeds to be calculated.

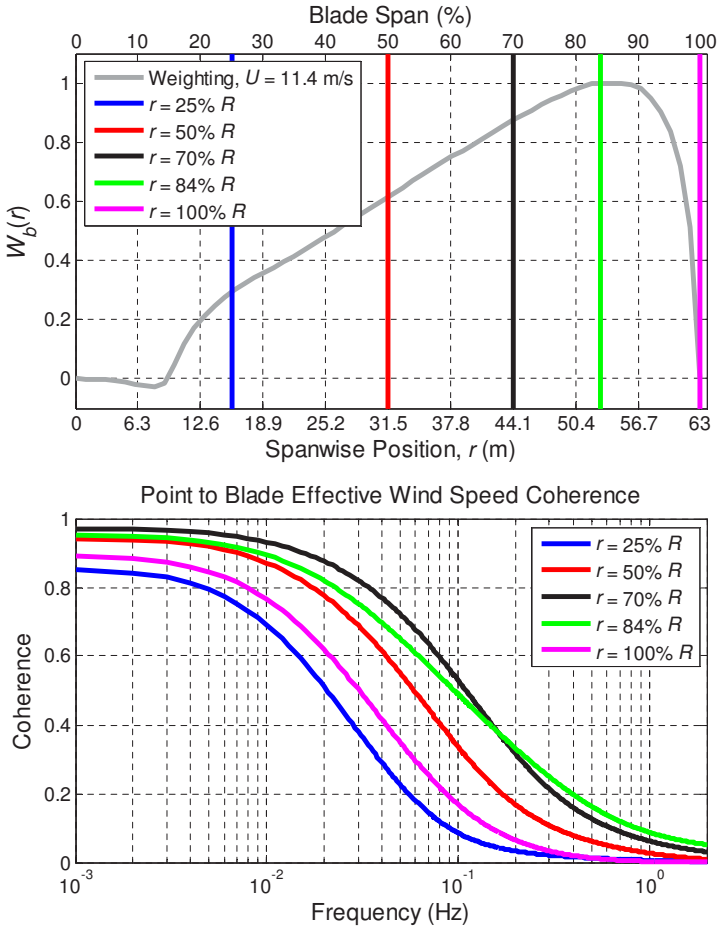

Figure 139: Coherence between the wind speeds at single points along the blade and overall blade effective wind speed for the NREL 5-MW model at $U = 11.4$ m/s.

The scan radius r of the circularly scanning lidar should be chosen to produce high measurement coherence between the measured wind and the blade effective wind speed. Figure 139 shows the coherence between perfectly measured u wind speeds at various points along the blade and blade effective wind speed. Coherence is highest for wind speed measurements near the outboard region of the blade, where torque production is highest. Note that low-frequency coherence happens to be maximized when the wind is measured at 70% blade span rather than at 84% span, where the peak of the weighting function is located, due to the particular spatial coherence model used. For control purposes, it is more important to maximize coherence at low frequencies, where the power in the turbulence spectrum is concentrated.

10.5.1 Range Weighting

As illustrated by the magenta curve on the lidar beam in Fig. 133, a CW lidar measures weighted line-of-sight wind speeds along the entire beam, where the peak of the weighting function is located at the intended focus point. A weighted line-of-sight lidar measurement can be described as

$$u_{wt,los} = -\ell_x u_{wt} - \ell_y v_{wt} - \ell_z w_{wt} \tag{234}$$

where $\hat{\ell} = [\ell_x, \ell_y, \ell_z]$ is the unit vector in the direction that the lidar is pointing. u_{wt}, v_{wt}, and w_{wt} are the weighted velocities along the lidar beam such that the vector $\vec{u}_{wt} = [u_{wt}, v_{wt}, w_{wt}]$ is given by

$$\vec{u}_{wt} = \int_0^\infty \vec{u}\left(R_\ell \vec{\ell} + [0,0,h]\right) W(F_\ell, R_\ell) dR_\ell \tag{235}$$

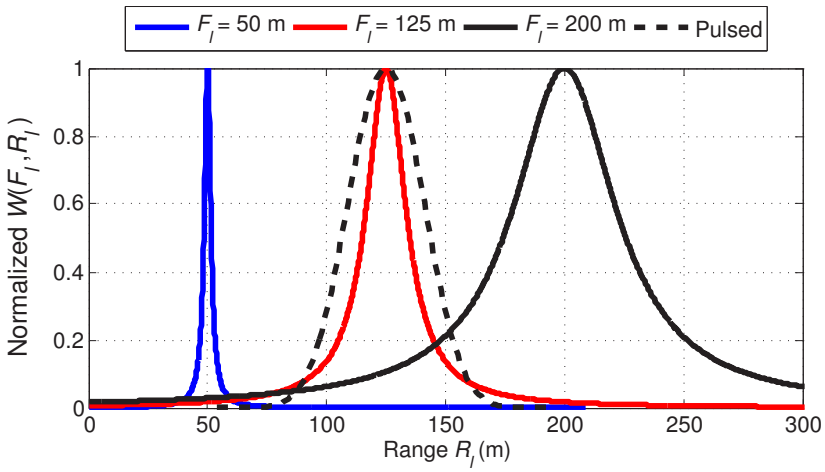

Figure 140: Normalized range weighting function $W\left(F_\ell, R_\ell\right)$ for a CW lidar similar to the ZephIR 300 at three different focus distances along with the range weighting function for a pulsed lidar similar to the Windcube WLS7.

where the velocity vector $\vec{u} = [u, v, w]$ is defined such that the u velocity is in the x direction, v is in the y direction, and w is in the z direction (see Fig. 133). Hub height is represented by h. The minus signs appear in Eq. (234) because the measured line-of-sight velocity is the projection of the velocity vector onto the direction from the measurement point to the lidar, opposite from the lidar look direction. $W\left(F_\ell, R_\ell\right)$ is the range weighting function with focus distance F_ℓ and range along the lidar beam R_ℓ as arguments.

The range weighting function for a CW lidar becomes broader as the focus distance increases (the Full width at half maximum of $W\left(F_\ell, R_\ell\right)$ scales with the square of the focus distance F_ℓ) (Frehlich and Kavaya 1991; Slinger and Harris 2012). $W\left(F_\ell, R_\ell\right)$ is plotted as a function of range along the lidar beam for three different focus distances in Fig. 140. Also included in Fig. 140 is the range weighting function for a pulsed lidar similar to the Windcube WLS7 (Frehlich et al. 2006; Mikkelsen 2009). Note that the pulsed lidar range weighting function does not vary with measurement distance. Additional details on CW and pulsed range weighting functions can be found in Simley et al. (2013c).

10.5.2 Geometry Errors

As mentioned in Section 10.4.1, the u component of the wind speed is of interest for wind turbine control. An estimate of the u component is formed by dividing the line-of-sight measurement in Eq. (234) by $-\ell_x$, yielding

$$\begin{aligned} \hat{u} &= -\tfrac{1}{\ell_x} u_{wt,los} \\ &= u_{wt} + \tfrac{\ell_y}{\ell_x} v_{wt} + \tfrac{\ell_z}{\ell_x} w_{wt}. \end{aligned} \tag{236}$$

As revealed in Eq. (236), detection of the v and w wind speed components causes a degradation in the estimate of the u component. For a fixed scan radius r, short preview distances d will result in large measurement angles, causing significant measurement error due to detection of the v and w components (Simley et al., 2013c). As preview distance increases, the $\frac{\ell_y}{\ell_x}$ and $\frac{\ell_z}{\ell_x}$ terms decrease and error caused by measurement geometry will decrease. Figure 141 contains coherence curves for a hub-mounted lidar without range weighting measuring at a scan radius of $r = 41$ m for different preview distances. The coherence curves represent the correlation between the lidar measurement and the wind speed at a single point downstream of the measurement, so that only geometry errors are included. As preview distance increases, the measurement coherence increases due to less contribution from the v and w components in Eq. (236).

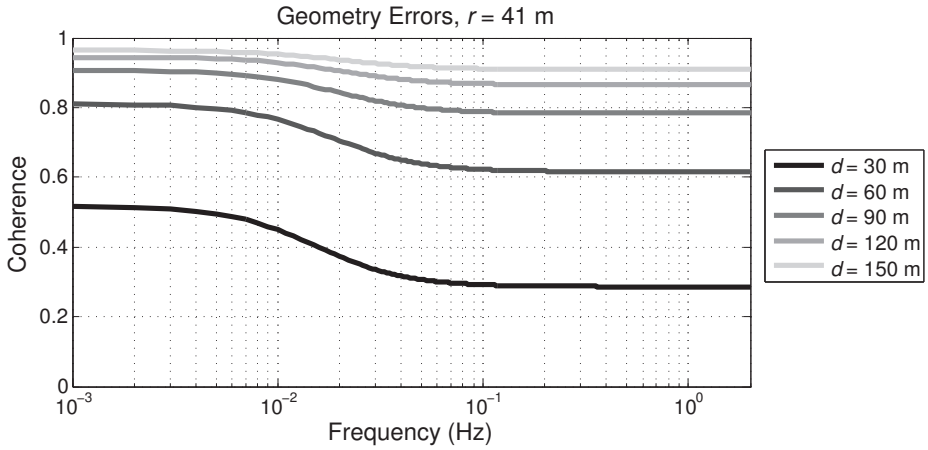

Figure 141: Measurement coherence for a hub-mounted lidar with a scan radius of 41 m at five different preview distances. Only geometry errors are included.

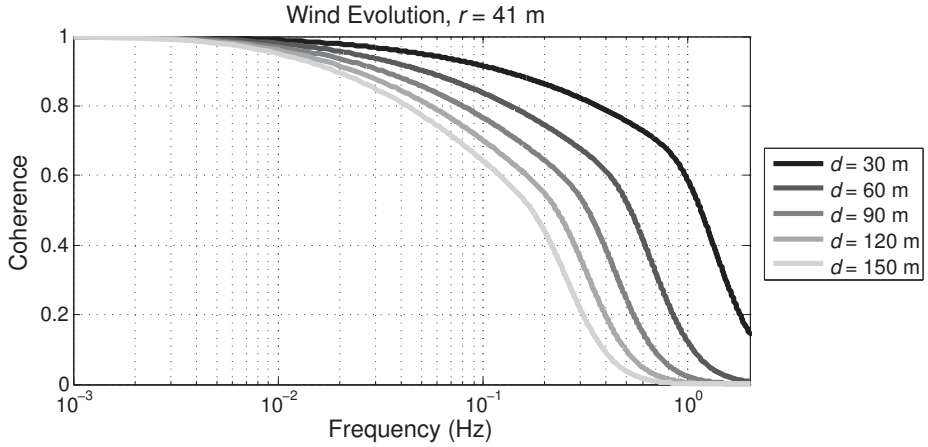

Figure 142: Measurement coherence for a hub-mounted lidar with a scan radius of 41 m at five different preview distances. Only wind evolution errors are included.

10.5.3 Wind Evolution

A major source of preview measurement error is the evolution of the turbulence between the time it is measured by the lidar and the time it appears at the turbine rotor as a wind disturbance. While for a fixed scan radius r, measurement errors due to the measurement geometry decrease as preview distance increases, errors due to wind evolution become more severe, since there is additional time for the turbulence to evolve.

Wind evolution can be described by a coherence function between wind speeds at two points separated in the longitudinal (along-wind) direction. A popular longitudinal coherence formula used in the wind turbine control community (Bossanyi et al. 2012b; Schlipf et al. 2012a; Laks et al. 2013) is presented in Kristensen (1979). The Kristensen coherence formula is a function of frequency, longitudinal separation, mean wind speed, turbulent kinetic energy, and a turbulence length scale. Wind evolution becomes more severe when longitudinal separation or turbulent kinetic energy are increased and becomes less severe as mean wind speed increases. Longitudinal coherence curves using the Kristensen (1979) formula are shown in Fig. 142 for several preview distances. A mean wind speed of 13 m/s is used with a turbulence intensity of 10%. Wind evolution tends to affect high frequencies more than low frequencies and, as a result, very low-frequency structures in the wind do not change significantly between the measurement point and the turbine.

The IEC von Karman wind model used in this chapter only defines spatial coherence in the transverse and vertical (yz) plane. This model assumes that wind speeds are perfectly

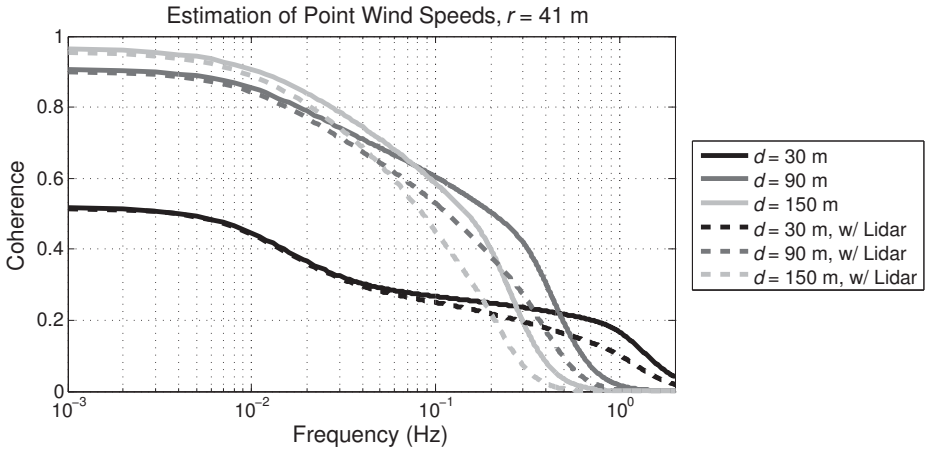

Figure 143: Coherence between lidar measurements and the wind speed at a point 41 m along the blade for a hub-mounted lidar with a scan radius of 41 m for three different preview distances. Geometry errors and wind evolution are included. The solid curves represent measurement coherence without lidar range weighting while the dashed curves include range weighting.

correlated in the x direction, i.e., wind speeds simply "march" downstream without evolving. Wind evolution is added to this wind field model by introducing imperfect longitudinal spatial coherence. We define spatial coherence for wind speeds at any two locations as the product between the spatial coherence defined in Jonkman (2009) due to the separation in the transverse (y) and vertical (z) directions and the longitudinal coherence due to separation in the x direction. Additional details on the application of the Kristensen (1979) wind evolution formula to wind field modeling can be found in Simley and Pao (2013a) and Laks et al. (2013).

10.5.4 Lidar Measurements of Blade Effective Wind Speed

Figures 141 and 142 reveal measurement coherence including the effects of geometry errors and wind evolution separately, where the variable of interest is the wind speed at a single point 41 m along the blade. Figure 143 contains measurement coherence curves for a fixed scan radius of $r = 41$ m including the combined effects of geometry errors and wind evolution for three different preview distances, with and without the effects of lidar range weighting. As preview distance increases, low-frequency correlation improves, due to diminishing measurement geometry effects, but high-frequency correlation becomes worse because of the additional wind evolution. Since more power in the wind is located at lower frequencies, it is important to have good low-frequency measurement correlation even if high-frequency correlation suffers. Lidar range weighting causes an overall drop in measurement coherence with the wind speed at a single point along the blade due to spatial averaging of the wind field.

As discussed earlier, blade effective wind speed is the wind speed quantity of interest for blade pitch control purposes, rather than the wind speed at a single point along the blade. The coherence between lidar measurements and blade effective wind speed for the same preview distances that are included in Fig. 143 are shown in Fig. 144. Measurement coherence tends to decrease compared to the results in Fig. 143 because of the spatial averaging of the wind field caused by blade effective weighting. However, when the variable of interest is blade effective wind speed, lidar range weighting actually improves measurement coherence. We attribute this improvement to the spatial averaging of the lidar measurement "mimicking" the spatial averaging of wind speeds along the blade. Further details on the calculation of lidar measurement coherence for measurement scenarios including geometry errors, wind evolution, and range weighting can be found in Simley et al. (2012).

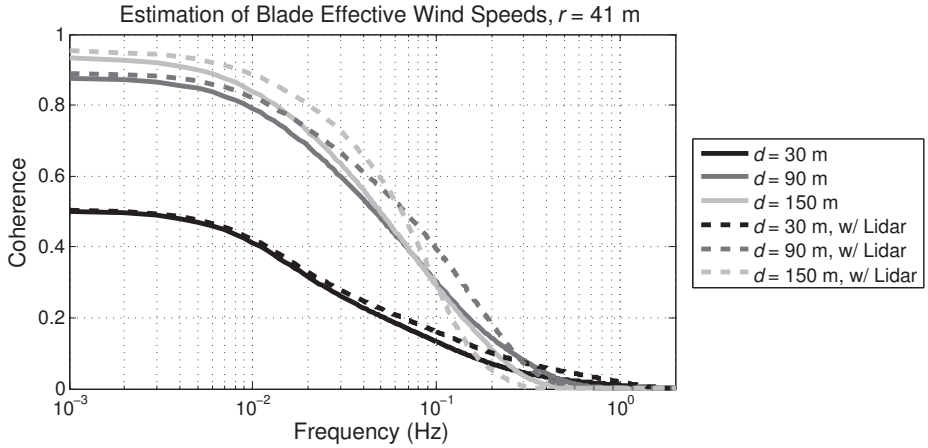

Figure 144: Coherence between lidar measurements and blade effective wind speed for a hub-mounted lidar with a scan radius of 41 m for three different preview distances. Geometry errors and wind evolution are included. The solid curves represent measurement coherence without lidar range weighting while the dashed curves include range weighting.

10.6 Lidar Measurement Example: Hub Height and Shear Components

In the previous section, the measurement quality between a lidar measurement and blade effective wind speed at a fixed location was investigated. In reality, the blades of a turbine rotate through the wind field and it is the total contribution from all blades comprising the rotor that affects the turbine. For a three-bladed turbine, such as the NREL 5-MW model, the wind speeds felt by the rotating blades can be described as the sum of a collective component, which all three blades experience; a linear vertical shear component, which describes the gradient of the wind speeds in the vertical z direction; and a linear horizontal shear component, which describes the wind speed gradient in the horizontal y direction. These collective and shear components describe the u component of wind speed in the rotor plane.

The three blade effective wind speeds, using the weighting function $W_b(r)$ defined in Eq. (232), can be written in terms of collective and shear components as

$$\begin{bmatrix} u_{blade,1} \\ u_{blade,2} \\ u_{blade,3} \end{bmatrix} = \begin{bmatrix} 1 & B\cos(\psi) & -B\sin(\psi) \\ 1 & B\cos\left(\psi+\frac{2\pi}{3}\right) & -B\sin\left(\psi+\frac{2\pi}{3}\right) \\ 1 & B\cos\left(\psi+\frac{4\pi}{3}\right) & -B\sin\left(\psi+\frac{4\pi}{3}\right) \end{bmatrix} \begin{bmatrix} u_{hh} \\ \Delta_v \\ \Delta_h \end{bmatrix} \tag{237}$$

where ψ is the azimuth angle in the rotor plane corresponding to blade number one, u_{hh} is the wind speed at hub height, Δ_v is the difference in the wind speed across the rotor disk in the vertical direction normalized by the mean wind speed U, Δ_h is the difference in the wind speed across the rotor in the horizontal direction normalized by the mean wind speed, and

$$B = \frac{U}{2R}\int_0^R W_b(r)\, r dr. \tag{238}$$

Azimuth angle is defined such that $\psi = 0°$ corresponds to the top of rotation (in the z direction) and $\psi = 90°$ corresponds to the left side of the rotor disk when facing upwind (in the $-y$ direction). By inverting Eq. (237), the collective and shear components can be described as a function of the three blade effective wind speeds as

$$\begin{bmatrix} u_{hh} \\ \Delta_v \\ \Delta_h \end{bmatrix} = \begin{bmatrix} \frac{1}{3} & \frac{1}{3} & \frac{1}{3} \\ \frac{2}{3B}\cos(\psi) & \frac{2}{3B}\cos\left(\psi+\frac{2\pi}{3}\right) & \frac{2}{3B}\cos\left(\psi+\frac{4\pi}{3}\right) \\ -\frac{2}{3B}\sin(\psi) & -\frac{2}{3B}\sin\left(\psi+\frac{2\pi}{3}\right) & -\frac{2}{3B}\sin\left(\psi+\frac{4\pi}{3}\right) \end{bmatrix} \begin{bmatrix} u_{blade,1} \\ u_{blade,2} \\ u_{blade,3} \end{bmatrix}. \tag{239}$$

Using the frequency domain description of the wind field with defined power spectra and spatial coherence functions, the spectrum of the wind experienced by a blade rotating through the wind field can be calculated, as explained in Simley and Pao (2013a). The method in

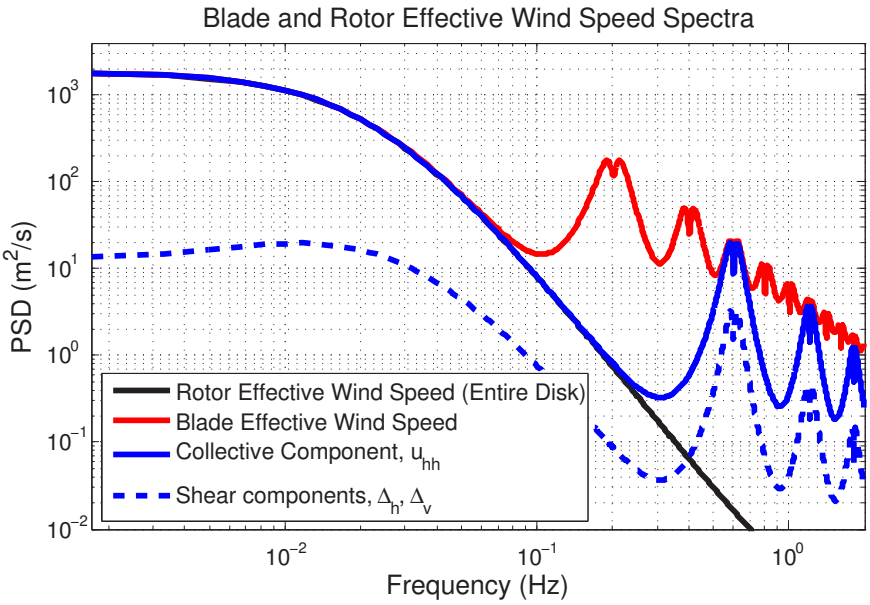

Figure 145: Power spectra of rotating blade effective wind speed as well as collective and shear components due to three rotating blades. The rotor effective wind speed, calculated by integrating wind speeds weighted according to their contribution to power over the entire rotor disk, is shown for comparison. Spectra are generated for the IEC von Karman wind field model using the NREL 5-MW turbine at mean wind speed 13 m/s.

Simley and Pao (2013a) can be extended to calculate the spectra of the collective and shear components due to three rotating blades, using Eq. (239). Using the IEC von Karman wind field and the NREL 5-MW model, the rotating blade effective wind speed and rotating collective and shear terms are plotted in Fig. 145 for the rated rotor speed 12.1 rpm (0.202 Hz) and above-rated wind speed 13 m/s. The blade effective wind speed spectrum contains peaks at the 1P frequency (0.202 Hz) and its harmonics, due to the blade passing through turbulent structures once per revolution. The collective and shear component spectra contain peaks at the 3P (three times per revolution) frequency (0.606 Hz) and its harmonics because each of the three blades passes through structures once per revolution. Also shown in Fig. 145 is the rotor effective wind speed averaged across the entire rotor disk, calculated using Eq. (229), to highlight the difference between modeling rotor effective wind speed as the wind felt by the rotor disk and the wind felt by three rotating blades.

For wind turbine controls, it is popular to use linear models of the turbine in the non-rotating frame because the resulting transfer functions do not vary with azimuth angle as much as in the rotating frame. Rotating variables at each of the three blades are instead represented as a collective component y_0, a vertical component y_v, and a horizontal component y_h. For example, the flapwise bending moment experienced by each blade can be represented as the average bending moment over all blades (y_0), the net bending moment of the rotor around the y axis (y_v), and the net bending moment around the vertical z axis (y_h). Transfer functions are calculated in the non-rotating frame using the multiblade coordinate (MBC) transform (Bir, 2008), which is used as the basis for Eqs. (237) and (239). The response of the collective component of a turbine variable is dominated by the collective wind component u_{hh}, and the vertical and horizontal components are dominated by the vertical Δ_v and horizontal Δ_h shear components of the wind, respectively. Figure 146 contains the magnitude squared frequency response of the transfer functions from hub height wind speed to the collective component of flapwise blade root bending moment as well as the transfer functions from horizontal shear and vertical shear to the horizontal component and vertical component of blade root bending moment generated using FAST (Jonkman and Buhl, 2005) with the 5-MW model at the above-rated wind speed 13 m/s. These transfer functions include blade pitch and generator

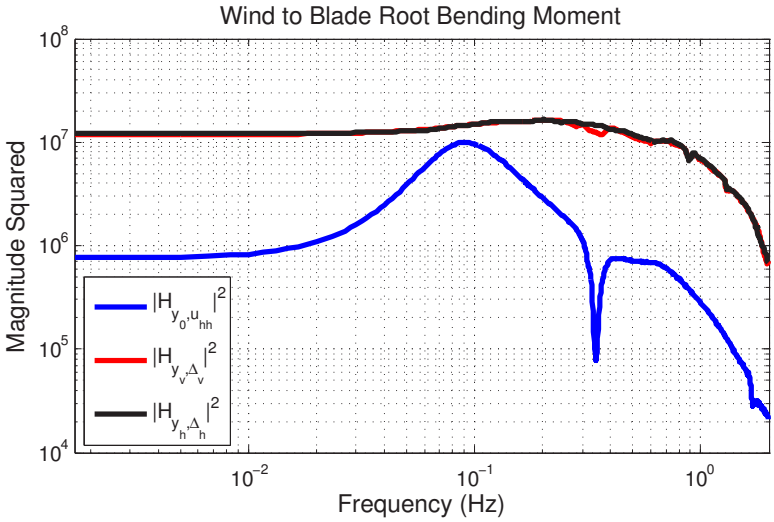

Figure 146: Transfer functions from hub height wind speed u_{hh} to the collective component of flapwise blade root bending moment y_0 as well as the transfer functions from vertical shear Δ_v and horizontal shear Δ_h to the vertical component y_v and horizontal component y_h of blade root bending moment. The transfer functions correspond to the NREL 5-MW turbine model at above-rated wind speed 13 m/s including feedback control of blade pitch and generator torque.

torque feedback control (Jonkman et al., 2009) using rotor speed measurements.

A lidar measurement scenario is proposed that uses three rotating measurements to estimate the three rotating blade effective wind speeds $\hat{u}_1$, $\hat{u}_2$, and $\hat{u}_3$, using Eq. (236). The collective and shear components of the wind are then estimated from the three lidar measurements using

$$\begin{bmatrix} \hat{u}_{hh} \\ \hat{\Delta}_v \\ \hat{\Delta}_h \end{bmatrix} = \begin{bmatrix} \frac{1}{3} & \frac{1}{3} & \frac{1}{3} \\ \frac{4}{3U}\cos(\psi) & \frac{4}{3U}\cos\left(\psi+\frac{2\pi}{3}\right) & \frac{4}{3U}\cos\left(\psi+\frac{4\pi}{3}\right) \\ -\frac{4}{3U}\sin(\psi) & -\frac{4}{3U}\sin\left(\psi+\frac{2\pi}{3}\right) & -\frac{4}{3U}\sin\left(\psi+\frac{4\pi}{3}\right) \end{bmatrix} \begin{bmatrix} \hat{u}_1 \\ \hat{u}_2 \\ \hat{u}_3 \end{bmatrix}. \tag{240}$$

A measurement scenario based on the lidar scenario in Fig. 133 is investigated for the purpose of minimizing the variance of the three blade root bending moment components using lidar-based estimates of the collective and shear wind speed terms and ideal feedforward control (Eq. (216)). Since the three lidars rotate at the rotor speed to provide measurements of blade effective wind speed, the only design variables are the scan radius r and preview distance d.

10.6.1 Optimizing the Measurement Scenario

The design problem is formulated to minimize the variance of the blade root bending moment felt by the three blades. The measurement geometry is to be chosen to minimize the sum of the variances of the three bending moment components:

$$(r^*, d^*) = \arg\min_{r,d} \left[\mathrm{Var}(y_0) + \frac{1}{2}\mathrm{Var}(y_v) + \frac{1}{2}\mathrm{Var}(y_h)\right]. \tag{241}$$

As a blade rotates through the wind field, it experiences the vertical and horizontal components of bending moment scaled by the cosine and sine of the azimuth angle ψ, respectively. Since variance is equivalent to the mean square value over time and thus azimuth angle, and the mean square value of a sinusoid is $\frac{1}{2}$, the factor of $\frac{1}{2}$ appears in front of the vertical and horizontal terms in Eq. (241). Using Eq. (219) from Section 10.2.1 for calculating variance based on measurement coherence with feedforward control and optimal prefiltering, the

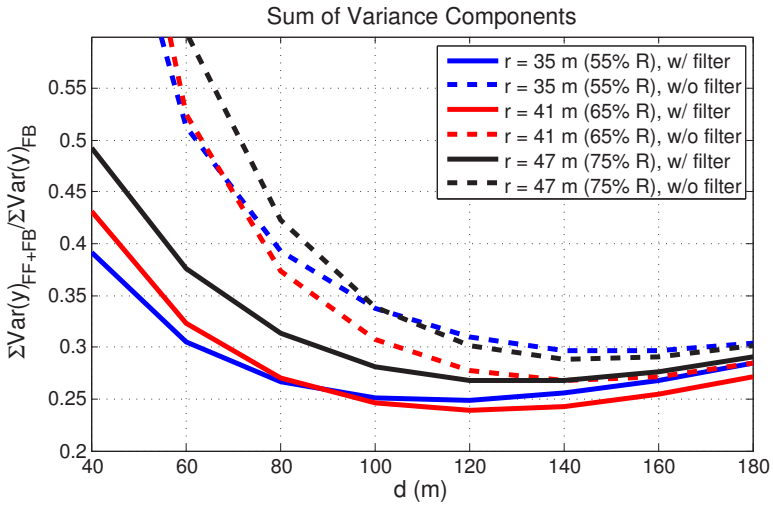

Figure 147: The sum of the variance terms of blade root bending moment $\mathrm{Var}\left(y_0\right) + \frac{1}{2}\mathrm{Var}\left(y_v\right) + \frac{1}{2}\mathrm{Var}\left(y_h\right)$ with feedforward control normalized by the sum of the variance terms with feedback only for a few scan radii r vs. preview distance d. The solid curves represent the variance with minimum mean square error prefiltering and the dashed curves show the performance without prefiltering ($H_{pre} = 1$). Measurement coherence is calculated using the ZephIR CW lidar model. The transfer functions are computed for the NREL 5-MW turbine at rated wind speed 13 m/s.

variances in Eq. (241) can be calculated using

$$\mathrm{Var}\left(y_0\right) = \int_0^\infty \left|T_{y_0 u_{hh}}(f)\right|^2 S_{u_{hh}u_{hh}}\left(f\right)\left(1 - \gamma^2_{u_{hh}\hat{u}_{hh}}(f)\right) df, \tag{242a}$$

$$\mathrm{Var}\left(y_v\right) = \int_0^\infty \left|T_{y_v \Delta_v}(f)\right|^2 S_{\Delta_v\Delta_v}\left(f\right)\left(1 - \gamma^2_{\Delta_v\hat{\Delta}_v}(f)\right) df, \tag{242b}$$

$$\mathrm{Var}\left(y_h\right) = \int_0^\infty \left|T_{y_h \Delta_h}(f)\right|^2 S_{\Delta_h\Delta_h}\left(f\right)\left(1 - \gamma^2_{\Delta_h\hat{\Delta}_h}(f)\right) df. \tag{242c}$$

In order to find the optimal r and d that satisfy Eq. (241), the variance terms in Eq. (242) are calculated for a number of scan radii and preview distances. Figure 147 shows the sum of the variance terms for scan radii $r = 35$ m (55% blade span), $r = 41$ m (65% blade span), and $r = 47$ m (75% blade span) plotted as a function of preview distance d. The variance is normalized by the sum of the variance terms without feedforward control (calculated using Eq. (220)). The solid curves indicate the variance achieved with the ideal feedforward controller and the optimal prefilter while the dashed curves represent the variance as a result of ideal feedforward control without prefiltering. The wind field model is comprised of the von Karman spectral model with wind evolution described in Section 10.5.3.

The results in Fig. 147 reveal that the variance of blade root bending moment is minimized using optimal measurement prefiltering with a scan radius $r = 41$ m (65% blade span) and a preview distance $d = 120$ m (almost one rotor diameter). This lidar geometry achieves a bending moment variance that is less than 25% of the value when feedforward control is not used. Without prefiltering, the variance is roughly 28% of the value with feedback only. Although the analysis in Fig. 139 showed that measurements at 70% blade span provide the highest correlation with blade effective wind speed, a scan radius of 65% blade span is optimal for this scenario, largely because of the implicit penalty on large scan radii caused by lidar geometry errors. Measurement performance suffers for preview distances less than 120 m because of additional errors caused by large measurement angles, as explained in Section 10.5.2. For preview distances beyond 120 m, on the other hand, the severity of wind evolution increases, as discussed in Section 10.5.3, causing measurement coherence to drop.

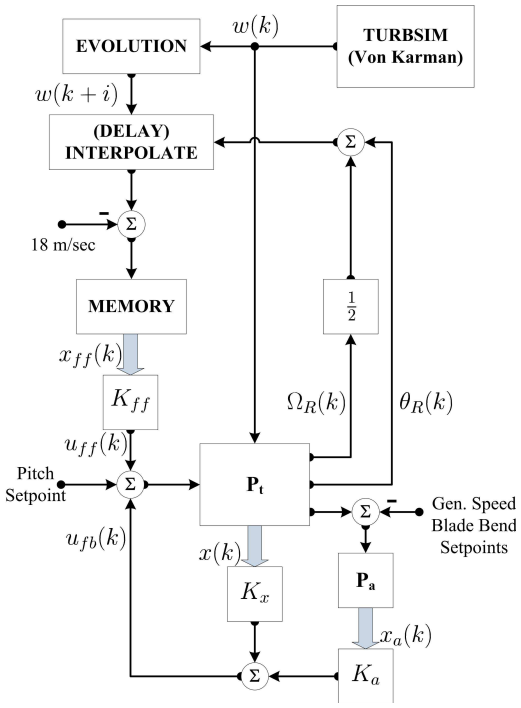

Figure 148: During simulation, FAST reads in wind speeds at the turbine directly from the TurbSim output; the controller estimates blade positions 1/2 second into the future and interpolates wind speeds at these positions from the annulus of evolved wind speeds. Signals and blocks are explained throughout Sections 10.7.1 and 10.7.2.

10.7 Control Example 1: Wind Turbine Preview Control In The Presence of Evolving Turbulence

In this control example, we use spectral methods discussed in Laks et al. (2013) so that a form of wind evolution described in Section 10.5.3 can be introduced into the simulation of preview control techniques. This is similar to the method proposed in Bossanyi et al. (2012b), but in our case TurbSim's von Karman spectral model (Jonkman, 2009) is generalized from the original transverse and vertical (y, z) implementation to one that encompasses (x, y, z) (directions defined in Fig. 133). This introduces changes in the measured wind speeds that increase with their displacement from the rotor, while keeping the spectral content and transverse and vertical spatial correlations consistent with those used by TurbSim.

A schematic of the simulation proposed for investigating the effects of evolution is shown in Fig. 148. A distribution of wind speeds is obtained from TurbSim (Jonkman, 2009) to provide inputs during simulation of the turbine using FAST (Jonkman and Buhl, 2005). These wind speeds are pre-processed to induce "evolved" wind speeds at locations within an annulus located at various distances in front of the turbine as depicted in Fig. 133. During simulation, preview measurements are taken from this annulus of evolved wind speeds. The pre-processing and simulations are done three times; first simply generating an annulus of wind speeds without evolution or lidar effects; then a second set with evolution effects; and then again with the addition of the geometry and range weighting effects of a continuous-wave lidar measurement system.

The controller is designed to regulate speed and mitigate blade loads. The design is based on a discrete-time equivalent of the turbine dynamics sampled at 20 Hz (0.05 s sample period). With this approach, the preview measurements are stored in a chain of delays and this storage can be viewed as a part of the state of a generalized turbine model. This allows implementation of preview control as a state-feedback design; that is, the turbine control is generated using feedback gains associated with each state of the generalized model and this

encompasses the storage of preview measurements. If the gains associated with the preview storage are partitioned from the gains applied to turbine measurements, then the former are correctly viewed as disturbance feedforward control and this is how they are depicted in Fig. 148. In the course of design, it is determined that the majority of benefit of preview is obtained using 0.5 s (10 samples) worth of feed-forward compensation, but this can change depending on the dynamics of the turbine involved.

The FAST simulation code marches the TurbSim wind distribution past the turbine at the mean speed of 18 m/s. The pre-processing induces evolution corresponding to distances $iT_s \times 18$ where T_s is the sample period and i is the number of preview samples used. Where the evolution distance is greater than $10T_s \times 18$, the process is equivalent to taking preview measurements further in front of the turbine, and then waiting the appropriate amount of time before applying the preview gains to the measurements.

10.7.1 $\mathcal{H}_2$ Optimal Preview Control

In this section, we describe the design of the preview controller and then evaluate its performance in the presence of emulated wind evolution. Linear models are obtained from the FAST wind turbine modeling code (Jonkman and Buhl, 2005) developed at NREL. The model is based on a 40 m diameter, three-bladed controls advanced-research turbine (CART3) located at NREL's National Wind Technology Center (NWTC). The nominal operating point for design (and simulation) is a uniform wind of 18 m/s, a blade pitch of 12.7°, and a rotor speed of 41.7 rpm.

As in Laks et al. (2011b), the FAST linearizations are used to obtain a discrete-time state-space model representing the turbine dynamics $\mathbf{P_t}$ with a 20 Hz sample rate. For controller design, the linearized model includes a first-order generator degree of freedom (DOF), second-order dynamics for each blade's out-of-plane blade flap compliance, and a second-order drive-train compliance. This model is then augmented with simple pitch actuator dynamics that provide the pitch rates generated by individual pitch commands. During simulation, all DOFs provided by FAST are used except for yaw and teeter (the freedom of the rotor to tilt).

In addition, integral control on generator speed error Ω_g ($= \Omega_R N_{gb}$ where N_{gb} is the gearbox ratio and Ω_R is the rotor speed) and rejection of 1P variation in the bending moments are obtained by augmenting the turbine model with additional dynamics $\mathbf{P_a}$ driven by measurements of these signals. We configure the control system to use individual point measurements of the longitudinal wind that the blades will encounter at 75% span after a fixed time delay of i samples, where the point measurements rotate in unison with the blades. As discussed in Laks et al. (2011b), this corresponds to using a blade-local model, that describes the effect on the turbine of wind speed perturbations local to each blade.

The state feedback is designed by forming the generalized plant (the FAST linearization with preview storage and augmented dynamics) with weighting on outputs that include generator speed perturbations and perturbations in out-of-plane blade bending moments. The state-feedback gains $[K_x \; K_a \; K_{ff}]$ are optimized to minimize the $\mathcal{H}_2$ norm from the preview wind measurement to weighted versions of flap and speed perturbations; this includes a penalty on excessive pitch rates so that the associated linear quadratic regulator problem is well posed. It is possible to compute the optimal state feedback independent of the amount of preview used (Hazell, 2008). This involves using the stabilizing solution of a Riccati equation to compute both the optimal state-feedback and feedforward gains. Details can be found in Laks et al. (2013).

In formulating the $\mathcal{H}_2$ cost, emphasis is initially focused on the flap response to wind perturbations. Then, the penalty on pitch effort is increased until the (linear) closed-loop response to a step change in collective wind produces pitch rates on the order of 10°/s. Generally, the $\mathcal{H}_2$ performance improves with the number of samples of preview, but remains bounded below so that there is a diminishing return; this lower bound is essentially reached with the use of about 4 samples of preview at 20 Hz. However, the goal is not the precise value of the $\mathcal{H}_2$ norm, but the attenuation of perturbations in blade load due to perturbations

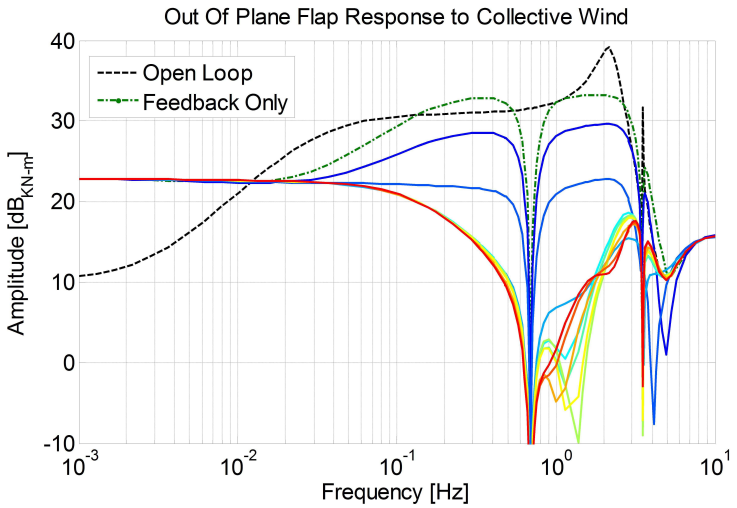

Figure 149: Collective flap response to collective wind: dashed line indicates open loop (no feedback control); each level of preview is indicated by the progression from blue to red. The notch near 0.7 Hz corresponds to the rejection of 1P loading that is provided by the augmented dynamics.

in wind speed. This goal is evident in the frequency responses provided in Fig. 149.

10.7.2 Controller Performance Simulations

As shown in Fig. 148, TurbSim is used to generate wind speeds at the turbine that are consistent with the von Karman spectral model. Then the technique presented in Laks et al. (2013) is used to induce evolved wind speeds located at 60 evenly spaced azimuths that are at a measurement radius of $r = 15$ m (= 75% blade span). The evolution distance $d = iT_s \times U$ is chosen based upon i samples at the control system sample rate of 20 Hz ($= 1/T_s$) and the nominal wind speed of $U = 18$ m/s.

The controller is simulated using feedback only, and also with increments of i samples of preview

$$K_{ff} = \begin{bmatrix} K_{w0} & \cdots & K_{wi} & 0 & \cdots & 0 \end{bmatrix}, \tag{243}$$

up to $i = 10$ samples. For previews $0 \leq i \leq 10$, the controller uses gains up through K_{wi}, and for $i > 10$, the controller uses preview gains through K_{w10}. In the latter case, this is equivalent to taking measurements further than $1/2$ s (at 18 m/s average wind speed) ahead of the turbine, and then waiting until those wind speeds are within $1/2$ s of reaching the turbine before storing them in the feedforward MEMORY.

The controller is simulated using the same base TurbSim wind field first using feedback only, and then multiple times using feedback plus preview feedforward. For the preview simulations, evolved wind speed measurements are pre-computed for the base wind field at distances that correspond to preview times in the range [0.05,10] s (or preview distances in the range [0.9,180] m). The computation done for each distance produces 60 time-varying measurement waveforms arranged spatially in a ring in front of the turbine as depicted in Fig. 133. As indicated in Fig. 148, the present rotor position $\theta_R(k)$ and speed $\Omega_R(k)$ are used to predict $1/2$ s worth of blade rotation, and then the evolved wind speeds at the 60 azimuth locations are interpolated to the predicted blade positions. This gives the controller a preview of wind speeds that the blades will encounter over a $1/2$ s horizon.

There are three sets of measurements generated corresponding to (i) an ideal preview case without evolution, (ii) a set that includes the evolution model, and (iii) a set that uses evolution and lidar distortion as discussed in Section 10.5. The turbine and controller simulation is repeated for each set of pre-computed wind measurements and the RMS blade load and preview measurement error (relative to the wind at the blades) are computed. The

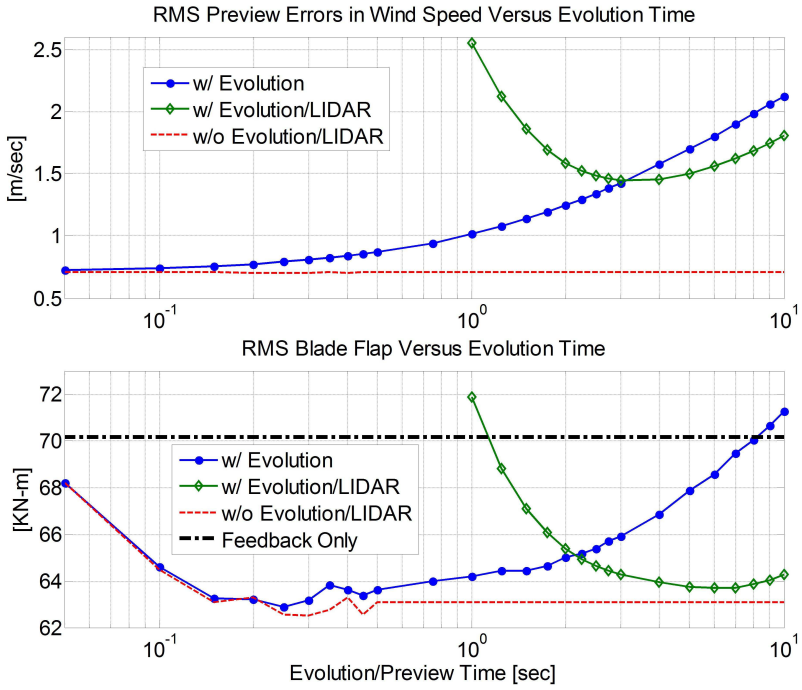

Figure 150: The accuracy (top plot) of evolved preview measurements w/o lidar distortion (blue/dots) and with lidar distortion (green/diamonds); RMS blade-loads (lower plot) w/o lidar distortion (blue/dots) and with lidar distortion (green/diamonds).

results are provided in Fig. 150. Simply introducing a set of wind speeds in the annulus that are properly correlated with the existing TurbSim field without evolution results in a base level of error relative to the wind speeds actually encountered by the blades; this is depicted by the red-dashed line in the top plot of Fig. 150.

10.7.3 Simulation Results

Given the 0.7 m/s RMS base level of measurement error, the maximum benefit potential of preview actuation is about a 10% drop in RMS blade flap relative to feedback-only control as shown in the lower plot of Fig. 150. As expected, the benefit of preview in terms of RMS blade loading reaches a maximum with 0.2 s (4 samples) of preview time. Without evolution or lidar effects, preview greater than 0.2 s does not really improve performance. With evolution and no lidar distortion, blade load mitigation performance deteriorates with preview distances greater than 0.2 s as measurement errors increase with distance from the rotor due to the applied evolution. Because of the frequency dependent nature of the evolution model, these measurement errors tend to be more significant at higher frequencies leading to over-actuation by the feedforward control. By 10 s (180 m) of preview, the advantage of preview control relative to feedback-only has been completely lost.

When applying preview based on a lidar measurement, large cone angles relative to the x (downstream) direction result in significant contributions of the transverse v and vertical w wind components to the estimate $\hat{u}$ of the downstream speed. This is apparent in the sharp upward trend of the green-diamond curve as preview times are reduced below 3 s (< 54 m preview, or equivalently a cone angle $> 15°$); at these shorter preview distances the geometry errors dominate the preview measurement errors. At larger preview times, evolution dominates the lidar measurement error, but the system is benefiting from the lidar range weighting, which low-pass filters the poorly correlated high frequencies in the wind. What is surprising is the magnitude of the effect this filtering has on the quality of the load mitigation. Since the

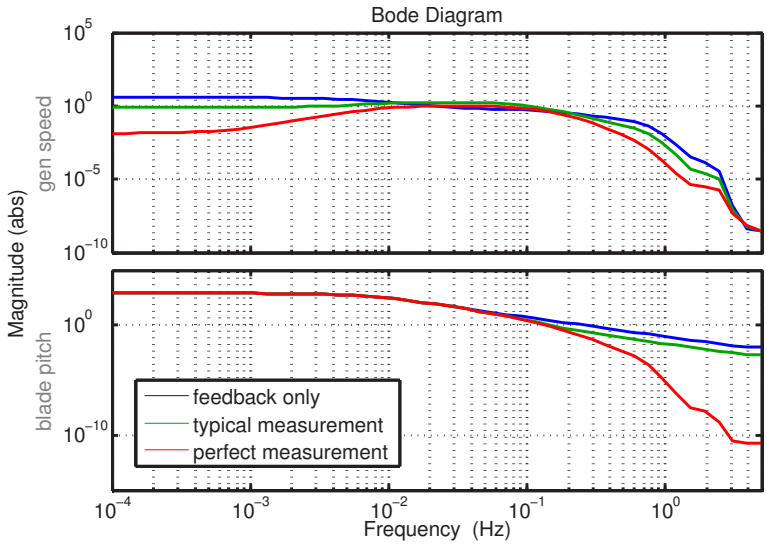

Figure 151: Frequency responses of closed-loop transfer functions, with wind spectrum included, showing generator speed error and blade pitch actuation with $\mathcal{H}_2$ optimal combined feedforward/feedback control for the NREL 5-MW turbine at a 13 m/s wind speed operating point with 9 seconds of available preview time.

lidar is removing high frequency content from the measurement, the remaining low frequency errors due to evolution do not become significant until at least 7 s (126 m) of preview, when even the low frequencies of turbulence have significantly evolved. Additional details regarding this control study can be found in Laks et al. (2013).

10.8 Control Example 2: $\mathcal{H}_2$ Optimal Control with Model of Measurement Coherence

In this section, an $\mathcal{H}_2$ optimal controller design is described where a model of wind measurement coherence is included in the design process. This combined feedforward/feedback controller is designed to minimize a weighted sum of RMS generator speed error and RMS blade pitch (deviation from the operating point) using the NREL 5-MW model, assuming the Kaimal wind spectrum, class B turbulence (medium turbulence) and the normal turbulence model (NTM) (Jonkman, 2009).

Figure 151 shows the resulting closed-loop generator speed and pitch actuation responses for three different cases: feedback only, typical measurements (measurement coherence is modeled as the magnitude squared of a single-pole low-pass filter with bandwidth of 0.2 Hz), and perfect measurements. We see that with lidar measurements, generator speed error is improved at both low and high frequencies, and pitch actuation is reduced at high frequencies.

Figure 152 shows the magnitudes of the optimal controllers. As the lidar measurement improves, the feedforward controller action increases at low frequencies, and the feedback controller action decreases at low frequencies, freeing it to act more at mid frequencies if necessary. The decrease in low-frequency feedback action is helpful because feedback control performance is fundamentally limited by the Bode sensitivity integral (Franklin et al., 2006), which essentially says that a decrease in sensitivity to disturbance at one frequency must be balanced by an increase in sensitivity to disturbance at another frequency. When feedforward takes over at low frequencies, feedback can increase sensitivity to low-frequency disturbance, and therefore can decrease sensitivity to mid-frequency disturbance. Thus low-frequency wind measurements can lead to reductions in mid-frequency loads. This increase in mid-frequency feedback action occurs for typical lidar measurements, but for perfect measurements, feedback is unnecessary because the feedforward controller takes over at all frequencies, assuming

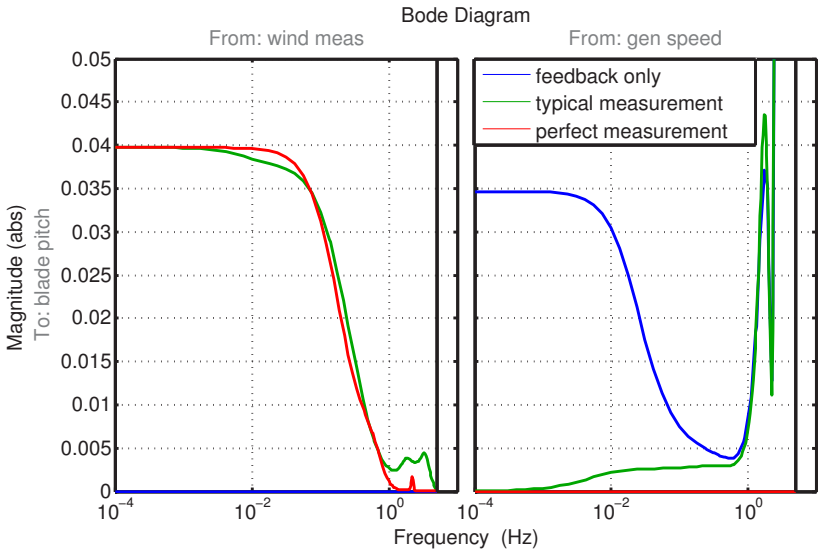

Figure 152: Frequency responses of $\mathcal{H}_2$ optimal feedforward (From: wind meas) and feedback (From: gen speed) controllers for the NREL 5-MW turbine at a 13 m/s wind speed operating point, with 9 seconds of available preview time.

perfect knowledge of the turbine model.

10.9 Summary

This chapter presented an introduction to wind turbine control using lidar, primarily focusing on a frequency domain analysis of lidar measurement quality. Two control examples were included to highlight the challenges that accompany the design of feedforward controllers that use lidar measurements. A summary of the main results presented in this chapter is provided here.

- With perfect preview measurements of wind speeds, a model-inverse feedforward controller can completely cancel the effect of the wind disturbance on a turbine variable of interest, assuming perfect turbine modeling. For imperfect preview measurements, a measurement filter can be introduced such that the mean square value of the turbine variable is minimized.
- A feedforward control system requires not only measurements of the wind disturbance, but also a certain amount of preview time required for implementation.
- For blade pitch control, the lidar system should be used to acquire an estimate of the "blade effective wind speed," a weighted integral of wind speeds along the blade that describes the equivalent wind speed experienced by the blade. Furthermore, the longitudinal component of the wind is of interest because it has the greatest impact on the rotor aerodynamics.
- The two main sources of lidar measurement error are geometry effects, or estimation of the longitudinal component using a line-of-sight measurement, and wind evolution, which represents the decorrelation of the turbulence as it travels downwind between the measurement location and the turbine. Spatial averaging, inherent in lidar measurements, appears to help with estimation of blade effective wind speed.
- Wind turbine control systems are often defined in the non-rotating frame, where estimates of the collective, vertical shear, and horizontal shear wind components are required, as opposed to measurements of the wind speed at individual blades.

- Measurement coherence, which can be calculated given a frequency domain wind field model, can be used to find the optimal lidar measurement configuration that minimizes the mean square value of a turbine variable of interest.
- For a hub-mounted lidar, there is an optimal preview distance that minimizes measurement error. For shorter preview distances, geometry effects cause error to increase. Beyond the optimal preview distance, wind evolution becomes more severe, thus increasing measurement error.
- A combined feedback/feedforward control system can be optimized given the measurement coherence. For perfect measurement coherence, the control system relies entirely on the feedforward controller. For measurements that are completely uncorrelated with the wind disturbance, the control system relies entirely on feedback. For imperfect measurements that have some correlation with the wind disturbance, the optimal control strategy utilizes both feedback and feedforward control.

Notation

1P	once per revolution
CPSD	Cross-Power Spectral Density
CW	continuous-wave
$C_P(r)$	radially-dependent coefficient of power
$C_Q(r)$	radially-dependent coefficient of torque
d	measurement preview distance
DEL	Damage Equivalent Load
f	frequency (Hz)
F	feedforward controller
F_ℓ	lidar focus distance
h	hub height
H_{pre}	lidar measurement prefilter
IEC	International Electrotechnical Commission
K_a	state feedback gains for augmented states
K_{ff}	state feedback gains for preview measurements
K_x	state feedback gains for turbine states
$\vec{\ell}$	lidar direction vector
NREL	National Renewable Energy Laboratory
N_{gb}	gear box ratio
PSD	Power Spectral Density
$\mathbf{P_a}$	augmented dynamics
$\mathbf{P_t}$	wind turbine dynamics
r	lidar scan radius
R	rotor radius
R_ℓ	range along lidar beam
RMS	root mean square
STD	standard deviation
$S_{aa}(f)$	power spectral density of signal a
$S_{ab}(f)$	cross-power spectral density between signals a and b
T_s	sample period of control system
T_{yw_t}	transfer function from wind disturbance to output y
$T_{y\beta_{FF}}$	transfer function from feedforward blade pitch command to output y
u	longitudinal wind speed
U	mean wind speed
u_{blade}	blade effective wind speed
u_{hh}	hub height or collective wind speed component
$\hat{u}_{hh}$	estimate of hub height wind speed component from lidar measurements
u_{rotor}	rotor effective wind speed
$u_{wt,los}$	range weighted line-of-sight measurement
$\hat{u}$	estimate of u component from lidar measurement
$\vec{u}_{wt}$	range weighted wind speed vector
v	transverse wind speed
w	vertical wind speed

$W_b(r)$	blade effective weighting function
$W(F_\ell, R_\ell)$	lidar range weighting function
w_m	wind speed disturbance preview measurement
w_t	wind disturbance at the turbine
x	longitudinal (along-wind) direction
y	transverse (horizontal) direction; output error variable from the turbine
y_0	collective component of output error variable from the turbine
y_h	horizontal component of output error variable from the turbine
y_v	vertical component of output error variable from the turbine
z	vertical direction
$\gamma^2_{ab}(f)$	coherence between signals a and b
Δ_h	horizontal shear wind speed component
$\hat{\Delta}_h$	estimate of horizontal shear component from lidar measurements
Δ_v	vertical shear wind speed component
$\hat{\Delta}_v$	estimate of vertical shear component from lidar measurements
θ_R	rotor position
ψ	azimuth angle in rotor plane
Ω_g	generator speed
Ω_R	rotor speed

References

Bir, B. (2008) Multiblade coordinate transformation and its application to wind turbine analysis. *Proc. AIAA Aerospace Sciences Meeting*, Reno, NV

Bossanyi, E. A. (2005) Further load reductions with individual pitch control. *Wind Energy* **8**:481–485

Bossanyi, E. A. (2012) Un-freezing the turbulence: Improved wind field modeling for investigating lidar-assisted wind turbine control. *Proc. European Wind Energy Association Annual Event (EWEA)*, Copenhagen, Denmark

Bossanyi, E. A., Kumar, A., and Hugues-Salas, O. (2012b) Wind turbine control applications of turbine-mounted lidar. *Proc. Science of Making Torque from Wind*, Oldenburg, Germany

Dunne, F., Pao, L. Y., Wright, A. D., Jonkman, B., Kelley, N., and Simley, E. (2011a) Adding feedforward blade pitch control for load mitigation in wind turbines: Non-causal series expansion, preview control, and optimized FIR filter methods. *Proc. AIAA Aerospace Sciences Meeting*, Orlando, FL

Dunne, F., Pao, L. Y., Wright, A. D., Jonkman, B., and Kelley, N. (2011b) Adding feedforward blade pitch control to standard feedback controllers for load mitigation in wind turbines. *Mechatronics* **21**:682–690

Dunne, F., Schlipf, D., Pao, L. Y., Wright, A. D., Jonkman, B., Kelley, N., and Simley, E. (2012) Comparison of two independent LIDAR-based pitch control designs. *Proc. AIAA Aerospace Sciences Meeting*, Nashville, TN

Franklin, G. F., Powell, J. D., and Emami-Naeini, A. (2006) Feedback control of dynamic systems, fifth edition, Pearson Prentice Hall

Frehlich, R. and Kavaya, M. (1991) Coherent laser performance for general atmospheric refractive turbulence. *Applied Optics* **30**:5325–5352

Frehlich, R., Meillier, Y., Jensen, M., Balsley, B. and Sharman, M. (2006) Measurements of boundary layer profiles in an urban environment. *Applied Meteorology and Climatology* **45**:821–837

Harris, M., Hand, M., and Wright, A. (2005) Lidar for turbine control, NREL/TP-500-39154, Tech. Rep., National Renewable Energy Laboratory, Golden, CO

Harris, M., Bryce, D., Coffey, A., Smith, D., Birkemeyer, J., and Knopf, U. (2007) Advance measurements of gusts by laser anemometry. *Wind Engineering and Industrial Aerodynamics* **95**:1637–1647

Hazell, A. (2008) Discrete-Time Optimal Preview Control, Ph.D. Thesis, Imperial College, University of London, London, England

IEC (2001) IEC 61400-13 Ed. 1: Wind turbine generator systems: Measurement of mechanical loads. Int. Electrotechnical Commission

IEC (2005) IEC 61400-1 Ed. 3: Wind turbines - Part 1: Design requirements. Int. Electrotechnical Commission

Jonkman, J. and Buhl, M. (2005) FAST user's guide, NREL/TP-500-38230, Tech. Rep., National Renewable Energy Laboratory, Golden, CO

Jonkman, B. (2009) TurbSim user's guide: Version 1.50, NREL/TP-500-46198, Tech. Rep., National Renewable Energy Laboratory, Golden, CO

Jonkman, J., Butterfield, S., Musial, W., and Scott, G. (2009) Definition of a 5-MW reference wind turbine for offshore system development, NREL/TP-500-38060, Tech. Rep., National Renewable Energy Laboratory, Golden, CO

Kodama, N., Matsuzaka, T., Tuchiya, K., and Arinaga, S. (1999) Power variation control of a wind generator by using feed-forward control. *Renewable Energy* **16**:847–850

Kragh, K. A., Hansen, M. H., and Mikkelsen, T. (2013) Precision and shortcomings of yaw error estimation using spinner-based light detection and ranging. *Wind Energy* **16**:353–366

Kristensen, L. (1979) On longitudinal spectral coherence. *Bound.-Layer Meteorol.* **16**:145–153

Laks, J., Pao, L. Y., Simley, E., Wright, A. D., Kelley, N., and Jonkman, B. (2011a) Model predictive control using preview measurements from lidar. *Proc. AIAA Aerospace Sciences Meeting*, Orlando, FL

Laks, J., Pao, L. Y., Wright, A. D., Kelley, N., and Jonkman, B. (2011b) The use of preview wind measurements for blade pitch control. *Mechatronics* **21**:668–681

Laks, J., Simley, E., and Pao, L. Y. (2013) A spectral model for evaluating the effect of wind evolution on wind turbine preview control. *Proc. American Control Conference*, Washington, D.C.

Mikkelsen, T. (2009) On mean wind and turbulence profile measurements from ground-based wind lidars: limitations in time and space resolution with continuous wave and pulsed lidar systems. *Proc. European Wind Energy Conference*, Stockholm, Sweden

Mikkelsen, T., Angelou, N., Hansen, K., Sjöholm, M., Harris, M., Slinger, C., Hadley, P., Scullion, R., Ellis, G., and Vives, G. (2013) A spinner-integrated wind lidar for enhanced wind turbine control. *Wind Energy* **16**:625–643

Mirzaei, M., Soltani, M., Poulsen, N. K., and Niemann, H. H. (2013) Model predictive control of wind turbines using uncertain lidar measurements. *Proc. American Control Conference*, Washington, D.C.

Moriarty, P.J. and Hansen, A.C. (2005) Aerodyn Theory Manual, NREL/TP-500-36881, Tech. Rep., National Renewable Energy Laboratory, Golden, CO

Pao, L. Y. and Johnson, K. E. (2011) Control of wind turbines: Approaches, challenges, and recent developments. *IEEE Control Systems Magazine* **31**:44–62

Pedersen, A. T., Sjöholm, M., Angelou, N., Mikkelsen, T., Montes, B. F., Pedersen, J. E., Slinger, C., and Harris, M. (2013) Full-scale field test of a blade-integrated dual-telescope wind lidar. *Proc. European Wind Energy Association Annual Event (EWEA)*, Vienna, Austria

Rettenmeier, A., Bischoff, O., Hofsäß, M., Schlipf, D., and Trujillo, J. J. (2010) Wind field analysis using a nacelle-based LIDAR system. *Proc. European Wind Energy Conference*, Warsaw, Poland

Schlipf, D. and Kühn, M. (2008) Prospects of a collective pitch control by means of predictive disturbance compensation assisted by wind speed measurements. *Proc. German Wind Energy Conference (DEWEK)*, Bremen, Germany

Schlipf, D., Trujillo, J. J., Basterra, V., and Kühn, M. (2009) Development of a wind turbine lidar simulator. *Proc. European Wind Energy Conference*, Marseille, France

Schlipf, D., Schuler, S., Grau, P., Allgöwer, F., and Kühn, M. (2010) Look-ahead cyclic pitch control using LIDAR. *Proc. Science of Making Torque from Wind*, Heraklion, Greece

Schlipf, D., Kapp, S., Anger, J., Bischoff, O., Hofsäß, M., Rettenmeier, A., Smolka, U., and Kühn, M. (2011) Prospects of optimization of energy production by lidar assisted control of wind turbines. *Proc. European Wind Energy Association Annual Event (EWEA)*, Brussels, Belgium

Schlipf, D., Mann, J., Rettenmeier, A., and Cheng, P. W. (2012a) Model of the correlation between lidar systems and wind turbines for lidar assisted control. *Proc. Int. Symp. for the Advancement of Boundary Layer Remote Sensing*, Boulder, CO

Schlipf, D., Schlipf, D. J., and Kühn, M. (2012b) Nonlinear model predictive control of wind turbines using LIDAR. *Wind Energy*

Scholbrock, A. K., Fleming, P . A., Fingersh, L. J., Wright, A. D., Schlipf, D., Haizman, F., and Belen, F. (2013) Field testing LIDAR based feed-forward controls on the NREL controls advanced research turbine. *Proc. AIAA Aerospace Sciences Meeting*, Grapevine, TX

Simley, E., Pao, L. Y., Kelley, N., Jonkman, B., and Frehlich, R. (2012) LIDAR wind speed measurements of evolving wind fields. *Proc. AIAA Aerospace Sciences Meeting*, Nashville, TN

Simley, E. and Pao, L. Y. (2013a) Correlation between rotating LIDAR measurements and blade effective wind speed. *Proc. AIAA Aerospace Sciences Meeting*, Grapevine, TX

Simley, E. and Pao, L. Y. (2013b) Reducing lidar wind speed measurement error with optimal filtering. *Proc. American Control Conference*, Washington, D.C.

Simley, E., Pao, L. Y., Frehlich, R., Jonkman, B., and Kelley, N. (2013c) Analysis of light detection and ranging wind speed measurements for wind turbine control. *Wind Energy*

Slinger, C. and Harris, M. (2012) Introduction to continuous-wave Doppler lidar. *Proc. Summer School in Remote Sensing for Wind Energy*, Boulder, CO

Wang, N., Johnson, K., and Wright, A. (2012a) Combined feedforward and feedback controllers for turbine power capture enhancement and fatigue loads mitigation with pulsed lidar. *Proc. AIAA Aerospace Sciences Meeting*, Nashville, TN

Wang, N., Johnson, K., and Wright, A. (2012b) FX-RLS-based feedforward control for lidar-enabled wind turbine load mitigation. *IEEE Transactions on Control Systems Technology* **20**:1212–1222

WT_Perf (2012). NWTC Design Codes (WT_Perf by Andrew Platt). http://wind.nrel.gov/designcodes/simulators/wtperf/. Last modified 26-November-2012

11 Lidars and wind profiles

Alfredo Peña
DTU Wind Energy, Risø Campus, Roskilde, Denmark

11.1 Introduction

Wind lidars have been able to observe wind profiles since the 70's and were first commercialized in 2005. The ZephIR continuous wave (cw) lidar, nowadays manufactured by Natural Power, entered the wind energy community to compete against the traditional instrumentation, such as cup anemometers and wind vanes, offering in advantage the measurement of wind speed and direction profiles up to 200 m above ground level (AGL), avoiding the flow distortion effects that the traditional instruments suffer when they are mounted on structures. The performance of the ZephIR, when compared with cup anemometers at several heights up to about 100 m, showed high agreement from first studies over land (Smith et al., 2006) and over the sea (Kindler et al., 2007).

Later, observations from cup anemometers were combined with ZephIR measurements at the Nysted (Antoniou et al., 2006) and at the Horns Rev (Peña et al., 2009) offshore wind farms to reproduce wind profiles up to about 160 m above mean sea level (AMSL). Although the results from the campaign at Horns Rev showed good agreement with the wind profile theory, limitations on the measurement range were found due to the contamination of the lidar's Doppler spectra by clouds, which gave the opportunity to Natural Power to improve the cloud correction algorithms of the ZephIR.

Since we are interested in wind profile retrieval within 30–200 m where large wind turbines operate, cloud contamination is a serious concern. In fact, when this issue was first addressed, the role of the aerosol profile on the lidar's probe volume (for any kind of lidar) became more important, specially since the expertise on this subject is rather limited. Mist and fog have also been realized as serious hazards for cws lidars (Peña et al., 2012), which for wind profile analysis results in high wind shears close to the ground, i.e. that–for example, wind profiles observed under stable atmospheric conditions might be interpreted as stable profiles.

Nowadays, many more wind lidars such as the Windcube and Galion systems, from the companies LeoSphere and Sgurr Energy, respectively, are also in the market. Both lidars offer instantaneous wind profile observation up to about 10000 m (there is a broad range of types with different ranges), but the instruments' range actually depends on the atmospheric conditions, namely on the amount of aerosols in the atmosphere, which is proportional to the signal-to-noise ratio (SNR). This is important as the SNR from wind lidars has been used for boundary-layer height (BLH) detection (Peña et al., 2013).

As with the ZephIR, a number of campaigns combining observations from cup and sonic anemometers at high meteorological masts and from pulsed lidars have been carried out. Peña et al. (2010b) described the neutral wind profile and Peña et al. (2010a) the diabatic wind profile, both for homogenous and flat terrain up to 300 m AGL, both using the Windcube to extend wind speed observations from traditional meteorological instrumentation at the National Test Station for Large Wind Turbines (NTWT) at Høvsøre, Denmark.

Other meteorological campaigns have looked even further; Floors et al. (2013) illustrated an intercomparison between wind speed observations from a long-range wind lidar and a numerical model up to 800 m and Peña et al. (2013) showed wind speed and direction profiles of the same instrument up to 1000 m. Such studies do not only help for increasing

By wind profile, it is meant the vertical wind speed profile

High agreement here refers to $1:1$ comparisons of wind velocity observations with linear correlation coefficients close to 1

By wind shear, it is meant the vertical wind shear

the accuracy in wind power calculations, but also for the improvement of the parameterizations used in boundary-layer meteorology and therefore of weather and numerical models. These 'high' observations have also started to 're-popularize' the study of the role of baroclinity on the wind profile and turning of the wind, and the ability of numerical models to predict such effects.

11.2 Wind profile theory

Mixing-length theory, firstly introduced by Prandtl (1932) for the description of atmospheric flow, is here chosen for the analysis of the wind profile. The local wind shear $\partial U/\partial z$, where U is the mean horizontal wind sped and z the height above the ground, is parameterized as

$$\frac{\partial U}{\partial z} = \frac{u_*}{l} \tag{244}$$

where u_* is the local friction velocity and l is the local mixing length.

11.2.1 Surface layer

In the surface layer, which covers the first 5–10% of the atmospheric boundary layer (ABL), the mixing length l_{SL} is given as

$$l_{SL} = \kappa z \phi_m \tag{245}$$

where κ is the von Kármán constant (≈ 0.4) and ϕ_m the dimensionless wind shear from Monin-Obukhov similarity theory (MOST) (Monin and Obukhov, 1954), which is defined as

$$\phi_m = \frac{\kappa z}{u_{*o}} \frac{\partial U}{\partial z} \tag{246}$$

where u_{*o} is the surface-layer friction velocity (u_* is rather constant in the surface layer). Several experiments have suggested expressions for the behaviour of ϕ_m with stability, which have resulted in the so-called flux-profile relationships. For unstable and stable conditions, respectively, these are given as

$$\phi_m = (1 - az/L)^p \qquad \text{and} \tag{247}$$

$$\phi_m = 1 + bz/L \tag{248}$$

where a, b, and p are empirical constants (Businger et al. 1971; Högström 1988) and L is the Obukhov length estimated as

$$L = -\frac{{u_{*o}}^3 T_o}{\kappa g \overline{w'\Theta_v{}'}_o} \tag{249}$$

where T_o is the mean surface-layer temperature, g is the gravitational acceleration, and $\overline{w'\Theta_v{}'}_o$ is the surface-layer kinematic virtual heat flux. Assuming $u_* = u_{*o}$ and $l = l_{SL}$ in Eq. (244), and combining it with Eqs. (245) and (246), the integration with height of Eq. (244) gives the surface-layer wind profile,

$$\frac{U}{u_{*o}} = \frac{1}{\kappa}\left[\ln\left(\frac{z}{z_o}\right) - \psi_m\right] \tag{250}$$

where z_o is the surface roughness length and ψ_m is the diabatic correction of the wind profile, which is derived from the integration with the dimensionless stability parameter z/L of ϕ_m in Eqs. (247) and (248) (Stull, 1988). For neutral conditions, which are favorable for wind energy due to high wind speed characteristics, $\phi_m = 1$ and $\psi_m = 0$, thus resulting in the well-known logarithmic wind profile.

Figure 153 illustrates the average dimensionless wind profiles observed for different stability conditions over flat and homogenous terrain at Høvsøre, Denmark. Each average wind profile is computed by classifying the individual 10-min wind profiles into stability classes, based on the Obukhov length as performed in Gryning et al. (2007) and Peña et al. (2010a). As shown

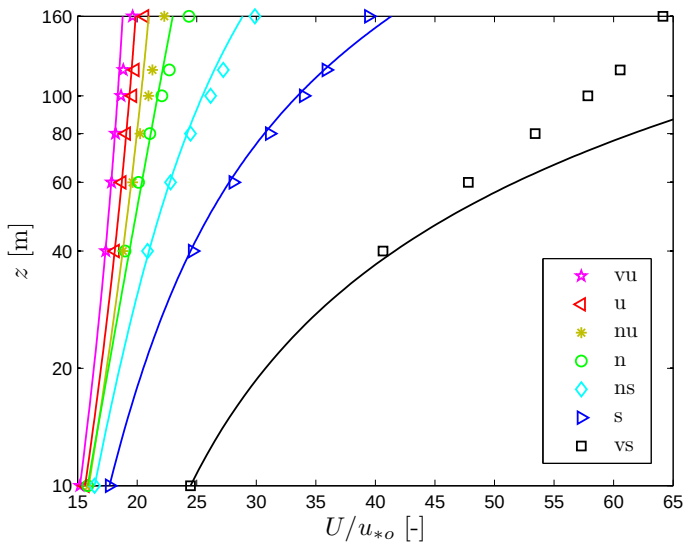

Figure 153: Wind profiles observed for different stability classes at Høvsøre, Denmark. The markers indicate the observations and the solid lines the predictions using Eq. (250). Legend: vu (very unstable), u (unstable), nu (near unstable), n (neutral), ns (near stable), s (stable), and vs (very stable).

in the figure, Eq. (250) fits well the observations in the surface layer and the observations start to departure from the surface-layer wind profile at about 100 m for near-neutral conditions and 60 m for very stable conditions. The roughness length is estimated fitting Eq. (250) to the first observational height only.

With such dimensionless x-axis, the wind profile is a function of roughness length and stability only. In the surface layer and over flat and homogenous land, Eq. (250) generally fits well the average observations and the wind profile can easily be studied using such dimensionless fashion, because z_o does not vary significantly. The standard error for the observations in Fig. 153 increases with height, indicating that other external parameters, such as the BLH z_i and baroclinity, start to play a more important role for the description of the wind profile. However, even for the observations at 160 m, the highest standard error is 0.35, i.e. the individual wind profiles concentrate close to the average.

11.2.2 Marine surface layer

Over water, the roughness length is not constant and depends, among others, on wind stress, waves, and fetch. The scaling U/u_{*o} is appropriate for the surface-layer wind profile for constant z_o values. Using the simple parameterization of Charnock (1955),

$$z_o = \alpha_c \frac{u_{*o}^2}{g} \tag{251}$$

where α_c is the Charnock's parameter (≈ 0.012), it is straightforward to realize that the scaling U/u_{*o} produces wind profiles that do not converge onto a straight line. Peña and Gryning (2008) analyzed this issue and suggested the following scaling for the marine wind profile,

$$\frac{U}{u_{*o}} + \frac{1}{\kappa}\ln\left[1 + 2\frac{\Delta u_{*o}}{\overline{u_{*o}}} + \left(\frac{\Delta u_{*o}}{\overline{u_{*o}}}\right)^2\right] = \frac{1}{\kappa}\left[\ln\left(\frac{z}{\overline{z_o}}\right) - \psi_m\right] \tag{252}$$

where $\Delta u_{*o} = u_{*o} - \overline{u_{*o}}$, i.e. Δu_{*o} is a *fluctuating* surface-layer friction velocity equal to the difference between the observation u_{*o} and the ensemble average $\overline{u_{*o}}$. $\overline{z_o}$ is a mean roughness length parameterized as Eq. (251), but replacing u_{*o} with the ensemble average $\overline{u_{*o}}$. Eq. (252) differs from Eq. (250), because it adds a dimensionless wind speed, the left term in square

brackets in Eq. (252), which allows the wind profiles to converge onto a straight line for the same stability class. It also uses a mean roughness length, which allows for an empirical estimation of the Charnock's parameter.

11.2.3 Boundary layer

The surface-layer wind profile was previously derived from the assumption that the length scale grows infinitively with height. At about 100 m AGL and neutral conditions–for example, this assumption is not longer valid. The IEC (2005) standard suggests to use surface-layer scaling for the length scale up to 60 m AGL and to assume a constant length scale upwards.

There has been a number of suggestions for the behaviour with height of the mixing length in the ABL, which departure from Eq. (245). Blackadar (1962) and Panofsky (1973) limited the growth of the length scale and proposed neutral mixing-length models, which were used to numerically compute the ABL wind profile. Lettau (1962) proposed a similar model to that of Blackadar (1962), but in which the length scale starts to decrease slowly beyond the surface layer. Gryning et al. (2007) proposed a mixing-length model, which assumes that the top of the boundary layer acts as the ground, and therefore, the length scale has a zero value at the top of the ABL. Based on the length-scale behaviour observed from turbulence measurements far beyond the surface layer, as shown in Caughey and Palmer (1979), and the close relation between the length scale of the wind profile and that derived from turbulence measurements as observed in Peña et al. (2010b), the idea of a decreasing mixing-length with height is rather reasonable.

Simple analytical models for the ABL wind profile can be derived, using such *limiting* mixing-length models and a model for the local friction velocity, by integrating with height Eq. (244). This was performed by Gryning et al. (2007) and Peña et al. (2010a) for the diabatic flow over flat land and homogeneous terrain, Peña et al. (2008) for diabatic flow over the sea, and Peña et al. (2010b) for neutral flow over flat and homogeneous land. The main results of the comparison of these models and wind speed observations at great heights at Høvsøre and at the Horns Rev wind farm are presented in the following section.

11.3 Comparison with observations at great heights

11.3.1 Marine observations

Marine wind speed observations from combined cup anemometer and ZephIR measurements up to 161 m AMSL, within a sector where the upstream flow is free and homogeneous at the Horns Rev wind farm, were compared to wind profile models in Peña et al. (2008) showing good agreement. The neutral and unstable wind profile models are identical to those traditionally used for the surface layer, Eq. (250), although the physics involved in their derivation are different. For the stable wind profile, a correction is applied to the stability parameter to take into account z_i:

$$\frac{U}{u_{*o}} = \frac{1}{\kappa}\left[\ln\left(\frac{z}{z_o}\right) - \psi_m\left(1 - \frac{z}{2z_i}\right)\right]. \tag{253}$$

Figure 154 illustrates the results using the scaling proposed in Peña and Gryning (2008), which can be used for wind profile comparison whenever the wind speed can be scaled with the friction velocity.

The stable BLH was estimated in Peña et al. (2008) by use of the Rossby and Montgomery (1935) formula,

$$z_i = C\frac{u_{*o}}{|f_c|} \tag{254}$$

where C is a proportionality parameter (≈ 0.15) and f_c is the Coriolis parameter. Eq. (254) is valid for neutral conditions only, thus, the buoyancy contribution was accounted for in stable conditions by decreasing the value of C.

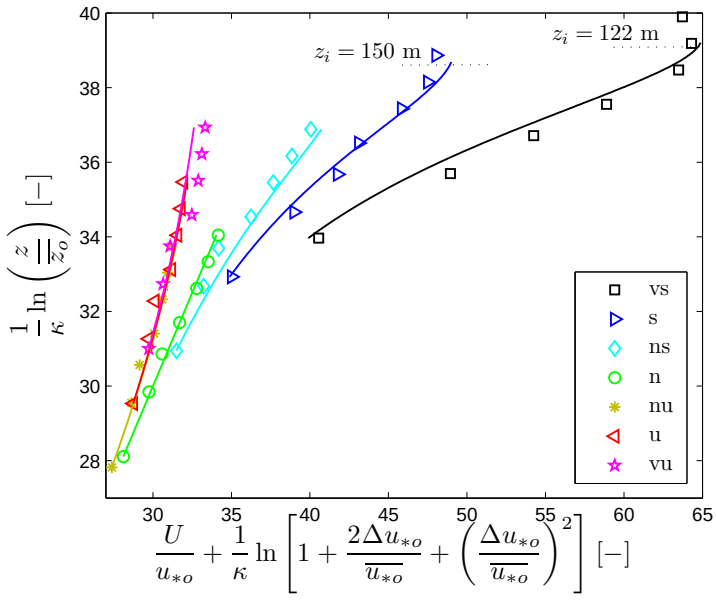

Figure 154: Wind profiles for different stability classes from combined lidar/cup anemometer observations at the Horns Rev wind farm in Denmark. The markers indicate the observations and the solid lines the predictions using Eq. (250) for unstable and neutral conditions and Eq. (253) for stable conditions. The boundary-layer height z_i is also indicated. Legend as in Fig. (153).

11.3.2 Neutral observations over flat land

Near-neutral wind speed observations from combined cup anemometer and Windcube measurements up to 300 m AGL, within an homogenous upwind sector at Høvsøre, were compared in Peña et al. (2010b) to a set of neutral wind profile models:

$$U = \frac{u_{*o}}{\kappa}\ln\left(\frac{z}{z_o}\right), \tag{255}$$

$$U = \frac{u_{*o}}{\kappa}\left[\ln\left(\frac{z}{z_o}\right) + \frac{1}{d}\left(\frac{\kappa z}{\eta}\right)^d - \left(\frac{1}{1+d}\right)\frac{z}{z_i}\left(\frac{\kappa z}{\eta}\right)^d - \frac{z}{z_i}\right], \tag{256}$$

$$U = \frac{u_{*o}}{\kappa}\left[\ln\left(\frac{\sinh\left(\kappa z/\eta\right)}{\sinh\left(\kappa z_o/\eta\right)}\right) - \frac{z}{z_i}\frac{\kappa z}{2\eta}\right], \tag{257}$$

$$U = \frac{u_{*o}}{\kappa}\left[\ln\left(\frac{z}{z_o}\right) + \frac{z}{l_{MBL}} - \frac{z}{z_i}\left(\frac{z}{2l_{MBL}}\right)\right], \tag{258}$$

which correspond to the logarithmic wind profile, a simple analytical solution for the wind profile from the mixing-length model of Blackadar (1962) ($d = 1$) and Lettau (1962) ($d = 5/4$), another simple solution using the mixing-length model of Panofsky (1973), and the wind profile model of Gryning et al. (2007), respectively. d is a parameter that controls the growth of the length scale, η is the limiting value for the length scale in the upper atmosphere, and l_{MBL} is a middle boundary-layer length scale.

η has traditionally been parameterized as,

$$\eta = D\frac{u_{*o}}{|f_c|} \tag{259}$$

where Blackadar (1965) suggested $D = 63 \times 10^{-4}$ and from the analysis of Lettau (1962) and assuming $\mathrm{Ro} = 5.13 \times 10^5$, where Ro is the surface Rossby number, $D = 96 \times 10^{-4}$. In this fashion, when combining Eq. (260) with Eqs. (255)–(258), the ratio $u_{*o}/|f_c|$ in can be

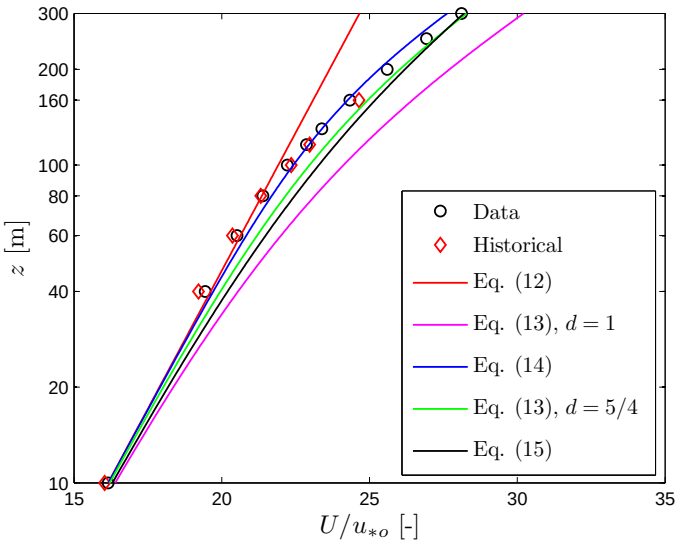

Figure 155: Neutral wind profile observed at Høvsøre, Denmark. The markers indicate combined lidar/cup anemometer observations (Data) and the mean wind profile from about 3 years of cup anemometer observations (Historical). The solid lines indicate the predictions using $C = 0.15$, $D = 73 \times 10^{-4}$, 58×10^{-4}, and 100×10^{-4} for Eq. (256) with $d = 1$, Eq. (257), and Eq. (256) with $d = 5/4$, respectively.

replaced by z_i/C from Eq. (254). l_{MBL} was parameterized by Gryning et al. (2007) as

$$l_{MBL} = \frac{u_{*o}/|f_c|}{-2\ln\left(\frac{u_{*o}}{|f_c|z_o}\right) + 55}. \tag{260}$$

The results of the comparison are illustrated in Figure 155. The models, which limit the growth of the length scale, have a better agreement with the wind speed observations beyond the surface layer (≈ 80 m). The logarithmic wind profile fits well the measurements within the surface layer only.

11.3.3 Diabatic observations over flat land

Wind speed observations from combined cup anemometer and Windcube measurements up to 300 m AGL, within an homogenous upwind sector and for different stability conditions at Høvsøre, were compared in Peña et al. (2010a) to a set of diabatic wind profile models. These models were derived by extending the surface-layer length scale of the mixing-length models of Blackadar (1962), Lettau (1962), and Gryning et al. (2007) to account for atmospheric stability using MOST. For example, using the extended mixing-length models of Blackadar (1962) and Lettau (1962), the wind profile is given as,

$$U = \frac{u_{*o}}{\kappa}\left[\ln\left(\frac{z}{z_o}\right) - \psi_m + \frac{1}{d}\left(\frac{\kappa z}{\eta}\right)^d - \left(\frac{1}{1+d}\right)\frac{z}{z_i}\left(\frac{\kappa z}{\eta}\right)^d - \frac{z}{z_i}\right], \tag{261}$$

$$U = \frac{u_{*o}}{\kappa}\left[\ln\left(\frac{z}{z_o}\right) + b\frac{z}{L}\left(1 - \frac{z}{2z_i}\right) + \frac{1}{d}\left(\frac{\kappa z}{\eta}\right)^d - \left(\frac{1}{1+d}\right)\frac{z}{z_i}\left(\frac{\kappa z}{\eta}\right)^d - \frac{z}{z_i}\right] \tag{262}$$

for unstable and stable conditions, respectively.

η was parameterized in Peña et al. (2010a) using Rossby-number similarity as,

$$\eta = \frac{\kappa z_i}{[d(1+d)]^{1/d}}\left[\left(\left[\ln\left(\frac{u_{*o}}{f_c z_o}\right) - A\right]^2 + B^2\right)^{1/2} + 1 - \ln\left(\frac{z_i}{z_o}\right)\right]^{-1/d} \tag{263}$$

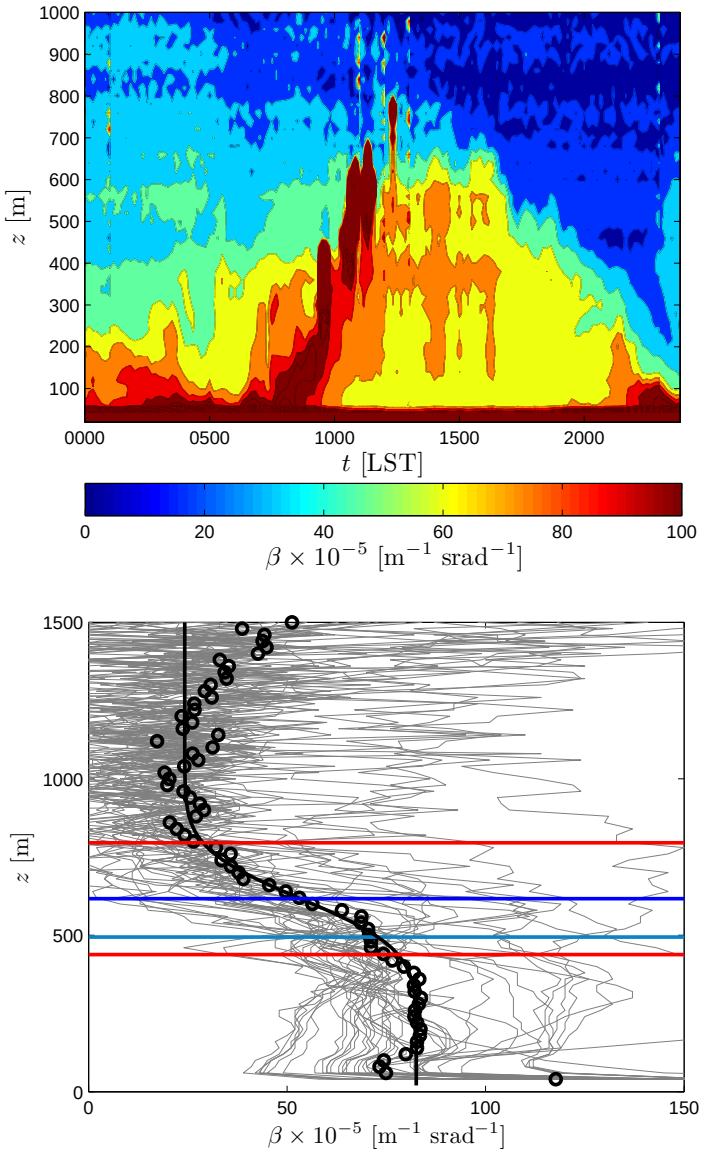

Figure 156: Top frame: Ceilometer observations of the aerosol backscatter coefficient β during a convective day at Høvsøre, Denmark. Bottom frame: Aerosol backscatter profile from ceilometer measurements at Høvsøre for neutral conditions. The gray lines show the aerosol profiles, the markers the average aerosol profile, the black line the fit function from Steyn et al. (1999), and the horizontal lines the estimation of z_i from the fit function (blue), the entrainment zone depth (red lines), and the estimation of z_i from Eq. (254) (cyan).

where A and B are the integration constants for a given stability from the resistant laws. A similar paramaterization is found in Gryning et al. (2007) for l_{MBL}. z_i was estimated from Eq. (254) for neutral and stable conditions, and from observations of the aerosol backscatter coefficient from a Vaisala CL31 ceilometer for unstable conditions. Figure 156 (top frame) illustrates the behaviour of the aerosol backscatter coefficient, β, during a day where most of the unstable profiles were measured. It is observed that during daylight time (1000–1800 LST), the aerosols reached 600–700 m marking the height of the unstable boundary layer. In Peña et al. (2010a), aerosol backscatter profiles observed simultaneously with the wind profiles for each stability class are used to estimate the boundary-layer height. The results for the neutral stability class are illustrated in Figure 156 (bottom frame). z_i is estimated using the modified error function suggested by Steyn et al. (1999) and a good agreement was found when compared to the estimation from Eq. (254) for neutral conditions.

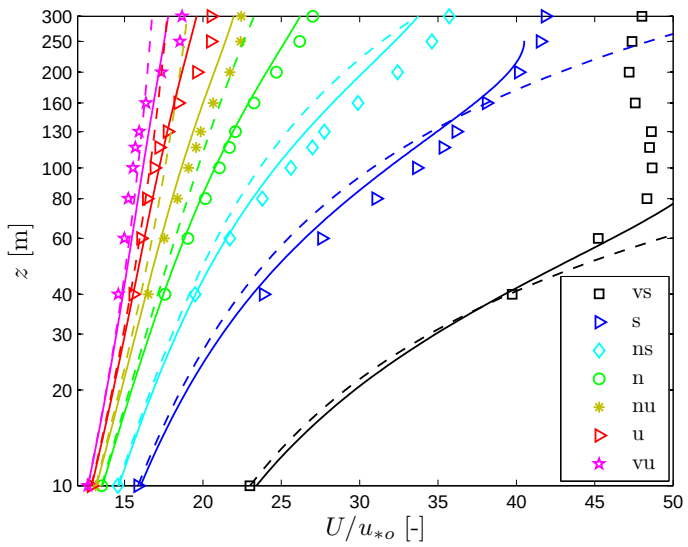

Figure 157: Wind profiles observed for different stability classes at Høvsøre, Denmark. The markers indicate the combined lidar/cup anemometer observations, the solid lines the predictions using Eqs. (261) and (262) with $d = 5/4$, and the dashed lines the predictions from Eq. (250). Legend as in Fig. 153.

Once η and z_i are estimated, the wind speed observations can be compared to the models. Figure 157 illustrates the comparison of the models in Eqs. (261) and (262) with $d = 5/4$, the surface-layer wind profile, Eq. (250), and the wind speed observations for the number of stability classes also used in Figures 153 and 154. As with the neutral observations, surface-layer scaling fits well the observations within the surface layer only. The wind profile model, which limits the value of the length scale, corrects for the departures of the observations beyond the surface layer. Similar results were obtained in Peña et al. (2010a) using Eqs. (261) and (262) with $d = 1$ and the wind profile models in Gryning et al. (2007).

11.4 Summary

- The use of ground-based remote sensing instruments has been useful for the study and description of the wind profile within and beyond the surface layer and for the improvement of the models that are traditionally used in wind power and boundary-layer meteorology.
- Over flat land and homogenous terrain and over the sea, the surface-layer wind profile fits well the observations for a wide range of atmospheric stability conditions within the surface layer only. For the analysis of wind profiles over water, however, a new scaling should be added in order to account for the variable roughness length.
- Wind speed observations from combined lidar/cup anemometer measurements up to 160 m AMSL at the Horns Rev offshore wind farm are well predicted by wind profile models that limit the value of the length scale, as suggested by Gryning et al. (2007), where the BLH becomes an important parameter, particularly for stable conditions.
- Near-neutral wind speed observations from combined lidar/cup anemometer measurements up to 300 m AGL at Høvsøre, Denmark, departure from the logarithmic wind profile beyond the surface layer. Simple analytical models, which limit the value of the length scale, predict such departure and fit well the observations.
- Wind profile models, extended for diabatic conditions, are compared to wind speed observations from combined lidar/cup anemometer measurements up to 300 m AGL at Høvsøre, Denmark, for a number of stability conditions. The models, which also limit

the growth of the length scale, agree better with the observations compared to the surface-layer wind profile, which under- and over-predicts the wind speed beyond the surface layer. The models also depend on the BLH, which is estimated under neutral and stable conditions using surface-layer turbulence measurements and under unstable conditions using ceilometer observations of the aerosol backscatter profile.

Notation

a	parameter for the convective dimensionless wind shear
A	integration constant for a given stability from the resistant laws
ABL	atmospheric boundary layer
AGL	above ground level
AMSL	above mean sea level
b	parameter for the stable dimensionless wind shear
B	integration constant for a given stability from the resistant laws
BLH	boundary-layer height
cw	continuous wave
C	proportionality constant for the boundary-layer height
d	parameter for the control of the length scale
D	proportionality parameter for the limiting length scale
f_c	Coriolis parameter
g	gravitational acceleration
l	local mixing length
l_{MBL}	middle boundary-layer length scale
l_{SL}	surface-layer mixing length
L	Obukhov length
LST	local standard time
MOST	Monin-Obukhov similarity theory
NTWT	National Test Station for Large Wind Turbines
p	parameter for the convective dimensionless wind shear
Ro	surface Rossby number
SNR	signal-to-noise ratio
T_o	mean surface-layer temperature
u_*	local friction velocity
u_{*o}	surface-layer friction velocity
$\overline{u_{*o}}$	average surface-layer friction velocity
U	horizontal mean wind speed
$\overline{w'\Theta_v{}'}_o$	surface-layer kinematic virtual heat flux
z	height above the ground or above mean sea level
z_i	boundary-layer height
z_o	surface roughness length
$\overline{z_o}$	mean surface roughness length
α_c	Charnock's parameter
β	aerosol backscatter coefficient
Δu_{*o}	fluctuating surface-layer friction velocity
η	limiting value for the length scale
κ	von Kármán constant
ϕ_m	dimensionless wind shear
ψ_m	diabatic correction of the wind profile
∂	partial derivative

References

Antoniou I., Jørgensen H. E., Mikkelsen T., Frandsen S., Barthelmie R., Perstrup C., and Hurtig M. (2006) Offshore wind profile measurements from remote sensing instruments. *Proc. of the European Wind Energy Conf.*, Athens

Blackadar A. K. (1962) The vertical distribution of wind and turbulent exchange in a neutral atmosphere. *J. Geophys. Res.* **67**:3095–3102

Blackadar A. K. (1965) A Single-layer theory of the vertical distribution of wind in a baroclinic neutral atmospheric boundary layer. In: Flux of heat and momentum in the planetary boundary layer of the atmosphere. AFCRL-65-531, The Pennsylvania State University, 1–22

Businger J. A., Wyngaard J. C., Izumi Y., and Bradley E. F. (1971) Flux-profile relationships in the atmospheric surface layer. *J. Atmos. Sci.* **28**:181–189

Caughey S. J. and Palmer S. G. (1979) Some aspects of turbulence structure through the depth of the convective boundary layer. *Quart. J. Roy. Meteor. Soc.* **105**:811–827

Charnock H. (1955) Wind stress over a water surface. *Quart. J. Roy. Meteorol. Soc.* **81**:639–640

Floors R., Vincent C. L., Gryning S.-E., Peña A., and Batchvarova E. (2013) The Wind profile in the coastal boundary layer: wind lidar measurements and numerical modelling *Bound.-Layer Meteorol.* in press

Gryning S.-E., Batchvarova E., Brümmer B., Jørgensen H., and Larsen S. (2007) On the extension of the wind profile over homogeneous terrain beyond the surface layer. *Bound.-Layer Meteorol.* **124**:251–268

Högström U. (1988) Non-dimensional wind and temperature profiles in the atmospheric surface layer: a re-evaluation. *Bound.-Layer Meteorol.* **42**:55–78

IEC (2005) IEC 61400-12-1 Wind turbines - Design requirements. Int. Electrotechnical Commission

Kindler D., Oldroyd A., MacAskill A., and Finch D. (2007) An eight month test campaign of the QinetiQ ZephIR system: Preliminary results. *Meteorol. Z.* **16**:479–489

Lettau H. H. (1962) Theoretical wind spirals in the boundary layer of a barotropic atmosphere. *Beitr. Phys. Atmos.* **35**:195–212

Monin A. S. and Obukhov A. M. (1954) Osnovnye zakonomernosti turbulentnogo peremeshivanija v prizemnom sloe atmosfery (Basic laws of turbulent mixing in the atmosphere near the ground). *Trudy Geofiz. Inst. AN SSSR* **24**(151):163–187

Panofsky H. A. (1973) Tower Micrometeorogy. Haugen D. A. (Ed.) Workshop on Micrometeorolgy. American Meteorology Society, 151–176

Peña A. and Gryning S.-E. (2008) Charnock's roughness length model and non-dimensional wind profiles over the sea. *Bound.-Layer Meteorol.* **128**:191–203

Peña A., Gryning S.-E., and Hasager C. B. (2008) Measurements and modelling of the wind speed profile in the marine atmospheric boundary layer. *Bound.-Layer Meteorol.* **129**:479–495

Peña A., Gryning S.-E., and Hasager C. B. (2010a) Comparing mixing-length models of the diabatic wind profile over homogeneous terrain. *Theor. Appl. Climatol.* **100**:325–335

Peña A., Gryning S.-E., Mann J., and Hasager C. B. (2010b) Length scales of the neutral wind profile over homogeneous terrain. *J. Appl. Meteorol. Climatol.* **49**:792–806

Peña A., Hasager C. B., Gryning S.-E., Courtney M., Antoniou I., and Mikkelsen T. (2009) Offshore wind profiling using light detection and ranging measurements. *Wind Energy* **12**:105–124

Peña A., Mikkelsen T., Gryning S.-E., Hasager C. B., Hahmann A. N., Badger M., Karagali I., and Courtney M. (2012) Offshore vertical wind shear. Final report on NORSEWInD's work task 3.1, DTU Wind Energy-E-Report-005(EN), DTU Wind Energy, Risø Campus, Roskilde

Peña A., Gryning S.-E., and Hahmann A. N. (2013) Observations of the atmospheric boundary layer height under marine upstream flow conditions at a coastal site. *J. Geophys. Res.: Atmosp.* **118**:1924–1940

Prandtl L. (1932) Meteorologische Anwendung der Strömungslehre (Meteorological application of fluid mechanics). *Beitr. Phys. Atmos* **19**:188–202

Rossby C. G. and Montgomery R. B. (1935) The layers of frictional influence in wind and ocean currents. *Pap. Phys. Oceanogr. Meteorol.* **3**(3):101 pp

Smith D. A., Harris M., Coffey A. S., Mikkelsen T., Jørgensen H. E., Mann J., and Danielian R. (2006) Wind lidar evaluation at the Danish wind test site in Høvsøre. *Wind Energy* **9**:87–93

Steyn D. G., Baldi M., and Hoff R. M. (1999) The detection of mixed layer depth and entrainment zone thickness from lidar backscatter profiles. *J. Atmos. Ocean. Technol.* **16**:953–959

Stull R. B. (1988) An introduction to boundary layer meteorology, Kluwer Academic Publishers, 666 pp

12 Complex terrain and lidars

Ferhat Bingöl
DTU Wind Energy, Risø Campus, Roskilde, Denmark

12.1 Introduction

The term "complex terrain" can be simply defined as any site where the wind is under effect of the terrain. This general definition includes landscapes with either vegetation or sudden elevation changes. In recent years, the interest of the European wind energy industry for such sites has increased. Formerly, they were considered as suboptimal for investments. This is not a coincidence and there are many reasons for such interest; most importantly the following two. Firstly, most of the suitable flat terrains have already been used. One example to this case is Northern Europe where the installed capacity is reaching its limit on flat terrain and the investors became more interested in complex sites. Secondly, the market is also growing in regions where wind resources are not fully utilized, like Mediterranean countries, where the land surface is dominated by rough terrain in the form of hills, mountains and forests.

In both cases, the terrain poses a challenge for flow modelling because the assumptions of classical boundary-layer theory are violated which which has a great impact on the site assessment. If one has to identify the wind conditions in complex terrain, knowledge beyond the classical site assessment methods would be needed. Hence, procedures are needed for the verification of the power curve for wind turbines erected in complex terrain because the power curve variation is $6-8\%$, higher compared to that measured over flat terrain (Pedersen et al., 2002). Therefore, current site assessment techniques are not *generally* reliable in such conditions, which may lead to reduced turbine/wind park life-time and loss of investment.

In addition to land cover and elevation complexity challenges in the terrain, the wind industry faces another equally important challenge related to the size of the wind turbines. In the last decade, the turbine hub heights have doubled, reaching a minimum of 100 m with 100 m of rotor diameter. The top and bottom edges of the blade of such turbines are typically at 150 and 50 m above ground level (a.g.l.), respectively.

This multitude of factors has created the need for a new generation of measurement devices with certain capabilities. The instruments;

1. should be able to measure up to 200 m to cover the whole rotor swept area,
2. must be able to perform in profile measurement standards (e.g. IEC (2005)),
3. and be easy to install/operate in complex terrains.

The above requirements cannot easily be fulfilled with conventional meteorological masts; installation of a meteorological mast and its maintenance, is a big logistical problem. Furthermore minor adjustments on the position of the meteorological mast entails almost the same amount of work as installing it. A category of instruments which can meet these goals is the wind energy Light Detection and Ranging instruments; mostly known as wind lidars or just lidars in wind energy. In this chapter, we will discuss on using the lidars in complex terrain.

12.2 Lidars

The lidars have become a part of wind energy meteorology after 1997 (Mayor et al., 1997). The capabilities of the instrument were well-known but the necessary investment was too high for many applications and the operating heights were not relevant to wind energy related studies. Therefore, the usage of them is recent and it has started after the "wind energy lidars" are developed (Jørgensen et al., 2004).

The main drawback of the wind lidars in complex terrain is that the horizontal wind measured from the instruments are based on the assumption that the data are collected on flat homogeneous terrain where the flow is homogeneous. Hence an adaptation to complex terrain is needed. Lidars have been previously adapted to various needs and used out of their designed envelope (Bingöl, 2005; Mikkelsen et al., 2008; Trujillo et al., 2011; Bingöl et al., 2009b). Such adaptations are of interest to wind turbine producers, wind park developers and the boundary layer meteorology community, as well as the lidar producers.

12.2.1 ZephIR

The British company QinetiQ designed a cost effective lidar model, ZephIR, in 2002. Risø DTU bought the first *prototype* (Figure 158-right) in 2004 and the *commercial* version (Figure 158-left) in 2005.

The prototype and the commercial models differ from each other mainly in physical appearance and in minor signal processing capabilities. The prototype is a combination of two parts; an optical head and the laser source/sensor. The parts are separated by means of an optical cable, while in the commercial model the two part have to be assembled directly together with a third containing a battery. For both versions, comparisons with several tall, meteorological masts have already proven the instrument to be accurate over flat homogeneous terrain (Antoniou et al., 2004; Smith et al., 2006). In complex terrain, the interpretation of the lidar data is still under development and Bingöl et al. (2009b) addresses this issue.

The instrument is a scanning tool that focuses the laser beam at different heights between 10 and 180 m and essentially assesses the radial velocity along the beam direction at the point of focus. The laser beam is deflected an angle $\phi \approx 30^\circ$ from the vertical by making use of a prism, which rotates one full revolution every second. The along beam or radial velocity component of the wind is thus measured on a circle as indicated in Figure 159-(left). The ZephIR is a continuous wave lidar, therefore it can only measure at the focus height. For each focus height, the prism rotates three times before the instrument changes focus to the next height. At each full revolution, 49 radial velocities are recorded and a total of 147 measurements in three seconds are used to derive the wind speed. It is possible to change the focus distance in 1 s. The number of prism rotations, the signal processing speed and the recursive focus height change can be adjusted freely for the prototype model (Bingöl, 2005; Bingöl et al., 2010).

In conical scanning mode, the measured radial wind speed, v_r, combined with the scan azimuth angles, θ, are fitted to the function (Harris et al., 2006, 2007):

$$v_r(\theta) = |A\cos(\Theta - \theta) + B| \tag{264}$$

where

$$U = \frac{A}{\sin\phi} \quad w = \frac{B}{\cos\phi} \quad . \tag{265}$$

The instrument can only measure the absolute value of the velocity. Therefore, the wind direction, Θ, is directly taken from the fit with a ambiguity of 180° which can be identified with the wind direction readings from the instrument's built-in mast. If the built-in vane is not present, as in prototype, a wind direction measurement is needed. The instrument records the 3 s statistics as well as the 10 min averages and one can use the raw data, which can be also recorded on demand, to calculate longer period averages or turbulence parameters. In this study, 30 min radial wind speeds are used, if the raw data are present, otherwise 10 min averages are preferred.

It is possible to remove the prism from a lidar and turn it into a "straight shooter" scanner where it measures the wind speed in the direction it is pointed. This working mode is referred as *staring mode* in this study. In staring mode, the beam direction is fixed and the instrument focuses at different distances and measures the component of the wind vector (Figure 159-right). The wind direction cannot be measured. Therefore, the beam direction must be known and the measured data must be used combined with a wind direction measurement instrument.

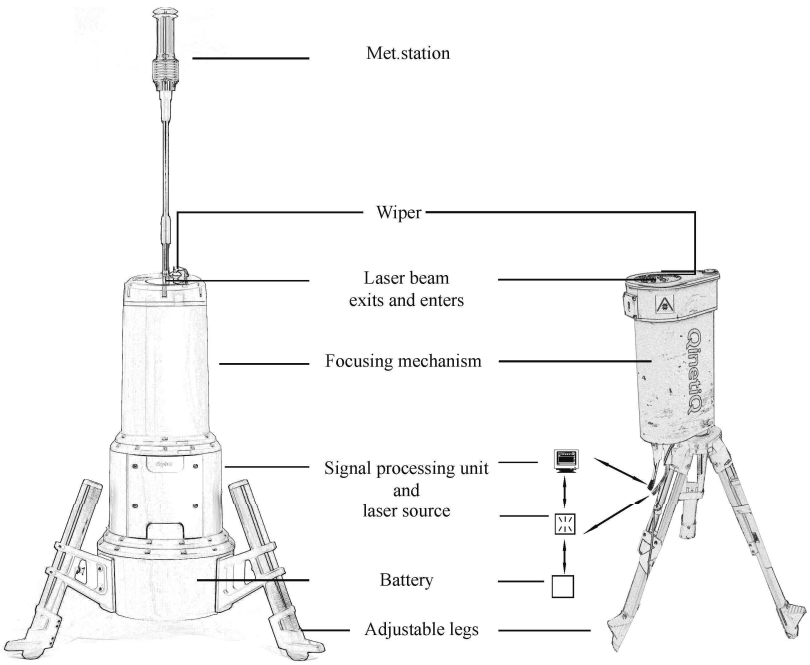

Figure 158: The ZephIR models which are used in the study. (Left) The commercial model which is 1.7 m tall and 0.5 m width. The instrument weights 100 kg. (Right) The prototype which is 1.5 m tall with adjustable legs. Including the signal processing unit, laser source/sensor and battery which are separated from the head by means of an optical cable, it weights 120 kg.

The staring mode approach was applied for the first time by Harris et al. (2006) with the aim of investigating possibilities for controlling the wind turbine based on upstream wind measurements with the prototype model of the ZephIR lidar. Subsequently, the prototype is used in other experiments in this context, like by mounting on a wind turbine to measure the wake behind (Bingöl et al., 2010; Trujillo et al., 2011), for synchronized multi-lidar field measurements (Mikkelsen et al., 2008) and horizontal wind profile measurements (Bingöl et al., 2009a).

12.2.2 Windcube

The second wind energy lidar that came into the market is the Windcube, developed by the French company LeoSphere. Evaluation reports, mostly for the measurements over flat terrain, are also available recently (Albers and Janssen, 2008).

Contrary to the ZephIR, Windcube is a pulse lidar, which measures the wind speed and direction at measurement points 90° apart from each other on the conical scan circle for all chosen heights simultaneously. Each sector is scanned for 1 s and every 6 s (2 extra seconds are used to move the wedge), the values are used to derive wind speed and direction profiles; calculated via (Lindelöw, 2007);

$$u = \sqrt{u_1^2 + u_2^2} \tag{266}$$

where u_1 and u_2 are the horizontal plane wind speed components, derived as

$$u_1 = v_r(0) - v_r(\pi), \quad u_2 = v_r(\tfrac{\pi}{2}) - v_r(\tfrac{3\pi}{2}) \tag{267}$$

and

$$w = \frac{v_r(0) + v_r(\pi)}{2\cos\phi} = \frac{v_r(\frac{\pi}{2}) + v_r(\frac{3\pi}{2})}{2\cos\phi}, \quad \Theta = \arctan(u_1, u_2) \tag{268}$$

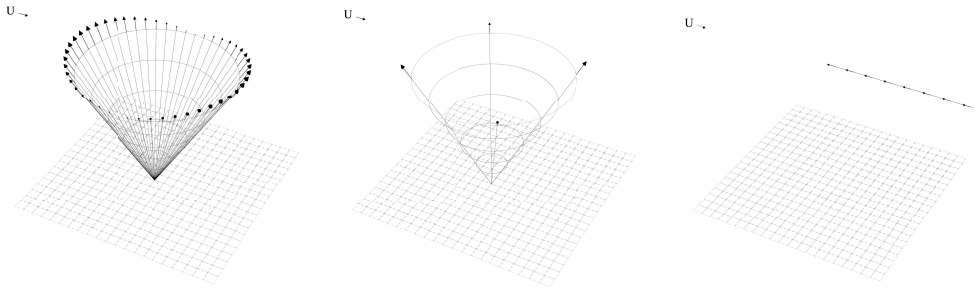

Figure 159: Lidar working modes. The arrows denote the laser beam direction and the measured wind components. (Top) The original conical scanning mode of ZephIR. At upwind and downwind directions the absolute value of the along beam velocity component has the maximum value. When the wind is perpendicular to the beam direction the wind component on the radial vector has a minimum value. (Middle) Conical Scanning Mode of the Windcube lidar. The data is recorded only in four equally separated sectors on the conical circle. (Bottom) Illustration of the Staring Mode. The beam direction is fixed and the instrument focuses at different distances and measures the component of the wind vector indicated by the arrows. In this mode, the lidar data is used combined with separate wind direction measurements

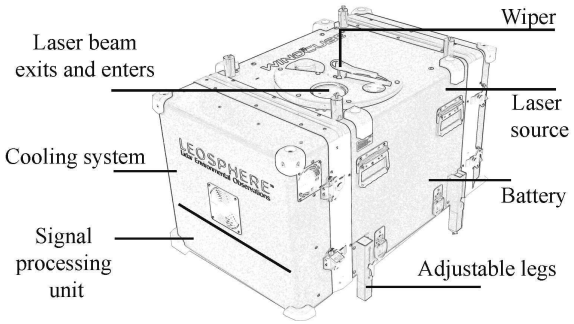

Figure 160: Leosphere Windcube; the laser source is located right on top of the unit and generates the beam in the direction to the the prism located under the beam exit lense where it is tilted to upwards. The dimensions are 0.7 m$\times 0.4$ m$\times 0.4$ m and the instrument weights ≈ 55 kg.

The Windcube is equally mobile to ZephIR with the added advantage that the wedge opening angle, ϕ, can be adjusted between $15°$ and $30°$. This option is introduced as a "bypass" for complex terrain problems such as inhomogeneous flow. This hypothesis is discussed in the section 12.3.1. For more information about latest working modes of windcube see Section 3 of this book.

12.3 Challenges and Known Issues

12.3.1 The conical scanning error in complex terrain

The success of the lidar conical scan operation is limited to flat terrain. In complex terrain, the flow is no longer homogeneous and that can give a large bias on the horizontal wind speed estimated from the lidar up to 10% in horizontal wind speed measurements (Bingöl et al., 2008a). Some of the lidar producers present the smaller half opening angle (Leosphere, 2009) as one of the possible solutions to overcome the problem caused by the inhomogeneous flow.

The error can be illustrated as in Figure 161 where the horizontal wind speed U is taken constant, but the vertical wind speed w is assumed to change linearly with the downwind position; parametrised with a factor of α. This is similar to the case over a hill. The upstream

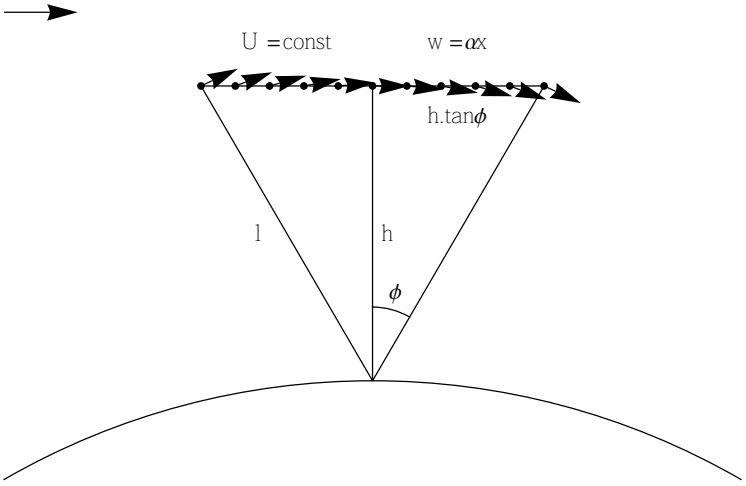

Figure 161: Simplified lidar scanning geometry in a linearly changing mean flow. The lidar is shooting upstream and downstream with a half opening angle ϕ.

has positive and the downstream has negative tilt relative to the top of the hill. The projected wind speed on the upwind and downwind beams are

$$v_{up} = -(U + h\alpha)\sin\phi \qquad v_{down} = (U + h\alpha)\sin\phi \quad . \tag{269}$$

Assuming horizontal inhomogeneity, the horizontal velocity can be calculated as

$$U_{lidar} = \frac{v_{down} - v_{up}}{2\sin\phi} = U + h\alpha, \tag{270}$$

which shows, in the case of a negative α that the horizontal wind is *underestimated* (Bingöl et al., 2008a). A simplified three dimensional analysis of the error is derived by Bingöl et al. (2008b), where the the mean wind field $\mathbf{U} = (u, v, w)$ is assumed to vary linearly. In such case, the wind vector estimations become:

$$u_{\text{lidar}} = u + h\frac{\partial w}{\partial x} \tag{271}$$

$$v_{\text{lidar}} = v + h\frac{\partial w}{\partial y} \tag{272}$$

$$w_{\text{lidar}} = w - \frac{l}{2}\tan^2\phi\frac{\partial w}{\partial z} \tag{273}$$

where l is the focus distance $h/\cos\phi$. Eq. 273 shows that the error due to inhomogeneity of the mean flow vanishes for the vertical component as the half opening angle ϕ goes to zero. The errors on the horizontal components are independent of ϕ.

12.3.2 Predicting the error by means of a flow model

Conical scanning mode of the lidar can be simulated in flow models. An automated script for commercial software WAsP Engineering has been written by the author for the ZephIR and Windcube lidars and has been published (Bingöl and Mann, 2009). The method can be simplified as below and can be adapted to different scanning regimes such as different ϕ.

A unit vector in the direction of the laser beam can be written as,

$$\mathbf{n} = (\cos\theta\sin\phi, \sin\theta\sin\phi, \cos\phi) \tag{274}$$

where ϕ is half opening angle and θ is the geographical angle in which the beam is pointing. As it is previously stated, assuming the flow field to be roughly homogeneous over the averaging

circle with a mean $U = (u, v, w)$. The radial velocity in the direction of the laser beam, the radial wind speed v_r, calculated at θ azimuth of the prism is the projection of **U** onto **n**:

$$v_r(\theta) = \mathbf{n}(\theta) \cdot \mathbf{U}\left(\mathbf{n}(\theta)l - (0, 0, z')\right), \tag{275}$$

where z' is absolute position of the instrument a.g.l. if it is placed on an artificial elevation (e.g. tower).

For ZephIR lidar, after calculating 60 points on the conical circle, all three velocity components can be obtained through a linear fit to trigonometric series

$$a + b\cos\theta + c\sin\theta, \tag{276}$$

as;

$$u = \frac{b}{\sin\phi} \qquad v = \frac{c}{\sin\phi} \qquad w = \frac{a}{\cos\phi} \qquad \Theta = \arctan\frac{v}{u} \quad . \tag{277}$$

For Windcube, radial wind speed v_r from calculated at four measurement points are used in Eq. (266)–(268) directly to derive wind speed components and direction.

12.4 Experimental studies

Conically scanning lidars assume the flow to be homogeneous in order to deduce the horizontal wind speed as it has been described in section 12.3.1. However, in moderately complex or complex terrain this assumption is not valid implying a risk that the lidar will derive an erroneous wind speed. The magnitude of this error was measured by collocating a meteorological mast and a lidar at two Greek sites, one hilly and one mountainous. In order to predict the error for various wind directions the flows at both sites were simulated with the linearised flow model LINCOM as described in section 12.3.2. The measurement data were compared with the model predictions with good results for the hilly site.

In both experiments lidar data are collected by the standard QinetiQ software and synchronized with mast data by the CRES WindRose software. Instruments are calibrated according to the requirements of IEC61400-12-1:2005/Annex F and MEASNET guidelines at CRES Laboratory for Wind Turbine Testing.

12.4.1 Hilly site; Lavrio

The Lavrio site is located 38 km SE of the center of Athens close to the coast of the Aegean Sea. The experiment took place between 2008-Dec-01 and 2008-Jan-15. The highest point is 200 m ASL and main wind direction is 0°. The 100 m triangular lattice reference meteorological mast is equipped with cup anemometers and vanes at five heights (10, 32, 54, 76, and 100 m). Cups are to the east and vanes are to the west. There are also ultrasonic 3D Gill anemometers at three heights (34, 78, and 98 m) which are not used in this study due to problems with icing but this does not influence the used cup anemometers and vanes. Additionally, the temperature profile is measured using differential thermometers, as well as, the atmospheric pressure and the solar radiation. Dedicated instrumentation is used for signal protection, filtering and conditioning. The lidar is located nearly 12 m north of the mast. The measurement heights are 32 and 78 m.

At Lavrio, most of the winds are northerly which means it is blowing from lidar to the mast. The scatter plots (Figure 162-top) show generally 5 to 7% errors in wind speed measurements. For the WAsP Engineering model we have used 3 km$\times 3$ km map with 4 m resolution simulating the wind direction from 0° to 360° with 6° bins. We have used all the data from the mast at each height and averaged them according to the wind direction in 10° bins.

The comparison between the model and the measurements is shown in Figure 162 (lower two plots) and shows good correlation in some sectors. The mast is voluminous, thus the selected data must be far from boom direction which is 113°. These sectors are marked with light grey areas in the plots for $\pm 30^\circ$. The ideal ratio line of one is also shown and it represents

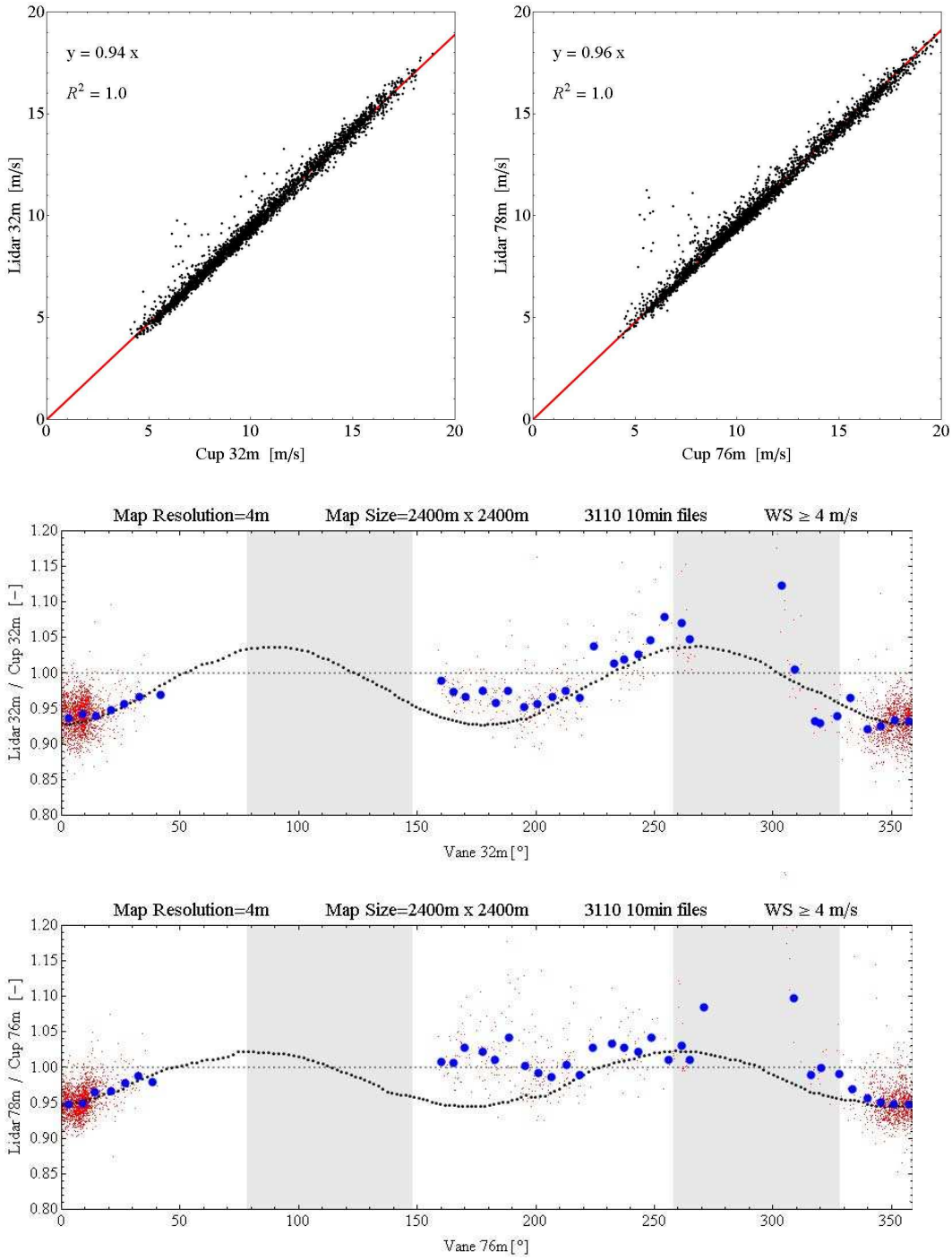

Figure 162: Lavrio: The scatter plots show generally 4% to 6% errors in wind speed measurements (top). Lower two plots are the comparison between the model and the measurement data for two different heights. Small red dots are the error ratio for each 10 min measurement, big blue dots are the averaged 6° bins according to the wind direction and medium black dots are the model results. The mast shadow is marked with grey rectangles. The ideal ratio line of one, dashed blue, is also shown and it represents the cases where there is no difference between the lidar and the mast measurements. Especially for northerly directions the model predicts the lidar error well for both heights, while for the southerly directions the prediction is not so good.

the cases where there is no difference between the lidar and the mast measurements. The black line is the model and the points are the measurement results.

Especially for northerly directions the model predicts the lidar error well for both heights, while for the southerly directions the prediction is not so good. We believe this can be a result of the limitation of WAsP Engineering. In southerly directions very close to the site there are steep slopes. In this sector and height, the flow model has difficulties predicting the tilt angles as compared to sonic measurements for periods with no icing problems.

12.4.2 Mountainous site; Panahaiko

The Panahaiko site is located 165 km northwest of Athens, at Vounogiorgis mountain south east of the village Sella, 14 km south of the Patras Sea. The experiment ran from 2007-Sep-19 to 2007-Oct-11. The terrain in the vicinity of the site is very complex. Highest point is 2000 m in the region where the experiment surrounding is between 1700 and 1750 m ASL. The prevailing wind directions are ENE and SW. The triangular lattice reference meteorological mast has six cup anemometers (10, 20, 30, 40, and 54 m) and two vanes (40 and 54 m). Additionally, there are also air temperature and relative humidity measurements at 54 m. The boom cross-section is 40 mm$\times 40$ mm. All wind sensors are mounted at a height of 75 cm above the boom and at a distance of 225 cm from the outer mast leg. The lidar is located nearly 20 m WSW of the mast. The lidar measurement heights are 30 m and 55 m.

The second site, Panahaiko, is much more complex than Lavrio, so there are many sectors which could be problematic for WAsP Engineering to model. The scatter plots in Figure 163 (top) show data for all directions. The mast at Panahaiko is smaller than at Lavrio so the sector with flow distortion is smaller ($\pm 25^\circ$) shown in grey in the figure. The boom direction is 210°.

The comparison between the modelled error and the measurements as a function of direction is shown in Figure 163 (lower two plots). It is not a perfect prediction, but the model gives the right order of magnitude for this complex site.

The outliers mainly seen for the larger heights in Figures 162 and 163 are probably due to cloud return as discussed in Courtney et al. (2008).

12.5 Conclusions

Lidars, used over flat homogeneous terrain, show errors in the mean wind speed of only a few percent. We have shown that in complex terrain of the type commonly used for wind turbine parks, errors in the horizontal wind speed as measured by a conically scanning lidar can be of the order of 10%. This is due to the lack of horizontal homogeneity of the flow, which is assumed in the interpretation of the lidar data. The findings are based on two experiments involving collocated lidars and meteorological masts in complex terrain, together with flow calculations over the same terrains. For that calculation we use WAsP Engineering, and we find that the calculations match the experiment except for some sectors where the terrain is particularly steep. This is not surprising, since the WAsP Engineering is built on a linearized flow model, which is only valid for limited terrain slopes.The model is not for highly complex terrain that can incorporate the stability effect in any reliable way. Furthermore most of the wind speeds analyzed, from both sites, are quite high so it is not unreasonable to assume neutral stratification. That is why there is concluding thoughts about stability. To make more reliable predictions of the error in very steep terrain, other more advanced flow models ((Castro et al., 2003)) must be used.

The hypothesis that the lidar conical scan error due to inhomogeneity of the mean flow is independent of the half opening angle ϕ on the horizontal components has been supported with experimental results from moderately-complex terrain site measurements. The synchronized measurements from the lidars with different half opening angles and meteorological mast instruments reported no positive effect of smaller half opening angle in horizontal wind speed measurements, contrary to what was being suggested by some of the producers and

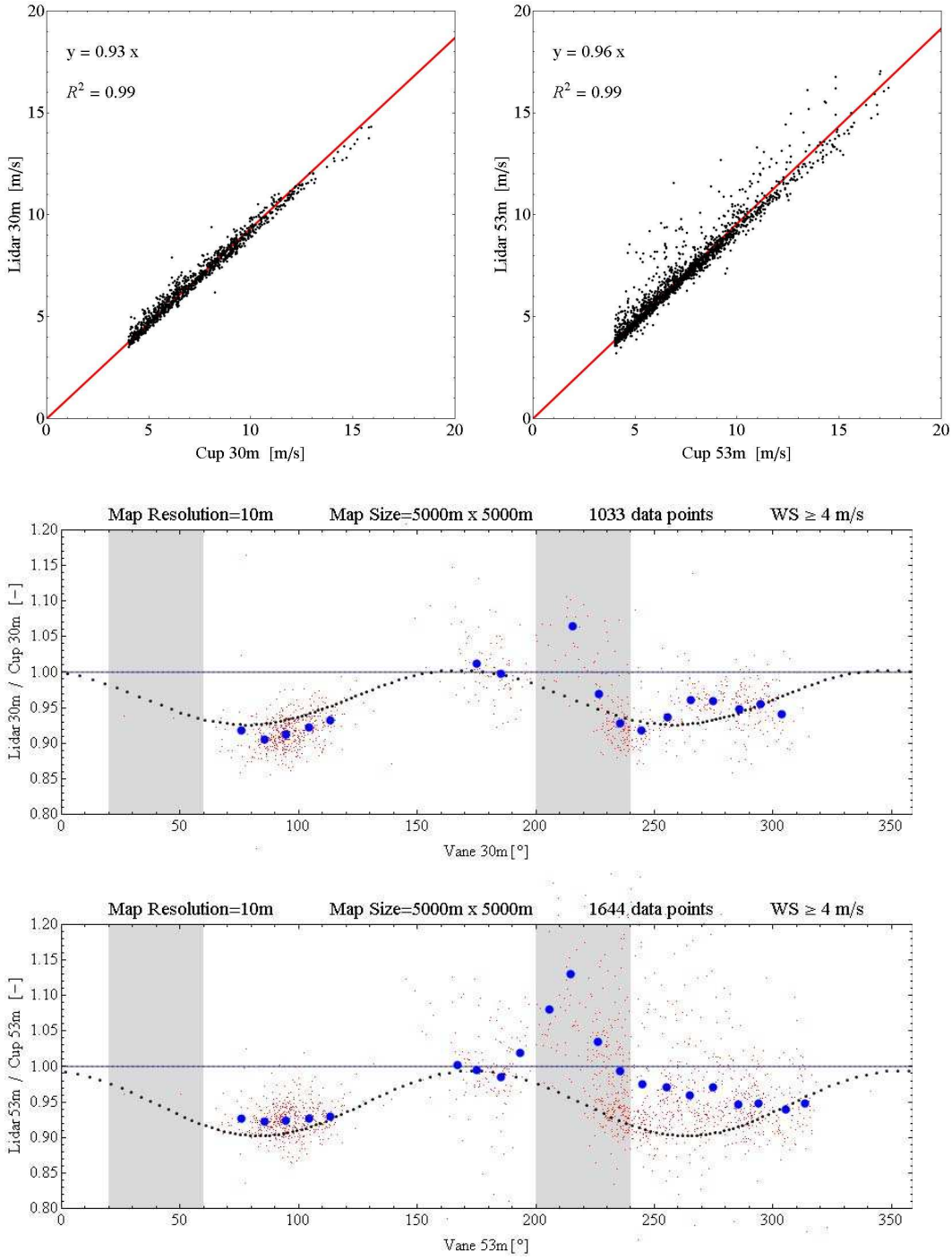

Figure 163: Panahaiko: The scatter plots show generally 4% to 7% errors in wind speed measurements (top). Lower two plots are the comparison between the model and the measurement data for two different heights. Small red dots are the error ratio for each 10 min measurement, big blue dots are the averaged 10° bins according to the wind direction and medium black dots are the model results. The mast shadow is marked with grey rectangles. The ideal ratio line of one, dashed blue, is also shown and it represents the cases where there is no difference between the lidar and the mast measurements. It is not a perfect prediction, but the model gives the right order of magnitude for this complex site.

academics. The measurements agreed with the described hypothesis and it can be concluded that smaller half opening angles can only be helpful in sites with the presence of dense canopy or obstacles, in order to measure the desired height easily.

As a general conclusion of this study, lidars can be used in complex terrain with support of flow models which should include well defined flow separation predictions. It is important to note that modelling must be accompanied by flow analysis before and after the measurements. Prior to the measurements, models should be used to detect possible suitable locations for lidar placement. This can be done with linearised or advanced CFD models because any of these can perform a simple assessment based on rough calculations of error values. Thus, the majority of sub-optimal locations can be eliminated. Subsequently, any attempt to correct the lidar data must be performed with an advanced flow model, preferably a CFD model that has already been tested in complex terrain with measurements. It is advised that the described modelling steps for lidar data correction should be included in wind turbine and site assessment and implemented in well established international standards (e.g. IEC 61400 series) after further studies.

The author also would like to bring to attention certain shortcomings of the current commercial versions of the lidar instruments. Some of the experiments, which are conducted in this study or cited in the manuscript, would not have been possible without full software and hardware access to the instruments. The re-formulation of signal processing methods and the physical manipulation of instrument parts were essential to achieve the necessary scanning speed and to create custom scan regimes. This underlines the importance of instrument flexibility for a wide range of uses (e.g. in complex terrain). Unfortunately, most of the producers of currently available commercial models are gradually stepping back from such an approach in an effort to create stable, robust instruments. In order to achieve faster development in lidar technology in complex terrain, the author believes that these instruments must be accessible in a software as well as a hardware level, and suggests a more detailed documented developer interface mode.

Concluding, current standards of the instruments are adequate to perform wind measurements over most of the terrain types and it is believed that it is possible for lidars to replace conventional meteorological mast in the future if the data interpretation is improved, particularly.

Notation

a.g.l.	above ground level
h	focusing height
l	focus distance
$\mathbf{n}$	unit vector in the direction of the laser beam
u	longitudinal wind speed component
u_i	wind speed component in the i direction
U	horizontal wind speed
$\mathbf{U}$	mean wind field
v	transversal wind speed component
v_{down}	projected wind speed in the downstream beam
v_{up}	projected wind speed in the upstream beam
v_r	radial wind speed
w	vertical wind speed
X'	fluctuation part of a variable X from the mean
z'	absolute position of the instrument a.g.l
α	linear factor for parametrization of the vertical wind speed
θ	scan azimuth lidar angle
Θ	wind direction
σ_X^2	variance of a variable X
ϕ	deflection lidar angle from the vertical or wedge angle
$\langle X \rangle$	time average of a variable X

References

Albers A. and Janssen A. (2008) Windcube evaluation report. Technical report, Deutsche WindGuard Consulting GmbH

Antoniou I., Jørgensen H. E., Mikkelsen T., Petersen T. F., Warmbier G, and Smith D. (2004) Comparison of wind speed and power curve measurements using a cup anemometer, a lidar and a sodar. *Proc. of the European Wind Energy Conf.*, London

Bingöl F. (2005) Adapting Laser Doppler Anemometer into Wind Energy. Master's thesis, Technical University of Denmark, Lyngby

Bingöl F. (2009) *Complex Terrain and Wind Lidars*. PhD thesis, Risø DTU, Roskilde

Bingöl F. and Mann J. (2009) Lidar performance estimation script for WAsP Engineering. Technical report, Risø DTU, Roskilde

Bingöl F., Mann J., and Foussekis D. (2008) Lidar error estimation with wasp engineering. *IOP Conf. Series: Earth and Environ. Sci.*, 012058 (9pp)

Bingöl F., Mann J., and Foussekis D. (2008) Modeling conically scanning lidar error in complex terrain with WAsP Engineering. Risø–R–1664(EN), Risø DTU, Roskilde

Bingöl F., Mann J., Dellwik E., Sogachev A., and Rathmann O. (2009) Flow over limited size forest; measurements and modelling. *Wind Energy*, under review.

Bingöl F., Mann J., and Foussekis D. (2009) Conically scanning lidar error in complex terrain. *Meteorologische Z.*, **18**:189–195

Bingöl F., Mann J., and Larsen G.-C. (2010) Lidar measurements of wake dynamics Part I: One Dimensional Scanning. *Wind Energy* **13**:51–61

Bradley S. (2008) Wind speed errors for lidars and sodars in complex terrain. *IOP Conf. Series: Earth and Environ. Sci.* 012061 (7pp)

Castro F., Palma J., and Lopes A. (2003) Simulation of the askervein flow. part 1: Reynolds averaged Navier-Stokes equations (k-epsilon turbulence model). *Bound.-Layer Meteorol.* **107**:501–530

Courtney M., Wagner R., and Lindelöw P. (2008) Testing and comparison of lidars for profile and turbulence measurements in wind energy. *IOP Conf. Series: Earth and Environ. Sci.* 012021 (14pp)

Harris M., Hand M., and Wright A. (2006) Lidar for turbine control. Technical Report NREL/TP-500-39154, NREL

Harris M., Bryce D. J., Coffey A. S., Smith D. A., Birkemeyer J., and Knopf U. (2007) Advance measurement of gusts by laser anemometry. *J. Wind Eng. Ind. Aerodyn.* **95**:1637–1647

IEC (2005) 61400-12-1: Power performance measurements of electricity producing wind turbines. Technical report, International Electrotechnical Commission

JRC (2006) Global land cover 2000 - Europe. Technical report, European Environmental Agency

Jørgensen H., Mikkelsen T., Mann J., Bryce D., Coffey A. S., Harris M., and Smith D. A. (2004) Site wind field determination using a CW Doppler lidar - comparison with cup anemometers at Risø. *Proc. EWEA Special Topic Conference: The Science of Making Torque from Wind* 261–266. Delft University, Delft

Leosphere (2009) Windcube information booklet

Lindelöw P. (2007) Uncertainties in wind assessment with lidar. Risø technical report, Risø-I-1234(EN), Risø DTU, Roskilde

Mayor S. D., Lenschow D. H., Schwiesow R. L., Mann J., Frush C. L., and Simon M. K. (1997) Validation of NCAR 10.6-μm co_2 Doppler lidar radial velocity measurements and comparison with a 915-MHz profiler. *J. Atmos. Oceanic Tech.*, **14**:1110–1126

Mikkelsen T., Mann J., Courtney M., and Sjöholm M. Windscanner: 3-D wind and turbulence measurements from three steerable doppler lidars (2008) *IOP Conf. Series: Earth and Environ. Sci.* 012018 (9pp)

Pedersen T. F., Gjerding S., Ingham P., Enevoldsen P., Hansen J. K., and Jørgensen H. K. (2002) Wind turbine power performance verification in complex terrain and wind farms. Technical report, Risø-R-1330(EN), Risø DTU, Roskilde

Smith D. A., Harris M., Coffey A. S., Mikkelsen T., Jørgensen H. E., Mann J., and Danielian R. (2006) Wind lidar evaluation at the Danish wind test site in Høvsøre. *Wind Energy* **9**:87–93

Trujillo J. J., Bingöl F., Larsen G. C., Mann J., and Kühn M. Lidar measurements of wake dynamics, Part II : Two dimensional scanning. *Wind Energy* **14**:61–75

13 Turbulence measurements by wind lidars

Ameya Sathe
DTU Wind Energy, Risø Campus, Roskilde, Denmark

13.1 Introduction

It is now well established that wind lidars (henceforth referred to as lidars) measure the 10-min mean wind speed with acceptable accuracy. Several measurement campaigns have been carried out in this regard, where cup anemometers are used as reference instruments (Smith et al., 2006; Kindler et al., 2007; Peña et al., 2009). Turbulence measurements using lidars is still a subject of research, and an acceptable method is yet to be established. At first it is important to understand which turbulence measurements we refer to in this chapter. They are the second-order moments of wind speeds. It is then interesting to know why turbulence measurements are useful for wind energy. Amongst a whole range of applications, we can list a few, such as,

- Load calculations of wind turbines - The driving loads causing fatigue of wind turbines is atmospheric turbulence. Currently, the three dimensional spectral tensor model of Mann (1994) is used to quantify turbulence. Expressions of turbulence spectra from Kaimal et al. (1972) are also used in load calculations. These theoretical and empirical models are obtained for neutral and homogeneous conditions. Wind turbines operate under all terrain types and atmospheric conditions. Hence, the best input of turbulence for load calculations is by directly measuring it at the site where wind turbines will operate.
- Power curve measurements - The power curve of a wind turbine is sensitive to turbulence intensity, especially in the region around the rated wind speed. Turbulence measurements will enable accurate power curve measurements that are vital for a wind farm developer.
- Validation of wind profile models - In recent years with the increase in the size of the wind turbines, wind profile models that extend in the entire boundary layer are developed (Gryning et al., 2007; Peña et al., 2010a). These models are based on the assumption that momentum flux changes linearly with height. If we are able to measure turbulence at several heights, we can verify these assumptions. Alternatively, empirical relations of the variation of momentum flux with height can also be derived.

The next interesting question is what is the current standard for the measurement of turbulence in wind energy. The answer is the sonic anemometer. They are compact instruments that can measure all three components of wind velocity in relatively small sample volume that for all practical purposes can be considered a point. They need to be mounted on a meteorological mast (met-mast), such that the flow distortion due to the mast itself is kept to a minimum. Despite this there are disadvantages of using sonic anemometers in turbulence measurements, the most important being that tall met-masts are very expensive, and offshore, the costs increase significantly. We thus have to look for alternatives. Remote sensing methods such as sodars and lidars are viable alternatives, but they are still a subject of research for turbulence measurements. In this chapter we restrict the discussion to turbulence measurements using lidars only.

Although lidars have been introduced in wind energy recently, for meteorology they have been investigated previously to measure turbulence using different scanning techniques. A common technique is by conical scanning and using the velocity azimuth display (VAD) technique of processing the data. One of the first remote sensing (Doppler radar) turbulence studies using a full 360° scan in a horizontal plane was carried out by Browning and

Wexler (1968), where the limitations of horizontal homogeneity and vertical wind shear are explained in detail. Wilson (1970) modified the technique from Browning and Wexler (1968) and performed turbulence measurements over snow. Kropfli (1986) extended the technique to accommodate turbulence scales of motion larger than those described in Wilson (1970) and showed that these techniques could be used to make reasonable estimates of turbulent kinetic energy and momentum flux by modelling the random errors in the measurements.

Eberhard et al. (1989) studied turbulence using Doppler lidar and modelled the random errors using a partial Fourier decomposition method, which gave better estimates of the errors than Wilson (1970) and Kropfli (1986). Gal-Chen et al. (1992) presented a technique to analyse lidar data for turbulence measurements using the scans at two levels, and produced estimates of fluxes in the mixed layer, and spectra of the horizontal velocity at the surface. Banakh et al. (1995) presented an analysis of estimating the random errors in the measurement of the mean wind speed by lidars using the theory of isotropic turbulence. Banta et al. (2002) studied the turbulence characteristics under the conditions of low-level jets, using the vertical-slice scans of radial velocities. Smalikho et al. (2005) presented a method to use lidar data for the estimation of turbulent energy dissipation rate to study wake vortices of an aircraft. A comprehensive review is given in Engelbart et al. (2007) that covers different remote sensing techniques for turbulence measurements including lidars. A review of the use of lidars for wind energy applications is also presented in Emeis et al. (2007). Pichugina et al. (2008) demonstrated the sensitivity of the streamwise velocity variance to the spatial and temporal averaging, also by using the technique of vertical-slice scans of radial velocities. Recently, studies have been carried out to model the spatial averaging effects (Sjöholm et al., 2009) and compare the 3D turbulence measurements using three staring lidars (Mann et al., 2009). Wagner et al. (2009) modelled the systematic errors by approximating the conical scan and the scan time as a length scale, providing first estimates of the variances of the longitudinal component of wind velocity. Mann et al. (2010) estimated the momentum fluxes using lidars and modelled the unfiltered turbulence from the CW lidar, where the model compares reasonably well with the measurements.

The main objective of this chapter is to understand if lidars can measure turbulence. Wind speeds are measured using the conical scanning and VAD technique is used to process the data. Much of the text is taken from Sathe et al. (2011). A theoretical model is developed to estimate the systematic errors in the second-order moments of wind speeds in the atmospheric surface layer measured by lidars. The systematic errors are those that arise due to the averaging effect in the sample or pulse volume and the relatively large circle in which Doppler lidars scan to obtain 2-component horizontal wind profiles. Two types of lidars are considered, a continuous wave (CW) ZephIR lidar developed by QinetiQ (Natural Power) and a pulsed WindCube lidar developed by Leosphere. The verification is carried out by comparing the variances measured by the ZephIR and WindCube with that of the sonic anemometers placed at different heights on a meteorological mast. Section 13.2 describes the theory, where the systematic errors in the second-order moments are modelled for the ZephIR and WindCube. Section 13.3 describes the results along with some inferences. Section 13.4 gives a discussion on the systematic errors, and section 13.5 provides a conclusion. Finally, section 13.6 provides future perspectives.

13.2 Theory

The approach is similar to Wyngaard (1968), Citriniti and George (1997), where turbulence measured by the hot-wire anemometer probe was modelled. The general working principle of lidars (in particular CW lidar) is explained in detail in chapter 3, but to familiarize the reader with the notations a brief explanation is also given here. Fig. 164 shows the lidar emitting the laser beam at different azimuth angles θ. The azimuth angles increase from 0°–360° in the clockwise direction as for the geographical convention. The line-of-sight velocity (also called radial velocity v_r) is measured by the lidar at each azimuth angle. The half-opening angle ϕ ($= 90^\circ -$ elevation angle) is kept constant throughout the scan. The CW and pulsed lidars

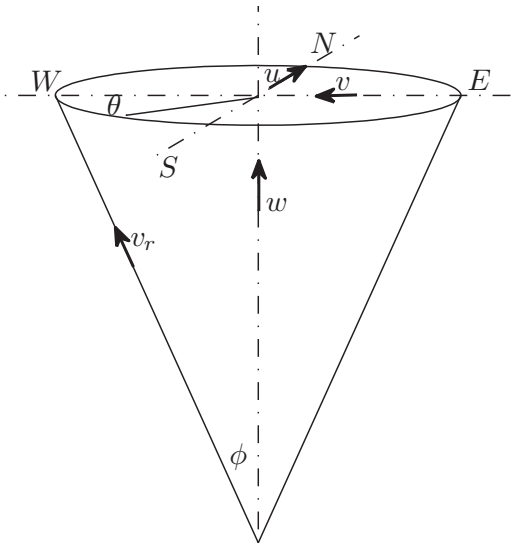

Figure 164: Schematic of the velocity azimuth display scanning

work on the principle of backscattering of the emitted radiation, and subsequent detection of the Doppler shift in the frequency of the received radiation. The Doppler shift in the frequency is related to v_r by,

$$\delta f = 2\frac{v_r}{\lambda}, \tag{278}$$

where f and λ are the frequency and wavelength of the emitted radiation. Mathematically, v_r is given as the dot product of the unit directional vector and the velocity field at the point of focus for a CW lidar, and the center of the range gate (Lindelöw, 2007) for the pulsed lidar,

$$v_r(\theta) = \mathbf{n}(\theta) \cdot \mathbf{v}(d_f \mathbf{n}(\theta)), \tag{279}$$

where d_f is the focus distance for the CW lidar or the distance to the center of the range gate for the pulsed lidar at which the wind speeds are measured, $\mathbf{v} = (u, v, w)$ is the instantaneous velocity field evaluated at the focus point or the center of the range gate $d_f\mathbf{n}(\theta)$, and $\mathbf{n}(\theta)$ is the unit directional vector given as,

$$\mathbf{n}(\theta) = (\cos\theta \sin\phi, \sin\theta \sin\phi, \cos\phi). \tag{280}$$

In practice it is impossible to obtain the backscattered radiation precisely from only the focus point, and there is always backscattered radiation of different intensities from different regions in space along the line-of-sight. Hence, it is necessary to assign appropriate weights to the backscattered intensity such that the weight corresponding to the focus point or the center of the range gate is the highest. Mathematically, the weighted average radial velocity can be written as,

$$\tilde{v}_r(\theta) = \int_{-\infty}^{\infty} \varphi(s)\mathbf{n}(\theta) \cdot \mathbf{v}(s\mathbf{n}(\theta) + d_f\mathbf{n}(\theta))\, ds, \tag{281}$$

where $\varphi(s)$ is any weighting function, integrating to one, and s is the distance along the beam from the focus or the center of the range gate. For simplicity we assume that $s = 0$ corresponds to the focus distance or center of the range gate.

Following are the main assumptions of the model:

1. The terrain is homogeneous
2. The flow field is frozen during the scan
3. Eq. (281) with an appropriately chosen $\varphi(s)$ models the averaging well
4. The spatial structure of the turbulent flow is described well by the spectral tensor model of Mann (1994)

13.2.1 Systematic turbulence errors for the ZephIR lidar

The ZephIR transmits the laser beam through a constantly rotating prism, giving the required half-opening angle of nominally 30°. Each of up to five heights are scanned for one or three seconds, corresponding to one or three complete rotations of the prism. The beam is then re-focused to the next height in the sequence and the scanning procedure is repeated. Up to five different heights can be selected, the sequence (with five heights and three second scans) taking up to 18 seconds to complete. Thus the lidar spends less than 20% of the time required to make a wind profile on any one of the five heights. A typical scan at each height consists of 50 measurements of v_r on the azimuth circle. If we assume the coordinate system such that u is aligned to the mean wind direction, v is perpendicular to the mean wind direction, w is the vertical component, and the mean wind comes from the North then $\tilde{v}_r(\theta)$ can be expressed as,

$$\tilde{v}_r(\theta) = A + B\cos\theta + C\sin\theta, \tag{282}$$

where the coefficients $A = w_{qq}\ \cos\phi$, $B = u_{qq}\ \sin\phi$ and $C = v_{qq}\ \sin\phi$ and the sign ambiguity in $\tilde{v}_r(\theta)$ is neglected (see Mann et al. (2010)). We use the subscript qq to denote the velocity components measured by ZephIR, since they are not the true velocity components u, v and w. The assumption that the mean wind comes from the North is only made for simplicity. For a lidar measuring at many points on the azimuth circle the choice of the mean wind direction does not matter since averaging over the entire circle is carried out. The values of the coefficients A, B and C are found using least squares method by fitting Eq. (282) to the measured values of $\tilde{v}_r(\theta)$ at all scanned azimuth angles. The coefficients can be written as Fourier integrals,

$$A = \frac{1}{2\pi}\int_0^{2\pi} \tilde{v}_r(\theta)\ d\theta, \tag{283}$$

$$B = \frac{1}{\pi}\int_0^{2\pi} \tilde{v}_r(\theta)\ \cos\theta\ d\theta, \tag{284}$$

$$C = \frac{1}{\pi}\int_0^{2\pi} \tilde{v}_r(\theta)\ \sin\theta\ d\theta. \tag{285}$$

We proceed by deriving expressions for the w_{qq} variance. The expressions for the (co-) variances of the remaining components of wind velocity can be derived in a similar manner.

The variance of A is defined as $\sigma_A^2 = \langle A'^2\rangle$, where $\langle\rangle$ denotes ensemble averaging of a variable and $'$ denotes fluctuations. From the above definition of A we can write,

$$\sigma_A^2 = \langle w_{qq}'^2\rangle \cos^2\phi. \tag{286}$$

Using Eq. (283) we can also write,

$$\sigma_A^2 = \left\langle \left(\frac{1}{2\pi}\int_0^{2\pi} \tilde{v}_r'(\theta)\ d\theta\right)^2 \right\rangle. \tag{287}$$

Substituting $\tilde{v}_r(\theta)$ from Eq. (281) into Eq. (287), converting the square of the integral into a double integral, interchanging the order of integration and averaging we get,

$$\begin{aligned}\sigma_A^2 =& \frac{1}{4\pi^2}\int_0^{2\pi}\int_0^{2\pi}\int_{-\infty}^{\infty}\int_{-\infty}^{\infty} \langle \mathrm{v}_i'(s_1\mathbf{n}(\theta_1) + d_f\mathbf{n}(\theta_1))\mathrm{v}_j'(s_2\mathbf{n}(\theta_2) + d_f\mathbf{n}(\theta_2))\rangle \\ & \varphi(s_1)\varphi(s_2)n_i(\theta_1)n_j(\theta_2)\ ds_1 ds_2 d\theta_1 d\theta_2, \\ =& \frac{1}{4\pi^2}\int_0^{2\pi}\int_0^{2\pi}\int_{-\infty}^{\infty}\int_{-\infty}^{\infty} R_{ij}(\mathbf{r})\varphi(s_1)\varphi(s_2)n_i(\theta_1)n_j(\theta_2)\ ds_1 ds_2 d\theta_1 d\theta_2,\end{aligned} \tag{288}$$

where $\langle \mathrm{v}_i'(s_1\mathbf{n}(\theta_1) + d_f\mathbf{n}(\theta_1))\mathrm{v}_j'(s_2\mathbf{n}(\theta_2) + d_f\mathbf{n}(\theta_2))\rangle = R_{ij}(\mathbf{r})$ is the covariance tensor separated by a distance $\mathbf{r} = (s_1\mathbf{n}(\theta_1) + d_f\mathbf{n}(\theta_1)) - (s_2\mathbf{n}(\theta_2) + d_f\mathbf{n}(\theta_2))$ and is related to the three dimensional spectral velocity tensor $\Phi_{ij}(\mathbf{k})$ by the inverse Fourier transform,

$$R_{ij}(\mathbf{r}) = \int \Phi_{ij}(\mathbf{k}) e^{\mathrm{i}\mathbf{k}\cdot\mathbf{r}}\ d\mathbf{k}, \tag{289}$$

where $\int d\mathbf{k} \equiv \int_{-\infty}^{\infty}\int_{-\infty}^{\infty}\int_{-\infty}^{\infty} dk_1 dk_2 dk_3$, $\mathbf{k} = (k_1, k_2, k_3)$ denotes the wave vector and the subscripts i, j take the values from 1 to 3. Inserting Eq. (289) into Eq. (288) we get,

$$\sigma_A^2 = \int \Phi_{ij}(\mathbf{k}) \left(\int_{-\infty}^{\infty} \varphi(s_1) \left[\frac{1}{2\pi} \int_0^{2\pi} n_i(\theta_1) e^{\mathrm{i}(s_1+d_f)\mathbf{k}\cdot\mathbf{n}(\theta_1)} \, d\theta_1 \right] ds_1 \right) \left(\int_{-\infty}^{\infty} \varphi(s_2) \left[\frac{1}{2\pi} \int_0^{2\pi} n_j(\theta_2) e^{-\mathrm{i}(s_2+d_f)\mathbf{k}\cdot\mathbf{n}(\theta_2)} \, d\theta_2 \right] ds_2 \right) \, d\mathbf{k}. \tag{290}$$

Let $\alpha_i(\mathbf{k}) = \left(\int_{-\infty}^{\infty} \varphi(s) \left[\frac{1}{2\pi} \int_0^{2\pi} n_i(\theta) e^{\mathrm{i}(s+d_f)\mathbf{k}\cdot\mathbf{n}(\theta)} \, d\theta \right] ds \right)$, which physically represents the line-of-sight and conical averaging. Eq. (290) can then be written as (using Eq. 286),

$$\langle w_{qq}'^2 \rangle \cos^2\phi = \int \Phi_{ij}(\mathbf{k}) \alpha_i(\mathbf{k}) \alpha_j^*(\mathbf{k}) \, d\mathbf{k}, \tag{291}$$

where $*$ denotes complex conjugation. Thus the integral reduces to evaluating $\alpha_i(\mathbf{k})$, since the analytical expressions for $\Phi_{ij}(\mathbf{k})$ are given in Mann (1994). Eq. (291) can then be estimated numerically. For a CW lidar, $\varphi(s)$ is well approximated by a Lorentzian function (Sonnenschein and Horrigan, 1971),

$$\varphi(s) = \frac{1}{\pi} \frac{l}{l^2 + s^2}, \tag{292}$$

where l is the Rayleigh length ($= \lambda d_f^2 / \pi r_b^2$, where $\lambda = 1.55$ μm and $r_b = 19.5$ mm is the beam radius). An attempt has been made to obtain analytical expressions for $\alpha_i(\mathbf{k})$. However, no general analytical solution exists for $\alpha_i(\mathbf{k})$ and at most the integral can be reduced (by integrating over s) to

$$\alpha_i(\mathbf{k}) = \frac{1}{2\pi} \, e^{\mathrm{i}d_f k_3 \cos\phi} \int_0^{2\pi} n_i(\theta + \theta_0) \, e^{\mathrm{i}d_f k_h \sin\phi\cos\theta} \, e^{-l|k_h \cos\theta \sin\phi + k_3 \cos\phi|} \, d\theta, \tag{293}$$

where $k_h = \sqrt{k_1^2 + k_2^2}$ is the magnitude of the horizontal wave vector, $\cos\theta_0 = k_1/k_h$, $\sin\theta_0 = k_2/k_h$, and $n_i(\theta + \theta_0)$ is the component of the unit directional vector obtained from Eq. (280). Thus numerical integration has to be applied also for the evaluation of $\alpha_i(\mathbf{k})$.

A similar approach is taken for deriving u_{qq} and v_{qq} variances, where we obtain,

$$\langle u_{qq}'^2 \rangle \sin^2\phi = \int \Phi_{ij}(\mathbf{k}) \beta_i(\mathbf{k}) \beta_j^*(\mathbf{k}) \, d\mathbf{k}, \tag{294}$$

$$\langle v_{qq}'^2 \rangle \sin^2\phi = \int \Phi_{ij}(\mathbf{k}) \gamma_i(\mathbf{k}) \gamma_j^*(\mathbf{k}) \, d\mathbf{k}. \tag{295}$$

The corresponding β and γ functions are,

$$\beta_i(\mathbf{k}) = \frac{1}{\pi} \, e^{\mathrm{i}d_f k_3 \cos\phi} \int_0^{2\pi} n_i(\theta + \theta_0) \cos(\theta + \theta_0) \, e^{\mathrm{i}d_f k_h \sin\phi\cos\theta} \, e^{-l|k_h \cos\theta \sin\phi + k_3 \cos\phi|} \, d\theta, \tag{296}$$

$$\gamma_i(\mathbf{k}) = \frac{1}{\pi} \, e^{\mathrm{i}d_f k_3 \cos\phi} \int_0^{2\pi} n_i(\theta + \theta_0) \sin(\theta + \theta_0) \, e^{\mathrm{i}d_f k_h \sin\phi\cos\theta} \, e^{-l|k_h \cos\theta \sin\phi + k_3 \cos\phi|} \, d\theta. \tag{297}$$

The derivation of the co-variances is merely a combination of the weighting functions $\alpha_i(\mathbf{k})$, $\beta_i(\mathbf{k})$, $\gamma_i(\mathbf{k})$ and their complex conjugates used with $\Phi_{ij}(\mathbf{k})$.

Modelling the low-pass filtering effect due to the three seconds scan

Since the ZephIR scans three circles in approximately three seconds, there will be a low-pass filter effect in turbulence measurements. We assume a length scale $L_f = \langle u \rangle \times 3$s such that it represents the three seconds averaging. We assume that the ZephIR scans a circle infinitely fast for three seconds. We model the corresponding filtering effect by a simple rectangular filter, such that,

$$f(x) = \begin{cases} \frac{1}{L_f} & \text{for } |x| < \frac{L_f}{2}; \\ 0 & \text{elsewhere,} \end{cases} \tag{298}$$

where x is the center of the scanning circle and $f(x)$ is any function of x. The corresponding spectral transfer function is given as,

$$\hat{T}_f(k_1) = \mathrm{sinc}^2\left(\frac{k_1 L_f}{2}\right), \tag{299}$$

where $\mathrm{sinc}(x) = \sin(x)/x$. The variances of u_{qq}, v_{qq} and w_{qq} are given as,

$$\langle u'^2_{qq}\rangle \sin^2\phi = \int \Phi_{ij}(\mathbf{k})\beta_i(\mathbf{k})\beta_j^*(\mathbf{k})\hat{T}_f(k_1)\ d\mathbf{k}, \tag{300}$$

$$\langle v'^2_{qq}\rangle \sin^2\phi = \int \Phi_{ij}(\mathbf{k})\gamma_i(\mathbf{k})\gamma_j^*(\mathbf{k})\hat{T}_f(k_1)\ d\mathbf{k}, \tag{301}$$

$$\langle w'^2_{qq}\rangle \cos^2\phi = \int \Phi_{ij}(\mathbf{k})\alpha_i(\mathbf{k})\alpha_j^*(\mathbf{k})\hat{T}_f(k_1)\ d\mathbf{k}. \tag{302}$$

13.2.2 Systematic turbulence errors for the WindCube lidar

The assumption made in section 13.2.1 that the mean wind direction comes from the North cannot be made for the WindCube, since it measures at four azimuth angles only (refer Fig. 164), e.g. North, East, South and West. In this case the coordinate system is such that u is aligned in the mean wind direction. Thus,

$$u_{wc} = u_{NS}\cos\Theta + u_{EW}\sin\Theta, \tag{303}$$

$$v_{wc} = u_{NS}\sin\Theta - u_{EW}\cos\Theta, \tag{304}$$

where u_{NS} and u_{EW} denote wind speeds in the North-South and East-West directions respectively, Θ denotes the wind direction, and the subscript wc denotes the velocity components measured by the WindCube. From simple geometrical considerations (refer Fig. 164),

$$u_{NS} = \frac{\tilde{v}_{rN} - \tilde{v}_{rS}}{2\sin\phi}, \tag{305}$$

$$u_{EW} = \frac{\tilde{v}_{rE} - \tilde{v}_{rW}}{2\sin\phi}, \tag{306}$$

where $\tilde{v}_{rN}$, $\tilde{v}_{rS}$, $\tilde{v}_{rE}$, $\tilde{v}_{rW}$ are the weighted average radial velocities in the North, South, East and West directions respectively. For the w component,

$$w_{wc} = \frac{P(\tilde{v}_{rN} + \tilde{v}_{rS}) + Q(\tilde{v}_{rE} + \tilde{v}_{rW})}{2\cos\phi}, \tag{307}$$

where P and Q are the weights associated with the wind direction such that $P + Q = 1$. Leosphere uses $P = \cos^2\Theta$ and $Q = \sin^2\Theta$, and hence, we use the same in our calculations.

We proceed by deriving expressions for the u_{wc} variance. The expressions for the (co-) variances of the remaining components of wind velocity can be derived in a similar manner. Substituting Eqs. (305), (306) into Eq. (303) we get,

$$u_{wc} = \frac{1}{2\sin\phi}[(\tilde{v}_{rN} - \tilde{v}_{rS})\cos\Theta + (\tilde{v}_{rE} - \tilde{v}_{rW})\sin\Theta]. \tag{308}$$

We define unit vectors in the four directions as,

$$\begin{aligned}
\mathbf{n}_N &= \mathbf{n}(-\Theta),\\
\mathbf{n}_S &= \mathbf{n}(\pi - \Theta),\\
\mathbf{n}_E &= \mathbf{n}(\frac{\pi}{2} - \Theta),\\
\mathbf{n}_W &= \mathbf{n}(\frac{3\pi}{2} - \Theta),
\end{aligned} \tag{309}$$

where $\mathbf{n}_N$, $\mathbf{n}_S$, $\mathbf{n}_E$ and $\mathbf{n}_W$ are the unit directional vectors in the North, South, East and West directions respectively. From Eq. (281), for the North direction,

$$\tilde{v}_{rN} = \int_{-\infty}^{\infty} \varphi(s)\mathbf{n}_N \cdot \mathbf{v}(s\mathbf{n}_N + d_f\mathbf{n}_N)\ ds. \tag{310}$$

To further simplify the notation we define the translation operator T_δ acting on any scalar or vector field $\xi(\mathbf{x})$,

$$T_\delta \xi(\mathbf{x}) = \xi(\mathbf{x} + \delta). \tag{311}$$

We also define a convolution operator $C_\mathbf{n}$ acting on any scalar or vector field as,

$$C_\mathbf{n}\mathbf{v}(\mathbf{x}) = \int_{-\infty}^{\infty} \varphi(s)\mathbf{n}\cdot\mathbf{v}(\mathbf{x}+\mathbf{n}s)\ ds. \tag{312}$$

For the North direction, Eq. (310) can be written as,

$$\tilde{v}_{rN} = C_{\mathbf{n}_N} T_{d_f \mathbf{n}_N}\mathbf{v}. \tag{313}$$

We get similar expressions for South, East and West directions. Eq. (308) can then be written as,

$$u_{wc} = \frac{1}{2\sin\phi}[(C_{\mathbf{n}_N}T_{d_f\mathbf{n}_N} - C_{\mathbf{n}_S}T_{d_f\mathbf{n}_S})\cos\Theta + (C_{\mathbf{n}_E}T_{d_f\mathbf{n}_E} - C_{\mathbf{n}_W}T_{d_f\mathbf{n}_W})\sin\Theta]\mathbf{v} \tag{314}$$

We also know that by definition,

$$\langle u'^2\rangle = \int \langle \hat{u}(\mathbf{k})\hat{u}^*(\mathbf{k})\rangle d\mathbf{k}, \tag{315}$$

where $\hat{}$ denotes Fourier transform and $*$ denotes complex conjugation. In the Fourier space we have,

$$\widehat{T_\delta \mathbf{v}}(\mathbf{k}) = e^{\mathrm{i}\mathbf{k}\cdot\delta}\hat{\mathbf{v}}(\mathbf{k}), \tag{316}$$

$$\widehat{C_\mathbf{n}\mathbf{v}}(\mathbf{k}) = \hat{\varphi}(\mathbf{n}\cdot\mathbf{k})\mathbf{n}\cdot\hat{\mathbf{v}}(\mathbf{k}), \tag{317}$$

where $\hat{\varphi}(k) = \mathrm{sinc}^2(kl_p/2)$, considering that the weighting function for a pulsed lidar is commonly defined as,

$$\varphi(s) = \begin{cases} \frac{l_p - |s|}{l_p^2} & \text{for } |s| < l_p; \\ 0 & \text{elsewhere,} \end{cases} \tag{318}$$

where l_p is the half length of the ideally rectangular light pulse leaving the lidar assuming the matching time windowing ($= 2l_p/c$, where c is the speed of light). Thus in Fourier space Eq. (314) can then be written as,

$$\begin{aligned}\hat{u}_{wc}(\mathbf{k}) =& \frac{1}{2\sin\phi}[(\mathbf{n}_N e^{\mathrm{i}d_f\mathbf{k}\cdot\mathbf{n}_N}\,\mathrm{sinc}^2(\mathbf{k}\cdot\mathbf{n}_N l_p/2) - \mathbf{n}_S e^{\mathrm{i}d_f\mathbf{k}\cdot\mathbf{n}_S}\,\mathrm{sinc}^2(\mathbf{k}\cdot\mathbf{n}_S l_p/2))\cos\Theta \\ &+ (\mathbf{n}_E e^{\mathrm{i}d_f\mathbf{k}\cdot\mathbf{n}_E}\,\mathrm{sinc}^2(\mathbf{k}\cdot\mathbf{n}_E l_p/2) - \mathbf{n}_W e^{\mathrm{i}d_f\mathbf{k}\cdot\mathbf{n}_W}\,\mathrm{sinc}^2(\mathbf{k}\cdot\mathbf{n}_W l_p/2))\sin\Theta]\cdot\hat{\mathbf{v}}(\mathbf{k}) \\ &\equiv \mathbf{b}(\mathbf{k})\cdot\hat{\mathbf{v}}(\mathbf{k}),\end{aligned} \tag{319}$$

and the variance (from Eq. 315),

$$\langle u_{wc}'^2\rangle = \int \Phi_{ij}(\mathbf{k})b_i(\mathbf{k})b_j^*(\mathbf{k})\ d\mathbf{k}, \tag{320}$$

where we have implicitly used the relation, $\Phi_{ij}(\mathbf{k}) = \langle \hat{\mathrm{v}}_i(\mathbf{k})\hat{\mathrm{v}}_j^*(\mathbf{k})\rangle$. The (co-) variances of other components can be estimated in a similar manner by first estimating the corresponding weighting functions $c_i(\mathbf{k})$ and $a_i(\mathbf{k})$ for v_{wc} and w_{wc} components respectively.

13.2.3 Definition of the systematic error

For simplicity we define systematic error as the ratio of the lidar second-order moment to the true second-order moment. Thus a ratio equal to one would signify no systematic error, whereas deviations from unity signify systematic error. By definition, the true second-order moment of a velocity component is given as,

$$\langle \mathrm{v}_i'\mathrm{v}_j'\rangle = \int \Phi_{ij}(\mathbf{k})d\mathbf{k}. \tag{321}$$

The theoretical systematic errors are calculated by taking the ratio of lidar second-order moments (Eqs. 291, 294, 295 and 319) to the true second-order moment (Eqn. 321). The numerical integration is carried out using an adaptive algorithm (Genz and Malik, 1980). For experimental comparison, the second-order moments measured by sonic anemometers are considered to be true second-order moments. Thus experimentally, the systematic errors are estimated by taking the ratio of the measured lidar second-order moments to sonic second-order moments.

13.3 Comparison of models with the measurements

The details of the measurement campaign are explained in Sathe et al. (2011). The estimation of Φ_{ij} using the model from Mann (1994) requires three input parameters, $\alpha\epsilon^{2/3}$, which is a product of the spectral Kolmogorov constant α (Monin and Yaglom, 1975) and the rate of viscous dissipation of specific turbulent kinetic energy $\epsilon^{2/3}$, a length scale L and an anisotropy parameter Γ. We use these input parameters obtained by fitting the sonic anemometer measurements under different atmospheric stability conditions, at several heights on the meteorological mast in the eastern sector (Peña et al., 2010b). The classification of atmospheric stability (table 19) is based on the Monin-Obukhov length (L_{MO}) intervals (Gryning et al., 2007). L_{MO} is estimated using the eddy covariance method (Kaimal and Finnigan, 1994) from the high frequency (20 Hz) measurements at 20 m. Mathematically, L_{MO} is given as,

Table 19: Classification of atmospheric stability according to Monin-Obukhov length intervals

very stable (vs)	$10 \leq L_{MO} \leq 50$ m
stable (s)	$50 \leq L_{MO} \leq 200$ m
near-neutral stable (nns)	$200 \leq L_{MO} \leq 500$ m
neutral (n)	$\mid L_{MO} \mid \geq 500$ m
near-neutral unstable (nnu)	$-500 \leq L_{MO} \leq -200$ m
unstable (u)	$-200 \leq L_{MO} \leq -100$ m
very unstable (vu)	$-100 \leq L_{MO} \leq -50$ m

$$L_{MO} = -\frac{{u_*}^3 T}{\kappa g \overline{w'\theta'_v}}, \tag{322}$$

where u_* is the friction velocity, $\kappa = 0.4$ is the von Kármán constant, g is the acceleration due to gravity, T is the absolute temperature, θ_v is the virtual potential temperature and $\overline{w'\theta'_v}$ (covariance of w and θ_v)is the virtual kinematic heat flux. u_* is estimated as,

$$u_* = \sqrt[4]{\overline{u'w'}^2 + \overline{v'w'}^2}, \tag{323}$$

where $\overline{u'w'}$ (covariance of u and w) and $\overline{v'w'}$ (covariance of v and w) are the vertical fluxes of the horizontal momentum.

13.3.1 Comparison with the ZephIR measurements

Figures 165–166 show the comparison of the modelled and measured systematic errors for u, v and w variances over 10 minute periods. The theoretical points are shown with and without the low-pass filter. For the low-pass filter, the model is dependent on the mean wind speed and the plots are shown for $\langle u \rangle = 9$ m/s at all heights, since this is the mean wind speed at Høvsøre. The measurements are represented as median (markers), first and third quartiles (error bars) respectively. We infer the following:

- The systematic errors vary considerably under different atmospheric stability conditions – The variation is up to 50% for u and v variances, and up to 20% for w variance. This

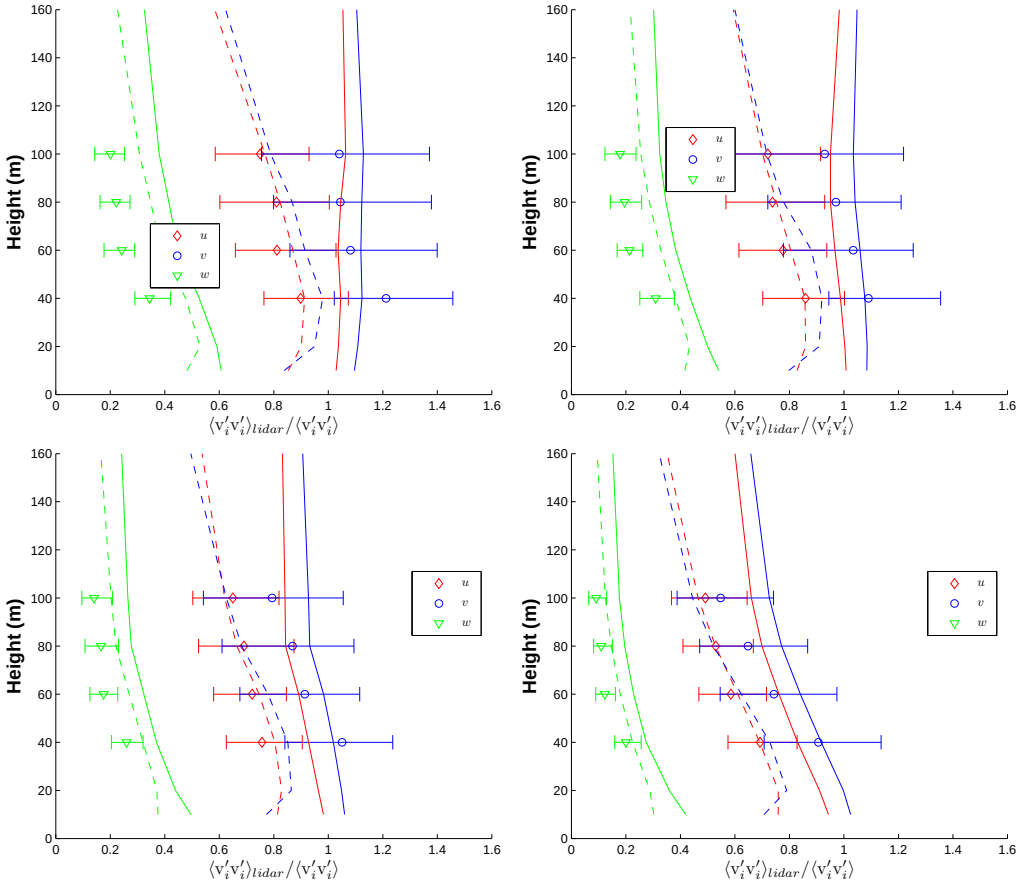

Figure 165: ZephIR systematic errors under different atmospheric stability conditions in the eastern sector. Very unstable (top left), unstable (top right), near neutral unstable (bottom left), and neutral (bottom right). The markers indicate measurements. The solid lines are the theory without the low-pass filter, and the dashed lines are with the low-pass filter.

is due to a large variation in the length scales of different velocity components resulting in varying attenuation of the variances.

- The systematic errors increase with height under all atmospheric stability conditions – This is due to a quadratic increase in the sample volume with height (Lindelöw, 2007). The diameter of the scanning circle also increases with height.
- The systematic errors in w variance are much larger (approximately 3-5 times) than that of the u and v variances – This is due to the very small length scales of the w component as compared to those for u and v, resulting in the attenuation of the w variance of up to 90%. The u and v variances are attenuated up to 70%.
- There is a significant spread (first and third quartiles) in the systematic errors of u and v variances – These are the random errors and most likely occur due to the disjunct sampling (Lenschow et al., 1994) of the ZephIR. A thorough scientific investigation is needed to quantify random errors, but is not the focus of this paper.
- The trend of the systematic errors predicted by both models is in agreement with the observations at all heights.
- With the exception of very stable conditions, the model with the low-pass filter (Eqs. 300–302) is in better agreement with the measurements at all heights than without the low-pass filter.

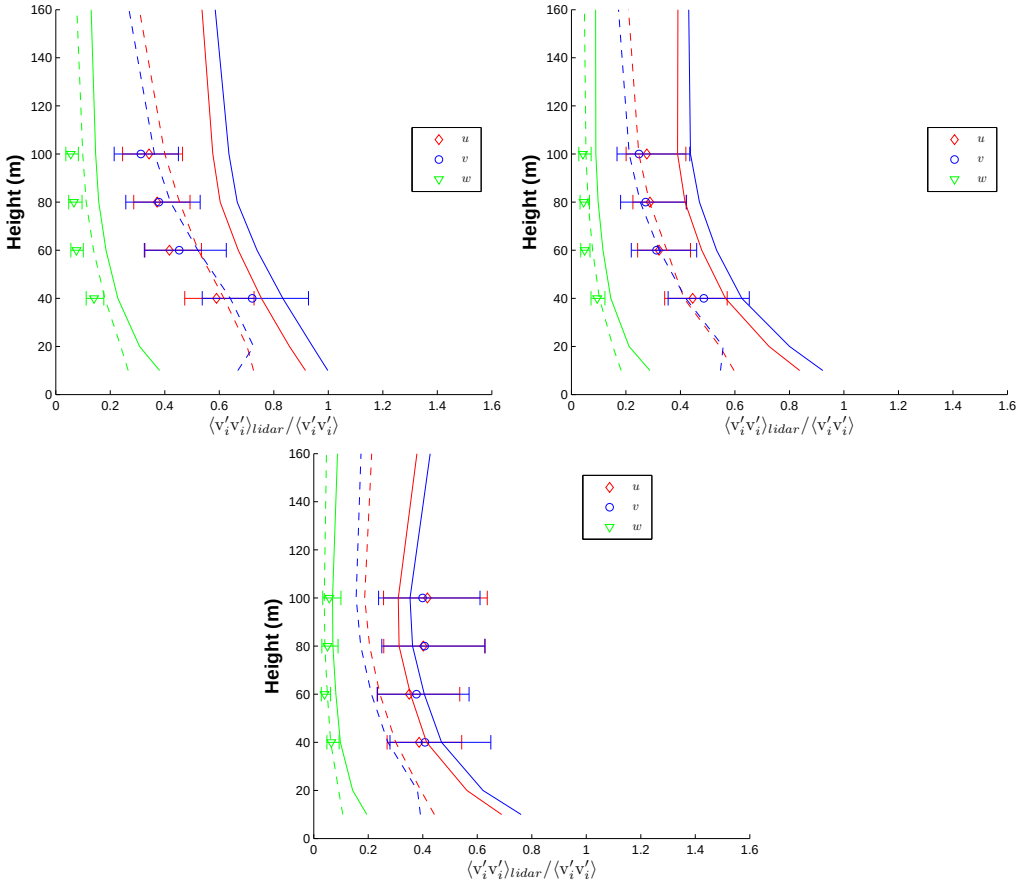

Figure 166: ZephIR systematic errors under different atmospheric stability conditions in the eastern sector. Near neutral stable (top left), stable (top right), and very stable (bottom). The markers indicate measurements. The solid lines are the theory without the low-pass filter, and the dashed lines are with the low-pass filter.

In order to quantify the improvement in the model predictions using the low-pass filter, we compute the root mean square percent errors (RMSPE) between the measured and the modelled systematic errors for each stability condition. RMSPE is given as,

$$RMSPE = \sqrt{\frac{\sum \left(\frac{\left(\frac{\langle v_i' v_i' \rangle_{lidar}}{\langle v_i' v_i' \rangle} \right)_{measured} - \left(\frac{\langle v_i' v_i' \rangle_{lidar}}{\langle v_i' v_i' \rangle} \right)_{modelled}}{\left(\frac{\langle v_i' v_i' \rangle_{lidar}}{\langle v_i' v_i' \rangle} \right)_{measured}} \times 100 \right)^2}{n}}, \tag{324}$$

where median values are used for the measurements.

Figure 167 shows the comparison of the RMSPE in the prediction of the systematic errors with and without the low-pass filter for the ZephIR. A significant decrease in the RMSPE (of the order of 30%) of u and w variances is observed under all atmospheric stabilities (except for the very stable condition for u variance), when the low-pass filtering is used. For the v variance, there is a slight increase (up to 10%) in the RMSPE under unstable conditions, whereas for stable conditions a decrease of up to 40% is observed. Thus, in general, using the low-pass filter, the model predicts the systematic errors better than without using the low-pass filter. We also performed the calculations using the beam radius $r_b = 24$ mm, and observed that the RMSPE for all three variance components changes only slightly ($\pm 5\%$).

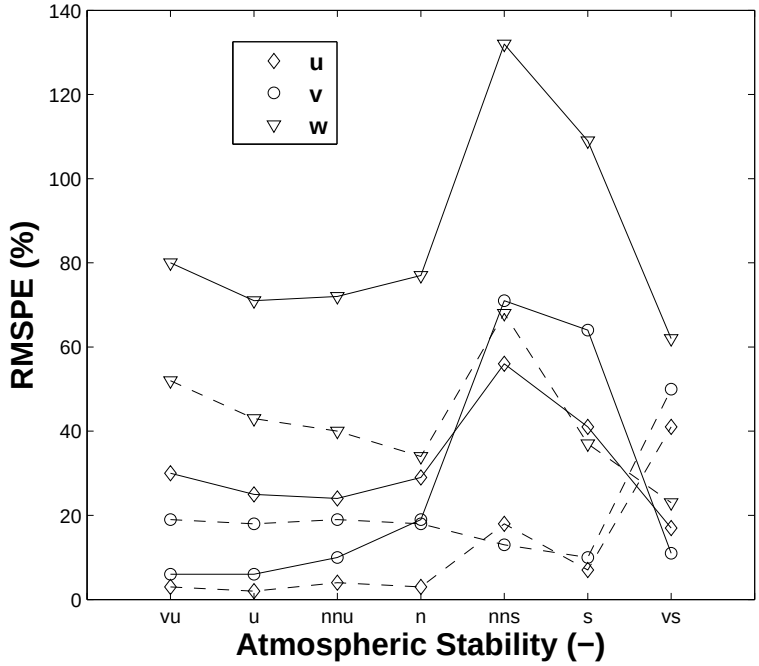

Figure 167: Root mean square percent error (RMSPE) in the prediction of the systematic errors for the ZephIR. The solid line shows the model without the low-pass filter and the dashed line shows the model with the low-pass filter. See table 19 for the meaning of the abbreviations on the x-axis.

13.3.2 Comparison with the WindCube measurements

Figures 168 and 169 show the comparison of the modelled and measured systematic errors (section 13.213.2.3) for u, v and w variances over 10-min periods. We infer the following:

- The systematic errors vary considerably under different atmospheric stability conditions – The variation is up to 50% for u and v variances, and up to 20% for the w variance. The same is also observed for the ZephIR.
- The systematic errors decrease with height for the u and v variances under all atmospheric stability conditions – For the WindCube, the probe length is constant (Lindelöw, 2007), and hence, at lower heights there is a combined averaging effect due to the probe length and the diameter of the scanning circle. Considering that at lower heights the length scales are smaller than at higher heights, it is likely that the variances are attenuated greater at lower heights than at higher heights. For w variance, the systematic error is approximately constant, and is most likely due to the small length scales.
- The systematic error in w variance is much larger (approximately 3-5 times) than that of the u and v variances. The same is also observed for the ZephIR.
- The spread in the systematic error (first and third quartiles) of the u and v variances is smaller than that of the ZephIR – This is most likely because the WindCube updates the velocity vector approximately every 6.5 seconds, whereas the ZephIR updates every 18 seconds.
- The systematic error varies significantly with the wind direction relative to the beam direction for w variance, and to a lesser degree for u and v variance under all stability conditions.

Fig. 170 shows the comparison of the RMSPE in the prediction of the systematic errors for the WindCube and ZephIR (with the low-pass filter). It is observed that for u and v variances, with the exception of the near-neutral stable condition, the RMSPE in both lidars

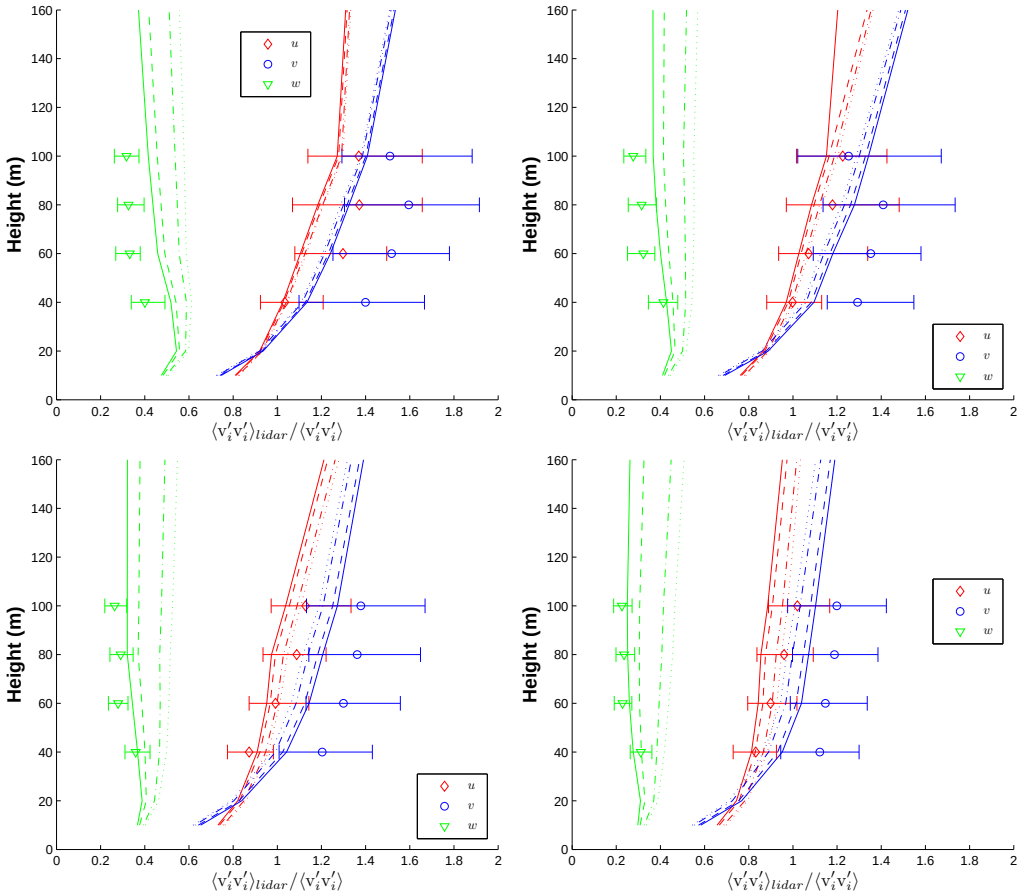

Figure 168: WindCube systematic errors under different atmospheric stability conditions in the eastern sector. Very unstable (top left), unstable (top right), near neutral unstable (bottom left), and neutral (bottom right). The markers indicate measurements. The model variation with wind direction is plotted as dotted line for $0°$, dash-dot line for $15°$, dashed line for $30°$ and solid line for $45°$

is approximately equal. There is a considerable variation in the RMSPE for the w variance. This is most likely because for the WindCube, the w variance is very sensitive to the wind direction due to its cosine and sine dependence. In general, for both lidars, except for the very stable condition, the model predicts the systematic errors for u variance reasonably well (RMSPE $\approx 6\%$), followed by v variance (RMSPE $\approx 12\%$). It is difficult to say whether the prediction for the w variance is less reliable or not (RMSPE of the order of 60%).

We do not model the filtering effect due to the scanning time (≈ 6.5 seconds) of WindCube for two reasons:

1. Since the measurement is carried out at only four points, each lasting 0.5 seconds on the scanning circle, we cannot assume that the WindCube measures infinitely fast on the scanning circle (as we did for the ZephIR). The translations in each direction have to be convolved with the corresponding spectral transfer function, if the filtering is to be included.
2. The calculation becomes too cumbersome if the above procedure is followed.

13.4 Discussion

Although the model is developed for specific lidars, the modelling framework would be the same for any other instrument. Additionally, we also model the low-pass filter for the three seconds scan in the ZephIR. We expected a large variation in the systematic errors under

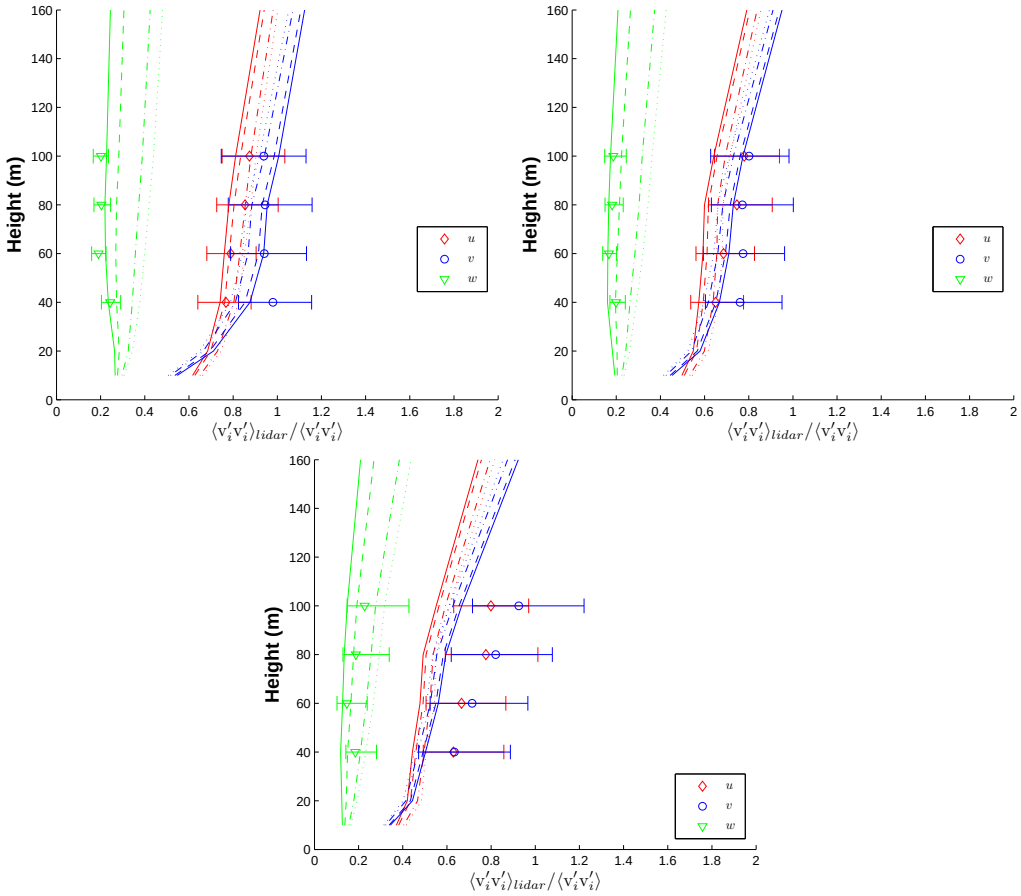

Figure 169: WindCube systematic errors under different atmospheric stability conditions in the eastern sector. Near neutral stable (top left), stable (top right), and very stable (bottom). The markers indicate measurements. The model variation with wind direction is plotted as dotted line for $0°$, dash-dot line for $15°$, dashed line for $30°$ and solid line for $45°$

different atmospheric stability conditions, and hence, performed the analysis accordingly. Figs. 165–169 indeed justify our analysis.

In general, except for the very stable conditions, the model predicts the systematic errors quite well, where the RMSPE for the u and v variances are of the order of 4% and 15% respectively. For the ZephIR, when the low-pass filter is not used then the RMSPE is quite large (of the order of 30%) for the u variance. For the w variance, the high values of RMSPE (of the order of 60%) under all atmospheric stability conditions is observed. We think that two reasons could contribute to this:

1. The attenuation in the w variance is quite large (up to 90%), as compared to the u and v variances (up to 70%). Thus, a small difference in the model prediction and the measurements results in amplifying the RMSPE.

2. For the ZephIR, when the low-pass filter is used in the model, there is dependence on the mean wind speed. The model results (Fig. 165) are shown for $\langle u \rangle = 9$ m/s only. Segregating the model and observations for different mean wind speeds will result in reducing the RMSPE.

For the WindCube, the model predicts a significant variation of the w variance with wind direction (Eq. 307). In order to estimate the influence of the weights P and Q on the prediction of systematic errors, we calculate $\langle w'^2_{wc} \rangle$ from the equation for w that corresponds to Eq. (315) with two different ways of calculating w. The first is the formula use by Leosphere, e.g. Eq. (307) with $P = \cos^2\Theta$ and $Q = \sin^2\Theta$, the second is $P = Q = 1/2$. The former is

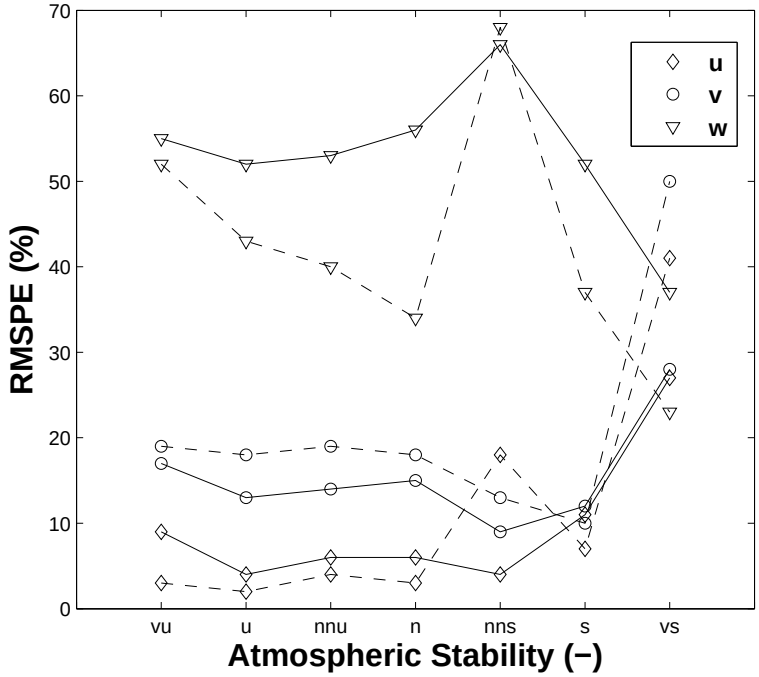

Figure 170: Comparison of the root mean square percent error (RMSPE) in the prediction of the systematic errors for the WindCube and ZephIR. The solid line is for the WindCube and the dashed line is for the ZephIR with the low-pass filter. See table 19 for the meaning of the abbreviations on the x-axis.

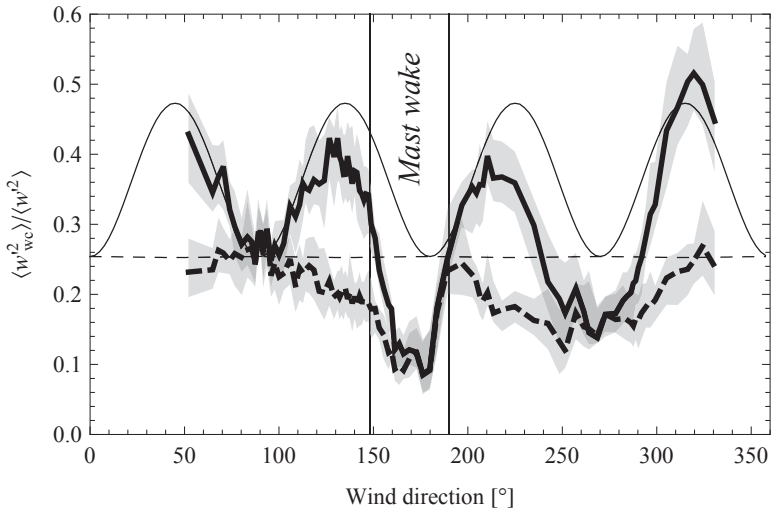

Figure 171: The ratio of the vertical velocity variance as measured by the WindCube and the actual variance measured and modeled at 100 m. The thin lines are the theoretical expectations using $P = \cos^2\Theta$ and $Q = \sin^2\Theta$ (solid line) and $P = Q = 1/2$ (dashed line) in Eq. (307), respectively. The corresponding measurements are shown as broad curves with the first and third quartiles displayed as shades

shown as a thin solid line in Fig. 171 and the latter as a thin dashed line. The spectral tensor parameters used are for neutral atmospheric stability from Peña et al. (2010b) at 100 m. The measurements of $\langle w'^2_{wc}\rangle/\langle w'^2\rangle$, shown as broad curves on Fig. 171, are from the same height, and both, measurements and theory show that $\langle w'^2_{wc}\rangle/\langle w'^2\rangle$ using Leosphere's choice of P and Q can vary by a factor of two solely by changing the wind direction. If $P = Q = 1/2$ is chosen the reduction of the vertical velocity variance does vary much less with wind direction,

but the overall attenuation is stronger.

Since the model predicts the trend in the systematic errors in the w variance reasonably well (Figs. 165–169), qualitatively it could be said that the model also agrees well with the measurements for the w variance.

While comparing the performance of our model, the following should also be considered:

- The model is dependent on the three dimensional spectral velocity tensor (Mann, 1994), which is strictly valid for neutral conditions only. Thus, one has to be careful while comparing under different atmospheric stability conditions. In this study, we have reduced the uncertainty by using the the three input tensor parameters that are fitted to the measurements under different atmospheric stability conditions (Peña et al., 2010b).
- While using Eqs. (300)–(302), we have used the same mean wind speed at all heights. In reality, there is always wind shear, which also depends significantly on atmospheric stability (Motta and Barthelmie, 2005). However, the calculations will become too cumbersome, and hence, we made a crude approximation.
- The very stable conditions are generally difficult to analyze. There could be different reasons for the large deviation in the u and v variances, e.g.,
  - Uncertainty in the input tensor parameters
  - Lack of validity of the spectral tensor model (Mann, 1994) under different atmospheric stability conditions

  Also, contrary to expectation, the measurements under very stable conditions (Figs. 166 and 169) show a decrease in the systematic errors for the u and v variances, as compared to the stable conditions.

There is also some room for reducing redundancy in the ZephIR measurements, which might reduce the spread of the systematic errors (quartile range). Instead of scanning at several points on the circle, only four points are required. Reducing the measurement points would increase the dependence of the second-order moments on the wind direction (refer section 13.213.2.2). However, it would considerably reduce the time required for completing a VAD. There is also no need to scan the circle three times, e.g. in the present configuration, 50 points are scanned in approximately one second. Thus four points would take only 0.08 seconds. If it measures five heights sequentially, the next measurement would be after 0.4 seconds, giving a measurement frequency ≥ 2 Hz. Alternatively, at each of the four points the scans can also be performed rapidly at different heights sequentially before scanning the next point.

13.5 Conclusion

The systematic errors of the second-order moments measured by lidars using the conical scanning and VAD technique to process the data are quite large due to

1. the spatial separation of the data points along the line-of-sight and
2. the spatial separation of the data points in the conical section.

Also, from Eqs. (291, 294, 295 and 320) the general lidar equation for the second-order moments using the VAD data processing technique can be written as,

$$\langle \mathrm{v}'_m \mathrm{v}'_n \rangle_{lidar} = \int \Phi_{ij}(\mathbf{k}) {X_i}^m(\mathbf{k}) X_j^{*n}(\mathbf{k})\, d\mathbf{k}; \tag{325}$$

$${X_i}^m(\mathbf{k}) = \begin{cases} \beta_i(\mathbf{k}) \bigwedge b_i(\mathbf{k}), & m = 1 \\ \gamma_i(\mathbf{k}) \bigwedge c_i(\mathbf{k}), & m = 2 \\ \alpha_i(\mathbf{k}) \bigwedge a_i(\mathbf{k}), & m = 3 \end{cases}$$

The weighting functions $\alpha_i(\mathbf{k})$, $\beta_i(\mathbf{k})$, $\gamma_i(\mathbf{k})$ are used for the ZephIR and $a_i(\mathbf{k})$, $b_i(\mathbf{k})$, $c_i(\mathbf{k})$ are used for the WindCube. Thus, the measurement of the second-order moment by lidar

involves interaction of all components of the spectral velocity tensor $\Phi_{ij}(\mathbf{k})$ weighted by the corresponding weighting functions ${X_i}^m(\mathbf{k})$ and ${Y_j}^{*n}(\mathbf{k})$. It is to be noted that Eqn. (325) is given in Einstein summation convention, and hence, in order to explicitly see the contribution of all components of $\Phi_{ij}(\mathbf{k})$ on the measurement of the second-order moments by lidar, this equation must be expanded for all values of the subscripts i and j. In most cases, this results in the attenuation of the second-order moments, whereas in some cases this also results in amplification of the second-order moment, e.g. as observed for the WindCube in the unstable conditions (see Fig. 168).

13.6 Future Perspectives

It is clear that using the conical scanning and VAD technique to process the data turbulence cannot be measured precisely. However, it should not be misunderstood that lidars can never measure turbulence. It depends greatly on the measurement configuration. We are currently looking into alternative ways of analyzing the lidar data and different beam configurations that would render turbulence measurements more feasible. One idea is to use two different half opening angles as in Eberhard et al. (1989), who show that all terms in the Reynolds stress tensor can be obtained by using the single beam statistics, without resorting to beam covariances, which is done in this paper. That would require significant hardware modifications to the instruments treated here. Another idea is to supplement the analysis with information on the width of the Doppler spectra, as done for the momentum flux in Mann et al. (2010), in order to compensate for the effect of along-beam averaging.

Notation

α	spectral Kolmogorov constant
α_i	ZephIR weighting function that represents the line-of-sight and conical averaging for the w component
β_i	ZephIR weighting function that represents the line-of-sight and conical averaging for the u component
$\mathbf{k}$	wave vector
$\mathbf{n}$	unit directional vector
$\mathbf{r}$	Separation distance
ϵ	rate of viscous dissipation of specific turbulent kinetic energy
Γ	turbulence anisotropy parameter
γ_i	ZephIR weighting function that represents the line-of-sight and conical averaging for the v component
$\hat{T}_f$	Spectral transfer function representing the three seconds averaging for the ZephIR
κ	von Kármán constant
λ	wavelength of the emitted radiation
$< \mathrm{v}'_i \mathrm{v}'_j >$	true second-order moment
v	instantaneous velocity field
$\overline{u'v'}, \overline{v'w'}$	vertical fluxes of the horizontal momentum
$\overline{w'\theta'_v}$	virtual kinematic heat flux
ϕ	half-opening angle
Φ_{ij}	spectral velocity tensor
Θ	Mean wind direction
θ	azimuth angle
θ_v	virtual potential temperature
$\bar{v}_r$	weighted average radial velocity
φ	lidar weighting function along the line of sight
a_i	Windcube weighting function that represents the line-of-sight and conical averaging for the w component
b_i	Windcube weighting function that represents the line-of-sight and conical averaging for the u component
c	speed of light
c_i	Windcube weighting function that represents the line-of-sight and conical averaging for the v component
d_f	focus distance/center of the range gate
f	frequency of the emitted radiation
g	acceleration due to gravity
L	Turbulence length scale
l	Rayleigh length
L_f	length scale that represents three seconds averaging in the ZephIR

L_{MO}	Monin-Obukhov length
l_p	half length of the ideally rectangular light pulse leaving the Windcube
r_b	beam radius
R_{ij}	Covariance tensor
$RMSPE$	root mean square percent errors
s	distance along the beam from the focus or center of the range gate
T	absolute temperature
u	Component of the velocity field in the mean wind direction
u_*	friction velocity
u_{qq}	Component of the velocity field in the mean wind direction measured by the ZephIR
u_{WC}	Component of the velocity field in the mean wind direction measured by the Windcube
v	Component of the velocity field perpendicular to the mean wind direction in a horizontal plane
v_{qq}	Component of the velocity field perpendicular to the mean wind direction in a horizontal plane measured by the ZephIR
v_r	radial velocity/line of sight velocity
v_{WC}	Component of the velocity field perpendicular to the mean wind direction in a horizontal plane measured by the Windcube
w	Component of the velocity field perpendicular to the mean wind direction in a vertical plane
w_{qq}	Component of the velocity field perpendicular to the mean wind direction in a vertical plane measured by the ZephIR
w_{WC}	Component of the velocity field perpendicular to the mean wind direction in a vertical plane measured by the Windcube

References

Banakh V. A., Smalikho I. N., Köpp F., and Werner C. (1995) Representativeness of wind measurements with a CW Doppler lidar in the atmospheric boundary layer. *Appl. Opt.*, **34**:2055–2067

Banta R. M., Newsom R. J., Lundquist J. K., Pichugina Y. L., Coulter R. L., and Mahrt L. (2002) Nocturnal low-level jet characteristics over Kansas during CASES-99. *Bound.-Layer Meteorol.*, **105**:221–252

Browning K. A. and Wexler R. (1968) The determination of kinematic properties of a wind field using a Doppler radar. *J. Appl. Meteorol.*, **7**:105–113

Citriniti J. H. and George W. K. (1997) The reduction of spatial aliasing by long hot-wire anemometer probes. *Exp. Fluids*, **23:**217–224.

Eberhard W. L., Cupp R. E., and Healy K. R. (1989) Doppler lidar measurements of profiles of turbulence and momentum flux. *J. Atmos. Oceanic Technol.*, **6**:809–819

Emeis S., Harris M., and Banta R. M.. (2007) Boundary-layer anemometry by optical remote sensing for wind energy applications. *Meteorol. Z.*, **16**:337–347

Engelbart D. A. M., Kallistratova M., and Kouznetsov R. (2007) Determination of the turbulent fluxes of heat and momentum in the ABL by ground-based remote-sensing techniques (a review). *Meteorol. Z.*, **16**:325–335

Gal-Chen T., Xu M., and Eberhard W. L. (1992) Estimation of atmospheric boundary layer fluxes and other turbulence parameters from Doppler lidar data. *J. Geophys. Res.*, **97**:409–423

Genz A. C. and Malik A. A. (1980) An adaptive algorithm for numerical integration over an n-dimensional rectangular region. *J. Comput. Appl. Math.*, **6**:295–302

Gryning S.-E., Batchvarova E., Brümmer B., Jørgensen H., and Larsen S. (2007) On the extension of the wind profile over homogeneous terrain beyond the surface layer. *Bound.-Layer Meteorol.* **124**:251–268

Kaimal J. C. and Finnigan J. J. (1994) *Atmospheric Boundary Layer Flows*, 255–257. Oxford University Press, New York

Kaimal J. C., Wyngaard J. C., Izumi Y., and Coté O. R. (1972) Spectral characteristics of surface-layer turbulence. *Q. J. Royal Meteorol. Soc.*, **98**:563–589

Kindler D., Oldroyd A., MacAskill A., and Finch D. (2007) An eight month test campaign of the QinetiQ ZephIR system: Preliminary results. *Meteorol. Z.* **16**:479–489

Kropfli R. A.. (1986) Single Doppler radar measurement of turbulence profiles in the convective boundary layer. *J. Atmos. Oceanic Technol.*, **3**:305–314

Lenschow D. H., Mann J., and Kristensen L. (1994) How long is long enough when measuring fluxes and other turbulence statistics? *J. Atmos. Oceanic Technol.*, **11**:661–673

Lindelöw P. (2007) *Fibre Based Coherent Lidars for Remote Wind Sensing*. PhD thesis, Technical University Denmark

Mann J. (1994) The spatial structure of neutral atmospheric surface-layer turbulence. *J. Fluid Mech.*, **273**: 141–168

Mann J., Cariou J., Courtney M., Parmentier R., Mikkelsen T., Wagner R., Lindelow P., Sjöholm M., and Enevoldsen K. (2009) Comparison of 3D turbulence measurements using three staring wind lidars and a sonic anemometer. *Meteorol. Z.*, **18**:135–140

Mann J, Peña A., Bingöl F., Wagner R., and Courtney M. S. (2010) Lidar scanning of momentum flux in and above the surface layer. *J. Atmos. Oceanic Technol.*, **27**:792–806

Monin A. S. and Yaglom A. M. (1975) *Statistical Fluid Mechanics*, volume 2. MIT Press,

Motta M. and Barthelmie R. J. (2005) The influence of non-logarithmic wind speed profiles on potential power output at Danish offshore sites. *Wind Energy*, 219–236

Peña A., Hasager C. B., Gryning S.-E., Courtney M., Antoniou I., Mikkelsen T. (2009) Offshore wind profiling using light detection and ranging measurements. *Wind Energy* **12**:105–124

Peña A., Gryning S.-E., and Hasager C. B. (2010a) Comparing mixing-length models of the diabatic wind profile over homogeneous terrain. *Theor. Appl. Climatol.* **100**:325–335

Peña A., Gryning S.-E, and Mann J. (2010) On the length scale of the wind profile. *Q. J. Royal Meteorol. Soc.*, **136**: 2119–2131

Pichugina Y. L., Banta R. M., Kelly N. D., Jonkman B. J., S C. Tucker S. C., R K. Newsom B. J., and Brewer W. A. (2008) Horizontal-velocity and variance measurements in the stable boundary layer using Doppler lidar: Sensitivity to averaging procedures. *J. Atmos. Oceanic Technol.*, **25**:1307–1327

Sathe A., Mann J., Gottschall J., and Courtney M. (2011) Can wind lidars measure turbulence? *Accepted for publication in the J Atmos. Oceanic Technol.*

Sjöholm M., Mikkelsen T., Mann J., Enevoldsen K., and Courtney M. (2009) Spatial averaging-effects on turbulence measured by a continuous-wave coherent lidar. *Meteorol. Z.*, **18**:281–287

Smalikho I., Kopp F., and Rahm S. (2005) Measurement of atmospheric turbulence by 2-μm Doppler lidar. *J Atmos. Oceanic Technol.*, **22**:1733–1747

Smith D. A., Harris M., Coffey A. S., Mikkelsen T., Jørgensen H. E., Mann J., and Danielian R. (2006) Wind lidar evaluation at the Danish wind test site in Høvsøre. *Wind Energy* **9**:87–93

Sonnenschein C. M. and Horrigan F. A. (1971) Signal-to-noise relationships for coaxial systems that heterodyne backscatter from atmosphere. *Appl. Opt.*, **10**: 1600

Wagner R., Mikkelsen T., and Courtney M. (2009) Investigation of turbulence measurements with a continuous wave, conically scanning lidar. Technical Report Risø-R-1682(EN), Risø DTU, 2009

Wilson D. A. (1970) Doppler radar studies of boundary layer wind profiles and turbulence in snow conditions. In *Proc.* 14^{th} *Conf. on Radar Meteorology*, 191–196,

Wyngaard J. C. (1968) Measurement of small-scale turbulence structure with hot wires. *J. Sci. Instrum.*, **1**:1105–1108

14 Ground based passive microwave radiometry and temperature profiles

Fabio Scanzani[1,2]
[1] *Institute of Atmospheric Sciences and Climate CNR, Roma, Italy*
[2] *Geoinformation Doctorate - Tor Vergata University Rome, Rome, Italy*

14.1 Introduction

The Earth's atmosphere is a layer of negligible thickness if compared to the Earth's diameter and is also, to a first approximation, transparent to electromagnetic radiation. Deviations from complete transparency are essential for life on Earth (e.g. importance of absorption of the ultraviolet radiation by ozone layer) and are the focus in the radiative physics of the atmosphere studies. At frequencies above 10 GHz, atmosphere continuously absorbs and emits electromagnetic radiation. The spectrum of this emitted radiation depends on a variety of atmospheric variables including temperature, water vapor concentration, and liquid water (e.g. clouds, rain and fog). Detecting and measuring the power of the thermal radiation emitted at certain frequencies allows to estimate some atmospheric parameters with very high spatial and temporal resolution.

The importance of the information that can be obtained from microwave observations of the atmosphere, is given in an excellent review article of the Environmental Research Laboratories of NOAA (Hogg et al., 1983): "... *Atmospheric observations form the essential base for almost all atmospheric research and services. Since the atmosphere is a variable three-dimensional fluid, these observations must be obtained in all three spatial dimensions. Ideally, such data sets should be continuous in both space and time; in practice, this has not been possible. Because existing observational systems use in situ instruments carried aloft by balloons, the National Weather Service has had to accept a compromise in which the data sets are neither continuous in time, nor continuous in space, but instead are taken once every 12 hours at stations spaced roughly 350 km apart across the United States. This system provides observations of upper air conditions that are suitable for identification and forecasting of synoptic scale phenomena such as cyclones and anti-cyclones (which have lifetimes of days and dimensions of 1000 km or more), but is not adequate for the observation and prediction of smaller scale, shorter lived phenomena such as thunderstorms, flash floods, etc. Other disadvantages of the existing system are that the profiles obtained are not usually vertical, and that significant man-hours per profile is required.* ..."

Hogg et al. (1983) also proposed an alternative observational network consisting of ground-based microwave systems upward-looking and satellite-borne, downward-looking radiometer systems. This network is envisioned to provide "profiles of wind, temperature, and to a lesser extent, humidity, continuously in time, in an unattended mode". In essence, the proposal integrates the capabilities of two complementary remote-sensing approaches to monitoring the atmosphere, one from below and the other from above. The retrieval of atmospheric parameters by passive remote sensing of thermal electromagnetic radiation at determinate frequencies is generally referred to as radiometry. A review of several radiometric techniques and the basics of the inversion algorithms to estimate the atmospheric temperature's profiles are here given.

14.2 Microwave radiometry fundamentals

Ground based radiometric measurements of lower tropospheric layers thermal emission, known as ground-based passive radiometric sensing, has been successfully used in a variety of ap-

plications, including meteorological observations and weather and climate forecasting, air quality pollution forecasting, power energy plants design, geodesy and long-baseline interferometry, communications and satellite data validation, air-sea interaction, and fundamental atmospheric molecular physics study.

Radiometers can be operated continuously – on time scales of seconds to minutes – and unattended mode under almost all weather conditions to continuously measure the temperature profiles and temperature gradients (Troitsky et al., 1993; Westwater et al., 1998). The remote sensing measurements (e.g. radiometer, RASS, sodar, lidar, etc.) have characteristics that could be largely different from those taken by in situ instruments as radiosondes, tethered balloon or traditional sensors. Remote sensing measurements are representative of a volume (e.g. related to a radio antenna's beam width or pulse length), whereas in situ measurements are usually only local point measurements. These differences must be considered in the comparison, interpretation and/or validation of data, and their use in models.

14.3 Upward-looking radiometric temperature profile measurements

The classical form of the radiative transfer theory describes the intensity of radiation propagating in a general class of medium which absorbs, emits, and scatters the radiation. The fundamental quantity measured by a radiometer is the radiant power, which is related to the specific intensity I_ν defined as the instantaneous radiant power that flows in a given point in the medium, per unit area, per unit-frequency interval at a specified frequency ν, and in a given direction per unit solid angle. As illustrated in Figure 172, its variation dI_ν at a point s along a elementary segment ds in the direction of propagation is obtained by considering the sources and sinks of the radiation in a elementary volume along that direction (in literature optical path) per unit solid angle.

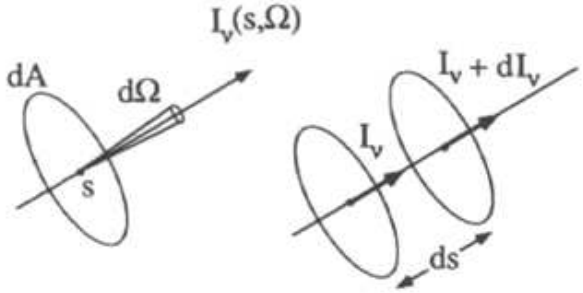

Figure 172: The specific intensity I_ν is the radiant energy flowing at each point in the medium per unit area normal to the flux, per unit solid angle, in the frequency range $\nu \; e \; \nu + d\nu$. The variation of intensity with position is governed by an equation of transfer that takes into account the sinks and sources of radiation

This leads to a following balancing power differential form of the radiative transfer equation (RTE):

$$dI_\nu = -\alpha_\nu(s) I_\nu(s) ds + S_\nu(s) ds, \tag{326}$$

where $alpha_\nu(s)$ is the local extinction coefficient and $S_\nu(s)$ is a local contributive source term at point s, which respectively describe the loss and gain of energy along the direction into the considered given elementary (Janssen, 1993).

The thermal radiation emitted from an ideal blackbody at a definite frequency ν, depends only on its thermodynamic temperature T: higher the temperature of the body more is its

emission. Its radiance also called brightness $B_\nu(T)$ is given by the Planck's law:

$$B(T,\nu) = B_\nu(T) = \frac{2h\nu^3}{c^2}\frac{1}{\exp\left(h\nu/kT\right)-1}, \tag{327}$$

where h is Planck's constant, k is Boltzmann's constant and c is the vacuum speed of light. The factor 2 in the numerator accounts for both polarizations according to the usual convention.

The related emission from a real body – often called grey body – at the same temperature is $A_\nu B_\nu(T)$ where A_ν is the fraction of incident energy absorbed from a certain direction. In the general theory, scattering into and from other directions can lead to both losses and gains to the intensity along a given propagation direction and can be taken into account in both the terms S_ν and α_ν. But if we assume a local thermodynamic equilibrium, so that each point into the elementary volume is characterized by the same temperature $T(s)$, the strict requirement of balance between the energy absorbed and emitted by any particular volume element leads to Kirchoff's law and for the S term we can suppose:

$$S_\nu(s,T) = \left[\alpha_\nu(s)\left(1-A_\nu\right)\right]B_\nu(T). \tag{328}$$

For our application we will consider a no-scatter isotropic medium. In these hypothesis the source term $S_\nu(s,T)$ expresses only the locally generated contribution to the radiation, and the absorption coefficient $\alpha_\nu(s)$ becomes a local scalar characteristic of the medium that describes a true loss of energy from the radiation field into the medium. Moreover, for a perfectly reflecting or transmitting body, A_ν is equal to zero and incident energy can be assumed to be redirected or pass through the body without being absorbed. Under these hypotheses for an upward looking radiometer we can rewrite Eq. (328) as:

$$S_\nu(s,T) \triangleq \alpha_\nu(s)B_\nu(T), \tag{329}$$

where $B_\nu(T)$ is always given by Planck's function Eq. (327).

Operating in the microwave frequency range $\nu < 300$ GHz, according to the Rayleigh-Jeans approximation of Planck's law, by expanding the exponential term $\exp\left(hv/kT\right)$ and truncating to the second term of Eq. (327)

$$\left[\exp\left(hv/kT\right) = 1 + \left(hv/kT\right) + \left(hv/kT\right)^2/2! + ... \cong 1 + \left(hv/kT\right)\right],$$

we obtained for $B_\nu(T)$ a well-known approximated linear form (see Fig. 173):

$$B_\nu(T) \cong \frac{2kv^2}{c^2}T(s), \tag{330}$$

from which Eq. (329) becomes:

$$S_\nu(s) = \alpha_\nu(s)B_\nu(T) \cong \alpha_\nu(s)\frac{2kv^2}{c^2}T(s) \tag{331}$$

$B_\nu(T)$ is the surface brightness, which is the flow of energy across a unit area, per unit frequency, from a source viewed through free space in an element of solid angle. Since the brightness and the intensity have the same units (according to Fig. 174) the two are locally equivalent in this case. It follows:

$$I_\nu(s) \equiv B_\nu(s) \cong \frac{2kv^2}{c^2}T(s), \tag{332}$$

in which I_ν is expressed as linear function of its relative thermodynamic temperature $T(s)$ as usually in the microwave frequency range formulation.

Substituting Eq. (331) form of $S_\nu(s)$ in Eq. (326) in the hypothesis of no scattering, in local thermodynamic equilibrium, plane horizontally stratified, perfectly transmitting (or reflecting) atmosphere we obtain the following radiance power transfer differential equation:

$$dI_\nu = -\alpha_\nu(s)I_\nu(s)ds + \frac{2k\nu^2}{c^2}\alpha_\nu(s)T(s)ds. \tag{333}$$

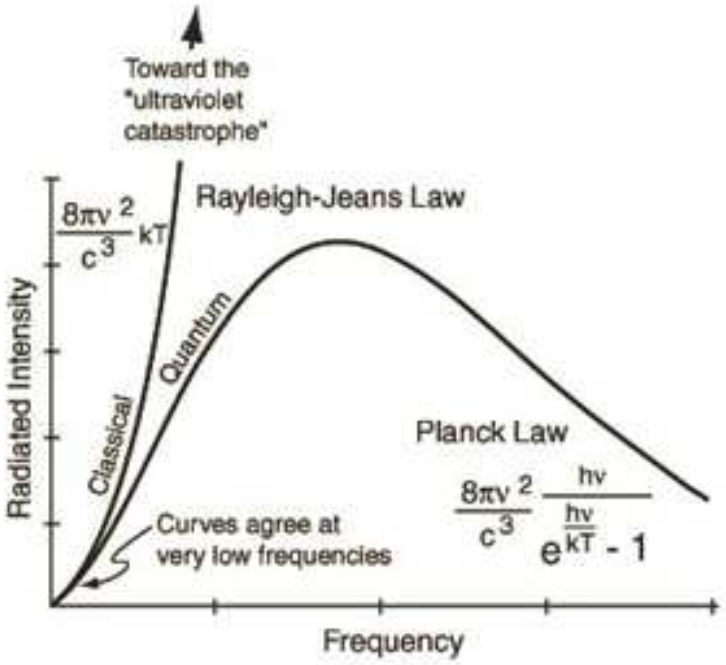

Figure 173: Rayleigh-Jeans' approximation assumed into the Planck'law

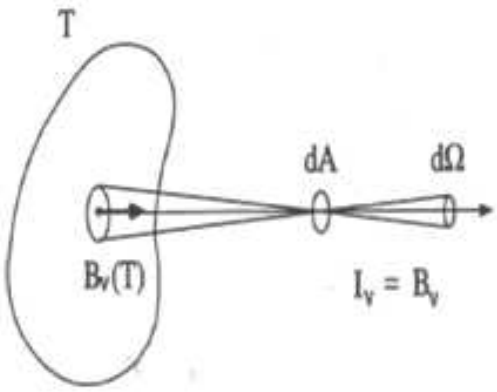

Figure 174: The surface brightness $B_\nu(T)$ of a blackbody emitter as viewed through free space in the solid-angle element $d\Omega$ produces a flow of energy given by the specific intensity $I_\nu \equiv B_\nu$

Referring to the conventions reported in Figure 175(a), the previous differential equation provides the following integral solution:

$$I_\nu(0) = I_\nu(s_0)\exp\left(-\int_0^{s_0}\alpha_\nu(s')ds'\right) + \frac{2k\nu^2}{c^2}\int_0^{s_0}\alpha_\nu(s)T(s)\exp\left(-\int_0^{s_0}\alpha_\nu(s')ds'\right)ds. \tag{334}$$

If we define the integral function of the absorption $\alpha_\nu(s)$ along the path as optical depth $\tau_\nu(s)$

$$\tau_\nu(s) \triangleq \int_0^s \alpha_\nu(s')ds', \tag{335}$$

we can rewrite Eq. (334) in the following more readable form for the ground level measured

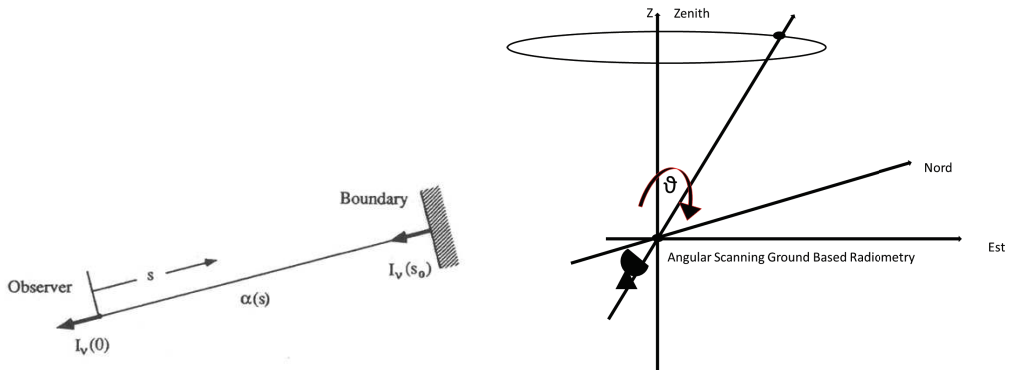

Figure 175: (a) Left: Conventions assumed into the integration of the RTE. (b) Right: Conventions assumed into the integration of the RTE

value $I_\nu(0)$:

$$I_\nu(0) = I_\nu(s_0)\exp\left(-\tau_\nu(s_0)\right) + \frac{2k\nu^2}{c^2}\int_0^{s_0}\alpha_\nu(s)T(s)\exp\left(-\tau_\nu(s)ds\right)ds. \tag{336}$$

Substituting the equivalent formulation of $I_\nu(s)$ expressed in Eq. (332) we can rewrite Eq. (336) as a function of the brightness temperature $T_b(s)$:

$$T_b(0) = T_b(s_0)\exp\left(-\tau_\nu(s_0)\right) + \int_0^{s_0} T(s)\alpha_\nu(s)\exp\left(-\tau_\nu(s)\right)ds, \tag{337}$$

where $T_b(s_0)\exp\left(-\tau_\nu(s_0)\right)$ is the brightness temperature contribute to the atmosphere from cosmic background sources attenuated by the optical depth $\tau_\nu(s_0)$ existing between ground level and the point s_0.

Referring to polar axis system of the Figure 175(b), operating the substitution $ds = dz/(\cos\theta)$, where θ is angle off zenith axis of the radiometer's beam (for zenith $\theta = 0°$) and assuming z as the atmosphere layer's level, the measured ground level brightness temperature for an upward looking radiometer expressed as function of frequency ν, and elevation angle θ it will become

$$T_b(0,\nu,\theta) \triangleq T_b(\nu,\theta) = T_b(\infty)\exp\left(-\tau_\nu(\infty)\right) + \frac{1}{\cos\theta}\int_0^{\infty} T(z)\alpha_\nu(z)\exp\left(-\tau_\nu(z)\right)dz \tag{338}$$

with the optical depth at z-layer's quote :

$$\tau_\nu(z,\theta) = \frac{1}{\cos\theta}\int_0^{z}\alpha_\nu(z')dz'. \tag{339}$$

Assuming the cosmic background contribute $T_b(\infty)\exp\left(-\tau(\infty)\right)$ as negligible for the effect of the opacity of the entire atmosphere, we can rewrite Eq. (338) at last as:

$$T_b(\nu,\theta) = \int_0^{\infty} T(z)\left(\frac{1}{\cos\theta}\alpha_\nu(z)\exp\left(-\tau_\nu(z,\theta)\right)\right)dz \tag{340}$$

or:

$$T_b(\nu,\theta) = \int_0^{\infty} T(z)W(\nu,z,\theta)dz, \tag{341}$$

in which the ground level measured brightness temperatures $T_b(\nu,\theta)$ is expressed as a convolution integral involving a temperature weighting function

$$W(\nu,z,\theta) \triangleq \frac{1}{\cos\theta}\alpha_\nu(z)\exp\left(-\tau_\nu(z,\theta)\right) \tag{342}$$

(also defined kernel function) and the thermodynamic temperature profile $T(z)$. From a physical point of view the brightness temperature $T_b(\nu,\theta)$ of Eq. (341) can be considered a "weighted" average over the thermodynamic temperature of the atmosphere along the integration path

numerically is the integral sum of the elementary emission term $T(z)dz$ from each volume's element,

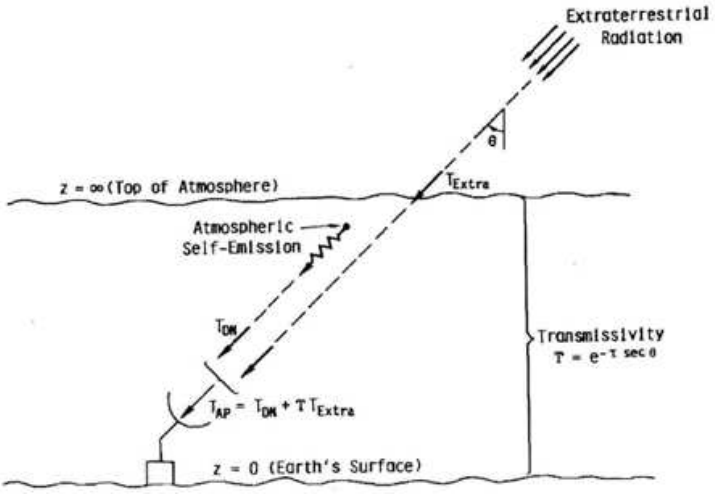

Figure 176: Brightness temperature also called apparent temperature that represents atmospheric radiation downwelling at angle θ measured by a radiometer

The integral Eq. (341) expresses the well known forward (or direct) problem: for a given weighting function $W(\nu, z, \theta)$. By the atmospheric temperature's profile $T(z)$, we can compute a measured ground level brightness temperature $T_b(\nu, \theta)$ using this equation.

However, in remote-sensing applications, we are concerned with the inverse problem in which $T_b(\nu, \theta)$ is generally measured by a radiometer at a discrete number of elevation angle θ^i (or at a discrete frequency ν^i or both) and the objective is to infer the atmospheric properties or simply to find a unknown function $T(z^i)$ that, when substituted in Eq. (340), will yield values of $T_b(\nu^i, \theta^i)$ approximately equal to the measured values. This is also known as the inverse problem and generally is more difficult to solve. A logic scheme of the two different procedures (direct and inverse) is shown in Figure 177.

Currently, there are three main absorption models that are widely used in these problems by the microwave propagation communities inside the recalled weighting function $W(\nu, z, \theta)$. A computer code has been developed and distributed of the microwave propagation model (MPM). More recently, Rosenkranz (1992) developed an improved absorption model that also is frequently used in the microwave propagation community. Another model that is used extensively in the US climate research community is the line by line radiative transfer model.

14.4 Upward-looking angular scanning microwave radiometry

The spectrum of received radiation depends on a variety of atmospheric variables including temperature, water vapor concentration, and liquid water (i.e. rain, clouds and fog). Through the measure of the received brightness temperature, it is possible to infer the atmospheric temperature profile $T(z)$ with a resolution that depends on the atmospheric absorption at the chosen frequencies. Therefore, the temperature weighting functions of upward-looking profiling radiometers above introduced in Eq. (341) have narrow peaks near the surface which decrease with altitude (see Figures 178(a) and (b)). In addition, sensitivity to oxygen is not degraded by radiation from the terrestrial surface. This allows accurate temperature profile retrievals with relatively high resolution in the lower troposphere's layer, typically until 2 km of height.

The retrieval of atmospheric temperature's profile by passive measurement of brightness

attenuated by a factor $\exp(-\tau_\nu(z, \theta))$ (by the intervening medium as it travels toward the point of measurement), weighted by $\alpha_\nu(z)/\cos\theta$. It is of fundamental importance to notice the difference between this $T_b(\nu, \theta)$, also called apparent temperature T_{AP} (shown in Fig. 176) sensed at ground level and a thermodynamic temperature profile $T(z)$ which remotely has originated it

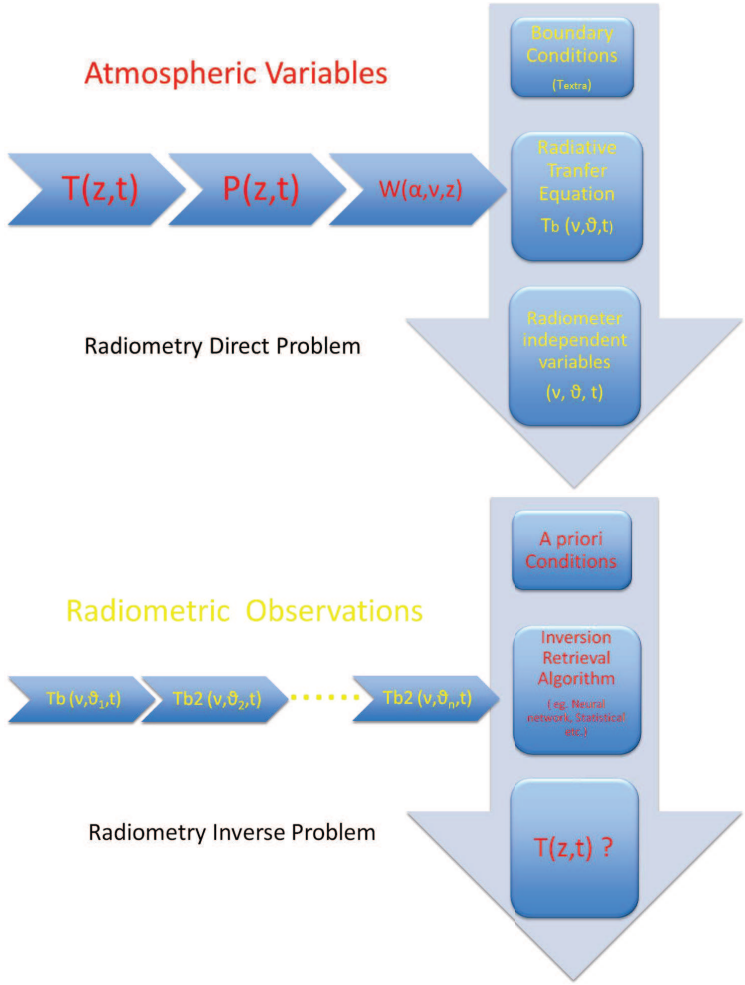

Figure 177: Schematics of the direct (top) and inverse (bottom) problem

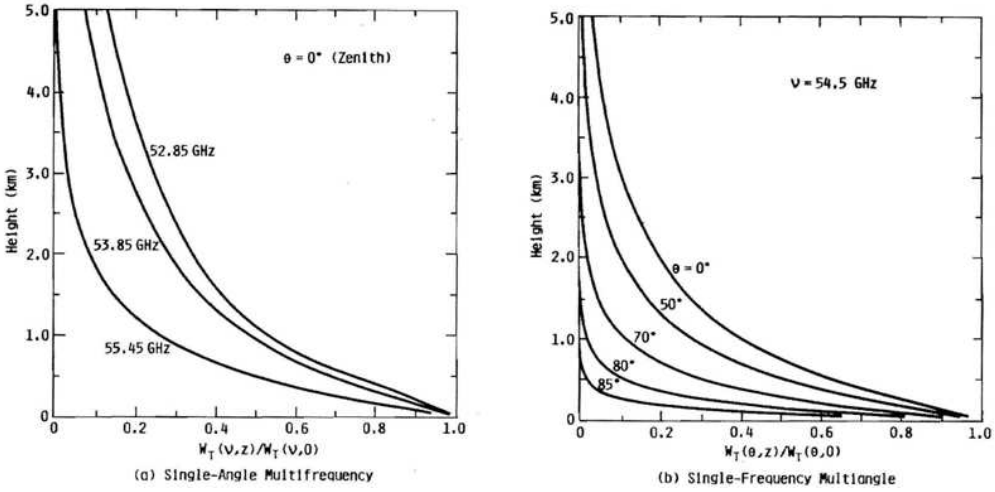

Figure 178: Normalized weighting functions

temperature $T_b(\nu, \theta)$ at one (or more) frequency and at various elevation angles is referred to as single (or multi) frequency angular scanning radiometry. For simplicity we will examine the single channel angular scanning typology but the conclusion are similar in the other cases.

The microwave atmospheric absorption (emission) in clear air and clouds, in which individual contributions from water vapor, cloud liquid, rain, and oxygen, and the attenuation associated

with rain are shown in Fig. 179. A strong emission peak is present around 60 GHz due to oxygen absorption (emission), which dominates the contribution from all other constituents except rain. The strong emission $T_b(\nu)$at frequencies near 60 GHz (see Figure 180) depends primarily on the concentration of molecular oxygen and layer's temperature. Since oxygen is well-mixed for altitudes below 80 km, its concentration is constant and well known so the only unknown associated with the high brightness emission near 60 GHz is atmospheric thermodynamic temperature.

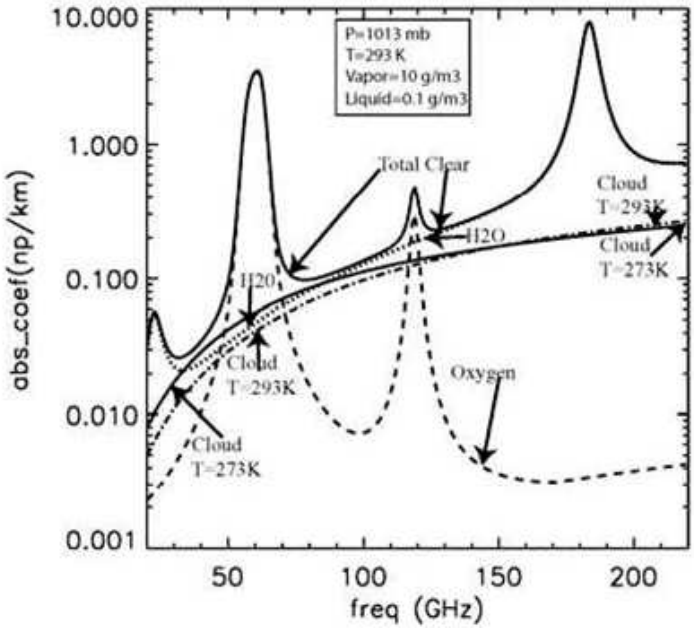

Figure 179: Atmospheric absorption normalized coefficient $\alpha_\nu(h)$ as frequency function notice the first narrow peaks at 60 Ghz

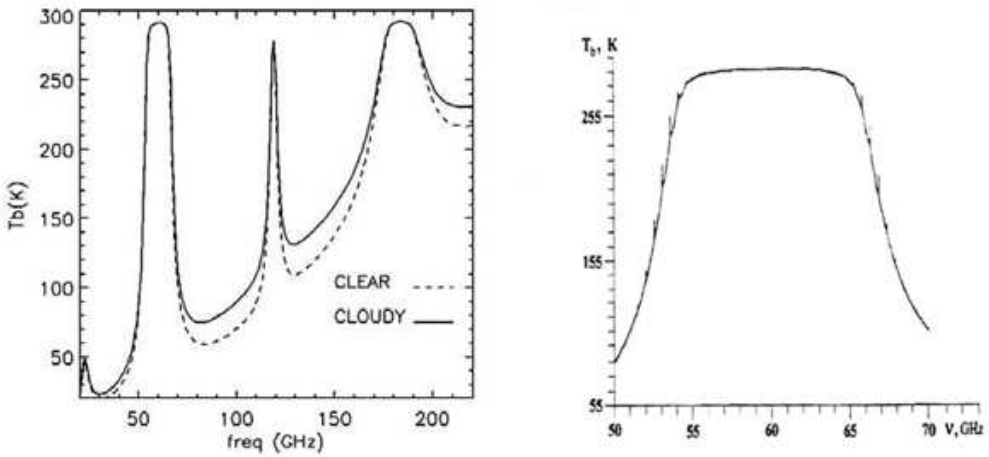

Figure 180: Spectral shape of the brightness temperature of atmospheric radio-emission, measured using ground based radiometric observation along the zenith direction in the oxygen absorption band at 60 Ghz

A ground-based radiometer looking upward detects the integrated emissions up to an heights which depends on the level of absorption associated to the observation frequency. Frequencies in the immediate vicinity of the absorption peak (Figure 180) experience the

largest attenuation, and only the lowest part of the atmosphere – in literature called skin depth – contributes to the signal detected by radiometer. The frequencies away from the peak, are less attenuated and radiation from higher layers in the atmosphere will contribute only to the deteriorating of the measured signal's noise ratio.

Askne and Westwater (1986); Troitsky (1986) described a multi-frequency (also called multi channel) passive microwave radiometer, which gave the possibility to measure temperature profiles in the troposphere (up to 10 km) but their lower troposphere's layers accuracy is not good. A more simple technique for the microwave remote sensing of the boundary layer temperature is based on measuring of the brightness temperature of the atmosphere proper in the center of the oxygen absorption band. Troitsky et al. (1993) and Kadygrov and Pick (1998) described an angular scanning single-channel microwave radiometer centered proper on molecular oxygen band at 60 GHz. For our application we will consider this second as case study.

As shown in Figure 180 at frequencies $\nu = 60$ Ghz we can suppose (with a good accuracy) an absorption coefficient independent with altitude h or $\alpha_\nu(h) = \alpha_\nu(0) =$constant and a skin depth around at $h = 300$ m. If we suppose that the skin depth equal to the boundary layer's height H_b at the zenith by integrating Eq. (339) follows:

$$\tau(H_b, \theta) = \frac{1}{\cos\theta} \int_0^{H_b} \alpha_\nu(z) dz = \frac{|\alpha_\nu(0)|(H_b - 0)}{\cos\theta} = \frac{|\alpha_\nu(0) 300 \text{ m}|}{\cos 0} \triangleq 1, \tag{343}$$

obtaining

$$|\alpha_\nu(0)| = |\alpha_\nu(h)| \triangleq \frac{1}{300 \text{ m}} \tag{344}$$

and also:

$$H(\theta) \leq H_b = \frac{\cos\theta}{|\alpha_\nu(0)|} \triangleq \cos\theta 300 \text{ m} \tag{345}$$

$$0 \leq H(\theta) \leq 300 \text{ m}. \tag{346}$$

Thus, the remote temperature sensing is conducted by measurements of the brightness temperature at the different elevation angles $\theta = 0$–90°. In this case the depth of contributing radiation layer is a range from 0–300 m (Troitsky et al., 1993) in the hypothesis that the layers of an atmosphere which are above than 300 m will not influence the measure of $T_b^{\nu_0}(\theta)$.

More in general we can rewrite the Eqs. (340) and (341) of brightness temperature as function of the elevation angle θ and expressed by a defined integral function of $T(z)$ and Eq. (342) weighting function calculated at the frequency ν_0

$$T_b^{\nu_0}(\theta) = \int_0^H T(z) W^{\nu_0}(z, \theta) dz. \tag{347}$$

This is a Fredholm integral of the first kind and the superior limit of integration is finite and coincident with the limit of atmosphere's altitude sensed generally not more than $H_b = 2$ km. In this hypothesis we are supposing the layers of an atmosphere which are higher than 2 km do not influence $T_b^{\nu_0}(\theta)$ measurements.

The previous integral function Eq. (347) may be solved for an unknown temperature profile $T(z)$, given a set of measured radiometer brightness temperature data $T_b(\theta)$ at different elevation angles θ.

One of the first inversion alghorithm used was a variation of the Twomey-Tikhonov retrieval algorithm (Tikhonov and Arsenin, 1977) in form of generalized variation (Troitsky et al., 1993). Inversion techniques for upward-looking radiometers are generally based on the temperature climatology at the site that is typically derived from in situ radiosonde measurements. The inversion method use an initial-guess profile, usually derived from radiosonde observations or tethered balloon, and use temperature brightness measurements to correct this initial guess.

At this purpose instead of $T(z)$ the deviation from the restriction function can be minimized on the manifold of positively determined function (a class of normalized function).

This method gives a good accuracy (about 0.5 K for accuracy of brightness temperature measurement better than 0.1 K) but sometimes results are not stable.

A more stable solution, having approximately the same accuracy, is given by a second method, which uses a variation of linear statistical retrieval (Turchin, 1967; Westwater et al., 1998). To implement this algorithm, it was constructed a covariance matrix which describes the brightness temperature differences at equally spaced zenith angles ranging from 0 to 90° with the in situ temperature. After having performed an eigenvector analysis on this covariance matrix a stable solution of the inverse problem is achieved. Other more modern frequently used method in radiometry include neural network inversion and Kalman filtering. A complete work on the most part of possible inversion methods is given in Janssen (1993).

14.5 An angular scanning temperature profile radiometer

A commercial example of an angular scanning temperature profiler radiometer is shown in Fig. 181 and was produced by the Russian scientific company ATTEX in cooperation with the Dutch company Kipp & Zonen: a polar regions version of the radiometer was realized in 2001 with improved vertical resolution and was called MTP-5P (P stands for polar). The MTP-5P has a microwave radiometer with the center frequency at about 60 GHz which measures the radio brightness temperature of the atmosphere with a high sensitivity (0.04 K at 1 s of integration time) at different discrete elevation angles. On the base of this discrete measurement, it is always possible to retrieve the discrete atmospheric temperature profile from the ground level around 5 m until to 600 m (instrument's intrinsic superior limit) with an accuracy 0.5 K at a vertical resolution at lower quotas of 10–20 m. The MTP-5P's electronics and parabolic antenna – beam aperture width of 0.5degrees – are housed into a thermostatic trailer (see Figure 182) whose temperature is controlled to within 5 K: over a year's time, the internal radiometer's receiver temperature should vary by less than 1 K.

Figure 181: Meteorological temperature profiler (polar version) MTP- 5P

Internal calibration of the instrument is achieved by sequentially switching between the antenna and a reference blackbody's radiation source (as a current controlled resistive dummy). The complete radiometer's technical specifications are reported in Table 20.

The brightness temperature data $T_b(\theta)$ for an angular scanning, MTP-5 radiometer has the previous integral form of Eq. (347) where atmospheric molecular oxygen absorption coefficient in weighted function $W^{\nu_0}(z,\theta)$ was calculated from Rosenkranz (1992) and upper limit of integration is $H = 1$ km. The statistical a priori database used for the setting up of the inversion process was a 2-year dataset of radiosonde's temperature profiles data from Russian upper air station network. In normal operation temperature profiles $T(z)$ are typically provided every 3 min.

Calibration factors require infrequent updating, perhaps once a year. External calibration

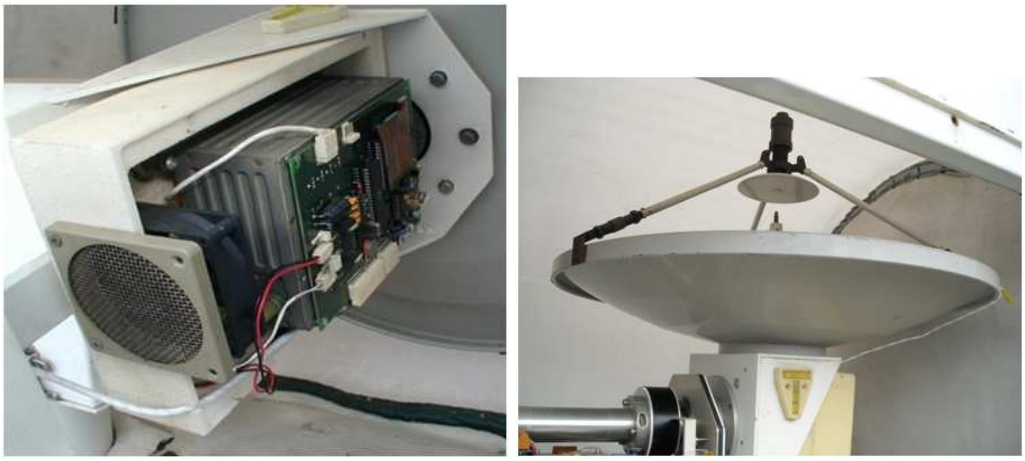

Figure 182: (MTP5 radiometer - microwave receiver assembly (for courtesy concession of ISAC CNR, Rome, Italy

Table 20: MTP-5P Technical Specifications

Parameter	Value/characteristic
Microwave (passive) radiometer	Single frequency angular scanning
Altitude range [m]	0–600
Altitude resolution [m]:	
$0 < H < 50$	10
$75 < H < 100$	25
$100 < H < 600$	50
Accuracy of temperature profile [K or °C]	0.5
Central measurement frequency [GHz]	60.4
Antenna bean width (at 3dB) [deg.]	0.5
Receiver sensitivity [K]	0.04
Integration time [s]	1
Measurement cycle [s]	300 (minimum)
Operational temperature [°C]	-50–40
Calibration	Self calibrating (internal and external sources)
Dimensions [mm]	$900 \times 900 \times 870$

procedures is necessary only in a long period maintenance's intervention and require a "tipping curves" (i.e. steering the antenna off-zenith by rotating the flat reflector to observe emission from a note source in a horizontal path) and/or radiative transfer calculations based on in situ comparison measurements (Figure 183).

14.6 Antarctica Dome C experimental site Radiometric measurements

In November 2002 a such MTP-5P radiometer was installed at the French-Italian Antarctic plateau station of Dome C (75°06'04" S, 123°20'52" E, altitude 3233 m) (Figure 183). The temperature profile measurements were provided from November 18 to December 17, 2002. The outside ground-based temperature range was -23.4°C– -45.7°C during the measurement period. The MTP-5P was installed at a height of 5 m above the Dome C surface and was in normal operational mode for all the period. Between November 18 and December 9 the data from the MTP-5P external in-situ temperature sensor were used for calibration. For the period December 9 to December 17 the data from the temperature sensor of a local me-

Figure 183: A recent maintenance intervention at the MTP5 radiometer – a microwave source for scanning angle's alignment – (F. Scanzani © 2009 by kind permission of ISCAC CNR Rome, Italy))

teorological station were used. Because of the strong influence of the radiation heating during the summer a shade-screen was installed in the near proximity of the instrument (Argentini et al., 2006).

One of the advantages of the MPT-5P is its continuity in acquiring data under all meteorological conditions, which allows to obtain time series and time-height cross sections of temperature. The MTP-5P recorded continuous measurements of the atmospheric boundary layer temperature profiles above the Antarctic plateau for the first time and made possible to calculate some parameters of the temperature inversion such as the height of elevated inversion base, the inversion depth and temperature difference across the inversion.

Referring to Figure 184, as an example, the temperature time series between 0 and 240 m for 12 December 2002 at Dome C. The lower surface temperature is reached at 06:30 Local Time (LT). From 01:00 until 10:00 LT inversion conditions prevail, with a stronger inversion at 07:00 LT. Between 09:30 and 11:00 LT neutral conditions are observed in the transition between the stable and the convective boundary layer. A narrow convective boundary layer is observed between 10:30 LT and 17:00 LT. Inversion conditions are present after this moment. Figure 185 shows the temperature profile during stable (a) and (b), neutral (c), and unstable (d) thermal conditions for the same day. The lapse rate at 06:30 LT (Figure 185(b)) is about 2.5°C/100 m. In Figure 186 the temperature behavior (top part of the figure) and the temperature cross section (bottom figure) during all field experiment are given (Argentini et al., 2006).

14.7 Summary

This chapter presents a general overview of physical fundamentals, measurement techniques and temperature profile retrieval methodology supported by a ground based microwave radiometry to derive meteorological temperature profiles. As case study is presented of a single channel multi angular scanning radiometer developed by Attex and Kipp&Zonen on request of the Italian ISAC CNR for the measure of the temperature profile in Antarctica.

From the concept of an ideal black body and Kickoff's law, it is known that the emission from a black body depends on its temperature and that the higher the temperature of the

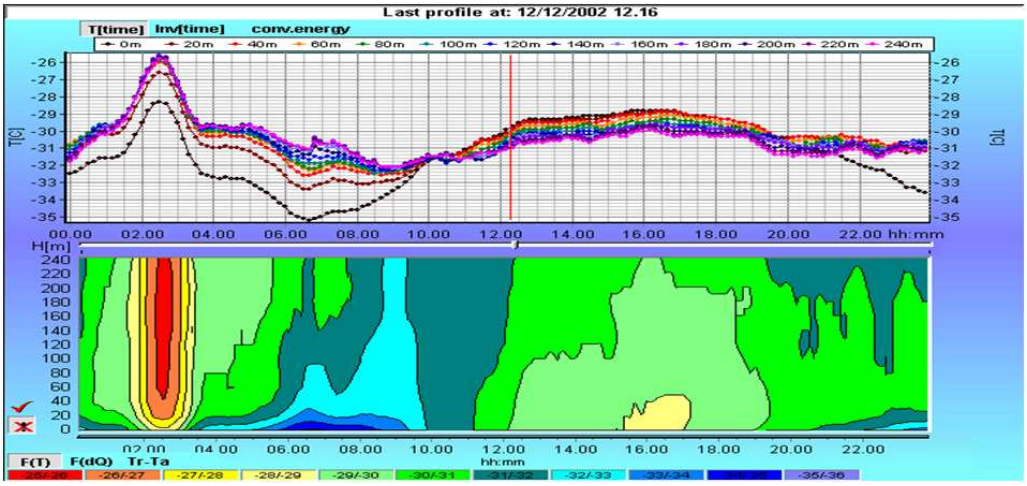

Figure 184: Temperature behaviour (top figure) and temperature cross section (bottom figure) during 12 December 2002

body, the more is its emission. The microwave energy emitted by the atmosphere, reflected from the surface, emitted from the surface, or transmitted from the subsurface can be recorded by a passive sensor a microwave radiometer.

In principle, temperature can be measured at any wavelength of the electromagnetic spectrum. Microwave radiometers measure brightness temperature whose values and variations at different frequencies can correlated with some atmosphere parameters. The atmosphere contains gaseous molecules, liquid and ice cloud particles. Microwave radiation from the atmosphere mostly is due to the absorption and scattering of gaseous molecules of molecular oxygen. For a well-mixed gas such as molecular oxygen, whose fractional concentration is independent of altitude below 80 km and the radiation contains information primarily on atmospheric temperature. In the case of atmospheric temperature profiling, advantage is taken of several properties of oxygen molecules, which comprise 23% of the mass of the Earth.s atmosphere. Moreover, molecular oxygen molecules radiate (and absorb) at a number of discrete frequencies between 50 and 70 GHz. These spectral lines are a consequence of rules of quantum mechanics which only allow oxygen molecules to have particular rotational energy states. Furthermore, since the oxygen molecules are in thermodynamic equilibrium with the local environment, this means that if we can measure the strength of the thermal emission from the oxygen molecules, then we can deduce the physical temperature of the molecules that produced this emission. The oxygen absorption is strong enough that the effective distance that emission is seen is of the order of a few kilometers, depending on the frequency.

Radiometer measurements are inexpensive compared to the cost of remote sensing system, and it can provide all-time observations in both cloudy and clear air situations. However, using radiometer measurements can have specific difficulties:

- the measured brightness temperature is proportional to cumulative emission from various layers
- both scattering and absorption contribute to the measured radiation, which is governed by an integral - differential Radiative transfer equation
- the relation between brightness temperature and the atmospheric parameters is nonlinear

To take advantage of continued improvements in radiometric techniques, it is important to provide such quality measurements with algorithms to calculate brightness temperature given the state of the atmosphere. Techniques to derive meteorological information from radiation measurements are generally based on numerically solving the radiative transfer equation (Tikhonov and Arsenin, 1977). For mildly nonlinear problems, a perturbation form of the RTE is frequently used as the basis of subsequent iteration. Microwave temperature profiling

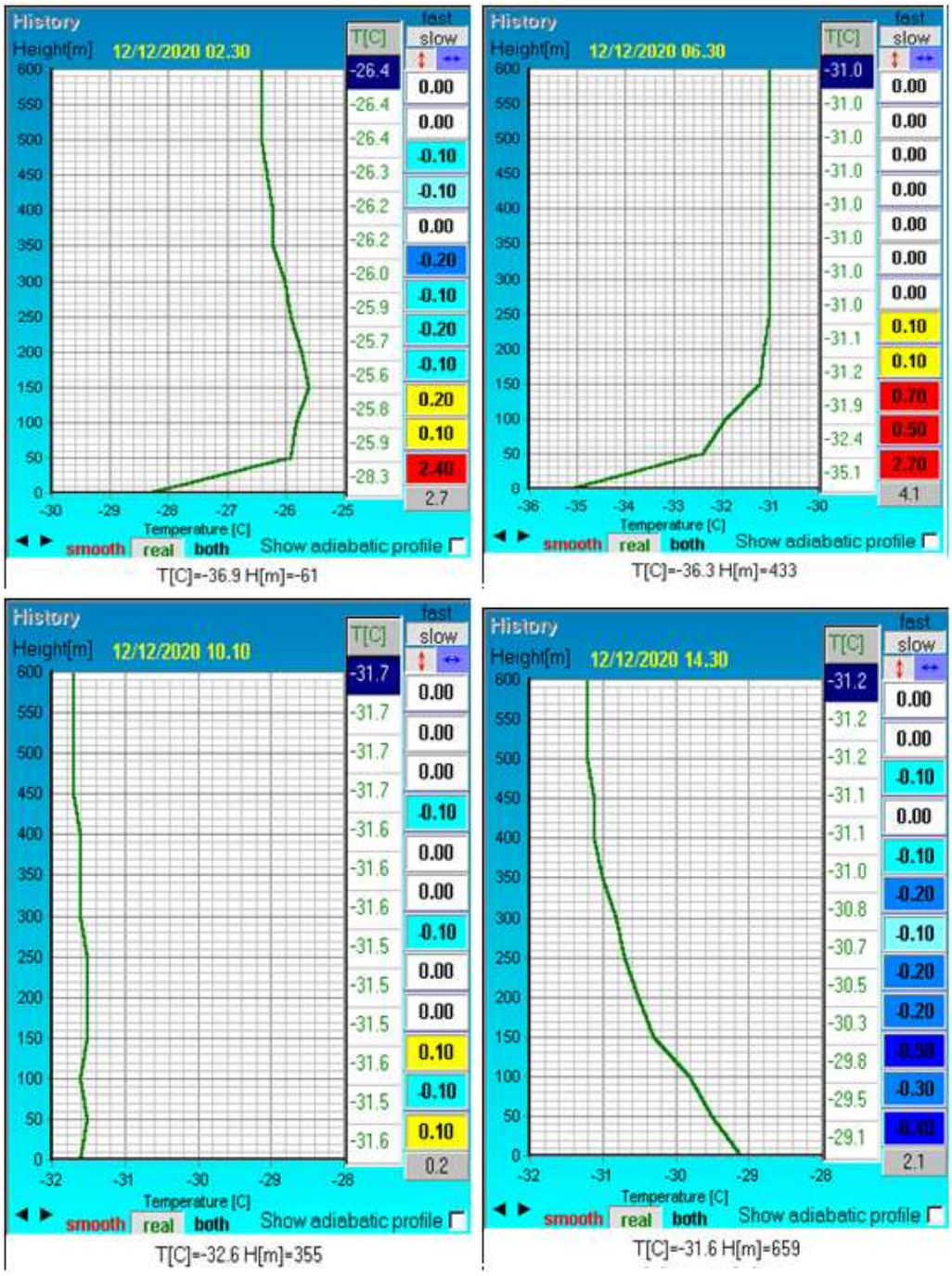

Figure 185: Temperature profiles in the first 250 me. The diurnal evolution of temperature is shown during (a)–(b) stable (c) neutral and (d) unstable conditions. The observation time is given at the top of each graph

radiometers have been designed primarily for downward viewing from a satellite. However, upward-looking instruments can provide useful high-temporal-resolution information about temperature structure at the low troposphere and atmospheric boundary layer.

Two techniques at present are mostly used for microwave temperature profiling. First is a well-known method that uses a zenith-viewing multi channel radiometer with frequencies between 53–58 GHz in the wings of the O_2 absorption band. It can measure temperature profile of the lower troposphere (up to about 5 km) (Troitsky, 1986). For good accuracy it is needed to have additional measurement channels for measurements of water vapor and cloud liquid (usually with channels at the frequencies between 23.8 GHz and 30 or 35 GHz). As

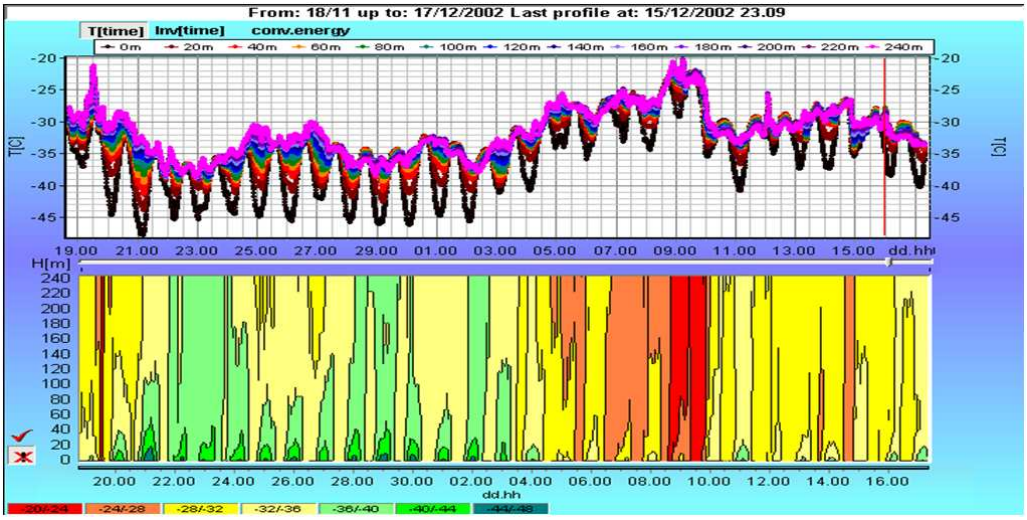

Figure 186: Temperature behaviour (top figure) and temperature cross section (bottom figure) during the all field experiment (18 November 2002 to 15 December 2002)

shown in Fig. 185, multi channel method without scanning had a low vertical resolution at the lowest part of the ABL (about 300 m).

The second method (our discussed case study) is based on using an angular-scanning single-channel radiometer with the central frequency of 60 GHz. This method and the instrument were proposed by Troitsky et al. (1993) and discussed in detail by Kadygrov and Pick (1998) and Westwater et al. (1999).

Due to the large atmospheric absorption by molecular oxygen at 60 GHz, angular-scanning method has some advantages for ABL temperature profiling over the multi channel method (Kadygrov et al., 2004a), which can be summarized as follows:

- it can really to operate in all weather conditions: the measurements do not depends on changes of water vapor density or on the presence of fog or low clouds
- better vertical resolution in the lower 300 m
- the bandwidth of the receiver is very wide which provides a high sensitivity of the receiver (about 0.04 K at 1 s integration time);
- instrument has a small sizes, is very portable, can provide reliable automated continuous profiling from a variety of sites and relatively small cost

However single-channel angular-scanning method, how we have seen, has its limitations in altitude measurement. It can measures only from the ground level up to 1000 m.

Notation

A_ν	fraction of incident energy absorbed from a direction
$B_\nu(T)$	brightness
c	vacuum speed of light
dI_ν	variation of specific intensity
ds	elementary segment in the direction of propagation
$d\Omega$	solid angle element
h	Planck's constant
	altitude
H_b	boundary-layer height
I_ν	specific intensity
k	Boltzmann's constant
MPM	microwave propagation model
RTE	radiative transfer equation

s	point in space
$S_\nu(s)$	local contributive source term at point s
T	temperature
T_{AP}	apparent temperature
$T_b(s)$	Brightness temperature
$W(\nu, z, \theta)$	temperature weighting function
z	layer level in the atmosphere
$\alpha_\nu(s)$	local absorption coefficient
θ	angle off zenith axis of the radiometer's beam
ν	frequency
$\tau_\nu(s)$	optical depth

References

Argentini S., Dargaud G., Pietroni I., Viola A., Mastrantonio G., Conidi A., Petenko I., and Pellegrini A. (2006) Behaviour of the temperature and inversion layer depth and strength at Dome C Antartica during the 2004–2006 field experiment. *Proc. of the 13th International symp. for the advancement of Bound.-layer Remote Sens.*, Garmish-Partenkirchen

Askne J. I. H., and Westwater E. R. (1986) A review of ground-based remote sensing of temperature and moisture by passive microwave radiometry. *IEEE Trans. Geosci. Remote Sens.* **24**:340–352

Hewison T. J., Cimini D., Martin L., Gaffard C., and Nash J. (2006) Validating clear air absorption model using ground-based microwave radiometers and vice-versa. *Meteorol. Z.* **15**:27–36

Kadygrov E. and Pick D. R. (1998) The potential for temperature retrieval from an angular-scanning single-channel microwave radiometer and some comparison with in situ observations. *Meteorol. Appl.* **5**:393–404

Kadygrov E., Koldaev A. V., Viazankin A. S., Argentini S., Viola A., and Mastrantonio G. (2004) First experience in monitoring the Temperature Profile over the Antarctic Plateau. Specialist meeting on Microwave Radiometry and Remote Sensing Application, Rome

Kadygrov E., Khaikin M., Miller E., Shaposhnikov A., and Troitsky A. (2004) Advanced atmospheric boundary layer temperature profiling with MTP-5HE microwave system. CAO Moskow region Russia

Janssen M. A. (1993) An introduction to the passive microwave remote sensing of atmospheres. In: Atmospheric Remote Sensing by Microwave Radiometry. Wiley, Interscience

Hogg D. C., Decker M. T., Guirand F. O., Eamshaw K. B., Merrit D. A., Moran K. P., Sweezy W. B., Stranch R. G., Westwater E. R., and Little C. G. (1983) An automatic profiler of the temperature, wind and humidity in the troposphere. *J. Clim. Appl. Meteorol.* **22**:807–831

Naumov A. P., Osharina N. N., and Trotsky A. V. (1999) Ground based microwave thermal sounding of the atmosphere *Radiophys. Quantum Elec.* **42**(1)

Rosenkranz P. W. (1992) Absorption of microwave by atmospheric gases. Atmospheric remote sensing by microwave radiometry, M. Janssen (ed). Wiley, Interscience

Troitsky A. V. (1986) Remote definition of the atmosphere temperature from spectral radiometric measurements in the line $\lambda = 5$ mm. *Izv. Vuzov Radiophysics* **XXIX**:878–886

Troitsky A. V., Gajkovich K. P., Gromov V. D., Kadygrov E. N., and Kosov A. S. (1993) Thermal sounding of the atmospheric boundary layer in the oxygen absorption band center at 60 GHz. *IEEE Trans. Geosci. Remote Sens.* **31**:116–120

Tikhonov A. N. and Arsenin V. Y. (1977) Solutions of III - Posed Problems. V. H. Winston and Sons, Washington

Turchin V. F. (1967) *J. Calc. Math. Mathematical Phys.* **102**, N3:In Russian

Ulaby F. T., Moore R. K., and Fung A. K. (1986) Microwave Remote Sensing: Active and Passive, from Theory to Applications - Vol III, chap 17-1.2

Westwater E. R. (1993) Ground-based microwave remote sensing of meteorological variables, Chapter 4 in atmospheric remote sensing by microwave radiometry, Janssen M. (ed). John Wiley & Sons, 145–213

Westwater E. R., Han Y., Irisov V. G., Ye V., Leuskiy V., Yu G., Trokhimovski G., Fairall C. W., and Yessup A. T. (1998) Air-sea and boundary-layer temperatures measured by a scanning 60-Ghz radiometer. Recent results. *Radio Sci.* **33**:291–302

Westwater E. R., Han Y., Irisov V. G., Leuskiy V., Kadygrov E. N., and Viazankin S. A. (1999) Remote sensing of boundary layer temperature profiles by a scanning 5-mm microwave radiometer and RASS: comparison experiments. *J. Atmos. Ocean. Tech.* **16**:805–818

15 SAR for wind energy

Charlotte B. Hasager and Merete Badger
DTU Wind Energy, Risø Campus, Roskilde, Denmark

15.1 Introduction

Satellite Synthetic Aperture Radar (SAR) can provide a wide range of information about the surface of the Earth. SAR instruments have been flown on several satellite platforms since the early 1990s. One of the purposes of the satellite SARs is research. The successful investigations have led to a variety of (near-) operational products including sea ice mapping, oil spill detection, ship movement, mapping of flooded land surfaces, earth quake, land slide and subsidence mapping, digital elevation mapping, urban development, vegetation and biomass changes, glacier coverage, ocean wave and ocean current information, and last but not least ocean surface wind mapping.

One advantage of SAR compared to optical remote sensing is that the radar carries its own illumination source, and is thus independent of daylight. This is particularly useful near the Arctic and Antarctic where daylight is limited for several months per year. SAR operates in the microwave bands. Microwave radiation is able to penetrate clouds and precipitation. SARs are all-weather instruments and so not limited by cloud cover. This is particularly useful in cloudy and rainy scenarios including hurricanes.

Ocean surface wind mapping from SAR has been described in numerous articles. A recent state-of-the-art white-paper on 'Wind retrieval from Synthetic Aperture Radar - an overview' from the SEASAR 2012 workshop 'Advances in SAR Oceanography' by the European Space Agency (ESA) (Dagestad et al., 2013) summarizes the technical fundamentals of satellite SAR ocean surface wind retrieval. A wide range of applications are also presented including ocean wind mapping for weather prediction, wind farming, tropical cyclones, polar lows, katabatic winds, gap winds, vortex streets, boundary layer rolls and atmospheric gravity waves. See this paper for references (157 in total).

SAR measurements are high-resolution observations of the Earth surface. Although no SAR sensor has been designed specifically for wind mapping, it has become clear that SAR data is very suitable for high-resolution wind retrievals over the ocean including near-shore areas. The spatial resolution of SAR makes it particularly useful for resolving mesoscale wind variability.

Planning of offshore wind farms has emphasized the need for reliable ocean wind observations. Ocean wind observations are generally costly to obtain from meteorological masts or ground-based remote sensing instruments. Furthermore, such data is only valid near the local point at which it is measured. In contrast, satellite SAR can provide spatially resolved ocean wind information. Most potential offshore wind farm sites are covered by archived SAR data. Wind resource mapping can thus be performed without any delay whereas it takes time to plan and conduct a ground based observational campaign.

15.2 SAR technical description

SAR is an active microwave sensor which transmits coherent microwaves. The images showing the normalized radar cross section (NRCS) are made from advanced signal processing of the original observations. NRCS is the recorded backscattered signal per unit area. The microwaves transmitted and received are either vertically (V) or horizontally (H) polarized. Co-polarized (VV or HH) images are made if the same polarization is used for both transmitting and receiving. Cross-polarized (VH or HV) images are made otherwise.

The co-polarized NRCS has traditionally been used for ocean surface wind retrieval at spatial pixel scales finer than 1 km. Cross-polarized NRCS has been tested for wind retrieval.

Also the Doppler Centroid anomaly can be used for wind retrieval. This method is particularly of interest for investigation of wind direction. This chapter focuses on wind retrieval from co-polarized SAR data (hereinafter co-pol).

The microwave wavelength in SAR ranges from around 2.5 to 30.0 cm. According to the standard radar frequency letter-band nomenclature (IEEE standard 521-1984), the X band wavelength band is $2.5 - 3.8$ cm ($8 - 12$ GHz), C band $3.8 - 7.5$ cm ($4 - 8$ GHz), S band $7.5 - 15.0$ cm ($2 - 4$GHz) and L band $15.0 - 30.0$ cm ($1 - 2$ GHz). In brackets is given the frequency bands.

Recent satellite SARs are listed in Table 1. Updated information is available at `http://database.eohandbook.com`. Long prior to the SARs listed in Table 1 the L-band SEASAT SAR was flown for three months in 1978. All SAR sensors provide co-pol NRCS data either VV and/or HH. Several SAR can provide selected cross-pol data or quad-pol (co-and cross pol together) data.

SAR	Agency / country	Operational	Radar band	Swath width (max)	No.
ERS-1	ESA	1991-2000	C	100 km	1
JERS-1	JAXA, Japan	1992-1998	L	75 km	1
ERS-2	ESA	1995-2011	C	100 km	1
RADARSAT-1	CSA, MDA, Canada	1995-2013	C	500 km	1
Envisat ASAR	ESA	2002-2012	C	420 km	1
ALOS / PALSAR	JAXA, Japan	2006-2011	L	350 km	2
RADARSAT-2	CSA, MDA, Canada	2007-	C	500 km	1
COSMO-SkyMed	ASI, Italy	2007-	X	200 km	4
TerraSAR-X					
TanDEM-X	DLR, Germany	2007-	X	100 km	1
HJ-1C	CAST, China	(2012-)	S	100 km	1
Sentinel-1	ESA	(2014-)	C	400 km	2
RCM	CSA	(2018-)	C	500 km	3

Table 22: Satellite SAR (adapted from Dagestad et al., 2013). The number of satellites is mentioned.

All SAR and scatterometer are on-board sun-synchronous polar orbiting satellites. The SAR image is not projected to a geographical coordinate system, is not calibrated, and the incidence angle dependence must be accounted for. The maximum swath width (see Table **??**) is determined from the radar band and incident angles. The incident angles for satellite SAR vary between sensors. The widest range is from 8 to 60 degrees for ALOS PALSAR. Other SARs are within this range. The Envisat ASAR Wide Swath Mode (WSM) and Radarsat-1/2 ScanSAR mode provide the maximum swaths of 420 to 500 km, with spatial resolutions of 100 m and 75 m, respectively. The capacity of the SAR processing facilities allows RADARSAT data to be made available for users in near-real-time; the same was true for Envisat. RADARSAT images can typically be downloaded via internet archives $1 - 3$ hours after the data acquisition. This opportunity has opened up for operational SAR-based wind mapping. Sentinel-1 and Radarsat Constellation Mission (RCM) will be future operational satellites.

From most SARs it is possible to order different products with different swath widths. From Envisat and RADARSAT a large suite of types of data are available. For the very high resolution products, the swath is narrow. For the wide swath mode products, the spatial resolution is lower. Thus there is a trade-off selecting either wide swath mode, i.e. more frequent coverage and large regions covered, versus high-resolution mode, i.e. finer spatial details but for smaller regions and less frequently.

Before introducing wind retrieval from SAR it is adequate to introduce satellite scatterometry. Scatterometers are also radar instruments observing in microwave bands. The scatterometers ERS-1/2 (ESA) and ASCAT-1/2 on-board the METOP-A and METOP-B satellites (EUMETSAT) are C-band while the scatterometer SeaWinds on-board the QuikSCAT satellite (NASA) and the scatterometer OSCAT on-board the OCEANSAT-2 satellite (ISRO) are Ku band $1.7 - 2.5$ cm ($12 - 18$ GHz). Scatterometers are purpose-built for operational ocean surface wind vector observations. Scatterometers have multiple antennae or disk antenna and observe each cell from different viewing angles. All scatterometers operate in VV. For wind retrieval, VV is preferred as the VV signals are stronger than HH. The spatial resolution of

the ocean surface wind vectors varies from 12.5 km, 25 km to 50 km. It may be noted that the swath of scatterometers is wide and this results in frequent coverage. QuikSCAT and OSCAT have swaths around 1800 km and ASCAT has two 500 km swaths. Near-global coverage is achieved twice per day for QuikSCAT and OSCAT and once per day for ASCAT-1/2 combined. For details see Karagali 2013.

15.3 Wind retrieval from SAR

NRCS is the observed quantity of a SAR. NRCS depends on the size and geometry of roughness elements on the scale of the radar wavelength at the Earth's surface (Figure 187-left). Over a calm ocean surface, the returned NRCS is limited because radar pulses are reflected away from the SAR at an angle equal to the angle of incidence. As the wind picks up, roughness in the form of capillary and short-gravity waves is generated by the surface wind stress. The dominant scattering mechanism is then diffuse and known as Bragg scattering (resonance scattering). The Bragg waves ride on longer-period waves (Valenzuela, 1978). Equation 348 gives the simple relationship between the wavelength of Bragg waves and radar wavelength:

$$\lambda_{Bragg} = \frac{\lambda_{radar}}{2\sin\theta} \tag{348}$$

where λ is the wavelength for Bragg and radar, respectively, and θ is the incidence angle.

The relation of NRCS to the local wind speed and direction, and to the radar viewing geometry forms the key principle in ocean wind retrievals from SAR. High-frequency radars (X- or Ku-band) are generally the most sensitive to small-scale waves generated by the instantaneous local wind. Lower-frequency SAR sensors (L-band) are more sensitive to longer-period surface waves that, because of their longer growth time are not so sensitive to local wind fluctuations.

SAR sensors operate with a single antenna and view each ground target from one angle only. As a consequence, several wind speed and direction pairs correspond to a given NRCS. The number of possible solutions may be reduced if *a priori* information about the wind direction is used to retrieve the wind speed.

The wind direction may be inferred directly from SAR images using FFT (Gerling, 1986; Lehner et al., 1998; Furevik et al., 2002), wavelet (Fichaux & Ranchin, 2002; Du et al., 2002) or gradient methods (Horstmann et al., 2000; 2003; Koch, 2004). The methods outline the orientation of km-scale wind streaks visible in many SAR images. These wind streaks are aligned approximately with the wind direction. The streaks originate from atmospheric roll vortices and other phenomena impacting the sea surface. However, the wind direction methods do not always produce reliable results. In addition the 180° ambiguity has to be resolved. In other words, the methods may resolve the orientation of linear features "the wind streaks" in the SAR images but none of the methods can identify the direction of the wind along the orientation lines. If the SAR image includes a coastline, the shadow effect from land may be visible, hence revealing the wind direction. Recent work on using the Doppler Centroid anomaly for more accurate wind direction retrieval is promising but not yet applicable for all SAR data (Mouche et al., 2013).

Reverting to external sources of information on wind direction, one option is wind direction from scatterometry. The method requires nearly simultaneous overpasses of a SAR and scatterometer, which becomes more practical with increasing latitudes (Monaldo et al., 2004; He et al., 2005).

For operational near real-time processing of SAR scenes into wind maps, the most frequently used external source is *a priori* wind direction from atmospheric models such as ECMWF (European Centre for Medium-range Weather Forecasting), NOGAPS (Navy Operational Global Atmospheric Prediction System), WRF (Weather Research and Forecasting) or similar.

At offshore sites with high-quality meteorological data, the locally observed wind direction has been tested for use as an input. The wind speeds were retrieved with a standard deviation error as low as ± 1.1 ms^{-1} (Hasager et al., 2004; Hasager et al., 2005; Hasager et al., 2006;

Christiansen et al., 2006). The results are only valid near the meteorological mast as wind direction cannot be assumed constant for a region.

In the case of ERS-1/2 it was possible to operate the radar in two modes: either scatterometer or SAR. When set in scatterometer mode the radar recorded from three antennae but when set in SAR mode the radar recorded from one antenna. Viewing of a given point at the surface from several different incidence and/or aspect angles allowed for unambiguous estimates of the wind speed and direction from a set of NRCS values at different aspect angles from the scatterometer. The Geophysical Model Functions (GMFs) were empirically developed to establish the wind-vector-to-backscatter relationship for the C-band scatterometer data (e.g. Stoffelen and Anderson, 1997).

The scatterometer model functions have later been proven to be suitable for SAR wind retrievals as well.

Figure 187 (right) shows the relationship between four GMFs for C-band VV for upwind and crosswind. The upwind and crosswind directions are defined from the SAR viewing geometry: the radar look angle difference to the prevailing wind direction. The GMFs are similar for upwind and downwind geometry but different for other angles with a minimum for crosswind. In other words, the GMFs are more sensitive to the NRCS for the upwind/downwind geometry than for the crosswind geometry. The signals are also weaker for crosswind.

The GMF for C-band SAR wind retrieval at low to moderate wind speeds CMOD4 is valid for wind speeds of $2-24$ ms^{-1} (Stoffelen & Anderson, 1997). For higher wind speeds CMOD-IFR2 (Quilfen et al., 1998) and CMOD5 (Hersbach et al., 2007) are typically used and are valid for wind speeds of $2-36$ ms^{-1}. CMOD4, CMOD5 and CMOD-IFR2 all have a nominal accuracy of ± 2ms^{-1}.

Generally, the empirical GMFs take the following form

$$\sigma^0 = U^{\gamma(\theta)} A(\theta) \left[1 + B(\theta, U) \cos\phi + C(\theta, U) \cos 2\phi\right] \tag{349}$$

where σ^0 is the normalized radar cross section (NRCS), U is wind speed at a height of 10 m for a neutrally-stratified atmosphere, θ is the local incident angle, and ϕ is the wind direction with respect to the radar look direction. The coefficients A, B, C and γ are functions of wind speed and the local incidence angle.

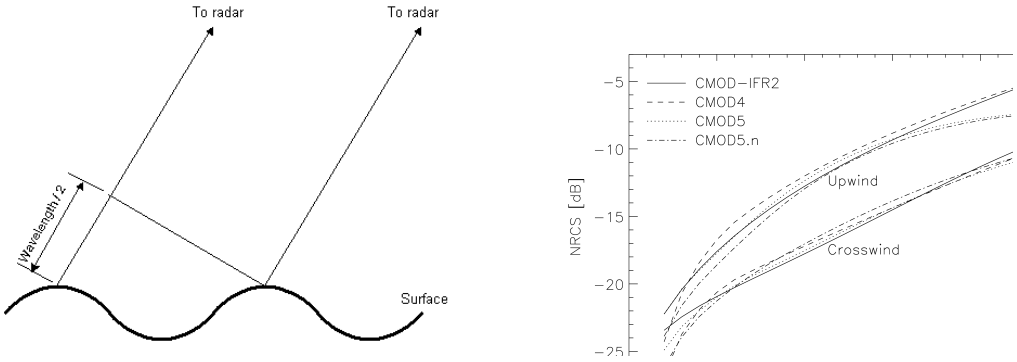

Figure 187: Left: Surface wave and microwave wavelength for radar. Right: Relationship between Normalized Radar Cross Section (NRCS) and wind speed for upwind and crosswind for three Geophysical Model Functions CMOD-IFR2, CMOD4 and CMOD5 for a given incidence angle.

The physical relationship between NRCS and the wind stress (friction velocity) is physically more direct than to the 10 m wind, hence friction velocity may empirically fit better to NRCS than 10 m wind. Most users, however, favour 10 m wind speed. Physical models describing the relationship between NRCS, the 2D wave spectrum, and the scattering mechanisms are complicated (Romeiser et al., 1997a; 1997b; Kudryavtsev et al., 2003). As a matter of fact, the empirical GMFs are so far best suited for wind retrieval.

The empirical model functions rely on the assumption that wind speed increases logarithmically with height above the sea surface. This is normally true if the atmospheric boundary layer is neutrally stratified. Stable stratification would typically lead to an underestimation and unstable stratification to an overestimation of the 10 m wind speed. Deviations from the logarithmic wind profile are mostly found in near-shore areas where the atmospheric boundary layer may be influenced by the land. GMFs can thus be expected to perform better over the open ocean than in near-shore areas.

The CMOD4 and CMOD5 were tuned empirically using co-located observations of NRSC and (mainly) ECMWF ocean wind vectors. On average the atmospheric stability of the marine boundary layer is not neutral. Therefore, to provide neutral 10 m wind retrieval CMOD5.N was developed (Hersbach, 2010). The differences of CMOD5 and CMOD5.N include the average stability correction of 0.2 ms^{-1} and the addition of 0.5 ms^{-1} to compensate for the negative bias of CMOD5.

In summary, the C-band GMFs conveniently available from scatterometry are suitable for wind retrieval from SAR VV data. The largest uncertainty is related to the necessary *a priori* wind direction input.

15.4 Beyond C-band VV

RADARSAT-1 only collects C-band HH data. There is no GMF from scatterometry for HH. It is therefore relevant to use C-band VV GMF with an additional function. This function is the so-called Polarization Ratio (PR) that relates the NRCS of HH to NRCS of VV as a function of radar incident angle. The HH should basically be translated to VV through this function. The first suggested relationship includes a coefficient (α) the value of which ranges from around 0.6 to 1.0 (Elfouhaily, 1997; Thompson et al., 1998; Vachon & Dobson, 2000). Later work has shown that PR is also a function of wind speed and direction (Mouche et al., 2005; Zhang et al., 2011).

SEASAT, JERS-1 and ALOS PALSAR collect L-band data. Based on JERS-1 and local wind data and based on ALOS PALSAR and observed scatterometer wind vectors, two L-band GMFs for HH are established (Shimada et al., 2004; Isoguchi and Shimada, 2009). The L-band GMFs appear less sensitive to moderate winds than C-band GMF. L-band could be advantageous for wind speeds larger than 20 ms^{-1} as L-band may not saturate for the high wind speeds as C- and X-band do.

TerraSAR-X, TanDEM-X and COSMO-SkyMed collect X-band data. Based on TerraSAR-X and in-situ buoy data the X-band GMF XMOD2 is established (Ren et al., 2012). The data set is sparse. Another XMOD function was developed by interpolating the well-known coefficients at two neighbouring bands from the C-band and Ku-band GMFs (Thompson et al., 2012).

Research on new GMFs for X-, C- and L-band can be based on quad-pol data from COSMO-SkyMed, RADARSAT2 and ALOS PALSAR, respectively. To establish and verify a new GMF requires many co-located samples covering a broad variety of wind conditions. Cross-pol data has a higher noise floor than co-pol data, thus cross-pol data cannot map low wind speeds. One advantage of cross-pol data for wind retrieval is that the GMF does not depend upon wind direction and moderate to high wind speeds may be mapped and be useful for observing hurricanes (Zhang and Perrie, 2012).

15.5 Current practices in SAR wind retrieval

SAR data is usually distributed as raw data (Level 1). The user has to calibrate the SAR data with (updated) calibration coefficients provided with the SAR product or separately. The calibration error should not exceed 0.5 dB. SAR images are not projected to a geographical coordinate system and the user has to do this. The correction for incidence angle across the swath also has to be made by the user. It is usual to block-average several SAR cells to pixels sizes around 500 m or more before wind retrieval. The block-averaging (multi-look) is done to

reduce speckle noise, a random noise in SAR data, and reduce effects of longer-period ocean waves.

It is possible to use the NEST open source toolbox from ESA (`nest.array.ca`) for calibration and geo-coding. NEST may also be used for wind retrieval, yet without many options. The commercial software SARTool from CLS offers various options for wind retrieval. It is used operationally by KSAT, EDISOFT and CLS at VIGISAT (`www.vigisat.eu`) to process data into wind fields in near real time. These data can be viewed on EODA GIS technology based web portal (`eoda.cls.fr`) with various examples on SAR applications. At Johns Hopkins University, Applied Physics Laboratory (JHU APL), the APL/NOAA SAR Wind Retrieval System (ANSWRS) wind retrieval software was developed. It is implemented at NOAA (National Oceanic and Atmospheric Administration), the Alaska SAR facility and DTU Wind Energy. Both SARTool and ANSWRS provide near real-time (NRT) SAR wind retrieval facility. In SARTool the ECMWF wind directions typically are used *a priori* while in the ANSWRS the NOGAPS wind directions are used *a priori*. It is possible to use other wind direction input in both.

Wind retrieval is only possible over open water such as ocean and large lakes. It is necessary to mask out land and sea ice before wind inversion. Hard targets such as large ships, oil and gas rigs, wind turbines, long bridges and other structures in the ocean should ideally also be masked out. This is not implemented yet but work is on-going to provide this (A. Mouche `pers.com`). Until then these hard targets contribute noise to the wind retrieval and may result in spurious high wind observations.

Another important issue to consider is the ocean surface. To first order the ocean surface can be described as modulated by the surface wind. However, looking into greater detail a wide range of phenomena influences the sea surface and hence the radar backscatter. Obviously, oil spill and oil slicks that are operationally monitored from SAR are visible. Ocean surface surfactants, oil and algae blooms dampen the radar backscatter resulting in winds which are too low. More complicated is the effect of oceanic processes of currents, fronts, eddies, swell and internal waves. The surface wave spectrum is modulated and generally speaking the NRCS modulation is positive for current convergence and negative for current divergence but also a function of radar frequency, local wind velocity, etc. (see Badger et al., 2008 for references). The use of Doppler Centroid anomaly may reveal some of these phenomena and may in combination with GMF based wind retrieval improve SAR wind retrieval.

Open access to SAR scenes is provided from ESA (`earth.esa.int`). The SAR scenes are stored in a searchable archive and may be accessed as Level 1 data with permission. In the archive many scenes can be inspected visually from Quicklook images. The image frames over a given site have different spatial coverage and orientations. The orbital characteristics reflect whether a particular frame is from a descending or an ascending track and the approximate local overpass time is given from this. At present the user has to perform this digital image processing before wind inversion. It is anticipated that wind fields (Level 2) will become available from Sentinel-1. This will be a major step forward making SAR wind maps more useful for end-users.

SAR retrieved winds have been validated by comparing to observations from meteorological masts, ships, buoys, scatterometer or atmospheric model results. In general, the validation results show a bias less than 0.5 ms^{-1} and standard deviation from 1.2 to 2.0 ms^{-1}. Please see Dagestad et al. 2013 and references herein. The accuracy of collocation, the uncertainty on the in-situ observations and atmospheric model results, and also the time-averaging method have to be considered. The fact is that satellite SAR provides spatial statistics and in-situ data are time-averaged statistics. The hypothesis of frozen turbulence (Taylor's hypothesis) is generally used. It is important to ensure that the spatial and temporal scales are adequate.

The SAR calibration of 0.5 dB gives an uncertainty on wind speed of roughly 0.5 ms^{-1}. As the standard deviation from the validation results is found to be much larger, around two to four times the calibration uncertainty, there is scope for improvement in SAR wind retrieval.

15.6 SAR wind retrieval at DTU Wind Energy

ANSWRS version 2.0 is currently being used for near real-time wind field retrieval at DTU Wind Energy. To meet the requirements of processing in near real-time, the ANSWRS software produces high-resolution (¡1 km) wind speed fields initialized using wind directions determined by the NOGAPS model and interpolated in time and space to match the satellite data. NOGAPS data is available at 6-hour intervals mapped to a 1° latitude/longitude grid. At present, DTU Wind Energy has a collection of around 15,000 Envisat scenes from 2002 to 2012. The study areas include the northern European seas, the coast of Iceland, parts of the coast of Greenland, parts of the Mediterranean Sea, parts of the Atlantic Sea along France, Spain and Portugal, parts of the Indian Ocean near India, parts of the Chinese coast, parts of the Persian Gulf, and Lake Erie among other sites. For most sites our aim was to map wind resources thus many images are retrieved and processed.

Comparison results for ANSWRS using NOGAPS wind directions have for the estimated wind speeds in the Gulf of Alaska and the US East coast yielded agreement with buoy measurements to within ± 1.76 ms^{-1} standard deviation (Monaldo et al., 2001) and with QuikSCAT wind speeds to within ± 1.25 ms^{-1} standard deviation (Monaldo et al., 2004). In the Baltic Sea comparison to in-situ wind speed and direction observed at meteorological masts show a root mean square error of ± 1.17 ms^{-1}, bias of -0.25 ms^{-1}, standard deviation of 1.88 ms^{-1} for wind speed and correlation coefficient of $R^2 = 0.78$. Wind directions compared to mast observations show a root mean square error of 6.3° with a bias of 7.8°, standard deviation of 20.1° and $R^2 = 0.95$ (Hasager et al., 2011a). Comparable results were obtained in the North Sea (Badger et al., 2010a).

15.7 Mesoscale wind phenomena from SAR

The high spatial resolution of SAR allows fine structures in ocean surface winds to be quantified. Each scene is recorded during a few seconds and so the SAR wind field is a snapshot of the conditions at the time of observation. The all-weather and day and night observing capability of SAR allow a great variety of marine atmospheric conditions to be observed across the oceans of the Earth. A few are presented here. More may be found in Badger et al. 2008 and Beal et al. 2005 with descriptions of the meteorological background. SAR wind maps may be viewed online at web-sites:

- `http://fermi.jhuapl.edu/sar/stormwatch/web_wind/` (USA and Canada),
- `http://polarlow.met.no/polar_lows/` (polar lows in the Nordic Seas),
- `http://soprano.cls.fr` (Europe),
- `http://galathea.dtu.dk/google/kmz/images/Wind/?C=M;O=D` (few from the world).

Below we present four selected wind maps from Greenland, Puerto Rico, Iceland and Gibraltar. The Envisat ASAR wind field in Figure 188 is from the east coast of Greenland observed 28 August 2006 at 12:47 UTC. During this time the Danish Galathea-3 circum-global ship expedition took place in the region. The winds were from the north. Katabatic flow is observed from the Kangerdlugssuaq Valley at 68° N, 31° W and penetrating 100 km across the Denmark Strait. The wind speed is around 12 ms^{-1} in the otherwise calm coastal sea. Further offshore a strong flow from the north more than 15 ms^{-1} is found. The frontal gradient is sharp.

The lee effect of the tropical island of Puerto Rico in the Caribbean Sea observed from Envisat ASAR on 16 March 2007 at 02:31 UTC is shown in Figure 189. The winds are moderate 7 to 12 ms^{-1} from the northeast. The lee is longer than 200 km.

On 24 September 2005 at 11:30 UTC the wind was flowing from the northwest in Iceland, see Figure 190. The mountainous island modulates the flow and along the eastern and southern coastline a pattern of lee effects and speed up from valleys is seen.

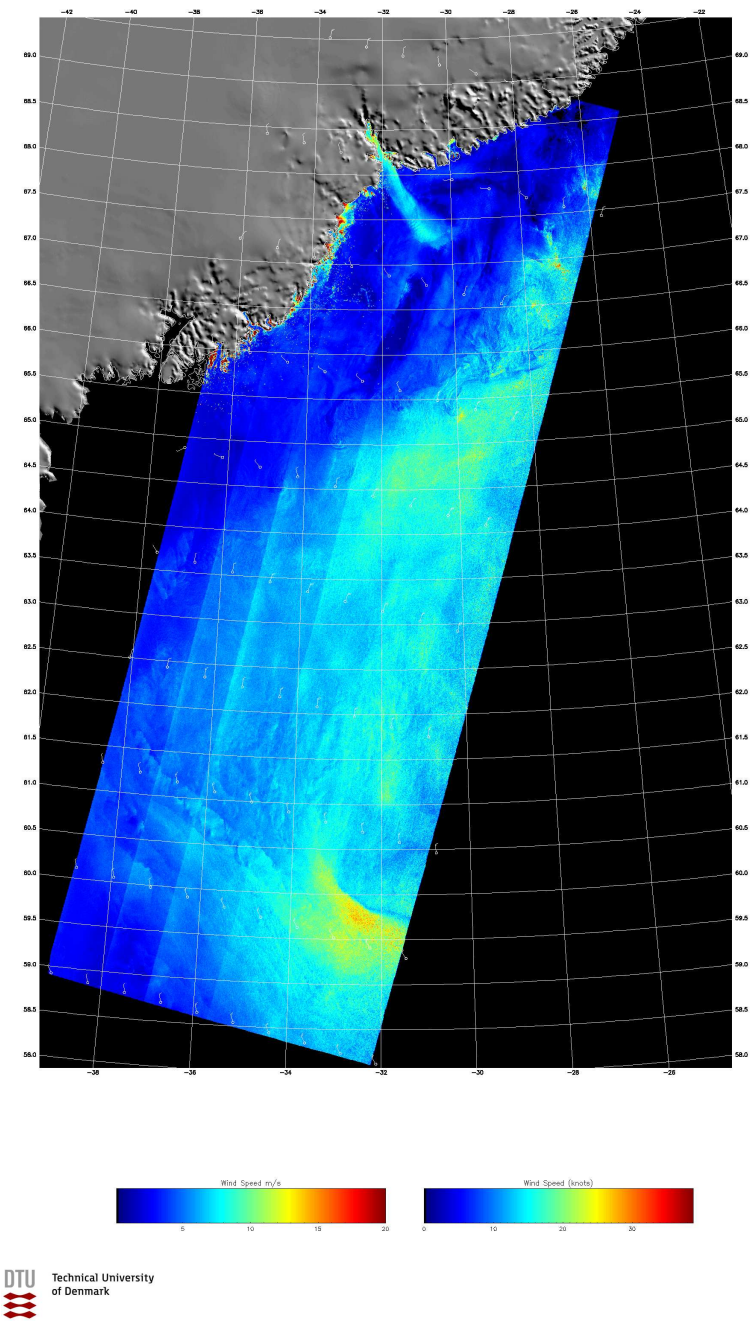

Figure 188: Envisat ASAR wind field from the east coast of Greenland observed 28 August 2006 at 12:47 UTC. Note the katabatic flow around 68° N, 31° W extending around 100 km into the Danish Strait.

Gap flow (acceleration flow) is clear on the Envisat ASAR wind map observed on 20 February 2009 at 22:22 UTC through and behind the Gibraltar Strait. The wind is from the east and the gap flow above 15 ms^{-1} whereas the wind is from 5 to 10 ms^{-1} in the area (Figure 191).

The spectral properties of Envisat ASAR wide swath mode wind fields have been analyzed and compared to the spectral properties of QuikSCAT wind fields for a region in the North Sea. The spatial resolution of SAR was varied from 2 km to 25 km and several resolutions

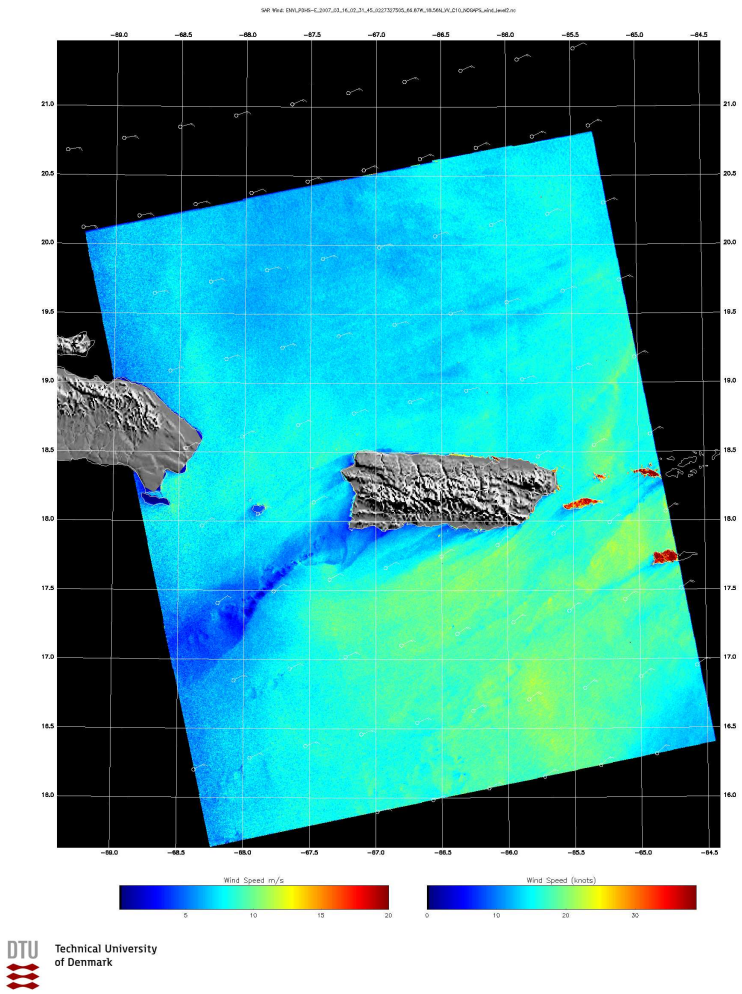

Figure 189: Envisat ASAR wind field from Puerto Rico in the Caribbean Sea observed on 16 March 2007 at 02:31 UTC. The lee effect is longer than 200 km.

between. The spectral analysis showed SAR to be able to resolve spatial details down to 6 km for the 2 km wind fields. The spectral content of SAR at 25 km is, as expected, higher than for QuikSCAT at the same resolution. The analysis indicates that SAR resolves the mesoscale details of marine winds with higher accuracy than scatterometer and mesoscale models (Karagali, 2012).

15.8 SAR wind fields near offshore wind farms

Large offshore wind farms have been constructed and operated since 2000. High-resolution SAR wind fields from ERS-2 and Envisat have been retrieved and analyzed. The data was recorded near the first two large offshore wind farms, Horns Rev-1 and Nysted-1. Also airborne E-SAR C- and L-band co- and cross-pol data from the Horns Rev-1 wind farm has been retrieved and analyzed (Christiansen & Hasager, 2005; 2006). High-resolution SAR wind fields in many cases show the wind farm wake, i.e. an area with reduced winds downwind of the wind farms. The magnitude of the wake near the wind farms was found to be similar to the wake effect predicted by wake models and observed from meteorological masts. More surprisingly the study demonstrated that the wind farm wake may extend as far as 20 km downwind of a large offshore wind farm. This is much further than predicted by current wake models. Therefore the potential power production from wind farms in clusters may be more affected by wakes than is assumed in general.

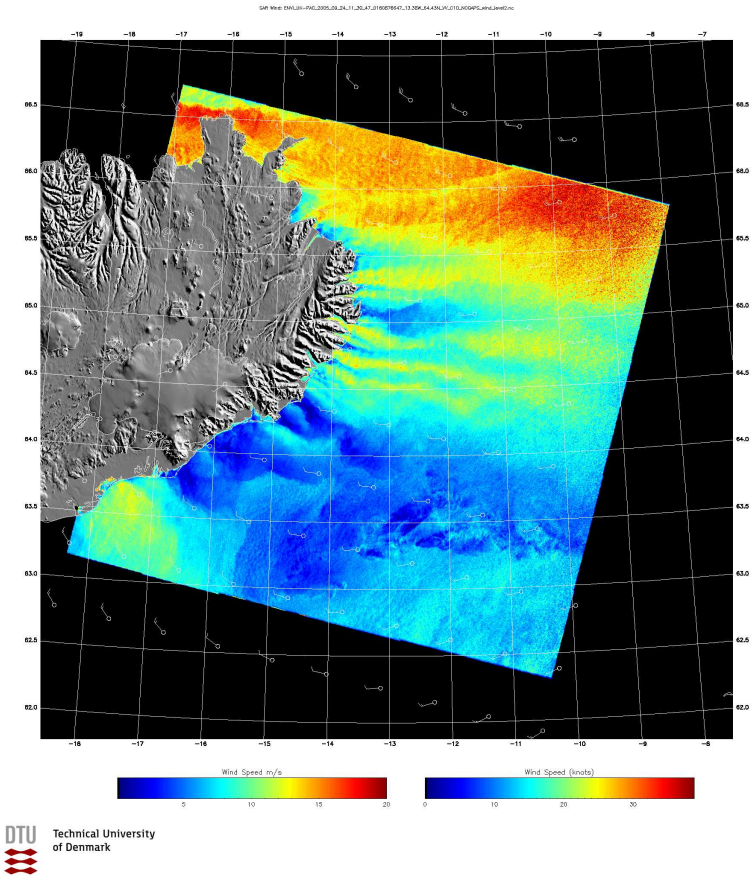

Figure 190: Envisat ASAR wind field from Iceland observed on 24 September 2005 at 11:30 UTC. The wind is flowing from the northwest. Along the eastern and southern coastline a pattern of lee effects and speed up from valleys is seen.

In the on-going FP7 (2012-2015) European Energy Research Alliance Design Tool for Offshore Wind Farm Clusters (EERA DTOC) project the wake effect of clusters of wind farms is being addressed. One project task is to analyze high-resolution SAR wind fields to quantify the wind farm wake field near large wind farms in operation. Figure 192 shows a RADARSAT-1 scene covering the Horns Rev -1 and -2 offshore wind farms and a very long wind farm wake, around 10 km wide and 88 km long. TerraSAR-X wind fields observed near the Alpha Ventus offshore wind farm also show wind farm wake effects (Li and Lehner, 2012).

15.9 Wind resources from SAR

Planning a wind farm includes the identification of the wind resource at the site. The potential wind power production is closely related to the prevailing wind climate. Wind observations from offshore meteorological masts may be used but due to high cost only few are established and mainly by private wind farm developers. If meteorological observations of wind speed and wind direction from a least one year from an offshore mast are available, the wind resource may be assessed using the de facto standard software, the Wind Atlas Analysis and Applications Program (WAsP, `www.wasp.dk`) (Mortensen et al., 2005).

The usual procedure in a WAsP analysis is to divide the data into twelve bins for 30 degree wind direction sectors and determine the Weibull wind-speed distribution for each of these. The method is described in the European Wind Atlas (Troen & Petersen, 1989). For land and offshore coastal sites the local scale maps of topography, roughness of the terrain and obstacles should be used. Wind resource assessment in the offshore coastal zone - where most offshore wind farms are located or are in development - is challenging as coastal wind systems

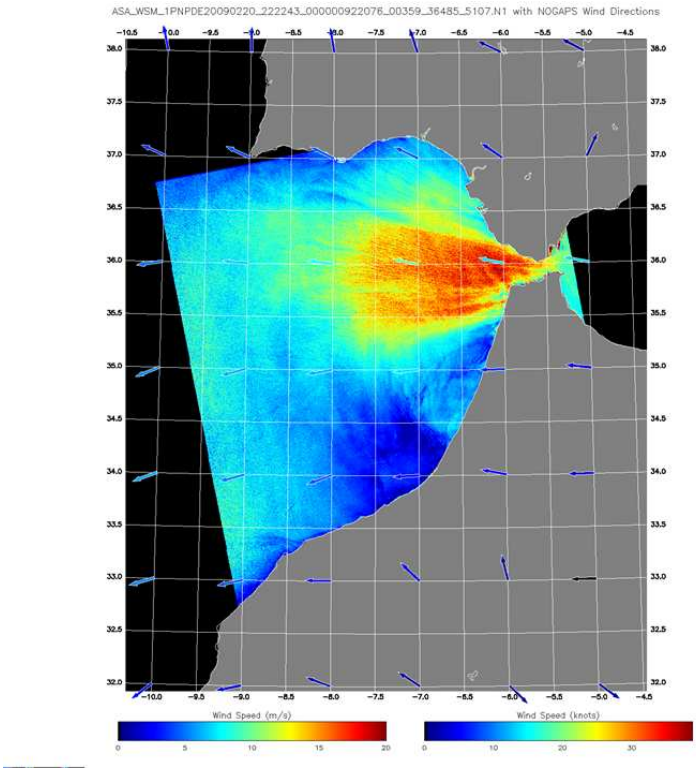

Figure 191: Envisat ASAR wind field observed on 20 February 2009 at 22:22 UTC. The wind map shows acceleration flow (gap wind) through and behind the Gibraltar Strait. The wind is from the east.

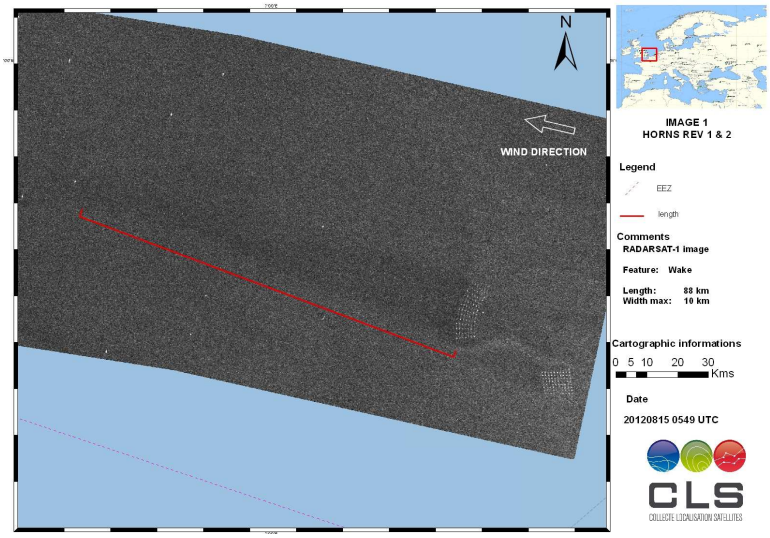

Figure 192: Wind farm wake at Horns Rev 1-/2 offshore wind farms in the North Sea observed from RADARSAT-1 from MacDonald, Dettwiler and Associates Ltd., 2012. From EERA DTOC project. Courtesy: Alexis Mouche, CLS.

are complicated and ocean wind observations are sparse.

Time-series data from meteorological masts typically include observations for every 10 minutes or each hour for a least one year. In this way one is certain to capture the wind conditions in all seasons both day and night. It is necessary to evaluate to what degree the one-year time-series is representative for the longer term (future 30 years). Long-term correlation/correction is not trivial; it adds some uncertainty to the wind resource (Hasager et al., 2008).

Satellites in sun-synchronous polar orbit observe a given local area at a certain local time in ascending (northbound) track and 12-hour shifted in descending (southbound) track. There are differences in the local acquisition time of the various satellites carrying radar instruments. If a local site has pronounced daily wind speed variations, the two fixed observational times may not be fully representative of the diurnal cycle. Far offshore diurnal variation is typically less pronounced than in some coastal areas, e.g. sites with pronounced land-sea breezes. Using observations from several satellites with different fixed observational times would be a possibility, but this has not yet been achieved.

Another challenge of using SAR for wind resource assessment is the relatively few observations available. For some sites less than 200 scenes may be available. In European coastal waters Envisat provides a somewhat higher number of observation. In the later years of operation many wide swath mode scenes were recorded. This makes it a unique archive for wind resource assessment. The available scenes can be seen at `http://earth.esa.int/EOLi`.

Barthelmie & Pryor (2003) and Pryor et al. (2004) investigated based on statistical analysis and using offshore meteorological observations from the Baltic Sea and North Sea, the number of randomly sampled wind observations necessary to carry out wind resource analysis within certain statistical bounds. The conclusion was that around 70 samples are sufficient to estimate mean wind speed and the Weibull scale parameter but around 2,000 samples are needed to estimate energy density and the Weibull shape parameter at the 10% confidence level (significance 95%). The result makes it clear that the accuracy of SAR-based wind resource statistics is adequate for pre-feasibility studies. In other words, the SAR-based wind resource map may be used as guide to site an offshore meteorological mast in a wind farm project. Alternatively, if high-quality offshore observations exist, the local wind gradients at 10 m above sea level may be evaluated from SAR wind resource maps. Also, combining or blending SAR wind resource statistics and mesoscale wind resource modelling is an option (Badger et al., 2010b).

When planning clusters of wind farms that cover 100 km^2 or more, it is advisable to have two meteorological masts if the wind resource should be assessed as accurately as possible. It is most likely that significant wind gradients exist within such areas, in particular in coastal zones (Barthelmie et al., 2007). At Horns Rev the first wind farm is located 14 to 21 km offshore from the closest coastal point and the second wind farm is located 26 to 31 km offshore. Using SAR, winds at $1-2$ km grid scale allow quantification of the local wind gradients. A third wind farm at Horns Rev in the North Sea is in planning.

15.10 S-WAsP

In-house software was developed for SAR wind resource wind mapping at DTU Wind Energy. The Satellite-WAsP (S-WAsP) software reads SAR wind fields from ANSWRS and SARTool (SOPRANO). In earlier versions of S-WAsP other formats were used as input (Nielsen et al., 2004; Hasager et al., 2008). The first step is to ensure geographical collocation of the series of wind fields (through a database) and select the desired data. The second step is to run the wind resource application routines to calculate the wind resource statistics: mean wind speed, Weibull scale, Weibull shape, and energy density and the statistical uncertainty for each parameter. The final results are output maps of the parameters (Hasager et al., 2012).

The number of satellite observations in a single directional bin may be small. Therefore to make it possible to fit a distribution, all data is used to derive the shape parameter. The shape parameter is assumed valid for every bin. The Weibull scale parameter is then estimated by the average wind speed in each sector. The frequency of occurrence in each sector is uncertain when observations are sparse and there is a risk of observing sectors without any observation and no estimate of the mean wind. An alternative to simple bin counting is to sort all observations after directions, estimate the probability density between the observations by the angle separating between them, and finally resample the densities in the standard sectors (Nielsen et al., 2004).

The available wind power density, $E\left(W/m^2\right)$ that is proportional to the wind speed cubed,

may be calculated from the two Weibull parameters, the scale parameter A and the shape parameter k, using the gamma function Γ, and the air density ρ ($\approx 1.245\text{kgm}^{-3}$ at $10°\text{C}$) as

$$E = \frac{1}{2}\rho A^3 \Gamma\left(1 + \frac{3}{k}\right) \tag{350}$$

The uncertainties for the four parameters; mean wind speed, Weibull A and k, and energy density can be calculated in S-WAsP. The uncertainty calculation estimates the difference of the Weibull A and k fitted function and the measured wind distribution based on the available number of samples. We follow the equations from the appendix in (Pryor et al., 2004). We assume that each SAR-based wind map is accurate and that the influence of time sampling is insignificant to the estimates. In other words, we assume the diurnal wind pattern to be described accurately using morning and evening observations only.

Studies from the North Sea and Baltic Sea have shown SAR wind maps to be a useful/valuable source of information for the estimation of Weibull A and k (Badger et al., 2010a; Christiansen et al., 2006; Hasager et al., 2011a).

15.11 The wind class method

Envisat ASAR and ERS-1/2 SAR scenes are nowadays freely available in large quantities over Europe. In earlier times there were limitations. For commercial application a relatively high cost was associated. This prompted a need for an alternative SAR-based wind resource method in S-WAsP: the wind class method (Badger et al., 2010a). The method is based on representative selected sampling of 135 SAR scenes each with wind conditions similar to representative long-term wind conditions as evaluated from the global atmospheric model results from NCAR NCEP re-analysis. Thus the first processing step is to evaluate the long-term statistics from large-scale models and assess the weighting function for the selected representative wind conditions. This method is also used in the KAMM/WAsP wind atlas methodology (Frank et al., 2001). The second step is to distribute the SAR scenes amongst the wind classes based on look-up tables with the specific dates and times when each given wind situation occurs. The third step is to retrieve and process the SAR scenes to wind fields. The fourth and final step is to use the relevant weighting functions from the first step to produce representative SAR-based wind resource statistics from the series of SAR wind fields. The final results are maps of Weibull A and k, mean wind speed and energy density. The method was used in United Arab Emirates and compared well with mesoscale model results (Badger et al., 2010b). Figure 193 shows the mean wind speed at 10 m over the United Arab Emirates.

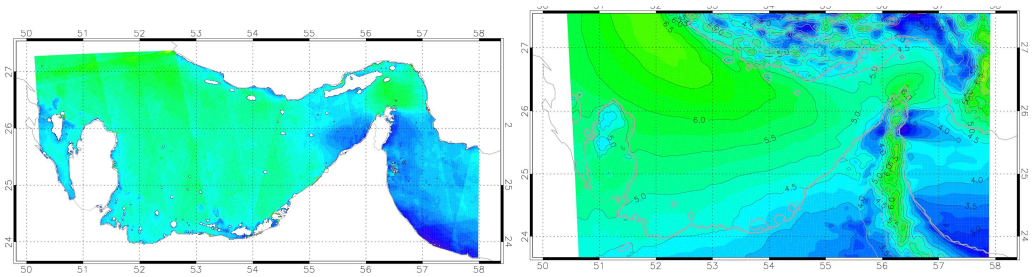

Figure 193: 10 m mean wind speed maps over the United Arab Emirates from (left) Envisat ASAR wind fields and (right) KAMM mesoscale modeling. From Badger et al. (2010b).

The wind class method was evaluated in the North Sea using in-situ data for comparison. The results were very good. The overall agreement with mast observations of the wind resource was within $\pm 5\%$ for mean wind speed and Weibull scale parameter and within $\pm 7\%$ for energy density and Weibull shape parameter. Similar results were obtained from using more than

500 overlapping scenes for wind resource assessment. In comparison, the accuracy of wind resources from mesoscale modeling is $10 - 15\%$ (Badger et al., 2010a).

The advantages of wind class sampling are that fewer images are needed and the long-term wind climatology may be obtained, even using SAR scenes covering a limited period.

15.12 SAR wind resource maps

In the Indian Ocean near India the mean wind speed from 164 Envisat ASAR wind fields is presented in Figure 194. Hasager et al. 2011b provide further detail.

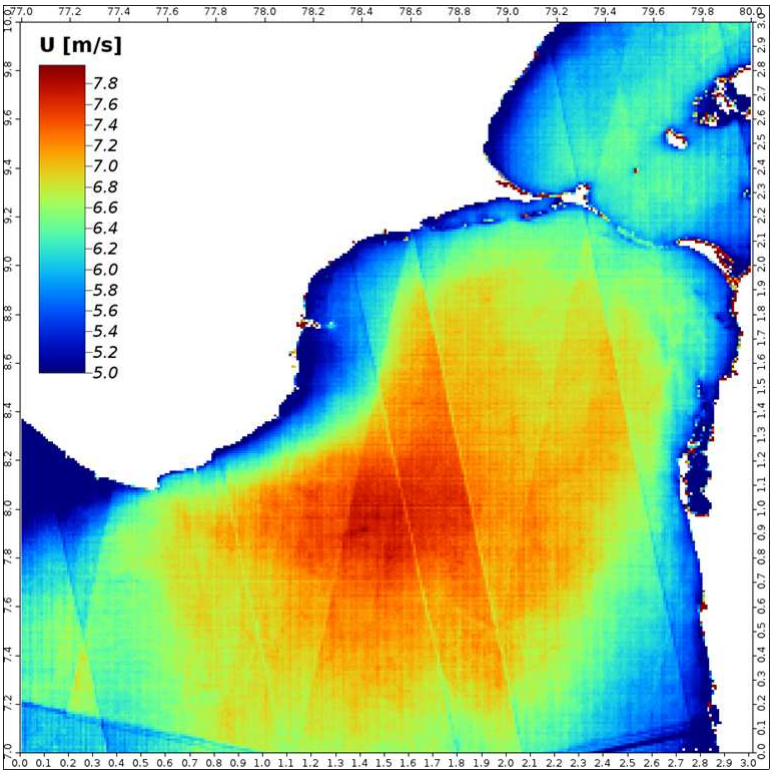

Figure 194: Mean wind speed map based on 164 Envisat ASAR wind fields at the Indian Ocean, India. From Hasager et al. 2011b.

Takeyama et al. 2013 compared in-situ winds for offshore and onshore winds in Japan and found large negative bias (above 1 ms^{-1}) for offshore flow but small bias for onshore winds. The wind maps are used to assess the mean wind speed in the region near Shirahama, see Figure 195.

In Figure 196 the maps of the 10 m mean wind speed and energy density over Hangzhou Bay in China are presented. Very high values (bright red) near the coastline are caused by a high radar return from exposed sand or mud and are not associated with the wind (Badger, 2009).

The most recent wind resource wind map produced by DTU Wind Energy is based on Envisat ASAR wide swath mode wind fields processed by A. Mouche at CLS using SOPRANO. The result is published online at `soprano.cls.fr` (select Wind/Statistics L3/Norsewind). The map covers the Northern European Seas and is based on 9,000 unique wind fields. It is part of the FP7 Northern European Seas Wind Index database (NORSEWInD) project final results (Hasager et al., 2012). The second moment fitting was chosen to be used for the Weibull scale and shape parameters (Pryor et al., 2004; Barthelmie and Pryor, 2003) for the final products in NORSEWInD. The uncertainty on mean wind speed and Weibull A is of the order 0.08 ms^{-1} in most of the study area and around 0.18 ms^{-1} in parts of the Irish Sea

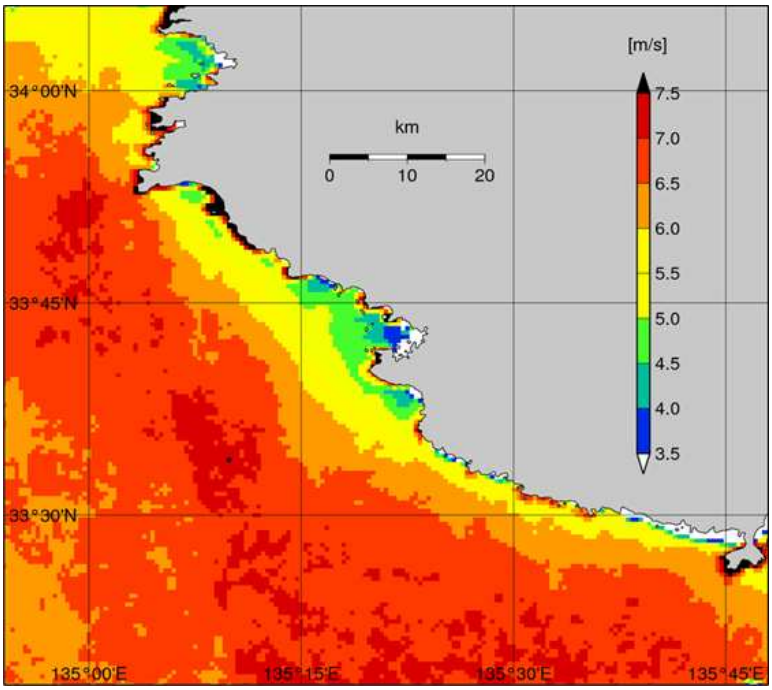

Figure 195: Mean wind speed map based on 104 Envisat ASAR wind fields at Shirahama, Japan. Courtesy: Yuko Takeyama.

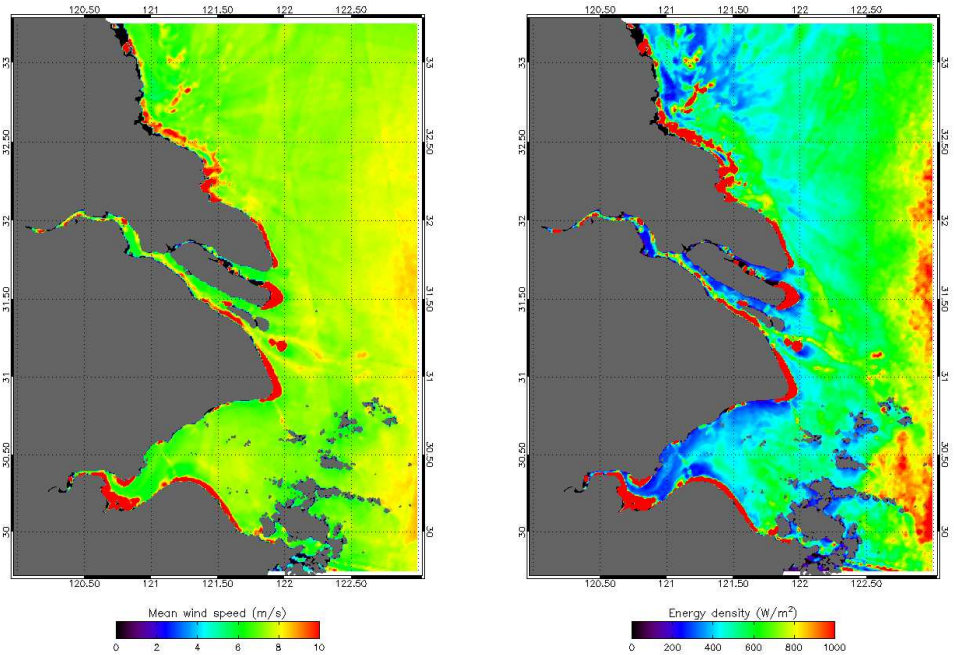

Figure 196: Maps of the 10-m mean wind speed (left) and energy density (right) from SAR over Hangzhou Bay in China. Very high values (bright red) near the coastline are caused by a high radar return from exposed sand or mud and are not associated with the wind. From Badger (2009).

(with the fewest samples). The uncertainty of Weibull k is around 0.04 and for energy density from 20 to 50 Wm^{-2}.

15.13 Lifting satellite winds to hub-height

The SAR-based wind results are valid at 10 m above sea level (modern turbines operate at 100 m). The vertical wind profile offshore is a function of atmospheric stability, roughness and boundary layer height (Peña et al. 2012). A method to extrapolate the satellite wind resource statistics to wind turbine hub-height is developed. It is based on combining atmospheric stability information from mesoscale models into the stability dependent wind profile equation. Preliminary results are presented (Hasager at al., 2012). The potential use of the lifting of satellite winds to hub-height is applicable for all types of 10 m satellite wind resource statistics including SAR and scatterometer. An improvement to the method is currently being investigated. The key difference is the use of stability information per scene versus average stability. It is expected to be more robust and reliable to use average stability for lifting winds to hub-height.

15.14 Future advances in ocean wind mapping from SAR

For end-users the level 2 wind product from Sentinel-1 is foreseen to be important new data. There will still be the need for evaluation and improvement on SAR wind retrieval. Investigations of Doppler shift anomaly in combination with GMF is one way as well as new adjustment to polarization ratio and validated GMFs for X- and L-band. Re-processing of the full Envisat archive to wind fields would be relevant for European scale wind resource mapping such as the New European Wind Atlas.

15.15 Acknowledgements

We are very thankful for collaboration with Frank Monaldo and Alexis Mouche. Envisat data provided by the European Space Agency and RADARSAT-1 data from MacDonald, Dettwiler and Associates Ltd are acknowledged. Projects we acknowledge are Offshore wind mapping in India with Centre for Wind Energy Technology (C-WET), FP7 NORSEWInD TREN-FP7-219048, FP7 EERA DTOC FP7-ENERGY-2011-1/ n°282797, ICEWIND Nordic Top-level Research Initiative, FP7 European Regional Development Fund and the South Baltic Programme: South Baltic Offshore Wind Energy Regions project, Off-Shore Wind Energy Resource Assessment and Feasibility Study of Off-Shore Wind Farm Development in China (EU-China Energy and Environment Programme), Offshore wind energy analyses over the United Arab Emirates is funded by Abu Dhabi Future Energy Company (Masdar). We enjoy the long-term visit of Yuko Takeyama.

Notation

A	function of wind speed and local incident angle in a GMF
A	Weibull scale parameter
ALOS	Advanced Land Observing Satellite (Japan)
ANSWRS	APL/NOAA SAR wind retrieval system
ASAR	advanced C-band SAR
ASCAT	Advanced Scatterometer
ASI	Italian Space Agency
B	function of wind speed and local incident angle in a GMF
C	function of wind speed and local incident angle in a GMF
CAST	China Association for Science and Technology
CSA	Canadian Space Agency

COSMO SkyMED	Constellation of small Satellites for the Mediterranean basin Observation (Italy)
DLR	German Aerospace Center
E	energy density
Envisat	Environmental Satellite (ESA)
ERS	European Research Satellite (ESA)
ESA	European Space Agency
EUMETSAT	European Organisation for the Exploitation of Meteorological Satellites
FFT	fast Fourier transformation
GMF	geophysical model function
HH	SAR operating at horizontal polarization in transmit and receive
HV	SAR operating at horizontal polarization in transmit and vertical in receive
H-pol	horizontally polarized radiation
HJ-1C	Huanjing (China)
IEEE	Institute of Electrical and Electronics Engineers
ISRO	Indian Space Research Organisation
JAXA	Japanese Space Agency
JERS	Japanese Earth Resource Satellite
JHU/APL	Johns Hopkins University Applied Physics Laboratory
k	Weibull shape parameter
KSAT	Kongsberg Satellite Service
MDA	MacDonald, Dettwiler and Associates Ltd
METOP	Meteorological polar orbiting satellites
NASA	National Aeronautics and Space Administration (USA)
NCAR	National Center for Atmospheric Research (USA)
NCEP	National Centers for Environmental Prediction (USA)
NEST	Next ESA SAR toolbox
NRCS	normalised radar cross section
NRT	Near real time
NOAA	National Oceanic and Atmospheric Administration
NOGAPS	navy operational global atmospheric prediction system
OCEANSAT	Ocean Satellite (India)
OSCAT	Ocean Scatterometer
PALSAR	Phased Array type L-band Synthetic Aperture Radar (Japan)
PR	polarization ratio
QuikSCAT	Quick Scatterometer (USA)
RADARSAT	Canadian Radar Satellite
Risø DTU	Risø National Laboratory for Sustainable Energy (Technical University of Denmark)
SAR	synthetic aperture radar
SEASAT	Sea Satellite (USA)
S-WAsP	satellite WAsP
TerraSAR-X	Terra Synthetic Aperture Radar X-band (Germany)
TanDEM-X	TerraSAR-X add-on for Digital Elevation Measurement (Germany)
U	wind speed at 10 m height
VH	SAR operating at vertical polarization in transmit and horizontal in receive
V-pol	vertically polarized radiation
VV	SAR operating at vertical polarization in transmit and receive
WAsP	Wind Atlas Analysis and Application Program
WSM	wind swath mode
γ	function of wind speed and local incident angle in a GMF
Γ	Gamma function
θ	radar's local incident angle
λ	wavelength
ρ	air density
σ^0	normalised radar cross section
ϕ	wind direction with respect to the radar look direction

References

Badger, M. (2009), Satellite SAR wind resource mapping in China (SAR-China), Risø-R-1706(EN), 17

Badger M., Badger J., Hasager C., Nielsen M., (2010b), Sampling of SAR imagery for wind resource assessment, In: Proceedings (on CD-ROM), SEASAR 2010, Frascati (IT), 25-29 Jan 2010, (European Space Agency, Paris, 2010) (ESA-SP-679), 6

Badger M., Hasager C. B., Thompson D., Monaldo F. (2008), Ocean winds from synthetic aperture radar, *Ocean Remote Sensing: Recent Techniques and Applications*, 31-54

Badger M., Badger J., Nielsen M., Hasager C.B., Peña P. (2010a), Wind class sampling of satellite SAR imagery for offshore wind resource mapping, *J. of Applied Meteorology and Climatology*

Beal R. C., Young G. S., Monaldo F., Thompson D. R., Winstead N. S., Schott C. A. (2005), High Resolution Wind Monitoring with Wide Swath SAR: A User's Guide, U.S. Department of Commerce, Washington, DC, USA, 1-155

Barthelmie R. J., Badger J., Pryor S. C., Hasager C. B., Christiansen M. B., Jørgensen B. H. (2007), Offshore coastal wind speed gradients: Issues for the design and development of large offshore windfarms, *Wind Engineering: The International Journal of Wind Power*, **31(6)**, 369-382

Barthelmie R. J. & Pryor S. C. (2003), Can satellite sampling of offshore wind speeds realistically represent wind speed distributions, *Journal of Applied Meteorology*, **42**, 83-94

Christiansen M. B. & Hasager C. B. (2005), Wake effects of large offshore wind farms identified from satellite SAR, *Remote Sensing of Environment*, **98**, 251-268

Christiansen M. B. & Hasager C. B. (2006), Using airborne and satellite SAR for wake mapping offshore, *Wind Energy*, **9**, 437-455

Christiansen M. B., Koch W., Horstmann J., Hasager C. B. (2006), Wind resource assessment from C-band SAR, *Remote Sensing of Environment*, **105**, 68-81

Dagestad K. F., Horstmann J., Mouche A., Perrie W., Shen H., Zhang B., Li X., Monaldo F., Pichel W., Lehner S., Badger M., Hasager C. B., Furevik B., Foster R.C., Falchetti S., Caruso M.J., Vachon P. (2013), Wind retrieval from Synthetic Aperture Radar – an overview, Proceedings of the SEASAR 2012, White paper, ESA (in press)

Du Y., Vachon P. W., Wolfe J. (2002), Wind direction estimation from SAR images of the ocean using wavelet analysis, *Canadian Journal of Remote Sensing*, **28**, 498-509

Elfouhaily T., Chapron B., Katsaros K., Vandemark D. (1997), A unified directional spectrum for long and short wind-driven waves, *J. Geophys. Res.*, 102(C7), **15**, 781–796

Fichaux N. & Ranchin T. (2002), Combined extraction of high spatial resolution wind speed and direction from SAR images: a new approach using wavelet transform, *Canadian Journal of Remote Sensing*, **28**, 510-516

Frank H. P., Rathmann O., Mortensen N. G., Landberg L., (2001), The numerical wind atlas - the KAMM/WAsP method, Risø-R-1252(EN), RisøNational Laboratory, Roskilde, Denmark, 60

Furevik B., Johannessen O., Sandvik A. D. (2002), SAR-retrieved wind in polar regions - comparison with in-situ data and atmospheric model output, *IEEE Transactions on Geoscience and Remote Sensing*, **40**, 1720-1732

Gerling T. W. (1986), Structure of the surface wind field from the SEASAT SAR, *Journal of Geophysical Research*, **91**, 2308-2320

Hasager C. B., Barthelmie R. J., Christiansen M. B., Nielsen M., Pryor S. C. (2006), Quantifying offshore wind resources from satellite wind maps: study area the North Sea, *Wind Energy*, **9**, 63-74

Hasager C. B., Dellwik E., Nielsen M., Furevik B. (2004), Validation of ERS-2 SAR offshore wind-speed maps in the North Sea, *International Journal of Remote Sensing*, **25**, 3817-3841

Hasager C. B., Nielsen M., Astrup P., Barthelmie R. J., Dellwik E., Jensen N. O., Jørgensen B. H., Pryor S. C., Rathmann O., Furevik B. (2005), Offshore wind resource estimation from satellite SAR wind field maps, *Wind Energy*, **8**, 403-419

Hasager C. B., Badger M., Peña A., Larsé n X. G. (2011a), SAR-based wind resource statistics in the Baltic Sea, *Remote Sens.*, **3(1)**, 117-144

Hasager C. B., Peña A., Christiansen M. B., Astrup P., Nielsen N. M., Monaldo F., Thompson D., Nielsen P., (2008), Remote sensing observation used in offshore wind energy, *IEEE Journal of Selected Topics in Applied Earth Observations and Remote Sensing*, **1(1)**, 67-79

Hasager C. B., Badger M., Mouche A., Stoffelen A., Driesenaar T., Karagali I., Bingöl F., Peña A., Astrup P., Nielsen M., Hahmann A. N., Costa P., Berge E., Bredesen R. E. (2012), NORSEWInD satellite wind climatology, DTU Wind Energy, (DTU Wind Energy E; No. 0007)

Hasager C. B., Bingöl F., Badger M., Karagali I., Sreevalsan E. (2011b), Offshore Wind Potential in South India from Synthetic Aperture Radar, Risoe-R; No. 1780(EN), Danmarks Tekniske Universitet, RisøNationallaboratoriet for Bæredygtig Energi, Roskilde, Danmark

He Y. J., Perrie W., Zou Q. P., Vachon P. W. (2005), A new wind vector algorithm for C-band SAR, *IEEE Transactions on Geoscience and Remote Sensing*, **43**, 1453-1458

Hersbach H., Stoffelen A., de Haan S. (2007), An improved C-band scatterometer ocean geophysical model function: CMOD5, *J. Geophys. Res.*, **112**, C03006

Hersbach H (2010), Comparison of C-band scatterometer CMOD5.N equivalent neutral winds with ECMWF, *J. Atm. Oceanic Tech.*, **27**, 721–736

Horstmann J., Koch W., Lehner S., Tonboe R. (2000), Wind retrieval over the ocean using synthetic aperture radar with C-band HH polarization, *IEEE Transactions on Geoscience and Remote Sensing*, **38**, 2122–2131

Horstmann J., Schiller H., Schulz-Stellenfleth J., Lehner S. (2003), Global wind speed retrieval from SAR, *IEEE Transactions on Geoscience and Remote Sensing*, **41**, 2277–2286

Isoguchi O. & Shimada M. (2009), An L-band ocean geophysical model function derived from PALSAR, IEEE Trans. Geosci. Remote Sens., **43**, 1925–1936

Karagali I. (2012), Offshore wind energy: wind and sea surface temperature from satellite observations, PhD dissertation, DTU Wind Energy, Roskilde, Denmark

Karagali I. (2013), Scatterometer for wind energy, PhD dissertation, DTU Wind Energy, Roskilde, Denmark

Koch W. (2004), Directional analysis of SAR images aiming at wind direction, *IEEE Transactions on Geoscience and Remote Sensing*, **42**, 702–710

Kudryavtsev V., Hauser D., Caudal G., Chapron B. (2003), A semiempirical model of the normalized radar cross-section of the sea surface - 1. Background model, *Journal of Geophysical Research - Oceans*, **108**

Lehner S., Horstmann J., Koch W., Rosenthal W. (1998), Mesoscale wind measurements using recalibrated ERS SAR images, *Journal of Geophysical Research - Oceans*, **103**, 7847–7856

Li X. & Lehner S. (2012), Sea surface wind field retrieval from TerraSAR-X and its applications to coastal areas, Presented at IGARSS 2012, Munich, Germany, 2059–2062

Monaldo F. M. & Beal R. (2004), Wind speed and direction, In C. R. Jackson & J. R. Apel (Eds.), Synthetic Aperture Radar Marine User's Manual, U.S. Department of Commerce, National Oceanic and Atmospheric Administration, Washingon, DC, 305–320

Monaldo F. M., Thompson D. R., Beal R. C., Pichel W. G., Clemente-Coló n P. (2001), Comparison of SAR-derived wind speed with model predictions and ocean buoy measurements, *IEEE Transactions on Geoscience and Remote Sensing*, **39**, 2587–2600

Monaldo F. M., Thompson D. R., Pichel W. G., Clemente-Colon P. (2004), A systematic comparison of QuikSCAT and SAR ocean surface wind speeds, *IEEE Transactions on Geoscience and Remote Sensing*, **42**, 283–291

Mortensen N. G., Heathfield D. N., Myllerup L., Landberg L., Rathmann O. (2005), Wind Atlas Analysis and Application Program: WAsP 8 Help Facility, RisøNational Laboratory, Roskilde, Denmark

Mouche A. A., Hauser D., Daloze J. F., Guerin C. (2005), Dual-polarization measurements at C-band over the ocean: Results from airborne radar observations and comparison with ENVISAT ASAR data, *IEEE Transactions on Geoscience and Remote Sensing*, **43**, 753–769

Mouche A., Collard F., Chapron B., Johannessen J.A. (2013), Doppler Centroid, Normalized Radar Cross Sections and Sea Surface Wind, Proceedings of SeaSAR 2012 Tromsø, Norway, ESA (in press)

Nielsen M., Astrup P., Hasager C. B., Barthelmie R. J., Pryor S. C. (2004), Satellite information for wind energy applications, Risø-R-1479(EN), RisøNational Laboratory, Roskilde, Denmark, 1–57

Peña A., Mikkelsen T., Grynin, S-E., Hasager C. B., Hahmann A. N., Badger M., Karagali I., Courtney M. (2012), Offshore vertical wind shear: Final report on NORSEWInD's work task 3.1, DTU Wind Energy, Roskilde, Denmark, DTU Wind Energy E; No. 0005,

Pryor S. C., Nielsen M., Barthelmie R. J., Mann J. (2004), Can satellite sampling of offshore wind speeds realistically represent wind speed distributions? Part II Quantifying uncertainties associated with sampling strategy and distribution fitting methods, *Journal of Applied Meteorology*, **43**, 739–750

Quilfen Y., Chapron B., Elfouhaily T., Katsaros K., Tournadre J. (1998), Observation of tropical cyclones by high-resolution scatterometry, *Journal of Geophysical Research*, **103**, 7767–7786

Ren Y. Z., Lehner S., Brusch S., Li X. M., He M. X., (2012), An Algorithm for the retrieval of sea surface wind fields using X-band TerraSAR-X data, *International Journal of Remote Sensing*, **33**

Romeiser R. & Alpers W. (1997a), An improved composite surface model for the radar backscattering cross section of the ocean surface. 2: Model response to surface roughness variations and the radar imaging of underwater bottom topography, *Journal of Geophysical Research-Oceans*, **102**, 25251–25267

Romeiser R., Alpers W., Wismann, V. (1997b), An improved composite surface model for the radar backscattering cross section of the ocean surface.1: Theory of the model and optimization/validation by scatterometer data, *Journal of Geophysical Research-Oceans*, **102**, 25237-25250

Shimada T., Kawamura H., Shimada M. (2004), Evaluation of JERS-1 SAR images from a coastal wind retrieval point of view, *IEEE Trans. Geosci. Remote Sens*, **42**, 491–500

Stoffelen A. & Anderson D. L. T. (1997), Scatterometer data interpretation: Estimation and validation of the transfer function CMOD4, *Journal of Geophysical Research*, **102**, 5767-5780

Takeyama Y., Ohsawa T., Kozai K., Hasager C.B., Badger M (2013), Comparison of Geophysical Model Functions for SAR Wind Speed Retrieval in Japanese Coastal Waters, *Remote Sens.*, **5(4)**, 1956–1973

Thompson D. R., Horstmann J., Mouche A., Winstead N. S., Sterner R., Monaldo F. M. (2012), Comparison of high-resolution wind fields extracted from TerraSAR-X SAR imagery with predictions from the WRF mesoscale model, *J. Geophys. Res.*, **117**, C02035

Thompson D., Elfouhaily T., Chapron B. (1998), Polarization ratio for microwave backscattering from the ocean surface at low to moderate incidence angles, Proceedings International Geoscience and Remote Sensing Symposium, Seattle, WA, 1671–1676

Troen I. & Petersen E. L. (1989), European Wind Atlas, RisøNational Laboratory, Roskilde, Denmark, 1–656

Vachon P. W. & Dobson E. W. (2000), Wind retrieval from RADARSAT SAR images: selection of a suitable C-band HH polarization wind retrieval model, *Canadian Journal of Remote Sensing*, **26**, 306–313

Valenzuela G. R. (1978), Theories for the interaction of electromagnetic and ocean waves - A review, *Boundary-Layer Meteorology*, **13**, 61–85

Zhang B., Perrie W., He Y. (2011), Wind speed retrieval from RADARSAT-2 quad-polarization images using a new polarization ratio model, *J. Geophys. Res.*, **116**, C08008

Zhang B. & Perrie W. (2012), Cross-polarized synthetic aperture radar: A new potential measurement technique for hurricanes, *Bull. Amer. Meteor. Soc.*, 531–541

16 Scatterometry for wind energy

Ioanna Karagali
DTU Wind Energy, Risø Campus, Roskilde, Denmark

16.1 Introduction

Scatterometry is a well established technique used for remote sensing of the oceans. Radiation is actively received in the microwave band. Scatterometers are active radars that send pulses towards the Earth's surface and measure the backscattered signal due to the small scale waves (in the order of 2 cm). Extended studies have related the backscattered signal to the surface stress and developed algorithms to relate this to wind speed. In addition, with a similar principle of function as the scatterometer, the Synthetic Aperture Radar (SAR) is an active instrument that measures the backscattered signal but only wind speed measurements can be retrieved. For details on SAR see the relevant chapter from Hasager and Badger (2013).

Radar scatterometers, operating at different sub-bands of the microwave, are widely used to derive near-surface wind speed and direction over the ocean from sun-synchronous satellites. The first operational space-borne wind scatterometer was the NASA Seasat-A Satellite Scatterometer (SASS), launched in 1978 and operated at the Ku-band frequency (14.6 GHz). In 1991, the European Space Agency (ESA) launched the ERS-1 satellite which failed in the year 2000. The Advanced Microwave Instrument (AMI) on board ERS-1 operated at 5.3 GHz (C band), allowing for a low resolution scatterometer mode and a high resolution SAR mode. ERS-2 was launched in 1995.

Table 23: List of the scatterometer missions taken from COAPS (2013)

Short Background	Period in Service	Spatial Resolution	Scan Characteristics	Operational Frequency
SeaSat-A Scatterometer	1978/7/7 - 1978/10/10	50 km with 100 km spacing	Two sided Double swath	Ku band (14.6 GHz)
ERS-1 Scatterometer	1991/7 - 1997/5/21	50 km	One sided Single swath	C band (5.3 GHz)
ERS-2 Scatterometer	1997/5/21 - 2011/7	50 km	One sided Single swath	C band (5.3 GHz)
NSCAT	1996/9/15 - 1997/6/30	25 km and 50 km	Two sided Double swath	Ku band (13.995 GHz)
SeaWinds on QuikSCAT	1999/7/19 - 2009/11/23	25 km	Conical scan One wide swath	Ku band (13.4 GHz)
SeaWinds on ADEOS II	2002/12 - 2003/10	25 x 6 km	Conical scan One wide swath	Ku band (13.4 GHz)
ASCAT	2006/10 - Present	50km	Two sided Double swath	C band (5.255 GHz)
OCEANSAT2	2009/9/23 - Present	25km	Conical scan One wide swath	Ku band (13.5 GHz)
HY-2A	2011/9? - Present	25km	Conical scan One wide swath	Ku band (13.256 GHz)

NSCAT was launched in 1996, on board the Japanese Advanced Earth Observing Satellite (ADEOS). NASA launched the SeaWinds scatterometer on-board the QuikSCAT platform in 1999. In 2002, NASA in collaboration with National Space Development Agency of Japan (NASDA) launched another SeaWinds instrument on board the Midori-II (ADEOS-II) satellite. ESA launched the Advanced Scatterometer (ASCAT) on-board the MetOp-A (2007) and MetOp-B (2012) platforms. The Indian Space Research Organization (ISRO) launched Oceansat-2 in 2009, carrying a Ku band scatterometer similar to QuikSCAT. A list of all the scatterometer missions and their technical characteristics is available in Table 23.

The range of applications for scatterometer winds is wide, including storm and hurricane

tracking, climate studies, air-sea interactions, propagation of polluted air masses, CO_2 fluxes (Boutin et al., 2009), assimilation in Numerical Weather Prediction (NWP) models and commercial applications, like wind energy. An overview of the progress in scatterometry applications is available in Liu (2002).

16.2 Principle of Function

Radars operate at different sub-bands within the microwave range of the electromagnetic spectrum (Table 24). Scatterometers are typically operational within the C and Ku subbands. For these wavelengths and for specific incidence angles, if the surface wave spectrum contains a component with wavelength similar to the incident radiation then the incident radar pulse is reflected due to Bragg resonant scattering (Martin, 2004). For more details on the relation between the sea surface and radar wavelengths see the chapter on SAR from Hasager and Badger (2013).

Table 24: IEEE standard radar band letter definitions and frequency ranges, taken from IEEE (2002)

Designation	Frequency	Wavelength
HF	3 - 30 MHz	100 m - 10 m
VHF	30 - 300 MHz	10 m - 1 m
UHF	300 - 1000 MHz	100 cm - 30 cm
L Band	1 - 2 GHz	30 cm - 15 cm
S Band	2 - 4 GHz	15 cm - 7.5 cm
C Band	4 - 8 GHz	7.5 cm - 3.75 cm
X Band	8 - 12 GHz	3.75 cm - 2.50 cm
Ku Band	12 - 18 GHz	2.50 cm - 1.67 cm
K Band	18 - 27 GHz	1.67 cm - 1.11 cm
Ka Band	27 - 40 GHz	1.11 cm - .75 cm
V Band	40 - 75 GHz	7.5 mm - 4.0 mm
W Band	75 - 110 GHz	4.0 mm - 2.7 mm
mm Band	110 - 300 GHz	2.7 mm - 1.0 mm

A microwave radar pulse is transmitted towards the Earth's surface and the reflected signal is measured. The small scale ripples on the water surface that are generated by the wind satisfy the wavelength requirement for Bragg scattering of the incident pulse. From the energy reflected back to the instrument due to Bragg scattering, the noise signal is defined as the instrument noise and the natural emissivity of the atmosphere-earth system at the frequency of the radar pulse. Subtracting the noise signal from the total measured reflected signal produces the backscattered signal which is used to estimate the normalized radar cross section (NRCS) σ_0.

The fraction of the radar signal backscattered to the instrument is mainly a function of the surface stress. But as surface stress observations are not available for the calibration and generation of an empirical relationship, the near-surface ocean wind velocity relative to the orientation of the instrument is used instead. The Geophysical Model Function (GMF) is the empirical relation between the wind velocity and the normalized radar cross section σ_0. During the decades of scatterometer applications, several GMFs have been developed and are constantly modified to improve the accuracy of the retrieved winds.

The GMFs are based on the correlation of the measured σ_0 at a location with in situ, modelled and other satellite winds. The general form of a GMF as described in Naderi et al. (1991), is

$$\sigma_0 = f\left(|u|, \xi, ...; \theta, f, pol\right). \tag{351}$$

$|u|$ is the wind speed, ξ the azimuth angle between the wind vector and the incident radar pulse (noted as χ in Figure 197), θ is the incidence angle of the radar signal measured in the vertical plane, "f" is the frequency of the radar signal and "pol" its polarization. The term ... accounts for non-wind variables such as long waves, stratification and temperature, the effects of which are considered small (Naderi et al., 1991).

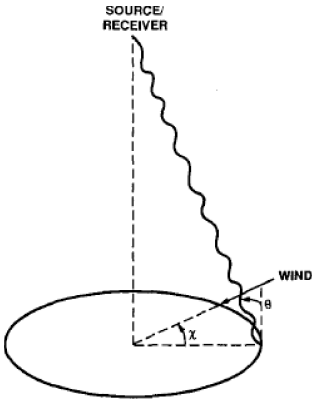

Figure 197: Scattering geometry sketch from Naderi et al. (1991).

A single σ_0 measurement is not sufficient to determine both the wind speed and direction. More measurements are required from different azimuth angles and different polarizations, obtained with more than one beams. During the wind inversion process, the set of wind speed and direction that maximizes the probability of the measured σ_0 is determined using a maximum-likelihood estimation (MLE) method. Typically, more than one solutions with extreme MLE values are obtained, known as "ambiguities". These ambiguities correspond to almost the same wind speed but different wind directions. The ambiguity that has the maximum value is chosen as the "best" estimate. The geometry of each σ_0 measurement or "footprint" depends on the specifications of the scatterometer. Many nearly-simultaneous, space-collocated σ_0 measurements are averaged in Wind Vector Cells (WVC). The dimensions of the WVC depend on the mission specifications.

GMFs have evolved during the decades of scatterometer applications, as more measurements become available and more validation studies are performed. The SASS-2 GMF was developed by Wentz et al. (1984), using the statistics from 3 months of SASS measurements and a mean global wind speed from a climatology. The NSCAT mission resulted in a new GMF, based on the correlation of the radar backscatter with modelled winds from ECMWF and SSMI wind speeds, as described in Wentz and Smith (1999). The SSM/I GMF was based on a model for the brightness temperature of the ocean and the atmosphere above, which is calibrated using buoy and radiosonde data as described in Wentz (1997).

ERS-1 required a new type of GMF due its different operating frequency compared to SASS. Data collected during several campaigns related σ_0 from air-borne instruments with in situ observations from research ships and buoys. This resulted in the pre-launch GMF known as CMOD2 (Offlier, 1994). The operational ERS-2 GMF was CMOD4, developed by Stoffelen and Anderson (1997), using satellite derived σ_0 and 10 m winds from the ECMWF analysis. The CMOD5 function (Hersbach et al., 2007) was released to correct for deficiencies in the CMOD4 version, fitting measurements of extreme backscatter and winds, obtained from aircraft and in situ data. CMOD5.N, described in Hersbach (2010), is tuned to wind at 10 m above the surface assuming neutral atmospheric stratification.

16.3 Equivalent Neutral Wind

GMFs are typically derived using open ocean buoy measurements and relating those to radar backscatter measurements. Once the empeirical relationship has been established, it is applied to the scatterometer σ_0 values to derive the wind speed and direction through the wind inversion process. As a convention, σ_0 values are related to the wind at 10 meters above the sea surface assuming a neutral atmospheric stratification, i.e. the Equivalent Neutral Wind (ENW) (Liu & Tang , 1996).

$$u = \frac{u_*}{\kappa}\left[\ln\left(\frac{z}{z_0}\right) - \Psi_M\right] \tag{352}$$

The modified logarithmic wind profile accounting for the atmospheric startification is defined in Equation 352. u is the wind speed at height z, z_0 is the sea roughness length, u_* is the friction velocity, κ is the von Kármán constant (0.4) and Ψ_M the stability correction. The ENW is computed using u_* and z_0 consistent with the actual stratification and setting the Ψ_M function to zero.

Wind observations from buoys, models or other satellite winds are used to estimate the friction velocity using the observed stability. The friction velocity is then used to estimate the 10 m wind assuming a neutral atmosphere. Finally, this neutral 10 m wind is related to the observed σ_0. The GMF resulting from the SASS scatterometer (Ku band) are tuned to ENW. The GMF of the CMOD family were tuned to non-neutral winds until CMOD5.N which is currently being used for the ASCAT scatterometer (Hersbach , 2010).

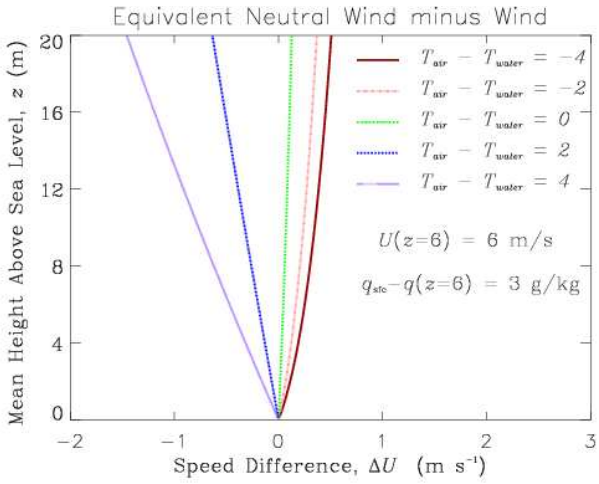

Figure 198: Example of the difference between ENW and true wind depending on the atmospheric stratification. Image taken from Bourassa (2013)

The atmospheric stability is not always neutral. Figure 198 shows how the stability can influence the difference between the ENW and the true wind. When the stratification is neutral (green line), the difference between the ENW and the true wind is negligible. When the stratification is stable (blue lines) the true wind is higher than the ENW. When the stratification is unstable (red lines) the ENW is higher than the true wind but the differences are much smaller compared to the stable cases. Brown et al. (2006) found that the globally averaged 10 m neutral winds from the European Centre for Medium Range Weather Forecasting (ECMWF) were 0.19 m s^{-1} stronger than the ECMWF standard 10 m winds and concluded that the marine boundary layer is overall slightly unstable.

16.4 Sources of error

The backscattered signal is affected by rain, currents, the sea surface temperature and the atmospheric stratification. Hilburn et al. (2006) stated that rain changes the ocean surface roughness, backscatters the radar pulse and reduces its transmission through the atmosphere. Ku-band instruments operate at shorter wavelengths than C-band ones which makes them more sensitive to raindrops either in the atmospheric path or because of the rougher sea surface.

The sea surface temperature (SST) influences the viscosity of the surface oceanic layer where the wind stress is applied. Higher SST results in lower viscosity. For a given wind speed, lower viscosity causes more surface roughness and thus, more backscattering. In such a case, the scatterometer will record higher σ_0 values and the derived wind speed will be higher. The overall effect is that over warm water the scatterometer-derived wind speed may be higher than from in situ measurements.

Moreover, SST partly adjusts the atmospheric stratification which also affects the backscattered signal. Under very stable conditions, the surface winds tend to be lower due to decoupling from the higher atmospheric levels. In such a case the surface stress is lower, thus σ_0 is lower. But, the atmospheric stability also controls if there is any discrepancy between the scatterometer derived wind and the "surface truth", due to the ENW convention.

Scatterometers observe relative to the sea surface. Strong currents can contaminate the wind velocity retrieval. Dickinson et al. (2001) used measurements from the Tropical Atmosphere Ocean (TAO) buoy array stating that when the current and wind had the same direction, the scatterometer speed was expected to be lower than in situ wind speeds.

As stated in Hoffman and Leidner (2005), light winds can pose a problem for the wind retrieval as in such cases the ocean surface is very smooth and acts more as a reflector rather than a scatterer. Very high winds can also be problematic as the buoy and modelled data used to calibrate the GMFs tend to under-represent very high winds.

16.5 QuikSCAT

The SeaWinds scatterometer on board NASA's QuikSCAT platform was the first scatterometer to operate for many consecutive years. It provided valuable, consistent and frequent observations of the global ocean both in terms of speed and direction. QuikSCAT was launched in June 1999 with a design life-time of 3 years, as a quick recovery mission to fill the gap from the loss of NSCAT. The scatterometer's antenna failed rotating on the 23rd of November 2009, far exceeding the design life-time.

At an altitude of 803 km, QuikSCAT completed each orbit in approximately 101 minutes, ascending in the morning and descending in the afternoon (see Figure 200 for an example). With a wide swath of 1800 km it covered 93% of the global ocean each day. SeaWinds was an active microwave radar operating at 13.4 GHz (Ku band), radiating microwave pulses through a 1 m diameter antenna, and measuring the power of the signal returning back to the instrument. The σ_0 "footprint" cell had dimensions of 25·37 km and the averaging area, the Wind Vector Cell was a square box of 25·25 km.

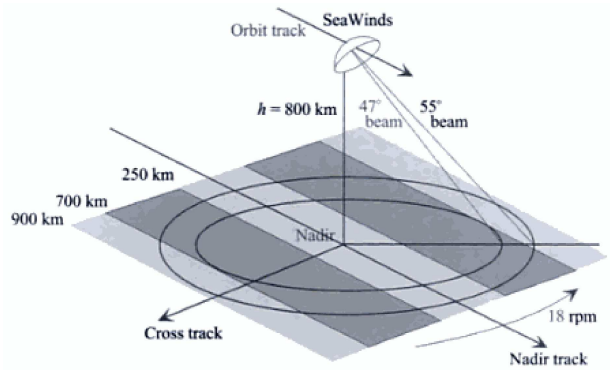

Figure 199: Graphical representation of the scanning geometry of the SeaWinds scatterometer on the QuikSCAT platform. The darker areas are covered by four looks of the antenna beams, while the light areas by two looks. Note that there is no gap in the nadir track. Taken from Martin (2004).

Each σ_0 "footprint" cell, also called "the egg", consisted of 12 slices. σ_0 was calculated for both the full "egg" and for each of the 8 inner slices. This meant that SeaWinds measured σ_0 at a variety of dimensions, i.e. the "footprint", the inner slices and a variety of "footprints" composed of combinations of slices. For more information, see Martin (2004). Backscattered signals were received from the sea, land and ice but the scattering processes over land and ice are different than those over open ocean. Therefore, the scattering from land and ice can contaminate the WVC and needs to be identified and removed. For this reason, a land and

sea ice mask was applied and σ_0 measurements falling over this mask were not included in the WVC.

The mission was managed by the Jet Propulsion Laboratory (JPL), operational products were produced at the National Oceanic Atmospheric Administration (NOAA) for the international meteorological community and were released near real time (NRT), i.e. within 3 hours of the data collection. More information can be found in `http://winds.jpl.nasa.gov/missions/quikscat/index.cfm`.

The mission requirements were i) an r.m.s. of 2 m s^{-1} for a wind speed range between 3-20 m s^{-1} and 10% within the 20-30 m s^{-1} range and ii) an r.m.s. of 20° for the direction within the wind speed range 3-30 m s^{-1}. Science products were distributed through the Physical Oceanography Data Archive Center (PODAAC). More information on the science data products can be found in JPL (2006).

Different scientific groups applied different GMFs and methodologies for the wind retrieval, resulting in a variety of different products. Some of these products are still being reprocessed when new, improved GMFs are released. The initial GMF was the NSCAT-2 but from 2000 to 2006 JPL derived wind velocity from QuikSCAT using the QSCAT-1 GMF (PO-DAAC, 2001), developed during the calibration/validation phase. From 06/2006 and afterwards, JPL used the QSCAT-1/F13, recalibrated for wind speeds above 16 m s^{-1} using speeds from SSM/I 13.

The Royal Netherlands Meteorological Institute (KNMI) has processed data using the NSCAT-2 GMF for the Ocean & Sea Ice Satellite Application Facility (OSISAF). They also applied a rather different methodology for the ambiguity removal and selection of the "best" solution for the WVC. Remote Sensing Systems (RSS) has been releasing swath and gridded QuikSCAT data using a family of descendants from the NSCAT-2 GMF, named Ku-2000, Ku-2001 and recently Ku-2011. For details, see `http://www.ssmi.com/qscat/qscat_browse.html`. In addition to the different GMF used to derive winds, various products exist ranging from the σ_0 observations time-ordered and earth-located (L1), ocean wind vectors in a swath grid (L2B) and gridded ocean wind vectors (L3).

Many validation studies exist that compare the QuikSCAT winds with in situ measurements from buoys and research ships and investigate potential biases. Pickett et al. (2003) compared QuikSCAT swath and gridded winds with near-shore and offshore buoy data and found a maximum wind speed bias of 0.5 m s^{-1} with a root mean square (r.m.s.) error of 1.6 m s^{-1}. The maximum mean bias, for the direction, was 11° with 26° r.m.s. error, while r.m.s. errors up to 38° were also found.

The quality of QuikSCAT retrievals using different algorithms (JPL L2B, DIRTH, RSS v2) has been discussed in Ebuchi et al. (2002). They used offshore buoy data and found wind speed r.m.s. differences of 1 m s^{-1} and ∼20° for the direction, when wind speeds higher than 3 m s^{-1} were used. Bourassa et al. (2003) evaluated the Ku-2000 QuikSCAT from RSS against winds from research vessels and found a maximum wind speed bias of 0.7 m s^{-1} and 10° for direction.

Especially for gridded (L3) products, Satheesan et al. (2007) compared the gridded QuikSCAT product from RSS with buoy data from the Indian Ocean; they reported a wind speed bias of 0.37 m s^{-1} and r.m.s. error of 1.57 m s^{-1} when all wind speeds were used. For the wind direction, the bias was 5.81° and the r.m.s. error was 44.1°. Pensieri et al. (2010) evaluated QuikSCAT L3 from JPL against buoy data in the Lingurian Sea, reporting maximum mean bias of 1.09 m s^{-1} and r.m.s. error of 1.97 m s^{-1} for wind speed and bias of –8.7° and r.m.s. error of 79.5° in direction.

In particular for the Northern European Seas, Winterfeldt et al. (2010) compared QuikSCAT L2B products with buoy wind speeds in the eastern North Atlantic Ocean and the North Sea, addressing the sensitivity of biases to collocation criteria and algorithms for converting in situ measurements to ENW. Average wind speed biases ranged from 0.18 to 0.30 m s^{-1} depending on collocation criteria and from 0.1 to 1.6 m s^{-1} depending on the conversion algorithm.

Winterfeldt (2008) compared a level2B 12.5 km QuikSCAT product with in-situ observations from buoys and rigs in the Eastern North Atlantic and the North Sea during one year

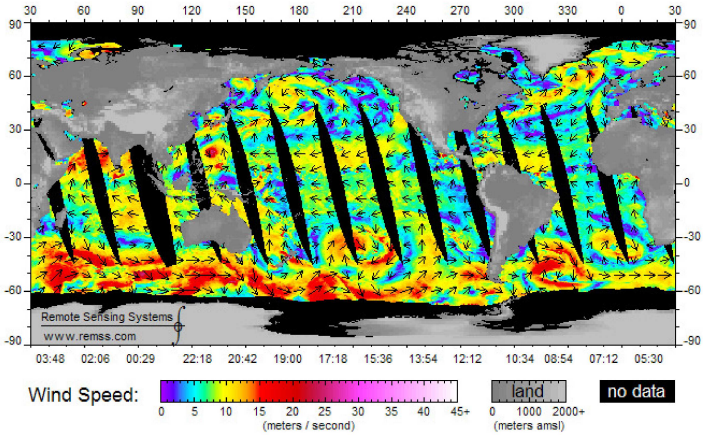

(a) Ascending mode (morning)

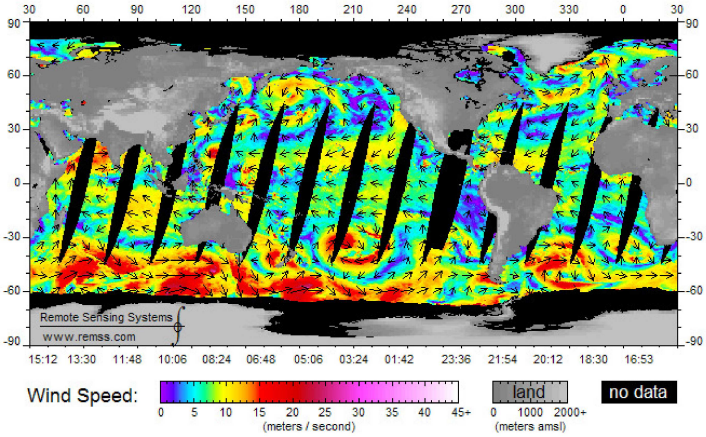

(b) Descending mode (evening)

Figure 200: Examples of the ascending, in the morning (top) and descending, in the afternoon (bottom) swath modes of QuikSCAT on the 4th of July 2006. Images are courtesy of RSS.

(2002). The study concluded that biases were negligible for all stations and that the mission requirements were met.

A study for wind resource assessment from Hasager et al. (2008) compared the RSS product with in situ measurements from an offshore met. mast with standard errors $\sim$1.3 m s^{-1} for the wind speed and $\sim$15° for the direction. Moreover, there was a very small difference in their estimation of the mean wind speed and the Weibull A and k parameters from $\sim$3.200 QuikSCAT observations and $\sim$260.000 in situ measurements.

Karagali et al. (2012) used the full QuikSCAT archive from RSS processed with the Ku-2001 GMF, which is a descendant of the NSCAT-2 GMF, the improved version of the NSCAT-1 (GMF) (Wentz and Smith, 1999). σ_0 values were mapped to a 0.25° Earth grid. This L3 product was compared with in situ derived ENW in the North Sea. Overall biases for the wind speed were found in the order of zero ($\pm$1.2 m s^{-1}), and 2.3° ($\pm$15°) for the wind direction.

Figure 201 shows the scatterplots for the wind speed and wind direction bewteen In situ observations from 4 meteorological masts in the North Sea and QuikSCAT. in situ observations have been adjusted to ENW using the in situ wind speed and stability information. Wind speeds lower than 3 m s^{-1} have been excluded due to the higher QuikSCAT uncertainties at very low wind speeds. Note the higher scatter and the fewer observations for winds above 15 m s^{-1}.

For wind energy related purposes the Weibull estimates are very relevant for site identification. Typically, 10-min in situ observations are used but at offshore locations, these are rarely available. Karagali et al. (2012) used twice daily QuikSCAT observations for the estimation

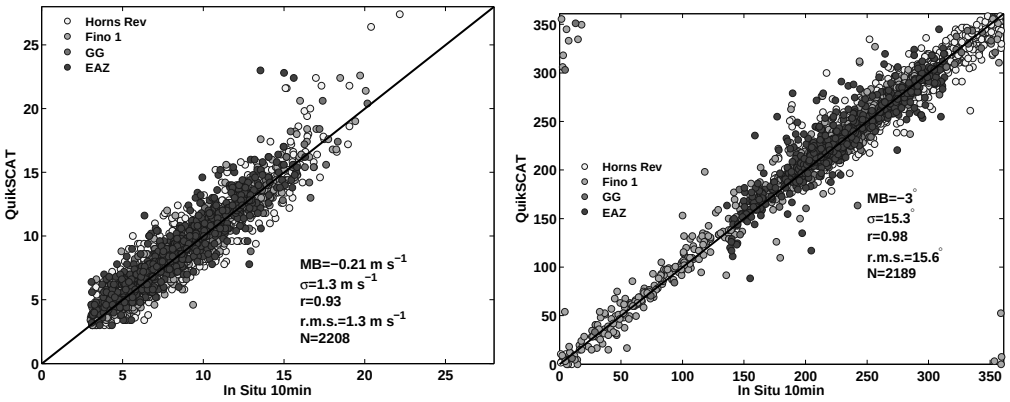

(a) Wind Speed (b) Wind Direction

Figure 201: Scatterplots and statistics of in situ and QuikSCAT wind speed and direction. Measurements from 4 meteorological masts in the North Sea have been used. The RSS v3 QuikSCAT data are used. The work was performed within the NORSEWInD project frame.

of the wind power and Weibull parameters and compared those estimates with the ones derived from offshore met. masts. For two offshore locations, a maximum 14% deviation in the wind power and 2.7% deviation in the mean wind speed was found between 1601 QuikSCAT observations and 137717 10-min measurements.

16.6 Applications of QuikSCAT Surface Winds

Due to their frequent, long and global nature, QuikSCAT data are ideal for an evaluation of the wind resources. A description of the mean spatial wind characteristics and the climatology of the Mediterranean Sea is available from Zecchetto and De Biasio (2007), for the Nordic Seas from Kolstad (2008) and for the global ocean from Risien and Chelton (2006).

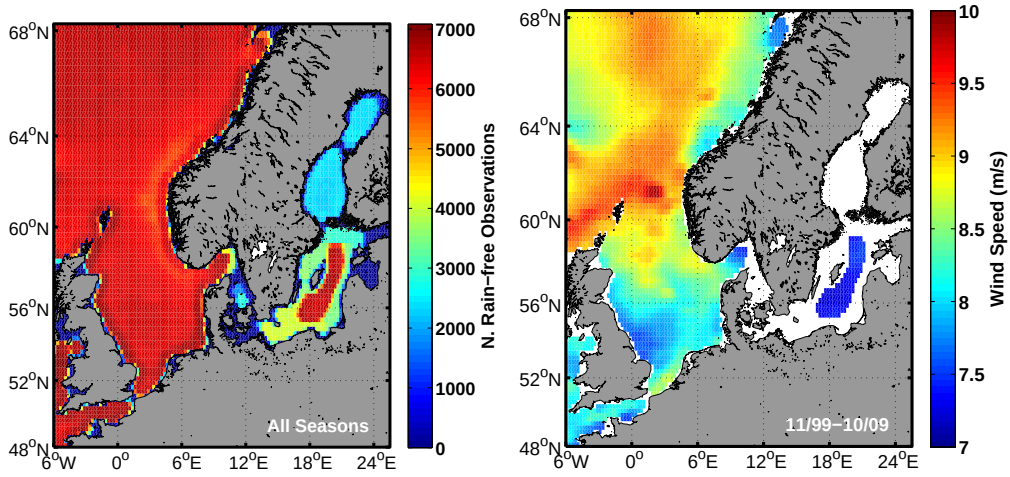

(a) (b)

Figure 202: a) Number of rain-free QuikSCAT observations from 11/99–10/09. b)Mean wind speed using rain-free QuikSCAT observations for the period 1999-2009. Taken from Karagali et al. (2013).

Within the context of offshore wind energy, Liu et al. (2008) estimated the wind power distribution over the ocean from eight years of QuikSCAT measurements. Capps and Zender (2010) estimated the global ocean wind power potential from QuikSCAT and lifted the satellite

winds from 10 m to 100 m, relevant for wind turbine hub heights. Furevik et al. (2011) used eight years of QuikSCAT for wind resource mapping in the Mediterranean Sea, concluding that the satellite observations are valuable for the first phase of wind farm planning, e.g. during the identification of promising sites.

Karagali et al. (2012) used the 10-year long QuikSCAT L3 product from RSS to study the seasonal 10 m wind characteristics in the North Sea and the Baltic Sea. They reported higher spatial variability of the mean wind speed in the North Sea compared to the Baltic Sea. Regarding the spatially coherent nature of the L3 product, they used the location of an offshore met. mast to calculate the spatial correlation between the grid cell containing the mast and all other grid cells. Correlation coefficients higher than 0.9 were reported for an area covering $\sim$4% of the North Sea.

QuikSCAT winds have been used for data assimilation in atmospheric and oceanic models. Comparisons between QuikSCAT and Numerical Weather Prediction (NWP) model reanalysis from NCEP/NCAR performed by Kolstad (2008), showed a 0.9 correlation of daily and monthly mean wind speeds. Root mean square (RMS) differences were 1.1–1.81 m s^{-1} for the daily and 0.75–1.00 m s^{-1} for the monthly means. Ruti et al. (2008) reported a lower accuracy of modelled winds compared to buoy data than that of QuikSCAT compared to the same buoy data in the Mediterranean Sea.

Karagali et al. (2013) compared the QuikSCAT L3 RSS product with modelled winds and found biases up to 1 m s^{-1} in the North Sea. Using the intra annual wind indices, they studied the temporal wind variability and concluded that QuikSCAT captures the wind variability and its amplitude as observed from 10-minute measurements at an offshore location in the North Sea. Modelled winds captured the overall seasonal trends but discrepancies were identified in the amplitude of the wind index and the wind variability.

16.7 Spatial Resolution of Scatterometer Winds

The effective spatial resolution of scatterometer winds has been examined through their spectral properties. Vogelzang et al. (2011) used QuikSCAT and ASCAT products with different characteristics, along with ECMWF model forecasts and buoy measurements to evaluate the quality of the scatterometer winds, concluding that the ASCAT-25 km product contains more intermediate scale information than the QuikSCAT product processed at the Royal Netherlands Meteorological Institute (KNMI). The advantages of the scatterometer spatial resolution compared to modelled wind fields have been studied using ERS (Chin et al., 1998; Halpern et al., 1999) and QuikSCAT (Zecchetto and De Biasio, 2003; Stoffelen et al., 2010).

Recently, Karagali (2012) examined the spectral properties of the ENVISAT ASAR winds of varying resolutions and RSS L3 (v3) QuikSCAT winds. A significant advantage of the SAR winds processed with the same resolution as QuikSCAT (25 km) was observed indicating the ability of SAR winds to resolve more small scale variability.

16.8 Contemporary Scatterometers

So far, emphasis on QuikSCAT has been given due to its unique mission lifetime which ended in 2009, after 10 years of operation. Currently, ASCAT is the longer available scatterometer in orbit. It is a C-band instrument onboard the platforms MetOp-A (operational since 2007) and MetOp-B (operational since April 2013). Due to its C-band nature, operating at 5.255 GHz with a longer wavelength, ASCAT is much less sensitive to rain compared to Ku band instruments like QuikSCAT. Because of this, C-band instruments are also less responsive to very small changes of the surface roughness.

At an altitude of 837 km, ASCAT has a 500 km wide swath on each side of the platform ground track. An example from an ASCAT wind retrieval is shown in Figure 203. The data are obtained from the coastal product developed at KNMI (`http://www.knmi.nl/scatterometer/ascat_osi_co_prod/ascat_app.cgi`). The missing data in the North Sea are due to the nadir gap.Note the high resolution features, showing an area of high winds

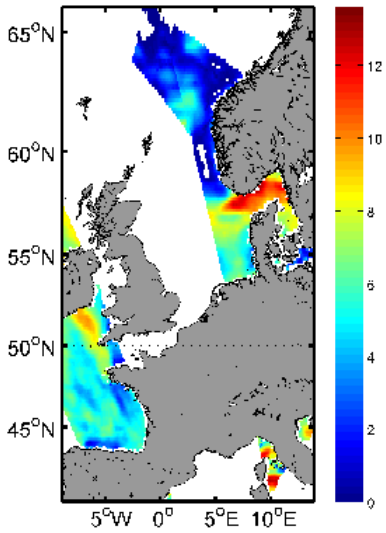

Figure 203: Example of an ASCAT coastal product from KNMI over the European Seas, taken from 01/06/2007 at 20:00. The wind speed is in m s^{-1}.

between Denmark and Norway.

ISRO launched Oceansat-2 (OSCAT) in 2009, carrying a Ku band (13.515 GHz) scatterometer with a ground resolution of 50×50 km. Data can be viewed online, available from KNMI at 50 km resolution (`http://www.knmi.nl/scatterometer/oscat_50_prod/oscat_app.cgi`) and from NOAA–NESDIS/Center for Satellite Applications and Research (`http://manati.star.nesdis.noaa.gov/products/OSCAT.php`), processed at 12, 25 and 50 km. See Figure 204 for an example of the available 12 km product.

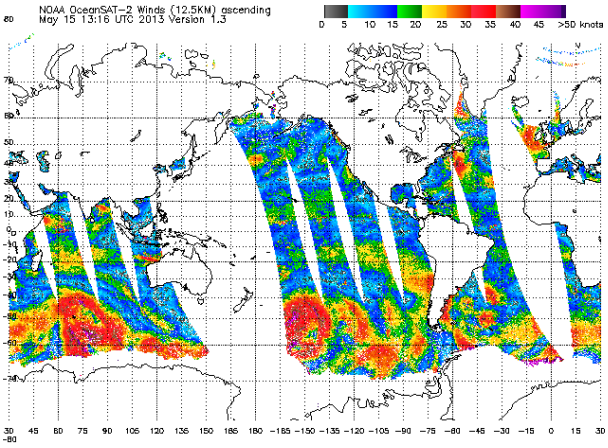

Figure 204: Example of the ascending pass of OSCAT, processed at 12 km, from the 15th of May 2013. The wind speed is in knots. Image taken from NOAA-NESDIS-STAR (2013)

16.9 Acknowledgements and Suggested Reading

A significant amount of work with QuikSCAT and ASCAT data has been performed in DTU Wind Energy within the FP7 NORSEWInD project (TREN-FP7-219048). Other projects include the FP7 European Regional Development Fund and the South Baltic Programme: South Baltic Offshore Wind Energy Regions project and the FP7 EU ORECCA. The QuikSCAT data used here are obtained from Remote Sensing Systems. ASCAT data are courtesy of KNMI. Data from Horns Rev (M2) are provided by Vattenfall and DONG Energy. Fino-1 meteorological data are obtained from DEWI (Deutsches Windenergie Institut, German Wind Energy Institute), oceanographic data from BSH, all through the NORSEWInD project. Greater Gabbard data are provided by SSE Renewables.

The bibliographic references in this chapter give a good overview of the scatterometry fundamentals and applications. The Martin (2004) book is highly suggested for throrough reading and extended descriptions. The International Ocean Vector Winds Science Team (IOVWST) holds annual meetings regarding the current advancements and applications of scatterometry (`http://coaps.fsu.edu/scatterometry/meeting/`). When using scatterometer data, the specific product's User Guide is a recommended document that describes in detail the nature of the data, the processing and quality flagging schemes.

Notation

σ_0 - (NRCS)	Normalised Radar Cross Section
$\|u\|$	wind speed
ξ	the azimuth angle between the wind vector and the incident radar pulse
θ	incidence angle of the radar signal measured in the vertical plane
"f"	frequency of the radar signal
"pol"	polarization of the radar signal
u	wind speed at height z
z_0	sea roughness length
u_*	friction velocity
κ	von Kármán constant
Ψ_M	stability correction
ADEOS	Advanced Earth Observing Satellite
AMI	Advanced Microwave Instrument
ASCAT	Advanced Scatterometer
ERS-1/2	European Remote Sensing-1/2
ESA	European Space Agency
ECMWF	European Centre for Medium-Range Weather Forecasting
ENW	Equivalent Neutral Wind
GMF	Geophysical Model Function
ISRO	Indian Space Research Organization
JPL	Jet Propulsion Laboratory
KNMI	Royal Netherlands Meteorological Institute
MetOp	Meteorological Operation
NASA	National Aeronautics Space Administration
NASDA	National Space Development Agency of Japan
NCAR	National Center for Atmospheric Research
NCEP	National Center for Environmental Protection
NOAA	National Oceanic Atmospheric Administration
NSCAT	NASA Scatterometer
NWP	Numerical Weather Prediction
O&SI-SAF	Ocean & Sea Ice Satellite Application Facility
PODAAC	Physical Oceanography Data Archive Center
RSS	Remote Sensing Systems
SAR	Synthetic Aperture Radar
SASS	Seasat-A Satellite Scatterometer
WVC	Wind Vector Cell

References

Bourassa M.A., Legler D.M., O'Brien J.J., and Smith S.R. (2003) SeaWinds validation with research vessels. *J. Geophys. Res.* **2003(108)**: C2-3019.

Bourassa M.A. (2013) `http://coaps.fsu.edu/~bourassa/BVW_html/eqv_neut_winds.shtml`

Boutin J., Quilfen Y., Merlivat L., and Piolle J.F. (2009) Global average of air-sea CO2 transfer velocity from QuikSCAT scatterometer wind speeds. *J. Geophys. Res.* **114**:C04007.

Brown A.R., Beljaars A.C.M., and Hersbach H. (2006) Errors in parametrizations of convective boundary-layer turbulent momentum mixing. *Q. J. R. Meteorol. Soc.* **132**:1859–1876.

Capps S.B., and Zender C.S. (2010) Estimated global ocean wind power potential from QuikSCAT observations, accounting for turbine characteristics and siting *J. Geophys. Res.* **2010(115)**:D09101.

Chin T.M., Milliff R.F., and Large W.G. (1998) Basin-scale, high-wavenumber sea surface wind fields from a multiresolution analysis of scatterometer data *J. Atmos. Ocean. Technol.* **1998(15)**:741–763.

COAPS (2013) Center for Ocean and Atmospheric Prediction Studies `http://coaps.fsu.edu/scatterometry/about/overview.php`

Dickinson S., Kelly K.A., Caruso M.J., and McPhaden M.J. (2001) Comparisons between the TAO buoy and NASA scatterometer wind vectors. *J. Atmos. Oceanic Technol.* **18**:799–806.

Ebuchi N., Graber H.C., and Caruso M.J. (2002) Evaluation of wind vectors observed by QuikSCAT/SeaWinds using ocean buoy data. *J. Atmosph. Ocean. Technol.* **2002(19)**:2049–2062.

Furevik B.R., Sempreviva A.M., Cavaleri L., Lefèvre J.M., and Transerici C. (2011) Eight years of wind measurements from scatterometer for wind resource mapping in the Mediterranean Sea. *Wind Energy* **2011(14(3))**:355–372.

Halpern D., Freilich M.H., and Weller R.A. (1999) ECMWF and ERS-1 surface winds over the Arabian Sea during July 1995 *J. Phys. Oceanogr.* **1999(29)**:1619–1623.

Hasager C.B., Peña A., Christiansen M.B., Astrup P, Nielsen M., Monaldo F., Thompson D., and Nielsen P. (2008) Remote sensing observation used in offshore wind energy. *IEEE J. Sel. Top. Appl. Earth Obs. Rem. Sens.* **1(1)**:67–79.

Hersbach H., Stoffelen A., and de Haan S. (2007) An improved C-band scatterometer ocean geophysical model function:CMOD5. *J. Geophys. Res.* **2007(112)**:C03006, 476–493.

Hersbach H. (2010) Comparison of C-band Scatterometer CMOD5.N equivalent neutral winds with ECMWF. *J. Atmos. Ocean. Techn.* **27**:721–736.

Hilburn K.A., Wentz F.J., Smith D.K., and Ashcroft P.D. (2006) Correcting active scatterometer data for the effects of rain using passive radiometer data *J. App. Meteor. Clim.* **45**:382–398.

Hoffman R.N., and Leidner S.M. (2005) An introduction to the near-real-time QuikSCAT data *Wea. Forec.* **20**:476–493.

IEEE (2002) IEEE-Standard-521 `http://www.radioing.com/eengineer/bands.html`

Jet Propulsion Laboratory (2006) NASA Quikck Scatterometer - QuikSCAT science data product user's manual: overview and geophysical data products. *JPL, California Institute of Technology* **2006(V3.0)**:D-18053-RevA.

Karagali I., Peña A., Badger M., and Hasager C.B. (2012) Wind characteristics in the North and Baltic Seas from the QuikSCAT satellite. *Wind Energy* , available online.

Karagali I. (2012) Offshore Wind Energy: Wind and Sea Surface Temperature from Satellite Observations. *Ph.D. thesis, DTU Wind Energy-PhD-003(EN)* **2012**, ISBN ISBN 978-87-92896-02-5.

Karagali I., Badger M., Peña A., Hahmann A., Hasager C.B., and Sempreviva A.M. (2013) Spatial and temporal variability of winds in the Northern European Seas. *Renewable Energy* **2013(57)**:200-210.

Kolstad E.W. (2008) A QuikSCAT climatology of ocean surface winds in the Nordic seas: Identification of features and comparison with the NCEP/NCAR reanalysis. *J. Geophys. Res.* **2008(113)**:D11106.

Liu W.T., Tang W. (1996) Equivalent neutral wind. *National Aeronautics and Space Administration, Jet Propulsion Laboratory, California Institute of Technology, National Technical Information Service, distributor.*

Liu W.T. (2002) Progress in Scatterometer Application *J. Oceanogr.* **58**: 121–136.

Liu W.T., Tang W., and Xie X. (2008) Wind power distribution over the ocean. *Geophys. Resea. Lett.* **2008(35)**: L13808.

Martin S. (2004) An introduction to ocean remote sensing. *Cambridge Un. Press*, ISBN 0521 802806, 286–290

Naderi F.M., Freilich M.H., and Long D.G. (1991) Spaceborne radar measurement of wind velocity over the ocean - an overview of the NSCAT scatterometer system. *Proc. IEEE.* **79(6)**:850–866.

NOAA-NESDIS-STAR (2013) National Oceanic Atmospheric Administration–National Environmental Satellite, Data, and Information Service–Center for Satellite Application and Research `http://manati.star.nesdis.noaa.gov/datasets/OSCATData.php`

Offiler D. (1994) The Calibration of ERS-1 Satellite Scatterometer Winds. *J. Atmos. Oceanic Technol.* **1994(11)**:1002-1017.

Pensieri S., Bozzano R., and Schiano M.E. (2010) Comparison between QuikSCAT and buoy wind data in the Ligurian Sea. *J. Mar. Sys.* **2010(81)**:286–296.

Pickett M.H., Tang W., Rosenfeld L.K., and Wash C.H. (2003) QuikSCAT satellite comparisons with nearshore buoy wind data off the U.S. West Coast. *J. Atmosph. Ocean. Technol.* **2003(20)**:1869–1879.

Physical Oceanography DAAC (2001) SeaWinds on QuikSCAT Level 3 Daily, Gridded Ocean Wind Vectors (JPL SeaWinds Project) Guide Document. *PODAAC, JPL* **2001(V1.1)**:D-20335.

Risien C.M., and Chelton D.B. (2006) A satellite-derived climatology of global ocean winds. *Rem. Sens. Envi.* **2006(105(3))**: 221–236.

Ruti P.M., Marullo S., D'Ortenzio F., and Tremant M. (2008) Comparison of analyzed and measured wind speeds in the perspective of oceanic simulations over the Mediterranean basin: Analyses, QuikSCAT and buoy data. *J. Mar. Sys.* **2008(70(1-2))**:33–48.

Satheesan K., Sarkar A., Parekh A., Ramesh Kumar M.R., and Kuroda Y. (2007) Comparison of wind data from QuikSCAT and buoys in the Indian Ocean. *Int. J. Rem. Sens.* **2007(28(10))**:2375-2382.

Stoffelen A., and Anderson D. (1997) Scatterometer data interpretation: estimation and validation of the transfer function CMOD4. *J. Geophys. Res.* **1997(102(C3))**:5767-5780.

Stoffelen A., Vogelzang J., and Verhoef A. (2010) Verification of scatterometer winds *10th International Winds Workshop, Tokyo, Japan, 20-26 February 2010, EUMETSAT P.56.* **2003**:Available from `http://www.eumetsat.int/Home/Main/AboutEUMETSAT/Publications/ConferenceandWorkshopProceedings/2010/SP_2010112211235289`.

Vogelzang J., Stoffelen A., Verhoef A., and Figa-Saldaña J. (2011) On the quality of high-resolution scatterometer winds. *J. Geophys. Res.* **2011(116)**:C10033.

Wentz F.J., Peteherych S., and Thomas L.A. (1984) A model function for ocean radar cross sections at 14.6 GHz. *J. Geophys. Res.* **89(C3)**:3689-3704.

Wentz F.J. (1997) A well-calibrated ocean algorithm for special sensor microwave/imager. *J. Geophys. Res.* **1997(102(C4))**:8703-8718.

Wentz F.J., and Smith D.K. (1999) A model function for the ocean-normalized radar cross section at 14GHz derived from NSCAT observations. *J. Geophys. Res.* **1999(104)**:11499-11514.

Winterfeldt J. (2008) Comparison of measured and simulated wind speed data in the North Atlantic. *PhD Thesis, GKSS 2008/2* ISSN 0344-9629.

Winterfeldt J., Andersson A., Klepp C., Bakan S., and Weisse R. (2010) Comparison of HOAPS, QuikSCAT and buoy wind speed in the Eastern North Atlantic and the North Sea. *IEEE Trans. Geosci. Rem. Sens.* **2010(48(1))**:338–347.

Zecchetto S., and De Biasio F. (2003) Wavenumber spectra of the Mediterranean sea winds derived from the NASA QuikSCAT data *Geoscience and Remote Sensing Symposium, 2003. IGARSS '03. Proceedings. 2003 IEEE International* **2003**:1907–1909

Zecchetto S., and De Biasio F. (2007) Sea surface winds over the Mediterranean basin from satellite data (2000-04): meso- and local-scale features on annual and seasonal time scales. *J. Appl. Meteorol. Climatol.* **2007(10)**:814–827.

DTU Wind Energy
Technical University of Denmark

Frederiksborgvej 399
4000 Roskilde
Denmark
Phone +45 4677 5024

www.vindenergi.dtu.dk